ARMOUR

Materials, Theory, and Design

SECOND EDITION

Paul J. Hazell

Armour

Updated throughout for the new edition, *Armour: Materials, Theory, and Design* covers extant and emergent protection technologies driving advances in armour systems. Covering materials, theory and design, the book has applications in vehicle, ship, personnel and building use.

Introducing a wide range of armour technologies, the book is a key guide to the technology used to protect against both blasts and ballistic attacks. Chapters cover bullets, blasts, jets and fragments, as well as penetration mechanics. The new edition builds on the previous, discussing ceramics and metallic materials as well as woven fabrics and composite laminates. Detailing modern technology advancements, the second edition has also been expanded to include improved explanations on shock mechanisms and includes significantly more figures and diagrams.

An essential guide to armour technology, this book outlines key ways to implement protective strategies applicable to many types of conflict.

Armour
Materials, Theory, and Design

Second Edition

Paul J. Hazell

Cover image: Shaped charge jet penetration of armour showing the formation of behind armour debris (courtesy of J Backofen Jr) - see Figure 11.7.

Dedicated to all the brave men and women of the military services who risk their lives in the defence of their nation.

Contents

Preface to the First Edition

Over the years, I have had the privilege of engaging with the brave men and women of the armed services from the United Kingdom and Australia, both at the UK Defence Academy at Shrivenham and at the Australian Defence Force Academy in Canberra. Many of my students have been serving military officers pursuing a technical career path where they are required to exercise strength in leadership, decision making and technical know-how. Many of my students had finished their undergraduate studies several years ago and were in the process of embarking on a master's programme. Some had never earned an undergraduate degree. Consequently, as they were not career scientists per se, many students would struggle with some of the more 'taken-for-granted' scientific principles. And this became all the more clear to me when I taught classes on impact dynamics, terminal ballistics, armour systems design and firepower and protection technologies. These are not traditional university courses! As such, there are relatively few texts that are available that can cover some of the more important theoretical elements of these courses as well as introduce in detail some of the materials that are used in constructing protective structures. This is what I have attempted to do in this book. Of course, there are some excellent texts that I regularly use for teaching purposes, each with their own strengths, and you will find references to some of these texts scattered in this book.

I suppose my overall aim in this text is to provide the student or engineer with an insight and the know-how for informing, choosing, buying and making protective structures that will be used in dangerous military environments. Hopefully, our troops will be safer as a result.

I would like to close this section by thanking some notable people who have helped me along the way with this manuscript. These include the staff at Taylor & Francis for their patience and encouragement during this project (particularly when using multiple equation editors). I particularly acknowledge Mr Jonathan Plant for his friendly counsel. I also thank my proofreaders and checkers: Dr. G. Appleby-Thomas, Dr. J. P. Escobedo, Maj (Retd) H. Pratt, Mr Hongxu Wang and Prof Stephen Yeomans.

Paul J. Hazell

Preface to the Second Edition

In my job as a university teacher, I have strived to convey concepts related to armour design clearly and succinctly. On occasions, I have failed. This is never a happy time for a teacher! Therefore, to improve on the first edition, I have endeavoured to expand on some of the theory with better explanations. New areas have been covered too. Chapter 4 has been substantially lengthened. Chapter 5 has been expanded to include improved explanations on shock mechanisms, given that many of my fourth-year engineering students at the Australian Defence Force Academy carry out thesis projects on shock. Computational modelling is becoming increasingly important and therefore it is appropriate to find a detailed treatise of this subject in this new edition (Chapter 6). Some of the figures have been enriched and I have increased the number by 50% compared with the first edition. A picture paints a thousand words, as the saying goes. A little historical context to some of the technical developments has been added too.

I also wanted to review the notation. There are many books for which the notation and the definitions are not clearly described and consistently presented. In the first edition of the book, there were a few areas where this needed tidying up and I have done that for the second edition.

As before, I would like to close this section by thanking some notable people who have helped me along the way with this manuscript. These include the staff at Taylor & Francis for their patience and encouragement during this project. I also want to thank my proofreaders and checkers: Dr Ali Ameri and Dr Hongxu Wang—both of whom are world-class scientists in their own right.

I hope you enjoy!

Paul J. Hazell
Canberra, 2022

Author

Paul J. Hazell is a professor of impact dynamics at UNSW Canberra. His main research interests are in the subjects of shock loading, penetration mechanics and lightweight armour optimization. He also teaches several courses related to terminal ballistics and armour design to undergraduate and postgraduate students at the Australian Defence Force Academy in Canberra.

Paul graduated from the University of Leeds in 1992 with a BEng (Hons) degree in mechanical engineering, and after a couple of years in the automotive industry, he pursued his doctoral studies at the Shrivenham campus of Cranfield University (at the Royal Military College of Science). He was subsequently taken onto the faculty to teach terminal ballistics—to a student cohort that mostly consisted of British Army Officers. He has been in the business of teaching the uniformed services ever since.

1 Introduction

The concept of armour is as old as the hills. The need to defend, protect, save, shield and guard from harm is engrained within the human consciousness. It is natural, so too is the propensity to progress. Advancements in armour technology have occurred so that we are no longer resorting to ever-greater thickness of material to provide resistance to penetration. Instead, we have relied on new advances in materials technology. This book will summarize some of the more recent advancements and the science behind them.

If we were to plot a graph showing the variation of armour performance with time, we would be left in no doubt that, in recent years at least, huge strides have been made in armour technology. The metric that would be used for armour performance is rather arbitrary—it could be described as 'some performance criteria' based on areal density (i.e. mass per unit area). That is to say, lighter-weight armour that provides sufficient protection is a good thing. Again, this is a concept that is as old as the hills. It is a notion that the shepherd boy David knew when he fought Goliath—spurning the heavy and clumsy armour of King Saul in favour of speed and agility (and a very good shot with a sling).

Of course, heavy armour, if you can wear it, or drive it, does provide a notable degree of reassurance. Perhaps this was the reasoning behind the German King Tiger tanks of World War II (WWII) that weighed in the region of 70t. As a fighting machine, they were an awesome sight and regularly struck fear into the Allied forces. These tanks were heavily armoured with their front hull armour being 150mm thick. However, they were regularly prone to mechanical failure that was caused, in part, by their enormous weight. And, in the end, only 489 vehicles of this type were manufactured (Ogorkiewicz, 1991).

With the introduction of advanced processing techniques, explosive-reactive armours, composite materials and ceramic materials around 30–40 years ago, the performance of armour systems improved dramatically. These developments were key to the drive for reduced armour weight. Further enhancements in performance were made by studying the penetration mechanisms of projectiles in armour materials using high-speed diagnostic equipment such as flash X-ray and high-speed photography. The system design was enhanced by the development of analytical and computational codes, with the latter being used to study penetration mechanisms. These codes have since enabled engineers to test different armour designs and conduct optimization studies without even leaving the office.

Much of this development in armour performance went hand in hand with weapon development but meant that lightweight vehicles could offer the same, if not better, protection than their heavier predecessors. Nevertheless, the basic structure of vehicle armour has not changed much in the past 100 years with most armoured vehicles being made from metal. Much of the existing armour development that has occurred has relied on using materials and systems applied to existing metallic hulls,

where the hulls have provided the last line of defence and are an integral part of the complete armour solution.

1.1   LESSONS FROM NATURE

Nature has many lessons to teach us in the field of engineering structures. There are many natural structures that have in-built resilience, and potentially, we can learn from nature in the way that we structure armour materials (Islam et al., 2021, Ghazlan et al., 2021). Scales have been used in armour for millennia and whether they were inspired by crocodilian armour is unclear. However, they have been found in Egypt in the tomb of Ḳen-Amūn at Thebes (ca. 1390–1353 BC). Such design of interwoven scales of leather, bronze, iron or steel has been used by various armies. Examples of such armour constructions have been found that point to use by the Scythians, Romans, Koreans, Chinese and Japanese, as well as medieval Europeans. The giant Goliath, of Biblical fame, wore an armour of 'mail' (1 Samuel 17 v 5) and was probably a hauberk composed of overlapping bronze scales sown onto an underlying tunic (Zorn, 2010).

It is known that in nature there are several strong and tough materials of interest, and much inspiration can be garnered from the construction of natural structures. For example, shell anatomies generally comprise a hardened protein layer, followed by a thin columnar calcite layer, which in turn is backed by a relatively thick nacre layer (Sun and Bhushan, 2012). Nacre is a relatively tough lamellar ceramic composite comprising of platelets arranged in a brick-and-mortar arrangement glued together with soft organic materials. This combination works well to protect the animal from extreme loads from attacking predators. The exterior layers of the shell are typically hard and brittle, which can provide resistance to penetration from external impact, while the nacre provides tough energy absorption capacity by dissipating the mechanical energy (Wang et al., 2001). Equally, fish scales generally comprise a flexible protective covering that has a hard bony outer layer to prevent penetration whilst the backing layer contains orthogonal collagen fibres to dissipate energy. Such scaled structures could find applications in ultra-light and flexible armour systems (Vernerey and Barthelat, 2014). As we will see, many modern armour systems adopt this hard/tough combination.

1.2   SURVIVABILITY AND ONIONS

There has been much written about the concept of the 'survivability onion'. This is a notion that is frequently used to talk about a layered concept of survivability. So, to maximize individual survivability, there need to be multiple layers of protection— with each layer exercising a particular purpose (see Figure 1.1).

The first layer of defence should always be camouflage. Today's military no longer simply relies on the shading and colouring of their clothing and equipment. There are much more advanced ways to hide from the enemy—mainly because the enemy has more advanced ways of detecting their foe. Armoured vehicles particularly will use signature management techniques to limit the thermal, audio, electromagnetic and radar cross section of the vehicle. However, if we are seen (or detected), then the next layer of defence is important: do not be acquired. By that, we mean that a gun,

1. Do not be seen

2. Do not be acquired

3. Do not be hit

4. Do not be penetrated

5. Do not be killed
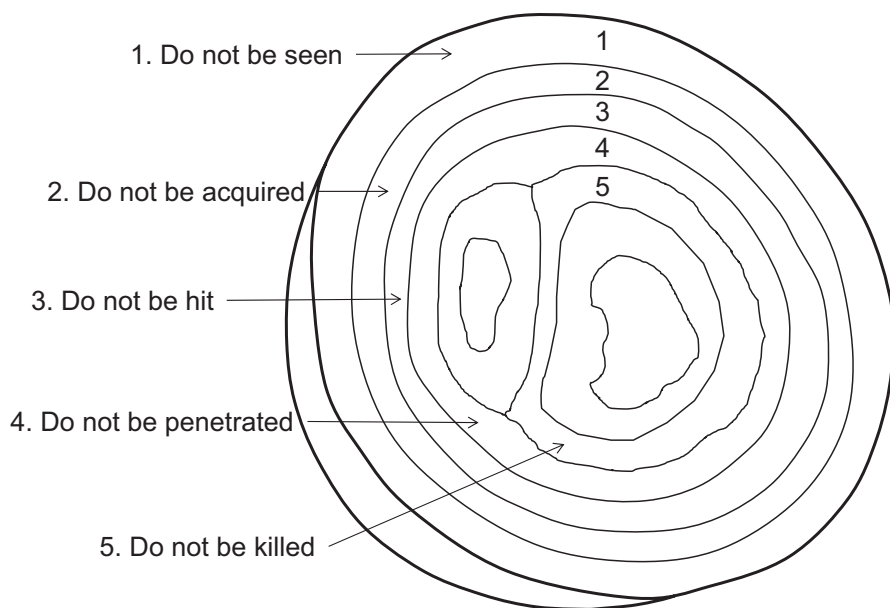
FIGURE 1.1   Onion approach to survivability.

missile or a person who is a very good shot with a bow and arrow has got you in their sights, and it is only a matter of time before they pull the trigger, push the button or release their arrow to hit you. Not being 'acquired' can be achieved by speed, mobility and agility. It can also be achieved by more technological options such as the use of obscurants such as smoke or electronic countermeasures to jam the enemies' targeting system or simply by unnerving the enemy by firing your weapon at them. So, if we are acquired, the next step is to ensure that we are not hit. This may be achieved by using some form of kinetic countermeasure (some of these will be discussed in Chapter 10). Then, if we are hit, we do not want to be penetrated. Well, technically, we do not want to be perforated. This is where this book comes in. Here, the fourth layer of the survivability onion will be discussed in that we will be looking at how armour works. This includes active armour and passive armour. The final layer is, of course, equally important. If we are penetrated/perforated, we should not be killed. This is achieved by using good spall liners, fire suppression systems and good exit strategies.

1.3   SOME BASIC CONCEPTS

Fundamentally, two types of armour are available to the armour designer: passive and reactive. Passive systems work by stopping the projectile by the material properties of the armour components alone. In contrast, reactive systems generally work by the projectile incurring a kinetic response in the armour material, the nature of which intends to reduce the lethality of the projectile by disruption or deflection. An example of the latter is explosive-reactive armour; this will be discussed in Chapter 10.

Ideally, the armour system should be as effective and as lightweight as possible, and not too bulky. Therefore, a desirable system would employ materials of low density and high resistance to penetration. The choice of materials used in passive armour depends on what the engineer wishes to achieve. Armour materials can be divided into two different categories that depend on their material properties and the way in which they deal with the energy of the projectile. Armour materials tend to be either energy 'disruptive' in nature or energy 'absorbing'. Disruptors (or 'disturbers') tend to be made from high-strength materials such as high-strength steel or ceramic materials. The purpose of these high-strength materials is to blunt the incoming projectile or rapidly erode it. If the projectile is fragmented, a hard material will tend to radially disperse the fragments, and therefore, the kinetic energy of the projectile is deflected and dispersed in the fragments. An absorber, on the other hand, works to absorb the kinetic energy of the projectile or fragments through large amounts of plastic deformation, thereby converting it to a lower form of energy such as heat. The disruptive component of an armour system is either a hard material such as ceramic or high-hardness steel; it can also be a moving material such as an explosive-reactive armour plate—if disruption of a shaped charge jet is the objective. The absorbing components of armour systems are generally materials that can undergo large amounts of plastic deformation before they fail. This is also important when ways of protecting against blast are examined. Usually, it is found that the disruptor plate is attached to an absorber plate—especially in the case of brittle disruptors such as ceramic (see Figure 1.2).

Some hard-facing disruptor materials such as ceramics or glasses are susceptible to brittle fracture, and therefore, it is frequently necessary to contain the material so that the fragments are retained in place after the tile has been perforated. In doing so, it is
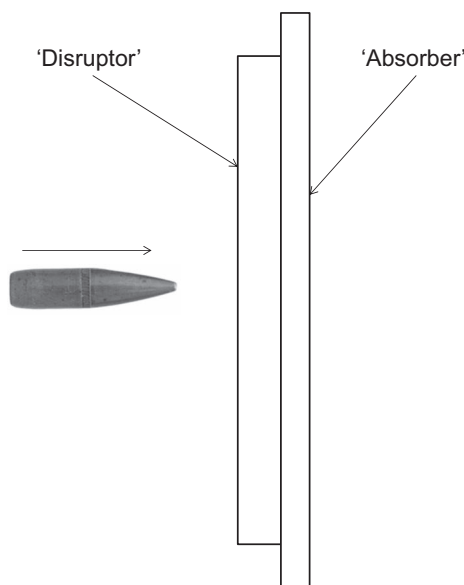
FIGURE 1.2 Disruptor–absorber concept. Most ceramic armours work best in this way.

possible to provide some level of multi-hit protection, although performance against subsequent hits would be compromised. Other disrupting materials such as certain high-hardness steels and hard aluminium alloy plates can be susceptible to gross cracking if penetrated, which means that the plate would need to be replaced. However, in these cases, a good multi-hit capability would still be retained despite the fracture.

1.4   THE DISPOSITION OF ARMOUR

Frequently, it is found that even with modern armour systems, providing all-round protection for a person or a vehicle is practically impossible. All-round protection often means that the system is too bulky or too heavy. Therefore, choices have to be made so that the location of the armour is most likely to provide the maximum amount of protection available whilst maintaining the required amount of comfort (for personnel protection) and mobility (for vehicle protection). For example, to maximize the life-saving ability of a bullet-resistant vest, ceramic inserts are provided to protect the vital organs such as the heart and lungs whilst providing minimal protection for the shoulders and arms. Furthermore, it is found that most protection offered by the vest is located at the front because, in the majority of cases, it is the frontal area that is attacked.

For vehicle armour, similar choices have to be made. These 'choices' have led to the development of 'directional probability variations (dpvs)'.

The term directional probability variation was first introduced as a means to assess the chance that an armoured fighting vehicle (AFV) is attacked from a particular direction. There have been several dpvs proposed for tank hulls, but that due to Lt Col J. M. Whittaker, published in 1943 (Gye, 1948), is the best known and is based on a theoretical model.

The basic assumption of Whittaker's model is that a tank is travelling towards a line of anti-tank guns with a constant velocity. The line of travel of the tank is straight and perpendicular to that of the anti-tank guns, and the total number of shots that can be fired at a certain aspect of a tank is directly proportional to the time that the tank presents that aspect to the gun. Additional assumptions are made about the range of the guns and their ability to fire in any direction. Whittaker's model predicted that it was more probable that a tank will be struck in a frontal segment of the vehicle.

Despite a rather simple model of a tank approaching a line of anti-tank guns at a constant velocity, analysis of tank casualties in Northwest Europe during WWII showed that Whittaker's theory fitted the battle data reasonably well. After the war, an important lesson was drawn that the weight of armour should be more concentrated at the front of the AFV.

How well the lessons learnt from this model fit with today's AFV design is questionable. This is mainly due to the variety of mechanisms that are now available to deliver anti-tank shaped-charge warheads to the target. Other factors such as the nature of the conflict and the speed and technological superiority of the attacking force will affect the chance of a hit in a particular segment. For example, subsequent battle data from the 1991 Gulf War have suggested that the number of hits on an Iraqi AFV was more evenly spread around the azimuth (Held, 2000); 70% of the hits that were assessed by this work were from shaped charge-type warheads with only 20%

of the hits being from a kinetic energy (KE) type round. Furthermore, 77% of the hits were on the turret, although it is noted that the most likely reason for this is because the majority of Iraqi main battle tanks (MBTs) were located in defensive trenches so that the hulls were not exposed to direct hits. The evidence suggests that we can no longer rely on Whittaker's initial concept for AFV design but rather a more evenly distributed system of protection to defeat the large variety of munitions, and their delivery method, is required. Thus, it is desirable to use the lightest and most ballistically efficient armour systems and materials possible.

1.5   EARLY APPLICATIONS

1.5.1   PERSONAL PROTECTION

Most armour has evolved to meet threats as they appeared. And, in recent conflicts, the nature of the threats that have been faced by the West has shifted from conventional projectiles fired from big guns to improvised explosive devices and mines. For the individual soldier, the threat will come from blast, high-velocity small-arm bullets and fragments. Therefore, wearable personal protection is important, although it is worth noting that in recent conflicts, fragments, not bullets, are still the major cause of military casualties.

Wearable protective equipment dates back millennia, although modern war-fighting equipment is considerably more lightweight, versatile and comfortable than its ancient predecessors that were made from bronze, steel or even gold.

An infamous early user of ballistic body armour was the Australian bushranger Ned Kelly. He was a notorious criminal who used body armour at the siege at Glenrowan in 1880 to defend himself from the bullets of the police Martini–Henry rifles. To do this, Kelly and his gang forged the now iconic-looking armour out of mould boards stolen from local ploughs (see Figure 1.3). The use of the armour was so unusual to the police at the time that they could not understand what it was that was taunting them.

The Argus (29 June 1880) captures the scene nicely as the scene unfolded at daybreak on Monday, 28 June 1880:

> He [Kelly] however, walked coolly from tree to tree, and received the fire of the police with the utmost indifference, returning a shot from his revolver when a good opportunity presented itself. Three men went for him, viz., Sergeant Steele of Wangaratta, Senior-constable Kelly, and a railway guard named Dowsett. The latter, however, was only armed with a revolver. They fired at him persistently, but to their surprise with no effect. He seemed bullet-proof. It then occurred to Sergeant Steele that the fellow was encased in mail, and he then aimed at the outlaw's legs.

Several years later, Kelly's exploits even led to the debate in the press as to whether it was sensible to wear body armour in conflict (Dean, 1915). In fact, Kelly's armour was arguably the inspiration behind the US Brewster Body[1] Shield that was tried in the early twentieth century.

FIGURE 1.3 The armour of the bushranger Ned Kelly on display at the Melbourne State Library.

Now, of course, it is generally a standard issue for troops who are going into conflict, and the modern vests use materials such as ceramic and Kevlar™. Body armour was revolutionized with the invention of Kevlar in 1962 and ceramic armour plates in 1963. These will be discussed in detail later in the book.

1.5.2 Vehicle Armour

Of course, military vehicles are a large user of armour. Much of the history here can be traced back to the original tank from WWI. These behemoths of the battlefield were slow lumbering beasts that could barely break 4 mph. Nevertheless, they provided a useful means of protecting advancing troops. This was achieved by constructing these vehicles from 6 to 8 mm of high-hardness steel. And this thickness of high-strength steel is still used today—albeit with a tougher formulation.

Of course, steel was the armour of choice, and there were some good advances in steel processing that served the production of warships from 1845 onwards. However, there was only so much steel you can put into an AFV—a lesson that Adolf Hitler had not learned when he approved the development of a superheavy tank—the Maus (mouse). Weighing in at 188 tonnes and with armour up to 240 mm thick, it was too heavy to cross most bridges. Its mass also meant that no engine was available to give

it reasonable speed. Only two were built with one incomplete before the invading Soviet forces overtook the testing grounds.

After WWII, an attempt to maximize the protection and survivability of tanks was achieved by lowering the overall height of the vehicle. This had two effects: Firstly, the silhouette of the tank was reduced (although notably, it was still a behemoth), and secondly, the weight that was saved from the height reduction could be put into the frontal armour. This was achieved by adopting a prone position for the driver.

However, there is a limit to the thickness of steel that can be employed. As the thickness of steel was increased, it was found that achieving consistency through the thickness became more difficult and working with the large thicknesses of steel became near-impossible. Therefore, new approaches to armour were required that included either spaced angled plates or alternative materials to steel.

1.5.3   AIRCRAFT ARMOUR

Ordinarily, it is difficult to armour an aircraft mainly due to the restrictions in adding weight to the structure. Nevertheless, towards the end of WWI, Germany introduced armoured aeroplanes: the single-engine two-seater ground attack Allgemeine Elektricitäts-Gesellschaft JI/II and a twin-engine three-seater bomber G.IVk. The armour on the single-engine machine was 5.1 mm thick—too thin to provide protection against the British armour-piercing bullets fired from the ground at a lower height than 500 ft. (152 m). It was parasitic too, adding a whopping 860 lb. (390 kg) to the mass of the aeroplane (Fox, 2006).

It seemed sensible to adopt a lower-density armour material than steel for aircraft armour applications, and some efforts were given over to this in WWII with the examination of whether magnesium alloys would make suitable ballistic armour plates (Sullivan, 1943). At that time, it appeared that the best solution was to armour the individual rather than the structure, and so the term 'flak jacket' was born due to the vests that the bomber crews used to protect them from anti-aircraft 'flak'. These were made from manganese steel encased in a canvas support structure (later nylon) and weighed in at 7.9 kg for front and back protection (Tobin and Iremonger, 2006). This was also the approach that was used by the crew of helicopters during the Vietnam conflict that had the benefit of the newly invented ceramic-based body armour vests. These vests, however, very often ended up on the floor of the aircraft to protect against small arms fire from the ground.

1.5.4   SHIP ARMOUR

Arguably, much of the theoretical understanding of armour penetration stems from the early work carried out on battleship armour. And much of the armour that was historically used on ships was made of iron and steel. The importance of naval armour is probably best summarized by the battle of the Denmark Strait where the German battleship Bismarck sank HMS Hood resulting in the death of all but 3 of

TABLE 1.1

Changes in Warship Armour from 1859 to 1901

Date	Ship	Type of Armour	Thickness (in.)	Thickness (mm)
1859	Gloire	Wrought iron (wooden frigate protected by a belt of armour)	4.75	121
1860	HMS Warrior	Wrought iron (first armour-clad ship to be built entirely from iron)	4.5	114
1876	HMS Inflexible	Sandwich (two plates of iron)	$2 \times 12 = 24$	610
1882	HMS Collingwood	Compound armour	18	457
1895	HMS Majestic	Nickel–steel armour	9	229
1901	HMS Duncan	Krupp armour	7	178

the 1418 crew. It is generally thought that the weak deck armour contributed to the Hood's sinking as it was penetrated by a 15-in. (380-mm) armour-piercing shell from the Bismarck resulting in the explosion of the Hood's 4-in. magazine.[2] Nowadays, advances in long-range anti-ship missile systems and torpedo technologies have led to the demise of large-calibre naval guns typified by Bismarck's Panzersprenggranate L/4.4 380-mm calibre shells.[3] Consequently, modern warships no longer rely on a belt of armour for protection but rather on a complex array of sensors and defensive aid suites that can detect, track and engage the incoming threat.

It was in 1805 that a proposal was made to clad wooden ships with iron to provide ballistic protection. Some early examples of ship armour employed wrought iron of many inches thick (typically 4.5 in. or 114 mm) backed by up to 36 in. (0.9 m) of teak or oak to combat the large-calibre naval shells. The French ship Gloire was the first armour-clad ship to sail, and this was completed in 1859 (Johnson, 1988). It was a wooden frigate employing a 4.75-in. (121-mm) belt of wrought iron armour. Two years later, the British ship HMS Warrior was completed and was the first ship to be completely made from iron. The hull was 4.5 in. (114 mm) thick and made from wrought iron plate.

The changes in battleship armour from 1845 to 1945 are nicely captured by W. Johnson (1988); some notable changes are summarized in Table 1.1.

By c. 1900, there was a tendency to reduce the thickness of the armour on the ship. The practice in the United States at that time was to protect the whole length of the waterline with approximately 8 ft. (2.44 m) of armour extending 4.5 ft. (1.37 m) above it and 3.5 ft. (1.07 m) below it. A schematic of the battleship Connecticut, commissioned in September 1906, is shown in Figure 1.4 (Lissak, 1907). The thickest sections of armour were reserved for the front turret (12 in. or 305 mm) and barbette (an armoured structure that protected the mechanisms of ammunition supply and turret operation), whilst various thicknesses of armour protected the waterline (4–11 in.).

It soon became clear that it was sensible to design ship armour such that it comprised a hard outer face and a tougher rear face. The first attempts to do this were by
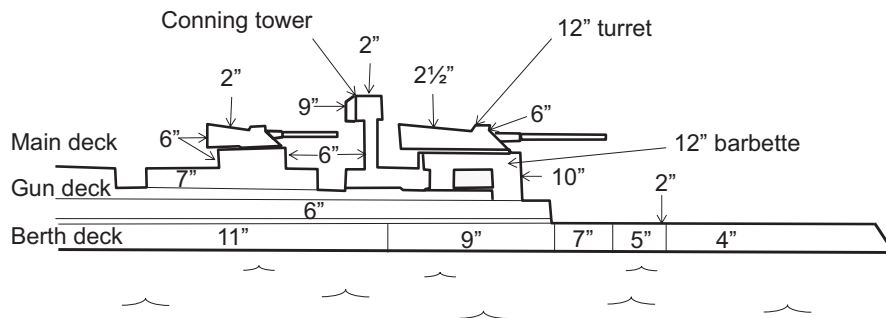
FIGURE 1.4 Distribution of armour in the United States Connecticut. (From Lissak, O. M. 1907. *Ordnance and Gunnery: A Text Book,* 1st ed. Copyright Wiley-VCH Verlag GmbH & Co. KGaA. Reproduced with permission.)

developing compound armour that was composed of a hard steel impact face (with perhaps 0.5%–0.6% C) joined to a softer but tougher wrought iron plate. The ballistic performance of the compound armour was judged to be down to the combination of the hardness of the steel face plate and the quality of the weld between the two plates. Best results were achieved with a thickness of one-third steel to two-thirds iron (Johnson, 1988).

Compound armour was soon replaced by the invention of nickel–steel armour where the addition of nickel led to an increase in the strength and toughness of the steel. When successfully treated, a 10-in. (254-mm) nickel–steel armour could be as effective as 13 in. (330 mm) of wrought iron plate. Other developments included carburizing the face of steel armour plate by holding in contact with bone, finely divided charcoal or other carbonaceous compounds at elevated temperature (this is a super-carburizing or 'cementing' process). This had the effect of increasing the carbon content close to the surface of the steel, and therefore, a product comprising a hard face and a tough body was produced.

Krupp was able to deepen the hardening process (cemented plates only had a carbon infusion to approximately 1 in. or 25.4 mm) by embedding nickel-chrome steel cemented plates in clay whilst leaving the cemented side exposed to air. Then, the exposed face was subjected to a process of rapidly heating and rapidly cooling the steel with water spray. This process of decremental face hardening produced a very hard face of between 30% and 40% of the plate's thickness with the remainder retaining the original properties of the plate.

Other inventions around the turn of the twentieth century included the use of laminated armour. A German engineer by the name of Schaumann developed a system whereby a compound plate comprising of 'several laminations cemented' together demonstrated good levels of resistance to penetration (Robinson, 1913). This is possibly the earliest example of laminated armour. Development of the Schaumann armour plate is further described by (Phelps, 1914) as:

> …not homogeneous, but is composed of an outer plate of nickel steel and an inner plate of soft metal, connected with each other at intervals.

Thickness values of this bi-layer system were quoted as 2 mm of nickel steel backed by 3 mm of soft steel—very similar to the disruptor/absorber system described previously.

1.5.5 FORTIFICATIONS

Fortifications have had a very long history, and there has been little change in the principles of protection throughout the centuries. Today, we use very similar (and in some cases, identical) materials to what was used over 2000 years ago. Take a well-known and well-used protection solution in HESCO Bastion. It uses the benefit of naturally occurring materials to provide cover and protection. In fact, it is found that rock, brick and concrete are pretty effective at stopping modern weapons as they were at stopping ancient projectiles. The reason for this lies in their hardness and the fact that there is rarely any limit on the amount of material that can be applied as protection, that is, given that there is sufficient space available. Therein lies the golden rule of protection: 'given enough space and not being limited by weight, all kinetic-energy-based weapons can be defeated'. The challenge, as will be seen in this book, is that rarely do we have the luxury of providing limitless space and accommodating large masses.

Concrete has long been known to provide an effective and cheap means of providing protection to fortifications. The Thornycroft Bison was developed in 1940 as a mobile pillbox with the intention that it would be deployed on and around airfields. Arguably, the Bison is a concrete AFV; an example located at the Bovington Tank Museum (United Kingdom) is shown in Figure 1.5.
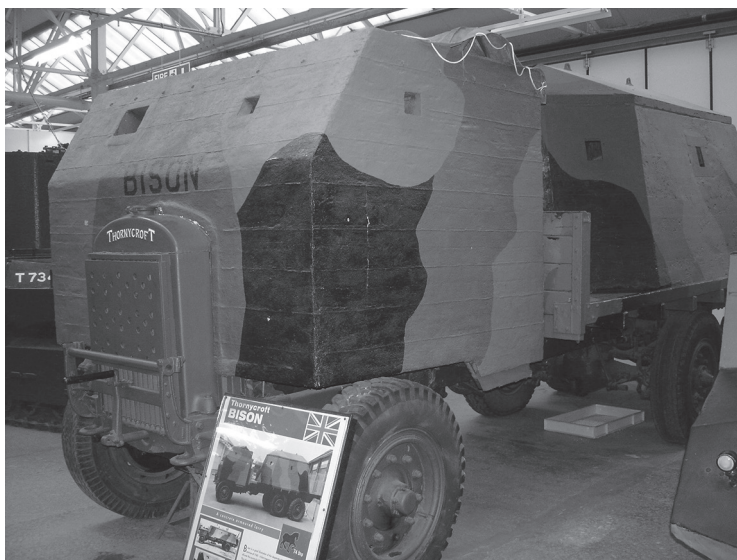
FIGURE 1.5   Thornycroft Bison.

Nowadays, the damage tolerance of concrete structures is enhanced by adding reinforcing fibres made from steel or polymer materials—such as polyvinyl alcohol or polyethylene. These fibres have been shown to enhance the blast resistance of concrete structures.

1.6   EARLY EMPIRICAL MODELS OF PENETRATION

We will finish this chapter with a brief review of some early empirical penetration models. The earliest known penetration equation is attributed to Benjamin Robins (1707–1751) and Leonhard Euler (1707–1783) (see (Allen et al., 1957)). They deduced the resistance of a medium to penetration was independent of velocity and was a constant (Robins, 1742). And so, from here on in, we must turn mathematical. The equation that describes this constant resistance is given by

$$-m_0 \frac{dv}{dt} = c_0 \tag{1.1}$$

where c_0 is a positive constant and m_0 is the initial mass of the projectile. The mass of the projectile is assumed to be constant throughout the penetration process. The minus sign indicates a constant deceleration in the medium. This was developed further by Euler (Allen et al., 1957) and (Poncelet, 1829) to *what* became known as the 'Poncelet equation'. Poncelet's equation will be given a thorough treatise in Chapter 4, however, in its final form it can be written as follows:

$$p = \frac{m_0}{2c_2} \left(\ln\left[1 + \frac{c_2 v_0^2}{c_0} \right] \right) \tag{1.2}$$

where p is the penetration, v_0 is the impact velocity and c_2 is a constant.

Much of the early work on attempting to predict the thickness of armour required to stop projectiles was carried out with the intention of providing better protection for ships. Much of this work was carried out from the late 1880s with semi-analytical equations proposed for predicting the thickness of a plate that could be penetrated. These were based on two different hypotheses of penetration (Bruff, 1896):

1. The projectile acted like a punch by shearing the metal along the circumference of a disc.
2. The projectile acted like a wedge forcing the particles of the metal apart.

For penetration into wrought iron, the formulas deduced under the first hypothesis were

$$(\text{Fairbairn}) \ h^2 = \frac{E}{\pi dk} \tag{1.3}$$

$$(\text{English Admiralty}) \ h^{2.0.5} = \frac{E}{0.86\pi d} \tag{1.4}$$

$$(\text{Muggiano}) \ h^{1.868} = \frac{E}{k\pi d} \tag{1.5}$$

For the case of the second hypothesis, the derived equations were

$$\left(\text{de Marre}\right) h^{1.3} = \frac{E}{5.8169d^{1.5}} \tag{1.6}$$

$$\left(\text{Maitland}\right) h = \frac{v_0}{608.3}\sqrt{\frac{w}{d}} - 0.14d \tag{1.7}$$

$$\left(\text{Krupp}\right) h^{1.33} = \frac{E}{4.156d^{1.67}} \tag{1.8}$$

$$\left(\text{Gâvre}\right) h^{1.4} = \frac{wv_0^2}{2265454d} \tag{1.9}$$

Here, we resort to imperial units: where h is the thickness of wrought iron, in inches, that the projectile would penetrate; E is the kinetic energy of the projectile (in foot tonnes); d is its diameter (in inches); w is its mass in pounds; v_0 is the projectile's striking velocity (in feet/seconds) and k is a constant.

As a rule of thumb, Captain Orde Browne was able to deduce a guide on how a projectile would penetrate the enemy's armour: 'The penetration of a projectile in wrought iron armour is one calibre for every thousand feet striking velocity' (Bruff, 1896, p. 327). So, for example, a 10-in. projectile striking with a velocity of 1000 ft./s will penetrate 1 calibre or 10 in.

Historically, for steel armour, engineers would calculate the penetration for wrought iron plate and add a percentage (varying from 10% to 30%) to accommodate the increased levels of strength and toughness. However, this was found to be unsatisfactory due to the variability in steel armour properties from one type of steel to the next. Therefore, equations for different steels were deduced based on the de Marre formula as follows.

For soft plates of Creusot steel (generally used for heavy armour), backed by wood,

$$h^{0.7} = 0.0009787\frac{w^{0.5}v_0}{d^{0.75}} \tag{1.10}$$

For perforation of the wooden backing only (Metcalfe, 1891),

$$h^{1.2} = \frac{E}{0.1823d^{1.8}} \tag{1.11}$$

where E is the kinetic energy of the projectile in foot tonnes given by

$$E = \frac{wv_0^2}{2g2240} \tag{1.12}$$

where g is the acceleration due to gravity (32.2 ft./s²) and noting that a tonne is defined as 2240 lb., giving

$$h^{0.6} = 0.006169\frac{w^{0.5}v_0}{d^{0.9}} \tag{1.13}$$

For thin hard steel plates used as protection against rapid-fire guns (unbacked),

$$h^{0.7} = 0.000734 \frac{w^{0.5} v_0}{d^{0.75}} \tag{1.14}$$

These equations are provided purely for historical context, and some analytical and empirical equations for penetration will be revisited later.

1.7   SUMMARY

In this book, the intention is to provide an overview of the science and technology that is used to provide protection against blast and ballistic attacks. The theory and applications will be mostly concerned with vehicles, ships and personnel with some reference to fortifications.

We will start by examining the theory of material behaviour and the typical threats that are out there. We will then examine projectile penetration and the theory behind stress waves and shock waves. Next, we will examine computational approaches and discuss some of the theories that underpins modern computational codes that help in examining penetration processes. We will then look at the materials technologies that have been used in protection, ranging from the common garden steel to ceramic- and composite-based systems. Reactive systems will be subsequently discussed. We will also discuss some of the system effects of adding blast-wave shaping to vehicles. Finally, we will close this book by examining the effect on the human body and blast and ballistic testing techniques.

NOTES

1 The Brewster Body Shield was a wearable 18-kg steel shield resembling Kelly's armour.
2 Although it should be noted that other theories on the demise of the *Hood* exist—particularly on the location of the fatal shell's strike location, e.g. Santarini (2013).
3 These shells had a mass of 800 kg and contained a small mass of explosives (~19 kg); the maximum range with a naval gun installation was 36 km.

REFERENCES

Allen, W. A., Mayfield, E. B. & Morrison, H. L. 1957. Dynamics of a projectile penetrating sand. *Journal of Applied Physics*, 28, 370–376.

Bruff, L. L. 1896. *A Text-Book of Ordnance and Gunnery: Prepared for the Use of Cadets of the U. S. Military Academy*. New York: John Wiley & Sons, Inc.

Dean, B. 1915. Should the warrior of today wear armor? *The New York Times,* SM4, Magazine section.

Fox, M. C. 2006. *Knights of the Skies: Armour Protection for British Fighting Aeroplanes*. Walton on Thames: Air Research Publications, Walton on Thames, UK.

Ghazlan, A., Ngo, T., Tan, P., Xie, Y. M., Tran, P. & Donough, M. 2021. Inspiration from nature's body armours – a review of biological and bioinspired composites. *Composites Part B: Engineering*, 205, 108513.

Gye, R. 1948. *Tank Armour Distribution Theory*. London: Operational Research Group (Weapons and Equipment).

Held, M. 2000. Warhead hit distribution on main battle tanks in the Gulf war. *Journal of Battlefield Technology*, 3(1), 1–9.

Islam, M. K., Hazell, P. J., Escobedo, J. P. & Wang, H. 2021. Biomimetic armour design strategies for additive manufacturing: A review. *Materials & Design*, 205, 109730.

Johnson, W. 1988. Some conspicuous aspects of the century of rapid changes in battleship armours, ca 1845–1945. *International Journal of Impact Engineering*, 7(2), 261–284.

Lissak, O. M. 1907. *Ordnance and Gunnery: A Text Book*, 1st ed. New York: John Wiley & Sons, Inc.

Metcalfe, H. 1891. *A Course of Instruction in Ordnance and Gunnery: Text*, 2nd ed. New York: John Wiley & Sons, Inc.

Ogorkiewicz, R. M. 1991. *Technology of Tanks, 2 vols.*, vol. 1. Coulsdon, Surrey, UK: Jane's Information Group Ltd.

Phelps, H. M. 1914. Bureau of standards furnace for testing building materials, Schaumann armor plate, and more. *Scientific American*, 111, 118–119.

Poncelet, J. V. 1829. *Cours de mécanique industrielle: fait aux artistes et ouvriers messins, pendant les hivers de 1827 à 1828, et de 1828 à 1829. Préliminaires et Applications.* Metz: Mme Ve Thiel.

Robins, B. 1742. *New Principles of Gunnery: Containing the Determination of the Force of Gunpowder, and an Investigation of the Difference in the Resisting Power of the Air to Swift and Slow Motions*, London, England: J. Nourse.

Robinson, C. N. 1913. Armour and ordnance. Ordnance tables. *In:* Hythe, V. (ed.) *The Naval Annual, 1913*. Portsmouth, UK: J. Griffin & Co Portsmouth.

Santarini, M. 2013. *Bismarck and Hood: The Battle of the Denmark Strait*. England: Fonthill Media Ltd.

Sullivan, J. F. 1943. *Aircraft Armor – Ballistic Characteristics of a Magnesium Alloy, Dowmetal (Type FS)*. Watertown, MA: Watertown Arsenal Laboratory.

Sun, J. & Bhushan, B. 2012. Hierarchical structure and mechanical properties of nacre: A review. *RSC Advances*, 2, 7617–7632.

Tobin, L. & Iremonger, M. 2006. *Modern Body and Helmets: An Introduction, Military Technology Series*. Canberra, Australia: Argos Press.

Vernerey, F. J. & Barthelat, F. 2014. Skin and scales of teleost fish: Simple structure but high performance and multiple functions. *Journal of the Mechanics and Physics of Solids*, 68, 66–76.

Wang, R. Z., Suo, Z., Evans, A. G., Yao, N. & Aksay, I. A. 2001. Deformation mechanisms in nacre. *Journal of Materials Research*, 16, 2485–2493.

Zorn, J. R. 2010. Reconsidering Goliath: an iron age I Philistine chariot warrior. *Bulletin of the American Schools of Oriental Research*, 360, 1–22.

Taylor & Francis
Taylor & Francis Group
http://taylorandfrancis.com

2 An Introduction to Materials

2.1 INTRODUCTION

Armour materials are subjected to large forces in very short timescales. In fact, they are doing their job very well if they are able to accommodate these forces. Therefore, to understand the behaviour of an armour material that has been impacted by a bullet or fragment from an exploding shell, or subjected to an explosive blast wave, we must take a look at its properties, and in particular, how those properties change with loading rate.

2.2 A QUICK INTRODUCTION TO THE STRUCTURE OF MATERIALS

The types of materials that are used in armour construction are quite extensive and range from low-density and low-stiffness materials such as polymers to high-density and high-hardness materials such as tungsten carbide. Naturally, the structure of these materials differs too. Most armour materials tend to be polycrystalline. That is to say that they are made up of multiple crystals 'stuck' together—each with a different orientation. Each crystal will be separated by a grain boundary. Materials in this category include most metals and ceramics. Additional structures include

- *Mono-crystalline materials (such as sapphire)*: where there is complete atomic order.
- *Glassy materials*: where there is limited order (i.e. glass).
- *Amorphous structures*: where there is no order. Many polymers fit into this category.

The way that a crystal is built is dependent on the atoms that make up the unit cell. The unit cell is the smallest repetitive unit that defines the relative locations of the atoms and forms the basic building block of the crystal. Multiple unit cells are stacked together to produce the crystal. And, in fact, there are a limited number of crystal systems known to science (seven is the current number). The three most common unit cell shapes in metals are body-centred cubic (BCC), face-centred cubic (FCC) and hexagonal close-packed (HCP). These crystal shapes define how the atoms are arranged, and the type of the crystal shape will affect the way in which plastic deformation is accommodated. A summary of crystal structures for 12 important metals used in defence applications is provided in Table 2.1. The corresponding structures representing BCC, FCC and HCP are shown in Figure 2.1.

17

TABLE 2.1

Crystal Structures for 12 Metals

Metal	Crystal Structure	Metal	Crystal Structure	Metal	Crystal Structure
Aluminium	FCC	Lead	FCC	Tantalum	BCC
Copper	FCC	Magnesium	HCP	Titanium (α)	HCP
Gold	FCC	Platinum	FCC	Tungsten	BCC
Iron (α)	BCC	Silver	FCC	Zinc	HCP

(a)   (b)   (c)
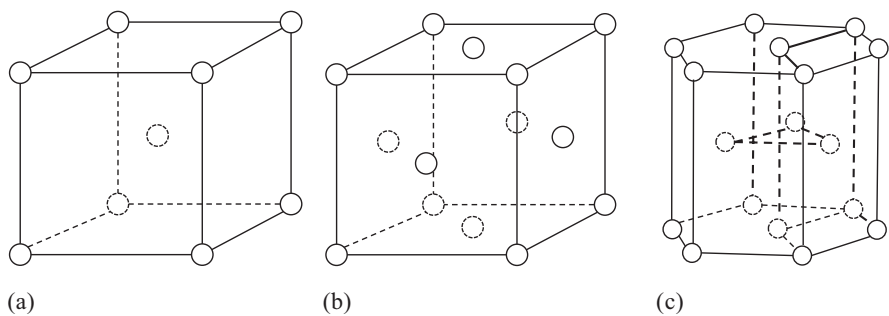
FIGURE 2.1 (a) BCC, (b) FCC and (c) HCP crystal structures. The circles indicate the position of the individual atoms.

2.2.1 MECHANISMS OF PLASTIC DEFORMATION

Both hardness and tensile (strength) tests result in plastic deformation of the sample. The mechanisms of plasticity are quite complex, and a readable explanation is provided by Callister (2007). The theory is largely based on the fact that crystals possess defects, and it is these defects that can move through a process called slip. These defects are known as *dislocations*. In an arrangement of atoms for a particular crystal, a dislocation is a defect about which there is a misalignment of atoms. Slip occurs because the stress that is applied in the tensile, compression or hardness tests (or indeed any stress for that matter) is transferred to the individual crystals in that material. This stress causes the movement of dislocations resulting in distortion of the crystal. The crystallographic plane along which this occurs is called the slip plane. This is the preferred plane for dislocation movement. For a particular crystal structure, the slip plane is the plane with the densest packing of atoms.

In addition to slip, plastic deformation can also occur by the formation of *mechanical twins* or *twinning*. Twinning occurs in metals that have a BCC and HCP structure at low temperatures and at high rates of loading—such as you would expect when a bullet penetrates an armour material. Twinning is a process whereby a shear force results in atomic displacement. An important characteristic of twinning is that atomic displacement results in a perfectly symmetrical atomic arrangement about the
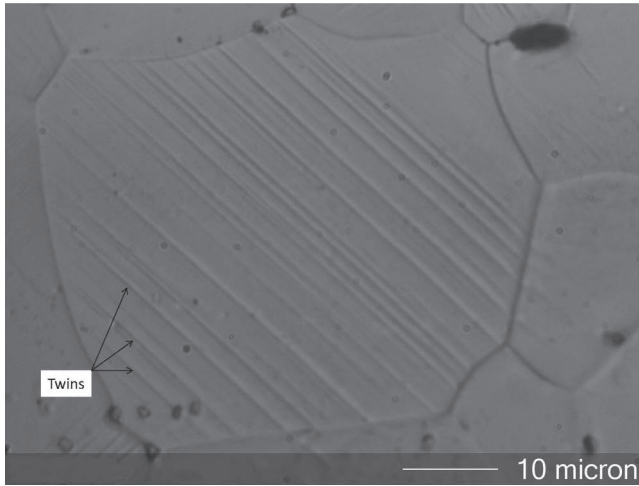
FIGURE 2.2   Examples of twinning in a magnesium material that has been shocked to 1.3 GPa.

twin plane. Figure 2.2 shows examples of twinning that have occurred in a shocked HCP magnesium material. The parallel lines that traverse the individual grain are due to the distortion that occurs due to twinning.

2.3   STRESS AND STRAIN

Let us start with the basics. We will be referring to different types of stress during the course of this book. Stress is simply a measure of the applied force divided by the area over which that force acts and has the SI-derived unit of N/m² or pascals (Pa).

In simple tension, the stress, σ, can be written as

$$\sigma = \frac{F}{A} \qquad (2.1)$$

where F is the applied force, and A is the area over which the force acts. A schematic of a simple tension case is shown in Figure 2.3a. Suppose that we have a case where the force no longer acts normal to the surface but at some angle to it. The force can now be resolved into two components: one component of force acting perpendicular to the surface, F_t, and other components of force acting parallel to the surface, F_s. The force acting parallel to the surface loads the element in shear. So, a shear stress, τ, that is acting on the element can now be defined, and this is given as

$$\tau = \frac{F_s}{A} \qquad (2.2)$$

Note too that in Figure 2.3b the forces acting on the vertical surfaces of the element due to the presence of shear have to be drawn. This is simply to satisfy equilibrium—otherwise, the element would spin clockwise.
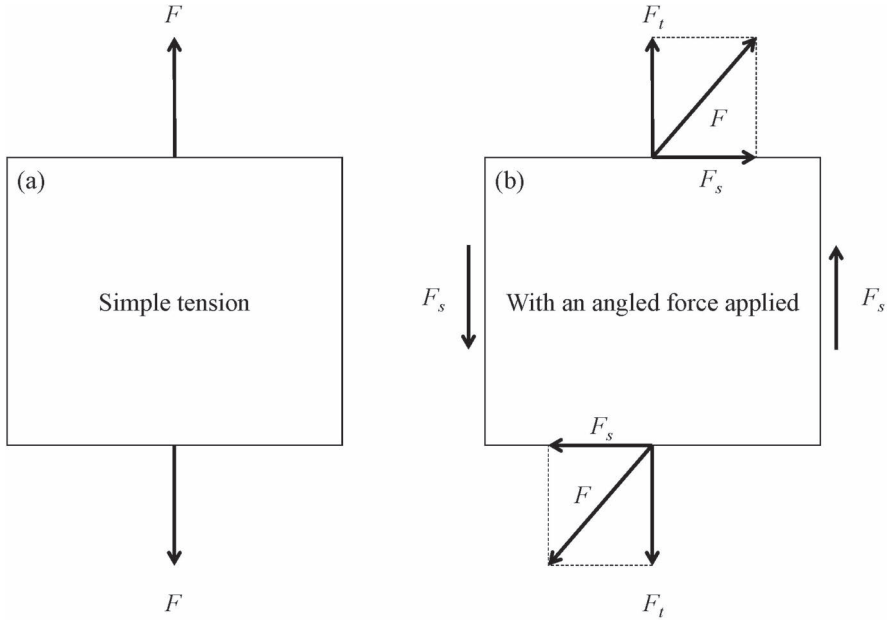
FIGURE 2.3 Schematic of (a) an element subjected to simple tension and (b) where the element is subjected to a force at an angle from the parallel surface.

There are three states of pure stress that will be discussed from time to time in this book. They are defined as *simple tension or compression* (the tensile case is shown in Figure 2.3a), *pure shear* (as defined in Equation 2.2) and *hydrostatic stress* or *pressure*. This occurs when a solid is subjected to equal compression on all sides. Pressure will be discussed in detail when we examine the role of shock waves in penetration and blast.

A material will accommodate stress by deforming or *straining*. Referring to a simple tensile case, then the amount of strain can be defined by measuring the amount of deformation and dividing that by the original length of the sample. So, strain, in simple tension, where a load is applied to a sample of length x_0 can be defined as

$$\varepsilon_n = \frac{x - x_0}{x_0} \tag{2.3}$$

where x is the new length due to the application of the load. This is the definition of *engineering or nominal strain* where the initial and final states of the sample are measured during an experiment. However, there is an additional important definition of strain that is frequently used in computational codes, or in the analysis of wave propagation, that the reader should be aware of, and that is *true strain* or *natural strain*. For a continually straining object, it is the precise measure of strain at one particular point in time. Therefore, an increment of true strain can be defined according to

$$d\varepsilon = \frac{dx}{x} \tag{2.4}$$

Integrating between x_0 and x, we have

$$\varepsilon = \int_{x_0}^{x} \frac{dx}{x} = \ln\left(\frac{x}{x_0}\right) \tag{2.5}$$

From Equation 2.3, it is seen that

$$x = x_0(1 + \varepsilon_n) \tag{2.6}$$

Therefore, the equation for true strain can be rewritten as:

$$\varepsilon = \ln\left(\frac{x_0(1 + \varepsilon_n)}{x_0}\right) \tag{2.7}$$

and so, true strain is defined as

$$\varepsilon = \ln(1 + \varepsilon_n) \tag{2.8}$$

This nicely gives us the relationship between true strain and engineering strain.

In simple tension, the length of the sample will increase, but the thickness, or diameter of a cylindrical specimen, will decrease. To describe this effect, Poisson's ratio is defined. This has the symbol of v and relates the longitudinal strain to the transverse strain, ε_t; thus,

$$v = -\frac{\varepsilon_t}{\varepsilon_n} \tag{2.9}$$

If the transverse dimension of the specimen is defined as d, then the transverse strain is defined as $\varepsilon_t = -\Delta d/d$.

Engineering shear strain is given to us with reference to Figure 2.4. This is defined as follows:

$$\gamma = \frac{w}{q} = \tan\theta. \tag{2.10}$$

For small angles $\gamma \approx \theta$.

In a similar fashion, volumetric strain can be defined as the change in volume divided by the original volume (V_0). So, the engineering definition of volumetric strain is given to us as

$$\varepsilon_{v\_n} = \frac{V - V_0}{V_0} \tag{2.11}$$
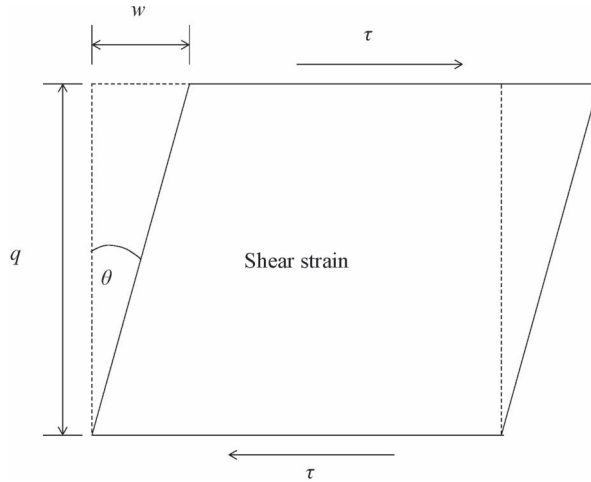
FIGURE 2.4   An element subjected to pure shear.

and the true volumetric strain is defined by

$$\varepsilon_v = \ln\left(\frac{V}{V_0}\right).$$

(2.12)

We will see this form of equation again in Section 5.8.4 where we will look at the volumetric strain in a shocked material.

Example 2.1

A steel test specimen is loaded by 10 kN as shown in Figure 2.5. Calculate the stress in each section. The diameters of each section are (1) 40, (2) 20 and (3) 30 mm.

This can be solved very simply with reference to Equation 2.1. The important point to learn here is that stress is a function of the cross-sectional area through which a force acts, and therefore, it is variable. Even though there is a single force acting through the specimen, the stress will vary throughout its length. In this case, it is remembered that 1 N/mm² = 1 MPa and that the equation for the area of a circle is given by

$$A = \pi\frac{d^2}{4}$$

(2.13)

Therefore, the answers can now be tabulated in Table 2.2.
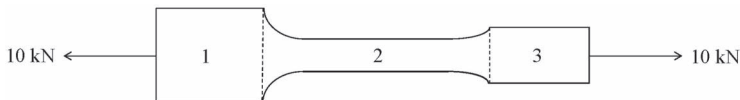
FIGURE 2.5   A steel test specimen with three cross-sectional areas.

TABLE 2.2

Answers to Example 2.1

Section	Diameter (mm)	Area (mm²)	Load (N)	Stress (MPa)
1	40	1257	10,000	8.0
2	20	314	10,000	31.8
3	30	707	10,000	14.1

2.4 ELASTICITY

When a load is applied to a material, initially it will deform elastically. In fact, all materials will deform elastically when subjected to small strains. Up to a predetermined stress limit, the amount of deformation is reversible as the material has incurred no permanent deformation. In this region, the stress is directly proportional to the strain; thus,

$$\sigma = E\varepsilon \tag{2.14}$$

where E is defined as the modulus of elasticity or Young's modulus of the material. This relationship was originally discovered by Robert Hooke in 1678 and is sometimes referred to as *Hooke's law*. At an atomic level, ε is a measure of the increase (or decrease) in atomic spacing due to the applied load. As the load is increased, the inter-atomic spacing increases, and when the load is removed, the atoms return to their equilibrium position. The greater the attraction between atoms—that is, the stronger the bonding—the greater the load required to increase the inter-atomic spacing. Certain ceramic armour materials are good examples of materials with high values of E due to their strong atomic bonding. Materials with relatively weak ionic bonding tend to possess relatively low values of E.

A common way of measuring the elastic properties of a material uses ultrasonic methods. An ultrasonic transducer is used to send a longitudinal elastic wave into the material. Knowing the sample's thickness and the time it takes for the ultrasonic wave to transit the thickness of the sample, we can work out how fast the wave travels through the sample. By knowing the material's density and the longitudinal and shear wave speed of the material, it is possible to calculate the Young's modulus, Poisson's ratio (v) and other important elastic properties including the shear modulus (G) and bulk modulus (K) according to the following equations:

$$v = \frac{1 - 2\left(\dfrac{c_s}{c_l}\right)^2}{2 - 2\left(\dfrac{c_s}{c_l}\right)^2}, \quad E = \frac{c_l^2 \rho_0 (1+v)(1-2v)}{(1-v)}, \quad G = c_s^2 \rho_0 \tag{2.15}$$

where c_l and c_s are the longitudinal and shear wave velocities, respectively. ρ_0 is the material density (note that the subscript '0' corresponds to initial conditions and as we will see later, the density will change under shock loading conditions).
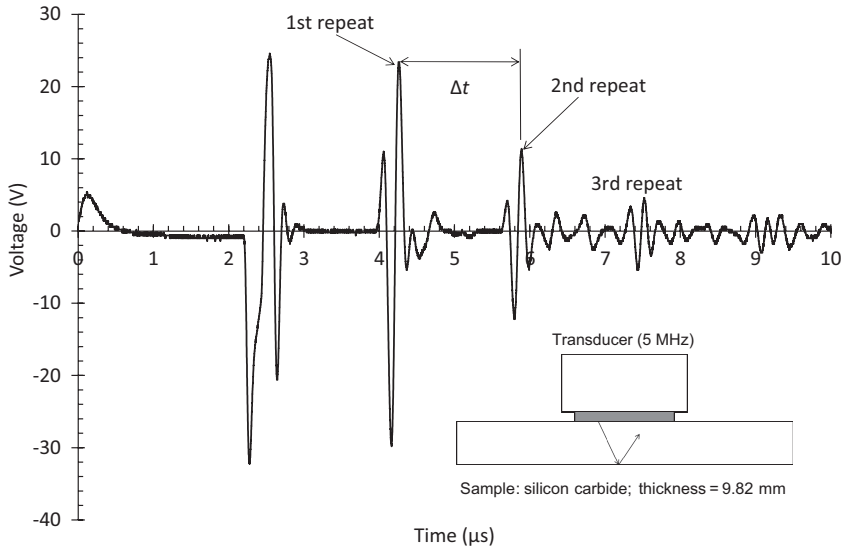
FIGURE 2.6 Longitudinal wave transmission through a silicon carbide target. Here, the transducer is used in 'pulse-echo' mode, which means that the transducer detects the reflection of the wave from the free surface of the target.

An example of a typical waveform from an ultrasonic transducer in contact with a silicon carbide tile is shown in Figure 2.6. The transducer is a longitudinal type (Olympus V109-RB) connected to an Olympus 5077PR square wave pulser/receiver. A digital storage oscilloscope captures the waveform. It can be seen that the pulse reflects back and forth from the surface of the sample, and as it does so, the magnitude drops. The time between each pulse is the time for the wave to transit twice the thickness of the sample.

In our example, it is known that

- The sample thickness, $h = 9.82$ mm
- The time between two pulses, $\Delta t = 1.64$ μs

Therefore, to calculate the longitudinal wave velocity in a sample of thickness of 9.82 mm, we have

$$c_l = \frac{2h}{\Delta t} = \frac{19.64}{1.64} = 11.976 \text{ mm/μs} \tag{2.16}$$

This is the longitudinal wave velocity for the silicon carbide.

In practice, it is common to use as many 'repeats' as possible where the identical feature is discernible in both pulses from which the measurements are taken. This is to minimize the error in timing acquisition. Furthermore, it is common that a contact medium is applied between the transducer and the sample to facilitate

TABLE 2.3
Elastic Properties of a Range of Materials

Material	Density (kg/m³)	c_l (m/s)	c_s (m/s)	c_b (m/s)	E (GPa)	G (GPa)	K (GPa)	ν
Epoxy resin (cured)	1141	2699.0	1283.5	2255.7	5.1	1.9	5.8	0.354
Perspex	1190	2768.0	1389.5	2255.6	6.1	2.3	6.1	0.332
Borosilicate glass	2200	5584.4	3411.8	3958.0	61.6	25.6	34.5	0.202
Float glass	2440	5797.9	3461.9	4199.5	71.5	29.2	43.0	0.223
Aluminium 5083-0	2660	6359.7	3187.7	5186.3	72.0	27.0	71.5	0.332
Aluminium 6082-T651	2703	6412.5	3188.3	5250.4	73.4	27.5	74.5	0.336
Aluminium 1318B	2780	6268.9	3112.0	5136.8	72.0	26.9	73.4	0.336
Silicon carbide (PS-5000)	3140	12,071.4	7629.8	8252.3	426.8	182.8	213.8	0.167
Alumina (Sintox™ FA)	3694	10,088.3	5933.0	7405.4	321.3	130.0	202.6	0.236
Alumina (AD-995)	3900	10,650.3	6260.3	7821.4	377.9	152.8	238.6	0.236
Steel (mild)	7800	5926.8	3241.3	4595.4	210.9	81.9	164.7	0.287
Steel (UK-RHA)	7838	5919.3	3300.8	4528.9	217.7	85.4	160.8	0.274
Stainless steel (304L)	7890	5739.5	3155.0	4435.0	201.6	78.5	155.2	0.283
Tungsten carbide	14,740	6829.0	4085.0	4938.2	600.9	246.0	359.4	0.221

wave transmission. For longitudinal transducers, something like a low-viscosity washing-up liquid is usually sufficient, whereas for shear wave transducers, something like higher viscosity honey or treacle is usually required.

A list of the elastic properties of a range of materials is presented in Table 2.3.

Materials of the same type generally have very similar elastic properties irrespective of their strength. For example, it is well known that rolled homogeneous armour (RHA) is much stronger steel than mild steel, yet their stiffness values are similar (±3%). The reason for this is that strength properties are dominated at the microstructural level, which is affected by processing, whereas the stiffness is very much affected by changes at the atomic scale.

2.5 STRENGTH

The theoretical strength that can be achieved by a material is defined by the elastic modulus, the inter-atomic spacing and the energy required to create a fracture surface—that is, the fracture surface energy. The theoretical strength can be defined by the following equation:

$$\sigma_{th} = \left(\frac{E\gamma}{a_0} \right)^{\frac{1}{2}} \quad (2.17)$$

where E is the elastic modulus, γ is the fracture surface energy and a_0 is the inter-atomic spacing. Sadly, many hard and brittle materials such as glass and ceramic never even come close to obtaining their theoretical strength as their structure

contains small flaws or pores that provide a source for crack propagation when the materials are placed under load. For example, fracture strengths for polycrystalline ceramics are typically of the order of 1% that of σ_{th}.

Griffith (1921), a British engineer, was the first to offer an explanation for the very low fracture strength of brittle materials compared to their theoretical strength. He deduced that it was due to the presence of small cracks or flaws in the material. He developed the foundation for the theory that led to the equation that defines the fracture strength of a brittle material in terms of the flaw size and fracture toughness:

$$\sigma_f = \frac{K_c}{\sqrt{\pi a}} \tag{2.18}$$

where a is half the defect size, and K_c is the fracture toughness of the material. Note that this is the equation for the plane stress condition and is a good approximation for thin plates under stress. K_c, like E, is a material property and as such can be measured. The important thing to realize from this equation is that the fracture strength is dependent on the largest flaw size in the material. The larger the flaw, the lower the fracture strength.

The measurement of the strength of metal materials is generally carried out in tension by what is called a 'simple tensile test'. Loading a ductile material such as mild steel in a simple tension results in a stress–strain profile shown in Figure 2.7. Inset is a typical 'dumbbell'-shaped specimen that may be used with metals showing a reduced section where the strain is measured. The curves for both true stress and engineering stress are shown. Consider the engineering stress behaviour: At point 'A', the yield strength (Y_0) of the material is reached. At this point, the material is no longer linear elastic and starts to deform plastically. This continues until at point 'B', the maximum engineering stress is reached, which is known as the ultimate tensile
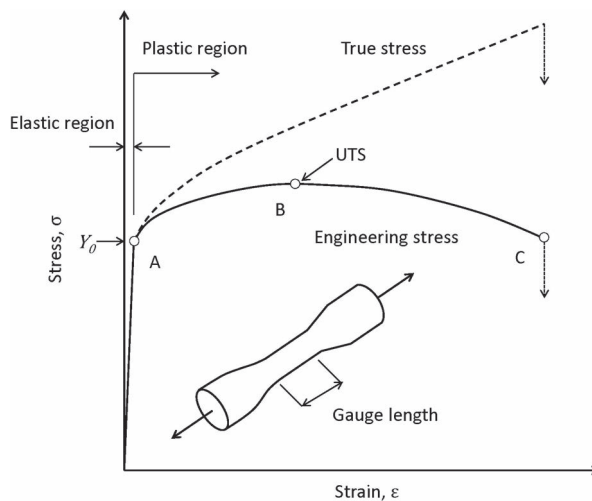
FIGURE 2.7   A schematic of a typical stress–strain curve for steel.

stress (UTS). At this point, the onset of necking occurs, and the stress is relaxed until fracture occurs at point 'C'.

The engineering (or nominal) stress curve sits lower than the true stress curve. This is because the calculation of engineering stress takes into account the original cross-sectional area before the sample is deformed. As the sample is stretched, it will narrow, and the true stress takes into account the reduced cross-sectional area, i.e. the instantaneous cross-sectional area.

The true stress and engineering stress are related by the following relationship:

$$\sigma = \sigma_n \left(1 + \varepsilon_n\right) \tag{2.19}$$

where σ_n is the engineering stress, and ε_n is the engineering strain.

The application of tensile load produces strains in the test specimen. The effect of these strains is to raise the energy levels in the bar itself. The increase in energy within the bar is called the *strain energy* and is equal to the work done on the bar provided that no energy is added or subtracted in the form of heat. The strain energy, U, can be calculated from

$$U = \int F.dx \tag{2.20}$$

where F is the load applied to the bar, and x is the distance through which the bar is stretched. The above equation including the cross-sectional area A and the original length L of the bar can be rewritten as follows:

$$U = A.L \int \frac{F}{A} \cdot \frac{dx}{L} \tag{2.21}$$

and therefore,

$$\frac{U}{V} = \int \sigma.d\varepsilon \tag{2.22}$$

Therefore, the area under the curve is a measure of the strain energy absorbed per unit volume, V, and is a measure of the material's toughness. For an armour designer, toughness is a desirable property as a tough material requires more energy to induce fracture. However, that is not the whole story as will be seen later. Ceramics are very brittle and cannot accommodate much plastic deformation. Yet, they are used extensively in armour.

For elastic collisions, the term *resilience* is often used to describe the behaviour of the material. Essentially, this is the capacity of the material to absorb energy when it is deformed elastically. So, assuming that the material has a linear elastic region, then the elastic strain energy absorbed is given to us by the area under the linear portion of the stress–strain curve. Therefore,

$$U_r = \frac{1}{2} Y_0 \varepsilon_Y \tag{2.23}$$

where Y_0 is the yield strength, and ε_Y is the strain at the yield point. Therefore, incorporating Equation 2.14, it is seen that

$$U_\mathrm{r} = \frac{Y_0^{\,2}}{2E} \tag{2.24}$$

U_r has the units of J/m³, and so it is the energy absorbed per unit volume of material. As this is strictly for the case of elastic deformation, this energy can also be released. Noting the above equation, it is therefore desirable to use a material with a high yield strength and low elastic modulus when faced with low-velocity collisions.

Example 2.2

A 10-mm diameter bar of 1040 carbon steel is subjected to a tensile load of 60 kN taking it beyond its yield limit ($Y_0 = 580$ MPa). Calculate the elastic recovery that would occur on the removal of the load given that $E = 200$ GPa.

Elastic recovery is assumed to occur in a linear fashion as the stress is released down an elastic path parallel to the elastic loading (see Figure 2.8).

First, the area needs to be calculated; this is given by

$$A = \pi \frac{d^2}{4} = \pi \frac{10^2}{4}$$

$$= 78.5 \ \mathrm{mm}^2$$

Using Equation 2.1, the stress can be calculated:

$$\sigma = \frac{F}{A} = \frac{60,000}{78.5}$$

$$= 764.3 \ \mathrm{MPa}$$
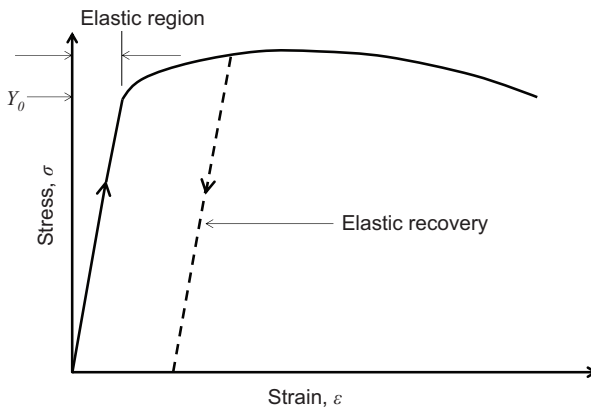
FIGURE 2.8   Elastic recovery from a plastic stress value.

The elastic recovery can be calculated from Hooke's law and therefore is given by

$$\varepsilon = \frac{\sigma}{E} = \frac{764.3 \times 10^6}{200 \times 10^9}$$

$$= 3.82 \times 10^{-3}$$

Note that the elastic recovery here is calculated as a value of strain and therefore is dimensionless.

Example 2.3

You are designing a new type of crash box for low-velocity collisions, and you are given the option of four materials. These are summarized in Table 2.4. During the collision, you expected that the structure would remain elastic at all times. Which material would you choose and why?

During a low-velocity elastic collision, we would want the structure to absorb as much kinetic energy as possible. Therefore, choosing a material that has high elastic resilience is sensible. From Equation 2.24, it is a relatively trivial task to work out the elastic resilience of our choices. Remember to write the equation so that the values are in base SI units. The answers are summarized in Table 2.5.

It can be seen from Table 2.5 that Ti–6A1–4V is the clear winner by virtue of its high yield strength, whereas AA 2024-T6 performs reasonably well and is ranked second by virtue of its low elastic modulus. Budgetary factors may well impact your choice, and given the cost of titanium alloys, the aluminium alloy option may turn out to be the better one (titanium alloys are very expensive).

TABLE 2.4
Properties of Selected Materials

Material	E (GPa)	Y_0 (MPa)
AA 2024-T6	72	350
AISI 304 stainless steel	193	205
AISI 1040 cold drawn steel	200	450
Ti–6Al–4V	110	825

TABLE 2.5
Elastic Resilience of Selected Materials

Material	U_r (J/m³)	Rank
AA 2024-T6	8.51×10^5	2
AISI 304 stainless steel	1.09×10^5	4
AISI 1040 cold drawn steel	5.06×10^5	3
Ti–6Al–4V	3.09×10^6	1
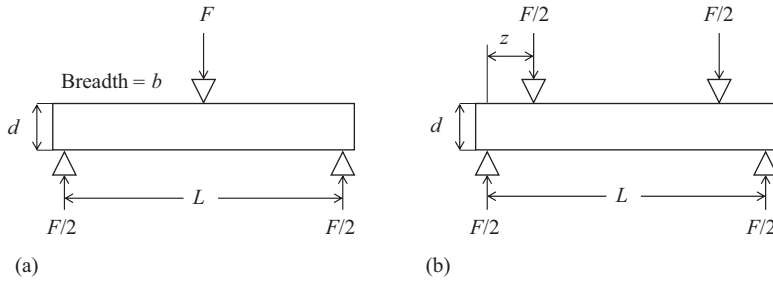
FIGURE 2.9   (a) Three-point bend test and (b) four-point bend test.

The strength of brittle materials is generally characterized by using a *bend test*, as illustrated in Figure 2.9. There are two types of tests that are principally used: the three-point bend test and the four-point bend test. In both cases, a rectangular beam of breadth *b* and depth *d* is loaded by a universal testing machine, as shown in Figure 2.9.

The bend strength of a rectangular specimen can be evaluated using the general bending equation; thus,

$$\sigma_b = \frac{My}{I} \tag{2.25}$$

where *M* is the applied moment calculated from the applied load that causes fracture, *y* is the distance from the neutral axis to the top surface of the beam (in this case, where the beam is perfectly symmetrical, the neutral axis sits in the central axis; therefore, $y = d/2$) and *I* is the second moment of area and for a rectangular beam can be calculated from

$$I = \frac{bd^3}{12} \tag{2.26}$$

The bend strength is often referred to as the modulus of rupture (*MOR*) and can be calculated from the following equations:

$$\text{Three-point bend test } MOR = \frac{3}{2} \frac{FL}{bd^2} \tag{2.27}$$

$$\text{Four-point bend test } MOR = \frac{3Fz}{bd^2} \tag{2.28}$$

However, there is a severe limitation in using the *MOR* for evaluating the fracture strength of brittle materials such as ceramics as the result will depend on the size of the sample and the test method used. For example, the three-point test method will tend to give higher results of the fracture strength of the sample when compared to the four-point test method. This has simply to do with the way in which the stress acts along the length of the specimen due to the applied moment.

The four-point test method produces a more uniform stress distribution when compared to the three-point test method, and therefore, more of the sample is loaded at an elevated stress level. For ceramics, the failure is determined by the

presence of a critical flaw, and so, the sample is more likely to fail under the action of a smaller applied load. Therefore, the measured fracture strength will be lower.

Brittle materials such as ceramics do not possess high toughness values, and the strain to failure under tensile loading conditions is very low (<0.001%); therefore, deformation is difficult to measure. The toughness of ceramic can be measured using a similar method shown in Figure 2.9. However, this time, a crack of known length is artificially machined into the sample on the tensile side of the specimen (in this case, the bottom), and the load increases until the crack propagates and the sample fails catastrophically. The fracture toughness of the sample can then be calculated from the load at fracture, the initial crack geometry and the geometrical aspects of the sample. Fracture toughness can also be measured by applying an indenter (usually a Vickers) under load to the sample as we do when measuring the hardness of the material (see Section 2.6). When the load is removed, the sizes of the cracks that emanate from the sides of the indentation are measured, and the toughness can be calculated from their length and the hardness of the ceramic. Fracture toughness has the units of MPa $m^{1/2}$ and for ceramic can be as little as 2 MPa $m^{1/2}$; for metals, the values will range from around 20 to 200 MPa $m^{1/2}$.

2.6   HARDNESS

For the disruption of a projectile, an important material property of armour is hardness. The hardness of a material is a measure of the material's resistance to indentation, abrasion and wear; there are a number of ways that this can be measured.

The Vickers hardness number (VHN), or Vickers pyramid number, is one of the most widely used measures of hardness, and it is evaluated by using a diamond indenter with an apex angle of 68°. A load is applied to the indenter such that it embeds itself within the sample material; the size of the indentation is a direct measure of the sample's hardness. The VHN is then calculated by

$$\text{VHN} = 1.854 \cdot \frac{F}{d^2} \tag{2.29}$$

where F is the load applied to the indenter, and d is the average distance between the opposite apexes of the diamond indentation (see Figure 2.10a).

(a)   (b)   (c)
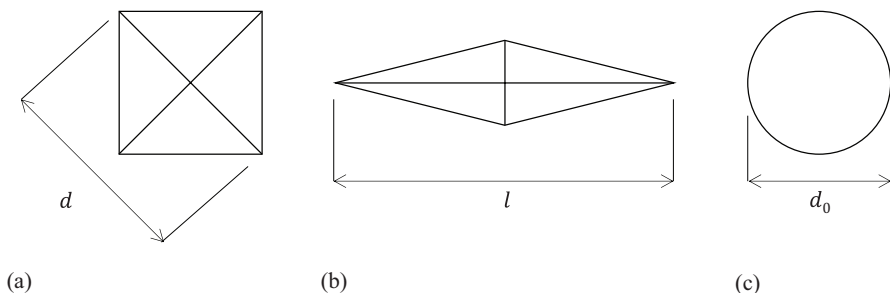
FIGURE 2.10   Top-view geometries of hardness indentations: (a) Vickers, (b) Knoop and (c) Brinell.

The Knoop hardness number (KHN) is measured using an elongated pyramid indenter, and it can be calculated from

$$KHN = 14.2 \cdot \frac{F}{l^2}$$ (2.30)

where l is the length of the indentation along its axis (see Figure 2.10b).

The Knoop hardness test is generally carried out on very hard ceramics. Other hardness measurement methods include the Brinell test where a hardened steel ball is used as the indenter. The Brinell hardness number (BHN) is the applied force F divided by the surface area of the indentation. Therefore,

$$BHN = \frac{2F}{\pi D \left(D - \sqrt{D^2 - d_0^2} \right)}$$ (2.31)

where D is the diameter of the ball (see Figure 2.10c), and d_0 is the diameter of the indentation. This hardness measurement is commonly used for metals and is not appropriate for most ceramics due to the hardness of the ceramic overmatching the steel ball indenter. This is a commonly used hardness metric that is quoted for armour-grade steels. Sometimes, it is convenient to use the *Meyer hardness* measurement instead of Brinell; this is simply calculated from the applied load divided by the projected surface area of the indenter.

Measuring the hardness of hard brittle materials such as engineering ceramics is problematic at best. If too small a load is applied to the indenter, then a very small indentation is left that can be difficult to measure accurately. If too large a load is applied, then the edges can spall, leading to problems in measuring the size of the indentation. Ideally, the sample should be polished, flat and parallel, and the indenter should be applied perfectly perpendicular to the sample to ensure a symmetrical indentation. Recording the applied load is also critical, as the measured hardness value will be affected by it. Typical VHN values of some armour materials are presented in Table 2.6 along with the UTS for each material.

For metals, the hardness of a material can be related to a material's UTS with a linear relationship. Table 2.6 shows why materials such as alumina and silicon carbide make very good disruptors. However, these materials are relatively brittle and therefore are susceptible to fragmentation.

TABLE 2.6

VHN Hardness and UTS Values of Some Typical Armour Materials

Material	VHN	UTS (MPa)
Aluminium alloy 7039 (armour plate)	130–150	450–480
RHA steel	270–350	900–1200
High-hardness armour (HHA) steel	500–550	1600–1900
Alumina (ceramic)	1300–1800	–
Silicon carbide (ceramic)	1900–2800	–

2.7   DYNAMIC BEHAVIOUR OF MATERIALS

When a bullet, penetrator or shaped-charge jet impacts and penetrates a material, the rate of deformation the projectile encounters is much higher than is observed when compared to conventional quasi-static material tests discussed in Sections 2.5 and 2.6. The behaviour of the metal (projectile) and the armour target is different at high rates of loading than at relatively low loading rates. Frequently, it is necessary to understand how the armour material behaves under dynamic loading, and there are various tests that can be used to assess behaviour and measure properties. Figure 2.11 summarizes the range of strain rates that are of interest to material scientists and engineers. Note that the unit of strain rate is s^{-1}. As the strain rates are increased, it is necessary to use different techniques to probe the response of the material and to measure the state of stress under dynamic loading.

For materials that are subjected to relatively high strain rates (when compared to quasi-static values), their strengths can change and, for most materials, increase markedly. Generally speaking, metals will get stronger but less ductile at elevated strain rates, but unlike some non-metals, their stiffness is relatively unaffected by increased deformation rates.

The reason for the increased strength with strain rate is due to complex microstructural behaviour that is dependent on the nature of the material. For example, with most metals, the mechanism can be explained by dislocation movements being impeded during plastic deformation. For long-chain polymers, the strain-rate sensitivity is due to molecules becoming entangled at high rates of loading, and therefore, their relative movement is impeded. A good demonstration of this effect can be shown with 'silly putty'. Rolling a sample of silly putty into a sausage and pulling it
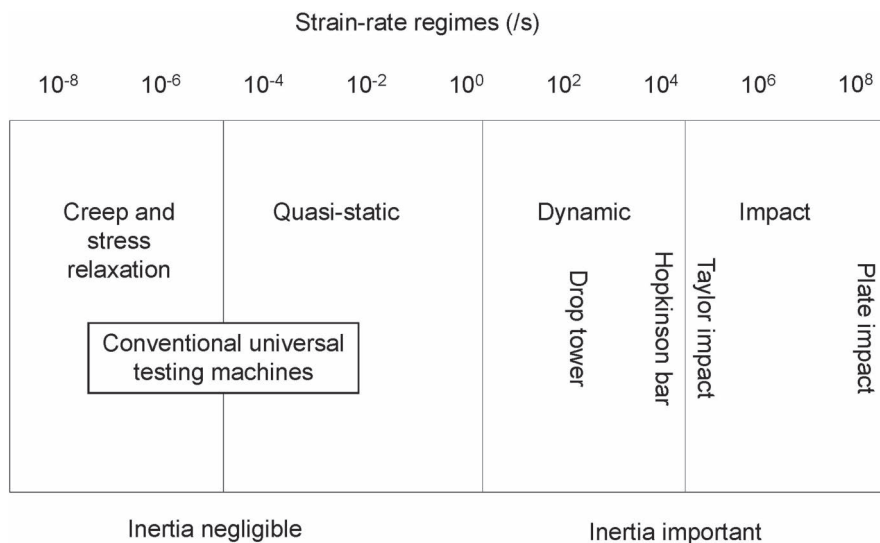
FIGURE 2.11   Strain-rate regimes. (Reprinted from Field, J. E., Walley, S. M., Proud, W. G., Goldrein, H. T. & Siviour, C. R. *International Journal of Impact Engineering*, 30(7), 725–775, Copyright 2004, with permission from Elsevier.)

apart (just using your hands) at different rates produces very different results. At low strain rates, the silly putty behaves much in the same way as a viscous fluid and is able to flow. Very little resistance to flow is offered by the material. At higher rates of loading, the user will experience resistance to flow as the long-chain molecules bind up. Brittle failure usually ensues.

For most metals, it is generally recognized that the dynamic yield strength of a material (or flow stress), Y, can be defined by the following proportionality:

$$Y \propto \ln \dot{\varepsilon}_\mathrm{p} \tag{2.32}$$

where $\dot{\varepsilon}_\mathrm{p}$ is the effective plastic strain rate; it has the unit of s^{-1}. The flow stress in this case is the stress taken at any point along the plastic stress–strain curve. During inelastic deformation, a considerable amount of work is converted to heat. This can lead to thermal softening of the metal where the flow strength of the material is reduced with increasing temperature. For high strain-rate applications, the process is adiabatic as there is little time for heat to be dissipated in the surrounding material. This gives rise to localized thermal softening. The effect of thermal softening on the yield strength of a metal can be described by the following equation:

$$Y = Y_0 \left[1 - \left(\frac{T - T_\mathrm{r}}{T_\mathrm{m} - T_\mathrm{r}} \right)^m \right] \tag{2.33}$$

where T_m is the melting temperature, and T_r is some reference temperature (such as the room temperature), T is the measured temperature and Y_0 is the quasi-static measure of yield strength of the material. The exponent m is called the thermal softening exponent and is constant for a known material.

Johnson and Cook (1983) brought these equations together along with a strain-hardening term to describe the tensile flow stress of a number of metals. It has now become one of the most widely used equations to describe the flow stress of a material subjected to large strains, strain rates and temperature and is regularly used within computational codes called hydrocodes that can simulate dynamic phenomena such as impact and penetration (mainly because of its elegant simplicity). The Johnson–Cook equation is given by (Johnson and Cook, 1985):

$$Y = \left(Y_0 + B\varepsilon_\mathrm{p}^n \right)\left(1 + \mathrm{C} \ln \dot{\varepsilon}_\mathrm{p}^* \right)\left(1 - \left(T^* \right)^m \right) \tag{2.34}$$

where
  Y_0 is the quasi-static yield strength of the material.
  B and n are the strain (or work) hardening constants.
  ε_p is the amount of equivalent plastic strain.
  $\dot{\varepsilon}_\mathrm{p}^*$ is the dimensionless plastic strain rate ($\dot{\varepsilon}_\mathrm{p}^* = \dot{\varepsilon}_\mathrm{p}/\dot{\varepsilon}_0$), $for\ \dot{\varepsilon}_0 = 1.0\ \mathrm{s}^{-1}$.
  C is a strain-rate constant.
  T^* is the homologous temperature defined by $T^* = (T - T_0)/(T_\mathrm{m} - T_0)$.
  T_0 is the ambient or reference temperature (usually 293 K).
  T_m is the melting temperature. The temperatures are measured in degrees Kelvin.
  m is the thermal softening exponent.

Notably, there are other constitutive models that describe the dynamic behaviour of materials, and the reader is directed to seminal works by Steinberg et al. (1980), Zerilli and Armstrong (1987) and Follansbee and Kocks (1988) as examples. A good overview of these and other constitutive models is provided by Meyers (1994). We will review constitutive models in some detail in Chapter 6.

For ceramic materials, it is generally accepted that their strength is relatively insensitive to strain rate until around $10^2 - 10^3$/s is reached. At this point, the strength of the ceramic becomes highly strain-rate sensitive. The reason for this is unclear, although some researchers have suggested that crack inertia plays a part (Lankford, 1981; Walley, 2010) (i.e. the crack growth rate determines the strain rate sensitive nature of these materials). However, ultimately, there are a multitude of problems with testing the high strain-rate response of ceramics due mostly to their highly brittle nature and high compressive strength (Walley, 2010).

There is a school of thought that suggests that the strain-rate response of ceramic materials in particular is less important than their pressure-dependent behaviour. Further, it is possible that during bullet penetration, the resistance offered by highly fractured material is affected by the local pressure. It is known that as a projectile penetrates a ceramic target, the material at the impact site changes very quickly from an intact state to a highly broken or comminuted state. The challenge is measuring the strength of this material during a penetration event. Various attempts have been made to assess the properties of comminuted ceramic materials, and the evidence suggests that there is a considerable stiffness reduction, and there is possibly a cap on the maximum strength that such material can withstand. However, what is surprising is that broken ceramic still has use in resisting penetration.

There are various tests that can be used to investigate the high strain rate of materials, and a brief review is given here. Notably, more extensive reviews can be found in studies by Meyers (1994) and Field et al. (2004). Each test will apply stress to the material in a slightly different fashion to another test. Table 2.7 summarizes these tests.

2.7.1   CHARPY IMPACT TEST

This test was developed to examine the amount of energy that was expended during an impact. It is sometimes referred to as the Charpy V-notch test. The Charpy V-notch test is an American Standards of Testing Materials (ASTM) standard.

A Charpy impact test consists of releasing a pendulum of a fixed mass and length such that it impacts a V-notched sample. Despite the fact that the velocity of impact is low (~5 m/s), the strain rate accessed in a Charpy test can be quite high due to the small dimension over which plastic deformation occurs (Meyers and Chawla, 1999). The sample is square in cross section and has a V-notch machined into one surface. Once a fracture occurs in the sample, the amount of energy that is transferred to the sample can be estimated by measuring the initial and final heights of the pendulum. This provides a measure of the energy to fracture the sample. Both the size of the notch and the size of the sample affect the result, and therefore, this test is only used to compare the impact toughness for identical geometries of samples. Hence,

TABLE 2.7

Summary of Common Material Testing Techniques

Test	Velocity of Impactor (m/s)	Stress/Strain Condition	Strain Rate (/s)	Result of Test
Quasi-static tensile/ compression test	Not measured	Uniaxial stress	10^{-4} to 10^{-2}	Stress–strain curve
Charpy impact test	Not measured	Combined stress	10^2–10^3	Impact energy required to break notched coupon
Instrumented drop tower	1–25	Variable	10–10^2	Force–time curve
Split-Hopkinson pressure bar (SHPB) test	5–40	Uniaxial stress	10^2–10^3	Dynamic stress–strain curve
Taylor test	100–500	Combined stress	10^2–10^4	Dynamic strength; validation of computational models
Flyer plate test	100–4000+	Uniaxial strain	10^5–10^7	Hugoniot curves; Hugoniot elastic limit (HEL) measurements; spall strengths

the results are more qualitative in nature and are generally of little use for design purposes—except in the sense of when comparing similar materials.

A variation on the theme of the test is the Izod test with the principal difference being the way in which the specimen is supported.

2.7.2 INSTRUMENTED DROP TOWER TEST

Instrumented drop towers are not usually used to measure the dynamic properties of materials, although they can be configured to do so. A single drop tower can be configured for both compression and tensile tests, and the main data collection is usually achieved through a piezo-elastic transducer located in the impactor (or 'tup'). Equally, strain data are acquired through the use of a strain gauge applied to the sample or by visual means using a high-speed camera. Velocities of impact are quite modest (~1–25 m/s), and the main purpose of the machine is to simulate an impact from a dropped mass at height by either dropping the tup mounted on a carriage from the actual height or from a 'simulated' height through the use of spring acceleration or a bungee cord attached to the carriage and base.

2.7.3 SPLIT-HOPKINSON PRESSURE BAR TEST

The split-Hopkinson pressure bar apparatus was developed in the 1940s by Herbert Kolsky (it is sometimes referred to as the Kolsky bar). It is principally used to derive a dynamic stress–strain curve for a material at varying temperatures, and therefore, it ideally lends itself for furnishing constitutive models, such as the Johnson–Cook strength model discussed in Section 2.7.

Essentially, a projectile (or striker bar) strikes an incident bar so that the pulse that is measured within it is large with respect to the size of the specimen. The incident bar must remain elastic, and therefore, the wave that is travelling along it is elastic in nature; typically, this means that the incident bar is made from a material with high (or relatively high) yield strength such as maraging steel. Other materials (including aluminium and magnesium alloys) are used when the specimen in question is of low impedance. The elastic wave traverses the incident bar and reaches the specimen that is sandwiched between it and the transmission bar. Again, the transmission bar remains elastic. As the wave enters the specimen reverberations occur in the sample such that the sample 'rings up' to equilibrium (see below). This typically occurs after approximately three reverberations. Strain gauges are attached to both the incident and transmitted bars to measure the strain. Measurements are made of the incident pulse, the reflected pulse (reflected from the sample) and the transmitted pulse. From these three pulses, a stress–strain relationship can be established for the sample; strain rates of 10^2–10^4/s are usually accessible by this technique.

It is important to note that the state of stress is not directly measured from the sample but rather calculated from the incident, reflected and transmitted pulses. The sample is plastically deformed during the process, and this is achieved either by using a sample of lower impedance and/or yield strength or cross-sectional area change that 'amplifies' the stress in the sample according to

$$\sigma(t) = E \frac{A_0}{A_s} \varepsilon_T(t) \tag{2.35}$$

where σ is the stress in the specimen, E is Young's modulus of the bars, A_0 is the cross-sectional area of the bar, A_s is the cross-sectional area of the specimen and ε_T is the transmitted strain measured in the transmission bar.

The strain rate $\dot{\varepsilon}(t)$ and strain $\varepsilon(t)$ in the specimen are then given by the following equations:

$$\dot{\varepsilon}(t) = -\frac{2c_0}{l_s} \varepsilon_R \tag{2.36}$$

$$\varepsilon(t) = -\frac{2c_0}{l_s} \int_0^t \varepsilon_R \cdot dt \tag{2.37}$$

where l_s is the current length (or thickness) of the specimen, ε_R is the reflected strain magnitude and c_0 is the elastic wave speed in the bar and can be calculated using

$$c_0 = \sqrt{\frac{E}{\rho_0}} \tag{2.38}$$

ρ_0 is the density of the bars and E is their Young's modulus.

Typical measurements of strain (from the strain gauges located on the incident and transmission bars) are shown in Figure 2.12. The negative strain is compressive.
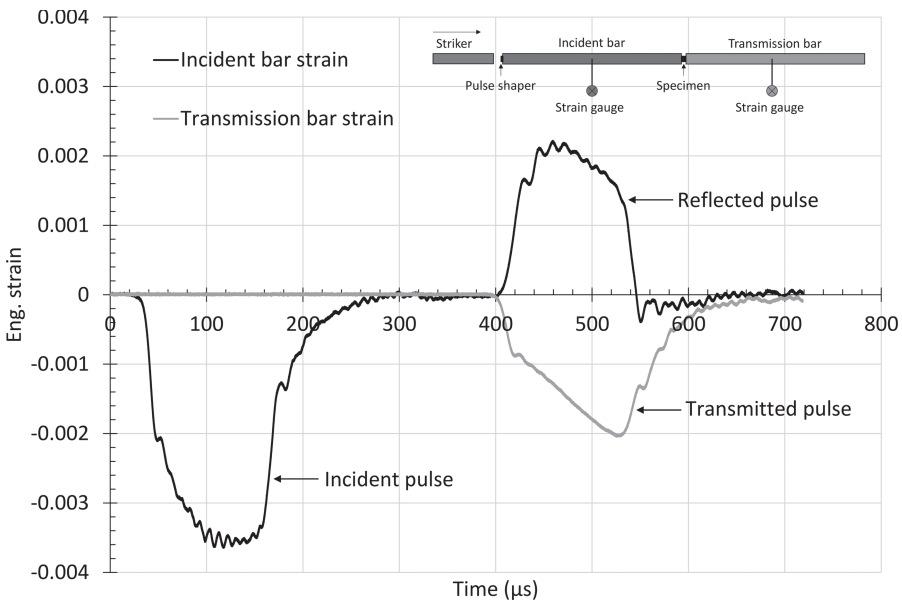
FIGURE 2.12 Split-Hopkinson Pressure Bar strain measurements in the incident and transmission bars for a duplex stainless steel (sample length = 4.5 mm, sample diameter = 7.5 mm, bar diameter = 19.05 mm, striker bar length = 304.8 mm and impact velocity of the striker = 33.6 m/s). A pulse shaper was used in this experiment to shape the incident pulse. (See Ameri et al., 2019.)

Two important assumptions are made in the derivation of these equations: (1) The forces on the two ends of the specimen are identical (that is, quasi-static stress equilibrium is achieved), and (2) the specimen plastically deforms at constant volume. If these two conditions are violated then unreliable test data is produced. The full theoretical derivation of the theory is provided in Gray III (2000).

The fact that quasi-static stress equilibrium is achieved means that the inertial effects are ignored. Consider a sample that is subjected to compression. Very simply, we can draw the free-body diagram of an SHPB sample in a test so that it looks like Figure 2.13. That is, the sum of the horizontal forces acting on the sample must add up to zero during the test.

This means that forces due to inertia (acceleration) are being ignored in the analysis. This is generally fine for materials undergoing large strains but is problematic
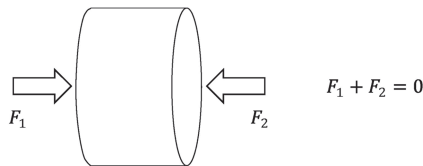
FIGURE 2.13 Split-Hopkinson Pressure Bar sample being subjected to quasi-static equilibrium.

where materials have low strains to failure (i.e. ceramics) or low wave speeds (and low strains to failure, i.e., polymer composites). In both cases, equilibrium is not reached before failure occurs and therefore it is not easily possible to derive the stress–strain response of the material.

It is important to confirm that during a test, a constant strain rate is realized. A constant strain rate demonstrates that stress equilibrium has occurred and a valid material characterization measurement has been done (Gray III, 2000, Ellwood et al., 1982). Standard SHPB tests involve the direct impact of a striker bar on an incident bar, generating a rectangular incident elastic stress-wave pulse with significant oscillations from dispersion effects. Using such a pulse violates the force equilibrium and constant strain-rate conditions during the test period for significant strain-hardening materials and for brittle materials, where failure occurs before equilibrium is achieved. To overcome this problem a 'pulse shaper' is often used as a mechanism for modifying the profile of the incident pulse and dampening out any oscillations. This is commonly in the form of a thin metal disc, or combination of metal discs, that are placed at the striker/incident bar interface. The design of the pulse shaper is often tailored to the specific test (Ameri et al., 2019).

Different materials can be tested in a Split-Hopkinson Pressure Bar, and typically, specimens are quite small in diameter. However, given that a large number of grains (crystals) are required to ensure that the specimen behaves as a bulk material, large-grained materials (or material with large aggregate present such as concrete) require larger specimen sizes and consequently larger apparatus (e.g. 200 mm × 200 mm; see Albertini et al., 1999).

2.7.4 TAYLOR TEST

The Taylor test was developed by G. I. Taylor (1946, 1948) to examine the high-rate response of ductile materials and is achieved by simply firing a rod onto a rigid anvil. Modern high-speed photographic techniques have provided a route to study the real-time deformation of the rod from which pertinent high strain-rate data can be derived. During the experiment, the rod is fired at the anvil and recovered, and the deformation is measured.

The mechanics of how the Taylor rod deforms can be described as follows. On impact, an elastic wave traverses along the length of the rod at the elastic wave speed. This is followed by the slower-moving plastic compression wave. When the elastic compression wave reflects off the rear surface of the rod, it travels back towards the impact face as a release wave. At some point, the elastic release wave and the plastic compression front collide, and the plastic deformation ceases due to the stress being released to zero. Thus, the recovered sample will have a plastically deformed section of a given length that can be measured.

An example of a Taylor test is shown in Figure 2.14. In this example, the test was carried out in a reverse ballistic mode. That is, an 'anvil projectile' was fired towards a stationary rod. However, the outcome is the same. This was achieved with a large calibre smooth-bore gun where a thick disc of high-strength steel was mounted onto a polymer sabot and accelerated to its target. The progression of the plastic wavefront in the rod can be seen by the arrows in Figure 2.14b–d.
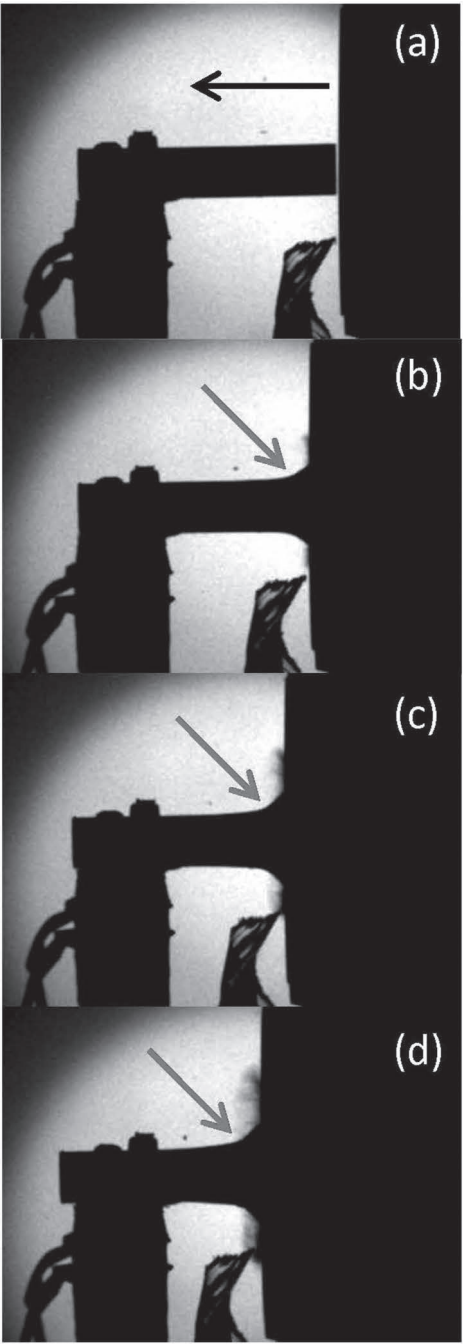
FIGURE 2.14   A Taylor test. In this case, the anvil is being fired at a stationary rod, which is made from a high-strength armoured steel. The anvil is moving from right to left (as shown in (a)), the progression of the plastic wavefront is indicated by the arrows in (b)–(d).

2.7.4.1 Introductory Concepts

The theoretical treatment of how a rod plastically deforms when striking an anvil will now be considered as this is relevant to the deformation of bullets during the impact of a target. It can be considered that the rod can plastically deform such that h is the temporal thickness of the plastically deformed section, x is the length of material that has not been plastically compressed and u is the velocity of the material that has not been compressed (i.e. including the end of the rod); U is the rod's impact velocity and is initially equal to u (the velocity of the rear boundary) until the arrival of the elastic wave. The following equations describe the small changes in u, h and x during one passage of the elastic wave from the plastic boundary and back to it.

The time taken for the passage of the elastic wave to traverse from the elastic boundary and back to it (see Figure 2.15) is

$$dt = \frac{2x}{c} \tag{2.39}$$

where c is the elastic wave velocity.

The extension to the plastic portion in the rod during this time (i.e. $2x/c$) is

$$dh = v\frac{2x}{c} \tag{2.40}$$

where v is the velocity of the plastic wavefront.
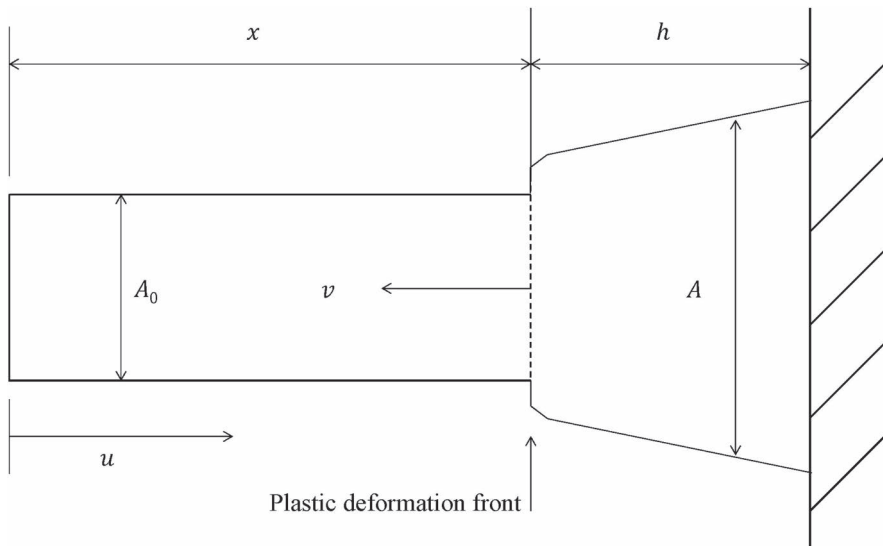
FIGURE 2.15 Taylor impact test showing the plastic deformation front and associated dimensions.

The reduction in length of the elastic portion during this time (i.e. $2x/c$) is

$$dx = -(u+v)\frac{2x}{c} \tag{2.41}$$

Remember that $dx \neq dh$ is due to the elastic portion continuing towards the anvil at velocity u.

2.7.4.2 Approximate Formula for Estimating the Yield Point

To establish an approximate formula for estimating the dynamic yield strength (Y) from the measurements of slugs after impact, Taylor (1948) presented the following analysis assuming that the plastic–elastic boundary moves outwards from the impact face at a uniform velocity to its final position. It should be noted that in the following analysis, the plastic wavefront velocity v is a constant.

It is already known (from Equation 2.39) that

$$dt = \frac{2x}{c} \tag{2.42}$$

But the velocity of the plastic wavefront is given to us by

$$v = \frac{dh}{dt} \tag{2.43}$$

Therefore,

$$dh = v.dt = v\frac{2x}{c} \tag{2.44}$$

And

$$\frac{dx}{dt} = -(u+v) \tag{2.45}$$

It is also known that the change in the velocity of the back portion of the velocity is given to us by

$$du = -\frac{2Y}{\rho_0 c} \tag{2.46}$$

It will be seen in Chapter 5 how this formula is derived; essentially, this is the formula for the particle velocity in the material at the free surface (Meyers, 1994). Here, it is assumed that the material is elastic–perfectly plastic, and therefore, the plastic stress is constant irrespective of strain.

As

$$dx = -(u+v)\frac{2x}{c} \tag{2.47}$$

$$\frac{du}{dx} = \frac{Y}{(u+v)\rho_0 x} \tag{2.48}$$

Integrating

$$\int (u+v)\,du = \frac{Y}{\rho_0}\int \frac{dx}{x} \tag{2.49}$$

$$\frac{(u+v)^2}{2} = \frac{Y}{\rho_0}\ln x + C \tag{2.50}$$

Initially, it is known that $u = U$ and $x = L$ (the initial length of the rod). So now, C can be solved, and this gives

$$\frac{(u+v)^2}{2} - \frac{(U+v)^2}{2} = \frac{Y}{\rho_0}\ln\left(\frac{x}{L}\right) \tag{2.51}$$

Expanding,

$$\frac{u^2}{2} + vu - \frac{U^2}{2} - vU = \frac{Y}{\rho_0}\ln\left(\frac{x}{L}\right) \tag{2.52}$$

However, in the final state, when $u = 0$, $x = X$; therefore,

$$-\frac{U^2}{2} - vU = \frac{Y}{\rho_0}\ln\left(\frac{X}{L}\right) \tag{2.53}$$

Now, to eliminate v, it is assumed that the time taken to decelerate the rod to zero could be given by

$$T = \frac{L_1 - X}{v} = \frac{2(L - L_1)}{U} \tag{2.54}$$

Therefore,

$$\frac{v}{U} = \frac{(L_1 - X)}{2(L - L_1)} \tag{2.55}$$

which, when substituted into Equation 2.53, becomes

$$Y = \frac{\rho_0 U^2 (L - X)}{2(L - L_1)\ln\left(\dfrac{L}{X}\right)} \tag{2.56}$$

Measurements are taken according to Figure 2.16. Taylor pointed out that this equation is only an approximation as a uniform deceleration has been assumed. In reality,
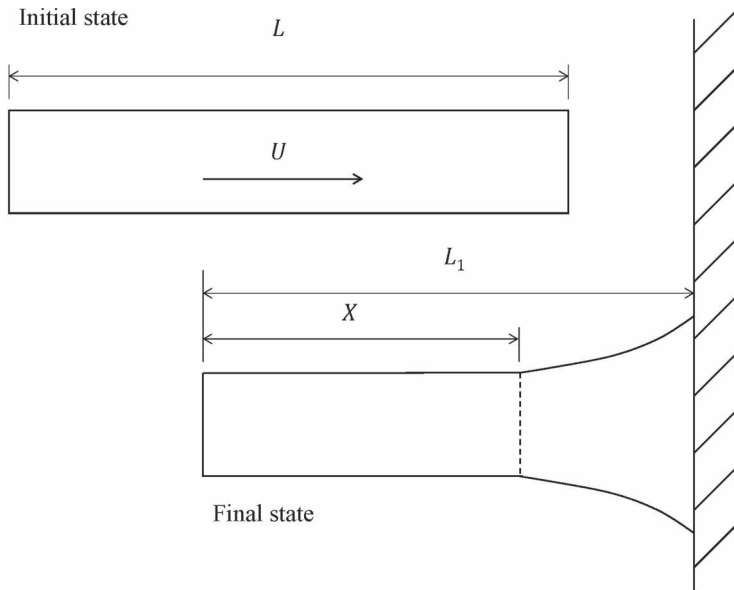
FIGURE 2.16   Taylor test showing before and after states.

deceleration is non-uniform. However, as a first-order approximation, it gives reasonable values when compared to Whiffin's (1948) experimental results.

Wilkins and Guinan (1973) built up Taylor's analysis and developed a similar model for establishing the yield point of a material from recovered specimens based on Newton's second law ($F = ma$). They showed that

$$\frac{L_1}{L} = \exp\left(-\frac{\rho_0 U^2}{2Y}\right)$$

(2.57)

Again, similar to Taylor, this implied that the only parameters that affected a cylinder's geometry after impact were the density and the yield strength of the material. Using computer simulations, they also showed that the profile of the projectile gives an erroneous location of the plastic front that decelerates the elastic portion, and it actually stays closer to the rigid boundary than originally thought (see Figure 2.17). To account for this, they showed that

$$\frac{L_1}{L} = \left(1 - \frac{h}{L}\right)\exp\left(-\frac{\rho_0 U^2}{2Y}\right) + \frac{h}{L}$$

(2.58)

where h is the distance from the anvil to the plastic wavefront that contributes to the deceleration.

In this analysis, they noted that the position to which the plastic wave moved was independent of velocity but proportional to the original length of the specimen (i.e. $h/L = const$).
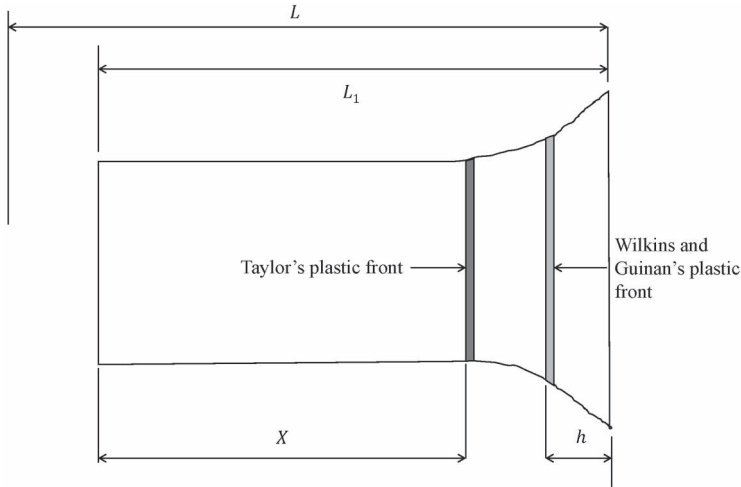
FIGURE 2.17 Deformation of the rod showing the positions of the deformation front as assumed by Taylor (1948) and Wilkins and Guinan (1973). (From Taylor, G. 1948, *Proceedings of the Royal Society of London. Series A. Mathematical and Physical Sciences*, 194(1038), 289–299; Wilkins, M. L. & Guinan, M. W. 1973, *Journal of Applied Physics*, 44(3), 1200–1206.)

Example 2.4

A mild steel-cored bullet strikes a rigid steel armour plate at 200 m/s. The original length of the bullet was 25 mm. If computer simulations show that the plastic wavefront ceased at $h = 5$ mm from the rigid surface, and the final length of the bullet was 15 mm, calculate the yield strength, Y of the bullet.

Firstly, let us look at Taylor's (1948) approach. We are going to assume that in this case, the position of the plastic boundary, h, is the same position of the plastic boundary as assumed by Taylor.

So,

$$X = L_1 - h = 15 \times 10^{-3} - 5 \times 10^{-3} = 10 \text{ mm}$$

From Equation 2.56, it is seen that

$$Y = \frac{\rho_0 U^2 (L - X)}{2(L - L_1) \ln\left(\frac{L}{X}\right)} = \frac{7800 \times 200^2 \left(25 \times 10^{-3} - 10 \times 10^{-3}\right)}{2\left(25 \times 10^{-3} - 15 \times 10^{-3}\right) \ln\left(\frac{25 \times 10^{-3}}{10 \times 10^{-3}}\right)} = 255 \text{ MPa}$$

This problem will now be analyzed using the work of Wilkins and Guinan (1973), but first, Equation 2.58 needs to be rearranged to find Y. This is given by

$$Y = \frac{-\rho_0 U^2}{2\left[\ln(L_1 - h) - \ln(L - h)\right]} \tag{2.59}$$

and therefore

$$Y = \frac{-7800 \times 200^2}{2\left[\ln\left(15 \times 10^{-3} - 5 \times 10^{-3}\right) - \ln\left(25 \times 10^{-3} - 5 \times 10^{-3}\right)\right]} = 225 \text{ MPa}$$

So, both types of analysis provide similar results for the yield strength of the bullet core with the Wilkins and Guinan method providing a more conservative result. Note that larger differences are observed when there are small deformations (i.e. $L_1 \rightarrow L$). This analysis assumes that the final plastic wavefront position is the same.

2.7.5 DYNAMIC EXTRUSION TEST

A modification to the Taylor test is the dynamic extrusion test where, instead of a rod being fired at a flat anvil, a sphere or bullet-shaped projectile is fired into a conical die. The purpose of this is to look at the main deformation modes and examine how the material fails as it is being stretched during the dynamic extrusion process. This technique was first proposed by Gray et al. (2006) for copper and has subsequently been used to investigate other materials. Figure 2.18 shows some results of dynamically extruded zirconium (Escobedo et al., 2012). Here, the necking and failure are captured using high-speed photography. The material is subsequently decelerated in a low-density medium to soft-capture the fragments for micro-structural analysis. The high-speed photography data are particularly useful for the validation of constitutive models and provide a route for tweaking material property data in the model.
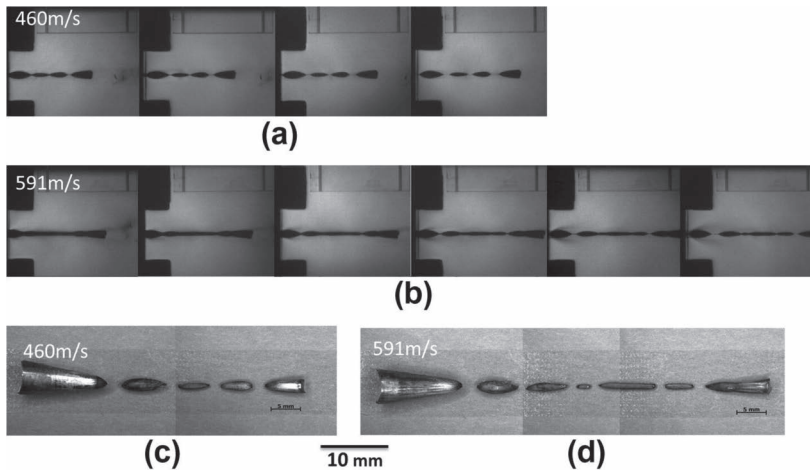
FIGURE 2.18   High-speed photography showing how zirconium samples exited a die after extrusion (a and b). Stereographic images of reassembled Z_r specimens (c and d). (Reprinted from Escobedo, J. P. et al. 2012, *Acta Materialia*, 60(11), 4379–4392, Copyright 2012, with permission from Elsevier.)

2.7.6   FLYER-PLATE TEST

Flyer-plate tests were developed to examine shock wave propagation in materials, and these experiments take the material to extremely high strain rates.

A typical experimental setup is shown in Figure 2.19. Here, a flyer plate is accelerated towards the target and arrives so that all points on the projectile's surface make contact with the target simultaneously. Consequently, both the flyer plate (projectile) and the target need to be lapped to very high tolerances (typically $<\pm5\,\mu$m). Projectile alignment before impact is also important. The impact of a flyer plate generates a planar shock wave in the target. In this situation, all strain is accommodated along the impact axis, whilst the orthogonal components of strain are zero due to inertial confinement. Consequently, the orthogonal components of stress are non-zero. Therefore, in summary, the conditions of stress and strain are written in the target as

$$\varepsilon_x \neq \varepsilon_y = \varepsilon_z = 0 \quad \text{and} \quad \sigma_x \neq \sigma_y = \sigma_z \neq 0, \tag{2.60}$$

where the subscript x denotes the condition along the impact axis, and the subscripts y and z denote the conditions orthogonal to the impact axis.

The setup shown in Figure 2.19 denotes a gun-launched flyer plate mounted on a sabot, although it is also possible to explosively accelerate a flyer plate. In this experimental setup, two spatially separated gauges are shown to measure the shock wave velocity in the material (attached to a suitable digital storage oscilloscope) and stress within the sample. A cover plate is necessary to protect the first gauge and would be made from the same material as the flyer plate. The first gauge records a rapid rise in stress due to the arrival of the shock wave followed by a plateau stress (referred to as the Hugoniot stress) and an elastic–plastic release. The second gauge records a precursor wave that has separated out from the main shock front, and this is apparent when the shock wave velocity is slower than the elastic wave speed in the material. The magnitude of the precursor is known as the Hugoniot elastic limit (HEL) and is analogous to the yield strength of the material. The HEL has been linked to the
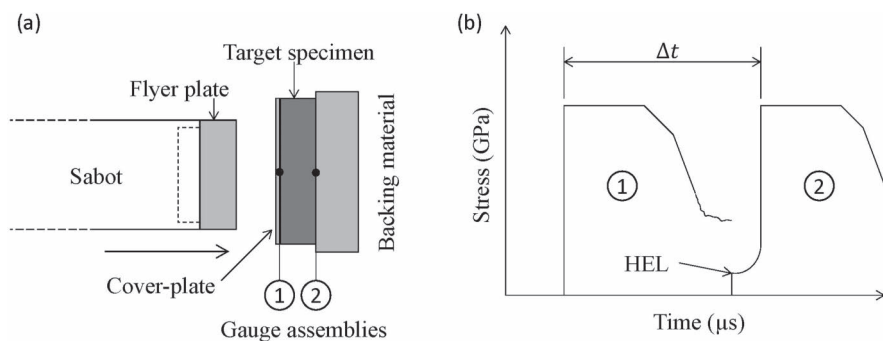
FIGURE 2.19   (a) A schematic of the flyer-plate technique where gauges are employed and (b) the expected gauge response when the backing material has the same shock impedance as the target material.

ballistic performance of certain materials such as ceramics. This is followed by post-yield flow and the 'plastic' shock front. The shock velocity is then established by measuring Δt, and with knowledge of the sample thickness, it is possible to calculate the shock wave velocity.

Using gauges is one of several diagnostic techniques that can be used. However more commonly it is non-invasive laser-based techniques that are preferred as these directly record the free-surface velocities of the target material during shock. This allows for the direct measure of the particle velocity in the material, which is an important parameter for establishing the shock conditions in the target. Examples of systems that employ this approach are Velocity Interferometer System for Any Reflector (VISAR) developed by Barker and Hollenbach (1972), and Photon Doppler Velocimetry (PDV), see (Strand et al., 2006).

These types of experiments are fundamental to the establishment of an equation of state for the material by providing a reference curve called a Hugoniot. The Hugoniot (named after the French engineer Pierre-Henri Hugoniot, 1851–1887) is empirically derived and is usually described in terms of shock velocity (U_s) and particle velocity (u_p), pressure (P) and u_p, or P and specific volume (V) where the specific volume is given by $V = 1/\rho$. Once a Hugoniot is established, the parameters for the equation of state can be calculated that can be input into hydrocodes (such as ANSYS AUTODYN™ or LS-DYNA), which are commonly used to simulate the ballistic response of materials. It is important to realize that the Hugoniot is not a plot of the history of pressure increase as a shock is formed but rather that it is a locus of all the possible shock states achievable. This will be discussed in more detail in Chapter 5 where stress waves and shock are examined.

2.8 SUMMARY

Material science plays a large role in armour design and having a good understanding of how materials behave under load is crucial for sound design. In particular, bullets, bombs and blast push materials to their extreme limits of strength, and therefore, it is good to know how materials fail. Materials have a theoretical strength—that is, the maximum strength that can be achieved for a perfectly uniform structure that is defect-free. However, all materials possess defects that compromise their ability to withstand load. We have seen in this chapter that crystals have natural defects called dislocations, and these play a role in how a material will deform plastically.

We have seen that the behaviour of materials at elevated deformation rates is generally different than at lower deformation rates. Therefore, the behaviour of a bullet striking a target cannot be predicted just from knowing the quasi-static values of strength and ductility (although they do serve as a good approximation in the first instance). A complete picture of the work hardening, strain-rate sensitivity and thermal softening characteristics of the jacket, core and target will help in the understanding of how the bullet penetrates.

There are a number of techniques that can be employed to investigate the high strain-rate response of a material, and these have been quickly reviewed here. These techniques subject the material to different loading rates and subject the sample to

different stress states. The results from these tests can then be used to input into computer codes to simulate complex loading problems. More on these in Chapter 6.

REFERENCES

Albertini, C., Cadoni, E. & Labibes, K. 1999. Study of the mechanical properties of plain concrete under dynamic loading. *Experimental Mechanics,* 39(2), 137–141.

Ameri, A. A. H., Brown, A. D., Ashraf, M., Hazell, P. J., Quadir, M. Z. & Escobedo-Diaz, J. P. 2019. An effective pulse-shaping technique for testing stainless steel alloys in a split-Hopkinson pressure bar. *Journal of Dynamic Behavior of Materials*, 5, 39–50.

Barker, L. M. & Hollenbach, R. E. 1972. Laser interferometer for measuring high velocities of any reflecting surface. *Journal of Applied Physics*, 43, 4669–4675.

Callister, W. D. 2007. *Materials Science and Engineering: An Introduction*. 7th ed. New York: John Wiley & Sons, Inc.

Ellwood, S., Griffiths, L. J. & Parry, D. J. 1982. Materials testing at high constant strain rates. *Journal of Physics E: Scientific Instruments,* 15, 280–282.

Escobedo, J. P., Cerreta, E. K., Trujillo, C. P., Martinez, D. T., Lebensohn, R. A., Webster, V. A. & Gray, G. T. 2012. Influence of texture and test velocity on the dynamic, high-strain, tensile behavior of zirconium. *Acta Materialia,* 60(11), 4379–4392.

Field, J. E., Walley, S. M., Proud, W. G., Goldrein, H. T. & Siviour, C. R. 2004. Review of experimental techniques for high rate deformation and shock studies. *International Journal of Impact Engineering,* 30(7), 725–775.

Follansbee, P. S. & Kocks, U. F. 1988. A constitutive description of the deformation of copper based on the use of the mechanical threshold stress as an internal state variable. *Acta Metallurgica,* 36(1), 81–93.

Gray III, G. T. 2000. Classic split Hopkinson pressure bar testing. *In:* Kuhn, H. & Medlin, D. (eds.) *ASM Handbook: Mechanical Testing and Evaluation*, vol. 8, pp. 462–476. Materials Park, OH: ASM International.

Gray, G. T., Cerreta, E., Yablinsky, C. A., Addessio, L. B., Henrie, B. L., Sencer, B. H., Burkett, M., Maudlin, P. J., Maloy, S. A., Trujillo, C. P. & Lopez, M. F. 2006. Influence of shock prestraining and grain size on the dynamic-tensile-extrusion response of copper: Experiments and simulation. *AIP Conference Proceedings,* 845(1), 725–728.

Griffith, A. A. 1921. The phenomena of rupture and flow in solids. *Philosophical Transactions A,* 221(582–593), 163–198.

Johnson, G. R. & Cook, W. H. 1983. A constitutive model and data for metals subjected to large strains, high strain rates and high temperatures. *In: Proceedings of the 7th International Symposium on Ballistics*, The Hague, The Netherlands: American Defense Preparedness Association.

Johnson, G. R. & Cook, W. H. 1985. Fracture characteristics of three metals subjected to various strains, strain rates, temperatures and pressures. *Engineering Fracture Mechanics,* 21, 31–48.

Lankford, J. 1981. Mechanisms responsible for strain-rate-dependent compressive strength in ceramic materials. *Journal of the American Ceramic Society,* 64(2), C33–C34.

Meyers, M. A. 1994. *Dynamic Behaviour of Materials*. New York: John Wiley & Sons, Inc.

Meyers, M. A. & Chawla, K. K. 1999. *Mechanical Behavior of Materials*. Upper Saddle River, NJ: Prentice Hall.

Steinberg, D. J., Cochran, S. G. & Guinan, M. W. 1980. A constitutive model for metals applicable at high-strain rate. *Journal of Applied Physics,* 51(3), 1498–1504.

Strand, O. T., Goosman, D. R., Martinez, C., Whitworth, T. L. & Kuhlow, W. W. 2006. Compact system for high-speed velocimetry using heterodyne techniques. *Review of Scientific Instruments,* 77, 083108.

Taylor, G. 1948. The use of flat-ended projectiles for determining dynamic yield stress. I. Theoretical considerations. *Proceedings of the Royal Society of London. Series A. Mathematical and Physical Sciences,* 194(1038), 289–299.

Taylor, G. I. 1946. The testing of materials at high rates of loading. *Journal of the Institution of Civil Engineers,* 26(8), 486–519.

Walley, S. M. 2010. Historical review of high strain rate and shock properties of ceramics relevant to their application in armour. *Advances in Applied Ceramics,* 109(8), 446–466.

Whiffin, A. C. 1948. The use of flat-ended projectiles for determining dynamic yield stress. II. Tests on various metallic materials. *Proceedings of the Royal Society of London. Series A, Mathematical and Physical Sciences,* 194(1038), 300–322.

Wilkins, M. L. & Guinan, M. W. 1973. Impact of cylinders on a rigid boundary. *Journal of Applied Physics,* 44(3), 1200–1206.

Zerilli, F. J. & Armstrong, R. W. 1987. Dislocation-mechanics-based constitutive relations for material dynamics calculations. *Journal of Applied Physics,* 61(5), 1816–1825.

3 Bullets, Blast, Jets and Fragments

3.1 INTRODUCTION

Before we look at the technologies that help in saving lives, we need to assess what has historically been designed to take life away. It is only with a full understanding of these technologies that we can begin to assess how to protect people. The mechanisms of damage from weapons can be quite varied, and therefore, an introduction to bullets, blast, jets and fragments is given here.

3.2 SMALL-ARMS AMMUNITION

The word 'ammunition' is the term given to describe a bullet and the associated components that give it velocity. So, in the case of small arms, the ammunition is composed of (see Figure 3.1)

a. The primer
b. The cartridge
c. The propellant
d. Any ancillary piece (such as propellant packing)
e. The projectile (bullet)
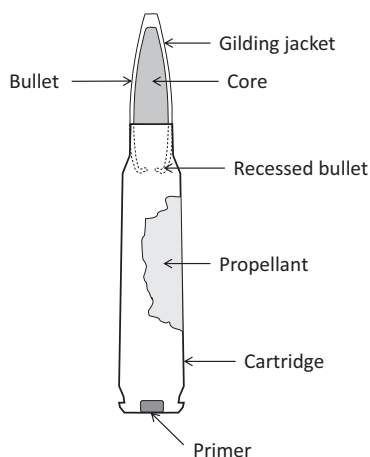
Ammunition	(v_0) (m/s)
5.56 mm x 45 mm SS109	920
7.62 mm x 39 mm PS Ball	720
7.62 mm x 51 mm Ball	820
7.62 mm x 51 mm FFV	950
14.5 mm x 114 mm BS41	1,000

FIGURE 3.1 Small-arms ammunition. Inset: a table of typical muzzle velocities (v_0) for different bullets.

Small-arms ammunition is typically characterized by the fact that the projectiles (or 'bullets') are small (relatively speaking), and the weapon system can be carried in an individual's 'arms'. The bullet generally consists of a penetrating mass (i.e. the bit that does all the work during penetration) surrounded by a gilding jacket that acts as a barrier, protecting the core of the bullet from the rifling of the barrel. Other types of bullets include incendiary and tracer rounds—these will not be covered here. The bullet itself comes in all sorts of shapes and sizes. Most bullets possess an ogival nose simply for aerodynamic stability and to reduce drag during flight. Similarly, some bullets may have a 'boat tail' (that is, a slightly reduced diameter at the base) to reduce drag at the rear of the projectile.

3.2.1 BULLET NOTATION

Ammunition is usually described in terms of the bullet's calibre and cartridge length. So, the ammunition that is described as 7.62×51 mm refers to a bullet of calibre of 7.62 mm and a cartridge length of 51 mm. Usually, the diameter of the bullet will be slightly larger than the stated calibre (by ~0.2 mm), and this is so that the bullet's jacket can engage in the grooves of the rifling with the calibre being measured to the 'lands' of the rifling in the gun barrel. A schematic showing the barrel and how the calibre is measured is given in Figure 3.2.

The purpose of the rifling is so that stability can be imparted to the projectile by causing it to spin during flight. As the projectile is fired, the rifle lands are driven into the jacket material. The rifling in the gun barrel is designed with a specific twist such that as the bullet moves along the gun barrel, it is forced to turn—thereby inducing its spin.

3.2.2 PENETRABILITY

The effect of the bullet depends largely on its weight, velocity, shape, calibre, stability and strength (hardness) of the core. For a bullet with a relatively high penetrative
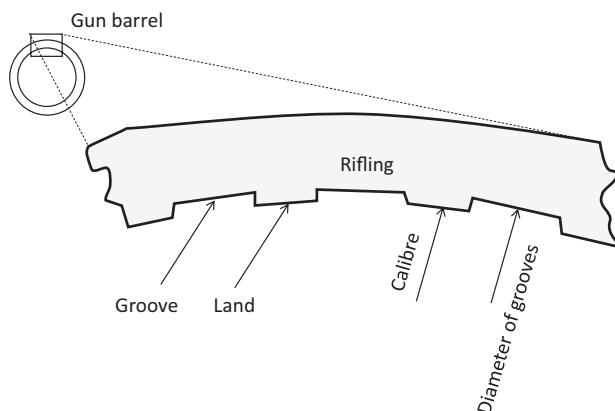
FIGURE 3.2 Definitions of rifling.
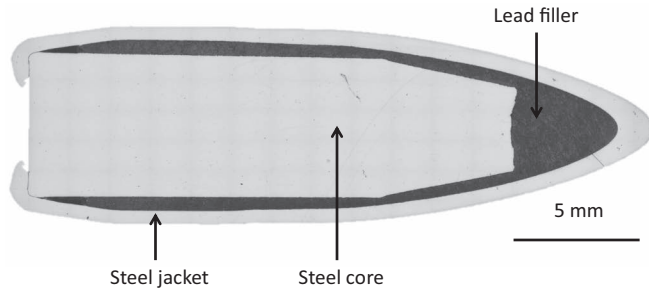
FIGURE 3.3 A polished section of a 7.62×3 9-mm Kalashnikov ball bullet showing the steel core, lead filler and jacket. (Courtesy of J. P. Escobedo.)

ability into armour, a fast, high-strength non-deforming core is important (such as tungsten carbide or hard steel). Such bullets are unsurprisingly called 'armour-piercing' (AP) bullets. For a bullet with relatively high stopping power in a human target, a heavy soft-deforming core is important (such as lead or 'soft' steel). Such bullets are normally called 'ball' rounds, presumably named after the first spherical lead shots.

An example of a ball round is shown in Figure 3.3. The core is made from a relatively soft steel (VHN=280), which enables it to deform when penetrating the target, and is enveloped by a lead filler and a steel jacket.[1] These types of bullets are relatively easy to stop with hard materials, and this projectile can be stopped (when fired from 10 m) by as little as 12 mm of mild steel (and less if the steel is an armour-grade). However, the other type of small-arms ammunition (the AP type) is more difficult to stop—mainly because of the relatively high kinetic energy (KE) densities and hardness values of the cores. KE density is a term that is frequently used to describe how penetrative an armour-piercing projectile is. It is given by the formula

$$KE_d = \frac{m_0 v_0^2}{2A} \tag{3.1}$$

where KE_d is the kinetic energy density, m_0 is the mass of the projectile, v_0 is its velocity and A is the cross-sectional area offered by the bullet.

For AP bullets, it is common to refer to the KE of the bullet's core—as it is this that does all the work in penetrating armour. The KE densities of various AP cores are presented in Table 3.1.

Figure 3.4 shows three different AP cores: (1) the Soviet 14.5×114-mm API BS41 core with a WC-Co core (v_0=~1000 m/s, ρ_0=14.9 g/cc, VHN=1400), (2) the Soviet 7.62×54-mm R API B32 steel core (v_0=~830 m/s, ρ_0=7.8 g/cc, VHN=920) and (3) the 7.62×51-mm FFV core with a WC-Co core (v_0=~950 m/s, ρ_0=14.9 g/cc, VHN=1550). Tungsten carbide is a hard and dense material, and therefore, the masses of these types of cores are high compared to similar steel-cored rounds

TABLE 3.1
KE Densities of a Selection of AP Cores

Designation	Core Material	Core Dia. (mm)	Mass of Core (g)	KE_d (MJ/m²)[a]
14.5-mm API BS41	Tungsten carbide	10.75	38.3	211
7.62-mm AP FFV	Tungsten carbide	5.60	5.9	108
7.62-mm API B32	Steel	6.09	5.4	63

[a] At muzzle velocity.

FIGURE 3.4   From left to right: 14.5×114-mm BS41 Armour-Piercing Incendiary (API) core, 7.62×54-mm R B32 API core and 7.62×51-mm Förenade Fabriksverken (FFV) core.

(of similar volumes). The muzzle velocities of these WC-Co cored bullets are relatively high too (for small-arms ammunition). Both of these factors lead to an increased KE density.

It is clear that reducing the diameter of the penetrator is important for increasing the level of penetration. Indeed, this is partly the reason why sub-calibre projectiles were invented in World War II. It was soon discovered that reducing the diameter of

TABLE 3.2

Typical Thicknesses of Armour That Are Required to Resist Perforation by a 7.62 mm×51 mm AP (Steel Core) Projectile and a 14.5 mm×114 mm AP B32 Projectile at Normal Incidence and Point-Blank Range

	Thickness (mm)	
Armour Material	7.62 mm×51 mm AP (Steel Core)	14.5 mm×114 mm AP B32
Mild steel	25	66
Rolled homogeneous steel	15	41
High hardness steel	13	36
Dual hardness steel (600/400 BHN)	8	-
AA 5083 alloy	48	134
AA 7017 alloy	-	97
AA 7020 alloy	45	-
AA 7039 alloy	38	91
Titanium alloy	17	48

Source: Ogorkiewicz, R. M. *AFV Armour and Armour Systems*. Course notes on: Survivability of Armoured Vehicles, Cranfield University, Shrivenham, Swindon, UK, 18–20 March 2002.

the round and housing it within a lightweight sabot, whilst maintaining a relatively large calibre of gun, improved penetrability dramatically.

Typical thickness of armour that is required to resist perforation from a 7.62 mm×51 mm AP projectile and a 14.5 mm×114 mm AP B32 projectile at normal incidence and point-blank range are provided in Table 3.2 (Ogorkiewicz, 2002). Both projectiles contain a steel core.

3.2.3 THE EFFECT OF THE BULLET'S JACKET DURING PENETRATION

With tungsten–carbide-cored bullets such as the 7.62-mm M993, the jacket metal is made from soft steel that envelopes a tungsten carbide core with an acute front tip. The jacket serves three main purposes: (1) to protect the barrel from the core, (2) to engage with the rifling of the barrel and (3) to provide a projectile shape optimized for free flight.

The bullet's jacket can affect penetration too—particularly into ceramic-faced armours. It has been known since 1878 that chilled cast iron projectiles would not penetrate a compound armour plate where the impact surface was hard, but when fired at the softer rear surface of the same plate, perforation occurred. This resulted in Captain English proposing that a projectile with a 'cap' of relatively soft wrought iron would stop the projectile from shattering to secure perforation against a hard face (Johnson, 1988). This was also proposed later in 1893 by Stepan Makarov (1849–1904), a Russian Admiral. Makarov realized that if a ductile cap was added to the shell, then the shock of the impact would be diminished thereby protecting the penetrator. It also had a secondary effect in that it provided confinement to the

(a) Uncapped AP shot   (b) APCBC shot
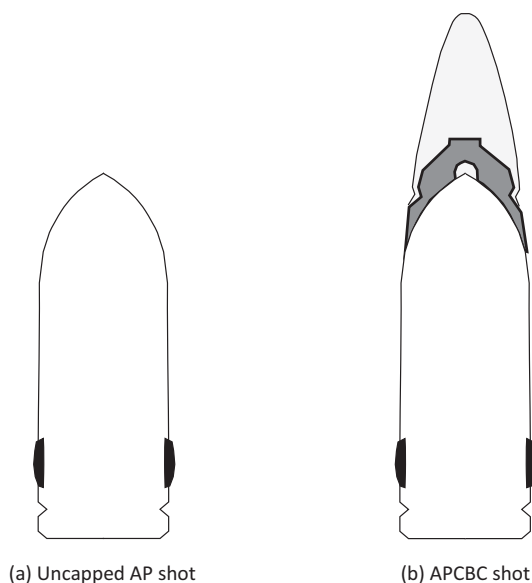
FIGURE 3.5 British 6-lb. AP shot showing (a) an uncapped AP projectile and (b) an APCBC shot. This shell was fired from a 2.24 in. (57 mm) calibre gun and had a mass of ~6 lb. (2.72 kg).

tip of the shell thereby hindering fractured material in the projectile separating and therefore enhancing the penetration. By 1915, this approach had been integrated into most Armour-Piercing shell designs (Anon, 1915). In WWII that this technique was extensively applied with the British 6-lb. armour-piercing cap (APC) projectile and armour-piercing cap, ballistic-cap (APCBC) projectile (see Figure 3.5). This was composed of the penetrator fitted with a ductile cap on the nose of the projectile. The purpose of the nose was to inhibit shattering when the projectile impacted a hard target (Goad and Halsey, 1982). With modern jacketed projectiles, the impact situation becomes slightly more complex in that hard-cored AP projectiles are designed to attack hard ceramic-based armour systems where both the core of the projectile and the ceramic plates are intrinsically brittle. Rosenberg et al. (1990) observed that removing the tip of the jacket from a 14.5-mm AP core resulted in a poor performance against a ceramic (AD-85) tile, whereas covering the ceramic with 3-mm copper plates appeared to result in the projectile performing better. They concluded that when the hard core impacted the ceramic tile, the lateral confinement of the cover plate prevented radial expansion of the core, and therefore, it could penetrate deeper into the target. Further results have been presented that showed that the jacket appeared to be pre-damaging the ceramic tile before the core arrives—further adding to the complexity (Hazell et al., 2013).

Additionally, against metal targets, it has been shown that when an AP projectile is subjected to non-zero yaw angles, the presence of the jacket helps to protect the core from fracture as it penetrates a finite thickness metal target (Francou and Giraud, 1998).

3.3   HIGHER-CALIBRE KE ROUNDS

Generally, there are two types of higher-calibre KE ammunition that are commonly fielded: the armour-piercing discarding sabot (APDS) round and the armour-piercing fin-stabilized discarding sabot (APFSDS) round (see Figure 3.6).

The APDS round normally consists of a dense core (usually tungsten carbide) with a length-to-diameter ratio (L/d) of between 6 and 7. These have been used in anti-tank guns since the latter part of WWII and have largely been superseded by the APFSDS round. An APFSDS round is usually made from tungsten-heavy alloy (WHA) or depleted uranium (DU) alloy, although some early Soviet APFSDS rounds were made from maraging steel. These projectiles have L/d ratios of between 15 and 25 and muzzle velocities in the range of 1400–1900 m/s.

The design shown in Figure 3.6 is typical for a large-calibre APFSDS round with a penetrator made from a heavy metal. The rod itself will be sub-calibre, that is, it will have a smaller diameter than the bore of the gun tube from which it is fired. For a 120-mm APFSDS round, rod diameters in the range of 25–35 mm are not uncommon. The rod itself will be carried along the gun tube by a sabot system, and in this case, there are three sabot segments that will become detached from the rod and separate out after the round has left the gun tube. The white plastic rings are the slipping driving bands that enable this particular round to be fired from a rifled gun tube—the United Kingdom's L30 120-mm gun, that is fitted to the Challenger 2. These rings engage with the rifling and reduce the amount of spin imparted to the sub-projectile (rod)—which is drag stabilized by six aluminium alloy fins. However, a small amount of spin is still desirable to maintain a stable trajectory as it cancels out any asymmetry in the rod due to manufacturing errors.

FIGURE 3.6   A tungsten alloy APFSDS round complete with sabot, slipping driving bands and fin protector.

TABLE 3.3

Armour-Piercing Capabilities of Machine Gun and Cannon Ammunition: Thickness of Homogeneous Steel Armour Penetrated at Normal Impact

Calibre (mm)	Type	Range (m)	Thickness (mm)
7.62×51	Ball	0	8
7.62×51	AP	0	15
7.62×51	AP (WC)	0	24
12.7×99	AP	200	24
12.7×99	AP (WC)	200	41
12.7×99	SLAP	200	30
14.5×114	AP	500	28
14.5×114	AP (WC)	500	35
20×139	AP	500	30
20×139	AP (WC)	500	38
25×137	APDS	1000	50
25×137	APFSDS	1000	80
30×165	AP	1000	36
30×165	APDS	1000	54
30×173	APDS	1000	61
30×173	APFSDS	1000	110
35×228	APDS	1000	90
35×228	APFSDS	1000	120
40×225	APFSDS (CTA)	1500	150
40×365	APFSDS	1500	135
50×330	APFSDS	1500	135
60×411	APFSDS	2000	240

Source: Ogorkiewicz, R. M. *AFV Armour and Armour Systems*. Course notes on: Survivability of Armoured Vehicles, Cranfield University, Shrivenham, Swindon, UK, 18–20 March 2002.

Penetration of these types of rods into semi-infinite rolled homogeneous armour (RHA) target stack usually results in a penetration depth roughly equal to the length of the penetrator, which corresponds to a penetration depth of between 400 and 600 mm for 105–120-mm calibre APFSDS rounds.

The typically expected penetration depths from a range of ammunition (including APDS and APFSDS penetrators) are summarized in (Table 3.3)

3.3.1 Depleted Uranium Penetrators

Depleted uranium or 'DU' is uranium that has had some of its U-235 content removed and therefore is only weakly radioactive. Furthermore, most modern DU projectile materials are also alloyed with a small (0.75%) amount of titanium to improve strength and corrosion resistance.

The idea of using uranium in projectiles is thought to originate with the Nazis as indicated by the memoirs of Albert Speer, translated into English in 1970

(Speer, 1970). Speer (1905–1981) served as the Minister of Armaments and War Production in Nazi Germany during most of WWII and he was a close ally of Adolf Hitler. Therefore, he would have had knowledge of the use of uranium. He notes:

> In the summer of 1943, wolframite imports from Portugal were cut off, which created a critical situation for the production of solid-core ammunition. I thereupon ordered the use of uranium cores for this type of ammunition. My release of our uranium stocks of about twelve hundred metric tons showed that we no longer had any thought of producing atom bombs.

(Speer, 1970)

This report was largely treated with scepticism. However, evidence of Nazi involvement in the nuclear arms race has since become apparent and therefore, it stood to reason that they had access to large uranium supplies that could be otherwise used for shells (e.g. see Bernstein and Cassidy (1995)).

DU possesses superior penetrative ability (when penetrating steel) than WHA for two reasons: Firstly, DU is relatively dense. This higher density is particularly important for maximizing penetration at elevated impact velocities. Secondly, and more importantly, DU has the ability to self-sharpen during penetration. This is due to a phenomenon called adiabatic shear and is principally caused by the rate of thermal softening exceeding the rate of work hardening during penetration. The disadvantage of DU, when compared to WHA, is the stiffness—with DU possessing Young's modulus of 170 GPa as opposed to 300 GPa for a WHA. This means that a DU rod will give a higher deflection for the same elastic stress as it passes through oblique targets. Furthermore, the long-term health consequences of this type of material in ingestible particulate form are, as yet, uncertain. However, due to DU being only weakly radioactive, it is possible to handle these penetrators for a long period of time without any adverse health effects.

A comparison of the penetration performance of DU vs WHA is shown in Figure 3.7. These data were for model scale penetrators (L/d = 20), with the WHA rods being made from a 93% W alloy. The difference in the penetration capabilities varies between 10% and 15% over the range of data points. However, this delta only narrows slightly when a 97%W is used (Magness and Farrand, 1990).

The mechanical properties and the ballistic limit velocity for the penetration of a 76.2 mm RHA plate by L/d penetrators are shown in Table 3.4. It can be seen that the density of a 97%W alloy is the same as the U-0.75Ti material, although its penetration performance is inferior due to the sharpening behaviour of the DU projectile. All of the DU penetrators are able to penetrate the plate at approximately 100 m/s lower than the WHA penetrators. The tungsten alloys are usually swaged (forged) to develop the various combinations of strength and ductility, whereas U–Ti alloys are able to undergo precipitation hardening (= ageing).

3.3.2 Lethality Calculations Using the Lanz–Odermatt Equation

Lanz and Odermatt developed an empirical model to determine the lethality of a large calibre KE projectile. Unlike many other studies, they used full-scale ammunition with 41 firings with tungsten alloy APFSDS projectiles of varying *L/d* ratios
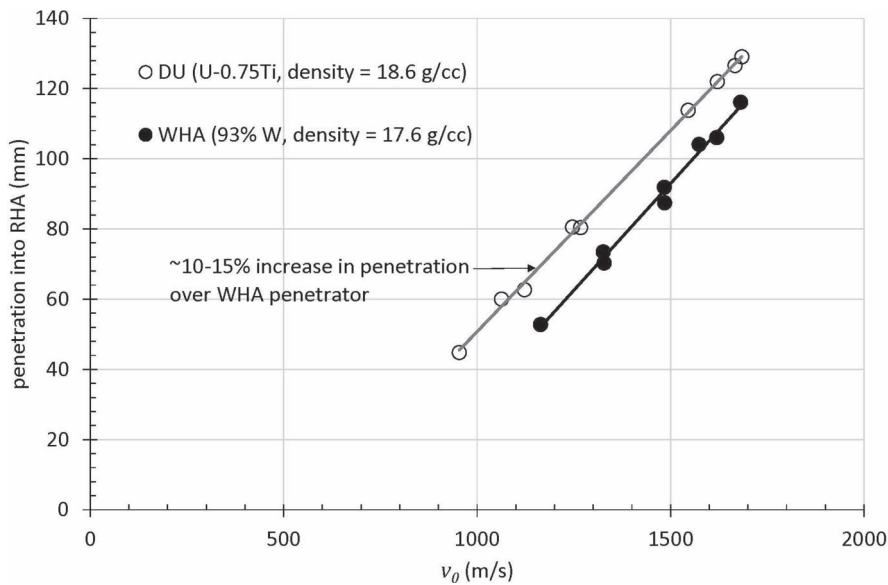
FIGURE 3.7 Comparison of the penetration performance of WHA and U-0.75Ti alloy projectiles (L/d=20) into Rolled Homogeneous Armour. (Replotted from data available in Magness and Farrand, 1990.)

TABLE 3.4

Properties of Uranium and Tungsten Heavy Alloy Penetrators, along with Ballistic Limit Velocities for the Perforation of a 76.2 mm Plate of Rolled Homogeneous Armour, After (Magness and Farrand, 1990)

Material	Density (g/cc)	Hardness (Rc)	0.2% Y_0 (MPa)	UTS (MPa)	Elong (%)	v_{bl} (m/s)
97W (Ni, Fe, Co) swg 20%	18.6	44	-	1208	4	1318
96W (Ni, Fe) swg 12%	18.3	40	1000	1037	7	1313
93W (Ni, Fe, Co) swg 25%, aged	17.7	47	-	1455	6	1326
93W (Ni, Fe) swg 18%	17.6	41	1116	1197	13	1338
90W (Ni, Fe) swg 20%	17.2	41	-	-	-	1350
U-0.1Be-0.7Ti	18.6	41	841	1379	11	1228
U-0.75Ti aged	18.6	40	848	1489	24	1221
U-0.75Ti >aged	18.6	47	1100	1580	12	1203
U-0.75Ti >>aged	18.6	49	1089	1689	6	1193
U-0.9Hf-0.5Ti	18.4	-	896	1620	20	1221
U-1Mo-0.5Ti	18.4	49	1396	1821	6	1177
U-3.5Zr-0.7Ti	17.3	54	1764	2051	1	1216

TABLE 3.5
Limits to the Lanz–Odermatt Equation (Lanz and Odermatt, 1992)

Parameter	Value	Units
Calibre	105, 120 and 140	mm
Penetrator length, L	330–900	mm
Length-to-diameter ratio, L/d	11–32	-
Penetrator densities (tungsten alloy), ρ_p	17,000–17,750	kg/m³
Penetrator impact velocities, v_0	1.1–1.9	km/s
Target plate thickness, h	150–400	mm
Ultimate tensile strength (UTS), R_m	800–1000	MPa
Obliquity, θ (from the normal)	30–74	°
Target density, ρ_t	7850	kg/m³
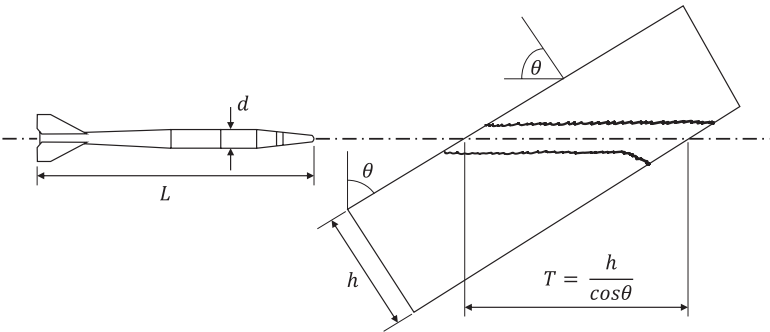
FIGURE 3.8 Penetration parameters for the Lanz–Odermatt equation. Note that d is assumed to be constant along the length of the rod. This is usually the case for many APFSDS projectiles.

(Lanz and Odermatt, 1992). The derived empirical parameters from their model are applicable according to Table 3.5:

Using the unit convention of Table 3.5 and referencing Figure 3.8, the following equation can be used:

$$\frac{h}{d} = a\left(\frac{L}{d}\right)\cos^{0.745}\theta \sqrt{\frac{\rho_p}{\rho_t}} e^{-\frac{25.9 R_m}{\rho_p v_0^2}} \tag{3.2}$$

where,

$$a\left(\frac{L}{d}\right) = \frac{L}{d} + 3.77\left(1 - \tanh\frac{L/d - 10}{6.89}\right) \tag{3.3}$$

where a is a dimensionless parameter. For $L/d \geq 20$, the expression $a(L/d)$ in the penetration equation simply transforms into (L/d). That is, $a \to 1.0$.

The parameter T is the total penetration achieved through the inclined plate and can be separately calculated (see Figure 3.8). The correlation of the equation for a given projectile-target combination (evaluated at varying velocities ranging from 1.1 to 2.3 km/s) is given in Figure 3.9. Here, dimensionless values of x and y are plotted on the x-axis and y-axis, respectively, where:

$$x = \frac{R_{\mathrm{m}}}{\rho_{\mathrm{p}} v_0^2} \tag{3.4}$$

and,

$$y = a\left(\frac{L}{d}\right)^{-1} \cos^{-0.745} \theta \sqrt{\frac{\rho_{\mathrm{t}}}{\rho_{\mathrm{p}}}} \frac{h}{d} \tag{3.5}$$

Inset (lower left) are the parameters used for the calculation (solid line). Correlation is seen to be quite good, even though some parameters are outside the limits defined by (Lanz and Odermatt, 1992). The model was further expanded by (Jeanquartier and Odermatt, 1995) by widening the applicability to lower calibres and providing more analysis on the effect of the target strength. Updated validity limits for this equation are provided in Table 3.6.
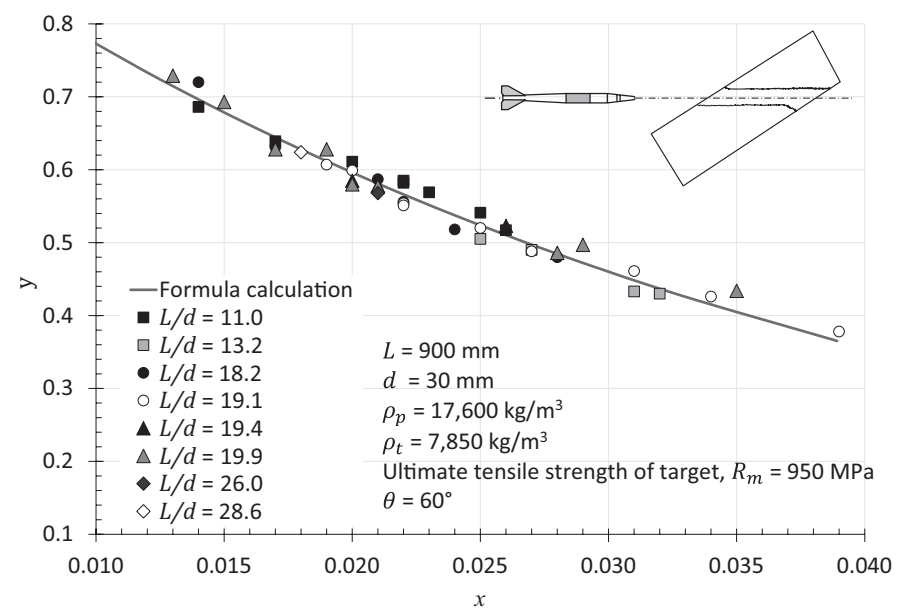
FIGURE 3.9 Correlation between the Lanz–Odermatt equation and 41 experiments. Plotted from data available in (Lanz and Odermatt, 1992). Inset: parameters used for the formula calculation for velocities from 1.1 to 2.3 km/s.

TABLE 3.6

Updated Limits to the Lanz–Odermatt Equation (Jeanquartier and Odermatt, 1995)

Parameter	Value	Units
Calibre	25, 30, 35, 105, 120 and 140	mm
Penetrator length, L	90–825	mm
Length-to-diameter ratio, L/d	11–31	-
Penetrator densities (tungsten alloy), ρ_p	17,000–17,750	kg/m^3
Penetrator impact velocities, v_0	1.1–1.9	km/s
Target plate thickness, h	40–400	mm
Ultimate tensile strength (UTS), R_m	800–1600	MPa
Obliquity, θ (from the normal)	0–74	°
Target density, ρ_t	7850	kg/m^3

In this case, the modified penetration formula is given by Jeanquartier and Odermatt (1995):

$$\frac{h}{d} = a\left(\frac{L}{d}\right)\cos^{0.775}\theta\sqrt{\frac{\rho_p}{\rho_t}}e^{-\frac{cR_m}{\rho_p v_0^2}} \tag{3.6}$$

$$a\left(\frac{L}{d}\right) = \frac{L}{d} + 3.94\left(1 - \tanh\frac{L/d - 10}{11.2}\right) \tag{3.7}$$

where,

and this time, a parameter c is introduced:

$$c = 22.1 + 1.274e^{-8}R_m - 9.47e^{-18}R_m^2 \tag{3.8}$$

Example 3.1

A 540-mm tungsten alloy penetrator is fired from a 120-mm smooth bore gun and hits a RHA target inclined at 60° at 1.6 km/s. Using the 1992 Lanz–Odermatt equation, calculate the maximum plate thickness that could be penetrated at that angle and the length of the penetration channel assuming the following penetrator and target parameters:

$$L/d = 20$$

$$\rho_p = 17,600 \text{ kg/m}^3$$

$$\rho_t = 7,830 \text{ kg/m}^3$$

$$R_m = 910 \text{ MPa}.$$

The diameter of the rod is given by $d = 540/20 = 27$ mm.

First, we calculate $a\left(\dfrac{L}{d}\right)$:

$$a\left(\frac{L}{d}\right) = \frac{540}{27} + 3.77\left(1 - \tanh\frac{540/27 - 10}{6.89}\right) = 20.4$$

Note we are at the cusp of where $a \approx 1.0$ for $L/d = 20$.

Now let us calculate the plate thickness:

$$h = \left(a\left(\frac{L}{d}\right)\cos^{0.745}\theta\sqrt{\frac{\rho_p}{\rho_t}}\, e^{-\frac{25.9 R_m}{\rho_p v_0^2}}\right)d$$

$$h = \left(20.4 \times \cos^{0.745}(60) \times 1.5 e^{-\frac{25.9 \times 910}{17600 \times 1.6^2}}\right) \times 27$$

Therefore, the maximum plate thickness that could be penetrated at 60° is

$$h = 292 \text{ mm}$$

The resulting length of the penetration channel is

$$T = \frac{292}{\cos(60)} = 584 \text{ mm}$$

3.4   EXPLOSIVE MATERIALS

Explosives are extensively used in the propulsion of high-velocity fragments or to damage structures by a blast wave, and it is worth mentioning these materials here. Notably, the rate of energy release in a detonation is incredibly quick and occurs within the microsecond timescale. Further, the detonation products are gases that are highly compressed, and their expansion produces shock waves in air.

Pure explosives are very difficult to handle, and so these are blended with other explosives or inert materials to change the mechanical behaviour or sensitivity of the material. Typical forms of products include the following: castings, slurries and gels, putties, machined polymer-bonded forms and rubberized materials.

Explosives are separated into two types:

- *Primary explosives*: sensitive to flame/heat, percussion or friction
- *Secondary explosives*: less sensitive to external stimuli but reliable in detonation

An example of the typical use of explosives in a warhead is shown in Figure 3.10. The detonator is used to initiate the secondary (booster) charge that provides an even detonation front for the main charge. The main purpose of separating out primary
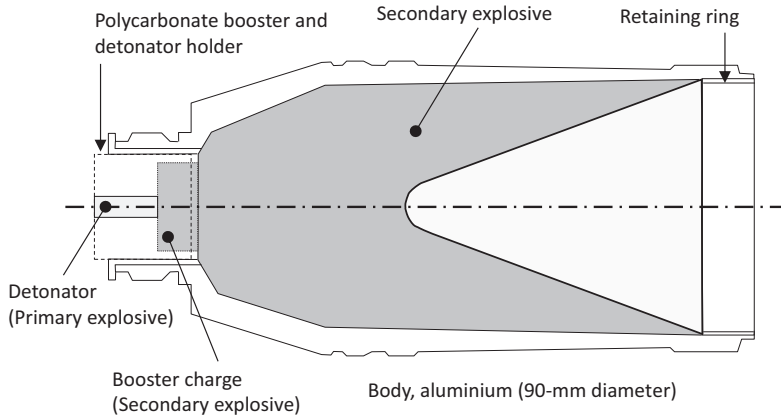
FIGURE 3.10 Shaped charge warhead showing the presence of the detonator (primary explosive), a booster charge (secondary explosive) and main explosive charge (secondary explosive).

and secondary explosives is so that the risk of a massive explosion due to an accident whilst the warhead is in storage is minimized. Thus, the detonators are usually mechanically (or completely) separated from the booster charge until the time comes to arm the warhead.

Once the detonator is initiated, the rapid pressure imparted to the secondary charge initiates the detonation. This process involves the formation of a chemically supported shock wave that traverses the length of the booster charge. This shock wave moves at the detonation velocity, U_D. As it does so, the unreacted material is converted to detonation products over the width of a reaction zone. The interface at which all the material has been converted to the gaseous explosion products is known as the Chapman–Jouguet (C–J) interface. The C–J (or detonation) pressure within the explosive can be estimated from the following equation:

$$P_{CJ} = \frac{\rho_0 U_D^2}{\gamma + 1} \tag{3.9}$$

where ρ_0 is the density of the unreacted explosive, and γ is the polytropic gas constant and for most explosives varies between 1.3 and 3.0.

3.4.1 BLAST

In the past couple of decades, this threat has been responsible for a large number of deaths and serious injuries within warzones of both civilians and troops, and therefore, a good understanding of the physics of blast is warranted. There have been numerous overviews provided that give a good insight into the physics of blast and the effect on structures, and the student is directed to works by Baker (1973), Baker et al. (1983) and Smith and Hetherington (1994).
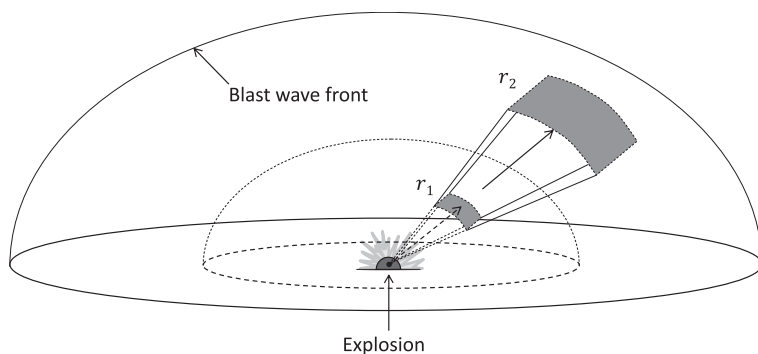
FIGURE 3.11 Expansion of a blast wave.

When an explosive material is detonated, a chemical reaction occurs in the explosive that results in the expulsion of a gas at such a high rate that a shock wave is formed in the air. It is this shock wave that can tear flesh, propel fragments and lift vehicles. Surprisingly, quite a small volume of gas is generated during the detonation. Roughly speaking, a 1-kg mass of trinitrotoluene (TNT) will produce 740 L of gas as a result of the explosion (at standard temperature and pressure).

The physics of blast waves is actually quite complicated; however, there is one golden rule for maximizing protection against explosive devices: maximize your distance from the explosion. The reason for this is that the blast resultants (pressure and impulse values) decrease very rapidly as the distance from the explosive and the structure that you wish to protect increases. This can be explained by the following qualitative analysis. Figure 3.11 shows a simplified schematic of what can be expected to happen when a mass of explosive is detonated on a flat and horizontal surface. Ignoring 'ground effects' such as the excavation of the surface and the inevitable reflection, it can be seen that as the radius of the blast increases from r_1 to r_2, the surface area of the blast also increases but so does the volume now occupied by the expanding element. The leading surface area of the blast element increases according to r^2 whereas the volume occupied by the expanding element increases according to r^3. Thus, the energy density (energy per unit volume) that is released by the detonation decreases as the volume expands. The energy density within the blast wave front decreases according to $1/r^3$ (Smith and Rose, 2005). Therefore, doubling your distance from a charge leads to a 7/8 reduction in energy density. This is why vehicles that have been designed to withstand mine blasts generally have the main cabin high off the ground. So, if you need to provide protection from a blast wave, then putting as much distance between the potential location of the bomb and you is going to help.

3.4.2 BLAST WAVE PARAMETERS

The pressure time history of a typical blast wave can be described by exponential functions such as the one given by the Friedlander equation (Baker, 1973):

$$P(t) = P_0 + P_s \left(1 - \frac{t}{T_s}\right) \exp\left[-\frac{bt}{T_s}\right] \tag{3.10}$$

where b is the waveform parameter, which is a function of the peak overpressure, P_s. Other parameters are defined in Figure 3.12. It should be pointed out that this equation is strictly empirical (i.e. it provides a good fit to observed experimental data) rather than theoretical. Other simpler and more complicated empirical equations exist (see Baker (1973) for a review).

A typical structure of an ideal blast wave is shown in Figure 3.12. Prior to the arrival of the blast wave, the pressure is at ambient (atmospheric) pressure, P_0. On arrival of the shock front (at time $= t_a$), the pressure jumps in a discontinuous fashion. The quantity, P_s, is termed the peak side-on overpressure or simply the peak overpressure. The portion of the wave above P_0 is called the positive phase, whereas the portion below P_0 is called the negative phase or the 'suction phase'.

Other significant parameters include

- $T_s =$ the duration of the positive phase
- $i_s =$ the impulse of the positive phase (calculated by taking the area under the curve in the positive phase). So, this is defined as

$$i_s = \int_{t_a}^{t_a+T_s} P(t).dt \tag{3.11}$$

The shock front is moving at U_s.

The various blast wave characteristics are related to the Rankine–Hugoniot equations in which there is a single shock. These will be covered in detail in Chapter 5.
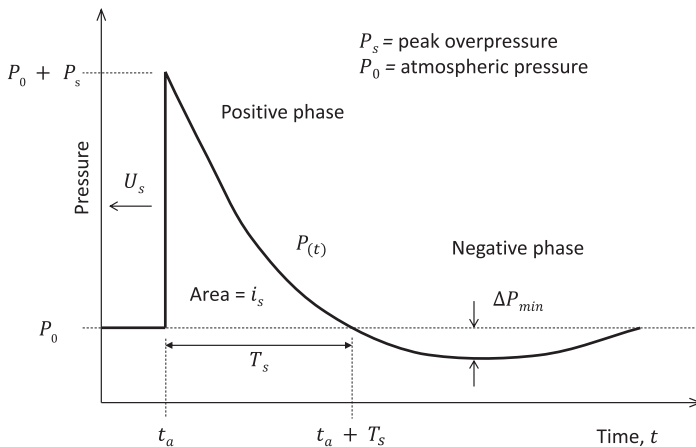
FIGURE 3.12 Ideal blast wave structure due to the detonation of an explosive in air.

The shock velocity in the air from an explosive blast, U_s, is governed by the following equation (Glasstone and Dolan, 1977):

$$U_s = c_0 \left(1 + \frac{\gamma + 1}{2\gamma} \frac{P_s}{P_0} \right)^{\frac{1}{2}} \qquad (3.12)$$

where c_0 is the ambient speed of sound (ahead of the shock front), P_s is the peak over-pressure (behind the shock front), P_0 is the ambient pressure (ahead of the shock) and γ is the ratio of specific heats (c_p/c_v) and for air, is nominally $= 1.4$. For $\gamma = 1.4$, the equation for the shock velocity becomes

$$U_s = c_0 \left(1 + \frac{6P_s}{7P_0} \right)^{\frac{1}{2}} \qquad (3.13)$$

The particle velocity (or 'wind velocity') behind the shock is given as

$$u_p = \frac{c_0 P_s}{\gamma P_0} \left(1 + \frac{\gamma + 1}{2\gamma} \frac{P_s}{P_0} \right)^{-\frac{1}{2}} \qquad (3.14)$$

so in air, $\gamma = 1.4$, and

$$u_p = \frac{5P_s}{7P_0} \frac{c_0}{\left(1 + \frac{6P_s}{7P_0} \right)^{\frac{1}{2}}} \qquad (3.15)$$

The density behind the shock front is related to the ambient density as follows:

$$\rho = \rho_0 \left(\frac{2\gamma P_0 + (\gamma + 1) P_s}{2\gamma P_0 + (\gamma - 1) P_s} \right) \qquad (3.16)$$

so in air

$$\rho = \rho_0 \frac{7P_0 + 6P_s}{7P_0 + P_s} \qquad (3.17)$$

3.4.3 Blast Scaling Laws

It is often convenient to scale the properties of blast waves so that is possible to pre-dict the properties of blast waves from large-scale explosions based on the measure-ments from small-scale explosions. The scaling law that is most frequently used is the Hopkinson–Cranz scaling law, which was independently developed by Hopkinson (1915) and Cranz (1926) and is sometimes referred to as the cube-root scaling law. The basis of the scaling law is as follows (Baker et al., 1983): Self-similar blast waves

are produced at identical scaled distances when two explosive charges of identical geometry and type but of different sizes are detonated in the same atmosphere.

So, from Smith and Hetherington (1994), consider two charge masses of W_1 and W_2 with diameters of d_1 and d_2. Note that here, we are breaking from the convention of listing mass by the letter 'W' instead of the letter 'm'

It is known that

$$W_1 \propto d_1^3$$

$$W_2 \propto d_2^3$$

and therefore

$$\frac{W_1}{W_2} = \left(\frac{d_1}{d_2}\right)^3 \tag{3.18}$$

and therefore

$$\frac{d_1}{d_2} = \left(\frac{W_1}{W_2}\right)^{\frac{1}{3}} \tag{3.19}$$

Therefore, if the two charge diameters (CDs) are in the ratio $d_1/d_2 = \lambda$, then for identical overpressures to be seen by an observer, the ratio of the ranges from the explosive to the observer will be given by

$$\frac{R_1}{R_2} = \lambda \tag{3.20}$$

where R_1 and R_2 are the ranges for the explosives of masses W_1 and W_2, respectively. Similarly, the same applies to the positive-phase duration:

$$\frac{T_{s1}}{T_{s2}} = \lambda \tag{3.21}$$

and the impulse of the positive phase:

$$\frac{i_{s1}}{i_{s2}} = \lambda \tag{3.22}$$

Thus, it follows that ranges at which a given overpressure will be produced by explosions from different masses of explosives can be calculated from

$$\frac{R_1}{R_2} = \left(\frac{W_1}{W_2}\right)^{\frac{1}{3}} \tag{3.23}$$

where R_1 is the range at which an overpressure is produced by an explosive with mass W_1, and R_2 is the range at which an identical overpressure is produced with a charge of mass W_2. An observer located at a distance R_2 from the centre of an explosive with a characteristic dimension of d_2 will be subjected to a blast wave of magnitude P_s with a duration of T_{s2} and impulse i_{s2}. So, the Hopkinson–Cranz scaling law states that another observer who is located at a distance of λR_2 from an explosive with size λd_2 will be subjected to a blast wave with magnitude P_s with a duration of λT_{s2} and impulse λi_{s2}. The blast wave overpressure, P_s, does not change (neither does its velocity nor temperature), whereas the duration and the impulse of the wave do. The Hopkinson–Cranz scaling law has been thoroughly verified over the years by many experiments conducted over a large range of explosive energies. See Figure 3.13 (Baker et al., 1983).

The Hopkinson–Cranz approach leads to the specification of a parameter known as the scaled distance, Z, which is a constant of proportionality. This is used to present normalized blast data in a general way so that from a single curve, it is possible to work out a blast wave parameter for variable ranges and masses. It is defined as

$$Z = \frac{R}{W^{\frac{1}{3}}} \tag{3.24}$$

where Z is the scaled distance, R is the range and W is the charge mass.

The charge mass is often expressed in kilograms of TNT, which is used as a reference explosive. To calculate the parameters from explosives other than TNT, it is convenient to convert the mass of the charge into a TNT 'equivalent mass'.
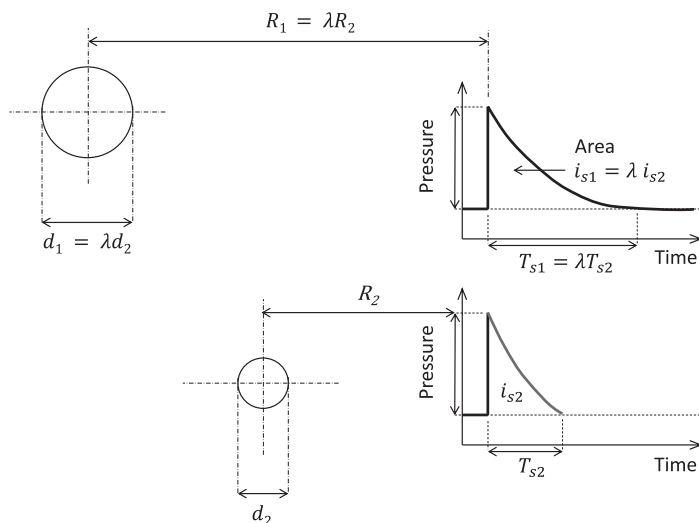
FIGURE 3.13   Hopkinson–Cranz scaling law. (Adapted from Baker, W. E. et al., *Explosion Hazards and Evaluation*, vol. 5, Fundamental Studies in Engineering.)

TABLE 3.7

Conversion Factors (TNT Equivalence) for Some High Explosives

Explosive	Density (kg/m³)	Mass-Specific Energy Q_x (kJ/kg)	TNT Equivalence (Q_x/Q_{TNT})
Amatol 80/20 (80% ammonium nitrate, 20% TNT)	1600	2650	0.586
Comp B (60% RDX, 40% TNT)	1690	5190	1.148
RDX (cyclonite)	1650	5360	1.185
HMX	1900	5680	1.256
Lead azide	3800	1540	0.340
Lead styphnate	2900	1910	0.423
Nitroglycerin (liquid)	1590	6700	1.481
Octol 70/30 (70% HMX, 30% TNT)	1800	4500	0.994
Pentaerythritol tetranitrate (PETN)	1770	5800	1.282
Pentolite 50/50 (50% PETN, 50% TNT)	1660	5110	1.129
Tetryl	1730	4520	1.000
TNT	1600	4520	1.000
C-4 (91% RDX, 9% plasticizer)	1580	4870	1.078
PBX 9404 (94% HMX, 3% nitrocellulose, 3% plasticizer)	1844	5770	1.277

To do this, a conversion factor is used based on the ratio of the specific internal energies of the explosive to TNT. A selection of properties and conversion factors for several explosives taken from Baker et al. (1983) are shown in Table 3.7.

So, a 100-kg charge of PETN converts to 128.2 kg of TNT since the ratio of the specific energies is 5800:4520 = 1.282. Note there are many ways to calculate the 'TNT equivalence' value for an explosive, including by calculating the explosive power—see Akhavan (1998).

3.4.4 PREDICTING BLAST LOADING ON STRUCTURES

There are several computational codes available for predicting the blast loading on structures for highly complex structures including ANSYS® AUTODYN and Cranfield University's Propagation of Shocks in Air (ProSAir). However, it is possible to carry out a desktop analysis of the types of loading on structure based on a series of empirical data fits that have been published in the open literature. A good collection of data based on the scaled distance (Equation 3.24) of a TNT charge is provided by Baker et al. (1983), a sample of which is presented in Figures 3.14 and 3.15.

These data are for free air bursts, that is, away from any reflecting surface such as the ground and strictly, these data should only be used for such applications. However, where an explosion occurs close to the ground, it is possible to use these data by adjusting the charge mass or yield and then applying the curves presented in Figures 3.14 and 3.15. Reasonable correlation for surface blasts of high explosives
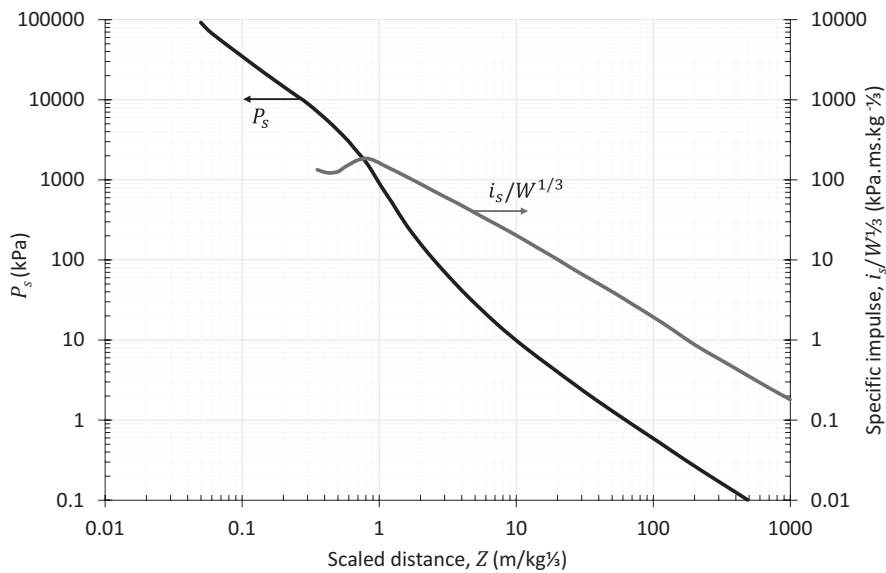
FIGURE 3.14 Side-on blast parameters for a spherical charge of TNT showing peak over-pressure and specific impulse data. (Adapted from Baker, W. E. et al., *Explosion Hazards and Evaluation*, vol. 5, Fundamental Studies in Engineering.)
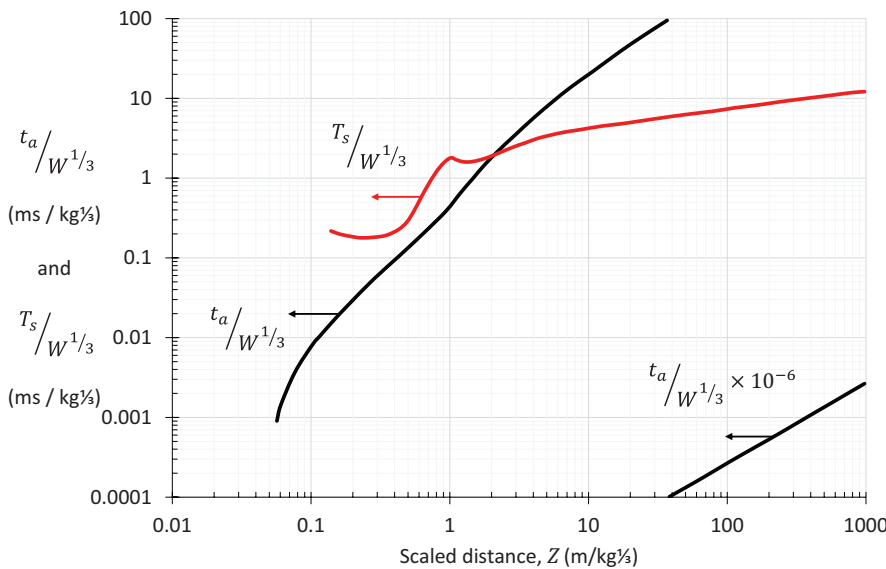
FIGURE 3.15 Side-on blast parameters for a spherical charge of TNT showing positive phase duration (T_s) and arrival time (t_a) data. (Adapted from Baker, W. E. et al., *Explosion Hazards and Evaluation*, vol. 5, Fundamental Studies in Engineering.)

with free-air burst data results if an enhancement factor of 1.8 is assumed (Smith and Hetherington, 1994). Where the ground is assumed to be a perfect reflector (i.e. no wave energy is absorbed by the ground), then an enhancement factor of 2.0 can be used as an approximation.

Figure 3.14 is presented as a log–log graph, with the left-hand vertical axis denoting the peak static over pressure. This is sometimes referred to as the incident, or 'side on' pressure. On the right-hand vertical axis, we have the specific impulse, $i_s/W^{1/3}$. An example of how to use this graph is provided in Example 3.2. Positive phase duration (T_s) and arrival time (t_a) data are presented in Figure 3.15 (Baker et al., 1983). Note that the section of the curve in the bottom right of Figure 3.15 demands that the y-axis value is divided by 1×10^6 to get the correct value of $t_a/W^{1/3}$.

Equally, for hemispherical charges located at the surface, Kingery and Bulmash (1984) developed a range of polynomials to describe the parameters seen from the range, R of a 1 kg hemispherical surface charge. Some of these parameters are summarized in the graph in Figure 3.16 where each of the parameters described on the graph can be read from the values on the y-axis. Arguably, this data is more meaningful than the data presented in Figures 3.14 and 3.15 as it has direct relevance to mine blast applications.

Note that due to the unavailability of data, the reflected impulse curve for a hemispherical surface burst was developed from spherical free-air data by using a 1.8 yield reflection factor, as discussed earlier.

Noting that Figure 3.16 summarizes parameters for a 1 kg TNT hemispherical charge detonated at a surface it is possible to equate the range in metres on the x-axis to the more usable parameter of scaled distance (Z) and therefore apply the curves
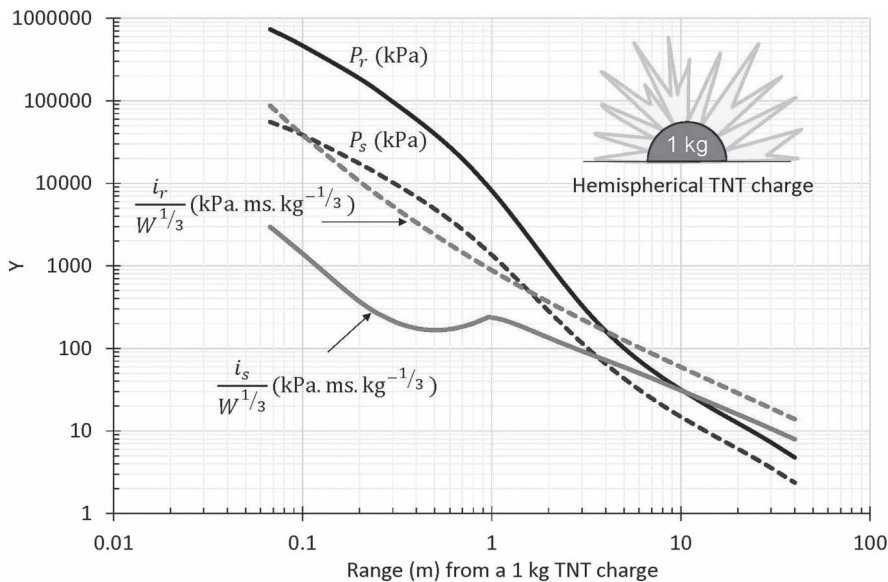
FIGURE 3.16 Parameters for a hemispherical 1 kg TNT surface blast, calculated from the relationships presented in (Kingery and Bulmash, 1984.)

to any mass and range of TNT (within the limits of $R = 0.0674\text{--}40.0\,\text{m}$). This is simply due to the fact that for 1 kg TNT charge mass, $Z = R/1^{1/3} = R$. Some researchers have presented the Kingery and Bulmash (1984) data that way (e.g. see Karlos and Solomos (2013)).

Example 3.2

An armoured vehicle is subjected to an air blast from an artillery shell that explodes at 20 m from its turret. If the artillery shell contains 6.75 kg of RDX, use Figure 3.14 to estimate the peak over pressure and the impulse experienced by the vehicle.

First, it is known that the explosive is RDX, and therefore we need to calculate the TNT equivalent mass so that we can use Figure 3.14. Therefore, from Table 3.7,

$$6.75 \text{ kg} \times 1.185 = 8.0 \text{ kg (equivalent mass of TNT)}$$

We now need to work out the scaled distance knowing that $R = 20\,\text{m}$.
Therefore,

$$Z = \frac{20}{8^{1/3}} = 10 \text{ m/kg}^{1/3}$$

Reading off Figure 3.14, we have:

$$P_s = 10 \text{ kPa}$$

$$i_s/W^{\frac{1}{3}} = 20 \text{ kPa.ms.kg}^{-1/3} \therefore i_s = 20 \times 8^{\frac{1}{3}} = 40 \text{ kPa.ms}$$

Example 3.3

An improvised explosive device (IED) is detonated at 10 m from an armoured fighting vehicle (AFV). The IED is manufactured with 8 kg of TNT which is assumed to have a hemispherical geometry. Calculate the peak static overpressure, reflected pressure and the incident impulse that is seen by the AFV. A schematic of the problem is shown in Figure 3.17.

Knowing the IED is located on the ground and is assumed to be a hemispherical charge we can use Figure 3.16.

IED explosion   AFV
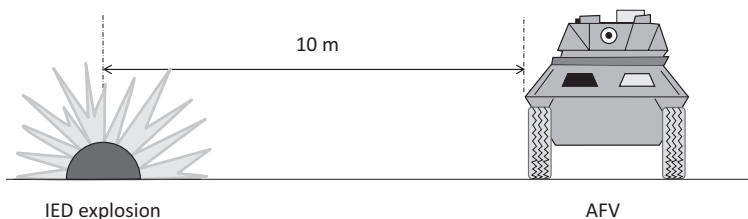
FIGURE 3.17   Attack on an AFV: calculating the expected pressure and impulse from an IED.

First, we calculate the scaled distance of the attacking charge, Z

From Equation 3.11, it is known that $Z = R/W^{1/3} = 10/8^{1/3} = 5.0$ m/kg$^{1/3}$.

Therefore, reading Figure 3.16 (noting that this is not straightforward), it is seen that

$$P_s = 40 \text{ kPa}$$

$$P_r = 100 \text{ kPa}$$

$$i_s / W^{\frac{1}{3}} = 60 \text{ kPa.ms.kg}^{-\frac{1}{3}} \therefore i_s = 60 \times 8^{\frac{1}{3}} = 120 \text{ kPa.ms}$$

It is worth noting that these values will be approximate given the difficulties of reading off a log–log graph from the pages of this book! For this problem, the analytical solution would be $P_s = 43.2$ kPa, $P_r = 100.7$ kPa and $i_s = 118.5$ kPa.ms. However, for most applications, the graph above will put you in the right 'ballpark'.

3.4.5   BLAST WAVE INTERACTIONS

When a blast wave encounters an immovable object, it will be reflected from it. The magnitude of the reflected pressure is governed by the following equation:

$$P_r = 2P_s + (\gamma + 1)q_s \tag{3.25}$$

where

P_r is the reflected pressure
P_s is the peak static overpressure
γ is the ratio of specific heats (C_p/C_v)
q_s is the dynamic (or 'wind') pressure (and has the units of Pa)

The dynamic pressure is defined by

$$q_s = \frac{1}{2}\rho u_p^2 \tag{3.26}$$

Introducing the previous Rankine–Hugoniot equations (Equations 3.14 and 3.16) we have,

$$q_s = \frac{P_s^2}{2\gamma P_0 + (\gamma - 1)P_s} \tag{3.27}$$

Or for air, ($\gamma = 1.4$)

$$q_s = \frac{5}{2}\frac{P_s^2}{7P_0 + P_s} \tag{3.28}$$

Substituting Equation 3.28 into Equation 3.25, we get the equation for the reflected pressure in the air:

$$P_r = 2P_s + \frac{6P_s^2}{(7P_0 + P_s)} \tag{3.29}$$

and rearranging,

$$P_r = 2P_s \frac{(7P_0 + 4P_s)}{(7P_0 + P_s)} \tag{3.30}$$

Examination of this equation determines an upper and lower limit to the value of P_r. When the value of P_s is a lot lower than atmospheric pressure, P_0 (that is, as P_s tends to zero), then the reflected pressure is defined as

$$P_r \approx 2P_s \tag{3.31}$$

This would be applicable to the case of a small charge located at a significant distance from the target (i.e. for weak shocks).

On the other hand, when P_s is a lot larger than P_0, such as the case where a large charge is located in close proximity to the target (strong shocks) then,

$$P_r \approx 8P_s \tag{3.32}$$

It is evident from Equation 3.25, that the increase in the reflected pressure above the expected value of twice the incidental value, i.e. $2P_s$ is due to the dynamic (or wind) pressure, governed by $(\gamma + 1)q_s$. The reflected overpressure arises due to the moving air abruptly changing direction as it hits the surface of the target, thereby changing momentum.

The calculation of the reflected pressure on the bottom hull of an AFV is shown in Figure 3.18. The calculations have been done based on the work of Kingery and Bulmash (1984) with reference to Figure 3.16 and assume a surface blast of a 10 kg hemispherical mass of TNT. It is the reflected pressure (and reflected impulse) that ultimately causes the vehicle to respond and will determine its acceleration and therefore the acceleration of the occupants. It can be seen in Figure 3.18, that as the standoff is increased, the reflected pressure drops significantly, and this knowledge has been used by vehicle designers to maximize occupant survivability.

3.4.6 UNDERWATER BLASTS

Underwater blasts have similar characteristics to air blasts except that the medium through which the shock wave is transmitted has a density of ~1000 kg/m³ as opposed to ~1.2 kg/m³. During an underwater explosion, the solid explosive material is converted into high-pressure gaseous products in a timescale of the order of microseconds. The expansion of the solid material to gas through the detonation process highly compresses the surrounding water leading to the formation of a supersonic shock wave that expands out radially.
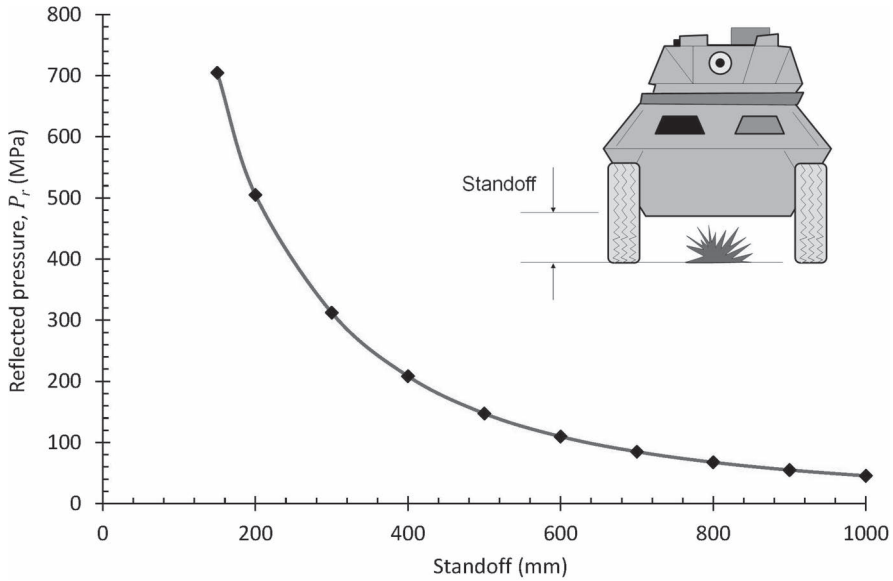
FIGURE 3.18   Reflected pressure variation with standoff for an armoured fighting vehicle subjected to an underbelly surface blast from 10 kg of TNT.

The shape of the shock wave and its decay characteristics (with time and distance) are given by Swisdak, Jr. (1978). The shape of the shock pulse in water follows a similar shape to Figure 3.12 and is shown in Figure 3.19.

It is generally assumed that the shock pressure decays from its peak exponentially for a period of one time constant (θ) after which the pressure decays more slowly with time (see the dashed line in Figure 3.19). This has been empirically established.

Assuming a full exponential decay, the shape of this pressure pulse is given by

$$P(t) = P_{\mathrm{s}} \exp\left(-\frac{t}{\theta}\right) \tag{3.33}$$

Swisdak, Jr. provides a summary of empirically derived constants and coefficients for various explosives to establish the peak pressure, P_{s}, impulse, i_{s}, and time constant, θ. For TNT, In terms of the mass (W) and the range (R), we have

$$P_{\mathrm{s}} = 52.4\left(\frac{W^{\frac{1}{3}}}{R}\right)^{1.13} \tag{3.34}$$

$$i_{\mathrm{s}} = 5.75 \times W^{\frac{1}{3}}\left(\frac{W^{\frac{1}{3}}}{R}\right)^{0.89} \tag{3.35}$$
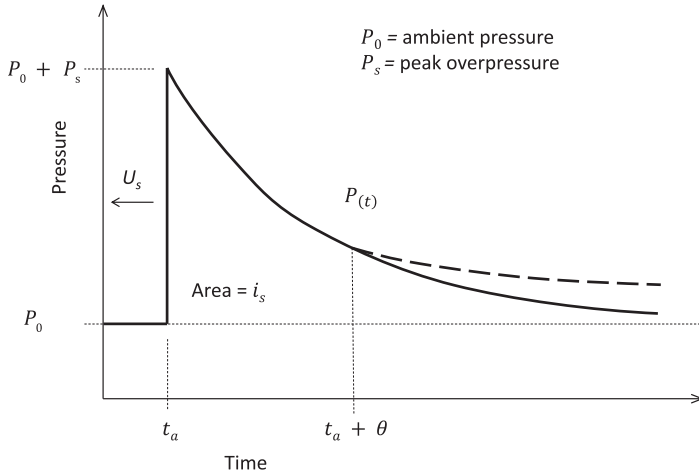
FIGURE 3.19 Ideal pressure pulse structure from an underwater explosion. (Adapted from Swisdak, Jr., M. M. 1978. *Explosion Effects and Properties: Part II – Explosion Effects in Water*. White Oak, Silver Spring, MD: Naval Surface Weapons Center.)

and

$$\theta = 0.084 \times W^{\frac{1}{3}} \left(\frac{W^{\frac{1}{3}}}{R} \right)^{-0.23} \tag{3.36}$$

Example 3.4

A 10-kg TNT blast mine is detonated underwater. Plot how the pressure and impulse decay with range (R) from the blast up to 10 m. Plot the shape of the expected pressure pulse at 10 m.

Equations 3.13 and 3.14 provide the solution. In this case, it is known that $W = 10$ kg, and therefore, substituting into the equations provides a solution shown in Figure 3.20.

Figure 3.20 shows that the pressure and impulse values drop off very rapidly with range – similar to an air blast. Note that two vertical axes have been plotted here: one to represent the peak pressure (right-hand axis) and one to represent the impulse.

The next step is to work out the profile of the wave at 10 m. To do this, we need the time constant θ.

Using Equation 3.36, it is seen that the time constant is given by

$$\theta = 0.084 \times 10^{\frac{1}{3}} \left(\frac{10^{\frac{1}{3}}}{10} \right)^{-0.23} = 0.257598 \text{ ms}$$
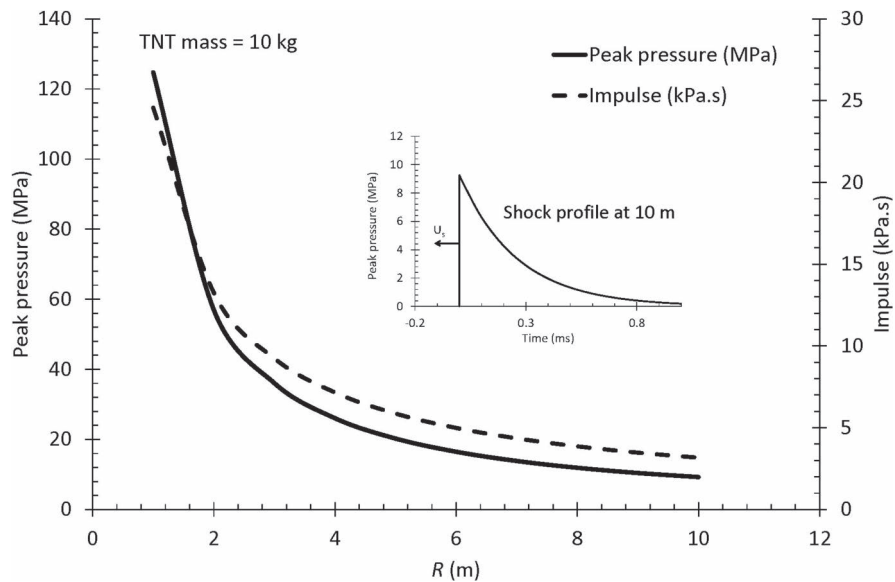
FIGURE 3.20 Peak pressure and impulse value of a spherically expanding shock wave in water. Inset: the shock profile at $R = 10\,\text{m}$ calculated by the means outlined in the text.

From Equation 3.34,

$$P_s = 52.4 \left(\frac{10^{\frac{1}{3}}}{10} \right)^{1.13} = 9.25 \text{ MPa}$$

Therefore, using Equation 3.33, the pressure profile for various arbitrary time values (e.g. ranging from 0 to 1 ms) can now be plotted. This is shown in the inset in Figure 3.20.

3.4.7 BURIED MINES AND IEDS

Up until the end of the Cold War, 80% of mines that were likely to be encountered were blast mines (mainly because of their relative simplicity). It was also apparent that 95% of these mines that were encountered contained not more than 9–10 kg of explosives. This was probably due to the fact that 9–10 kg is about the mass limit that someone can easily handle whilst deploying multiple mines. Because of these factors, most battle tanks and APCs were designed to withstand 9 kg of TNT (or equivalent) exploding under their wheels or tracks.

However, since the end of the Cold War, AFVs have been subjected to an ever-increasing threat from buried weapon systems that include IEDs. IEDs are particularly insidious in that they are, as the name implies, 'improvised', and this means that it is often difficult to predict the mass of the explosive, the type of explosive used and the nature of the fragmentation that it will produce. The effect that these weapons

(a) Loss of structural integrity   (b) Perforation

(c) Floor plate deformation   (d) Lift
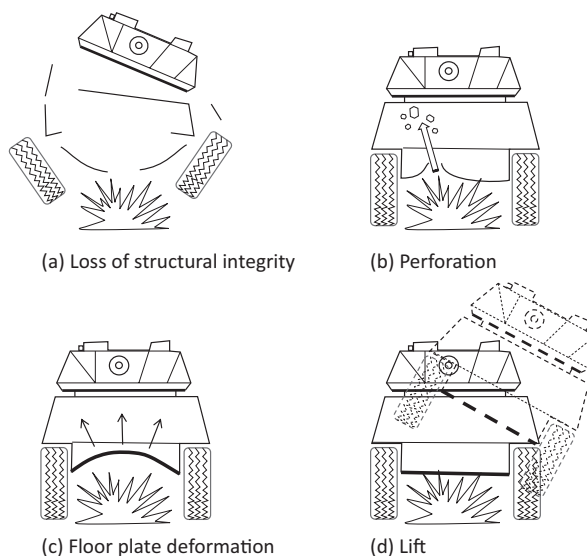
FIGURE 3.21 The effect of an IED or mine on an armoured vehicle detonated under the vehicle. (a) Loss of structural integrity, (b) perforation, (c) floor plate deformation and (d) lift.

may have on a vehicle is, as most readers would be aware from the news reports, devastating. In Figure 3.21, there are four examples of what can happen to an AFV when an explosive device is detonated under the centre of the vehicle. Failure will occur according to one of these examples or even a combination of events. They are summarized as follows:

1. *Loss of structural integrity*: The explosive load is powerful enough to bend the steel structure beyond its strain-to-failure limits, the weld lines fail and parts of the structure are propelled radially outward.
2. *Floor plate perforation*: The bottom plate is perforated by either a fragment, explosively formed projectile (EFP) or a piece of debris that is explosively accelerated from the ground into the AFV. The floor plate fails as it is unable to resist the penetration and ultimately perforation of the fragment.
3. *Floor plate deformation*: The impulse delivered by the explosion causes the bottom of the vehicle to deform. The floor plate is accelerated up into the cabin of the AFV; anybody who is in direct contact with the floor is likely to suffer serious injury due to the fast acceleration of the plate.
4. *Lift*: It is caused when the expanding blast wave is unable to be diverted away from the underside of the vehicle, and consequently, the vehicle is accelerated upward. Again, the acceleration loads are going to be huge; injury is most likely. Anybody who is not strapped in will almost certainly suffer serious injury or death as they are thrown around the inside of the cabin. Any loose object will turn into a lethal projectile.

Thankfully, considerable progress has been made in recent years in providing defence against improvised devices. More about this will be discussed in Chapter 11.

It should be noted that the use of IEDs is not a modern phenomenon, and modern concepts can be traced back to medieval examples such as the 'Fougasse'. These were first used in Italy in c. 1530 and were simply composed of a hole in the ground into which black powder and various projectiles (rock/iron) were filled. The black powder was lit by a fuze resulting in an explosion that propelled the numerous rocks and other projectile materials towards the enemy.

3.5   SHAPED CHARGE

A shaped-charge warhead consists of a mass of explosives surrounding a conically shaped metal, usually copper, and some form of detonator to initiate the explosive. The most infamous weapon system that employs a shaped-charge warhead is the rocket-propelled grenade (RPG-7). Although it is called a grenade, and it does have some fragmentation effects, it is in fact a shaped-charge system. This is its primary means of attack. The formation of a shaped-charge jet is schematically shown in Figure 3.22.

A shaped-charge jet is formed by the collapse of a liner of material (usually copper) due to a high-compressive detonation wave evolving in an explosive charge. The resulting jet possesses a tip velocity in the range of 5–11 km/s and is determined by several factors including the apex angle of the conical liner, the detonation wave velocity and the material from which the liner is made. The smaller the apex angle (α), the faster the jet. In fact, it can be shown from a trigonometric point of view that as $\alpha \to 0$ (i.e. as the apex angle is reduced to zero), the maximum velocity that can be achieved is

$$v_{\max} = 2U_{D} \tag{3.37}$$

where U_{D} is the detonation wave velocity of the explosive.
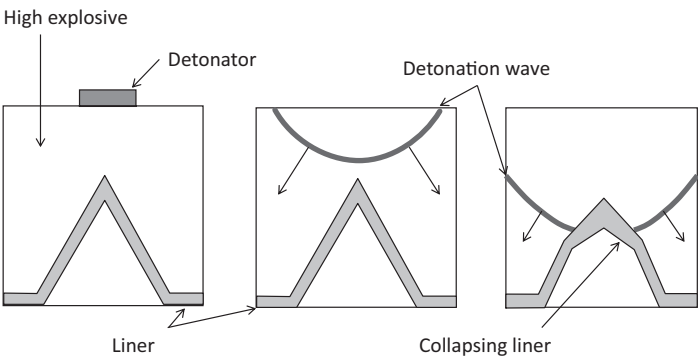
FIGURE 3.22   Initial stages of shaped charge jet formation.

So, the velocity of the shaped-charge jet can never exceed twice the detonation wave velocity in the explosive. In reality, α needs to be a finite value to get a good length of jet (which is also very important for penetration).

3.5.1 PENETRATION PREDICTION

The penetration of a shaped-charge jet into a target material is assumed to be hydrodynamic due to the high pressures formed on contact. There are excellent reviews on shaped-charge technology that are covered in Chou and Flis (1986) and Walters and Zukas (1989).

An equation to predict jet penetration is

$$p = l_j \sqrt{\frac{\lambda \rho_j}{\rho_t}}$$

(3.38)

where

l_j is the length of the jet (which, on first approximation, can be taken to be the standoff).

ρ_j is the density of the jet.

ρ_t is the density of the target.

λ is a constant (for cohesive jets $= 1$; for particulating jets $= 2$).

The derivation of this type of equation will be discussed in Chapter 4. A slight modification to this penetration mode was provided by Pack and Evans (1951), which took into account both the strength of the target and the velocity of the jet. The Pack and Evans equation is

$$p = l_i \sqrt{\frac{\rho_j}{\rho_t}} \left(1 - \frac{\alpha_1 Y_0}{\rho_j v^2} \right)$$

(3.39)

where

v is the velocity of the jet.

Y_0 is the yield strength of the target.

α_1 is a function of the densities of the jet and target.

They showed that for armour with a very high yield stress, the correction term $\alpha_1 Y_0 / \rho_j v^2$ can be as high as 0.3 (i.e. the penetration can be reduced by as much as 30% for a high-strength target).

Alternative penetration equations are provided by DiPersio and Simon (1964) for three cases: (1) penetration before the jet break-up, (2) the jet breaks up during penetration and (3) the jet breaks up before reaching the target. For case (1), where a cohesive jet is expected during penetration,

$$p = s \left[\left(\frac{v}{v_{min}} \right)^{\frac{1}{\gamma}} - 1 \right]$$

(3.40)

where

$$\gamma = \sqrt{\frac{\rho_t}{\rho_j}} \tag{3.41}$$

s = the effective standoff, which is calculated from the virtual origin of the shaped charge to the target, and v_{min} = minimum jet velocity that contributes to material penetration. v is the velocity of the jet tip.

For case (2), where particulation occurs during penetration, it is found that

$$p = \frac{(1+\gamma)(vt_b)^{[1/(1+\gamma)]} s^{[\gamma/(1+\gamma)]} - v_{min} t_b}{\gamma} - s \tag{3.42}$$

Finally, for the third case (3), it is found that

$$p = \frac{(v - v_{min})t_b}{\gamma} \tag{3.43}$$

where t_b = the time of jet break-up.

For a shaped-charge jet with a constant liner thickness, the stretching of the jet occurs in a linear fashion. Therefore, there is a linear velocity distribution from the fast-moving tip all the way to the slow-moving slug at the rear. Counter-intuitively, it also can be assumed that each particle in the jet has a constant velocity. This is because it can be assumed that each portion of the jet is accelerated nearly instantaneously by the high explosive.

It should be noted that v_{min} is not a constant and varies as the penetration ensues. Rearranging Equation 3.40 gives a relationship of how v_{min} varies as it penetrates a target. So,

$$v_{min} = \frac{v}{\left(\dfrac{p}{s} + 1\right)^\gamma} \tag{3.44}$$

This relationship is plotted graphically in Figure 3.23 for a copper jet penetrating a steel target at different initial values of v.

Note that Equation 3.23 also provides the exit velocity of the jet after penetrating a target of finite thickness, p. In other words, the exit velocity (v_{out}) of the jet after it has penetrated through a finite thickness of the plate is given by

$$v_{out} = \frac{v}{\left(\dfrac{p}{s} + 1\right)^\gamma} \tag{3.45}$$

3.5.2 Jet Formation

The first real analysis of how shaped-charge jets were formed occurred just after WWII when Birkhoff et al. (1948) published an analysis of shaped-charge formation.
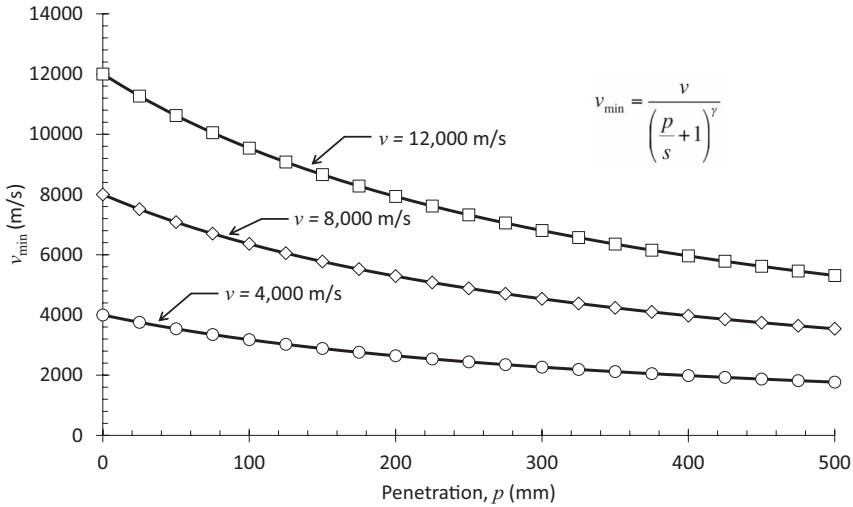
FIGURE 3.23   Variation of v_{min} with penetration depths for different values of initial jet velocities, v. The jet is made from copper ($\rho_j = 8900\,\text{kg/m}^3$), and the target is made from steel ($\rho_t = 7800\,\text{kg/m}^3$); $s = 360\,\text{mm}$ for each case.

They recognized that the detonation pressure is much larger than the strength of the liner and therefore treated the liner material as if it behaved like a non-viscous fluid (hence the word 'jet'). Later, the development of Birkhoff et al.'s work was carried out by Pugh et al. (1952) who built on the hydrodynamic concepts postulated by Birkhoff et al. and provided a theory for liner collapse and subsequent jet stretching. They theorized that the velocity of liner collapse changed continuously from the apex of the cone to its base, and this led to the stretching phenomena seen with shaped-charge jets. Good reviews of the history of shaped-charge jets are provided in Kennedy (1990) and Walters (1990).

   An example of a 100-mm shaped-charge jet penetrating steel with time is shown in Figure 3.24 (Held, 1976). Electrical 'make-contact' probes were installed in the target in between discrete plates and this allowed for the evaluation of penetration with time. During the initial phases of penetration the penetration rate is astonishingly high (~4000 m/s) however this drops off as penetration ensues resulting in ~650 mm of steel being penetrated in 400 µs. This drop off in penetration rate is due to the fact that the jet is stretching and there is a velocity gradient from the tip to the slug. Thus, as subsequent jet material makes contact with each steel target plate, its impact velocity is less, and this reduces the subsequent penetration rate. This can be seen by analyzing the following equation that can be used to calculate the penetration rate of a homogeneous rod penetrating a target hydrodynamically:

$$u = \frac{v}{\left(1 + \sqrt{\dfrac{\rho_t}{\rho_p}}\right)} \tag{3.46}$$
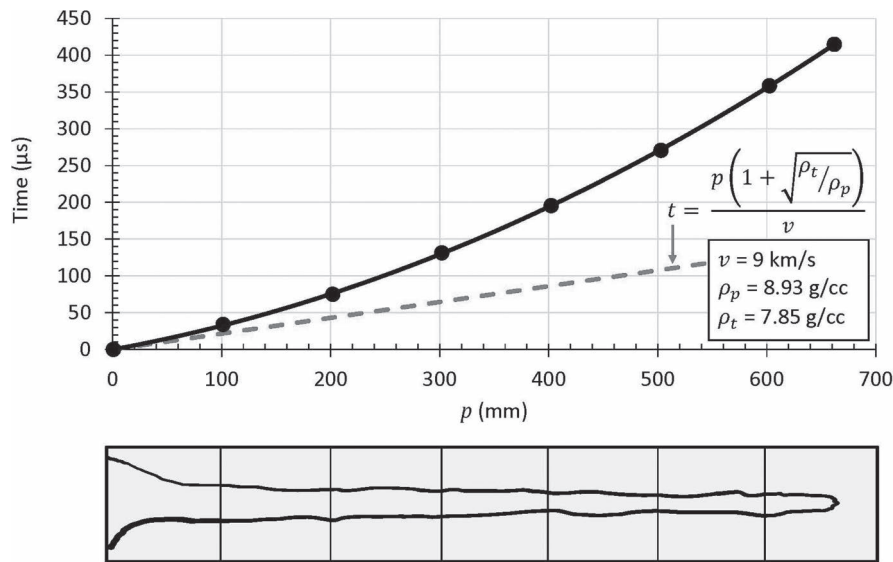
FIGURE 3.24 A 100-mm shaped-charge jet penetrating steel with time. The straight dashed line indicates the expected penetration velocity from a homogeneous copper rod penetrating steel after impacting at 9 km/s. (Experimental penetration data adapted from Held, 1976.)

where,

u = penetration velocity (crater growth rate in the direction of penetration)
v = impact velocity
ρ_p = density of the penetrator
ρ_t = density of the target

This equation, including its derivation, will be discussed in Chapter 4. The penetration rate is clearly a function of the impact velocity. It can be seen that for a solid rod (as opposed to a stretching jet), impacting the steel at 9 km/s, the penetration rate is expected to be constant and faster than the shaped-charge jet (in this instance). This is presented by the dashed line in Figure 3.24.

A schematic of a shaped charge jet formation is shown in Figure 3.25. The explosive charge is detonated and forms a high-pressure detonation wave that expands hemispherically within the cylinder of high explosive. Eventually, the detonation front engulfs the liner and locally deforms the liner material to very high strains over a very short period of time. After the formation of the jet (>40 μs), a residual slug follows the jet at a much-reduced velocity (1–2 km/s).

The cone is usually made from copper, but jets can also be made from brittle materials such as glass and ceramic. Copper has a face-centred cubic (FCC) crystalline structure, which lends itself to achieving good ductility. However, molybdenum (a body-centred cubic [BCC] metal, which is inherently less ductile) has also been used in shaped charge weapon design. BCC metals (such as Fe, Mo and Ta) tend to produce chunky jets, whereas FCC metals produce long thin ductile jets.
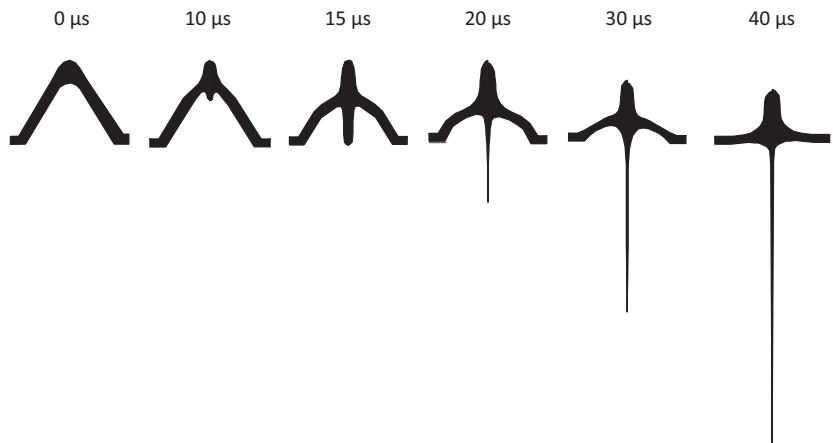
FIGURE 3.25 Formation of a copper shaped charge jet.

Hexagonal close-packed materials such as magnesium and titanium tend to produce powdery jets; this is due to the limited modes available to accommodate plastic deformation in these structures.

Of course, a shaped charge liner can be formed into all sorts of shapes and sizes as can be seen in Figure 3.26. Each shape can bestow a different velocity gradient and therefore different jet length and jet shape. Liners with steeper gradients will result in a jet with high velocity. Variable gradient liners will produce jets with a large velocity gradient. For example, a trumpet liner (see Figure 3.26) will produce a longer and more penetrating jet, whereas a Norman helmet shape will produce a shorter but larger-diameter jet.

Shaped charge liners can also be very large as exemplified by the Mistel (mistletoe) warhead developed by the Germans in WWII. A fighter aircraft was mounted piggyback on the top of a large unmanned bomber aircraft that carried the Mistel warhead. Amazingly, the warhead consisted of a 2-m-diameter conical-shaped charge with an explosive mass of 1720 kg. It is thought that the liner had a 120° apex angle and was about 30 mm thick (and made from aluminium or steel). The fighter pilot flew the warhead to the target who, after aiming it, released it before returning to base (Walters, 2008).
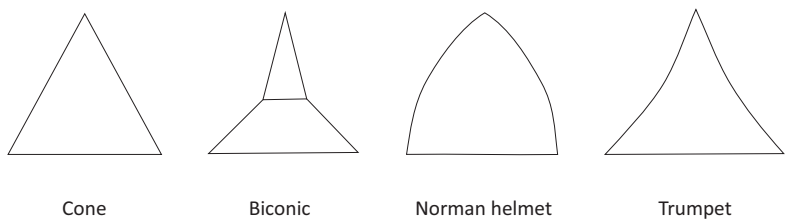
FIGURE 3.26 Examples of liner shapes.

Due to the nature of the formation of the jet, a standoff distance from the armour is required to achieve optimum penetration. If the standoff distance is too large, the jet will begin to particulate, and its penetration depth will be compromised. If the standoff is too low, the jet will not have the space to form, and therefore, again, the penetration depth into the armour will be reduced. Typically, a standoff distance of 4–5 CDs is required for the optimum standoff distance. However, a much-reduced standoff is usually employed. Standoff is engineered by using a spigot (or elongated nose) protruding from the front of the warhead casing. This spigot cannot be too long due to potential manual handling problems, especially in confined turrets. However, more importantly, the warhead needs to be able to fly straight and an extra-long spigot would not be conducive to that outcome. So, for example, the Milan 1 (Ø103 mm) has a standoff of 1.53 CD whereas the Milan-K (Ø115 mm) has a standoff of 2.50 CD (see Figure 3.28). This is despite the fact that using a higher standoff would result in deeper penetration and therefore better lethality.

The relationship between standoff and penetration for two jet materials is shown in Figure 3.27. Not only does the standoff affect penetration, but also the length and density of the jet play a role. The higher the density of the jet, the greater the penetration depth, and that is why copper ($\rho_0 = 8900\,\text{kg/m}^3$) provides a higher penetration than aluminium ($\rho_0 = 2800\,\text{kg/m}^3$). Both are FCC metals.

Shaped charge jets are not jets of fluid as their name implies, but rather, they are thought to be super-plastic solids. Temperature measurements taken from copper jets
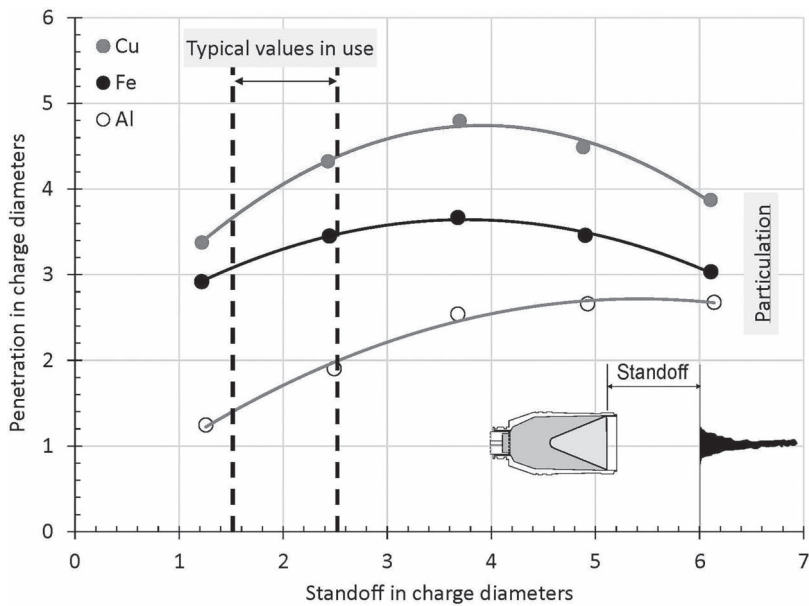
FIGURE 3.27 Effect of weapon stand-off on the penetration of a shaped charge jet formed from different liner materials. Data for a 66° cone warhead with a wall thickness of 0.023 charge diameter with penetration into mild steel. (Adapted from data presented in Peters and Cummings, 1957.)

formed from 81.3-mm-diameter liners have resulted in a mean temperature of 432°C (with a standard deviation of 76°C; Von Holle and Trimble, 1976). Although the authors acknowledged that these measurements were preliminary, it is worth noting that this temperature is less than half the melting temperature of copper (1085°C). Other work based on a one-dimensional theoretical model has suggested that most of the heating of a copper jet is caused by the plastic deformation during liner collapse and jet elongation (130°C for each mechanism) and the temperature increase due to the explosive shock wave is relatively low (30°C) (Racah, 1988). Again, these calculations suggest that the temperature of the jet is much lower than the melting temperature of copper.

An advanced PG-7 shaped charge grenade that can be launched from these weapons can penetrate up close to 1 m of RHA. Penetration depths are dependent on the geometry and material of the liner, the explosives used and the manufacturing tolerances that are applied (see Table 3.8). Typically, a 40-mm high-precision shaped charge will penetrate ~200 mm of RHA and a 50-mm high-precision shaped charge will penetrate ~300 mm of RHA.

However, penetration can be quite variable. Figure 3.28 shows the penetration expected into RHA by two well-known shaped-charge warheads, the MILAN and MILAN-K. The MILAN-K has a charge diameter of 115 mm and a characteristic spigot protruding from its nose to enhance standoff whereas the MILAN has a charge diameter of 103 mm and a rounded nose. Both warheads exhibit considerable scatter in penetration data, especially as the standoff increases beyond the optimal value. Furthermore, it is again clear that the actual standoff (as intended by design) is lower than the optimal penetration that could be expected. These are shown by the vertical lines in Figure 3.28 and are 158 mm for the MILAN and 290 mm for the MILAN-K. Nevertheless, the scatter in the penetration data at these values is relatively small and therefore allows for a predictable penetration performance on the battlefield.

Some shaped-charge devices (particularly those used as anti-tank mines) do not employ liners but instead they rely on a focused explosive force to cut holes into the belly of tanks and the like. They comprise a hollowed-out explosive fill, the hollow of which is conical or hemispherical in shape (Backofen Jr. and Williams, 1981). With these mines, the absence of any metal makes detection more difficult.

TABLE 3.8

Armour Penetration Data for Some Grenades Launched from the RPG–7 Knut 40-mm Portable Rocket Launcher

Grenade	Charge Diameter (mm)	Armour Penetration (mm)
PG–7VM	70	300
PG–7N	–	400
PG–7L	93	600
PG–7LT[a]	93	700
PG–7M 110	110	600–700

[a] Tandem warhead.
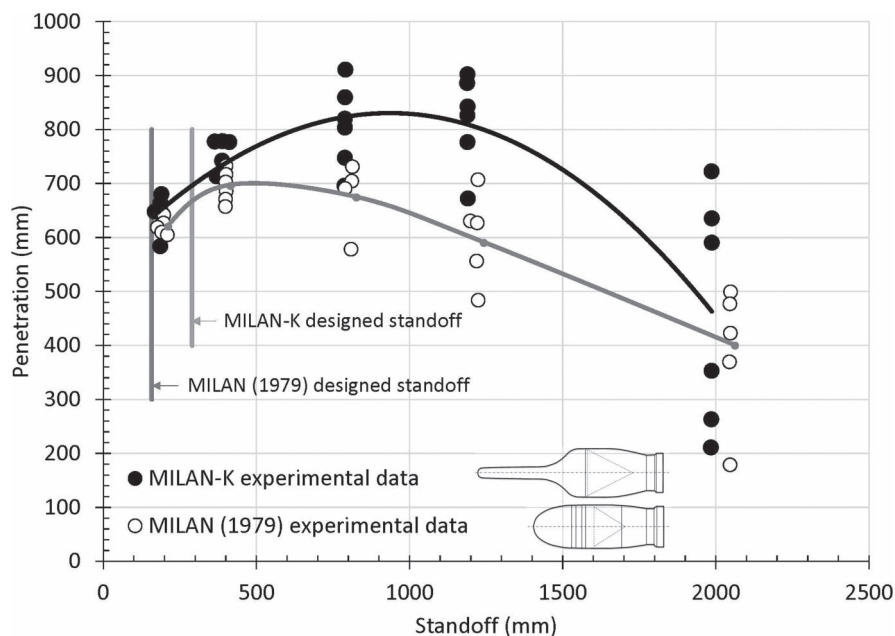
FIGURE 3.28 Penetration data for the MILAN (1979) and MILAN-K with variable stand-off, adapted from data presented from (Held, 2002). Actual standoff (as intended by design), also shown.

3.6 EXPLOSIVELY FORMED PROJECTILES

The use of an EFP, otherwise known as a Misznay–Schardin slug or self-forging fragment, remains one of the most versatile methods of attacking armour. The projectile is formed by the dynamic deformation of a metallic dish due to the detonation of an explosive charge located behind it. The formation of the EFP is illustrated in Figure 3.29, and a soft-captured EFP (captured by using large thicknesses of ever-increasing densities of layered materials) is shown in Figure 3.30. The mechanism of dish deformation is very similar to that of a shaped charge warhead (see Section 3.5), and indeed, this warhead is sometimes described as a shaped charge warhead. The fundamental difference is that instead of a conical liner being deformed into a jet, a relatively shallow dish is formed into a slug or projectile. The nature and size of the projectile can be optimized for a particular application by the use of different explosives, CDs, various 'wave-shaping' techniques, case and dish materials. The dish is often made of a relatively soft material to ensure that it deforms into an appropriate projectile-like shape. Relatively dense metals such as steel ($\rho_0 = 7850\,\text{kg/m}^3$), iron ($\rho_0 = 7870\,\text{kg/m}^3$), copper ($\rho_0 = 8930\,\text{kg/m}^3$) and, more recently, tantalum ($\rho_0 = 16{,}690\,\text{kg/m}^3$) are used to ensure effective penetrative performance, especially in the lower part of the hydrodynamic regime (2–3 km/s).

Unlike shaped charge warheads, an explosively formed projectile is insensitive to standoff distance (the distance between the warhead at initial slug formation and
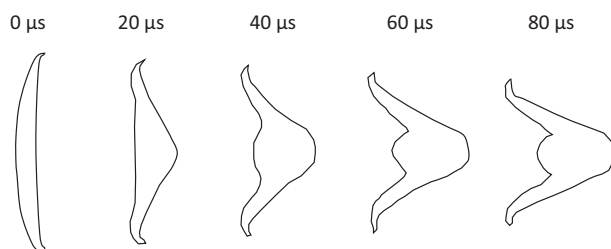
FIGURE 3.29   Result from a numerical simulation showing the formation of an EFP.
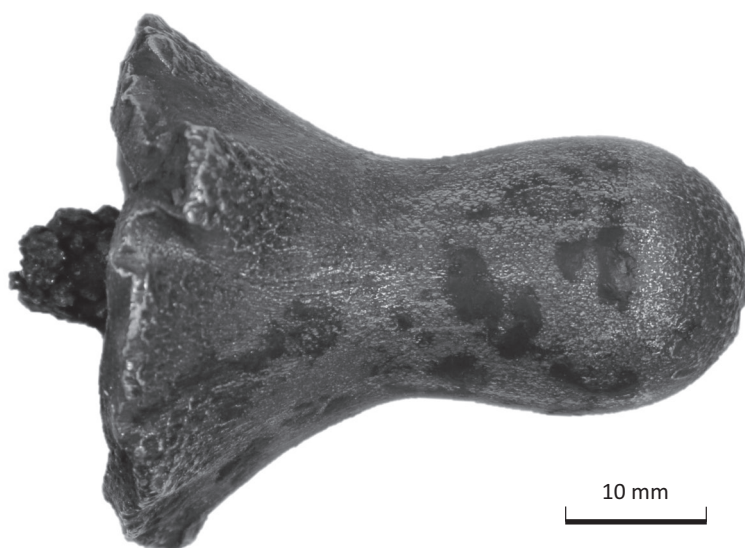
FIGURE 3.30   A well-designed soft-captured EFP.

the target). Hence, it can be used in a wide variety of applications such as mines (for example, the M70 Remote Anti-Armour Mine and the Yugoslav TMRP-6 anti-tank mine). It is also used in top-attack sub-munitions such as those available in the M898 Sense and Destroy Armour (SADARM) projectile and guided weapons.

Explosively formed projectiles can trace their history back to 1936 when Professor R W Wood reported on the death of a young woman inspecting her 'house furnace' to see if the fire was burning properly (Wood, 1936). According to Wood's report, the young lady 'was struck by a small particle of metal which flew out of the fire and penetrated the breastbone, slitting a large artery and causing death in 2 or 3 minutes from internal hemorrhage'. It turned out that the culprit was part of a detonator that had been delivered by mistake along with the coal for the furnace. At that time, the detonators that were used in coal mines for blasting were around 40 mm in length and 5 mm in diameter and formed from thin sheets of copper. The head of the detonator was comprised of a concave component of copper. The mercury fulminate charge

(usually detonated by an electrically heated wire) was set off by the fire in the furnace resulting in the detonator's head being projected towards the young lady, who was opening the furnace door at the unfortunate time! So, infamously, she became the first victim of an explosively formed projectile. Wood proceeded to report all types of experiments that showed that the denotator heads were effectively turned inside out as they were projected at a high velocity (6000 ft/s, 1830 m/s) by the mercury fulminate composition—similar to our modern understanding of how modern explosively formed projectiles are produced.

It is entirely possible that Wood's paper could have prompted a Hungarian army officer, by the name Misznay, to develop this observed phenomenon into a weapon during World War II. That is, this could have led to the Misznay–Schardin charge. It is not clear how Professor Hubert Schardin contributed to the weapon design however it is thought that Schardin once visited Misznay in Hungry and on his return wrote a technical paper describing the so-called Misznay–Schardin effect. And so the name stuck! (Kennedy, 1990).

Relatively little research has been published in the open literature providing specific details on protecting against this threat. Instead, researchers have been preoccupied with disseminating information regarding protection against KE ammunition (long-rod penetrators [LRPs]) and shaped charge jets. EFPs have a lower length-to-diameter ratio than LRPs, travel faster, are traditionally made of less-dense materials and are softer in construction. Conversely, the shaped charge jet is almost universally formed from a copper liner and extends at a velocity far in excess of the flight velocity of an EFP. These factors alone would lead us to conclude that the penetration mechanics of an EFP are likely to be different from that of a shaped charge jet or an LRP.

Rondot (1998) studied the performance of tantalum EFPs as they penetrated semi-infinite steel target plates as well as pre-armoured steel plates. With the latter, a finite thickness plate of steel of different hardness values (BHN=107 and 480) and at two different angles of obliquity (0° and 60°) were perforated and the depth of penetration into a steel (BHN=320) witness plate was recorded. The results showed that the mass effectiveness of the system at normal incidence did not exceed 1.15, whereas, at the 60° oblique angle, the mass effectiveness improved and reached 1.25 for L/d=6.0 projectiles.

In this case, mass effectiveness (E_m) was defined as a ratio of areal densities, viz,

$$E_m = \frac{p_\infty \rho_{st}}{h \rho_{st} + p_r \rho_{st}} \tag{3.47}$$

where ρ_{st} is the density of the steel targets and front armour, p_∞ is the penetration into the witness plate (no armour) and p_r is the penetration into the witness plate (with armour), and h is the thickness of the steel armour plate, spaced from the witness plate (see Chapter 12 for a discussion of this technique).

3.7 HIGH-EXPLOSIVE SQUASH HEAD

The use of high-explosive squash head (HESH) rounds is gradually diminishing due to the interest in fitting smoothbore guns into main battle tanks (MBTs). HESH has been mainly used to attack bunkers and occasionally thin-skinned vehicles where the
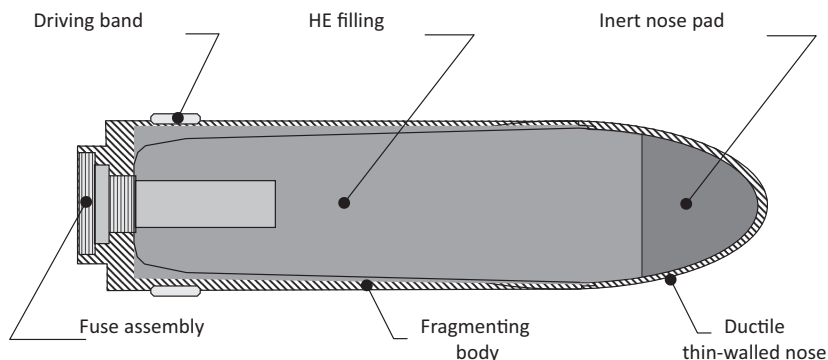
FIGURE 3.31   A typical HESH shell.

use of an APFSDS round would completely overmatch the armour and therefore not transfer sufficient energy to the target. A HESH round consists of a base-fuze explosive shell that is spin-stabilized. On contact with the target, the thin shell nose rapidly deforms and spreads a layer of polymer-bonded explosive over the target (a typical 120-mm round will contain approximately 4 kg of explosive). The fuze is embedded in the explosive and then detonates the explosive leading to a compressive stress wave propagating into the target. An inert filling is normally placed in the nose to lessen the shock directly imparted to the explosive on impact with the target. A schematic of a typical HESH round is shown in Figure 3.31.

If the compressive wave front that is moving into the target encounters a free surface, then the wave is reflected back as a tensile wave. During reflection, the leading edge of the tensile wave overlaps the trailing edge of the compressive wave. Therefore, the resultant stress in the target can be calculated by summing the compressive stress at a specific point with the tensile stress. The magnitude of the tensile stress increases as it moves towards the point of impact, and eventually, the entire compressive wave is reflected.

Because most materials are weaker in tension than they are under compression, tensile failure normally follows and occurs when the net tensile stress exceeds the tensile strength of the material. This process is called spalling and can lead to the formation of a lump of material (sometimes referred to as a 'scab') that becomes separated from the target material (Figure 3.32). A steel scab can travel at velocities of around one-third the speed of sound.

HESH is effective against thick concrete structures and has reasonable fragmentation effects that can threaten thin-skinned vehicles.

3.8   FRAGMENTS

The final consideration in this chapter is that of fragments that are propelled by a blast wave produced from an exploding shell, pipe bomb or IED, etc. These shells produce fragments of varying velocities and shapes. A modern 155-mm shell can propel up to 10,000 fragments on detonation that are lethal up to approximately 50 m. Because
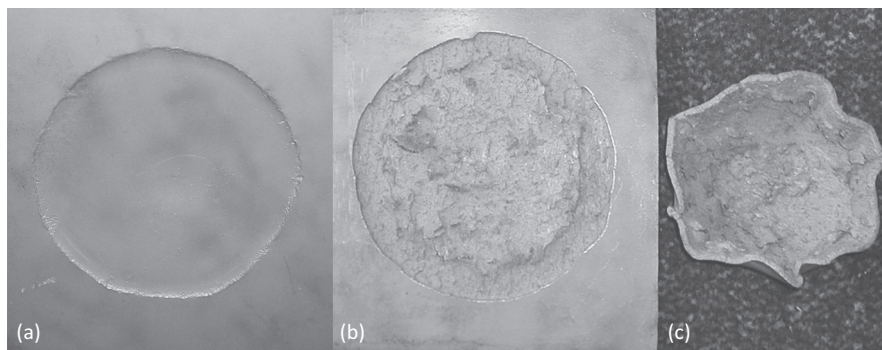
FIGURE 3.32 A steel target that has been subjected to attack from a HESH round, showing (a) the impact surface, (b) the scabbed surface and (c) the scab.

these fragments have a somewhat irregular shape and tend to be unstable in flight, they lose velocity fairly quickly with distance travelled with lighter-weight fragments exhibiting a faster drop-off than heavier fragments. Their penetration characteristics are similar to high-velocity rifle bullets in that they are of a similar average mass to, say, 14.5-mm bullets, and although they may be travelling at a relatively high velocity when compared to a bullet, their shapes are not ideal for maximizing penetration.

There are various ways in which fragmentation occurs in a shell casing. This can be achieved by making grooves in the case that act as stress concentration points for the shock wave. Alternatively, notched wire has sometimes been used where the wire has been brazed together. Adding grooves in an explosive is sometimes employed where the grooves in an explosive provide a mini shaped charge focusing effect. Similarly, a metal liner can be added in between the explosive and shell casing to modify the shape of the shock wave interacting with the case metal to focus the stress on the metal casing. Such a liner is often called a 'Buxton liner'.

3.8.1 Gurney Analysis to Predict Fragment Velocity

Gurney (1943) provided an analysis of the estimation of fragment velocity from an exploding shell. Gurney realized that the important parameters for estimating the velocity of a fragment were the internal energy per unit mass of the explosive material (E) and the ratio of the mass of the metal to the mass of the charge (M/C). This ratio is known as the 'loading factor'. Assuming that all the internal energy of the explosive was translated over to KE of the metal fragments (i.e. ignoring heat, light and the KE of the air that is exposed to the blast gases), Gurney arrived at a series of equations to predict the velocities of fragments for different initial geometries. The theory for a cylindrical pipe bomb is provided here.

Assume that there is a cylindrical pipe bomb such that the ends are closed off, and there is no leakage (see Figure 3.33). When the explosive detonates, there is little resistance to fragmentation, and the material in the cylinder expands uniformly at velocity v_0 (sometimes referred to as the Gurney velocity). It is assumed that the velocity of the gases that result from the detonation varies linearly from the centre
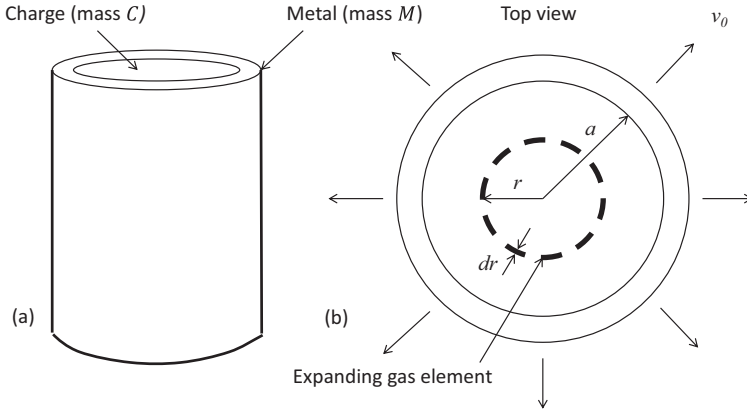
FIGURE 3.33 (a) A cylindrical charge and (b) the top view showing the gas element expanding at velocity v with the metal tube expanding at velocity v_0.

of the core to the interface with the metal. At the interface, the velocity of the metal cylinder is equal to the velocity of the detonation gases, whereas, at the centre of the cylinder, the velocity is equal to zero. Detonation is assumed to be instantaneous. For a cylinder of internal radius, a, the velocity of the gas, v, at radius, r, is given by

$$v = v_0 \left(\frac{r}{a} \right) \tag{3.48}$$

The KE of the gas is given by

$$KE_g = \frac{1}{2} \int v^2 \cdot dm_g \tag{3.49}$$

and

$$dm_g = \rho_0 \, 2\pi r \cdot dr \tag{3.50}$$

Therefore,

$$KE_g = \frac{1}{2} \int_0^a v_0^2 \frac{r^2}{a^2} \rho_0 \, 2\pi r \cdot dr \tag{3.51}$$

leading to the solution of

$$KE = \frac{1}{4} v_0^2 \pi a^2 \rho_0 \tag{3.52}$$

However, it is known that

$$C = \pi a^2 \rho_0 \tag{3.53}$$

Therefore, the KE of the gases is given by

$$KE_g = \frac{1}{4}Cv_0^2 \tag{3.54}$$

Remembering that KE=EC, the total KE is given by

$$KE = \frac{1}{2}Mv_0^2 + \frac{1}{4}Cv_0^2 \tag{3.55}$$

$$EC = \frac{1}{2}Mv_0^2 + \frac{1}{4}Cv_0^2 \tag{3.56}$$

and rearranging

$$v_0^2 = \frac{2EC}{\left[M + \frac{1}{2}C \right]} \tag{3.57}$$

and again

$$v_0 = \sqrt{2E}\left[\frac{M}{C} + \frac{1}{2} \right]^{-\frac{1}{2}} \tag{3.58}$$

The equation above provides a first-order approximation of the velocities that would be expected from a cylindrical bomb. And, actually, it works quite well—particularly where the shell material is ductile enough to expand up to diameters where the force acting by the detonation gases is small. For brittle materials, the actual velocity of the fragments will be lower than that predicted by this theory—mainly due to the fact that fracture occurs allowing for gas blow-by, although work with explosively accelerated ceramic tiles (very brittle materials) has shown pretty good correlation (Hazell et al., 2012). The equation for the velocities will vary slightly depending on the initial geometry of the set-up; good overviews of the various calculations for the different geometries are presented here (Meyers, 1994; Cooper, 1996). It should be noted that in all the derivations for the various geometries, there is one variable that keeps cropping up, namely $\sqrt{2E}$. This is known as the Gurney constant, and it has the units of velocity. It is possible to measure the Gurney constant for explosives by measuring the terminal velocities of explosively driven metals (Kennedy, 1970); a selection of constants is presented in Table 3.9 (Kennedy, 1972).

Generally speaking, the Gurney constant is similar for similar types of explosives and is linked to its detonation velocity (Koch et al., 2002). Figure 3.34 shows the calculated fragment velocities for three explosives in terms of the ratio between the mass of the metal and the mass of the explosive charge (M/C). The three explosives are HMX (a powerful and relatively insensitive nitroamine high explosive), Comp B (a castable mixture of RDX and TNT) and nitromethane (a relative insensitive liquid explosive). You will notice that there is not a great deal of difference between them.

TABLE 3.9
Gurney Constants for a Selection of Explosives

No.	Explosive	Density (g/cc)	$\sqrt{2E}$ (mm μs)
1	RDX	1.77	2.93
			2.83
2	Composition C-3	1.60	2.68
3	TNT	1.63	2.37
			2.44
4	Tritonal (TNT/Al=80/20)	1.72	2.32
5	Comp B (RDX/TNT)	1.72	2.71
			2.77
			2.70
			2.68
6	HMX	1.89	2.97
7	PBX-9404	1.84	2.90
8	Tetryl	1.62	2.50
9	TACOT	1.61	2.12
10	Nitromethane	1.14	2.41
11	PETN (duPont sheet)	1.76	2.93
12	EL506D	1.46	2.28
			2.50
13	EL506L	1.56	2.20
14	Trimonite No. 1[a]	1.10	1.04

Source: Kennedy, J. E. 1972. Explosive output for driving metal. *In: Behavior and Utilization of Explosives in Engineering Design, Proceedings of the 12th Annual Symposium of the New Mexico Section of the ASME.* Albuquerque, New Mexico: ASME. Preferred value of the Gurney constant for each explosive is listed first (Kennedy, 1972).

[a] Detonates nonideally.

Additionally, Figure 3.35 shows a plot of the dimensionless velocity, $\left(v_0/\sqrt{2E}\right)$ of the metal, M, for various configurations summarized in Table 3.10. This is plotted in terms of the loading factor (M/C). You will see that all configurations, apart from the symmetric sandwich and the asymmetric sandwich (assuming $N = 2M$) converge at high loading factors. Note that if we set $N = M$, for the asymmetric sandwich, we would expect the same behaviour as shown for the symmetric sandwich. However, due to the notation for the symmetric sandwich (where each plate$=M/2$) this is not the case—this is purely down to the notation used. This plot can be used to estimate metal velocity from any given metal/explosive system of simple geometry.

Of course, the Gurney analysis presented above is limited to a cylindrical example. Additional analysis is required where the geometry of the initial set-up is varied. These have been presented in a number of sources (e.g. Kennedy (1970), Zukas (1990), Meyers (1994), Cooper (1996) and Zukas and Walters (1998)), and the velocity equations are summarized in Table 3.10.
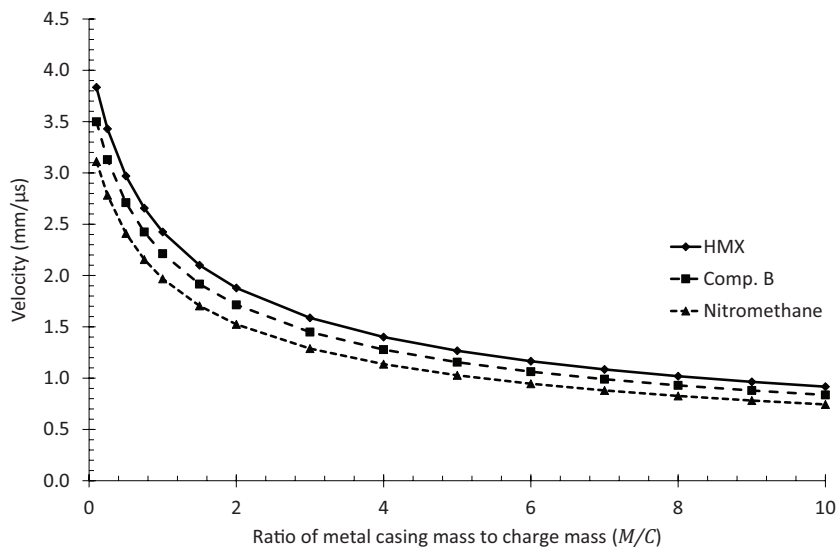
FIGURE 3.34 The effect of the M/C ratio on fragment velocities.
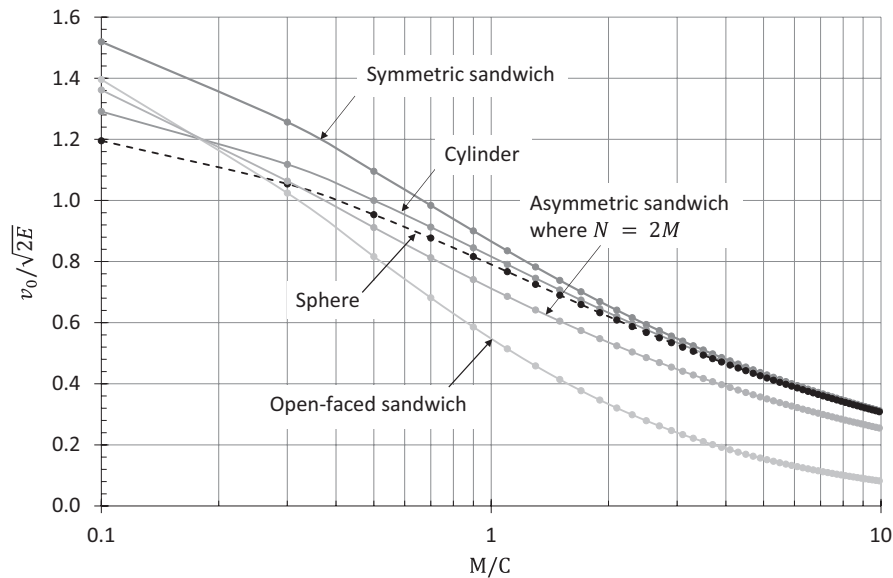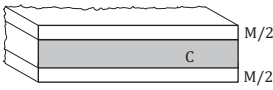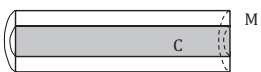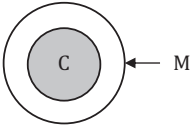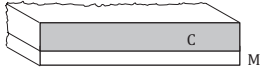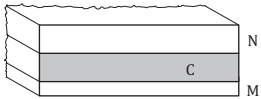
FIGURE 3.35 Dimensionless velocity of metal as a function of loading factor, M/C. (Adapted from Kennedy, 1970.)

TABLE 3.10
Gurney Equations

Type	Schematic	Equation
Symmetric flat sandwich	M/2 / C / M/2	$v_0 = \sqrt{2E}\left[\dfrac{M}{C}+\dfrac{1}{3}\right]^{-\frac{1}{2}}$
Cylinder	M / C	$v_0 = \sqrt{2E}\left[\dfrac{M}{C}+\dfrac{1}{2}\right]^{-\frac{1}{2}}$
Spherical	C ← M	$v_0 = \sqrt{2E}\left[\dfrac{M}{C}+\dfrac{3}{5}\right]^{-\frac{1}{2}}$
Open-faced sandwich	C / M	$v_0 = \sqrt{2E}\left[\dfrac{\left(1+2\dfrac{M}{C}\right)^3+1}{6\left(1+\dfrac{M}{C}\right)}+\dfrac{M}{C}\right]^{-\frac{1}{2}}$
Asymmetric sandwich	N / C / M	$v_0 = \sqrt{2E}\left[\dfrac{1+A^3}{3(1+A)}+\dfrac{N}{C}A^2+\dfrac{M}{C}\right]^{-\frac{1}{2}}$ where $A=\dfrac{1+2\dfrac{M}{C}}{1+2\dfrac{N}{C}}$

Source: After (Kennedy, 1970).

Example 3.5

Calculate the velocity of the metal casing from a pipe bomb that is made from steel (density = 7800 kg/m³) and is 200 mm long with an external diameter of 150 mm and an internal diameter of 75 mm. Assume that the internal part of the tube is filled with an explosive (density = 1500 kg/m³) and has a Gurney constant value of 2.9 mm/μs.

First, the mass of the explosive and the mass of the metal casing need to be calculated.

The mass of the explosive (C) is given by

$$\rho_0 \pi \frac{d_i^2}{4}l = 1500 \times \pi \times \frac{\left(75\times10^{-3}\right)^2}{4}\times 200\times 10^{-3}$$

$$C = 1.33 \text{ kg.}$$

The mass of the steel (M) is given by

$$\rho_0 \frac{\pi}{4}\left(d_0^2 - d_i^2\right)l = 7800 \times \frac{\pi}{4} \times \left[\left(150 \times 10^{-3}\right)^2 - \left(75 \times 10^{-3}\right)^2\right] \times 200 \times 10^{-3}$$

$$M = 20.68 \text{ kg}.$$

The velocity of the casing is given in Table 3.6 and is

$$v_0 = \sqrt{2E}\left[\frac{M}{C} + \frac{1}{2}\right]^{-\frac{1}{2}} = 2.9 \times \left[\frac{20.68}{1.33} + \frac{1}{2}\right]^{-\frac{1}{2}}$$

$$v_0 = 0.724 \text{ mm/μs} = 724 \text{ m/s}.$$

3.8.2 FRAGMENT SIZE PREDICTIONS

The first in-depth consideration of fragment sizes and their distribution was published by Mott (1947) just after WWII (although this was a culmination of extensive work and published internal reports—see Grady (2006) for a thorough treatise of Mott's work). Mott's fragmentation theory provided the foundation for what we understand of the mechanism of natural fragmentation today (Figure 3.36), that is to say, fragmentation that occurs due to the material's microstructure as opposed to prenotched bombs. Mott realized that if a uniform cylinder was subjected to an internal blast pressure, then in an ideal material, it would expand continually until fragmentation occurs simultaneously, and an infinite number of fragments are formed. Of course, this does not happen. Instead, as a crack begins to propagate, the presence of the free surface generated by the crack leads to a release in stress in the surrounding material. Consequently, a 'release wave' propagates away from the position of the crack, and this releases the stress in the surrounding material, thereby inhibiting
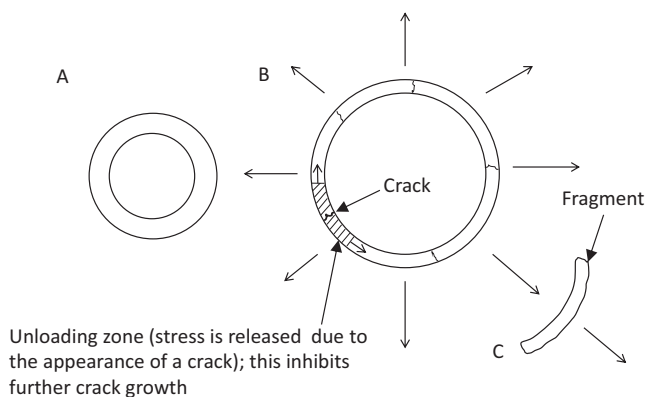
FIGURE 3.36 Mott's fragmentation theory: A – the cylinder is at rest, B – the cylinder expands due to an explosion and C – a fragment is formed.

crack growth. Thus, the number and size of fragments that are formed are determined by the balance between the rate of increasing hoop strain and the velocity of the release wave.

Mott showed that the average fragment length is proportional to a number of properties according to

$$l_f \propto \sigma_f \sqrt{\frac{1+\varepsilon_f}{\rho_0 B}} \qquad (3.59)$$

where

σ_f is the true stress at fracture of the shell casing.
ε_f is the plastic strain at fracture.
ρ_0 is the density of the shell casing.

B is the strain hardening characteristic of the shell casing assuming that the true stress–strain (σ–ε) response of the material (for large strains) can be written as

$$\sigma = Y_0 + B\ln(1+\varepsilon) \qquad (3.60)$$

Thus, a shell casing material that has a high fracture strength gives large fragments, and a high ductility also results in large fragments. Increasing the density of the material and the strain hardening parameter, B, results in smaller fragments.

For the prediction of fragment sizes due to natural fragmentation, the work carried out by Grady (1982a, b) also helps. This can be particularly insightful when trying to predict what happens when armour is attacked by an IED (such as a pipe bomb), for example. In this work, the average fragment diameter was linked to the strain rate and is given by:

$$d = \left(\frac{\sqrt{20}K_{Ic}}{\rho_0 c_0 \dot{\varepsilon}}\right)^{2/3} \qquad (3.61)$$

Where d is the fragment diameter (assuming a spherical fragment), K_{Ic} is the fracture toughness, ρ_0 is the density of the casing from which the fragment is formed, c_0 is the speed of sound in the casing material and $\dot{\varepsilon}$ is the strain rate. Grady compared this model with the experimental results of (Weimer and Rogers, 1979) with a reasonable correlation.

3.8.3 DRAG ON FRAGMENTS AND OTHER PROJECTILES

Anything flying through the air will be subjected to drag forces, and that includes bullets. There are several aerodynamic forces acting on free-flying projectiles. The most important ones are forebody drag and base drag. Skin friction also exists and, of course, gravity. However, for a first-order calculation, these effects can be ignored. A useful equation to describe the effect of drag on a free-flying fragment (or bullet) is given below. This is derived from the original work carried out by Lord Rayleigh who calculated the force acting on an object moving through a fluid.

Following Newton's second law,

$$F = m\frac{dv}{dt} \tag{3.62}$$

where
    m is the mass of the projectile.
    v is the velocity of the projectile.
    F is the drag force acting on the projectile.

It is assumed that the drag force acting on the object is given by

$$F = -\frac{1}{2}C_D\rho_{air}Av^2 \tag{3.63}$$

where
    C_D is the coefficient of drag of the projectile and is assumed to be constant.
    ρ_{air} is the density of air ($1.225\,\mathrm{kg/m^3}$).
    A is the presented area of the projectile.

Newton's second law then becomes

$$m\frac{dv}{dt} + \frac{1}{2}C_D\rho_{air}Av^2 = 0 \tag{3.64}$$

Assuming that C_D is not a function of velocity (a rather simplified assumption), then all of the constants can be lumped together in terms of L:

$$L = \frac{2m}{C_D\rho_{air}A} \tag{3.65}$$

Therefore, the equation becomes

$$L\frac{dv}{dt} + v^2 = 0 \tag{3.66}$$

and

$$L\int\frac{dv}{v^2} = -\int dt \tag{3.67}$$

where the solution is (in terms of the initial velocity, v_0)

$$v = \frac{Lv_0}{(v_0t + L)} \tag{3.68}$$

Integrating this equation, knowing that

$$v = \frac{dx}{dt} \tag{3.69}$$

where x is the displacement, and eliminating t, rearranging such that

$$t = L\left(\frac{1}{v} - \frac{1}{v_0}\right)$$
(3.70)

and substituting gives

$$v = v_0 \exp\left(-\frac{x}{L}\right)$$
(3.71)

when expanded gives

$$v = v_0 \exp\left[-C_D \rho_{air} x\left(\frac{A}{2m}\right)\right]$$
(3.72)

where v is the velocity of the fragment after flying distance x, v_0 is the velocity at detonation, ρ_{air} is the density of the air (1.225 kg/m³ at sea level), A is the projected area of the fragment offered to the flow, m is its mass, and C_D is the coefficient of drag. C_D is a dimensionless constant and depends on the fragment's geometry and velocity. The higher the drag coefficient, the higher the drag forces acting on the projectile and consequently, the faster its velocity will drop off. The fact that C_D also changes with velocity markedly around the transonic region (Mach 0.8–Mach 1.2) also complicates things—particularly for flat-headed projectiles (see Figure 3.37). However, for a first-order calculation, it is possible to calculate the velocity decay as a consequence of drag using a constant value of C_D.
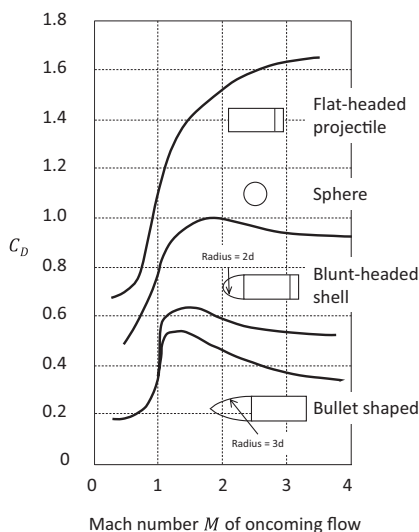
FIGURE 3.37 Variation of C_D with Mach number. (Adapted from Massey, B. S. 1989. *Mechanics of Fluids*, 6th ed. London: Van Nostrand Reinhold [International].)

It can be seen from this equation that heavier fragments will decelerate less than lighter-weight fragments when they both have the same initial velocity.

Example 3.6

A 9-mm calibre bullet with a mass of 10 g is fired from a muzzle of a gun at 300 m/s. Assuming a C_D of 0.2, calculate the velocity drop-off in the air at 500 m.
    First, the presented area, A, must be calculated:

$$A = \pi \frac{d^2}{4} = \pi \frac{\left(9 \times 10^{-3}\right)^2}{4} = 63.62 \times 10^{-6} \text{ m}^2.$$

From Equation 3.72, it is known that

$$v = v_0 \exp\left[-C_D \rho_{\text{air}} x \left(\frac{A}{2m}\right)\right] = 300 \exp\left[-0.2 \times 1.225 \times 500 \times \left(\frac{63.62 \times 10^{-6}}{20 \times 10^{-3}}\right)\right]$$

$v = 203.2$ m/s. So, the velocity would have dropped by a third.

3.8.4 FRAGMENT PENETRATION

A series of equations were developed in the 1960s by the Project THOR working group (Ballistic Analysis Laboratory, The Johns Hopkins University, 1961) specifically for understanding the penetration characteristics of various materials by explosively propelled fragments. The equations were derived from a large number of empirical tests. The Project THOR equation given for the ballistic limit velocity is given as follows (in SI units) after (Crull and Swisdak, Jr., 2005)

$$v_{\text{bl}} = 0.3048.10^{C_1} \left(0.061024 h A\right)^{\alpha_1} \left(15432.4 m\right)^{\beta_1} \left(\sec\theta\right)^{\gamma_1} \tag{3.73}$$

where
    v_{bl} is the ballistic limit velocity in m/s.
    h is the target thickness in cm.
    A is the average impact area of the fragment in cm^2.
    m is the mass of the original fragment in kg.
    C_1, α_1, β_1 and γ_1 are empirical constants of the material to be penetrated.

A selection of empirical constants for different materials is provided in Tables 3.11 and 3.12.
    Therefore, Equation 3.73 can be rearranged to calculate the thickness required to stop a fragment of a given mass, projected area and velocity, according to

$$h = \left(\frac{v_0}{0.3048.10^{C_1} \left(15432.4 m\right)^{\beta_1}}\right)^{\frac{1}{\alpha_1}} \left(0.061024 A\right)^{-1} \tag{3.74}$$

where v_0 is the impact velocity in m/s. The impact is at normal incidence.

TABLE 3.11
Empirical Constants for the Project THOR Equation (No Particular Fragment Shape Assumed); Metallic Materials

Material	Hardness (BHN)	C_1	α_1	β_1	γ_1
AA 2024-T3	120	6.185	0.903	−0.941	1.098
Cast iron	150–220	10.153	2.186	−2.204	2.156
Copper	42	14.065	3.476	−3.687	4.27
Lead	5.5	10.955	2.735	−2.753	3.59
Magnesium alloy	72	6.349	1.004	−1.076	0.966
Steel, face hardened	480–550 (front) 331–375 (rear)	7.694	1.191	−1.397	1.747
Steel, homogeneous hard	380	6.601	0.906	−0.963	1.286
Steel, homogeneous mild	150	6.523	0.906	−0.963	1.286
Titanium alloy	190	7.552	1.325	−1.314	1.643

TABLE 3.12
Empirical Constants for the Project THOR Equation (No Particular Fragment Shape Assumed); Non-Metallic Materials

Material	Hardness (Rockwell)	C_1	α_1	β_1	γ_1
Doron (glass-fibre reinforced plastic [GFRP])	R74	5.581	0.75	−0.745	0.673
Glass, bullet-resistant	–	6.991	1.316	−1.351	1.289
Lexan (polycarbonate)	R70–R118	7.329	1.814	−1.652	1.948
Nylon, bonded[a] (Nylon 66)	–	7.689	1.883	−1.593	1.222
Nylon, unbonded[a] (Nylon 66)	–	5.006	0.719	−0.563	−0.852
Plexiglass, cast	R93	6.913	1.377	−1.364	1.415
Plexiglass, stretched	–	11.468	3.537	−2.871	2.274

[a] Material unable to break up the projectile in the velocity range tested.

Data are also available for non-metallic materials (Ballistic Analysis Laboratory, The Johns Hopkins University, 1963) and are presented in Table 3.12.

The applicability of the THOR equation is summarized by King (2010; Table 3.13).

Figure 3.38 shows the results of the THOR prediction for the thickness of metal required to defend against a specific fragment ($m = 15$ g, $A = 4$ cm^2) travelling at velocity. The thinnest material that is able to provide protection against this threat is hard steel. However, it will not be the lightest in weight. In fact, the lightest solution (per square metre) is a competition between the aluminium alloy and titanium alloy with the aluminium alloy performing well at the lower-impact velocities and the titanium alloy performing better at the elevated velocities.

Penetration equations will be explored further when the subject of penetration is again examined in Chapter 4.

TABLE 3.13

Applicability of Project THOR Parameters

Target Material	Target Thickness Range h (mm)	Impact Velocity v_0 (m/s)	Fragment Mass Range m (g)
AA 2024-T3	0.5–51.0	366–3353	0.32–16.0
Cast iron	4.8–14.0	335–1859	0.97–16.0
Copper	1.5–25.0	335–3475	0.97–16.0
Doron	1.3–38.0	152–3353	0.16–38.9
Glass, bullet-resistant	5.0–42.0	61–3048	0.97–30.8
Lead	1.8–25.0	152–3170	0.97–16.0
Lexan	3.2–25.0	305–3505	0.32–15.6
Magnesium alloy	1.3–76.0	152–3200	0.97–16.0
Nylon, bonded	11.0–51.0	305–3658	0.32–53.5
Nylon, unbonded	0.5–76.0	91–3048	0.32–13.4
Plexiglass, as cast	5.0–28.0	61–2897	0.32–30.8
Plexiglass, stretched	1.3–25.0	152–3353	0.32–30.8
Steel, face hardened	3.6–13.0	762–2987	0.97–16.0
Steel, homogeneous	8.0–25.0	183–3658	0.32–53.0
Titanium alloy	1.0–30.0	213–3170	1.9–16.0

Source: King, K. 2010. Fragmentation. *In:* Dusenberry, D. O. *Handbook for Blast Resistant Design of Buildings*, pp. 215–238, Hoboken, New Jersey: Wiley.
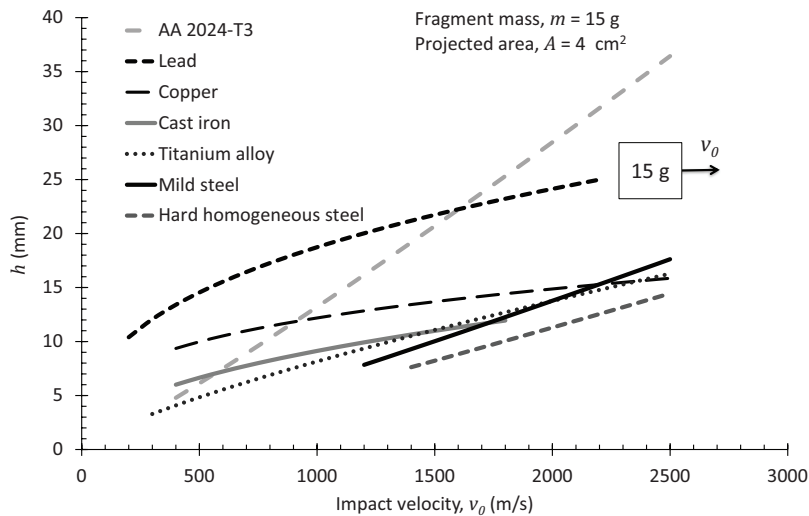
FIGURE 3.38 THOR predictions (using Equation 3.74) for the thickness of metal required to defend against a fragment of 15 g and a projected area of 4 cm².

3.9 SUMMARY

Sadly, there are a wide variety of ingenious ways to attack a building, vehicle or person. For protection, recent attention has been turned towards providing better survivability against blast mines and IEDs. The latter is particularly insidious because often, we do not know the weapon's construction (hence the word 'improvised'). This redirected attention has mainly been driven by the problems encountered in peacekeeping operations after the second Gulf War and in Afghanistan. However, the science behind these threats, whether it is the way the explosive detonates or how the fragments are formed, is quite well understood and has been studied for more than 70 years. The challenge, however, is to mitigate against them.

NOTE

1 There are a large number of variants of this type of projectile, and the design depends largely on the country of origin.

REFERENCES

Akhavan, J. 1998. *The Chemistry of Explosives*, Cambridge, UK: The Royal Society of Chemistry.

Anon 1915. *Treatise on Ammunition*, 10th ed. London, UK: War Office.

Backofen Jr., J. & Williams, L. W. 1981. Antitank Mines. *Armor*, July-August, 26–30.

Baker, W. E. 1973. *Explosions in Air*. Austin, TX: University of Texas Press.

Baker, W. E., Cox, P. A., westine, P. S., Kulesz, J. J. & Strehlow, R. A. 1983. *Explosion Hazards and Evaluation*, vol. 5, Fundamental Studies in Engineering. Amsterdam: Elsevier Science.

Ballistic Analysis Laboratory, The Johns Hopkins University. 1961. *The Resistance of Various Metallic Materials to Penetration by Steel Fragments; Empirical Relationships for Fragment Residual Velocity and Residual Weight*. Aberdeen Proving Ground, MD: Ballistic Research Laboratories.

Ballistic Analysis Laboratory, The Johns Hopkins University. 1963. *The Resistance of Various Non-Metallic Materials to Penetration by Steel Fragments; Empirical Relationships for Fragment Residual Velocity and Residual Weight*. Aberdeen Proving Ground, MD: Ballistic Research Laboratories.

Bernstein, J. & Cassidy, D. 1995. Bomb apologetics: Farm hall, August 1945. *Physics Today*, 48, 32–36.

Birkhoff, G., MacDougall, D. P., Pugh, E. M. & Taylor, G. 1948. Explosives with lined cavities. *Journal of Applied Physics*, 19(6), 563–582.

Chou, P. C. & Flis, W. J. 1986. Recent developments in shaped charge technology. *Propellants, Explosives, Pyrotechnics*, 11(4), 99–114.

Cooper, P. W. 1996. *Explosives Engineering*. New York: Wiley-VCH.

Cranz, C. 1926. *Lehrbuch der Ballistik*. Berlin, Germany: Springer-Verlag.

Crull, M. & Swisdak Jr., M. M. 2005. *Methodologies for Calculating Primary Fragment Characteristics*. Alexandria, VA: Department of Defense Explosives Safety Board.

DiPersio, R. & Simon, J. 1964. *The Penetration-Standoff Relation for Idealized Shaped Charge Jets*. Aberdeen Proving Ground, MD: Ballistic Research Laboratory.

Francou, T. & Giraud, M. 1998. Jacket effects on penetration and perforation of 0.5 AP projectile. *In:* Nel, P. & Van Niekerk, C. (eds.) *Proceedings of the 17th International Symposium on Ballistics*. Midrand, South Africa: South Africa Ballistics Organisation.

Glasstone, S. & Dolan, P. J. 1977. *Effects of Nuclear Weapons*. 3rd ed. Washington, DC: United States Department of Energy, Technical Information Center.

Goad, K. J. W. & Halsey, D. H. J. 1982. Ammunition (including grenades & mines). *In:* Lee, R. G. (ed.) *Battlefield Weapons Systems and Technology, X vols.*, vol. III. Oxford: Brassey's Publishers Ltd.

Grady, D. E. 1982a. Fragment size prediction in dynamic fragmentation. *AIP Conference Proceeding*, 78, 456–459.

Grady, D. E. 1982b. Local inertial effects in dynamic fragmentation. *Journal of Applied Physics*, 53, 322–325.

Grady, D. E. 2006. *Fragmentation of Rings and Shells: The Legacy of N.F Mott*. Heidelberg: Springer-Verlag.

Gurney, R. W. 1943. *The Initial Velocities of Fragments from Bombs, Shell and Grenades*. Aberdeen Proving Ground, MD: Ballistic Research Laboratories.

Hazell, P. J., Appleby-Thomas, G. J., Philbey, D. & Tolman, W. 2013. The effect of gilding jacket material on the penetration mechanics of a 7.62 mm armour-piercing projectile. *International Journal of Impact Engineering*, 54, 11–18.

Hazell, P. J., Lawrence, T. & Stennett, C. 2012. The defeat of shaped charge jets by explosively driven ceramic and glass plates. *International Journal of Applied Ceramic Technology*, 9(2), 382–392.

Held, M. 1976. The performance of the different types of conventional high explosive charges. *In: Proceedings of the 2nd International Symposium on Ballistics*, Daytona Beach, FL: American Defense Preparedness Association.

Held, M. 2002. Lecture notes from the survivability of armoured vehicles course (18–20 March). *In:* Coombs, M. E. C. (ed.). *The Royal Military College of Science*. Shrivenham: Cranfield University.

Hopkinson, B. 1915. British Ordnance Board Minutes 13565.

Jeanquartier, R. & Odermatt, W. 1995. Post-penetration length and velocity of KE projectiles with single oblique targets. *In:* Mayseless, M. & Bodner, S. R. (eds.) *Proceedings of the 15th International Symposium on Ballistics*. Jerusalem, Israel.

Johnson, W. 1988. Some conspicuous aspects of the century of rapid changes in battleship armours, ca 1845–1945. *International Journal of Impact Engineering*, 7(2), 261–284.

Karlos, V. & Solomos, G. 2013. *Calculation of Blast Loads for Application to Structural Components*. Luxembourg: Institute for the Protection and Security of the Citizen.

Kennedy, D. R. 1990. *The History of the Shaped Charge Effect: The First 100 Years*. Los Alamos, NM: Los Alamost National Laboratory.

Kennedy, J. E. 1970. *Gurney Energy of Explosives: Estimation of the Velocity and Impulse Imparted to Driven Metal*. Albuquerque, NM: Sandia Laboratories.

Kennedy, J. E. 1972. Explosive output for driving metal. *In*: Davison, L.W., et al. (eds.). *Behavior and Utilization of Explosives in Engineering Design, Proceedings of the 12th Annual Symposium of the New Mexico Section of the ASME*. Albuquerque, New Mexico: ASME.

King, K. 2010. Fragmentation. *In:* Dusenberry, D. O. (ed.) *Handbook for Blast Resistant Design of Buildings*, pp. 215–238. Hoboken, NJ: Wiley.

Kingery, C. N. & Bulmash, G. 1984. *Airblast Parameters from TNT Spherical Air Burst and Hemispherical Surface Burst*, Maryland: US Army Armament and Development Center, Ballistic Research Laboratory.

Koch, A., Arnold, N. & Estermann, M. 2002. A simple relation between the detonation velocity of an explosive and its gurney energy. *Propellants, Explosives, Pyrotechnics*, 27, 365–368.

Lanz, W. & Odermatt, W. 1992. Penetration limits of large caliber anti tank guns/kinetic energy projectiles. *In:* Persson, A., et al. (eds.) *Proceedings of the 13th International Symposium on Ballistics, Stockholm, Sweden*. Sundbyberg, Sweden: National Defence Research Establishment.

Magness, L. S. & Farrand, T. G. 1990. Deformation behavior and its relationship to the penetration performance of high-density KE penetrator materials. *In: Proceedings of the 1990 Army Science Conference*. Durham, NC: Department of the Army, Washington, DC.

Massey, B. S. 1989. *Mechanics of Fluids*, 6th ed. London: Van Nostrand Reinhold (International).

Meyers, M. A. 1994. *Dynamic Behaviour of Materials*. New York: John Wiley & Sons, Inc.

Mott, N. F. 1947. Fragmentation of shell cases. *Proceedings of the Royal Society of London, Series A*, 189(1018), 300–308.

Ogorkiewicz, R. M. 2002. *AFV Armour and Armour Systems. Course Notes on: Survivability of Armoured Vehicles*. Shrivenham, Swindon, UK: Cranfield University.

Pack, D. C. & Evans, W. M. 1951. Penetration by high-velocity ('Munroe') jets: I. *Proceedings of the Physical Society. Section B*, 64(4), 298–302.

Peters, R. E. & Cummings, E. L. 1957. *Ordnance Engineering Design Handbook, Section 2: Design for Terminal Effects. Artillery Ammunition Series*. Washington, DC: Office of the Chief of Ordnance.

Pugh, E. M., Eichelberger, R. J. & Rostoker, N. 1952. Theory of jet formation by charges with lined conical cavities. *Journal of Applied Physics*, 23(5), 532–536.

Racah, E. 1988. Shaped charge jet heating. *Propellants, Explosives, Pyrotechnics*, 13, 178–182.

Rondot, F. 1998. Performance of tantalum EFP simulants. *In:* Nel, P. & Van Niekerk, C. (eds.) *Proceedings of the 18th International Symposium on Ballistics*. Midrand, South Africa: South Africa Ballistics Organisation.

Rosenberg, Z., Yeshurun, Y. & Tsaliah, J. 1990. More on the thick-backing screening technique for ceramic tiles against AP projectiles. *In: Proceedings of the 12th International Symposium on Ballistics, San Antonio, TX, 30 October–1 November*.

Smith, P. D. & Hetherington, J. G. 1994. *Blast and Ballistic Loading of Structures*. Trowbridge: Butterworth-Heinemann.

Smith, P. D. & Rose, T. A. 2005. *Blast Loading, Structural Response and Design*. Hong Kong: Centre for Research and Professional Development.

Speer, A. 1970. *Inside the Third Reich*. New York: Simon & Schuster.

Swisdak Jr., M. M. 1978. *Explosion Effects and Properties: Part II – Explosion Effects in Water*. White Oak, Silver Spring, MD: Naval Surface Weapons Center.

Von Holle, W. G. & Trimble, J. J. 1976. Temperature measurement of shocked copper plates and shaped charge jets by two-color ir radiometry. *Journal of Applied Physics*, 47 (6), 2391–2394.

Walters, W. 2008. A brief history of shaped charges. *In:* Bless, S. & Walker, J. D. (eds.). *Proceedings of the 24th International Symposium on Ballistics, New Orleans, LA, 22–26 September*. Arlington: National Defense Industrial Association.

Walters, W. P. 1990. *The Shaped Charge Concept, Part II: The History of Shaped Charges*. Aberdeen Proving Ground, MD: US Army Ballistics Research Laboratory.

Walters, W. P. & Zukas, J. A. 1989. *Fundamentals of Shaped Charges*. New York: Wiley-Interscience.

Weimer, R. J. & Rogers, H. C. 1979. Dynamic fracture phenomena in high-strength steels. *Journal of Applied Physics*, 50, 8025–8030.

Wood, R. W. 1936. Optical and physical effects of high explosives. *Proceedings of the Royal Society of London A: Mathematical, Physical and Engineering Sciences*, 157, 249–261.

Zukas, J. A. 1990. *High Velocity Impact Dynamics*. New York: John Wiley & Sons, Inc.

Zukas, J. A. & Walters, W. P. 1998. Explosive effects and applications. *In:* Graham, R. A. (ed.) *High- Pressure Shock Compression of Condensed Matter*. New York: Springer.

4 Penetration Mechanics

4.1 INTRODUCTION

To try and solve how best to protect people from flying projectiles, it is useful to have an understanding of how projectiles penetrate materials and structures. Penetration processes are affected by material properties of the penetrator and the target, the impact velocity and the geometry of the incoming projectile. Furthermore, it is found that how a projectile penetrates a target is frequently divided into two fundamental processes: sub-hydrodynamic—where the strength of the material is of great importance, and hydrodynamic, where the material strength takes a lesser role. These will now be reviewed in this chapter.

4.2 FAILURE MECHANISMS

A projectile penetrating a target subjects the material to a complex state of stress that can and will result in material failure. There are several types of failure that will occur and can be compartmentalized into five failure mechanisms:

1. Brittle failure will occur with materials of low fracture toughness—such as a ceramic or glass. Generally speaking, for brittle materials, kinetic energy (KE) from the projectile is required to create the fracture surfaces within the material during penetration; however, very little KE in the projectile is expended in doing this in brittle materials (Woodward et al., 1994). More of the KE of the projectile is often transferred to the KE of the resulting fragments. Brittleness is not always a disadvantage as it is the generation of fracture surfaces that leads to the 'bulking' of the material. This is very useful for defeating shaped charge jets—as will be seen in Chapter 8.
2. Gross cracking is a failure that will occur in hard strong materials such as metals. Cracks propagate at a velocity that is close to the speed of sound in the material, and therefore, the cracking process happens very quickly. Armours that have welded joints are susceptible to this (Edwards and Mathewson, 1997) as are high-carbon steels. Frequently, however, this type of failure does not impede the protective ability of the material as long as the plates are restrained from flying apart. Gross cracking can compromise the load-bearing capability of the structure, however.
3. Shear plug failure is a problem when materials are susceptible to adiabatic shear processes and are impacted by blunt compact fragments. This is particularly problematic in that the energy required to generate shear bands in metals is quite low and depends on several material properties including the material's propensity to thermally soften and low work-hardening coefficients. This is particularly important as ballistic penetration events are,

by their very definition, over in a very short time. This means that the heat generated through plastic deformation processes does not have time to dissipate and therefore can lead to the separation of a shear plug in the armour material.

4. Lamination failure occurs when the material is subjected to stress wave reflections, which ultimately results in the tensile strength of the material being exceeded. If this occurs in a planar impact, then ultimately, the material will be pulled apart by inertial forces (this will be discussed again later).

5. Viscous flow results in the parting of the material due to localized melting. This is usually associated with hard-pointed projectiles.

The sixth failure mechanism is due to hydrodynamic flow. This is a special case that is reserved for very-high-velocity collisions that result in the superplastic flow of the material due to high-confining pressures that are present. More on that later.

4.3   PENETRATION ANALYSIS

Comprehensive reviews of penetration equations are provided by Backman and Goldsmith (1978), Wright (1983), Zukas (1990), Corbett et al. (1996), Ben-Dor et al. (2005) and more recently by (Anderson Jr. (2017) and Schonberg and Ryan (2021). There are many models available and to cover all would be beyond the scope of this publication. Nevertheless, the readers are recommended to familiarize themselves with the aforementioned publications.

In this section, we will review several models and apply them to real-world data where appropriate.

We will start simply with a rudimentary analysis of a rigid body penetrating a plastically deforming target medium. Consider a flat-nosed cylinder striking a plate of a specific thickness, h, with a velocity of less than 1000 m/s and normal to the target. The cylinder does not deform, and the penetration occurs due to the plate plastically deforming. The fact that the cylinder does not deform means that we describe this process as 'rigid-body penetration'.

On impact, the cylinder (of diameter d) is subjected to a resisting force, F_r, from the target's strength. It is assumed that the force is governed by the stress (σ) required to open up a cavity in the target material. That is, $F_r = \sigma A_1$, where A_1 is the projected area of the projectile. For the projectile to be arrested, the KE of the cylinder must be transferred to the work done in plastically deforming the target through a thickness, h. The relevant equations are shown below:

$$\frac{1}{2}mv_0^2 = (\sigma A_1)h \tag{4.1}$$

where A_1 is the cross-sectional area and is given by

$$A_1 = \frac{\pi d^2}{4} \tag{4.2}$$
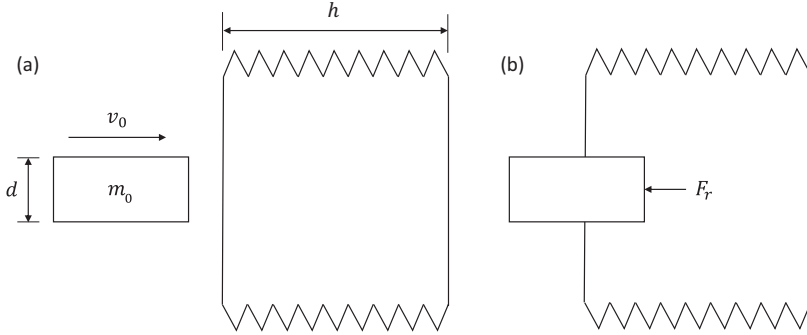
FIGURE 4.1 Schematic of, (a) a projectile of mass m travelling at velocity v_0 to a target of thickness h, and (b) rigid-body penetration of the projectile being resisted by a force F_r by the target material.

where m_0 is the initial mass of the cylinder and is a constant throughout the penetration process, and v_0 is the impact velocity of the projectile. See Figure 4.1.

Substituting and rearranging

$$\left[\frac{\frac{1}{2}mv_0^2}{A_1}\right] \times \frac{1}{d} = \sigma\left[\frac{h}{d}\right] \tag{4.3}$$

Notice how that on the left-hand side, we have a measure of the KE density. It is then convenient to rearrange and simplify:

$$\frac{mv_0^2}{d^3} = \frac{\pi}{2}\sigma\left[\frac{h}{d}\right] \tag{4.4}$$

If we take into account an oblique impact, then the equation can be modified using the angle of obliquity θ; thus,

$$\frac{mv_0^2}{d^3} = \frac{\pi}{2}\sigma\left[\frac{h}{d}\right]\left[\frac{1}{\cos\theta}\right]^k \tag{4.5}$$

where k is an empirical constant that determines a material's ability to turn the projectile during penetration. Note that $h/\cos\theta$ is the effective through-thickness offered to the projectile by a plate of thickness h set at an angle of obliquity θ.

The above model is a simplification of what occurs in real life; it is very unlikely that a target would suffer from pure plastic flow as prescribed by the above derivation. Consequently, one should exercise caution when employing this model due to the (very) simplified approach that is used.

Occasionally, shear failure occurs resulting in a cylindrical plug forming. Consequently, the above derivation can be repeated assuming that pure shear failure

is occurring. The target is penetrated when the *shear strength,* as described by τ_0, is exceeded. Therefore, the resistance offered by the target is given by $F_r = \tau_0 A_2$, where,

$$A_2 = \pi dh \tag{4.6}$$

Following the logic outlined previously, it is found that the penetration equation can be given by

$$\left[\frac{\frac{1}{2} m_0 v_0^2}{A_2} \right] \times \frac{1}{d} = \tau_0 \left[\frac{h}{d} \right] \tag{4.7}$$

and finally,

$$\frac{m_0 v_0^2}{d^3} = 2\pi \tau_0 \left[\frac{h}{d} \right]^2 \tag{4.8}$$

For most metallic penetration examples, penetration will be a combination of cavity expansion and plug formation and therefore a general equation for penetration is required, following:

$$\frac{m_0 v_0^2}{d^3} = c \left[\frac{h}{d} \right]^n \tag{4.9}$$

where c and n are empirically derived constants.

Jacobson used the above analysis to describe the transition from plugging to piercing (plastic flow; see Carlucci and Jacobson (2014)). If it is assumed that at some ratio h/d, the projectile will transition from a state of plugging to a state of piercing (plastic flow), then the analysis outlined above can be used to predict the value of h/d at which that occurred. So, to recap, the energy for a piercing-type flow is

$$E_{\text{piercing}} = \sigma \frac{\pi d^2}{4} h = \sigma \frac{\pi d^3}{4} \left(\frac{h}{d} \right) \tag{4.10}$$

The energy required for plugging failure is

$$E_{\text{plugging}} = \tau \pi dh^2 = \tau_0 \pi h^3 = \left(\frac{h}{d} \right)^2 \tag{4.11}$$

If it is assumed that

$$\tau_0 \approx 0.6\sigma \tag{4.12}$$

then

$$E_{\text{plugging}} = 0.6\sigma \pi d^3 \left(\frac{h}{d} \right)^2 \tag{4.13}$$

Therefore, the transition will occur when $E_{piercing} = E_{plugging}$:

$$0.6\sigma \pi d^3 \left(\frac{h}{d}\right)^2 = \sigma \frac{\pi d^3}{4}\left(\frac{h}{d}\right) \rightarrow \left(\frac{h}{d}\right)_{crit} = 0.42 \tag{4.14}$$

This analysis implies that once the ratio of (h/d) exceeds 0.42, then piercing would be expected, whereas below this, plugging would be anticipated. This is illustrated in Figure 4.2 where the energy required to penetrate a plate is plotted for both piercing and plugging. The projectile diameter is 7.62 mm and is assumed to be rigid. The stress required to open up a cavity in the plate is set to 500 MPa, and its thickness is varied to provide a variable (h/d) value. The projectile will penetrate at the lowest possible energy, and therefore, below $h/d = 0.42$, the projectile causes plate plugging. This is a simple analysis and, as will be seen later, does not always hold true. In fact, it is known that the propensity to plug is very much determined by the material properties of the material (Walley, 2007) as well as the shape of the projectile tip.

This energy-based approach was originally taken by de Marre in 1886 who derived an empirical model for the energy required to achieve complete penetration in a thin hard steel plate (see Chapter 1), viz.,

$$E_0 = cd^{1.5}h^{1.4} \tag{4.15}$$

where E_0 is the KE of the projectile required to perforate the plate, and c is an empirically derived constant. The thickness of the plate penetrated is given by

$$h^{0.7} = k\frac{m_0^{0.5}v_0}{d^{0.75}} \tag{4.16}$$

where k is an empirically derived constant.
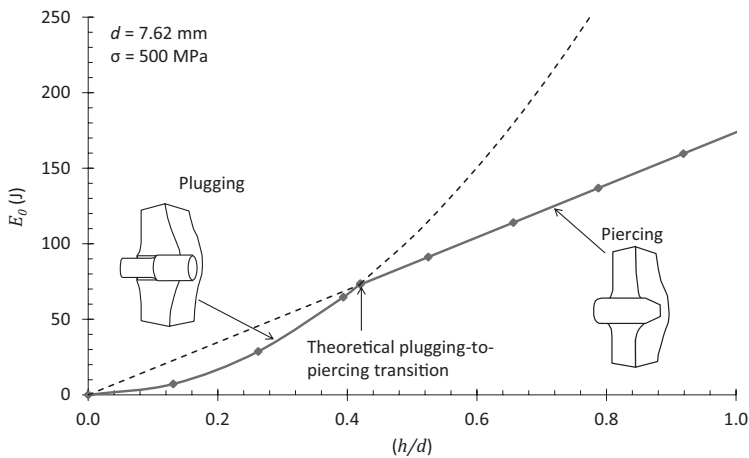
FIGURE 4.2 Transitioning from plugging to piercing during penetration (E_0=energy required to perforate the plate, $\sigma = 500$ MPa and $d = 7.62$ mm).

4.3.1 PENETRATION ANALYSIS INTO THICK PLATES

The simplest way to analyze the penetration of a material is to consider it as a semi-infinite plate. That is to say that the depth of penetration is considerably less than the depth of penetration achieved by the projectile and there is no effect on the penetration due to the proximity of any free surfaces. The resulting value of the penetration depth gives a crude approximation of the thickness that would be required to stop the projectile; however, it is usually sufficient for design purposes.

A common approach is to use the equation of motion to determine penetration (as opposed to the conservation of energy that was used above). So, for example, a generalized equation can be used that defines the resistive force applied to the projectile during penetration. This equation will be a function of velocity, v, and can be written as:

$$F = c_0 + c_1 v + c_2 v^2 \tag{4.17}$$

where c_0, c_1 and c_2 are constants. Using the above-mentioned generalized force equation, we can now proceed to derive a series of penetration equations.

From the equation of motion, we note:

$$F = -m_0 \frac{dv}{dt} = m_0 \frac{dx}{dt} \frac{dv}{dx} = -m_0 v \frac{dv}{dx} \tag{4.18}$$

where m_0 is the mass and v is the velocity of the projectile at any given point in time. Note, that the minus sign is added as we are assuming deceleration (i.e. a negative acceleration). Therefore, rearranging we have,

$$\int_0^p dx = -m_0 \int_{v_0}^0 \frac{v}{F} dv \tag{4.19}$$

where F is the resisting force and p is the penetration. Note that 'p' is lowercase to distinguish from pressure, 'P' that will be used later in this book. This is the starting point for many analytical penetration models.

4.3.1.1 Robins–Euler Penetration Formula (Robins, 1742)

As we saw in Chapter 1, The earliest known penetration equation is attributed to Benjamin Robins (1707–1751) and Leonhard Euler (1707–1783) (see Allen et al. (1957)). They deduced the resistance of a medium to penetration was independent of velocity and was a constant (Robins, 1742). That is,

$$F = c_0 \tag{4.20}$$

Noting

$$\int_0^p dx = -m_0 \int_{v_0}^0 \frac{v}{F} dv \tag{4.21}$$

Our integral then becomes

$$\int_0^p dx = -m_0 \int_{v_0}^0 \frac{v}{c_0} dv \tag{4.22}$$

Integrating both sides we get:

$$p - 0 = -m_0 \left(0 - \frac{1}{2c_0} v_0^2 \right) \tag{4.23}$$

$$p = \frac{m_0}{2c_0} v_0^2 \tag{4.24}$$

This does have some bearing in reality, especially for low velocities of impact.

The Robins–Euler equation uses one term from the generalized force definition in Equations 4.17. Let us now look at whether using another parameter is useful for developing a penetration equation. See the following worked example (Example 4.1).

Example 4.1

A generalized force equation that can be used to describe the resistive force acting on a projectile during penetration of a target medium is given by:

$$F = c_0 + c_1 v + c_2 v^2 \tag{4.25}$$

For the case of where c_0 and $c_1 = 0$, evaluate whether this equation has any foundation in reality as to how projectiles behave as they penetrate targets.

So, the generalized force equation now becomes

$$F = c_2 v^2 \tag{4.26}$$

This is not a million miles from reality as we know from the conservation of energy that the resisting force must be proportional to the kinetic energy of the projectile (kinetic energy of the projectile = work done on the target = force × displacement into the target).

To evaluate this equation, we need to substitute $F = c_2 v^2$ into the following:

$$\int_0^p dx = -m_0 \int_{v_0}^0 \frac{v}{F} dv \tag{4.27}$$

Our integral then becomes

$$\int_0^p dx = -m_0 \int_{v_0}^0 \frac{v}{c_2 v^2} dv = -m_0 \int_{v_0}^0 \frac{1}{c_2 v} dv \tag{4.28}$$

Integrating both sides we get:

$$p = \frac{m_0}{c_2} \ln(v_0) \tag{4.29}$$

Unfortunately, there is a large body of evidence that tells us that non-deforming projectiles penetrating ductile targets do not follow a natural logarithmic pattern when plotting penetration with impact velocity. This is clearly wrong (although note that some deforming projectiles behave exactly like this when penetrating something like ballistic gelatin, for example!). Therefore, we need to increase the complexity of the force definition. This leads us nicely to the Poncelet derivation.

4.3.1.2   Poncelet Penetration Formula (Poncelet, 1829)

One of the first engineers to carefully examine the penetration of a non-deforming projectile into a thick target was Jean-Victor Poncelet (1788–1867). Poncelet deduced that there are two terms at play that are important for establishing resistance force (F) during penetration, e.g. see Backofen Jr (1980). This approach was also suggested by Leonhard Euler (1707–1783), see (Allen et al., 1957). We therefore now increase the complexity of the force definition by combing a 'static resistance term', c_0 with a 'drag' function, $c_2 v^2$, viz.

$$F = \left(c_0 + c_2 v^2 \right) \tag{4.30}$$

Out integral now becomes:

$$\int_0^p dx = -m_0 \int_{v_0}^0 \frac{v dv}{\left(c_0 + c_2 v^2 \right)} \tag{4.31}$$

On integration,

$$p = m_0 \left(\frac{1}{2c_2} \ln \left(c_0 + c_2 v_0^2 \right) - \frac{1}{2c_2} \ln \left(c_0 \right) \right) \tag{4.32}$$

On simplification,

$$p = \frac{m_0}{2c_2} \left(\ln \left[1 + \frac{c_2 v_0^2}{c_0} \right] \right) \tag{4.33}$$

This form of equation is seen time and time again in different penetration equations. Unfortunately, there are two unknowns in this equation (c_0 and c_2) and these will need to be derived for each material from penetration data. Figure 4.3 shows the Poncelet model that has been calibrated to data presented by Hazell et al. (1998) where a 6.35 mm diameter steel sphere ($m_0 = 1.05$ g) penetrated an aluminium alloy, AA 6082-T6. The model is able to show the expected penetration at lower impact velocities. Calibration was carried out in MS Excel® using the Solver function.

It is important to note that this model, like many others, is only relevant to non-deforming projectiles and will lose fidelity when the projectile deforms. Furthermore, it also assumes zero frictional contact between the penetrator and the target and therefore has been used to study the penetration of sands and soils, where this would be expected.
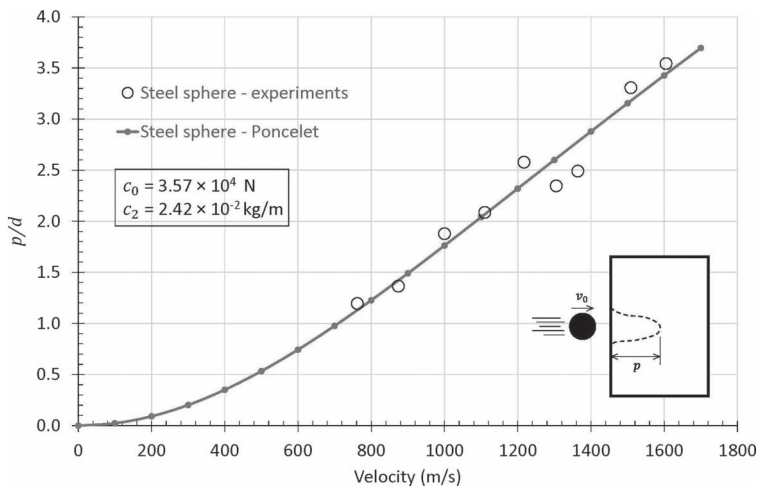
FIGURE 4.3   A calibrated Poncelet model for a 6.35 mm steel sphere penetrating AA 6082-T6 with $c_0 = 3.57 \times 10^4$ N and $c_2 = 2.42 \times 10^{-2}$ kg/m. (Data from Hazell et al., 1998.)
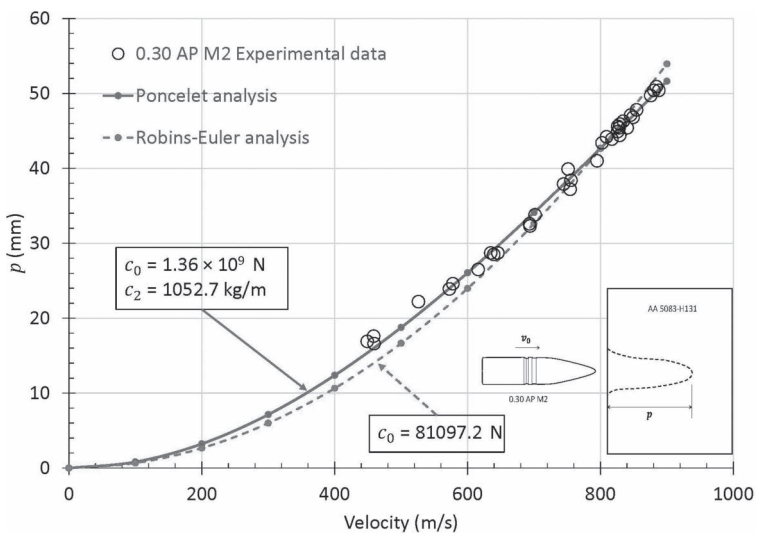
FIGURE 4.4   Data showing the results from a 0.30 AP M2 projectile that has penetrated an AA 5083-H131 semi-infinite target; data after Moynihan et al. (2000). Also plotted are the calibrated models for Poncelet and Robins–Euler. Projectile mass $= 10.8$ g and projectile diameter $= 7.836$ mm.

We can compare the Poncelet and Robins–Euler formulations as follows by plotting depth-of-penetration data with velocity and comparing that data to each respective model. Figure 4.4 shows data after Moynihan et al. (2000) for an 0.30 AP M2 projectile penetrating an aluminium-grade armour, AA 5083-H131.

The Poncelet model fits the data quite nicely, whereas the Robins–Euler model is less satisfactory. This is purely down to the latter's simplicity, and one would expect a larger difference to become apparent as v_0 is increased. Of course, we should continue to remember that this is an empirical model, that is, the constants are fitted to the data, and does not inform any physical processes such as the effect of the jacket stripping.

4.3.1.3 Poncelet with Increasing Complexity

We can now try using the full force definition of Equation 4.17. Unfortunately, the right-hand side of this integral is not trivial when F is a complex function of v. So, when the force is defined in terms of Equation 4.17, the mathematics gets rather messy. Nevertheless, the equations are derived here for completeness.

Assuming that we use Equation 4.17 as our definition of the resisting force, then we have

$$\int_0^p dx = -m_0 \int_{v_0}^0 \frac{v}{c_0 + c_1 v + c_2 v^2}\, dv \tag{4.34}$$

For the case where $4c_2 c_0 - c_1^2 > 0$, the solution becomes

$$p = \frac{m_0}{2c_2}\left(\ln\left|\frac{c_0 + c_1 v_0 + c_2 v_0^2}{c_0}\right| + \frac{2c_1}{\sqrt{4c_2 c_0 - c_1^2}}\left(\tan^{-1}\left(\frac{c_1}{\sqrt{4c_2 c_0 - c_1^2}}\right) - \tan^{-1}\left(\frac{2c_2 v_0 + c_1}{\sqrt{4c_2 c_0 - c_1^2}}\right) \right) \right) \tag{4.35}$$

For the case where $4c_2 c_0 - c_1^2 = 0$ the integral simplifies to

$$p = \frac{m_0}{2c_2}\left(\ln\left|\frac{c_0 + c_1 v_0 + c_2 v_0^2}{c_0}\right| - \left(\frac{c_2 v_0}{(2c_2 v_0 + c_1)}\right) \right) \tag{4.36}$$

For the case where $4c_2 c_0 - c_1^2 < 0$, the solution becomes

$$p = \frac{m_0}{2c_2}\left(\ln\left|\frac{c_0 + c_1 v_0 + c_2 v_0^2}{c_0}\right| + \frac{c_1}{a}\left(\ln\left|\frac{c_1 - a}{c_1 + a}\right| - \ln\left|\frac{2c_2 v_0 + c_1 - a}{2c_2 v_0 + c_1 + a}\right| \right) \right) \tag{4.37}$$

where $a = \sqrt{c_1^2 - 4c_2 c_0}$

It is largely accepted, that the increased complexity adds very little to the fidelity of the model!

4.3.1.4 Poncelet with a Physical Force Definition

Analytical models are generally more complex when the resisting force definition is tweaked to provide a more physical rationale. A nice overview of this is provided by Recht (1990). Recht summarized several analytical modes where he described the resisting force as follows:

Force = active area × (inertial pressure term + distortion pressure term).

Mathematically we can write this as

$$F = A_x \left(c_3 \rho_t v^2 + p_d \right) \tag{4.38}$$

where A_x is the active area, c_3 is a constant, ρ_t is the density of the target and p_d is a distortion pressure term or target deformation pressure and is constant. This has the units of Pa, whereas c_3 is dimensionless. Note that this is similar to the form presented before but with a couple of additional terms, A_x and ρ_t.

Assuming A_x is constant and therefore equal to the projected area of the projectile, A_p, our integral now becomes

$$\int_0^p dx = -\frac{m_0}{A_p} \int_{v_0}^0 \frac{v dv}{\left(c_3 \rho_t v^2 + p_d \right)} \tag{4.39}$$

And on integration (as before) this gives us:

$$p = \frac{m_0}{2 A_p c_3 \rho_t} \left(\ln \left[1 + \frac{c_3 \rho_t v_0^2}{p_d} \right] \right) \tag{4.40}$$

We can simplify further for a spherical projectile knowing that the mass of the sphere can be defined by:

$$m_0 = \frac{4}{3} \pi r^3 \rho_p \tag{4.41}$$

where r is the radius of the projectile and ρ_p is its density. Substituting and simplifying, we get

$$p = \frac{\rho_p d}{3 \rho_t c_3} \left(\ln \left[1 + \frac{c_3 \rho_t v_0^2}{p_d} \right] \right) \tag{4.42}$$

where d is the diameter of the sphere.

A general equation, where the penetration into the target can be calculated after the projectile has been decelerated to a specific velocity can be written as:

$$p = \frac{m_0}{2 A_p c_3 \rho_t} \left(\ln \left[\frac{c_3 \rho_t v_0^2 + p_d}{c_3 \rho_t v^2 + p_d} \right] \right) \tag{4.43}$$

A series of Poncelet parameters corresponding to this form of the model have been presented by Bless et al. (2014) and are summarized in Table 4.1.

4.3.1.5   Other Related Penetration Models

Before we increase the complexity further, it is worth just listing other penetration models that have been examined in the past. These tend to be a variation of the Poncelet formula. They are:

TABLE 4.1

Poncelet Coefficients for Various Granular Media (Derived from Fitting Deceleration Data from 300 m/s to 100 m/s)

Material	Density (g/cc)	c_3	p_d (MPa)
Crushed quartz glass	1.30	0.52	22
Oil saturated quartz glass	1.52	0.21–0.26	0
Loose packed sand	1.59	0.79–0.81	0
Water saturated loose sand	1.99	0.40	0
Dry dense packed sand	1.82	0.75	17
Water saturated dense sand	2.12	0.50	10

Source: After (Bless et al., 2014).

$$\left(\text{Resal, } 1895\right)$$

$$p = \frac{m_0}{c_4}\left(\ln\left[1 + \frac{c_4 v_0}{c_5}\right]\right) \tag{4.44}$$

$$\left(\text{Petry, } 1910\right)$$

$$p = c_6 \frac{m_0 g}{A_\text{p}}\left(\log\left[1 + \frac{v_0^2}{20{,}000}\right]\right) \tag{4.45}$$

where c_4, c_5, c_6 are constants and A_p is the projected area of the projectile.

Additional models can be found in Chapter 1 and it is worth also reviewing the works of Herrmann and Jones (1961), Backman and Goldsmith (1978) and Ben-Dor et al. (2013).

4.3.1.6   Awerbuch and Bodner Formulae

In the late 1960s to early 1970s, there was a push to develop more predictive models for ballistic penetration. Empirical and semi-empirical models are all very well, however ballistic experiments are still required to calibrate constants. Building off the work of Awerbuch (1970), Awerbuch and Bodner reported a model that predicts the projectile penetration and subsequent perforation of finite plates (Awerbuch and Bodner, 1974a). They assumed penetration occurs in three stages, namely (see Figure 4.5):

1. *Stage 1*: An inertial force and compressive force are acting on the projectile to decelerate it.
2. *Stage 2*: The onset of shearing occurs in the target plate and therefore three forces are now considered to act on the projectile (a shear force, in addition to an inertial and compressive force). The mass of the projectile is effectively changed as there is now a mass of material moving with it. This stage ends when the plug is completely joined to the projectile.
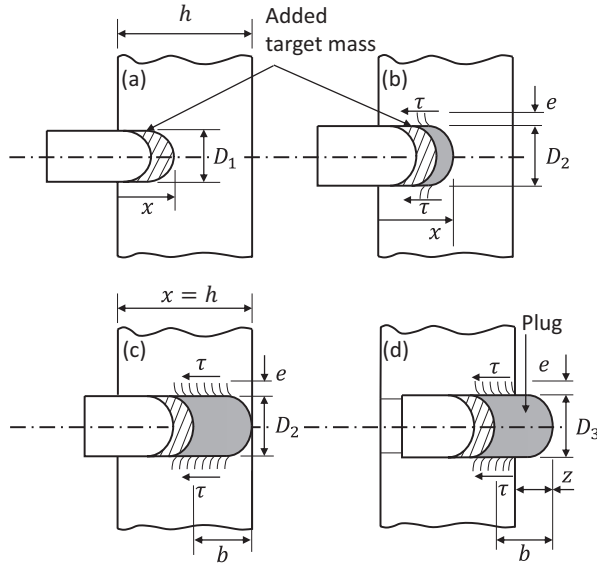
FIGURE 4.5 The three stages of penetration showing (a) the first stage, (b) the second stage, (c) the end of the second stage and, (d) the third stage. (Adapted from Awerbuch and Bodner, 1974a.)

3. *Stage 3*: The projectile and the plug that has been formed are effectively moving as a rigid body. The only force acting at this stage is a shearing force that acts on the plug's circumference along its whole length.

Their model appeared to correlate well with experimental data presented separately by the same authors (Awerbuch and Bodner, 1974b). Unlike other researchers such as Jacobson (1975) and Recht (1990), Awerbuch and Bodner ignore the effects of friction due to the assumption that a small film of liquid is produced between the projectile and the target plate. This would be caused, it is assumed, by localized melting. Elastic and plastic wave propagation is also neglected.

Again, the equation of motion is invoked and in general, the resisting force is regarded as a resultant of the three main forces acting on the projectile. These are:

F_i – the inertial force
F_c – the compressive force, and
F_s – the shearing force

Thus, we can write:

$$\frac{d}{dt}(mv) = -\left(F_i + F_c + F_s\right) \tag{4.46}$$

Two further assumptions were made:

1. It is assumed that the element of mass of the target material in contact with the projectile is set in motion while the remainder of the target material remains at rest. Each mass element is considered to move normal to the surface of the nose of the projectile.
2. The projectile mass increases during penetration due to the addition of displaced target material to the total mass of the projectile (see Figure 4.5).

Stage 1—inertial and compressive forces

If we consider a small mass element, dm, in the target that is being displaced by the projectile, we can equate the work done by the reaction of the inertial force on the target material to the change in kinetic energy of the displaced mass. Therefore,

$$dF_{in}dx = \frac{1}{2}dmv^2 \tag{4.47}$$

where dF_{in} is the normal inertial force acting on the elemental area dA_n of the projectile. The parameter dx is the displacement of the mass element dm and v is the velocity of that mass element. The mass element can be further defined assuming the density of the target is defined by ρ_t and knowing mass = density × volume.

$$dm = \rho_t(dx)(dA_n) \tag{4.48}$$

Substituting, we have

$$dF_{in} = \frac{1}{2}\rho_t(dA_n)v^2 \tag{4.49}$$

F_i can be determined by integrating dF_i over the contact surface (between the projectile's nose and the target material), S, of the projectile and so for a cylindrical projectile with a flat end,

$$\int_S dF_{in} = F_i \quad \text{and} \quad \int_S dA_n = A \tag{4.50}$$

So, we have,

$$F_i = \frac{1}{2}\rho_t Av^2 \tag{4.51}$$

Note that this is very similar to Equation 3.63 where we examined a flying projectile subjected to drag forces.

For projectile shapes other than those where the nose shape is flat, then a constant K, is introduced as defined in Table 4.2.

$$F_i = K\frac{1}{2}\rho_t Av^2 \tag{4.52}$$

TABLE 4.2

Shape Factors for the Awerbuch–Bodner Model

Nose Shape	K
Flat	1
Spherical	0.5
Cone with half-angle of α	$\sin^2 \alpha$

The compressive force, derived from the compressive strength of the target material $(F_c = \sigma_c A)$ is also added resulting in the following equation of motion:

$$\frac{d}{dt}(mv) = v\frac{dm}{dt} + m\frac{dv}{dt} = F_1 = -\frac{1}{2}K\rho_t A_1 v^2 - \sigma_c A_1 \tag{4.53}$$

The projected area, A_1, is introduced here to account for possible effects of the projectile's nose being flattened during penetration and is assumed to be constant during penetration.

The rate of change of mass of the projectile is given by:

$$\frac{dm}{dt} = \rho_t A_1 \frac{dx}{dt} = \rho_t A_1 v \tag{4.54}$$

Using the Chain rule,

$$\frac{dv}{dt} = \frac{dv}{dx}\frac{dx}{dt} = v\frac{dv}{dx} \tag{4.55}$$

Leading to:

$$\rho_t A_1 v^2 + (m_0 + \rho_t A_1 x)\, v\frac{dv}{dx} = -\frac{1}{2}K\rho_t A_1 v^2 - \sigma_c A_1 \tag{4.56}$$

Where $(m_0 + \rho A_1 x)$ is the effective mass of the combined projectile and target material, where m_0 is the original mass of the projectile and $\rho A_1 x$ is the additional contribution from the target element in front of the projectile.

Through the separation of the variables and integration of Equation 4.56, the following equation arises:

$$v_1(x) = \left[\left(v_0^2 + \frac{\sigma_c}{\rho_t(1+0.5K)}\right)\left(\frac{m_0/\rho_t A_1}{x+m_0/\rho_t A_1}\right)^{2+K} - \frac{\sigma_c}{\rho_t(1+0.5K)}\right]^{\frac{1}{2}} \tag{4.57}$$

where $v_1(x)$ is the velocity of the projectile and added mass from the target material and v_0 is the impact velocity.

The time for the projectile to penetrate a distance (x) through the following integration:

$$t(x) = \int_0^x \left[\left(v_0^2 + \frac{\sigma_c}{\rho_t (1 + 0.5K)} \right) \left(\frac{m_0 / \rho_t A_l}{x + m_0 / \rho_t A_l} \right)^{2+K} - \frac{\sigma_c}{\rho_t (1 + 0.5K)} \right]^{-\frac{1}{2}} .dx \qquad (4.58)$$

The first stage ends when $x = (h - b)$ and when $t = t_1$. It has been seen experimentally that the ratio of the plug length to target thickness (b/h) is approximately constant for a range of ordnance velocities and for a given projectile and target material. Ranges of (b/h) values have been estimated by Awerbuch and Bodner (1974b) for ballistically perforated plates and were 0.80–0.85 for mild steel and various steel alloys and from 0.65 to 0.75 for AA 6061-T6. This allows for an estimate of the value, b for a known plate thickness.

An example of some analysis for Stage 1 penetration is presented in Figure 4.6. Here a 5.59 mm projectile is penetrating a 10-mm thick aluminium alloy. In this case, the entrance hole, D_1 is increased from 5.6 to 7.6 mm resulting in (1) an increase in the time of Stage 1 penetration, (2) an increase in the resisting force acting on the projectile, and (3) a consequent reduction in the velocity of the projectile at the end of Stage 1 penetration. This shows that the penetration characteristics are quite sensitive to the value of D_1, which needs to be determined empirically (although can be assumed to equal the diameter of the projectile in the first instance) (Figure 4.6).

In the second stage, the plug begins to form (= incipient plugging) and the equation of motion is dominated by inertial forces, compressive forces and shear forces. The inertial force is again given by
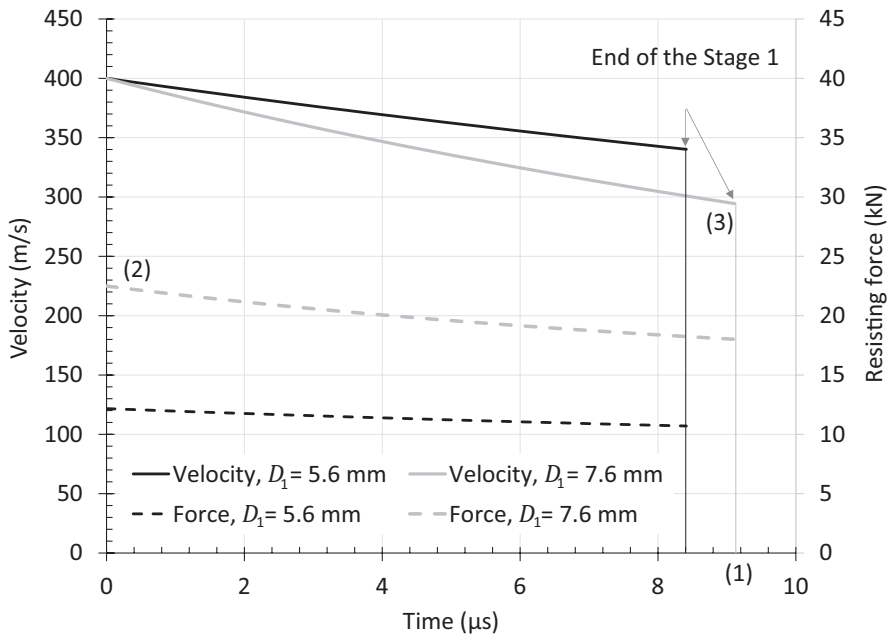
FIGURE 4.6 Stage 1 penetration calculation based on a 5.59 mm (0.22 cal) lead projectile impacting an aluminium alloy at 400 m/s. The parameters used for these calculations were $m_0 = 2.68$ g, $K = 1.0$, $\rho_t = 2700$ kg/m³, $\sigma_c = 280$ MPa, $h = 10$ mm.

$$F_{i2} = \frac{1}{2} K \rho_t A_2 v^2 \tag{4.59}$$

In the second stage, the K value is set to 0.5 as non-armour-piercing projectiles will deform to a spherical shape during penetration. The projected area of the plug, A_2 is generally regarded as constant and experimental results indicated that it was very close to A_1. The compressive force given by $F_c = \sigma_c A_2$ also initially acts at the beginning of Stage 2 however it diminishes to 0 by the end of this stage as the full plug is formed and moves at the same velocity as the projectile. When the full plug is formed, there is simply no more compressive force from the material acting—see Figure 4.5c. The reduction to zero is given by a parabolic function, although a simple, linear form will also closely approximate the actual force on the projectile. The parabolic function is presented here:

$$F_{c2}(x) = \sigma_c A_2 \left(1 - \left[\frac{x - (h - b)}{b} \right]^2 \right) \tag{4.60}$$

In addition to the compressive force, a shear force acts along the surface of the plug that is moving with the projectile, that is, along the surface $\pi D_2 [x - (h - b)]$. The shear force is therefore given by:

$$F_{s2} = \tau \pi D_2 [x - (h - b)] \tag{4.61}$$

The shear strength of dynamically strained metals can be defined by the following:

$$\tau = \tau_0 + \mu \dot{\gamma} \tag{4.62}$$

where τ_0 is the quasi-static shear strength, μ is the coefficient of viscosity and $\dot{\gamma}$ is the shear strain rate. In the context of a projectile penetrating a target, the shear strain rate can be defined as follows:

$$\dot{\gamma} = \frac{v}{e} \tag{4.63}$$

where v is the velocity of the moving material and e is the width of the shear zone—see Figure 4.5. Summing all of these effects together, the equation of motion for Stage 2 becomes:

$$F_2 = -\frac{1}{2} K \rho_t A_2 v^2 - \left(\tau_0 + \mu \frac{v}{e} \right) \pi D_2 [x - (h - b)] - \sigma_c A_2 \left(1 - \left[\frac{x - (h - b)}{b} \right]^2 \right) \tag{4.64}$$

A_2 and D_2 are constant. The velocity during this stage should be integrated using the following expression.

$$\frac{dv_2(x)}{dx} = \left[-(1+0.5K)\rho_t A_2 v^2 - \tau_0 \pi D_2 x - \frac{\mu D_2}{e} vx + \frac{\mu \pi D_2 (h-b)}{e} v \right.$$

$$\left. + \tau_0 \pi D_2 (h-b) - \sigma_c A_2 \left(1 - \left[\frac{x-(h-b)}{b} \right]^2 \right) \right] / \left[(m_0 + \rho_t A_2 x) v \right] \quad (4.65)$$

The duration of the second stage is given by.

$$t_2 = \int_{x=h-b}^{x=h} \frac{1}{v} dx \quad (4.66)$$

The third stage starts when all of the material ahead of the projectile moves forward as a rigid body. The effective mass of the moving material is, therefore $m_2 = m_0 + \rho_t \bar{A} h$. Where $\bar{A}$ is the average area of the entire cavity. During this stage, the only active force is due to the shear stresses acting over the surface of the plug. In this stage, the displacement of the combined projectile and added mass is related to e, as follows.

$$x^* = \gamma e \quad (4.67)$$

The equation of motion for the third stage is

$$m_2 \frac{d^2 x^*}{dt^2} = F_3 = -\tau A_p \qu(4.68)$$

where $A_p = \pi D_2 b$ and D_2 is the average cavity diameter in the second stage.

The solution to this equation is

$$x^* = \left(v_{f2} + \frac{\tau_0 e}{\mu} \right) \left(\frac{m_2 e}{\mu A_p} \right) \left[1 - \exp\left(-\frac{A_p \mu}{m_2 e} t \right) \right] - \frac{\tau_0 e}{\mu} t \quad (4.69)$$

where v_{f2} is the velocity at the end of the second stage. The force is therefore expressed as:

$$F_3 = -A_p \left(\tau_0 + \mu \frac{v_{f2}}{e} \right) \left[\exp\left(-\frac{A_p \mu}{m_2 e} t \right) \right] \quad (4.70)$$

This is a complex model and involves several stages of analysis. However good results have been claimed for a 5.59 mm lead projectile perforating 5.0 mm of an aluminium alloy plate (see Figure 4.7). The interesting aspect of this model is that there is a methodology for deriving the force acting on the projectile, along with displacement and velocity. However, this model is overly reliant on the assumption of plug formation that may not happen for thick targets penetrated by armour-piercing projectiles and during the penetration of semi-infinite targets. A number of assumptions are made too around the length of the plug, the width of the shear zone and the evolution of the diameter of the plug from D_1 to D_3. Like many other models, the limitation of the Awerbuch and Bodner model is its one-dimensional nature of
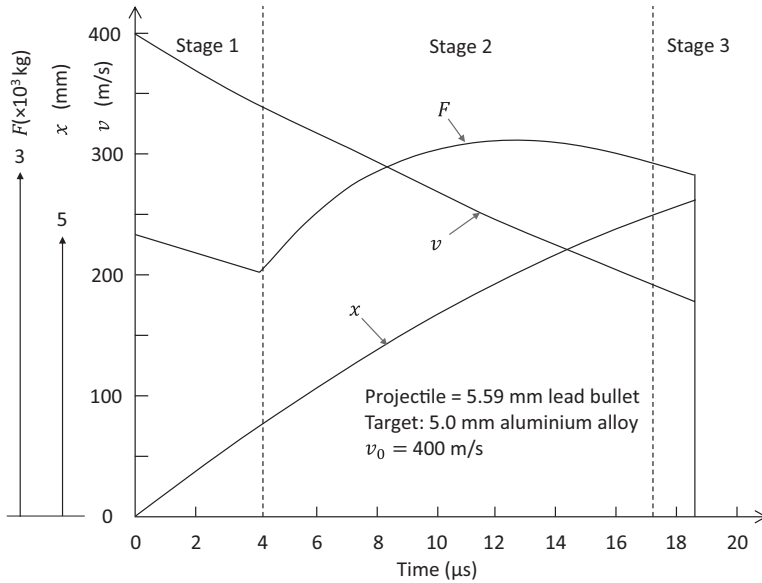
FIGURE 4.7 Penetration of a 5.0 mm aluminium alloy by a 5.59 mm lead projectile showing what happens during the three stages of penetration; the exit velocity predictions correlated well with experimental results. (Adapted from Awerbuch and Bodner, 1974a.)

what is essentially a two-dimensional process (or three-dimensional when obliquity is considered). Two-dimensional solutions are significantly more complex and are often avoided given the success and simplicity of one-dimensional models. Further discussions on this model are provided by Nixdorff (1983, 1984).

4.3.1.7 Jacobson Penetration Formulae

Jacobson reports a model for the resisting force applied to a blunt and conical projectile during penetration of polycarbonate (Jacobson, 1975), although it is applicable to ductile materials in general. This model decomposes the penetration stages into five regimes:

1. *Regime 1*: the penetrator tip enters the target and proceeds to $x = l$ inside the target (where x is the displacement of the tip of the projectile and l is the length of the conical/ogive part of the projectile). See Figure 4.8.
2. *Regime 2*: the cylindrical part of the penetrator enters the target and proceeds to $x = l + L$, such that the projectile is fully immersed into the target (where L is the length of the cylindrical section of the projectile).
3. *Regime 3*: the full penetrator is immersed in the target and proceeds to $x = h$, the total thickness of the armour plate.
4. *Regime 4*: the penetrator tip emerges from the rear face of the target and proceeds to $x = h + l$, such that the penetrator is sticking out from the target by length l.
5. *Regime 5*: The projectile leaves the target at $x = h + l + L$
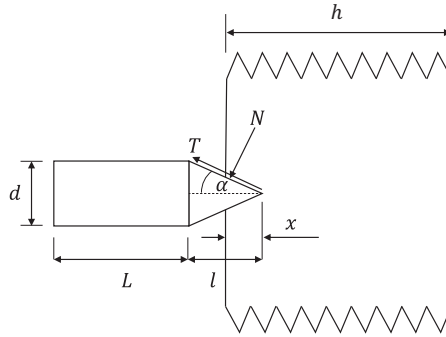
FIGURE 4.8 Regime 1 of the Jacobson model showing the key variables. (Adapted from Jacobson, 1975.)

For each regime, there is a different force definition and initially (in Regime 1), the penetration can be analyzed in terms of a normal resisting force to the cone (N) and a frictional force (T)—see Figure 4.8. Where,

$$m_0 \frac{d^2 x}{dt^2} = -T \cos \alpha - N \sin \alpha = F_1(x) \tag{4.71}$$

$$T = fN \tag{4.72}$$

and,

$$N = \frac{1}{2} \rho_t A_n v_n^2 \tag{4.73}$$

and so,

$$N = \left(\frac{\pi \rho_t}{2} \frac{\tan \alpha}{\cos \alpha} \sin^2 \alpha \right) x^2 \left(\frac{dx}{dt} \right)^2 \tag{4.74}$$

$F_1(x)$ is the force (for Regime 1) resolved along the trajectory of penetration (x) and m is the mass of the projectile. f is the dynamic coefficient of friction, and between a steel projectile and polycarbonate target was derived to be $=0.25$ by correlating the model with penetration experiments. In Jacobson's 1975 paper, he used the definition of specific weight, as opposed to mass density of the target, ρ_t, and therefore was required to divide the density by the gravitational constant, g. In keeping with modern notation, mass density is used here. The parameter A_n is the lateral area of the nose of the penetrator subjected to the forces of N and T and v_n is the normal velocity along the surface A_n.

The derived resisting force equations are now presented for each of the regimes in terms of the penetration in terms of x, as defined in Figure 4.8:

Regime 1: $0 < x \le l$

$$F(x) = -\left(A_1 v^2 + B_1 \right) x^2 \tag{4.75}$$

Where,

$$A_1 = \frac{\pi \rho_t}{2} \tan \alpha \sin^2 \alpha \left(\tan \alpha + f \right) \tag{4.76}$$

$$B_1 = \pi \sigma_c \tan \alpha \left(\tan \alpha + f \right) \tag{4.77}$$

Regime 2: $l < x \le l + L$

$$F(x) = -\left[A_2 v^2 + B_2 (x - l) + C_2 \right] \tag{4.78}$$

$$A_2 = \frac{\pi \rho_t}{2} \tan^2 \alpha \sin^2 \alpha \left(\tan \alpha + f \right) l^2 \tag{4.79}$$

$$B_2 = \pi f \sigma_c d \tag{4.80}$$

$$C_2 = \pi \sigma_c \tan \alpha \left(\tan \alpha + f \right) l^2 \tag{4.81}$$

For Regime 2, Jacobson (1975) separated the force calculation into two sections due to:

a. the retardation force acting only on the nose at the beginning of penetration, and
b. the retardation force that acts on the nose plus the force that becomes apparent due to friction on the projectile's body as penetration ensues.

For expediency, (a) has been ignored and so only (b) is summarized here, as per the approach by Backman and Goldsmith (1978). In any event, the effect of (a) is likely to be relatively small.

Regime 3: $(l + L) < x \le h$

$$F(x) = -\left(A_2 v^2 + P_3 \right) \tag{4.82}$$

where,

$$P_3 = B_2 L + C_2 \tag{4.83}$$

Regime 4: $h < x \le h + l$

$$F(x) = -\left(A_4 e^{\left[-K_2 (x - (l + L)) \right]} + B_4 (x - h)^2 e^{\left[-K_1 (x - h)^3 \right]} + C_4 \right) \tag{4.84}$$

where,

$$A_4 = A_2 v_{(l+L)}^2 - \frac{A_2 Q_3}{K_2} \tag{4.85}$$

$$B_4 = -\left(A_1 v_l^2 + B_1\right) \tag{4.86}$$

$$C_4 = \frac{A_2 Q_3}{K_2} + B_2 L + C_2 \tag{4.87}$$

where v_l is the computed velocity of the projectile when $x = l$ and $v_{(l+L)}$ is the velocity computed when $x = l + L$.

Regime 5: $h + l < x \le h + L + l$

$$F(x) = -\left(\pi f d \sigma_c (h + l + L - x)\right) \tag{4.88}$$

This is a complex model. Nevertheless, test data involving the penetration of polycarbonate targets ($\sigma_c = 75.8\,\text{MPa}$) by 12.7-mm calibre blunt, conical, hemispherical and ogival-tipped projectiles correlated reasonably well with the model in terms of the calculation of in-material velocities.

Force and velocity predictions are all very well, however, most engineers are more interested in predictive penetration capacity. For deep penetration of a semi-infinite target, we can ignore Regimes 4 and 5. Regimes 1 and 2 are likely to have relatively little effect on the overall prediction of deep penetration events and therefore we can use the integration method presented previously to arrive at a predictive equation (using the equation for Regime 3).

Thus, in this condition,

$$F(x) = -\left(A_2 v^2 + P_3\right) \tag{4.89}$$

And substituting, we get:

$$\int_0^P dx = -m_0 \int_{v_0}^0 \frac{v\,dv}{\left(A_2 v^2 + P_3\right)} \tag{4.90}$$

On integration,

$$p = m_0 \left(\frac{1}{2A_2} ln\left(P_3 + A_2 v_0^2\right) - \frac{1}{2c_2} ln\left(P_3\right)\right) \tag{4.91}$$

On simplification,

$$p = \frac{m_0}{2A_2}\left(ln\left[1 + \frac{A_2 v_0^2}{P_3}\right]\right) \tag{4.92}$$

Noting that:

$$A_2 = \frac{\pi \rho_t}{2} \tan^2 \alpha \sin^2 \alpha \left(\tan \alpha + f\right) l^2 \tag{4.93}$$

$$P_3 = B_2 L + C_2 \tag{4.94}$$

$$B_2 = \pi f \sigma_c d \tag{4.95}$$

$$C_2 = \pi \sigma_c \tan\alpha (\tan\alpha + f) l^2 \tag{4.96}$$

Figure 4.9 shows predictions of the simplified Jacobson model for an AP M2 projectile penetrating AA 5083-H131 (derived from the Regime 3 penetration analysis). The model is sensitive to both the coefficient of friction (f) and α. The model has been fitted to the data assuming $\alpha = 28°$ and $f = 0.03$. Although arguably this is unsatisfactory, the AP M2 projectile shed its jacket and filler during penetration with the solid core remaining intact (Moynihan et al., 2000). This makes correlation with a rigid-body penetration troublesome. The angle of 28° is somewhat larger than the approximated half-angle of the AP M2 jacket ($= 14°$) but surprisingly close to the approximated half-angle of the core ($= 27°$)—see Figure 4.10. This may explain why the fit at the elevated velocities is closer (i.e. where more of the penetration is dominated by the exposed core tip). The coefficient of friction also has an influence on the fit. This reducing it from 0.25 (as suggested by Jacobson for metal on polycarbonate) to 0.03 provides a good fit and is closer to the 0.01 value for metal-metal interfaces as used by Recht (1990) noting that friction accounts for 3% retardation in longitudinal motion of a projectile during penetration, as per the experimental measurements of Krafft (1955).

The dashed line represents a fit for $\alpha = 23.5°$ with the Jacobson value of $f = 0.25$. This appears to fit the penetration data at the lower velocities however is less satisfactory for elevated velocities of impact. A half-angle of 23.5° is suggested by
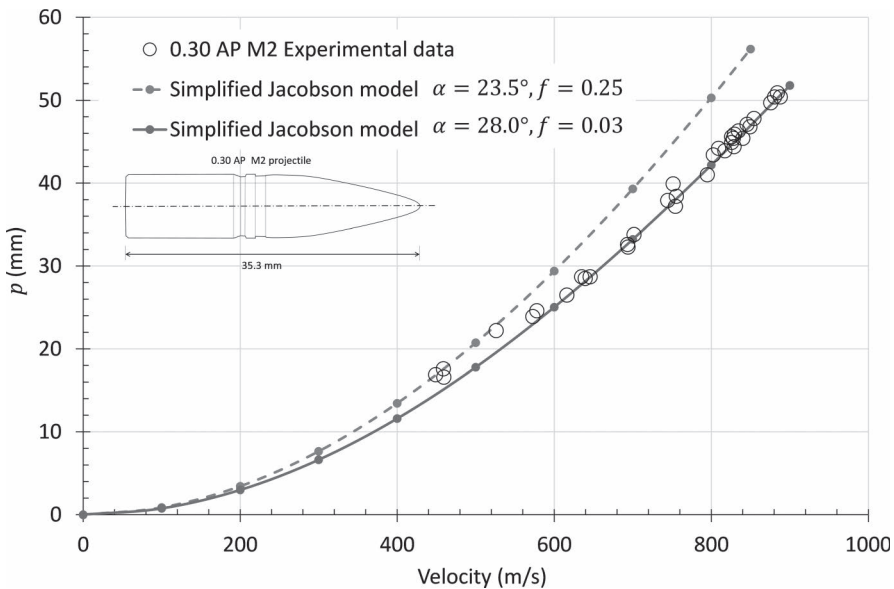
FIGURE 4.9 Correlation of a simplified Jacobson model (derived from Regime 3 penetration) with 0.30 AP M2 penetration data (into AA 5083-H131) from (Moynihan et al., 2000.)
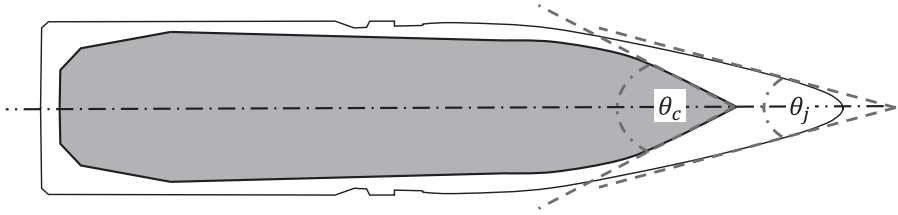
FIGURE 4.10 A schematic of a section of the AP M2 projectile showing the included angle of the core, θ_c which is larger than the included angle of the jacket, θ_j. For this projectile, $\theta_c = 54°$ and $\theta_j = 28°$ corresponding to half-angles (α) of 27° and 14°, respectively.

Recht (1990) for most ogival projectiles (including the AP M2) and increases to 37.5° for blunt projectiles, due to the evolution of a 'false nose' of material ahead of the penetrating projectile (see next).

4.3.1.8 Recht Penetration Formulae

Recht (1967, 1990) described the resisting force in a more complex fashion that included mechanical strength terms and a dynamic friction coefficient. The force definition is compartmentalized as follows:

$$\text{The inertial pressure term} = C_n\left(C_v v \sqrt{K\rho}\ \sin\alpha\right) \tag{4.97}$$

$$\text{The distortion pressure term} = 2\tau_0 \ln(2Z_m) \tag{4.98}$$

$$\text{A frictional term} = \left(1 + \frac{f}{\tan\alpha}\right) \tag{4.99}$$

These three terms (Equations 4.97–4.99) are brought together in the following equation:

$$F = A_x\left[C_n\left(C_v v \sqrt{K\rho_0}\ \sin\alpha + 2\tau_0 \ln(2Z_m)\right) \times \left(1 + \frac{f}{\tan\alpha}\right)\right] \tag{4.100}$$

Where A_x is the active area of the projectile and during penetration is assumed constant, C_n is an empirical dimensionless constant dependent on nose shape (= 0.62 for conical penetrators and for ogive projectiles where the radius of tangent ogive divided by the penetrator diameter is between 1 and 8), C_v is an empirical dimensionless constant that recognizes that inertial pressure decreases with time due to wave dispersion (=0.25) and α is the half-angle of the conical nose of the projectile, as described previously. K is the bulk modulus of the target material, τ_0 is the static shear strength of the target material, f is the dynamic friction coefficient (≈ 0.01 for metal on metal) and Z_m is given by

$$Z_m = \left(\frac{E}{Y_0}\right) \times \left(1 + 2\frac{E}{Y_0}\right)^{-0.5} \tag{4.101}$$

where E is Young's modulus of the target material and Y_0 is its static yield strength.

We can simplify the force definition (Equation (4.100)) by substituting the following:

$$a = 2\tau_0 \ln(2Z_m)\left(1 + \frac{f}{\tan\alpha}\right) \tag{4.102}$$

and

$$b = C_v\sqrt{K\rho_0}\left(1 + \frac{f}{\tan\alpha}\right)\sin\alpha \tag{4.103}$$

Therefore, the resisting force is simply given by:

$$F = A_x C_n(a + bv) \tag{4.104}$$

Integrating as before, we get

$$\int_0^p dx = -\frac{m_0}{A_x C_n}\int_{v_0}^v \frac{vdv}{(a + bv)} \tag{4.105}$$

This gives

$$p = -\frac{m_0}{A_x C_n}\left(\frac{v}{b} - \frac{a}{b^2}\ln(a + bv) - \frac{v_0}{b} - \frac{a}{b^2}\ln(a + bv_0)\right) \tag{4.106}$$

Leading to

$$p = \frac{m_0}{A_x C_n b}\left((v_0 - v) - \frac{a}{b}\ln\frac{(a + bv_0)}{(a + bv)}\right) \tag{4.107}$$

Assuming $A_x = $ constant $= A_p$

$$p = \frac{m_0}{A_p C_n b}\left((v_0 - v) - \frac{a}{b}\ln\frac{(a + bv_0)}{(a + bv)}\right) \tag{4.108}$$

Similar to the simplified Jacobson model presented previously, the beauty of Recht equation is that it is purely analytical. Predictions can be made simply by using a handbook of engineering properties.

Figure 4.11 shows the penetration prediction by using the Recht equation when compared to experimental penetration values into AA 6082-T651. The properties of the aluminium are presented in Table 4.3. The details of the bullet (7.62-mm FFV AP) are presented in Table 4.4, and the experimental data for the aluminium alloy were deduced from Hazell (2010). It can be seen that there is excellent agreement between the absolute penetration data and the predicted values of p (the penetration depth when the penetrator is fully immersed in the target—see Equation 4.108). Also included is the prediction of the penetration depth (p) when only the core is taken into
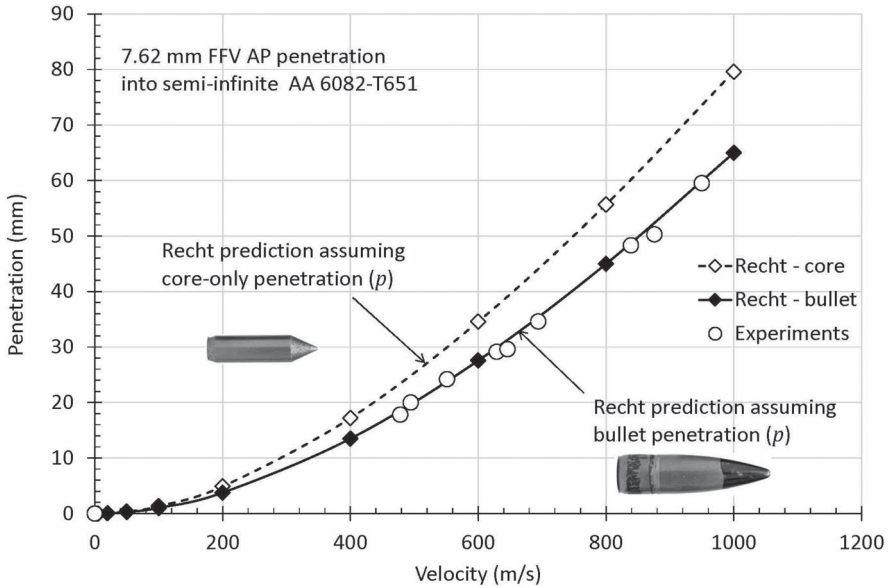
FIGURE 4.11 Penetration curves for AA 6082-T651 showing the comparison between the Recht predictions and experimental data for the 7.62-mm FFV AP bullet—with and without a jacket. The model values are calculated using Equation 4.108 and setting v_0 to the impact velocity and $v = 0$.

account. With the core-only data, it is seen that Recht overpredicts the penetration depth, as the penetration through the jacket and the energy required to remove it have not been taken into account. However, it shows nicely the differences in penetration that could be expected with and without a jacket (Figure 4.11).

The results are less satisfactory with other rigid-projectile penetration data, however. A comparison between the simplified Recht prediction noted above and the data presented by Piekutowski et al. (1999) is presented in Figure 4.12. Here the Recht prediction is not exact but close to the experimental measurements.

If higher-fidelity calculations are required, where there is a distinct conical or ogival shape for the projectile nose, the calculation can be done in two steps. This is achieved by knowing the length of the cone/ogive, l. First, for the case where $x < l$, the velocity is calculated at the point where the projectile has become immersed into the target, taking into account the varying change of the nose of the penetrator. To account for the change in the area of the projectile nose, the left-hand side of the above penetration equation is replaced with the following:

$$\int_0^x \frac{A_x}{A_P} \cdot dx = \int_0^x \frac{\pi x^2 \tan^2 \alpha}{A_p} = \frac{\pi x^3}{3A_P} \tan^2 \alpha \qquad (4.109)$$

where A_x is the incremental area presented by the conical/ogival part of the penetrator and for the condition of $x < l$, can be written as $A_x = \pi x^2 \tan^2 \alpha$ (see Recht (1990)).

TABLE 4.3
Engineering Material Properties for Some Common Metals

Material	Hardness (Brinell Hardness Number [BHN])	Density (kg/m³)	Bulk Modulus, K (×10^9 N/m²)	Young's Modulus, E (×10^9 N/m²)	Yield Strength, Y_0 (×10^6 N/m²)	Compressive Shear Strength, τ_0 (×10^6 N/m²)
Steel alloys						
Steel–soft	100	7830	158	206	172	206
Steel–mild	150	7830	158	206	309	275
Ship armour	200	7830	158	206	549	377
Ship armour	250	7830	158	206	756	470
Armour	300	7830	158	206	893	549
MIL-12560	350	7830	158	206	1030	618
Aluminium alloys						
AA 7075-0	60	2765	69	71	103	151
AA 5083-0		2660	71	72	145	172
AA 5083-H113	75	2765	69	71	227	185
AA 6082-T651		2680	69	70	240	210
AA 2024-T3	120	2765	69	71	343	281
AA 7075-T6	150	2765	69	71	500	330
Titanium alloys						
Ti–6Al–4V	285	4500	126	114	827	483
Magnesium Alloys						
Mg–13Li–6Al	55	1720	41	45	200	152

Source: Recht, R. F. 1990. High velocity impact dynamics: Analytical modeling of plate penetration dynamics. *In:* Zukas, J. A. (ed.) *High Velocity Impact Dynamics*, pp. 443–513. New York: John Wiley & Sons, Inc.

TABLE 4.4

Parameters for the 7.62-mm AP FFV Bullet for Use with the Recht Model

Parameter	Symbol	Bullet	Core
Mass ($\times 10^{-3}$ kg)	M	8.23	5.90
Diameter ($\times 10^{-3}$ m)	D	7.62	5.59
Projected area ($\times 10^{-6}$ m^2)	A_p	45.60	24.50
Half-angle of cone (°)	A	23.50	29.95
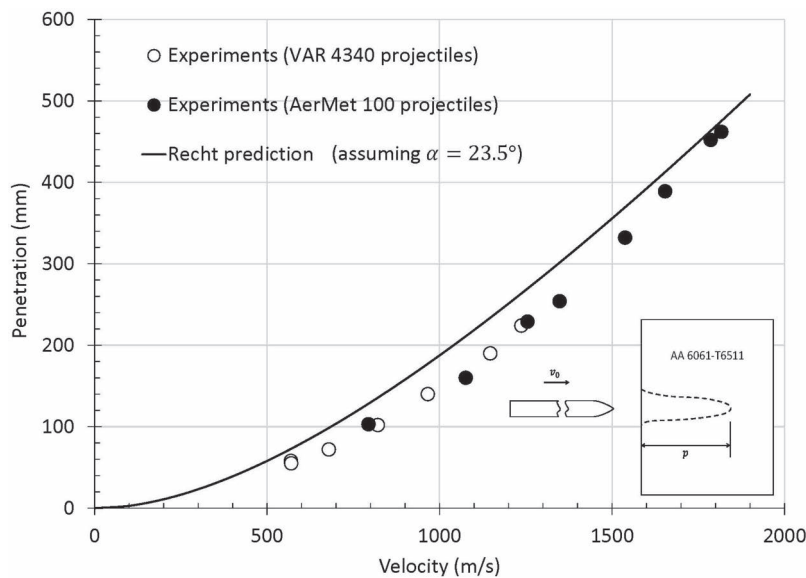
FIGURE 4.12 Penetration of an AA 6061-T6511 target ($Y_0 = 276$ MPa) by an ogival rod of length 71.1 mm and diameter 7.11 mm with a calibre-radius-head (CRH) of 3. Assumed projectile mass for the Recht prediction $= 20.4$ g. Experimental data from Piekutowski et al. (1999).

The constant A_p is the area presented by the projectile once it is completely immersed in the target, and v_0 is the initial impact velocity.

So that the penetration equation (Equation 4.108) becomes:

$$\int_0^x \frac{A_x}{A_\mathrm{p}}\, dx = \frac{\pi x^3}{3 A_\mathrm{p}} \tan^2 \alpha = \frac{m_0}{A_\mathrm{p} C_n b}\left[(v_0 - v) - \frac{a}{b} \ln\left(\frac{a + b v_0}{a + bv}\right)\right] \qquad (4.110)$$

Noting that the impact velocity $= v_0$, the velocity, v is computed for when $x = l$. This is the velocity that the penetrator has decelerated to after the ogive/cone section has immersed in the target (see Figure 4.13).
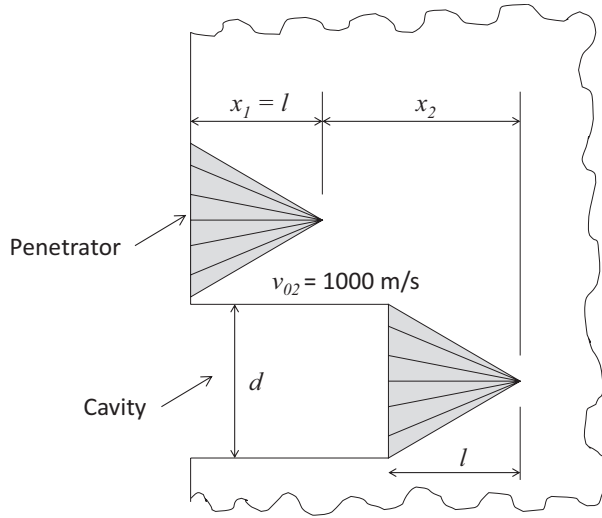
FIGURE 4.13 Penetration of a non-deforming cone-shaped projectile into ductile media. After penetrating a distance of x_1, where $x_1 = l$, the velocity, $v_{02} = 1000$ m/s.

If the penetrator is completely immersed in the target material, then the left-hand side of the above penetration equation is simply 'x_2' (the displacement into the target), and so the penetration equation becomes

$$x_2 = \frac{m_0}{A_P C_n b}\left[(v_{02} - v) - \frac{a}{b}\ln\left(\frac{a + bv_{02}}{a + bv}\right)\right]$$
(4.111)

where v_{02} is the velocity of the projectile as it becomes completely immersed in the target (i.e. after penetrating the nose length, see Figure 4.13). Maximum penetration can be calculated by setting $v = 0$.

The total depth of penetration is then given by

$$p = l + x_2$$
(4.112)

where l is the length of the conical/ogival part of the penetrator and assuming that $p > l$.

Knowing that

$$A_P = \frac{\pi d^2}{4}$$
(4.113)

and dividing both sides of the penetration equation by the diameter – d gives

$$\frac{x_2}{d} = \frac{4\left(\dfrac{m_0}{\pi d^3}\right)}{C_n b}\left[(v_{02} - v) - \frac{a}{b}\ln\left(\frac{a + bv_{02}}{a + bv}\right)\right]$$
(4.114)

This equation gives a dimensionless value of penetration (x_2/d) that can be used to compare predicted computations for different calibres of projectiles.

For ogives described above, Recht deduced that these can be described as conical with a half-angle, α, of 23.5°. That is, the ogival projectile is modelled as if it is replaced with a conically-tipped projectile with the same mass and velocity as the ogival projectile but with the conical part possessing a half angle of 23.5° with a corresponding cone height. Further, for conical shapes where $\alpha > 37.5°$ (i.e. blunt projectiles), α can be assumed to be equal to 37.5°. This is because a non-deforming blunt projectile develops a 'false nose' of target material which modifies its shape and mass. Recht deduced that for rigid flat cylinders the false nose possesses an effective apex half-angle of about 37.5° and therefore all penetrators having nose geometries more blunted than 37.5° should be assigned a massless false nose with such an angle.

Various material properties that are used for penetration analysis are presented in Table 4.3. The majority of the data are from Recht (1990).

This equation has been used extensively to predict penetration into various ductile target materials and is a useful tool for armour designers. Figure 4.14 shows some predicted penetration values of a projectile shaped like a cone with a half-angle of 23.5° into various ductile metals using the data from Table 4.3; the solid lines indicate the prediction of the projectile velocity as it penetrates deeper into the target. The x-axis is presented in the form (x_2/d) (m/d^3), which is a measure of penetration. Recht (1990) has shown that these penetration curves correlate very well with experimental data (Figure 4.14).

The Recht penetration formula has also been shown to be quite satisfactory in predicting penetration of rigid body penetrators of a variety of calibres into

FIGURE 4.14 Penetration into ductile target media by a conical projectile.

TABLE 4.5

Parameters for Armour-Piercing Bullets for Use in the Recht Model

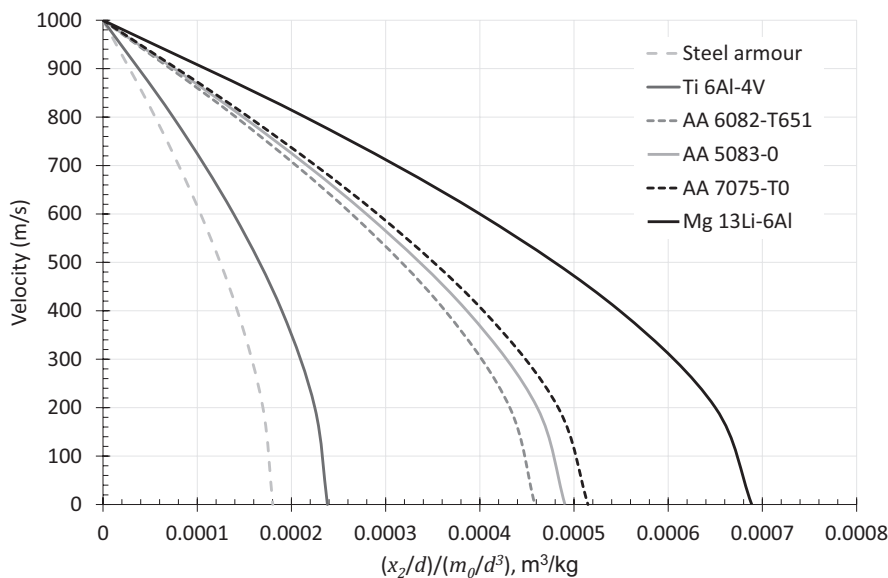| Projectile	Mass ($\times10^{-3}$ kg)	Diameter ($\times10^{-3}$ m)	Projected Area ($\times10^{-6}$ m²)	Assumed Half-Angle of Cone (°)	Typical Muzzle Velocity[a] (m/s)
	m	D	Ap	A	v_0
5.56 mm M995 AP	4.0	5.66	78.54	23.5	1000
7.62 mm B32 API	10.3	7.87	25.16	23.5	800
7.62 mm P80 AP	9.8	7.82	48.65	23.5	850
7.62 mm AP M2[b]	10.8	7.84	48.03	23.5	840
12.7 mm M8 API	43.1	12.96	131.92	23.5	910
12.7 mm B32 API	48.3	12.95	131.71	23.5	840
14.5 mm B32 API	63.4	14.50	174.37	37.5	975
14.5 mm BS41 API	64.4	14.50	174.37	37.5	975

Source: Basic data such as mass, diameter and muzzle velocity taken from Cutshaw and Ness (2003).
[a] Sometimes recorded as velocity at 25 m from the muzzle.
[b] This is the same as the 0.30 calibre AP M2 AP projectile.

ductile plates. From the analysis presented by Recht, it is possible to establish the projectile parameters for a variety of different calibres. These are shown in Table 4.5. However, caution should be exercised when computing penetration—particularly for complex small-arm projectiles, for the following reasons:

1. The Recht model does not directly account for strain-rate strengthening effects of the material (although there is an indirect account for this in the constant, C_v). This may not be a problem for heavily strain-hardened alloys, however.
2. The model relies on the measure yield strength of the material (Y_0) whereas a better property to use perhaps would be the ultimate tensile strength which is normally reported in manufacturers' material data sheets.
3. Real armour-piercing projectiles with ogival noses are complex and commonly the nose will deform readily on contact with the target material and therefore the condition for the projectile to behave like a rigid body is somewhat compromised. Therefore, the half-angle of the cone value may require some calibration.
4. The compressive strength of the material is rarely available in manufacturer-supplied material data sheets and needs to be measured or calculated. See later.

Table 4.6 presents some penetration data for 14.5-mm projectile presented by Woolmore (2005) and the Recht predictions taking into account the cone half-angle of 23.5° and 37.5°. For these projectiles, it can be seen that using a half angle of 23.5° over-predicted the penetration into different materials whereas 37.5° provides

TABLE 4.6

Recht Comparison for Different Cone Half-Angles for 14.5 Armour-Piercing Projectiles

Projectile	Target Material	Velocity (m/s)	Experimental DoP (mm)	Recht Prediction ($\alpha=23.5°$), DoP (mm)	Recht Prediction ($\alpha=37.5°$), DoP (mm)
14.5 mm BS41 API	Mild steel	1016	75	104.2	77.4
14.5 mm BS41 API	AA 1318B	1017	105	135.0	111.6
14.5 mm B32 API	Mild steel	1002	68	101.0	75.0

Source: Experimental Data from Woolmore (2005).

a better correlation. The material properties for the analysis of the Recht model are shown in Table 4.7 along with some other relevant armour materials currently available. The compressive shear strength of the materials is often missing from mechanical property data sheets and in this case, it has been assumed to be given according to:

$$\tau_0 = \frac{1}{\sqrt{3}} Y_0 \tag{4.115}$$

This is a reasonable approximation.

4.3.1.9 Forrestal Penetration Formula

Forrestal et al. (1988, 1992) examined the penetration performance of rods into aluminium alloys. In these works, they developed a formula for the axial force on an ogival nose as it penetrated an aluminium alloy target.

The projectile is shown in Figure 4.15. The shape of the nose is important, and it is commonplace to define the shape of an ogive in terms of its calibre-radius-head (CRH). With reference to Figure 4.15, CRH is defined by

$$CHR = \frac{s}{d} = \psi \tag{4.116}$$

The nose length, l, is given by

$$l = \frac{d}{2}\left(4\psi - 1\right)^{1/2} \tag{4.117}$$

The projectile strikes the target at velocity v_0 and penetrates at a constant velocity (as a rigid body) at velocity, v_z.[1] The axial force acting on the ogival nose was derived as

TABLE 4.7
More Properties of Target Materials for Use with the Recht Model

Material	Hardness (Brinell Hardness Number [BHN])	Density (kg/m³)	Bulk Modulus, K (×10^9 N/m²)	Young's Modulus, E (×10^9 N/m²)	Yield Strength, Y_0 (×10^6 N/m²)	Compressive Shear Strength, τ_0 (×10^6 N/m²)
Mild steel	-	7830	158	206	265	153
AA 1318B	-	2780	73	72	460	265
AA 2139-T8	165	2820	69	73	475	274
AA 5083- H131	105	2660	69	71	319	184

It is assumed that $\tau_0 = \dfrac{1}{\sqrt{3}} Y_0$.
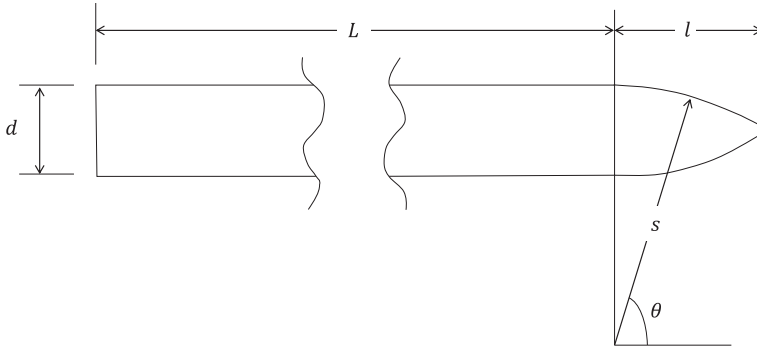
FIGURE 4.15   Ogival-nosed rod used for the Forrestal analysis. (Adapted from Forrestal, M. J. et al. 1992, *International Journal of Solids and Structures*, 29(14–15), 1729–1736.)

$$F_z = 2\pi s^2 \int_{\theta_0}^{\pi/2} \left\{ \left[\sin\theta - \left(\frac{s - \dfrac{d}{2}}{s} \right) \right] (\cos\theta + \mu\sin\theta) \right\} \sigma_n(v_z,\theta) \cdot d\theta \qquad (4.118)$$

where

$$\theta_0 = \sin^{-1}\left(\frac{s - \dfrac{d}{2}}{s} \right) \qquad (4.119)$$

In this equation, v_z is the instantaneous axial velocity during penetration, and s, d and θ are defined in Figure 4.15. The normal stress component $\sigma_n(v_z, 0)$ is the normal stress approximated assuming that the penetration of the rod causes a spherical cavity to grow in the material from rest to a constant velocity, v.

The derivation of the penetration formula will now be outlined according to Forrestal et al. (1992) which takes into account a cavity expansion that considers the strain hardening of the material. This is different from Forrestal et al.'s (1988) paper that only considered elastic–perfectly plastic behaviour (i.e. no strain hardening).

The coefficient of sliding friction introduced previously (f) is calculated by noting that the tangential stress is directly proportional to the normal stress according to

$$\sigma_t = f\sigma_n \qquad (4.120)$$

For a spherically expanding cavity, a radial stress is applied to the material that results in cavity growth at a velocity v. This is defined as

$$\frac{\sigma_r}{Y_0} = A + B\left(\sqrt{\frac{\rho_t}{Y_0}}\, v \right)^2 \qquad (4.121)$$

where A and B are dependent on the material properties of the target material and v is the cavity-expansion velocity. For an *incompressible* material, the following equations were derived (Luk et al., 1991):

$$A = \frac{2}{3}\left[1 + \left(\frac{2}{3}\frac{E}{Y_0}\right)^n I\right]$$

(4.122)

$$B = 1.5$$

(4.123)

$$I = \int_0^{1-(3Y_0/2E)} \frac{(-\ln x)^n}{1-x}\,dx$$

(4.124)

where

I is evaluated numerically (Forrestal and Romero 2007).

E is Young's modulus.

Y_0 is the yield strength of the material.

n is the work-hardening exponent used to curve-fit the stress–strain data.

For an AA 7075-T651, $I = 3.896$, and $A = 4.609$. It is important to point out that these equations are valid for incompressible material flow. That is to say that the density remains constant. For compressible behaviour, the density becomes a dependent variable. Based on previously published procedures (Luk et al. 1991), the radial stress at the cavity surface can be plotted against the cavity expansion velocity for both incompressible and compressible flow; the results for AA 7075-T651 (including the stress–strain response) are shown in Figure 4.16. It is then possible to curve-fit Equation 4.121 such that the parameters A and B are found. For a compressible AA 7075-T651, these results are $A = 4.418$ and $B = 1.068$.

Next, the particle velocity associated with the penetrating ogival-nosed projectile needs to be established. As the material is being penetrated, the material surrounding the ogival tip will be 'pushed away' at a velocity given by

$$u_P(v_z, 0) = v_z \cos\theta$$

(4.125)

The normal stress on the nose of the projectile is approximated by replacing the spherically symmetric cavity expansion velocity v with the particle velocity of the target material, u_p.

Therefore, Equation 4.121 becomes

$$\frac{\sigma_n(v_z, \theta)}{Y_0} = A + B\left[\left(\frac{\rho_t}{Y_0}\right)^{1/2} v_z \cos\theta\right]^2$$

(4.126)

Substituting into Equation 4.118 and integrating gives

$$F_z = \frac{\pi d^2}{4} Y_0\left(\alpha + \frac{B\rho_t v_z^2}{Y_0}\right)$$

(4.127)
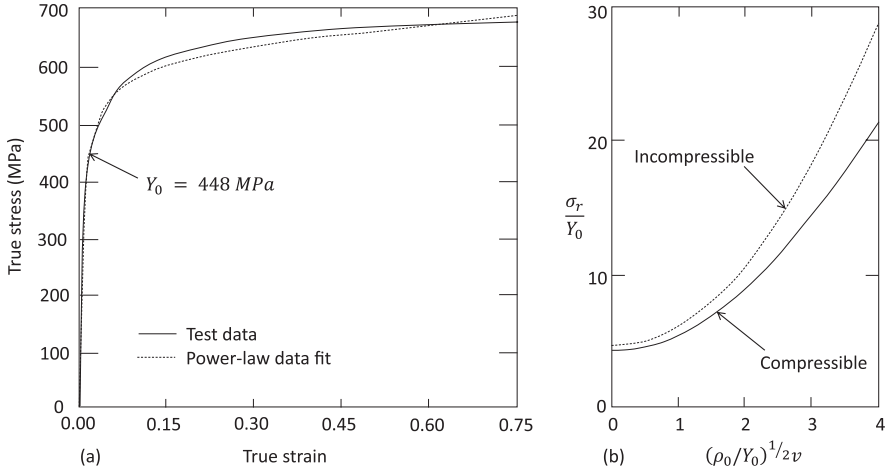
FIGURE 4.16 (a) Compression stress–strain data for 7075-T651 target material and the power law data fit and (b) radial stress at the cavity surface versus cavity expansion velocity for an elastic, strain-hardening material. (Adapted from Forrestal, M. J. et al., *International Journal of Solids and Structures*, 29(14–15), 1729–1736.)

$$\alpha = A\left[1 + 4f\psi^2\left(\frac{\pi}{2} - \theta_0\right) - f(2\psi - 1)(4\psi - 1)^{1/2}\right] \tag{4.128}$$

$$\beta = B\left[\frac{(8\psi - 1)}{24\psi^2} + f\psi^2\left(\frac{\pi}{2} - \theta_0\right) - \frac{f(2\psi - 1)(6\psi^2 + 4\psi - 1)(4\psi - 1)^{1/2}}{24\psi^2}\right] \tag{4.129}$$

$$\theta_0 = \sin^{-1}\left(\frac{2\psi - 1}{2\psi}\right) \tag{4.130}$$

The final penetration depth is obtained from

$$m_0\left(\frac{dv_z}{dt}\right) = m_0 v_z\left(\frac{dv_z}{dz}\right) = -F_z \tag{4.131}$$

where m_0 is the intial projectile mass, and z is the penetration depth.

The mass of the cylindrical portion of the rod is given by

$$m_c = \rho_p \frac{\pi d^2}{4} L \tag{4.132}$$

The mass of the ogival part of the projectile is given by

$$m_{og} = \rho_p \frac{\pi d^3}{8} k \tag{4.133}$$

where k is given by

$$k = \left(4\psi^2 - \frac{4\psi}{3} + \frac{1}{3} \right)(4\psi - 1)^{1/2} - 4\psi^2 (2\psi - 1)\sin^{-1}\left[\frac{(4\psi - 1)^{1/2}}{2\psi} \right] \quad (4.134)$$

Therefore, the total mass of the projectile is

$$m_p = m_c + m_{og} = \rho_p \frac{\pi d^2}{4}\left(L + \frac{kd}{2} \right) \quad (4.135)$$

Equations 4.127 and 4.135 can now be inserted into Equation 4.131 to give

$$-dz = \rho_p \left(L + \frac{kd}{2} \right)\frac{v_z}{\alpha Y_0 + \beta \rho_t v_z^2}\, dv_z \quad (4.136)$$

This is then integrated between 0 and v_0 to give the final penetration depth (p):

$$p = \frac{1}{2\beta}\left(L + k\frac{d}{2} \right)\left(\frac{\rho_p}{\rho_t} \right)\ln\left[1 + \left(\frac{\beta}{\alpha} \right)\left(\frac{\rho_t v_0^2}{Y_0} \right) \right] \quad (4.137)$$

The predicted penetration results due to varying the impact velocity into AA 7075-T651 are given in Figure 4.17. It is clear that the coefficient of the sliding friction
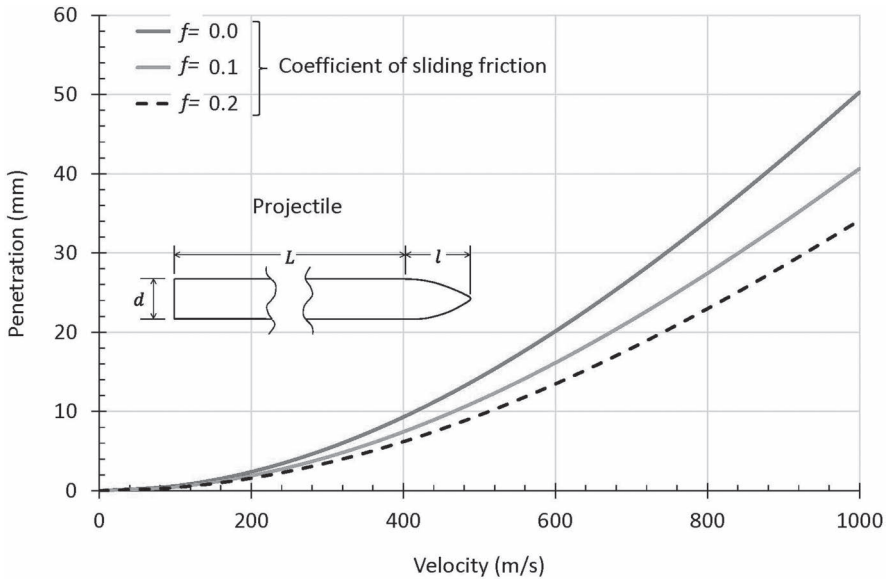
FIGURE 4.17 Calculated penetration results into an AA 7075-T651 by the projectile shown in the chart $d = 10\,$mm, $L = 25\,$mm and $l = 9\,$mm. The coefficient of sliding friction is varied to show its effect.

plays a moderate role in reducing the penetration depth. However, measuring the coefficient of sliding fraction during fast penetration is problematic. Forrestal et al. (1992) used values between 0.0 and 0.06 that appeared to correlate well with the experimental results, which, given the extent of thermal softening that would be expected to occur, is reasonable. In fact, subsequent models assumed that $f = 0.0$ due to the expectation that a thin layer of melted material existed between the projectile/target material interface allowing for nearly frictionless contact (Forrestal and Warren, 2008).

Example 4.2

A conically-nosed steel penetrator 25 mm long and 10 mm in diameter, d impacts an AA 7075-T6 target at 1000 m/s. The length of the conical portion of the projectile, $l = 9$ mm. Using the data from Table 4.3, calculate the penetration depth into the aluminium alloy using the Recht equation. See Figure 4.18 for the key projectile parameters that are provided (or will need to be calculated).

$C_n = 0.62$
$C_n = 0.25$
$f = 0.01$

Firstly, the half-angle of the cone needs to be calculated; this is done according to

$$\tan \alpha = \frac{\frac{d}{2}}{l} \tag{4.138}$$

The projected area is calculated from

$$A_p = \frac{\pi d^2}{4} \tag{4.139}$$

And the volume (V_{proj}) of the projectile (to calculate its mass) needs to be calculated according to

$$V_{proj} = \frac{\pi d^2}{4}\left(L + \frac{l}{3}\right) \tag{4.140}$$

FIGURE 4.18   Projectile parameters for Example 4.2.

where L is the length of the cylindrical section.

The penetration needs to be calculated in two steps:

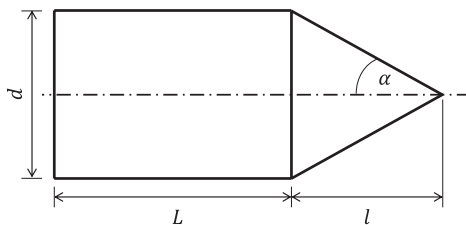Firstly, the velocity of the projectile is calculated at the point that the conical section is completely immersed in the target by setting $x = l$, and solving for the velocity, v, in the following equation using trial and error,

$$\frac{\pi x^3}{3 A_p} \tan^2 \alpha = \frac{2\left(\dfrac{m_0}{2 A_p}\right)}{C_n b}\left[(v_0 - v) - \frac{a}{b}\ln\left(\frac{a + bv_0}{a + bv}\right)\right] \tag{4.141}$$

This can be solved very easily using Goal Seek in Microsoft Excel®.

So, in this first step, the volume of the projectile (V_{proj}) is needed:

$$V_{proj} = 1.49 \times 10^{-6}\ \text{m}^3$$

which then gives us the mass ($m = \rho \times V$)

$$m_0 = 11.67\ \text{g} = 11.67 \times 10^{-3}\ \text{kg}$$

The half-angle of the cone is given by

$$\alpha = \tan^{-1}\left(\frac{5}{9}\right) = 29.055°$$

And the left-hand side of the penetration equation gives us

$$\frac{\pi x^3}{3 A_p}\tan^2 \alpha = \frac{4\pi l^3}{3\pi d^2}\frac{\dfrac{d^2}{2^2}}{l^2} = \frac{l}{3} = 9/3 = 3 \times 10^{-3}\ \text{m}$$

From Table 4.3, the values for Z_m, a and b can be calculated. They are

$$Z_m = 8.41,\ a = 1.90 \times 10^9\ \text{N/m}^2\ \text{and}\ b = 1.71 \times 10^6\ \text{Ns/m}^3$$

Therefore, the penetration equation now becomes

$$3.0 \times 10^{-3} = 1.4 \times 10^{-4}\left(1000 - v - 1111\ \ln\left(\frac{3.61 \times 10^9}{1.90 \times 10^9 \times 1.71 \times 10^6\, v}\right)\right)$$

Solving for v gives 954 m/s.

The second step is to replace v_0 with the calculated value of v from the previous step so that it is now v_{02} ($= 954$ m/s), and use the following equation to calculate the penetration depth by the fully immersed penetrator and setting $v = 0$:

$$x_2 = \frac{2\left(\dfrac{m_0}{2 A_p}\right)}{C_n b}\left[(v_{02} - v) - \frac{a}{b}\ln\left(\frac{a + bv_{02}}{a + bv}\right)\right] \tag{4.142}$$

Doing this, we arrive at a value of $x_2 = 37.3 \times 10^{-3}$ m $= 37.3$ mm.
Total penetration is then given by

$$p = l + x_2 \tag{4.143}$$

So, the total penetration $= 9.0 + 37.3 = 46.3$ mm.

Example 4.3

An ogival-nosed steel penetrator 25 mm long and 10 mm in diameter impacts an AA 7075-T6 target at 1000 m/s. The length of the ogival portion of the projectile is 9 mm. Using the Forrestal equation, calculate the penetration depth into a compressible aluminium alloy.

First, the projectile parameters shall be dealt with.

The projectile parameter s needs to be calculated. From Equations 4.116 and 4.117,

$$s = \frac{1}{d}\left(l^2 + \frac{d^2}{4}\right) \tag{4.144}$$

For our projectile,

$d = 0.010$ m
$L = 0.025$ m
$l = 0.009$ m
$s = 0.0106$ m

Next, the other parameters need to be established (noting that the angles are in radians). These can be calculated simply by substituting into the equations presented previously and are summarized in Table 4.8.

Here too, it is being assumed that the properties of AA 7075-T6 are pretty much identical to AA 7075-T651 (they are pretty close), and therefore, $A = 4.418$ and $B = 1.068$ are adopted for a compressible material; $Y_0 = 448$ MPa. Substituting into Equation 4.137, we get

$$p = \frac{1}{2 \times 0.296}\left(0.025 + 1.041 \times \frac{0.01}{2}\right)\left(\frac{7850}{2710}\right)\ln\left[1 + \left(\frac{0.296}{4.420}\right)\left(\frac{2710 \times 1000^2}{448 \times 10^6}\right)\right]$$

$$= 50.3 \times 10^{-3} \text{ m } (50.3 \text{ mm}).$$

TABLE 4.8
Parameters Calculated for Example 4.3

Parameter	k (Radians)	m_p (kg)	θ_0 (Radians)	α (Radians)	β (Radians)	f
Value	1.041	1.862×10^{-2}	0.556	4.420	0.296	0.00

This is similar to the Recht prediction with a conical-shaped nose projectile. The small difference is due to the different approaches used, and the expectation of a slightly different behaviour with a conical nose, as opposed to an ogival nose. Full penetration curves for this projectile into AA 7075-T651 are shown in Figure 4.17.

4.3.2 PENETRATION OF FINITE-THICKNESS PLATES

Penetration prediction of finite thickness plates is necessarily an important part of the armour design process. We can analyze this problem for ductile plates by considering the energy required to force open a cavity in such a plate. Figure 4.19 shows the comparison of a symmetrical hole formed on a lathe using a broaching tool to a hole formed by the penetration of a conical projectile. Qualitatively, they are similar and therefore it seems reasonable to apply similar models to both scenarios. The energy required to cause the former was derived by Taylor in 1948 and has been extensively discussed by Woodward (1978a, 1978b, 1990) in the context of penetrating projectiles. This energy can be calculated by,

$$E = \frac{\pi}{2} d^2 Y h \qquad (4.145)$$

where Y is a measure of the effective flow stress such as yield strength or ultimate tensile strength. Investigations have shown that this is not a terrible estimate for the perforation of a 5083 plate by conical projectile (see Figure 4.20).

If we take the work done in forming the hole and equate that to the kinetic energy of the projectile, it is possible to establish a ballistic limit velocity (e.g. see Figure 4.20b). This is one way that models for the ballistic limit velocity are established. We will discuss several of these models in the following section.

Woodward went on to discuss the energy required to cause dishing, shear and adiabatic shear in ductile targets (Woodward, 1990). These are:

(a)   (b)
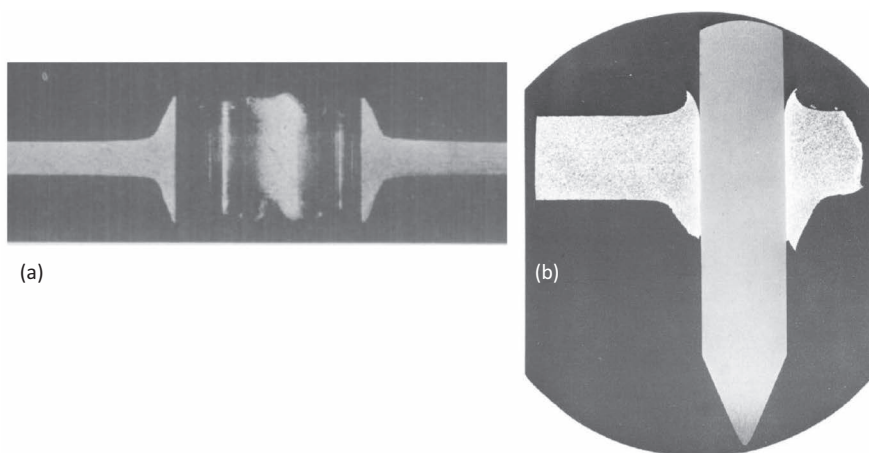
FIGURE 4.19 (a) Expansion of hole in a plate by a broaching tool on a lathe, after Taylor (1948) and (b) perforation of a mild steel plate by a pointed projectile after Woodward (1978a.)
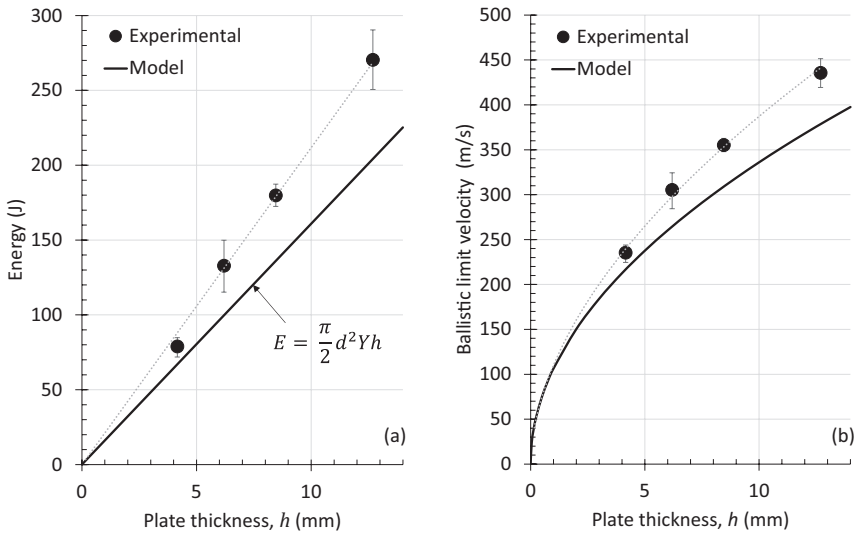
FIGURE 4.20   Plot of energy and ballistic limit velocity to just perforate an AA 5083 target plate compared with Taylor's simple model for penetration. Target: AA 5083 (cold rolled), $Y = 452\,\text{MPa}$. Projectile: 45°conical tip, $m = 2.85\,\text{g}$, $d = 4.76\,\text{mm}$. (After Woodward (1978b).)

Dishing:

$$E = \frac{\pi}{8} dYh(d + \pi h) \tag{4.146}$$

Where the first term on the right is the stretching work and the second term is the energy required for bending during the dishing process. Dishing is favourable when $h < (\pi/3)d$ because in this circumstance it takes less energy for this to occur than to form a hole through radial expansion.

Shearing (thick plate, flat projectile, assuming that the shear strength, $\tau_0 = \frac{1}{\sqrt{3}}Y$):

$$E = \frac{\pi}{2\sqrt{3}} dYh^2 \tag{4.147}$$

Adiabatic shear (where the shear strength, $\tau_0 = 0$)

$$E = \frac{\pi d^2}{2}\left(h - \frac{\sqrt{3}}{2}d\right)Y + \frac{\pi d^3 Y}{12\tan\theta/2} \tag{4.148}$$

Shear in thin plates, where $h < (\sqrt{3}/2)d$ and when the penetrator is buried to a diameter of $(2/\sqrt{3})h < d$.

$$E = \frac{2\pi Yh^3}{9\sqrt{3}\tan\theta/2} \tag{4.149}$$

4.3.2.1 Ballistic Limit Equations for Finite-Thickness Plates

All armour systems are of finite thickness and therefore researchers have (sensibly) developed equations to allow for the prediction of the velocity at which we would expect 50% of the projectiles to perforate the target and 50% to be stopped. This velocity is known as the v_{50} velocity, or 'ballistic limit velocity' (v_{bl}). We will review a few here (although others are covered elsewhere in the book).

1. (Nishiwaki, 1951)

    Nishiwaki presented a model for the penetration of aluminium plates by sharp-nosed conical projectiles by considering a force equilibrium approach at various stages of the penetration. At each stage of the penetration process, the resisting force acting on the projectile is related to the contact pressure which is assumed to be constant. The residual velocity of the projectile is given as follows:

$$v_r = \left[\exp\left(-\frac{\rho_t}{2m_0} \pi d^2 h \sin^2 \alpha \right) \left\{ v_0^2 - \frac{g P_0}{\rho_t \sin^2 \alpha} \left[\exp\left(\frac{\rho_t}{2m_0} \pi d^2 h \sin^2 \alpha \right) - 1 \right] \right\} \right]^{1/2}$$

(4.150)

where,

   ρ_t = the density of the target plate (which for aluminium = 2700 kg/m³)
   h = plate thickness
   g = acceleration due to gravity
   m_0 = projectile mass (assumed constant)
   d = projectile diameter
   α = the half-angle of the projectile nose
   τ_t = a function of the dynamic shear strength of the target material (units of stress)

The quantity P_0 is the contact pressure that was assumed to be constant and derived by penetrating the different thicknesses of aluminium plate by a mandrel and measuring the load during penetration. This resulted in a relationship where, $P_0 = Ch$. Assuming the units of kg/mm², for P_0 and the units of mm for h, a value $C = 5.4$ kg/mm³ was measured for aluminium.

It is important to note that in Nishiwaki's original 1951 paper, the specific weight of the aluminium target plate ($= \rho_t g$) was used. Further, the radius of the projectile was used, which has been substituted for $d = 2r$ above.

By setting $v_r = 0$, we can solve for v_0 which in this circumstance $= v_{bl}$, viz,

$$v_{bl} = \left(\frac{g P_0}{\rho_t \sin^2 \alpha} \left[\exp\left(\frac{\rho_t}{2m_0} \pi d^2 h \sin^2 \alpha \right) - 1 \right] \right)^{1/2}$$

(4.151)

Overall, the model appeared to work reasonably well for non-deforming projectiles perforating thin plates (see Figure 4.21). Comparison with experimental data for impacts with fragment simulating projectiles
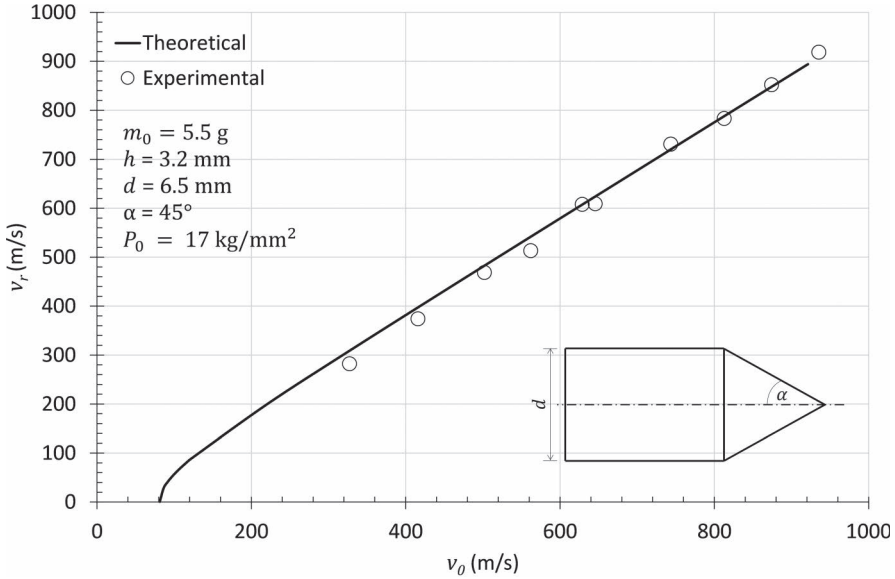
FIGURE 4.21 Comparison between theoretical and experimental values of residual velocity for a 5.5 g projectile perforating 3.2 mm of aluminium plate, $v_{bl} = 81$ m/s. (Adapted from the data presented by Nishiwaki, 1951.)

(i.e. assuming $\alpha = 90°$) against relatively strong aluminium alloys showed less satisfactory results (Schonberg and Ryan, 2021), however, in this case, a recalibration of the parameter P_0, was probably required.

2. (Recht and Ipson, 1963)

Recht and Ipson presented a model for the minimum penetration velocity ($= v_{bl}$) for a non-deforming flat-nosed cylinder perforating a thick plate. The premise of the model is that shearing occurs during penetration, leading to a plug formation that in length, is less than the plate thickness. The principles of wave mechanics were employed, and it was assumed that the average dynamic shear strength of the target remained constant. It was claimed that against mild steel plates, the model worked well however it was less successful when fragment simulators and steel armour were tested. The model is as follows:

$$v_{bl} = \frac{4\Omega h^2 \psi \tau_t}{Ld} \left\{ 1 + \left[\frac{L + \Omega h}{\Omega h} \left(1 + \frac{d}{4\rho_t h \tau_t \psi^2} \right) \right]^{1/2} \right\} \qquad (4.152)$$

where,

$$\psi = \frac{\rho_p c_p + \rho_t c_t}{\rho_p c_p \rho_t c_t} \qquad (4.153)$$

$\rho_p, \rho_t =$ densities of the projectile and target

$\Omega = \rho_t / \rho_p =$ ratio of plate to projectile density

$c_p, c_t =$ longitudinal wave velocities of in the projectile and target materials

$h =$ plate thickness

$L =$ projectile length

$d =$ projectile diameter

$\tau_t =$ a function of the dynamic shear strength of the target material (units of stress)

3. (Awerbuch, 1970)

Similar to the three-stage model presented by Awerbuch and Bodner (1974a), Awerbuch has presented a model that considers the resisting forces acting on a target plate. The final velocity of the projectile is given by:

$$v_f = \frac{-AB + \sqrt{(AB)^2 + 4C\left(EB^2 - F\right)}}{2C} \tag{4.154}$$

where

$$A = \rho_0 A_p b \tag{4.155}$$

$$B = \left[\left(v_0^2 + \frac{\sigma}{3\rho_t/2}\right)\left(\frac{m_0/\rho_t A_p}{h - b + m_0/\rho_t A_p}\right)^3 - \frac{\sigma}{3\rho_t/2}\right]^{1/2} \tag{4.156}$$

$$C = m_0 + \rho_t A_p h \tag{4.157}$$

$$E = m_0 + \rho_t A_p (h - b) \tag{4.158}$$

$$F = 2\pi d h b^2 \tau_0 \tag{4.159}$$

This equation can be converted into a ballistic limit equation simply by setting $v_f = 0$ and solving for v_0. This has been presented by Schonberg and Ryan (2021) and is:

$$v_{bl} = \left[\frac{\left(\dfrac{8d_h b^2 \tau_0}{\rho_0 d^2 (h - b + C)} + \dfrac{2R_m}{3\rho_t}\right)}{\left(\dfrac{4m_0}{\rho_t \pi d^2 (h - b + C)}\right)} - \frac{2R_m}{3\rho_t}\right]^{1/2} \tag{4.160}$$

where

$A_p =$ projectile face area

$d =$ diameter of the projectile

$m_0 =$ projectile mass (assumed constant)

d_h = hole diameter in the target plate (that can be estimated or measured, or assumed = d)

h = target plate thickness

R_m = target plate material ultimate tensile strength

τ_0 = target plate material maximum shear stress

b = plug thickness (that can be estimated or measured, or assumed = h)

ρ_t = target plate material density.

For this model to work, plug thickness, b, and hole diameter, d_h, should be empirically obtained. Nevertheless, reasonable results for metallic targets have been obtained assuming the plug thickness was equal to the target plate thickness, and the hole diameter was equal to the projectile diameter (Schonberg and Ryan, 2021).

4. (Forrestal et al., 1987)

Forrestal et al developed a simple model based on a cylindrical cavity expansion approach and energy conservation. The model only includes forces from radial cavity expansion and neglects frictional resistance and the projectile shape function. The ballistic limit is evaluated as follows:

$$v_{bl} = \left(\frac{\pi d^2 h \sigma_s}{2m_0} \right)^{1/2} \tag{4.161}$$

This is very similar in form to the rudimentary model discussed at the beginning of the chapter except that the stress (σ_s) required to open up a cylindrical cavity is based on the work of (Bishop et al., 1945) and is given by the following equation:

$$\sigma_s = \frac{Y_0}{2} \left(1 + \ln\left[\frac{6(1-v)K}{(5-4v)Y_0} \right] \right) \tag{4.162}$$

where,

m_0 = projectile mass (assumed constant)

h = target plate thickness

d = diameter of the projectile

v = Poisson's ratio

K = Bulk modulus of the target plate

Y_0 = the yield strength of the target plate.

This model is also discussed by Rosenberg and Forrestal (1988).

5. (Forrestal and Hanchak, 1999)

Forestal and Hanchak presented a model for the penetration of a plastic beam-like target by a rigid projectile. The analysis is based on an equation of lateral momentum and an equation of angular momentum during the bending of the beam. The ballistic limit velocity (limited to thin plates) is consequently given as:

$$v_{bl} = \left[\left(1 + \frac{\rho_t h b_d d}{m_0} \right)^2 \frac{2Y_0}{3\rho_t} \left(1 + \frac{3\rho_t h^2 b_d}{m_0 + \rho_t h b_d d} \right) \right]^{1/2} \tag{4.163}$$

where,

m_0 = projectile mass (assumed constant)

d = width of the projectile which is assumed to be equivalent to its diameter

h = target plate thickness

b_d = breadth of the target beam which is only assumed to be the width of the projectile = d

ρ_t = density of the target plate

Y_0 = the yield strength of the target.

This equation is slightly different from the one presented by the original authors as the term $\rho_t h b_d$ has replaced the mass per unit length for the target plate used in the original. Schonberg and Ryan (2021) found this model to work particularly well for titanium penetration data.

6. (Chen and Li, 2003)

Chen and Li presented a model for the perforation of a thick plate, of thickness h, by a rigid projectile of diameter d, and provided two separate equations for:

a. The case where a rigid projectile with a sharp nose (no plugging), and

b. The case for a rigid projectile with a flat nose (plugging expected).

For a projectile with a sharp nose the ballistic limit equation is defined as follows:

$$v_{bl} = \left[\frac{AN_1 Y_0}{BN_2 \rho_t} \left\{ \exp\left(\frac{\pi \chi}{2N} \right) - 1 \right\} \right]^{1/2} \tag{4.164}$$

where $\chi = h/d$, N, N_1 and N_2 are a function of the geometry function of the projectile. The effect of the geometry of the nose has been extensively discussed by Chen and Li (2002) and is based on a dimensionless nose parameter, $\psi = l/d$, and for a conical nose, l is the height of the nose and d is the projectile diameter. Therefore, for a conical nose (different equations are provided for ogival noses), the following applies to the ballistic limit equation and includes a dynamic frictional coefficient, f:

$$N_1 = 1 + 2f\psi, \; N_2 = N^* + \frac{2f\psi}{1 + 4\psi^2}, \; N^* = \frac{1}{1 + 4\psi^2}, \; 0 < N^* \leq 1 \tag{4.165}$$

$$N = \frac{\lambda}{BN_2} \tag{4.166}$$

$$\lambda = \frac{m_0}{\rho_t d^3} \tag{4.167}$$

Clearly, where friction is ignored ($f = 0$), then $N_1 = 1$, and $N_2 = N^*$. A and B are dimensionless material constants. $B = 1.5$ for all incompressible materials, and for an elastic-perfectly plastic material,

$$A = \frac{2}{3}\left\{1 + \ln\left[\frac{E}{3(1-v)Y_0}\right]\right\}$$

(4.168)

where, E, v and Y_0 are Young's modulus, Poisson's ratio and yield strength, respectively.

For the perforation of a thick plate by a flat-nosed projectile,

$$v_{bl} = \left[\frac{AY_0}{B\rho_t}\left\{\left[1 + \frac{8B\chi\eta}{\sqrt{3}A}\left(1+\frac{b}{h}\eta\right)\left(\frac{b}{h}\right)^2\right]\exp\left[2\eta B\left(1-\frac{b}{h}\right)\right] - 1\right\}\right]^{1/2}$$

(4.169)

Where b and h are the thickness of the plug and the thickness of the plate, respectively and,

$$\eta = \frac{\rho_t \pi d^2 h}{4m_0} = \frac{\pi\chi}{4\lambda}$$

(4.170)

A comparison between the Forrestal et al (1987) model and Chen and Li (2003) model is shown in Figure 4.22. The models were computed for a 25.4 mm plate of aluminium alloy, with varying hypothetical yield strengths. The single experimental data point and projectile parameters were taken from Rosenberg and Forrestal (1988) with $\chi = 3.58$, $\psi = 1.51$, $m_0 = 24.8$ g, $d = 7.1$ mm, $l = 10.7$ mm, $f = 0.02$. From the experimental data, the point is clear that the more complex Chen and Li (2003) model performs better than the Forrestal et al (1987) model. Nevertheless, given the simplicity of the Forrestal et al (1987) model, it does reasonably well. Having the ability to account for the nose shape of the projectile during cavity expansion makes a difference and we will look at that next.

4.3.2.2 The Effect of Projectile Shape on Penetration

How a thin plate fails during ballistic penetration is largely driven by the shape of the projectile nose, the projectile's strength, and its mass. It also depends on the target material and particularly how susceptible it is to adiabatic shear failure. Investigations of the projectile nose shape on Weldox steel have been carried out by Børvik et al. (2002) and Dey et al. (2004). It is quite clear from these works that flat-nosed projectiles resulted in the lowest ballistic limit velocity for the plate, whereas conical, ogival and hemispherical projectiles result in similar ballistic limit velocities. The reason why flat (blunt)-nosed projectiles were able to perforate the plate at a lower velocity was because of the nature of plate failure, i.e. adiabatic shearing resulting in plug formation. Whereas with the more pointy projectiles, the higher ballistic limit result was due to ductile hole enlargement. This is an energy-expensive process.
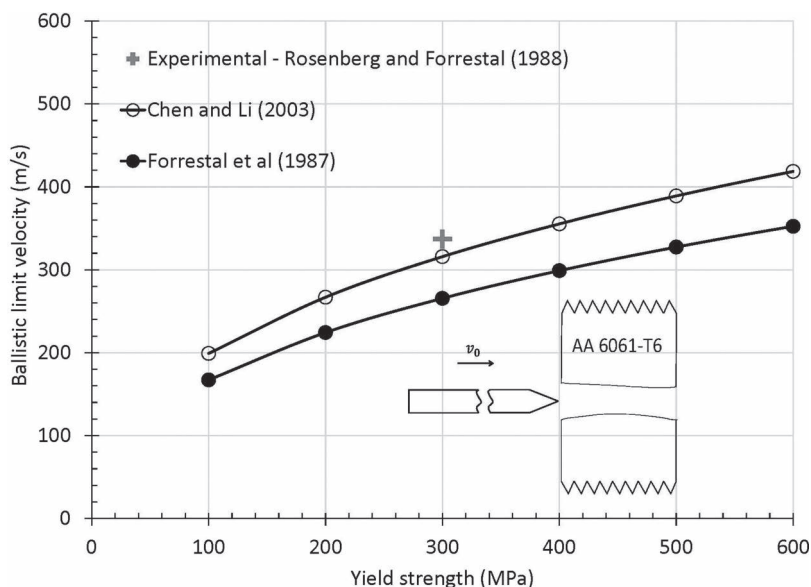
FIGURE 4.22 Comparison between the Chen and Li (2003) model with the Forrestal et al (1987) model for the predicted ballistic limit velocity based on the perforation of aluminium alloy plates with different (hypothetical) yield strengths. Projectile definition and single experimental result for an AA 6061-T6 plate (25.4 mm thick, $Y_0 = 300$ MPa) from Rosenberg and Forrestal (1988.)

An example of the various penetration processes at play for projectiles with different nose shapes is shown in Figure 4.23. Here, flat-nosed, hemispherical-nosed and conical-nosed steel projectiles ($d = 20$ mm, $m_0 = 197$ g) have been accelerated towards 12-mm thick Weldox 460 E steel plates. Each target has not been perforated but nicely shows the phenomenon at play for each projectile. For the flat-nosed projectile example (left) it is clear that deformation localizes in narrow shear bands prior to the formation of a plug. This is caused by the material in front of the projectile being accelerated to relatively high velocities compared with the surrounding material. In these localized zones, very large strains, strain rates and temperatures appear prior to plug separation. For the hemispherical projectile (centre), the penetration process results in a bulge forming at the rear of the target resulting in the emergence of large tensile strains. Eventually, the material begins to neck and thin prior to failure and eventually when a critical value of strain is reached, a small plug is ejected. The conical projectile's penetration process is different again and this occurs by the conical tip radially pressing the target material outward as it penetrates.

4.3.2.3 Penetration of Thin Plates by Blunt-Nosed Projectiles

As we have discussed, penetration of thin plates is a little more complex as we have to take into account the role of petalling or plugging—particularly with regards to energy absorption. There are a number of analytical expressions that one can use to

(a) Test B8   (b) Test H2   (c) Test C5
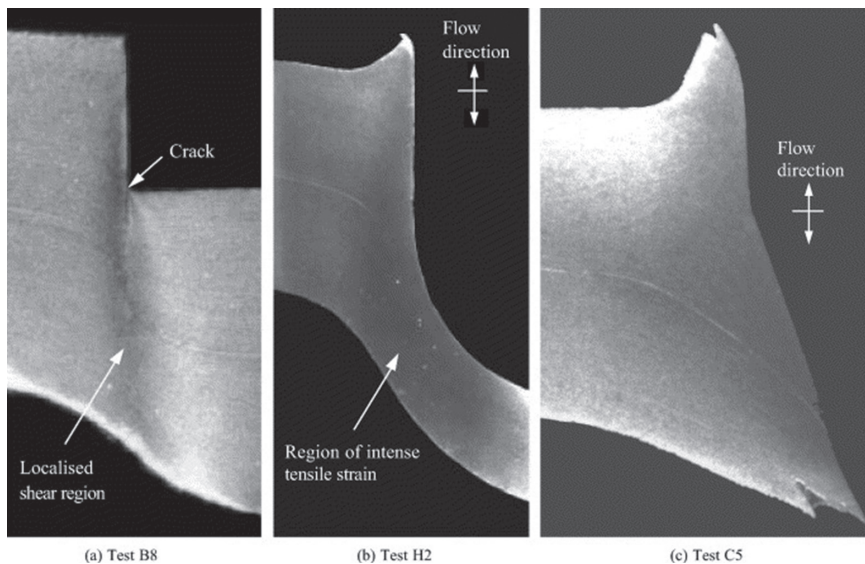
FIGURE 4.23 Macrographs of sectioned and etched target plates close to perforation (not in scale) for a flat-nosed projectile (left), a hemispherical-nosed projectile (centre) and a conical-nosed projectile (right). (Reproduced with permission from Borvik et al., 2002.)

predict the v_{bl} of thin plates, some of which have already been discussed. Equations for targets impacted by compact blunt fragments are summarized below (Recht 1971):

Modified de Marre (imperial units)

$$v_{bl} = 2.34 \times 10^4 \left(\frac{h}{m_0^{0.333}} \right)^{3/4} \tag{4.171}$$

Thor (imperial units)

$$v_{bl} = 4.05 \times 10^4 \left(\frac{h^{0.906}}{m_0^{0.359}} \right) \tag{4.172}$$

Recht–Ipson (imperial units)

$$v_{bl} = 810 \frac{h^2}{Ld} \left\{ 1 + \left[(1 + L/h)(1 + d/0.098h) \right]^{0.5} \right\} \tag{4.173}$$

where
h is the plate thickness (in).
L is the cylindrical fragment length (in).
d is the cylindrical fragment diameter (in).
m_0 is the fragment mass (gr).

It should be pointed out that the coefficients present in these equations have been derived using imperial units (inches, grains), and therefore, they need to be converted into SI units.

Figure 4.24 shows the data for the ballistic limit velocity (v_{50}) for compact blunt steel fragments impacting steel plates of varying hardness. These data are plotted here in SI units (m, s, kg), although they were originally plotted in Recht (1971) using imperial units; the unit of mass used was grains rather than pounds, as, at that time, most ballistic fragment studies used that unit. It can be seen that the modified de Marre equation for compact ballistic fragments fitted through the data is now given to us as

Modified de Marre (SI units)

$$v_{50} = 0.89 \times 10^4 \left(\frac{h}{m_0^{1/3}} \right)^{3/4} \tag{4.174}$$

There is also a lesson from Figure 4.24 on the type of steel plates that are best used to contain ballistic fragments. Mild steel plates (100–200 BHN) have low shear strengths, and therefore, they have low v_{50} values. The Hadfield manganese steel is especially tough and is a good performer in stopping the projectiles at small plate thicknesses. However, the high-hardness steel plates (400–550 BHN) do not perform so well. The reason for this is that these steels have a low coefficient of work hardening but are strong and generate high heat when deformed. This means that they are susceptible to adiabatic shear failure early on in the penetration process, and therefore, a plug shear occurs before much plate deformation occurs.
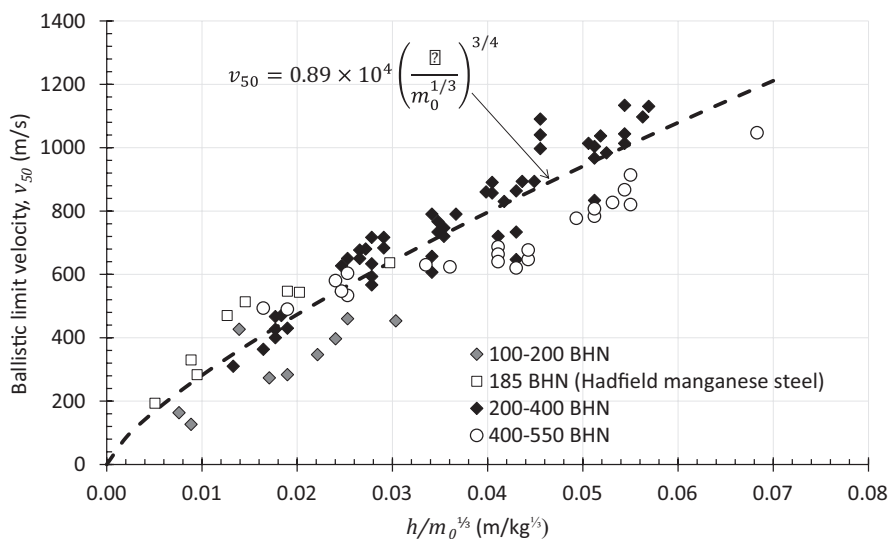

FIGURE 4.24   Ballistic limit correlations for steel plate. (Data extracted and converted from Recht, R. F. 1971, Containing ballistic fragments. *In:* Pugh, H. L. D. (ed.) *Engineering Solids under Pressure*, pp. 50–60. London: The Institution of Mechanical Engineers.)

TABLE 4.9
Parameters for Blunt-Nosed Deformable
Projectile Penetration

Parameter	Steel (300 BHN)	AA 2024-T4
C (m/s)	1297	227
K (m/s)	−164	141
J (m/s)	1544	1450
B	0.61	1.75

A good fit for the mild steel targets (from Figure 4.24) for low velocities is given below (Equation 4.175):

Modified de Marre (SI units) – mild steel

$$v_{50} = 0.89 \times 10^4 \left(\frac{h}{m_0^{1/3}} \right)^{0.84} \tag{4.175}$$

Further data are provided by Recht (1990). For blunt deformable penetrators impacting ductile plates, the following equations can represent the data well:

$$h/d \geq 0.1: v_{50} = \frac{\left[C(h/d)^b + K \right]}{(L/d)^{1/2}} \tag{4.176}$$

$$h/d < 0.1: v_{50} = \frac{J(h/d)}{(L/d)^{1/2}} \tag{4.177}$$

where
C, K, J = empirical constants (units of m/s).
b = dimensionless empirical constant.
L = length of the penetrator.

The typical values for 300-BHN steel and AA 2024-T4 are provided in Table 4.9.

4.3.2.4 Penetration of Thin Plates by Sharp-Nosed Projectiles

As one would expect, the penetration process as outlined for a blunt-nosed projectile will differ from the case where a sharp-nosed projectile penetrates the target. An example of a sharp-nosed projectile would be an armour-piercing core. Recht and Ipson (1963) developed an analytical description that appears to work well for a variety of data.

The energy balance for the case where a projectile perforates a thin plate is given by

$$\frac{1}{2} m_0 v_0^2 = \frac{1}{2} m_0 v_r^2 + W \tag{4.178}$$

where

    m_0 is the mass of the projectile.

    v_0 is the impact velocity.

    v_r is the residual velocity.

    W is the work done during perforation.

If $v_r = 0$, then $v_0 = v_{bl}$.

    And therefore,

$$W = \frac{1}{2} m_0 v_{bl}^2 \tag{4.179}$$

where v_{bl} is the ballistic limit velocity—i.e. the velocity required to just completely penetrate the target (this can be approximated to v_{50}).

    Therefore, combining the equations leads to

$$v_0^2 = v_r^2 + v_{bl}^2 \tag{4.180}$$

And therefore, normalizing and rearranging,

$$\frac{v_r}{v_{bl}} = \left(\frac{v_0^2}{v_{bl}^2} - 1 \right)^{1/2} \tag{4.181}$$

So, knowing the impact velocity and the ballistic limit velocity, it is possible to calculate the residual velocity of the projectile (after the plate has been perforated). This equation is seen to work especially well where the impact velocities exceed the ballistic limit velocities by at least 50%.

    In a more general sense, this is sometimes used for curve-fitting ballistic data such that Equation 4.181 is rearranged in terms of the residual velocity, and empirical parameters are introduced, viz.,

$$v_r = a \left(v_0^p - v_{bl}^p \right)^{1/p} \tag{4.182}$$

where a and p are the Recht–Ipson parameters and are dimensionless. Figure 4.25 shows an example of how these data are frequently presented (for a fictitious series of experiments). This methodology for presenting ballistic data has been used as early as 1951 by Nishiwaki (1951).

    Recht (1990) provides an empirical equation for the ballistic limit for the penetration of an armour-piercing projectile into a 300-BHN steel.

    For cases where $h/d \geq 0.5$, this is given by

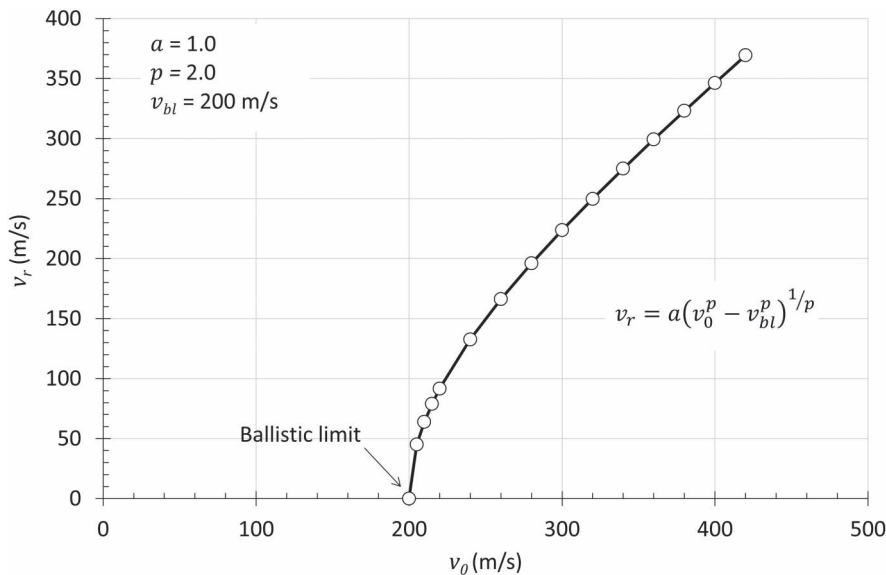$$v_{50} = C_s \left[\frac{\rho_0 (h/d)}{m_0 / d^3} \right]^{b_s} \tag{4.183}$$

FIGURE 4.25 Recht–Ipson model where the ballistic limit velocity of the projectile $=200\,\text{m/s}$; $a=1.0$ and $p=2.0$.

where
  $\rho_0=$ density (units of kg/m³).
  $m_0=$ mass of the penetrator (kg).
  $C_s=$ empirical constants (units of m/s).
  $b_s=$ dimensionless empirical constant.

For a 300-BHN steel, C_s and b_s are estimated to be 781 m/s and 0.63, respectively ($h/d\geq0.5$). Where $h/d<0.5$, different constants would apply as petalling is a dominant failure process in the target.

Example 4.4

A 7.62 mm cylindrical rod projectile has a muzzle velocity of 820 m/s and with a mass of 14 g completely penetrates a 15 mm plate of aluminium and goes on to penetrate into a semi-infinite copper plate located 20 mm behind the aluminium. If the ballistic limit velocity of the aluminium plate $=700\,\text{m/s}$ and the yield strength of the copper $=200\,\text{MPa}$, using a simplified energy balance equation (Equation 4.1), calculate the penetration depth into the copper plate. Assume the Recht–Ipson parameters a and $p=1.0$ and 2.0 respectively.

From the 'Recht–Ipson' analysis we must first calculate the residual velocity of the projectile after it exits the aluminium plate:

$$v_r = \sqrt{v_0^2 - v_{bl}^2}$$

$$v_r = \sqrt{820^2 - 700^2}$$

$$v_r = 427.1 \text{ m/s}$$

Recall that the simple energy balance equation for penetration (Equation 4.1) is given by:

$$\frac{1}{2}m_0 v_0^2 = (\sigma A_1)h \tag{4.183}$$

where h is the penetration thickness, σ is the stress required to open up a cavity in the plate (which, we will simply assume to be equal to the yield strength, Y_0 in this case), m_0 is the mass of the projectile, and v_0 is the impact velocity. And therefore, penetration into the copper plate with a projectile of velocity v_r, can be given by:

$$h = \frac{m_0 v_r^2}{2Y_0 A_1} \tag{4.184}$$

where A_1 is the cross-sectional area of the projectile and is given by

$$A_1 = \pi \frac{d^2}{4} \tag{4.185}$$

Therefore, $A_1 = 45.6\,\text{mm}^2$ ($d = 7.62\,\text{mm}$) and using v_r calculated previously, $h = 140\,\text{mm}$.

4.3.3 INTRODUCING OBLIQUITY

Introducing obliquity to an armour plate will lead to an increase in the effective path length that will be offered to the projectile. This is clearly advantageous, although the advantage offered is often marred by the prospect of using a longer plate of armour to achieve height. The T34 is widely recognized for being the first mass-produced armoured vehicle that used angle plates deliberately to improve the ballistic performance of its armour. Since then, there have been many vehicles that have adopted similar strategies. Take the BMP-1 for instance; the thickness of the steel armour on the front upper glacis plate of the hull was only 7 mm thick, but due to its steep angle to the vertical plane (80°), this thickness of steel offered 40 mm of effective thickness to a horizontal attack.

There are further advantages of inclining a plate of steel to an incoming projectile: namely, encouraging the projectile to turn. This can be an energy-expensive process. A projectile will usually exit a plate perpendicular to the plane of the plate and so therefore will be subjected to turning forces (see Figure 4.26). The harder the plate, the better. Harder materials encourage more ricochet compared to their softer counterparts. Certainly, for ceramics, it has been shown for small-arms ammunition that the ballistic limit velocity (v_{50}) increases with obliquity, although there is evidence that the increase in performance with obliquity does not match that of steels (Hetherington and Lemieux, 1994).
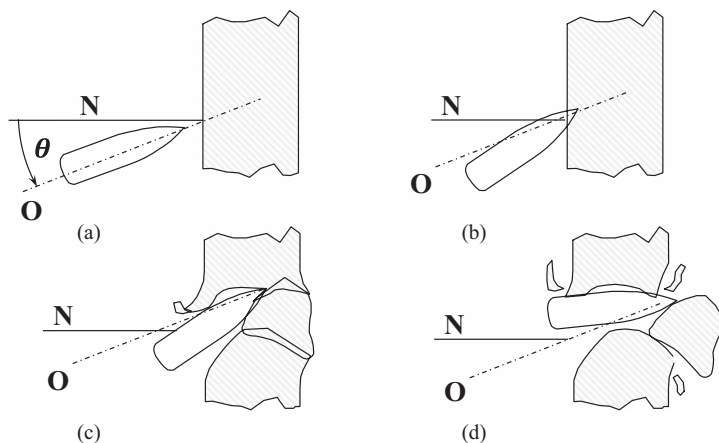
FIGURE 4.26 Bullet penetration at an oblique angle showing the sequence of events: (a) before impact, (b) the bullet embeds into the target, (c) the target fails and (d) the bullet perforates the target.

A demonstration of the advantage of obliquity in steels can be shown by plotting the energy absorbed by the plate that has been shot at increasing thickness and comparing that for a single thickness inclined at an increasing angle. The relevant equations are as follows.

The percentage of energy absorbed by the plate (assuming that the mass of the projectile is not eroded during penetration, i.e. $m_i = m_r$) is given by

$$KE_a = 1 - \left(\frac{v_r}{v_0}\right)^2 \tag{4.186}$$

where KE_a is the fraction of the KE absorbed by the plate, v_r is the measured residual velocity after the plate has been perforated and v_0 is the initial velocity of the projectile before it strikes the target. Sequentially, shooting projectiles (say, 5.56×45-mm SS109) at a mild steel plate of thicknesses 3, 6, 8 and 10 mm will result in a linear correlation between the fraction of the KE absorbed by the plate and the thickness of the plate. Taking a 6-mm plate and inclining at angles ranging from 10° to 55° will result in an increase in effective path length from 6.09 to 10.46 mm (according to the equation $h_\theta = h/\cos\theta$). This will result in a relationship as shown in Figure 4.27. For the normal incident example, the steel plate stops the projectile at a thickness of ~12 mm, whereas, for the 6-mm inclined plate, this is accomplished at an angle of 55° and a resultant effective path length of 10.46 mm. As the plate is inclined, the effective path length that is offered to the projectile is also increased and appears to outperform equal thickness of steel at normal incidence. Thus, the obliquity is working positively to take energy out of the bullet. For more of a discussion on this, see Hazell et al. (2004).

Other studies have concentrated on mapping obliquity results with velocity and inclination. A good example of this is provided by Backman and Goldsmith (1978) (Figure 4.28).
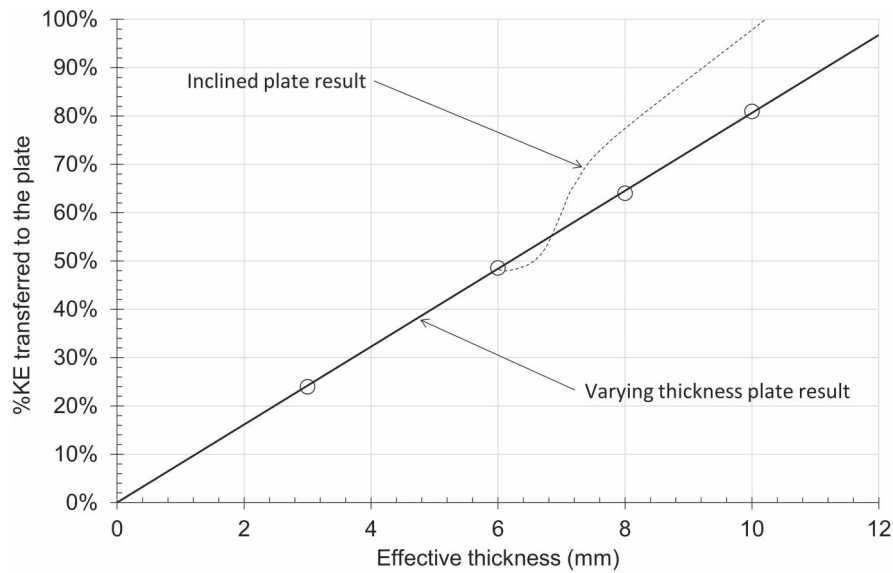
FIGURE 4.27 Calculation of the fraction of KE transferred to a mild steel plate ($Y_0 = 300\,\text{MPa}$) with increasing thickness compared to a 6-mm plate that is angled between $10°$ and $55°$.
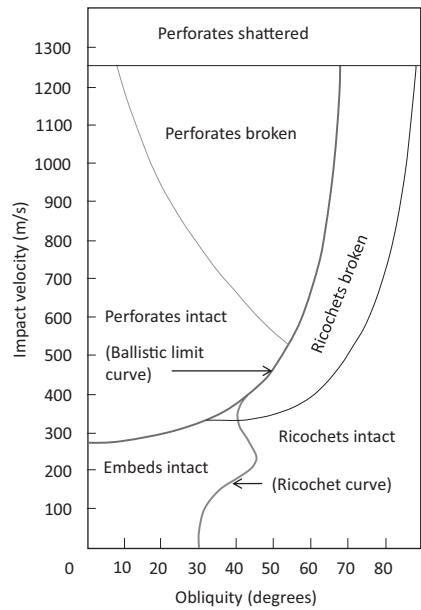
FIGURE 4.28 Phase diagram for a 6.35-mm-diameter ogival-nosed projectile impacting and penetrating a 6.35-mm-thick aluminium alloy target. (Adapted from Backman, M. E. & Goldsmith, W. The mechanics of penetration of projectiles into targets, *International Journal of Engineering Science*, 16, 1, 1–99.)

4.3.4 Perforation of Oblique Plates of Finite Thickness by Rods

Of considerable interest over the past 40 years has been the examination of the perforation of inclined target plates by rods. These studies are especially of interest where there is a requirement to defeat APFSDS penetrators. Figure 4.29 shows a typical example of a flash radiograph of a rod before, during and after the complete penetration of an oblique steel target ($\theta = 60°$). It is immediately obvious that the obliquity of the target plate invokes asymmetric forces on the penetrator such that it is forced to bend. An analysis of tungsten heavy rods perforating inclined thin plates has been provided by Hohler et al. (1978). They showed that as the rod penetrated oblique targets the nose of the projectile is initially forced to flow in one direction and then forced to flow in the opposite direction on the plate exit (Figure 4.30). When the penetrator is particularly brittle, these disruptive forces can result in fracture of the penetrator. Positioning subsequent angled plates to the line of penetration enhances protection greatly and such multi-plate armour systems are used extensively in armoured fighting vehicle designs (Hohler and Stilp, 1990).
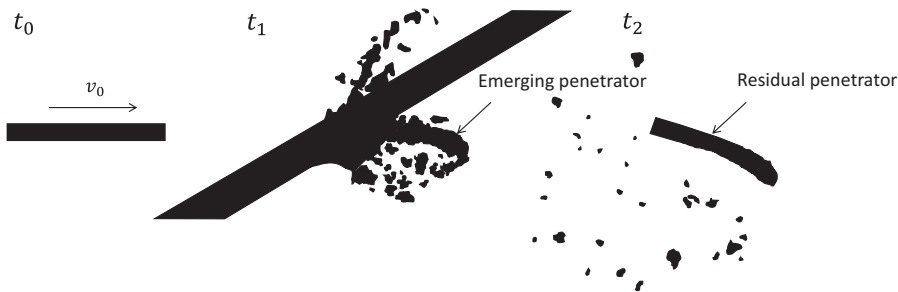

FIGURE 4.29 Perforation of an oblique ($\theta = 60°$) mild steel plate by a rod at ~1000 m/s. (Adapted from Hohler et al., 1978.)
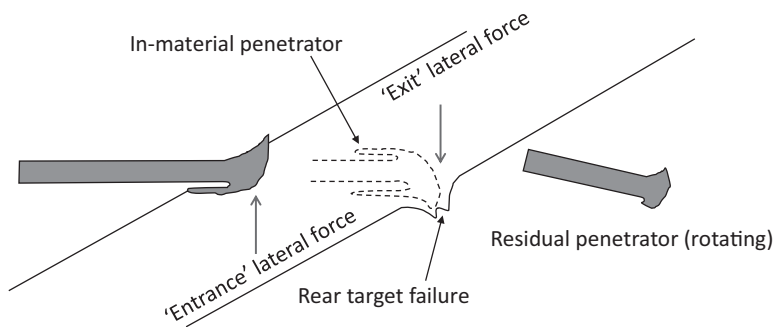

FIGURE 4.30 Perforation of an oblique target showing the lateral forces acting on the head of the perforating projectile. (Adapted from Hohler et al., 1978.)

4.3.5 MINIMUM TARGET OBLIQUITY TO INDUCE ROD RICOCHET

Clearly, the best outcome when being attacked by APFSDS projectiles is that the incoming projectile ricochets off your armour. This can be achieved by a suitably thick plate angled at a high angle of obliquity. Thick plates allow for asymmetric forces to be applied to the deformation front of the projectile and if allowed to continue for a suitable amount of time, the rod will ricochet. However thin plates that do not fulfil such a condition will not induce ricochet. Tate (1979) developed an analytical model to provide a simple estimate of the minimum target obliquity required for the ricochet of such a projectile. It is given by Tate (1979):

$$\tan^3 \theta > \frac{2}{3} \frac{\rho_p v_0^2}{Y_p} \left(\frac{L^2 + d^2}{Ld} \right) \left[1 + \left(\frac{\rho_p}{\rho_t} \right)^{1/2} \right] \tag{4.187}$$

where Y_p is the strength of the rod.

From this equation, it can be quickly seen that the angle to induce ricochet against high-speed rods is within several degrees of 80°. For example, consider a tungsten alloy penetrator ($\rho_p = 17,600 \, \text{kg/m}^3$), impacting a steel target ($\rho_t = 7850 \, \text{kg/m}^3$) at 1800 m/s. The critical angles required to induce ricochet (assuming, $Y_p = 2 \, \text{GPa}$) for a range of L/d values are given in Table 4.10

Rosenberg et al developed Tate's theory further by assuming that the ricochet is largely affected by the pressure applied to the rod by the angled plate. This results in bending and so an appropriate model needs to take this into account (Tate's model assumed a rigid penetration). It was argued that in most cases the rod bends at the impact location and therefore ricochet is achieved by successive bending of rod elements as opposed to rigid body rotation. They developed a model for the critical angle of obliquity, as follows (Rosenberg et al., 1989):

$$\tan^2 \theta > \frac{\rho_p v_0^2}{R_t} \left(\frac{v_0 + u}{v_0 - u} \right) \tag{4.188}$$

TABLE 4.10
Critical Angles to Induce Obliquity in High-Speed Rods of Various L/d Ratios

L/d	θ ricochet
5	80.942°
10	82.719°
15	83.620°
20	84.195°

The rods are travelling at 1800 m/s and $\rho_p = 17,600 \, \text{kg/m}^3$, $\rho_t = 7850 \, \text{kg/m}^3$, and, $Y_p = 2 \, \text{GPa}$.

In this case, R_t is a target strength term (in Pa) and u is the penetration velocity of the rod (see later).

4.4   PENETRATION OF RODS INTO THICK PLATES

As we have already seen, rod projectiles are extensively used on the battlefield and thus there have been various academic studies that have explored the penetration behaviour into a variety of targets including thick semi-infinite plates. These are plates where the proximity of the target free surfaces has no bearing on the penetration process.

Into soft targets, it has been shown that a rod projectile will initially behave like a rigid body penetrator. At a threshold velocity, the projectile will deform before an erosion process begins that is characterized by mass loss in the penetrator. An example of data that showed this process was presented by Forrestal and Piekutowski (2000) and their results are shown in Figure 4.31. Hemispherically nosed rods manufactured from 4340 steel and with a length 71.1 mm and diameter 7.11 mm were launched at AA 6061-T5511 targets at velocities in-between 0.5 and 3.0 km/s. Three different rod hardness values were tested (two are presented in Figure 4.31). From these results, it was clear that the velocity at which the penetration transitioned from rigid-body penetration to penetration where the rod deformed was higher with stronger rods. This was also validated numerically by Rosenberg and Dekel (2010). It appeared from these works that the following three phases of penetration occur during penetration by rods (Rosenberg and Dekel, 2012):
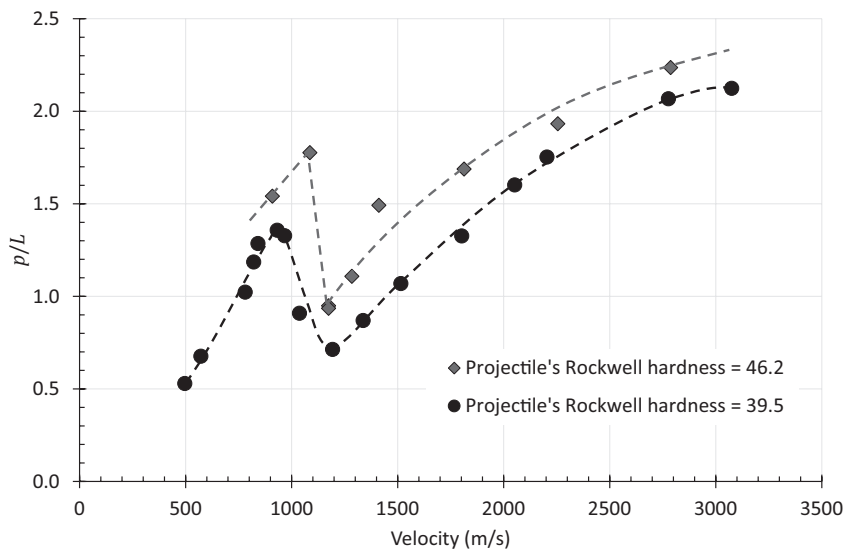

FIGURE 4.31   Ballistic penetration of two rods of differing hardness values penetrating an AA 6061-T5511 target. Plotted from the data presented by (Forrestal and Piekutowski, 2000). Penetration values normalized by the length of the projectile ($L=71.1$ mm) are presented here. Note that the penetration 'drop off' occurs at a higher velocity with the stronger rod.
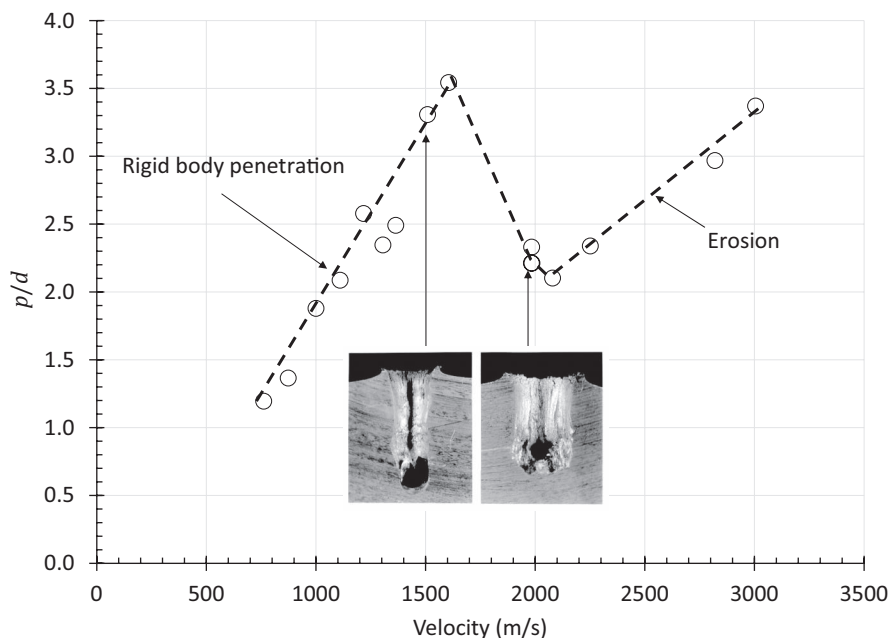
FIGURE 4.32 Penetration of a steel sphere into AA 6082-T6 targets. Penetration values normalized by the diameter of the projectile ($d = 6.35$ mm) are presented here. Data from (Hazell et al. (1998).

1. At low velocities, the rod penetrates as a rigid body up to a certain threshold velocity when,
2. the rod deforms without mass loss but leads to reduced penetration until,
3. erosion occurs in the rod as the velocity is increased and the penetration depth increases again.

Very similar penetration behaviour has also been shown with spherical projectiles. Data is presented in Hazell et al. (1998) for a 6.35-mm diameter steel spherical projectiles ($R_c = 63$) striking AA 6082-T6 targets (very similar to the alloy used by Forrestal and Piekutowski). These results showed the rigid body penetration continued to extend to around 1800 m/s before the penetration depth was reduced (see Figure 4.32). Inset there are a couple of images of the recovered targets that have been sectioned. The image on the left-hand side clearly shows rigid body penetration with some mass loss in the spherical penetrator. Whereas, the image on the right-hand side shows a wider, relatively shallow crater. This is indicative of radial plastic flow as the projectile made contact with the target and is a hint of 'hydrodynamic' effects that we will discuss next.

The data from the experiments by Hazell et al. (1998) are presented in Table 4.11.

4.5 HYDRODYNAMIC PENETRATION

Armour-piercing fin-stabilized discarding sabot (APFSDS) rounds will commonly have an impact velocity in the range of 1300–1900 m/s, and therefore, penetration

TABLE 4.11

Data from the Experiments Presented in Hazell et al. (1998) for a Steel Sphere Penetrating an AA 6082-T6 Target Showing Data for the Impact Velocity (v_0), Penetration (p), and Penetration Normalized by the Diameter (p/d)

v_0 (m/s)	p (mm)	p/d
762	7.6	1.20
874	8.7	1.37
1000	11.9	1.88
1110	13.3	2.09
1217	16.4	2.58
1305	14.9	2.35
1364	15.8	2.49
1509	21.0	3.31
1605	22.5	3.54
1983	14.1	2.21
1984	14.8	2.33
1985	14.1	2.21
2079	13.4	2.10
2252	14.9	2.34
2820	18.9	2.97
3005	21.4	3.37

is approaching what we call hydrodynamic behaviour. Hydrodynamic penetration is described as a regime when the pressure below the tip of the penetrator is sufficiently high so as to cause the materials to behave like fluids (that is, with no resistance to shear). In essence, hydrodynamic penetration is governed by shock processes that we will discuss in detail in Chapter 5. For tungsten alloy penetrators impacting steel, fully hydrodynamic penetration will not occur until an impact velocity of approximately 3000 m/s. This velocity is known as the *hydrodynamic limit*. Below this velocity, the strength of the steel target is important and provides a principal role in decelerating the rod. However, the required velocity for full hydrodynamic interaction depends on the materials and can be as high as 5000 m/s for ceramic materials, and therefore, this type of penetration regime will only be approached by a very high-velocity rod projectiles and shaped charge jets. For a soft projectile penetrating a polymer, the hydrodynamic limit may be as low as 500 m/s.

Figure 4.33 shows an example of what happens during hydrodynamic penetration. Presented here are results from a computational simulation. Here, we have a strengthless W penetrator impacting a strong steel target at 3000 m/s. The first thing to realize is that despite the target being strong (tool steel) and the penetrator having zero strength (which is artificially set within the code), the penetrator is still able to penetrate. This is because the penetrator is still able to exert huge pressures on
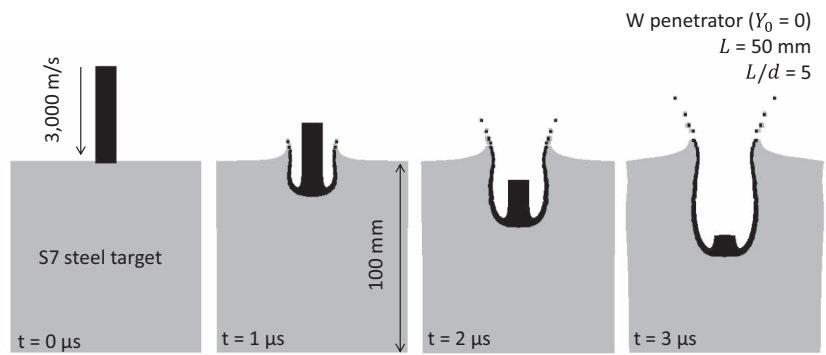
FIGURE 4.33   Hydrodynamic penetration.

the target. In fact, similar results would be seen if the penetrator was given realistic strength values—although the strength of the penetrator does play a role as will be seen later. Secondly, as the penetrator penetrates, it is continually eroded by the target. Furthermore, the crater growth rate (that is to say, the velocity at which the crater moves downward in Figure 4.33) is constant. Thirdly, we see that the penetrator material is being deposited on the inside of the crater—a phenomenon that is readily observed after shaped charge penetration.

There are four phases to hydrodynamic penetration that are summarized by the diagram in Figure 4.34 (Christman and Gehring, 1966).
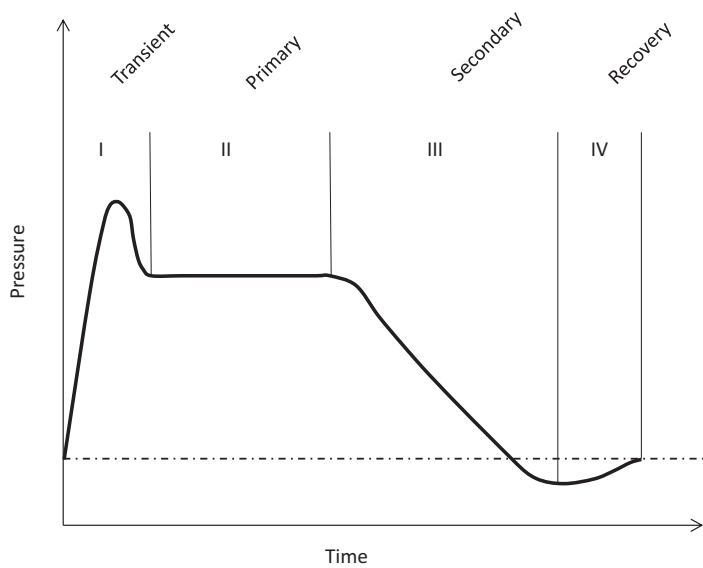

FIGURE 4.34   Four phases of penetration. (Adapted from Christman, D. R. & Gehring, J. W. Analysis of high-velocity projectile penetration mechanics, *Journal of Applied Physics*, 37(4), 1579–1587.)

During the initial penetration, high transient pressures in the penetrator and the target material occur. This lasts for only a few microseconds as the material is rapidly compressed. During this time, an impact flash is generated, and this can be partially attributed to the conversion of the thermal energy due to shock heating to visible light. At this point, a shock wave detaches from the interface between the penetrating projectile and the target, and the crater grows. The pressure spike from the primary phase of penetration then rapidly decays to a steady state (phase II) when, for a long-rod penetrator or shaped charge jet, the majority of the penetration occurs. This penetration is known as *primary penetration,* and at this stage, the rate of penetration is constant and can last for tens of microseconds. During the first two phases, the penetrator deforms and erodes and becomes increasingly shorter with increasing penetration depth. If the penetrator is completely eroded, as is the case when the impact velocity is sufficiently high, then phase III penetration occurs. This is *secondary penetration* when, under certain conditions, target material at the penetrator-target interface retains a proportion of inertia, and therefore, the crater continues to grow even after the penetrator has eroded or ceased penetration. During this time, the pressure decays in the target. Historically, this has sometimes been referred to as cavitation. The final phase (phase IV) is the elastic return of the target material and is normally very small and therefore ignored.

4.5.1 FLUID JET PENETRATION MODEL

The theory to predict the primary phase of penetration was presented by Birkhoff et al. (1948). Consider a jet of material penetrating a target block hydrodynamically. The tail of the jet is travelling into the material at velocity v (this is also equivalent to the initial impact velocity). However, the penetration velocity is somewhat lower than v, and the tip of the jet penetrates into the target at velocity u. It is convenient to change the co-ordinate system to Lagrangian such that the origin or stagnation point is at the interface between the tip of the jet and the crater (Figure 4.35).

At this point, the velocity of the material is regarded as being zero, and the pressure on the left-hand side of the stagnation point equals the pressure on the right-hand side. Note that for hydrodynamic penetration, it is assumed that the velocity of penetration into the target by the tip of the jet is constant—that is, the penetration is said to be in a steady state (no acceleration or deceleration). This is illustrated by the primary (phase II) penetration in Figure 4.34. From our new co-ordinate system, the tail of the jet is approaching the stagnation point at $v-u$, and the target material is approaching the stagnation point (from right to left) at a velocity u.

Consequently, the penetration can be described by a modified one-dimensional incompressible flow equation from the field of fluid mechanics:

$$\frac{1}{2}\rho_p (v-u)^2 = \frac{1}{2}\rho_t u^2 = \text{const.} \tag{4.189}$$

where ρ_p and ρ_t are the densities of the penetrator and the target, respectively, v is the impact velocity, which is also equal to the penetrator's tail velocity, and u is the penetration velocity (Figure 4.35).
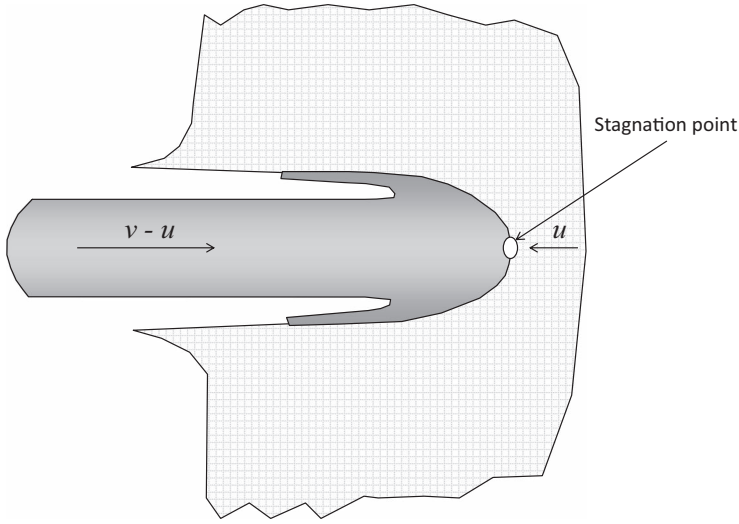
FIGURE 4.35   A jet of material penetrating a target hydrodynamically.

This equation holds true for a projectile penetrating a target hydrodynamically with a constant penetration velocity and a constant erosion rate of $v-u$. From here, we can derive an equation that describes the total depth of penetration that is achievable through hydrodynamic penetration.

The time t taken for the total rod of length l to completely erode is given by

$$t = \frac{L}{v-u} \tag{4.190}$$

Therefore, the total penetration depth, p, is given by

$$p = u \cdot t \tag{4.191}$$

and substituting gives

$$p = \frac{L \cdot u}{v-u} \tag{4.192}$$

Furthermore, we obtain

$$\frac{u}{v-u} = \sqrt{\frac{\rho_p}{\rho_t}} \tag{4.193}$$

Therefore, by substituting, we get

$$p = L \cdot \sqrt{\frac{\rho_p}{\rho_t}} \tag{4.194}$$

This equation tells us that when a jet penetrates a target hydrodynamically, the depth of penetration does not depend on the velocity of the penetrator. Instead, the depth of penetration depends on the length of the penetrator and the densities of the penetrator and the target. Therefore, it can be seen that maximum penetration can be achieved with long and dense penetrators.

We can also work out the desirable density of the material that, during fully hydrodynamic penetration, will provide the most weight-efficient means of eroding the penetrator. Multiplying both sides by ρ_t, we get

$$p \times \rho_t = L \cdot \sqrt{\rho_p \times \rho_t} \tag{4.195}$$

Therefore, for a known penetrator of length L and density ρ_p, the relationship between the areal density (A_D) of the material required to completely erode the penetrator and the bulk density of the material is

$$A_D \propto \sqrt{\rho_t} \tag{4.196}$$

Therefore, water, with its low density, offers weight-efficient protection against hydrodynamic attack. However, you will need a lot of it. The lower the density of the material, the lower the areal density required to provide protection. However, the 'thickness' of the material you require would be quite large. This is shown graphically in Figure 4.36 with annotations for water (H_2O), copper (Cu), mercury (Hg) and platinum (Pt).
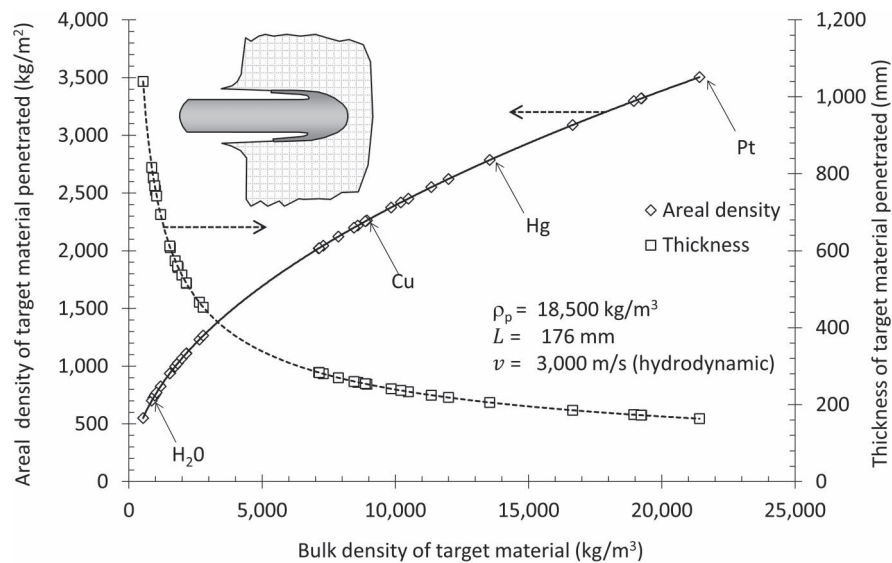

FIGURE 4.36 Effect of the bulk density of material on the resultant areal density (the curve sloping upward from left to right) and thickness of material (the curve sloping downward from left to right) penetrated by a hydrodynamic threat.

Christman and Gehring (1966) fired a steel rod into two transparent plastics (polystyrene and polymethacrylate). Using a framing camera, they observed the shock wave as it swept through the thickness of the material. Using the Hugoniot properties of the target and the projectile, they deduced the impact pressure in the transient phase of the penetration. We will discuss how to do this in Chapter 5; however, in short, this is achieved by taking the known Hugoniot properties of the projectile and the target and using an impedance matching technique to establish the particle velocity and shock pressure.

The shock wave turned the transparent plastic opaque, and therefore, it was possible to track the shock front using a high-speed framing camera. Using the conservation of momentum across a shock front and the linear shock velocity–particle velocity relationship, Christman and Gehring were able to calculate the shock pressures (P) in the target and particle velocities (u_p) behind the shock wave (see Chapter 5).

The appropriate equations are

$$U_s = c_0 + s \cdot u_p \tag{4.197}$$

$$P = \rho_0 U_s u_p \tag{4.198}$$

and therefore

$$P = p_0 \left(c_0 + s \cdot u_p \right) u_p \tag{4.199}$$

For methacrylate: $U_s = 2.68 + 1.61 \cdot u_p$, for $U_s < 6.9$ km/s
For polystyrene: $U_s = 2.48 + 1.63 \cdot u_p$, for $U_s < 6.7$ km/s

The measured shock waves in the methacrylate and polystyrene were 3.0 and 2.7 km/s, respectively, corresponding to primary-phase-penetration pressures of 0.71 and 0.38 GPa—much lower than the impact shock pressures.

Christman and Gehring also examined the penetration rate for a range of materials by taking a flash X-ray of the rod/cavity at about half the penetration depth. The results are shown in Table 4.12. They observed that the penetration rate was close to the initially calculated particle velocities (i.e. in the initial transient contact phase); however, the particle velocities exceeded the penetration velocity by between 6% and 19%. Also, assuming that the material behaved like an incompressible fluid, assuming a fluid jet penetration model provided better results for the penetration rate when compared to experimental data. The penetration rate can be calculated by rearranging Equation 4.189 to get

$$u = \frac{v}{1 + \sqrt{\dfrac{\rho_t}{\rho_p}}} \tag{4.200}$$

It can also be seen that the calculated pressures were much higher than the yield strengths of these materials, and therefore, the strengths can be ignored, and the penetration can be described as hydrodynamic.

Their data are presented in Table 4.12.

TABLE 4.12

Rod Penetration Rate Data for a C1015 Steel Rod ($L/d=10$, $m=0.6\,g$) Impacting Various Target Materials

Target Material	Density ρ_0	Impact Velocity (km/s) v	Penetration Rate (km/s) (Measured) u_e	Initial Hugoniot Conditions Pressure (GPa) P	Shock Velocity (km/s) U_s	Particle Velocity (km/s) u_p	Penetration Rate (km/s) (Calculated) u
AA 2024-T3	2770	3.84	2.2	6.20	8.76	2.53	2.40
AA 2024-T3	2770	4.95	2.9	8.85	9.73	3.25	3.10
AA1100-0	2720	3.32	2.0	5.11	8.32	2.20	2.09
AZ31B-F	1770	3.54	2.5	3.59	7.65	2.65	2.40
Methacrylate	1190	3.66	2.5	2.56	7.23	2.98	2.63
Polystyrene	1050	3.66	2.6	2.19	6.89	3.04	2.68
Water	1000	3.72	2.8	2.09	6.70	3.12	2.74
Polyethylene	940	3.63	2.8	2.06	7.25	3.04	2.70

Source: Christman, D. R., & Gehring, J. W. 1966, *Journal of Applied Physics*, 37(4), 1579–1587.

4.5.2 Improvements on the Fluid Jet Penetration Model

With that said, it has been found that materials exhibit a dynamic strength capability even when the penetration is hydrodynamic. And, of course, a 1D model is being examined here. Therefore, it is prudent to add a dynamic strength coefficient that represents the resistance of the material to plastic flow. This approach was first suggested by Mott et al., 1944 in an unpublished Ministry of Supply report. It was later published in the open literature by Pack and Evans (1951) and Eichelberger (1956). Additionally, Christman and Gehring (1966) noted that an extremely good correlation could be achieved when comparing penetration depths from rods into various semi-infinite targets over a velocity range of 2.0–6.7 km/s with the following equation

$$p = (L-d)\left(\frac{\rho_p}{\rho_p}\right)^{1/2} + 0.13\left(\frac{\rho_p}{\rho_p}\right)^{1/3}\left(\frac{E_1}{B_{max}}\right)^{1/3} \tag{4.201}$$

where E_1 is the kinetic energy of the last calibre-length portion of the rod that penetrates the target and B_{max} is the maximum hardness (a strength term), in kg/mm². L and d are the length and diameter of the rod, respectively. In this equation, B_{max} was intended to account for the strain hardening in the target and can be assessed by measuring the maximum hardness just below the crater in a sectioned target. Indeed, an increase in hardness values of up to 80% was noted as a result of high-velocity impact. See Table 4.13.

TABLE 4.13

Target Hardness Data, Showing Increase in Hardness of Several Materials as a Result of High-Velocity Impact

Material	Hardness before Impact (BHN)[a]	Maximum Hardness after Impact, B_{max} (BHN)[a]	Increase in Hardness (%)
AA 1100-0	25	45	80
AA 2024-T3	125	155	24
C1015 steel	110	165	50
AZ31B-F	57	72	26

Source: Christman, D. R. & Gehring, J. W. 1966. *Journal of Applied Physics*, 37(4), 1579–1587.
[a] Standard Brinell, 500-kg load, 10-mm ball.

Early work to improve the fluid jet penetration model was also carried out by Allen and Rogers (1961) who examined the penetration of Au, Pb, Cu, Sn, Al and Mg rods into aluminium targets using a modified Bernoulli equation:

$$\frac{1}{2}\rho_p(v-u)^2 = \frac{1}{2}\rho_t u^2 + R' \qquad (4.202)$$

Allen and Rogers regarded the quantity R' as a strain rate function involving the material strength of both the rod and the target. Assuming that the yield strength of the rod $=0$ (i.e. it acts purely like a fluid), then the strength of the target $=R'$ can be written. Solving the above equation for u, we get

$$u = \frac{\rho_p v - \left[\rho_p^2 v^2 - 2(\rho_p - \rho_t)(0.5\rho_p v^2 - R')\right]^{1/2}}{(\rho_p - \rho_t)} \qquad (4.203)$$

and, substituting this equation into Equation 4.191 and using Equation 4.190, we get

$$p = L\frac{-\rho_p v + \left[\rho_p v^2 - 2(\rho_p - \rho_t)(0.5\rho_p v^2 - R')\right]^{1/2}}{\rho_t v - \left[\rho_p v^2 - 2(\rho_p - \rho_t)(0.5\rho_p v^2 - R')\right]^{1/2}} \qquad (4.204)$$

In the special case where $\rho_p = \rho_t = \rho$, then the above equations simplify to

$$u = \frac{v}{2}\left(1 - \frac{2R'}{\rho v^2}\right) \qquad (4.205)$$

$$p = L\frac{1 - (2R'/\rho v^2)}{1 + (2R'/\rho v^2)} \qquad (4.206)$$

At very high velocities $R' = 0$ and the equations for penetration velocity and penetration revert to

$$u = \frac{v}{1 + \sqrt{\dfrac{\rho_t}{\rho_p}}} \tag{4.207}$$

$$p = L \cdot \sqrt{\frac{\rho_p}{\rho_t}} \tag{4.208}$$

The beauty of this approach is that it now gives a way of predicting penetration velocities and penetration depths in the intermediate velocities as well as at the very high velocity.

From consideration of Equation 4.205, if the penetration velocity, $u = 0$, then the strength can be defined in terms of a critical velocity to allow penetration. In essence,

$$v_c = \sqrt{\frac{2R'}{\rho_p}} \tag{4.209}$$

where v_c is a critical velocity at which the rod will start to penetrate. Below this velocity, no penetration occurs ($u = 0$). From this, Allen and Rogers used an analytical model to deduce the strength of their 7075-T6 targets as being 1.87 GPa ± 0.12 GPa. The static compressive strength of 7075-T6 is 0.496 GPa. However, it had also been observed that the dynamic yield strength of a similar alloy was ~50% higher than its quasi-static yield strength. Also, it was noted that Tabor's (1951) analysis stated that plastic yielding occurred when the mean pressure applied by a penetrating punch is approximately 2.8 Y_0; for the case of a spherical punch, plastic flow occurs at 2.6 Y_0 (Allen and Rogers 1961), where Y_0 is the quasi-static yield strength of the material. Therefore, the value of R' could be calculated from

$$R' = 0.496 \text{ GPa} \times 1.5 \times 2.6 = 1.93 \text{ GPa}$$

which is very close to the value predicted by the penetration experiments.

In fact, the best fit for R' gives a value of 2.22 GPa. This was based on the average value from the penetration experiments carried out on the rod metals that Allen and Rogers tested. The results are shown in Figure 4.37.

Allen and Rogers also observed that the gold rods appeared to penetrate deeper into the aluminium targets than expected. They deduced that this was down to a process that they called 'secondary' or 'residual penetration' and is caused by the high relative density between the gold rods and the aluminium targets. They also noted that this effect was proportional to the jet length. This can be explained as follows: When the rod material is penetrating the aluminium, the rod material that has not been eroded has a velocity = $v - u$ (relative to the position of the crater, moving at velocity u). When the material is eroded at the crater, the material is reflected rearward with a velocity of $2u - v$. So, as the rod length is completely consumed, the
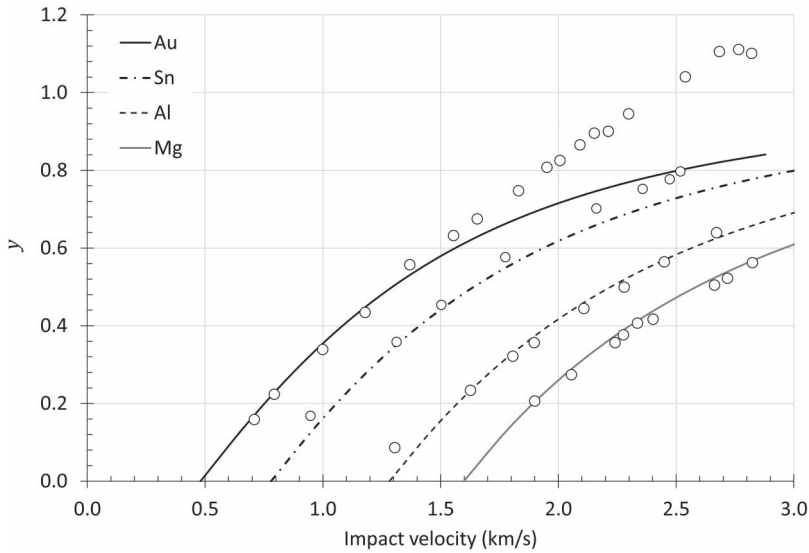
FIGURE 4.37 Comparison of theory and experiment. (Adapted from Allen W. A. & Rogers, J. W. Penetration of a rod into a semi-infinite target, *Journal of the Franklin Institute*, 272(4), 275–284.)

eroded mass retains a velocity $= 2u - v$. If $2u > v$ (which is determined by the densities of the projectile and the target), then deeper penetration can be expected.

Allen and Rogers' model is a good approximation where it is assumed that the strength of the rod is zero. Of course, for most tank gun applications, this is not the case.

This has led to the introduction of two terms by Alekseevskii (1966) and Tate (1967). The resulting equation indicating the pressure equality at the stagnation point is given by

$$\frac{1}{2}\rho_p(v-u)^2 + Y_p = \frac{1}{2}\rho_t u^2 + R_t \tag{4.210}$$

where Y_p is the projectile's dynamic strength, and R_t is the target's strength. The term R_t is not the shear or yield strength of the material but can be described as a measure of the overall resistance to penetration of the target. This takes into account the strength of the material and the dimensional effects due to approximating a two-dimensional penetration phenomenon (assuming axial symmetry) with a strictly one-dimensional equation. A material with a large R_t term will perform well as an armour system when it is subjected to attack by an APFSDS projectile.

As outlined by Tate (1967), from Equation 4.210, the following equations can be derived that describe the penetration velocity:

$$u = \frac{1}{1-\mu^2}\left[v - \mu\sqrt{v^2 + A}\right] \tag{4.211}$$

where

$$\mu = \sqrt{\frac{\rho_t}{\rho_p}} \quad \text{and} \quad A = 2\frac{\left(R_t - Y_p\right)\left(1 - \mu^2\right)}{\rho_t} \tag{4.212}$$

Tate observed that some experiments had shown that the rod came to rest before it was all used up, and therefore, some deceleration had occurred, and therefore, the rear of the rod is slowing down.

Tate considered that the dynamic yield strength as measured from plate impact experiments was a good indicator for the value of Y_p and R_t. This property can be calculated from the Hugoniot Elastic Limit (HEL) of the material measured under uniaxial strain shock-loading conditions and is given by

$$Y_d = \left[\frac{(1 - 2v)}{(1 - v)}\right]\sigma_{\text{HEL}} \tag{4.213}$$

where Y_d is the dynamic yield strength (under uniaxial stress conditions), v is Poisson's ratio and σ_{HEL} is the HEL. The HEL is discussed in detail in Chapter 5.

Now, Alekseevskii and Tate took into account the deceleration of the residual rod as the elastic waves travelled up the length of the rod and reflected from its free surface. The force per unit area retarding the rod is approximately Y_p. Therefore, knowing the momentary velocity of the back of the rod $= v_b$ (i.e. it is not constant), we have

$$Y_p = -\rho_p l \frac{dv_b}{dt} \tag{4.214}$$

where l is the length of the rod at any point in time. Now, noting that any decrease in length in time is given to us by

$$\frac{dl}{dt} = -\left(v_b - u\right) \tag{4.215}$$

Equation 4.214 gives us the time integral, i.e. rearranging, we have

$$dt = \frac{-l\rho_p dv_b}{Y_p} \tag{4.216}$$

and substituting into Equation 4.215, we have

$$\frac{dl}{l} = \frac{\rho_p\left(v_b - u\right)dv_b}{Y_p} \tag{4.217}$$

By substituting Equation 4.211 into Equation 4.217 and integrating both sides, we arrive at an equation that describes the momentary rod length and the momentary rod velocity.

$$\frac{l}{L} = \left\{ \frac{v_b + \sqrt{v_b^2 + A}}{v + \sqrt{v^2 + A}} \right\}^{\left(\frac{R_t - Y_p}{\mu Y_p} \right)} \exp \left[\frac{\mu \rho_p}{2\left(1 - \mu^2\right) Y_p} \left(\left[v_b \sqrt{v_b^2 + A} - \mu v_b^2 \right] - \left[v \sqrt{v^2 + A} - \mu v^2 \right] \right) \right]$$

(4.218)

remember that v is the initial velocity and v_b is the momentary velocity of the rear of the rod.

As before, the penetration depth is given by integrating with time the penetration rate; therefore,

$$p = \int_0^t u \cdot dt.$$

(4.219)

And, until the rod penetrates as a rigid body, Equation 4.219 can be rewritten as

$$p = \frac{\rho_p}{Y_p} \int_0^v ul \cdot dv_b$$

(4.220)

For the special case where $R_t = Y_p$, it is found that the equation for u (Equation 4.211) and l (Equation 4.218) is somewhat simplified, and the resultant penetration equation is given as

$$\frac{p}{L} = \left(\frac{1}{\mu} \right) \left[1 - \exp \left\{ -B \left(v^2 - v_b^2 \right) \right\} \right]$$

(4.221)

where

$$B = \frac{\mu \rho_p}{2\left(1 + \mu\right) Y_p}$$

(4.222)

Setting $v = 0$ in Equation 4.221 gives the penetration depth in terms of L, μ, B and v. In general, Equation 4.220 needs to be integrated numerically; however, for a very specific case where $\rho_p = \rho_t = \rho$ and the ratios of the target/projectile strengths are $R_t/Y_p = 1, 3, 5$ and so on, the penetration equations can be easily written.

Establishing two velocity parameters,

$$\overline{V}^2 = \frac{\rho v^2}{4 Y_p} \text{ and } \xi = \frac{v_b}{v}$$

(4.223)

the penetration equations are given for the special case $\rho_p = \rho_t = \rho$ as follows:

$$R_t/Y_p = 1 \quad \frac{p}{L} = 1 - \exp \left[\left(\xi^2 - 1 \right) \overline{V}^2 \right]$$

(4.224)

$$R_t/Y_p = 3 \quad \frac{p}{L} = \left(1 - \frac{2}{\overline{V}^2} \right) - \left(\xi^2 - \frac{2}{\overline{V}^2} \right) \exp \left[\left(\xi^2 - 1 \right) \overline{V}^2 \right]$$

(4.225)

$$R_t/Y_p = 5 \quad \frac{p}{L} = \left(1 - \frac{4}{\bar{V}^2} + \frac{4}{\bar{V}^2}\right) - \left(\zeta^4 - \frac{4\zeta^2}{\bar{V}^2} + \frac{4}{\bar{V}^2}\right)\exp\left[\left(\zeta^2 - 1\right)\bar{V}^2\right] \qquad (4.226)$$

To calculate the final depth of penetration, we simply set $\zeta = 0$ in the above equations. In his original paper, Tate presented the predictions in terms of $\bar{V}$; the same data are presented in the following in terms of the impact velocity (m/s) (see Figure 4.38). The strength of the steel penetrator (Y_p) was assumed to be 1.1 GPa, and the predictions and experimental data are for a steel penetrator penetrating a steel target (i.e. $\rho_p = \rho_t = 7800\,\text{kg/m}^3$).

The way that the tail of the rod decelerates can also be plotted according to theory. This is shown below for two cases: $v = 1500\,\text{m/s}$ and $v = 3000\,\text{m/s}$ ($\bar{V} = 2$ and 4, respectively) using Equation 4.108 ($R_t/Y_p = 3$). Two important points can be seen from these data (see Figure 4.39):

1. The constant velocity of penetration is a reasonable assumption during most of the penetration process.
2. Increasing the velocity of impact results in less deceleration of the rod material over a given displacement in the primary phase of penetration.

To evaluate the R_t term, the erosion rate of the rod needs to be assessed (assuming a constant penetration rate), and therefore, it is possible to calculate the strength difference ($R_t - Y_p$) knowing that
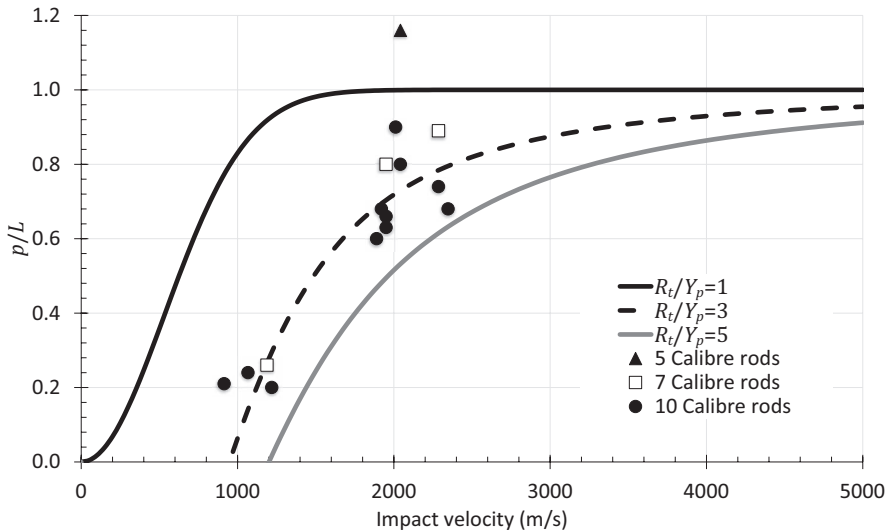

FIGURE 4.38 Theoretical predictions for the cases where $\rho_p = \rho_t$ and $R_t/Y_p = 1$, 3 and 5 with experimental data points. (Adapted from Tate, A. A theory for the deceleration of long rods after impact, *Journal of the Mechanics and Physics of Solids*, 15(6), 387–399.)
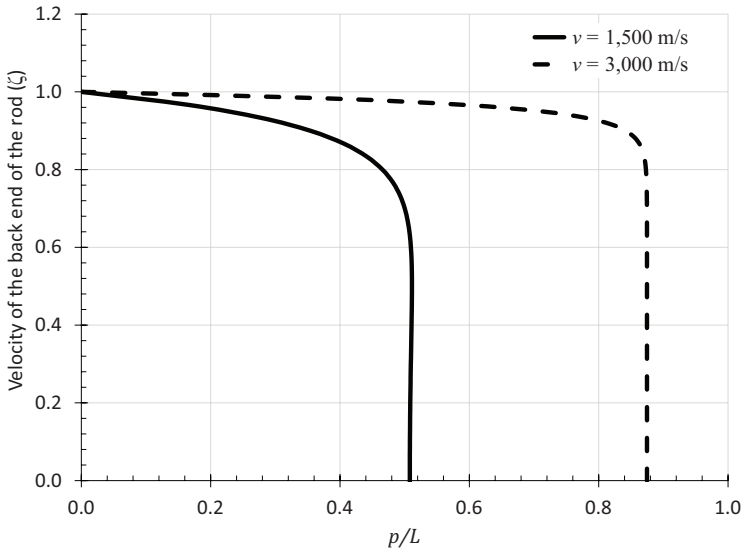
FIGURE 4.39   Theoretical prediction of the deceleration of the rear portion of the rod assuming that $\rho_p = \rho_t$ and $R_t/Y_p = 3$; the data for impact velocities of 1500 and 3000 m/s are presented.

$$R_t - Y_p = \frac{1}{2}\rho_p v_e^2 - \frac{1}{2}\rho_t u^2 \qquad (4.227)$$

where v_e is the measured erosion rate of the rod during penetration (normally taken from flash X-rays). If an estimate of Y_p can be made, then it is a relatively trivial task to calculate R_t.

Kozhushko et al. (1991) fired copper rods at ceramic targets at velocities between 5 and 8 km/s. Assuming that $Y_p \ll R_t$, they were able to estimate the value of R_t for the ceramic materials. Again, they showed that their calculated R_t correlated with the dynamic yield strength of the material.

Orphal and Franzen (1997) and Orphal et al. (1996, 1997) specify broad ranges of R_t values that are somewhat less than the values quoted by Kozhushko et al. Orphal et al. used a tungsten rod and assumed that $Y_p = 2.0\,GPa$. The large discrepancy in the results from the two researchers may suggest that the magnitude of R_t is sensitive to loading conditions and velocity of impact. Certainly, with alumina, it has been suggested that R_t may in fact vary with impact velocity (Subramanian and Bless, 1995). It has also been shown that R_t varies with target confinement (Anderson, Jr. and Royal-Timmons, 1997).

Example 4.5

A material comprising three layers of material is subjected to attack by a shaped charge jet with a tip velocity of 8 km/s. Assuming that the front 100-mm portion of the jet is travelling at a constant velocity (i.e. there is no velocity gradient in this portion of the rod), calculate the penetration velocities into the structure given that the layers are AA 1100-0, water and methacrylate.

Using Equation 4.200 will give us the penetration velocities:

$$\text{So, for the AA } 1100 - 0 \; u = \frac{8000}{1 + \sqrt{\dfrac{2720}{8930}}} = 5155 \text{ m/s}$$

$$\text{For water, } u = \frac{8000}{1 + \sqrt{\dfrac{1000}{8930}}} = 5994 \text{ m/s}$$

$$\text{For methacrylate, } u = \frac{8000}{1 + \sqrt{\dfrac{1190}{8930}}} = 5861 \text{ m/s}$$

There are two things to note: Firstly, the velocity that is used in each case is 8000 m/s. This is because the value 'v' is the velocity of the rod material, from the tail to the crater (ignoring wave effects). Secondly, it is seen that the penetration rate changes as the material changes. This is to be expected as the penetration rate is governed by the densities of the materials.

Example 4.6

A solid, strengthless copper penetrator of length 200 mm impacts a target that comprises 20-mm W, 10-mm polycarbonate (PC) and 10-mm Cu. The projectile is travelling at 5 km/s. Assuming that one-dimensional penetration and all materials are strengthless, calculate the velocity of the penetrator in each layer assuming that each plate behaves like a semi-infinite plate. What is the length of the rod that exits the target?
The densities of materials are as follows:

W: 19,250 kg/m³
PC: 1210 kg/m³
Cu: 8960 kg/m³

From Equation 4.200, we have

$$u = \frac{v}{1 + \sqrt{\dfrac{\rho_t}{\rho_p}}} \tag{4.228}$$

Therefore, the velocities of penetration are

W: $u = 2028$ m/s
PC: $u = 3656$ m/s
Cu: $u = 2500$ m/s

To calculate the length of the rod that exits the target, we need to calculate how much of the rod is consumed during the penetration of each plate. This can be done very simply by knowing that

$$dL = h \sqrt{\frac{\rho_t}{\rho_p}} \qquad (4.229)$$

where dL is the length of rod consumed in each thickness (h) of plate. Therefore, the lengths consumed are

W: $dL = 29.3$ mm
PC: $dL = 3.7$ mm
Cu: $dL = 10.0$ mm

Therefore, the length of the remainder of the rod after it perforates the target can be calculated by subtracting these lengths from the original length of the rod, viz.,

$$200.0 - 29.3 - 3.7 - 10.0 = 157 \text{ mm}$$

4.5.3   SEGMENTED PENETRATORS

It has been well known for some time that at high velocity, shorter penetrators are more efficient at penetrating deeper than their longer counterparts. Early indications of this were seen in 1956 when Eichelberger (1956) observed that 40% of the total penetration in a lead target by a shaped charge jet was due to the relatively slow-moving particles at the jet's tail. A good (and more recent) illustration of the effect is shown by the work of Hohler and Stilp (1987). They showed that the penetration normalized by the length of the penetrator was much higher when the length was equal to the diameter ($L/d = 1$) than when it was 9 or 10 times the diameter ($L/d = 9$ or 10). Notably, the increased performance of the short penetrator occurred at modest velocities (~1000 m/s) (see Figure 4.40).

Also shown in Figure 4.40 is the theoretical prediction of penetration based on the hydrodynamic theory that was discussed in Section 4.5.1 ($p/L = 1.5$). It can be seen that the long rods more or less obey the theory and plateau at a p/L value of 1.5, whereas the shorter rods do not. This behaviour was first described by Pack in 1951 as secondary penetration (Pack and Evans, 1951). That is to say that after the pressure has been released from the bottom of the penetration cavity due to penetrator erosion, the material continues to flow until the motion has been damped out by the material's resistance to flow. This phenomenon is independent of penetrator length and is different from the secondary penetration observed by Allen and Rogers and discussed in Section 4.5.2.

All this suggests that if a continuous rod is broken up into discrete well-aligned segments separated by some distance, then penetrator performance can be enhanced. The trick is to ensure that the first segment is completely consumed before penetration from the second segment ensues. Engineering this is problematic, which has led to a range of solutions including the concept of segmented-telescopic (seg-tel) penetrators (Tate, 1990; Brissenden, 1992; Anderson Jr. et al., 1997; see Figure 4.41).
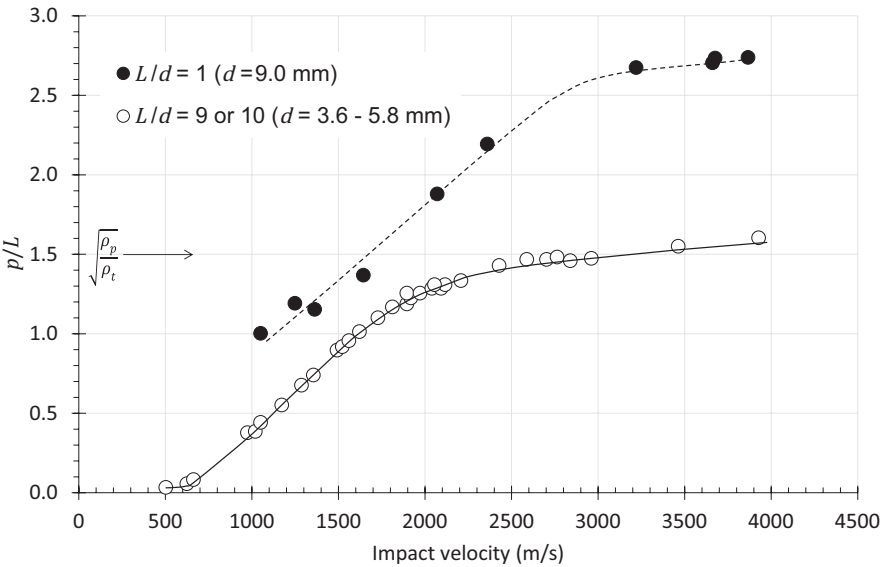
FIGURE 4.40 Penetration into a steel target (BHN = 360) by a tungsten alloy rod ($p = 17.6$ g/cc, BHN = 420); results are shown where the penetrator has an L/d value of 1 and 9 or 10. (Adapted from Hohler, V. & Stilp, A. J., *International Journal of Impact Engineering*, 5(1–4), 323–331, 1987.)
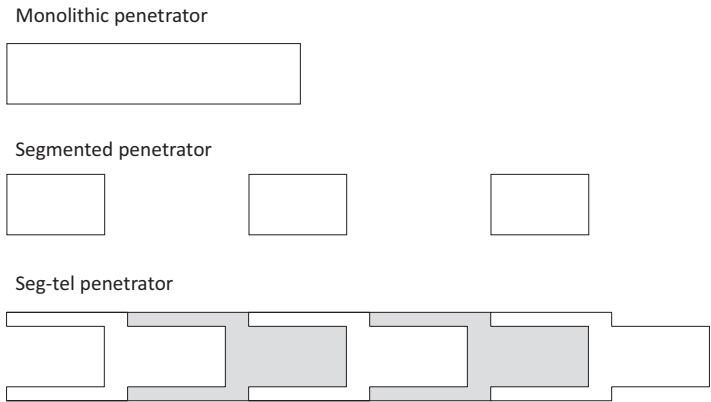

FIGURE 4.41 Monolithic, segmented and seg-tel penetrators. The seg-tel penetrator here shows the presence of low-density spacers.

4.6 SUMMARY

In this chapter, some very simple approaches to understand the penetration mechanisms of a projectile into a target have been covered. It is worth noting that students can do some sensible work using some well-thought-out analytical models that are available in the literature; some of the more pertinent ones have been summarized here. Our understanding of penetration phenomena continues to advance and this has

been due to advances in property measurements including measuring strain visually using digital image correlation, improvements in high-speed camera technologies and fidelity improvements in data acquisition systems. Code developments also continue to improve. In recent years, we have seen that computational codes have become extremely adept at predicting penetration into targets. Of course, it is also notable that computer technology continues to move forward in leaps and bounds, and with them the complexity of problems that can be simulated. We will pick up this theme again in Chapter 6.

NOTE

1 Note: previously the axis of penetration has been described as in the x-direction, however the notation from the original authors has been kept where it is prudent to do so.

REFERENCES

Alekseevskii, V. P. 1966. Penetration of a rod into a target at high velocity. *Combustion, Explosion and Shock Waves*, 2(2), 63–66.

Allen, W. A., Mayfield, E. B. & Morrison, H. L. 1957. Dynamics of a projectile penetrating sand. *Journal of Applied Physics*, 28, 370–376.

Allen, W. A. & Rogers, J. W. 1961. Penetration of a rod into a semi-infinite target. *Journal of the Franklin Institute*, 272(4), 275–284.

Anderson Jr., C. E. 2017. Analytical models for penetration mechanics: A review. *International Journal of Impact Engineering*, 108, 3–26.

Anderson Jr., C. E. & Royal-Timmons, S. A. 1997. Ballistic performance of confined 99.5%-Al$_2$O$_3$ ceramic tiles. *International Journal of Impact Engineering*, 19(8), 703–713.

Anderson Jr., C. E., Subramanian, R., Walker, J. D., Normandia, M. J. & Sharron, T. R. 1997. Penetration mechanics of seg-tel penetrators. *International Journal of Impact Engineering*, 20(1–5), 13–26.

Awerbuch, J. 1970. *A Mechanics Approach to Projectile Penetration*. Haifa, Israel: Israel Institute of Technology.

Awerbuch, J. & Bodner, S. R. 1974a. Analysis of the mechanics of perforation of projectiles in metallic plates. *International Journal of Solids and Structures*, 10, 671–684.

Awerbuch, J. & Bodner, S. R. 1974b. Experimental investigation of normal perforation of projectiles in metallic plates. *International Journal of Solids and Structures*, 10, 685–699.

Backman, M. E. & Goldsmith, W. 1978. The mechanics of penetration of projectiles into targets. *International Journal of Engineering Science*, 16(1), 1–99.

Backofen Jr., J. E. 1980. Armor/armor penetration: Land, sea, air and space. *In: Proceedings of the 5th International Symposium on Ballistics*. Toulouse, France.

Ben-Dor, G., Dubinsky, A. & Elperin, T. 2005. Ballistic impact: Recent advances in analytical modeling of plate penetration dynamics–a review. *Applied Mechanics Reviews*, 58, 355–371.

Ben-Dor, G., Elperin, T. & Dubinsky, A. 2013. *High-Speed Penetration Dynamics: Engineering Models and Methods*. Singapore: World Scientific Publishing Company.

Birkhoff, G., MacDougall, D. P., Pugh, E. M. & Taylor, G. 1948. Explosives with lined cavities. *Journal of Applied Physics*, 19(6), 563–582.

Bishop, R. F., Hill, R. & Mott, N. F. 1945. The theory of indentation and hardness tests. *Proceedings of the Physical Society*, 57, 147–159.

Bless, S., Peden, B., Guzman, I., Omidvar, M. & Iskander, M. 2014. *Poncelet Coefficients of Granular Media*, pp. 373–380. Cham: Springer International Publishing.

Børvik, T., Langseth, M., Hopperstad, O. S. & Malo, K. A. 2002. Perforation of 12mm thick steel plates by 20mm diameter projectiles with flat, hemispherical and conical noses - Part I: Experimental study. *International Journal of Impact Engineering*, 27(1), 19–35.

Brissenden, C. 1992. Performance of novel KE penetrator designs over the velocity range 1600 to 2000m/s. *In: Proceedings of the 13th International Symposium on Ballistics*. Stockholm: National Defence Research Establishment.

Carlucci, D. E. & Jacobson, S. S. 2014. *Ballistics: Theory and Design of Guns and Ammunition*. 2nd ed. Boca Raton, FL: CRC Press.

Chen, X. W. & Li, Q. M. 2002. Deep penetration of a non-deformable projectile with different geometrical characteristics. *International Journal of Impact Engineering*, 27, 619–637.

Chen, X. W. & Li, Q. M. 2003. Perforation of a thick plate by rigid projectiles. *International Journal of Impact Engineering*, 28, 743–759.

Christman, D. R. & Gehring, J. W. 1966. Analysis of high-velocity projectile penetration mechanics. *Journal of Applied Physics*, 37(4), 1579–1587.

Corbett, G. G., Reid, S. R. & Johnson, W. 1996. Impact loading of plates and shells by free-flying projectiles: A review. *International Journal of Impact Engineering*, 18(2), 141–230.

Cutshaw, C. Q. & Ness, L. (eds.) 2003. *Jane's Ammunition Handbook 2003–2004*. Coulsdon, Surrey, UK: Jane's Information Group Ltd.

Dey, S., Børvik, T., Hopperstad, O. S., Leinum, J. R. & Langseth, M. 2004. The effect of target strength on the perforation of steel plates using three different projectile nose shapes. *International Journal of Impact Engineering*, 30(8–9), 1005–1038.

Edwards, M. R. & Mathewson, A. 1997. The ballistic properties of tool steel as a potential improvised armour plate. *International Journal of Impact Engineering*, 19(4), 297–309.

Eichelberger, R. J. 1956. Experimental test of the theory of penetration by metallic jets. *Journal of Applied Physics*, 27(1), 63–68.

Forrestal, M. J. & Hanchak, S. J. 1999. Perforation experiments on HY-100 steel plates with 4340 Rc 38 and maraging T-250 steel rod projectiles. *International Journal of Impact Engineering*, 22, 923–933.

Forrestal, M. J., Luk, V. K., Rosenberg, Z. & Brar, N. S. 1992. Penetration of 7075-T651 aluminum targets with ogival-nose rods. *International Journal of Solids and Structures*, 29(14–15), 1729–1736.

Forrestal, M. J., Okajima, K. & Luk, V. K. 1988. Penetration of 6061-T651 aluminum targets with rigid long rods. *Journal of Applied Mechanics, Transactions ASME*, 55(4), 755–760.

Forrestal, M. J. & Piekutowski, A. J. 2000. Penetration experiments with 6061-T6511 aluminum targets and spherical-nose steel projectiles at striking velocities between 0.5 and 3.0 km/s. *International Journal of Impact Engineering*, 24, 57–67.

Forrestal, M. J. & Romero, L. A. 2007. Comment on 'Perforation of aluminum plates with ogive-nose steel rods at normal and oblique impacts' (*Int J Impact Eng* 1996; 18:877–887). *International Journal of Impact Engineering*, 12(34), 1962–1964.

Forrestal, M. J., Rosenberg, Z., Luk, V. K. & Bless, S. J. 1987. Perforation of aluminum plates with conical-nosed rods. *Journal of Applied Mechanics*, 54, 230–232.

Forrestal, M. J. & Warren, T. L. 2008. Penetration equations for ogive-nose rods into aluminum targets. *International Journal of Impact Engineering*, 35(8), 727–730.

Hazell, P., Iremonger, M., Barton, P. & Broos, J. 2004. Anomalous target failure at small angles of obliquity. *In:* Burman, N., Anderson, J. & Katselis, G. (eds.) *Proceedings of the 21st International Symposium on Ballistics*. Adelaide.

Hazell, P. J. 2010. Measuring the strength of brittle materials by depth-of-penetration testing. *Advances in Applied Ceramics*, 109(8), 504–510.

Hazell, P. J., Fellows, N. A. & Hetherington, J. G. 1998. A note on the behind armour effects from perforated alumina/aluminium targets. *International Journal of Impact Engineering*, 21, 589–595.

Herrmann, W. & Jones, A. H. 1961. *Survey of Hypervelocity Impact Information*. Massachusetts: Massachusetts Institute of Technology.

Hetherington, J. G. & Lemieux, P. F. 1994. The effect of obliquity on the ballistic performance of two component composite armours. *International Journal of Impact Engineering*, 15(2), 131–137.

Hohler, V., Shneider, E., Stilp, A. J. & Tham, R. 1978. Length and velocity reduction of high density rods perforating mild steel and armor steel plates. *In:* Dowd, R. S. (ed.) *Proceedings of the 4th International Symposium on Ballistics*, Monterey, CA: Naval Postgraduate School, American Defense Preparedness Association.

Hohler, V. & Stilp, A. J. 1987. Hypervelocity impact of rod projectiles with L/D from 1 to 32. *International Journal of Impact Engineering*, 5(1–4), 323–331.

Hohler, V. & Stilp, A. J. 1990. Long rod penetration mechanics. *In:* Zukas, J. A. (ed.) *High Velocity Impact Dynamics*. Chichester: John Wiley & Sons, Inc.

Jacobson, S. S. 1975. Penetration of a transparent medium by rigid blunt-and conical-nosed bodies of revolution.

Kozhushko, A. A., Rykova, I. I. & Sinani, A. B. 1991. Resistance of ceramics to penetration at impact velocities above 5 km/s. *Journal de Physique IV France*, 1(C3), C3-117–C3-122.

Krafft, J. M. 1955. Surface friction in ballistic penetration. *Journal of Applied Physics*, 26, 1248–1253.

Luk, V. K., Forrestal, M. J. & Amos, D. E. 1991. Dynamic spherical cavity expansion of strain-hardening materials. *Journal of Applied Mechanics, Transactions ASME*, 58(1), 1–6.

Mott, N. F., Hill, R. & Pack, D. C. 1944. Armament Research Establishment of the Ministry of Supply Report, 2 January.

Moynihan, T. J., Chou, S.-C. & Mihalcin, A. L. 2000. *Application of the Depth-of-Penetration Test Methodology to Characterize Ceramics for Personnel Protection*. Aberdeen Proving Ground, MD: Army Research Laboratory.

Nishiwaki, J. 1951. Resistance to the penetration of a bullet through an aluminium plate. *Journal of the Physical Society of Japan*, 6, 374–378.

Nixdorff, K. 1983. Some remarks on the penetration theory of J. Awerbuch and S.R. Bodner. *Transactions of the Canadian Society for Mechanical Engineering*, 7, 148–153.

Nixdorff, K. 1984. Some applications of the impact theory of J. Awerbuch and S.R. Bodner. *Transactions of the Canadian Society for Mechanical Engineering*, 8, 16–20.

Orphal, D. L. & Franzen, R. R. 1997. Penetration of confined silicon carbide targets by tungsten long rods at impact velocities from 1.5 to 4.6 km/s. *International Journal of Impact Engineering*, 19(1), 1–13.

Orphal, D. L., Franzen, R. R., Charters, A. C., Menna, T. L. & Piekutowski, A. J. 1997. Penetration of confined boron carbide targets by tungsten long rods at impact velocities from 1.5 to 5.0 km/s. *International Journal of Impact Engineering*, 19(1), 15–29.

Orphal, D. L., Franzen, R. R., Piekutowski, A. J. & Forrestal, M. J. 1996. Penetration of confined aluminum nitride targets by tungsten long rods at 1.5–4.5 km/s. *International Journal of Impact Engineering*, 18(4), 355–368.

Pack, D. C. & Evans, W. M. 1951. Penetration by high-velocity ('Munroe') jets: I. *Proceedings of the Physical Society. Section B*, 64(4), 298–302.

Petry, C. 1910. *Monographies de systèmes d'artillerie*. Brussels, Joseph Polleunis.

Piekutowski, A. J., Forrestal, M. J., Poormon, K. L. & Warren, T. L. 1999. Penetration of 6061-T6511 aluminum targets by ogive-nose steel projectiles with striking velocities between 0.5 and 3.0 KM/S. *International Journal of Impact Engineering*, 23, 723–734.

Poncelet, J. V. 1829. *Cours de mécanique industrielle: fait aux artistes et ouvriers messins, pendant les hivers de 1827 à 1828, et de 1828 à 1829. Préliminaires et applications.* Metz: Mme Ve Thiel.

Recht, R. F. 1967. *Ballistic Perforation Dynamics of Armor-Piercing Projectiles*. China Lake, CA: Naval Weapons Center.

Recht, R. F. 1971. Containing ballistic fragments. *In:* Pugh, H. L. D. (ed.) *Engineering Solids under Pressure*, pp. 50–60. London, England: The Institution of Mechanical Engineers.

Recht, R. F. 1990. High velocity impact dynamics: Analytical modeling of plate penetration dynamics. *In:* Zukas, J. A. (ed.) *High Velocity Impact Dynamics*, pp. 443–513. New York: John Wiley & Sons, Inc.

Recht, R. F. & Ipson, T. W. 1963. Ballistic perforation dynamics. *Journal of Applied Mechanics*, 30(3), 384–390.

Resal, H. 1895. Sur la penetration d'un projectile dans les semi-fluides et les solides. *Compte Rendus*, 120, 397–401.

Robins, B. 1742. *New Principles of Gunnery: Containing the Determination of the Force of Gunpowder, and an Investigation of the Difference in the Resisting Power of the Air to Swift and Slow Motions*. London, England: J. Nourse.

Rosenberg, Z. & Dekel, E. 2010. On the deep penetration of deforming long rods. *International Journal of Solids and Structures*, 47, 238–250.

Rosenberg, Z. & Dekel, E. 2012. *Terminal Ballistics*. Berlin Heidelberg: Springer-Verlag.

Rosenberg, Z. & Forrestal, M. J. 1988. Perforation of aluminium plates with conical-nosed rods—additional data and discussion. *Journal of Applied Mechanics*, 55, 236–238.

Rosenberg, Z., Yeshurun, Y. & Mayseless, M. 1989. On the ricochet of long rod projectiles. *In:* Celens, E. & Meysmans, R. (eds.) *Proceedings of the 11th International Symposium on Ballistics*. Belgium: Brussels Congress Centre.

Schonberg, W. & Ryan, S. 2021. Predicting metallic armour performance when impacted by fragment-simulating projectiles – model review and assessment. *International Journal of Impact Engineering*, 158, 104025.

Subramanian, R. & Bless, S. J. 1995. Penetration of semi-infinite AD995 alumina targets by tungsten long rod penetrators from 1.5 to 3.5 km/s. *International Journal of Impact Engineering*, 17(4–6), 807–816.

Tabor, D. 1951. *The Hardness of Metals*. Oxford: Clarendon Press.

Tate, A. 1967. A theory for the deceleration of long rods after impact. *Journal of the Mechanics and Physics of Solids*, 15(6), 387–399.

Tate, A. 1979. A simple estimate of the minimum target obliquity required for the ricochet of a high speed long rod projectile. *Journal of Physics D: Applied Physics*, 12, 1825–1829.

Tate, A. 1990. Engineering modelling of some aspects of segmented rod penetration. *International Journal of Impact Engineering*, 9(3), 327–341.

Taylor, G. I. 1948. The formation and enlargement of a circular hole in a thin plastic sheet. *The Quarterly Journal of Mechanics and Applied Mathematics*, 1, 103–124.

Walley, S. M. 2007. Shear localization: A historical overview. *Metallurgical and Materials Transactions A: Physical Metallurgy and Materials Science*, 38(11), 2629–2654.

Woodward, R. L. 1978a. The penetration of metal targets by conical projectiles. *International Journal of Mechanical Sciences*, 20, 349–359.

Woodward, R. L. 1978b. The penetration of metal targets which fail by adiabatic shear plugging. *International Journal of Mechanical Sciences*, 20, 599–607.

Woodward, R. L. 1990. Material failure at high strain rates. In: Zukas, J. A. (ed.) High Velocity Impact Dynamics. New York: John Wiley & Sons, Inc.

Woodward, R. L., Gooch Jr., W. A., O'Donnell, R. G., Perciballi, W. J., Baxter, B. J. & Pattie, S. D. 1994. A study of fragmentation in the ballistic impact of ceramics. *International Journal of Impact Engineering*, 15(5), 605–618.

Woolmore, N. J. 2005. The Failure of a Tungsten Carbide - Cobalt Cored Projectile Penetrating a Hard Target. PhD, Cranfield University.

Wright, T. W. 1983. A survey of penetration mechanics for long rods. *In:* Chandra, J. & Flaherty, J. E. (eds.) *Computational Aspects of Penetration Mechanics*, pp. 85–106. Berlin, Heidelberg: Springer.

Zukas, J. A. 1990. *High Velocity Impact Dynamics*. New York: John Wiley & Sons, Inc.

5 Stress Waves

5.1 INTRODUCTION

Projectile impacts and explosions result in the formation of waves of stress that can propagate deep into a target. Stress waves (and indeed shock waves) are important as they travel at very high velocities, and consequently, failure of the target linked to these waves can occur a long distance ahead of the penetrating projectile. This is very important when the spall failure of materials is considered. Understanding wave propagation mechanisms is also important when the design of armour is considered—especially in the case of brittle-based systems where small tensile waves can cause catastrophic failure. In this chapter, the physics behind stress waves and the special case where a shock wave is formed within the target material are examined.

Any contact between a moving object and a stationary object produces a wave that emanates from the point of impact and moves into the projectile and the target simultaneously. For very low-velocity collisions in strong materials (metals and ceramics), the wave is most likely to be elastic in nature. Increasing the velocity of impact will result in an inelastic (plastic) wave being formed. Elastic wave velocities can be easily measured using ultrasonic techniques, as discussed in Chapter 2. Transducers are comprised of a piezo-electric crystal that can be forced to oscillate when a voltage is applied; the oscillation results in an ultrasonic waveform with a frequency that is typically within the range of 0.02–20 MHz.

It is possible to design a multi-layered armour such that the stresses that are transmitted and reflected between each individual layer are optimized to minimize the degree of damage caused by the impacting projectile. First, the velocity of the material that is picked up by the wave and carried along with it will be established. This velocity is called the 'particle velocity'.

5.2 CALCULATION OF THE PARTICLE VELOCITY

The velocity of the particles in the elastic region is given by applying the principle of conservation of mass to an elastic wave front propagating at a velocity c (see Figure 5.1). Here we consider the mass per unit area entering the elastic wave front (see also Section 5.6.1).

$$\rho_0 c = \rho(c - u_P) \tag{5.1}$$

Therefore, rearranging, it is seen that the velocity of the particles in the elastically compressed region (where the elastic wave compresses the material from ρ_0 to ρ) is given by

$$u_P = c\left(1 - \frac{\rho_0}{\rho}\right) \tag{5.2}$$
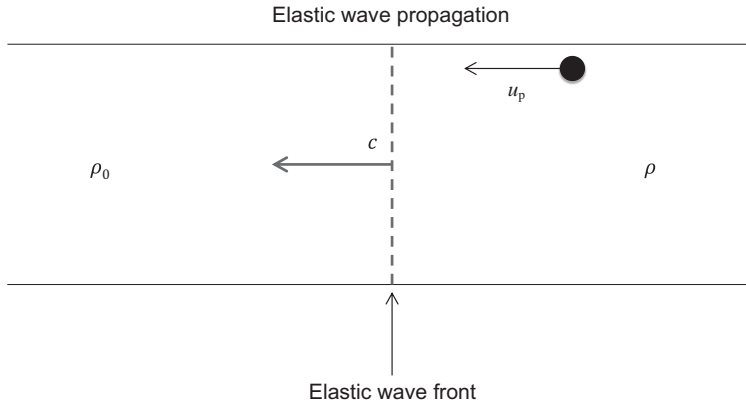
Elastic wave propagation

FIGURE 5.1   Elastic wave propagation with the elastic wavefront moving from right to left.

Now, for a unit mass, the specific volume is given by

$$V_0 = \frac{1}{\rho_0} \tag{5.3}$$

Assuming that the area is constant over the increment, the elastic strain in the sample is given by

$$\varepsilon = \frac{l_0 - l}{l_0} = \frac{V_0 - V}{V_0} = \frac{\rho - \rho_0}{\rho} = \left(1 - \frac{\rho_0}{\rho}\right) \tag{5.4}$$

Substituting Equation 5.4 into Equation 5.2 and assuming that the material follows Hooke's law in that $\varepsilon = \sigma/E$, we find that

$$u_P = \varepsilon c = \frac{\sigma}{E} c \tag{5.5}$$

Given that it is known that $E = \rho_0 c^2$, it, therefore, follows that

$$u_P = \frac{\sigma}{\rho_0 c} = \frac{\sigma}{\sqrt{\rho_0 E}} \tag{5.6}$$

We will see in Section 5.4 an example of where elastic waves travel faster than plastic waves. Now, when the elastic wave separates out from the plastic wave, it can be assumed that the magnitude of the elastic wave is equal to the (dynamic) yield stress, Y, of the material. Therefore, the equation becomes

$$u_P = \frac{Y}{\rho_0 c} \tag{5.7}$$

5.3   ELASTIC WAVES

For an elastic wave (where the stress is less than the dynamic yield strength of the material), the speed is fixed and depends on the Young's modulus (E) and density (ρ_0). For a wave travelling in a bounded medium (such as a cylindrical bar or bullet), it is given by

$$c_0 = \sqrt{\frac{E}{\rho_0}} \tag{5.8}$$

For elastic wave transmission, it is assumed that $\rho \sim \rho_0$ as compressions are small.

For an elastic wave travelling in a semi-infinite medium (such as a target), the wave speed will be slightly higher than the value calculated in Equation 5.8 and is a function of Poisson's ratio (ν) of the material as well as the Young's modulus and density. That is,

$$c_0 = \sqrt{\frac{E(1-\nu)}{\rho_0(1+\nu)(1-2\nu)}} \tag{5.9}$$

When two different materials are joined together, a portion of the elastic wave that arrives at the interface will be transmitted into the secondary layer, whilst a portion will be reflected. The relative elastic impedances of each material govern the proportion that is transmitted and reflected. The elastic impedance (Z) can be calculated from

$$Z = \sqrt{E\rho_0} = \rho_0 c_0 \tag{5.10}$$

It has the unit of $kg/m^2 s$.

There are different forms of elastic waves, and in Sections 5.3–5.5, we are only going to concern ourselves with longitudinal waves, that is to say, where the particle motion is parallel to the wave propagation. Other types of waves include shear waves (we briefly looked at these in Chapter 2). These are evident where the particles are moving perpendicular to the direction in which the wave is propagating. For a description of other types of waves such as Rayleigh (surface) waves and waves that are particularly important in seismology (such as Love waves), consult Meyers (1994).

5.3.1   ELASTIC WAVE TRANSMISSION AND REFLECTION AT AN INTERFACE

Elastic wave transmission and reflection across an interface will now be considered. Consider a laminate consisting of two materials (A and B), where an elastic wave of intensity σ_I travels through material A and comes into play with the interface. It will be assumed that a compressive stress wave of intensity σ_T is transmitted into material B, and a wave of intensity σ_R is reflected (see Figure 5.2). The subscripts I, T and R represent incident, transmitted and reflected, respectively.
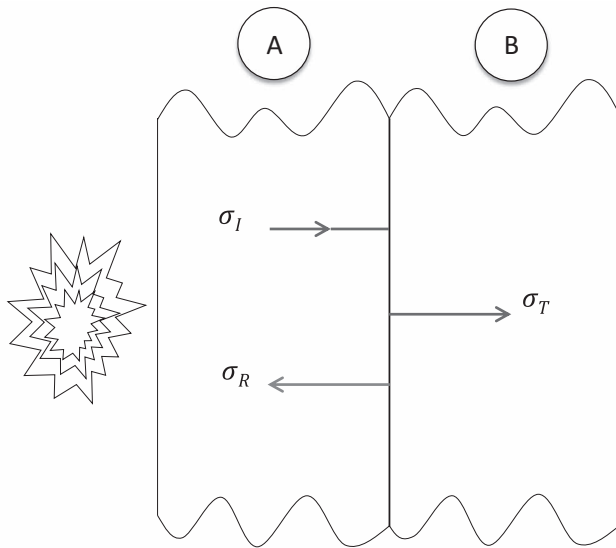
FIGURE 5.2 Transmission and reflection of an elastic wave at an interface.

The interface will be in force equilibrium. Therefore,

$$(\sigma_I + \sigma_R)A_A = \sigma_T A_B \tag{5.11}$$

where A is the cross-sectional area of each material in contact and subscripts A and B represent the two different materials as per Figure 5.2. For the case where the areas are equal, Equation 5.11 becomes

$$(\sigma_I + \sigma_R) = \sigma_T \tag{5.12}$$

We will assume a constant area of contact for the subsequent derivation.

For continuity at the interfaces (no gaps can be created, and matter cannot superimpose itself),

$$u_{p^I} + u_{p^R} = u_{p^T} \tag{5.13}$$

where u_p represents the particle velocity, and the subscript letters I, R and T represent incident, reflected and transmitted, respectively. In a continuum sense, the particle velocity can be assumed to be the velocity of any single particle within the material behind the wave front. This is much less than the velocity at which the wave front propagates.

Now, considering two materials A and B, the incident stress wave front (σ_A) makes contact with the interface between the two materials, and some of the energy is transmitted into material B, whilst the remainder of the energy is reflected back into material A (see Figure 5.2). The particle velocities of these waves are therefore (see Equation 5.6)

$$u_{p^I} = \frac{\sigma_I}{\sqrt{E_A \rho_A}}, \quad u_{p^T} = \frac{\sigma_T}{\sqrt{E_B \rho_B}}, \quad u_{p^R} = \frac{-\sigma_R}{\sqrt{E_A \rho_A}} \tag{5.14}$$

Assuming continuity,

$$\frac{\sigma_I}{\sqrt{\rho_A E_A}} - \frac{\sigma_R}{\sqrt{\rho_A E_A}} = \frac{\sigma_T}{\sqrt{\rho_B E_B}} \tag{5.15}$$

And solving Equations 5.12 and 5.15 simultaneously gives

$$\frac{\sigma_T}{\sigma_I} = 2 \left(\frac{\sqrt{E_B \rho_B}}{\sqrt{E_A \rho_A} + \sqrt{E_B \rho_B}} \right) \tag{5.16}$$

$$\frac{\sigma_R}{\sigma_I} = \left(\frac{\sqrt{E_B \rho_B} - \sqrt{E_A \rho_A}}{\sqrt{E_A \rho_A} + \sqrt{E_B \rho_B}} \right) \tag{5.17}$$

From Equations 5.16 and 5.17, the level of stress that is transmitted and reflected depends on the impedances of the individual materials. It is therefore possible to list the relative transmission and reflection values assuming that material A is steel. These are shown in Table 5.1.

It can be seen from Table 5.1 that depending on the properties of the material that adjoins the face plate, the magnitude of the reflected stress can either be positive or negative. That is to say that the stresses are either compressive or tensile. The stress transmitted into material B is always positive (compressive). So, consider a steel face plate with an epoxy rear layer. It will be seen that 89% of the wave is reflected back

TABLE 5.1

Ratios of the Transmitted and Reflected Stress from a Wave Transiting an Interface between Steel and a Secondary Material (B) of the Same Cross-Sectional Area

Material A	Material B	ρ_B (kg/m³)	E_B (GPa)	$Z_B \times 10^6$ (kg/m²s)	σ_A/σ_I	σ_R/σ_I
Steel	Air	1.225	0	0	0.00	−1.00
Steel	Epoxy	1140	5	2.41	0.11	−0.89
Steel	PMMA	1190	6	2.69	0.12	−0.88
Steel	Magnesium (AZ31B)	1780	41	8.55	0.35	−0.65
Steel	Aluminium (6082-T6)	2703	73	14.09	0.52	−0.48
Steel	Ti–6Al–4V	4400	114	22.40	0.71	−0.29
Steel	Copper	8900	122	33.01	0.90	−0.10
Steel	Steel	7840	210	40.58	1.00	0.00
Steel	Tungsten	19,250	411	88.95	1.37	0.37
Steel	WC	14,740	601	94.11	1.40	0.40

Note: The impedance of steel, $Z_A = 40.58 \times 10^6$ kg/m²s.

into the steel as a tensile wave. If the steel is not backed by anything (i.e. material B is air), then the stress wave is completely reflected back. This can be damaging to the steel and is the reason why high-explosive squash head (HESH) causes such signifi-cant spall damage in metals.

However, it can also be seen that when material B has a higher impedance than material A, then the reflected wave is compressive. This can have positive implica-tions for armour design—particularly where the face plate is brittle.

Example 5.1

A stress wave with a magnitude of 100 MPa propagates into a Rolled Homogeneous Armour (RHA) face layer of a two-component armour. The rear face is made from the aluminium alloy AA 7017. Calculate the magnitude of the stress wave in the aluminium, and sketch the wave interaction at the interface assuming an infinitely long stress pulse. Repeat the process for a case where the second material is W (as opposed to AA 7017). The properties of all materials are summarized in Table 5.2. Assume both materials have identical contact areas.

First, the impedance values are calculated for each of the materials:

$$RHA: Z = \sqrt{E\rho_0} = \sqrt{218 \times 10^9 \times 7838} = 41.34 \times 10^6 \, kg/m^2 s$$

$$AA\ 7017: Z = \sqrt{E\rho_0} = \sqrt{72 \times 10^9 \times 2780} = 14.15 \times 10^6 \, kg/m^2 s$$

So, substituting into Equation 5.16,

$$\sigma_T = 2\left(\frac{14.15 \times 10^6}{41.34 \times 10^6 + 14.15 \times 10^6}\right) \times 100 \times 10^6 = 51 \times 10^6 \, Pa = +51 MPa$$

To sketch the wave interaction, the reflected stress at the interface that travels back into the steel needs to be calculated. This can be easily done by knowing that equilibrium at the interface for a unit area dictates:

$$\sigma_I + \sigma_R = \sigma_T \tag{5.18}$$

Therefore,

$$\sigma_R = 51 \times 10^6 - 100 \times 10^6 = -49 \times 10^6 \, Pa = -49 \, MPa$$

TABLE 5.2
Properties of RHA and AA 7017

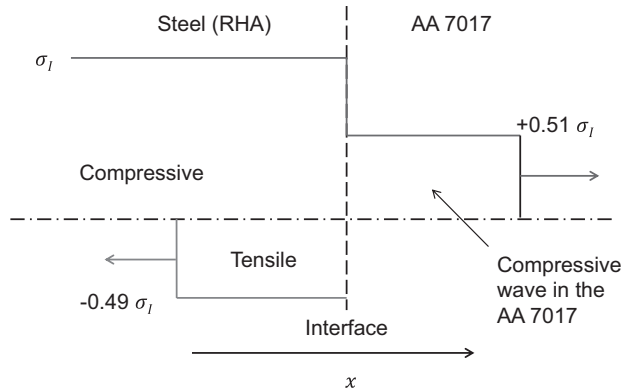| Material	ρ_o (kg/m³)	E (GPa)
RHA	7838	218
AA 7017	2780	72
W	19,250	411

FIGURE 5.3 Stress wave transmission at the interface between steel (RHA) and an aluminium alloy (7017).

Therefore, tensile stress (indicated by the '−' sign) is reflected back into the steel. This is shown in Figure 5.3. The tensile stress that has been reflected back into the steel will be deducted from the compressive wave in the steel.

The above calculations can now be repeated but this time using W as the second material as opposed to AA 7017. So, the impedance of the W (see Table 5.2) is given by

$$W : Z = \sqrt{E\rho_0} = \sqrt{411 \times 10^9 \times 19{,}250} = 88.95 \times 10^6 \, \text{kg} / \text{m}^2 \text{s}$$

And the stress transmitted into the W will be given by

$$\sigma_T = 2 \left(\frac{88.95 \times 10^6}{41.34 \times 10^6 + 88.95 \times 10^6} \right) \times 100 \times 10^6 = 137 \times 10^6 \, \text{Pa} = +137 \text{MPa}$$

It can now be seen that the stress transmitted into the W is higher than the stress that was seen in the RHA, i.e. the stress is amplified. To calculate the reflected stress back into the steel, we again can refer to the equilibrium:

$$\sigma_R = 137 \times 10^6 - 100 \times 10^6 = +37 \times 10^6 \, \text{Pa} = +37 \, \text{MPa}$$

Therefore, compressive stress (indicated by the '+' sign) is reflected back into the steel. This is shown in Figure 5.4. The compressive stress that has been reflected back into the steel has been added to the original compressive wave in the steel.

Example 5.2

A closed-cell aluminium foam[1] (see Chapter 7) is encased by two thin layers (skins) of aluminium. An impact results in a stress propagation through the front skin and is transmitted through the porous foam layer. It is estimated that the area of transmission of the foam is about one-quarter of the skin. Calculate the stress
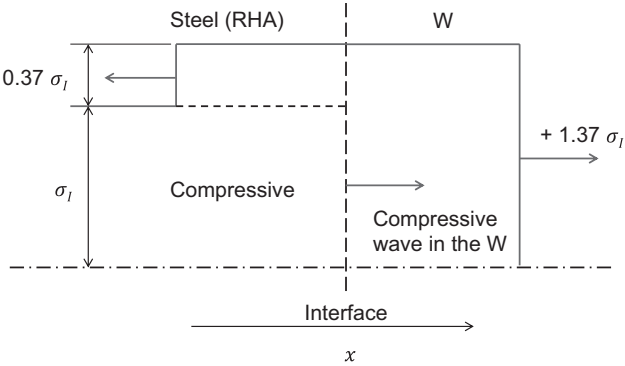
FIGURE 5.4 Stress wave transmission at the interface between steel (RHA) and tungsten (W).

transmitted to the rear layer when a 100-MPa stress is suddenly applied to one face and maintained.

For this problem, we now need to adapt our 'equilibrium equation' to take into account the change in the area. The problem can be summarized in Figure 5.5.

The equilibrium equation now becomes

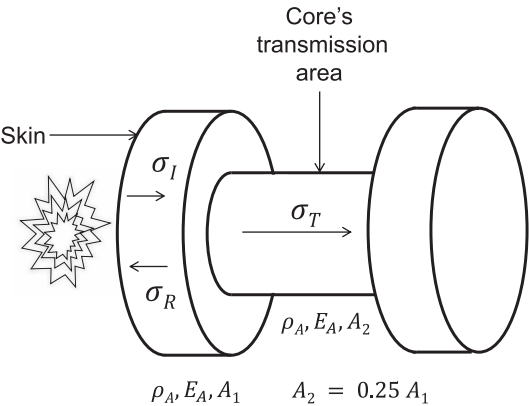$$(\sigma_I + \sigma_R)A_1 = \sigma_T A_2 \tag{5.19}$$

or

$$(\sigma_I + \sigma_R)A_1 = \sigma_T n A_1 \tag{5.20}$$

FIGURE 5.5 Stress wave transmission through a sandwich panel with a porous core—a simple approach.

where n is the fraction of the area, A_1, and in this case $= 0.25$ if we are looking at transmission from the skin into the core.

The compatibility equation for identical materials is

$$\frac{\sigma_I}{\sqrt{\rho E}} - \frac{\sigma_R}{\sqrt{\rho E}} = \frac{\sigma_T}{\sqrt{\rho E}} \tag{5.21}$$

Therefore, solving Equations 5.20 and 5.21 simultaneously gives

$$\sigma_T = \frac{2}{n+1}\sigma_I \tag{5.22}$$

and

$$\sigma_R = \frac{n-1}{n+1}\sigma_I \tag{5.23}$$

Therefore, from Equations 5.22 and 5.23, referring to our problem, it is seen that

$$\sigma_T = \frac{2}{0.25+1} \times 100 \text{ MPa}$$

$$= +160 \text{ MPa}$$

$$\sigma_R = \frac{0.25-1}{0.25+1} \times 100 \text{ MPa}$$

$$= -60 \text{ MPa}$$

The next step is to calculate the stress transmitted into the second skin.

This time, the area is four times the area from which the stress arrives, and therefore, $n = 4$.

Back to Equations 5.22 and 5.23,

$$\sigma_T = \frac{2}{4+1} \times 160 \text{ MPa}$$

$$= +64 \text{ MPa}$$

$$\sigma_R = \frac{4-1}{4+1} \times 160 \text{ MPa}$$

$$= +96 \text{ MPa}$$

It should be pointed out that, in reality, the transmission of stress waves into foam materials is quite complex as the face plate is driven into the foam and compacts it, and therefore, the volume of the core is not constant. Further, the waves navigate through the cell walls in a convoluted way, and the stress in the cell wall is released by virtue of their proximity to the voids (e.g. see Kader et al. (2017)). However, as an illustrative example, it is an interesting problem! Next, we will look at a problem where there is a change in both materials and area.

Example 5.3

A 50-MPa elastic wave from an aluminium bar is transmitted into a steel bar where the steel bar has half the diameter (see Figure 5.6). Calculate the stress transmitted into the steel bar and the reflected wave back into the aluminium.

If the diameter of the steel bar is half the diameter of the aluminium bar, then the area of the steel bar is one-quarter of the aluminium bar, i.e. $d_2 = 0.5\,d$, and therefore, $A_2 = 0.25\,A_1$. Therefore, $n = 0.25$ (as before) and

$$(\sigma_I + \sigma_R)A_1 = \sigma_T n A_1 \ (\text{equilibrium})$$

$$\frac{\sigma_I}{\sqrt{\rho_A E_A}} = \frac{\sigma_R}{\sqrt{\rho_A E_A}} = \frac{\sigma_T}{\sqrt{\rho_B E_B}} \ (\text{compatibility})$$

Solving these equations simultaneously gives

$$\sigma_T = 2\left(\frac{\sqrt{E_B \rho_2}}{\sqrt{E_A \rho_A} + n\sqrt{E_B \rho_B}}\right)\sigma_I \tag{5.24}$$

$$\sigma_R = \left(\frac{n\sqrt{E_B \rho_B} - \sqrt{E_A \rho_A}}{\sqrt{E_A \rho_A} + n\sqrt{E_B \rho_B}}\right)\sigma_I \tag{5.25}$$

Recalling that the impedance of the aluminium is: $Z_A = 14 \times 10^6$ kg/ m²s, and the steel bar is $Z_B = 41 \times 10^6$ kg/m²s and using Equations 5.24 and 5.25:

$$\sigma_T = 2\left(\frac{41 \times 10^6}{14 \times 10^6 + 0.25 \times 41 \times 10^6}\right)\sigma_I$$

$$= +169.1 \text{ MPa}$$

$$\sigma_R = \left(\frac{0.25 \times 41 \times 10^6 - 14 \times 10^6}{14 \times 10^6 + 0.25 \times 41 \times 10^6}\right)\sigma_I$$
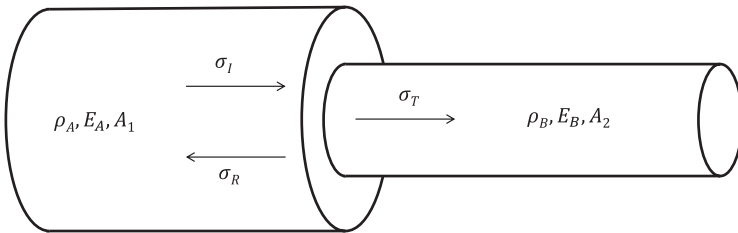
$$= -7.7 \text{MPa}$$

FIGURE 5.6   Wave transmission at an interface where there is a change of material and area.

We should now double-check that equilibrium is maintained by substituting our results into Equation 5.20, namely,

$$(50.0 - 7.7) = 169.1 \times 0.25 = 42.3 \text{ MPa}$$

5.4 INELASTIC WAVES

In most practical military applications where a dynamic load is applied, the magnitude of the stress wave will be much higher than the yield stress of the material. This gives rise to a two-wave structure consisting of elastic and plastic parts.

The equation for the velocity of an inelastic wave travelling in a bounded medium is similar for an elastic wave—Equation 5.8—and is given by

$$c_i = \sqrt{\frac{S}{\rho}} \tag{5.26}$$

where S is the slope of the stress–strain curve beyond the elastic limit. This is often called the plastic modulus (as opposed to the elastic modulus). Because $E > S$, the elastic wave will travel faster than the inelastic wave, and therefore, the wave fronts will become separated over the distance travelled (see Figure 5.7).

If the inelastic response of the material is non-linear (as is the case with most ductile materials), then we will need to calculate the slope at each increment of stress. If the stress–strain curve for a material is considered, then the velocities at specific stress levels can be evaluated (in this case, at three locations—see Figure 5.7):

$$c_1 = \sqrt{\frac{E}{\rho_0}}, \quad c_2 = \sqrt{\frac{S_2}{\rho_0}}, \quad c_3 = \sqrt{\frac{S_3}{\rho_0}} \tag{5.27}$$
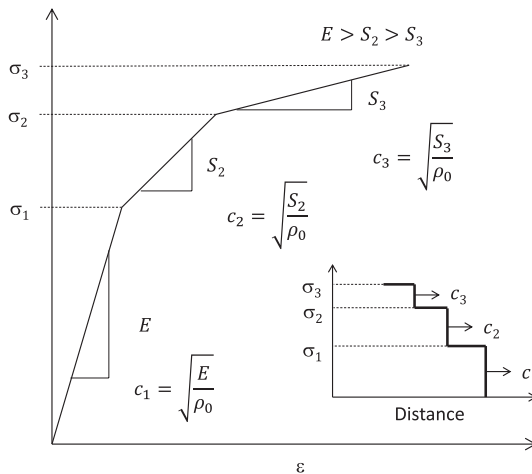

FIGURE 5.7 Stress–strain curve for a material showing three discrete gradients resulting in three different wave speeds. Inset: an idealized wave shape after the wave has travelled a certain distance.

Again, this assumes small compressions $(\rho \sim \rho_0)$. In the above case, it can be seen that as $E > S_2 > S_3$, then $c_1 > c_2 > c_3$—in other words, the shape of the wave changes as the wave progresses through the material.

5.4.1 INELASTIC WAVE TRANSMISSION AND REFLECTION AT AN INTERFACE

In Section 5.3.1, elastic wave reflection and transmission at an interface were discussed. For inelastic waves, the same principles apply; however, the solution is a little more complicated in all but the simplest of cases. It is appropriate to separate the elastic wave calculations from the inelastic wave calculations as the following example shows.

Example 5.4

Consider a ceramic-faced armour system consisting of a ceramic front plate and an aluminium alloy back plate. The ceramic is subjected to an incident stress wave of magnitude 1500 MPa. If the yield strength (Y_0) of the aluminium alloy is 450 MPa and has a stress–strain curve that can be approximated in a bilinear fashion where $E = 70$ GPa and $S = 30$ GPa $(\rho_0 = 2710 \, \text{kg/m}^3$—see Figure 5.8), calculate the magnitude of the elastic and inelastic stress waves that are transmitted into the aluminium alloy. The ceramic remains elastic throughout the process. For the ceramic, $\rho_0 = 3840 \, \text{kg/m}^3$; $E = 380$ GPa.

Firstly, the ceramic will remain elastic throughout the process; however, the aluminium will experience an elastic stress wave with a magnitude equal to the yield strength of the material and an inelastic stress wave of unknown magnitude. Therefore, the compatibility equation is modified to take this into account:
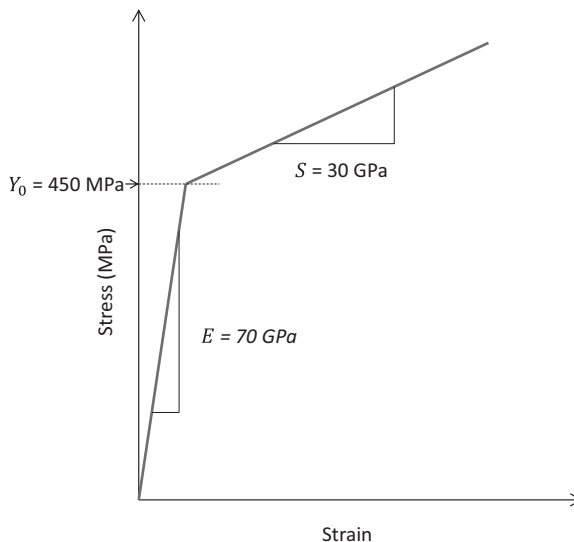

FIGURE 5.8 Strain–strain diagram for the aluminium alloy back plate in Example 5.4.

$$\frac{\sigma_I}{\sqrt{\rho_A E_A}} - \frac{\sigma_R}{\sqrt{\rho_A E_A}} = \frac{Y_0}{\sqrt{\rho_B E_B}} + \frac{\sigma_T^P}{\sqrt{\rho_B S_B}} \tag{5.28}$$

After calculating the impedance values, this becomes

$$\frac{1500}{38.2 \times 10^6} - \frac{\sigma_R}{38.2 \times 10^6} = \frac{450}{13.8 \times 10^6} + \frac{\sigma_T^P}{9.0 \times 10^6}$$

Considering equilibrium,

$$(\sigma_I + \sigma_R) A = (Y_0 + \sigma_T^P) A \tag{5.29}$$

and solving simultaneously, $\sigma_T^P = 248.7$ MPa.

Therefore, it is seen that an elastic wave with a magnitude of 450.0 MPa and an inelastic wave with a magnitude of 248.7 MPa are transmitted into the aluminium alloy.

5.5   SHOCK WAVES

Shock waves are normally associated as occurring in fluids or gases where the material has no shear strength. However, in the 1940s, it was realized that shock waves do occur in solid materials as well as liquids and gases. Early work deduced that if the magnitude of the stress amplitude greatly exceeds the strength of the material, then we can effectively ignore its shear strength and treat the problem hydrodynamically. That is to say, it is assumed that the medium that is shocked has no strength. Thus, much of the mathematical treatment of shock waves is done by hydrodynamic methods that are appropriate to fluids. Shock propagation in solid materials has been extensively studied, and various reviews have been presented elsewhere (Davison, 2008; Kanel, 2019; Skidmore, 1965; Davison and Graham, 1979).

There are various analogies that explain the mechanics by which shock waves propagate through the materials. One such analogy is that of a snow plough clearing a path of freshly laid snow. As the plough moves forward, more and more snow is accumulated in front of the blade. A quick analysis will show that the 'front' of moving snow is travelling at a velocity that is faster than that of the plough. So, the front (which is synonymous with the shock front) is moving at U_s, and the plough blade and the snow are travelling at u_p (i.e. the particle velocity). This is synonymous with the shock and particle velocity in a material system (see Figure 5.9).

Shock waves are very steep in nature. The shock front appears infinitely steep, and the properties of the material change discontinuously from one side of the front to the other. As a material is shocked, its volume is compressed as interatomic distances are being reduced. This results in pressure. Therefore, a shock wave can be defined as a 'discontinuity of pressure, temperature (or internal energy) and density occurring over a very thin front'. Unlike elastic–plastic waves travelling in a cylindrical bar, shock waves 'steepen' with amplitude; they are also supersonic. This is because higher amplitude stresses are transmitted faster than lower amplitude stresses. Consequently, researchers have been able to shock compress materials by
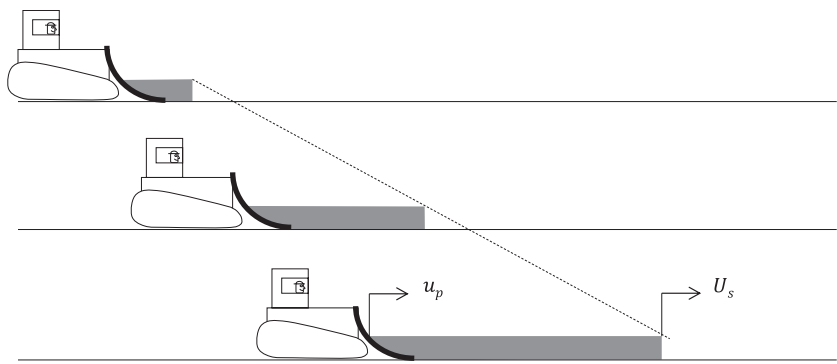
FIGURE 5.9   Analogy of a shock front propagating in a material: the snow plough model.

a factor of two or more, which results in densification that can only be otherwise encountered in the centre of cosmic bodies.

In nature, it would be expected to find shock waves where the unshocked medium is being overdriven by a fast-moving material (e.g. a supersonic jet) or where the type of loading provides a unique set of uniaxial-strain conditions within the material. Previously, elastic and inelastic waves where the material was not constrained and allowed to flow in all directions have been discussed. However, if the material is constrained so that it can only flow in one direction, then it is possible to form a shock in the material. This is because under such uniaxial-strain loading, the stress–strain curve is concave upwards (see Figure 5.10). Thus, following the rationale of Figure 5.7, instead of wavelets of stress becoming slower as the stress is increased, they speed up. This is because the gradient of the inelastic portion increases with stress (see Figure 5.10). The ultimate consequence of this is a sharp fast-moving shock front.

Eventually, it can be seen that, at some point, the gradient of the plastic part is greater than the elastic part, and at this point, the inelastic shock will overtake the elastic wave. Thus, it is no longer possible to detect the elastic wave.
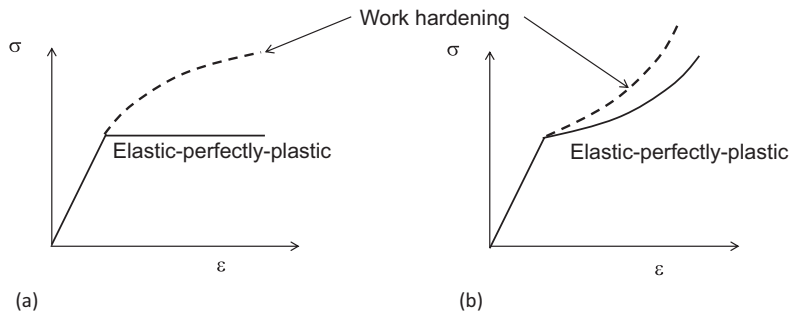

FIGURE 5.10   Strain–strain curves for conditions of (a) uniaxial stress and (b) uniaxial strain. The dashed line indicates how the material would work-harden.
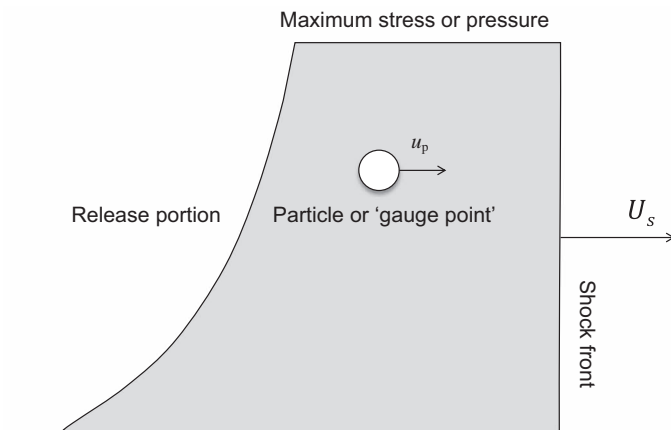
FIGURE 5.11 An ideal shock wave.

5.5.1 AN IDEAL SHOCK WAVE

A shock wave formed by the impact of a projectile will look something like Figure 5.11. This shows a theoretical shock profile captured in an instant of time. Actually, very often nature is much more complicated than this, and there will be other facets present due to strength, microstructural changes, phase changes and the type of loading. It will also change in shape with time as it propagates through the medium. However, this ideal-looking shock wave is useful for describing some key parameters. Firstly, it can be seen that the shock comprises an instantaneous increase in stress at the shock front. This is also accompanied by an increase in density and temperature as will be seen in Section 5.6. Theoretically, the thickness of this shock front rise will be of the order of atomic distances. So, it is very thin. At the peak stress (the maximum stress experienced by the material due to shock loading), the stress level is constant, and the length of this plateau is the shock duration. The duration of the shock is determined by the geometry of the projectile and target and their properties that in turn defines how quickly the stress is released. The release profile is shown at the rear of the wave.

As the shock wave sweeps through, the material is 'picked up' by the wave and travels at the particle velocity, u_p, as seen earlier. A particle is best thought of in the continuum sense as a gauge point that moves with the material.

5.5.2 ARE SHOCK WAVES RELEVANT IN BALLISTIC-ATTACK PROBLEMS?

During penetration by a bullet, fragment, armour-piercing discarding sabot or armour-piercing fin-stabilized discarding sabot projectile, a very complex state of stress exists within the material and around the tip of the penetrating object (Figure 5.12). Just below the surface of the penetrating object, a uniaxial state of strain arises that gives rise to the formation of shocks. However, this zone is fairly small and is most probably localized within a calibre's depth of material. Further away from
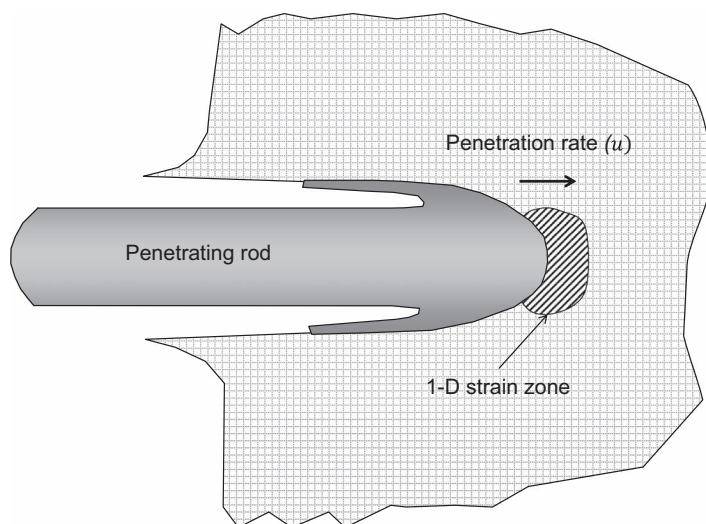
FIGURE 5.12   1D strain zone ahead of a penetrating rod.

this point exists a complex state of stress that adds to the complexity of the analysis (which, incidentally, can only be sensibly done using a hydrocode—see Chapter 6). Consequently, it would be anticipated that the influence of the shocked zone would be relatively small in most ballistic-penetration examples. Nevertheless, it is important to understand what is happening to the material in that locality.

However, it should be pointed out that shock waves are readily formed where the material is being overdriven. That is to say that the rate of penetration is faster than the speed of sound in the medium. The analogy here is of a supersonic jet exceeding the speed of sound in air (i.e. Mach 1). As the jet approaches Mach 1, pressure waves are formed that are able to dissipate away from the jet at the speed of sound. However, when the jet flies at Mach 1, the pressure waves are unable to 'get out of the way' of the jet and consequently compress together to form a shock front. This results in the characteristic sonic boom.

Therefore, when the velocity of a projectile is increased, and the subsequent penetration is higher than the speed of sound in the material in which it is penetrating, then shock waves readily propagate from the penetration interface. For example, this would occur when a shaped charge jet penetrates a polymer such as polymethylmethacrylate (PMMA) or even some low-density metals.

Assume that a shaped charge jet has a tip velocity of 10,000 m/s. The jet is made from copper that has a density of 8940 kg/m³ and is penetrating into PMMA with a density of 1190 kg/m³. Ignoring the fact that the jet will be stretching, the penetration rate into the PMMA can be calculated from (see Chapter 4)

$$u = \frac{v}{1+\sqrt{\dfrac{\rho_t}{\rho_p}}} = \frac{10,000}{1+\sqrt{\dfrac{1190}{8940}}} = 7327 \text{m} / \text{s}$$

where

  u is the penetration rate into the material.

  v is the impact velocity.

  ρ_t is the density of the target.

  ρ_p is the density of the projectile.

    Given that the speed of sound in PMMA is 2260 m/s, the material would be substantially overdriven and consequently shock-compressed ahead of the penetrating jet tip.

5.6 RANKINE–HUGONIOT EQUATIONS

The equations governing the conservation of mass, momentum and energy across a shock front will now be derived assuming that a shock wave is moving in a strengthless fluid (i.e. hydrodynamic). It is considered that a 1D shock wave is progressing through a material, and the reference point from which all measurements are taken is at the shock front (see Figure 5.13). Further, it is assumed that the material ahead of the shock wave is at rest (i.e. unshocked). Ahead of the shock front, the pressure in the material is P_0, the density is ρ_0, and the internal energy (temperature) is e_0. Behind the shock front, there has been a jump in conditions such that the pressure, density and internal energy are now P_1, ρ_1 and e_1, respectively. So, an observer at the shock front will be moving at a velocity U_s. In front of the observer, they see a material moving towards them at a velocity U_s. Behind the observer, it appears that the material has a velocity of $U_s - u_p$, and a specific particle (shown by the circle) is gradually moving away from them.

A general case where the material ahead of the shock wave is already shocked will now be considered, and the material in this zone has a particle velocity of u_0. For most problems that students will face, this overcomplicates things a little, and for the vast number of problems that are solved with pen and paper, $u_0 = 0$. For more complicated problems, it is better to rely on a computer.
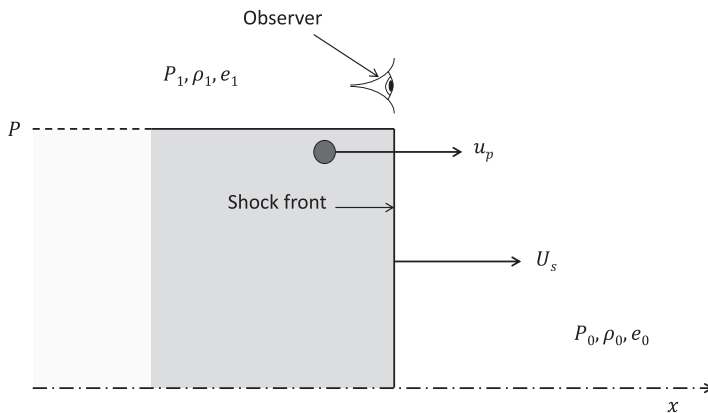

FIGURE 5.13 Schematic of a shock wave showing the position of the observer.

Before we derive the important Rankine–Hugoniot equations, it is important to establish the assumptions behind the derivation. These are as follows:

1. A shock is a discontinuous surface and has no apparent thickness.
2. The shear modulus of the material is assumed to be zero, therefore it responds to the wave as a fluid. Naturally, there is no elastic–plastic behaviour.
3. Body forces and heat conduction at the shock front are negligible.
4. The material does not undergo phase transformation.
5. The initial and final states of the shocked material are in mechanical equilibrium.

5.6.1 CONSERVATION OF MASS

Consider the mass per unit area of a material moving into the shock front. The mass of the material moving into the shock is given by

$$\text{Mass in} = \rho_0 A (U_s - u_0) dt \tag{5.30}$$

$$\text{Mass out} = \rho_1 A (U_s - u_p) dt \tag{5.31}$$

Therefore, as mass in $=$ mass out,

$$\rho_0 A (U_s - u_0) dt = \rho_1 A (U_s - u_p) dt \tag{5.32}$$

and this simplifies to

$$\rho_0 (U_s - u_0) = \rho_1 (U_s - u_p) \tag{5.33}$$

For the case where $u_0 = 0$, this simplifies to

$$\rho_0 U_s = \rho_1 (U_s - u_p) \tag{5.34}$$

This is similar to Equation 5.1 where we were discussing elastic wave propagation.

5.6.2 CONSERVATION OF MOMENTUM

The momentum of the particles can be calculated from their mass $\times$ velocity. The change in the momentum due to the passage of the shock must be equal to the impulse per unit area. The impulse due to the passage of the shock is given by

$$\text{Impulse} = F dt = A (P_1 - P_0) dt \tag{5.35}$$

Knowing that the material behind the shock front has a velocity of u_p, and the material ahead of the shock front has a velocity u_0 (or is at rest), we can work out the change in momentum across the shock front by

$$\text{change in momentum} = \left[(\text{mass})_1 \times (\text{velocity})_1\right] - \left[(\text{mass})_0 \times (\text{velocity})_0\right]$$

$$= \left[\rho_1 A (U_s - u_p) dt \times u_p\right] - \left[\rho_0 A (U_s - u_0) dt \times u_0\right] \quad (5.36)$$

Therefore,

$$\left[\rho_1 A (U_s - u_p) dt \times u_p\right] - \left[\rho_0 A (U_s - u_0) dt \times u_0\right] = A(P_1 - P_0) dt \quad (5.37)$$

Simplifying

$$\left[\rho_1 (U_s - u_p) \times u_p\right] - \left[\rho_0 (U_s - u_0) \times u_0\right] = (P_1 - P_0) \quad (5.38)$$

However, it is recalled from the conservation of mass that

$$\rho_0 (U_s - u_0) = \rho_1 (U_s - u_p) \quad (5.39)$$

Therefore, substituting and simplifying,

$$\left[\rho_o (U_s - u_0) \times u_p\right] - \left[\rho_0 (U_s - u_0) \times u_0\right] = (P_1 - P_0) \quad (5.40)$$

$$\rho_o (U_s - u_0)(U_p - u_0) = (P_1 - P_0) \quad (5.41)$$

For the case where $u_0 = 0$, this simplifies to

$$\rho_o U_s u_p = (P_1 - P_0) \quad (5.42)$$

For most cases of interest, $P_1 \gg P_0$, and therefore, we simplify further

$$\rho_o U_s u_p = P_1 \quad (5.43)$$

5.6.3 Conservation of Energy

We now look at the change in work due to the passage of the shock wave. The work done on a particle of a material behind the shock front is given to us by considering its force $\times$ displacement in a small increment of time, dt. Therefore, this can be calculated from

$$W = (P_1 A)(u_p dt) \quad (5.44)$$

Therefore, the change in energy due to the passage of a shock is

$$\Delta W = (P_1 A)(u_p dt) - (P_0 A)(u_0 dt) \quad (5.45)$$

Now, the kinetic energy of a particle behind the shock front is given to us by

$$KE_1 = \frac{1}{2}\left[\rho_1 A(U_s - u_p)dt\right]u_p^2 \qquad (5.46)$$

and the internal energy of a particle behind the shock front is given to us by

$$\text{internal energy behind shock front} = e_1\rho_1 A(U_s - u_p)dt \qquad (5.47)$$

Note that the internal energy per unit mass, e_1, is multiplied by the mass to get the total energy behind the shock front. Therefore, the difference in total energy due to the passage of the shock front is given to us by

$$= \frac{1}{2}\left(\left[\rho_1 A(U_s - u_p)dt\right]u_p^2 + e_1\rho_1 A(U_s - u_p)dt\right)$$

$$-\left(\frac{1}{2}\left[\rho_0 A(U_s - u_o)dt\right]u_o^2 + e_o\rho_o A(U_s - u_o)dt\right) \qquad (5.48)$$

This can now be equated to ΔW; at the same time, the equation will be simplified by assuming that $u_0 = 0$:

$$(P_1 A)(u_p dt) = \left(\frac{1}{2}\left[\rho_1 A(U_s - u_p)dt\right]u_p^2 + e_1\rho_1 A(U_s - u_p)dt\right) - (e_o\rho_o A U_s dt) \qquad (5.49)$$

Simplifying

$$P_1 u_p = \frac{1}{2}\rho_1 (U_s - u_p)u_p^2 + e_1\rho_1 (U_s - u_p) - e_o\rho_o U_s \qquad (5.50)$$

However, it is known that from the conservation of mass, $\rho_0 U_s = \rho_1(U_s - u_p)$; therefore, substituting and rearranging,

$$P_1 u_p = \frac{1}{2}\rho_0 U_s u_p^2 + e_1\rho_0 U_s - e_o\rho_o U_s \qquad (5.51)$$

or

$$P_1 u_p = \frac{1}{2}\rho_0 U_s u_p^2 + \rho_0 U_s(e_1 - e_o) \qquad (5.52)$$

Now, this equation can be further simplified to use the more commonly used form as follows:

$$e_1 - e_o = \frac{P_1 u_p}{\rho_0 U_s} - \frac{1}{2}u_p^2 \qquad (5.53)$$

From the conservation of momentum, it is known that

$$u_p = \frac{(P_1 - P_0)}{\rho_o U_s} \qquad (5.54)$$

Therefore, substituting into Equation 5.53, we get

$$e_1 - e_o = \frac{P(P_1 - P_0)_1}{\rho_0^2 U_s^2} - \frac{1}{2} \frac{(P_1 - P_0)^2}{\rho_0^2 U_s^2} \tag{5.55}$$

To simplify this equation further, an equation that describes the term $\rho_0^2 U_s^2$ in terms of pressure and specific volume is needed. To achieve this, we refer back to the conservation of momentum; thus,

$$-\rho_1 u_p = -\rho_1 \frac{(P_1 - P_0)}{\rho_0 U_s} \tag{5.56}$$

and from the conservation of mass,

$$-\rho_1 u_p = U_s (\rho_0 - \rho_1) \tag{5.57}$$

So,

$$\rho_0 U_s^2 = -\rho_1 \frac{(P - P_0)}{(\rho_0 - \rho_1)} \tag{5.58}$$

Simplifying leads to

$$\rho_0^2 U_s^2 \left(\frac{1}{\rho_1} - \frac{1}{\rho_0} \right) = -(P - P_0) \tag{5.59}$$

Knowing that $\rho = 1/V$ gives

$$\rho_0^2 U_s^2 = \frac{(P - P_0)}{(V_0 - V_1)} \tag{5.60}$$

This equation is then substituted into Equation 5.55 to give

$$e_1 - e_o = \frac{P_1 (P_1 - P_0)(V_0 - V_1)}{(P_1 - P_0)} - \frac{1}{2} \frac{(P_1 - P_0)^2 (V_0 - V_1)}{(P_1 - P_0)} \tag{5.61}$$

or,

$$e_1 - e_o = \frac{1}{2}(P_1 + P_0)(V_0 - V_1) \tag{5.62}$$

Again, for most cases of interest, $P_1 \gg P_0$, and therefore, it can be simplified further to give

$$e_1 - e_o = \frac{1}{2} P_1 (V_0 - V_1) \tag{5.63}$$

In summary, for a shock wave that is travelling through an unshocked strengthless medium, the conservation of mass, momentum and energy across the shock front can be written as follows:

$$\rho_0 U_s = \rho_1 (U_s - u_p) \text{—conservation of mass} \qquad (5.64)$$

$$P_1 = \rho_0 U_s u_p \text{—conservation of momentum} \qquad (5.65)$$

$$e_1 - e_0 = \frac{1}{2} P_1 (V_0 - V_1) \text{—conservation of energy} \qquad (5.66)$$

We now have five unknowns (e_1, P_1, U_s, u_p and ρ_1). By measuring one of these parameters and combining these equations with the equation of state for the material (see Section 6.7.1), viz.,

$$P_1 = fn(e_1, \ \rho_1) \qquad (5.67)$$

it is possible to calculate all the other variables.

5.6.4   A CONSISTENT SET OF UNITS

It is worth mentioning that in the field of shock physics, base SI units are not the most commonly used form of unit. Shock velocities are very fast, and therefore, all velocities are expressed in kilometres per second or millimetres per microsecond. Therefore, times and displacements are expressed as microseconds (μs) and millimetres (mm), respectively. Pressures and stresses are generally extremely high and quoted in gigapascals (GPa). To provide a consistent set of units, density is therefore quoted in grams per cubic centimetre (g/cc) and specific volume in cubic centimetres per gram (cc/g) and so on.

5.7   THE HUGONIOT

A useful form of the equation of state is the Hugoniot curve (named after the French engineer Pierre-Henri Hugoniot [1851–1887]). This curve is empirically derived and is usually described in terms of U_s and u_p, P and u_p or P and V. Typical shapes of Hugoniot curves are presented in Figure 5.14.

It is important to point out that when a material is shocked, it does not follow the path as described by the Hugoniot, but rather, it jumps from one state to the next. The linear line that links the two states is called the Rayleigh line (see Figure 5.15a) and shows how a strengthless material is shocked from V_0 to V_1. Consequently, the Hugoniot is a locus of attainable jump conditions. On unloading, however, the material follows the isentrope, which is a curve usually lying quite close to the Hugoniot (and for small shocks can be assumed to follow the Hugoniot). This is shown in Figure 5.15b. Due to the loading and unloading following different paths, energy is dissipated in the form of heat and the final volume is larger (e.g. see Ahrens (1993)). This is shown as V_2 in Figure 5.15b. So, a material that has been shocked will be hotter than it was before loading.
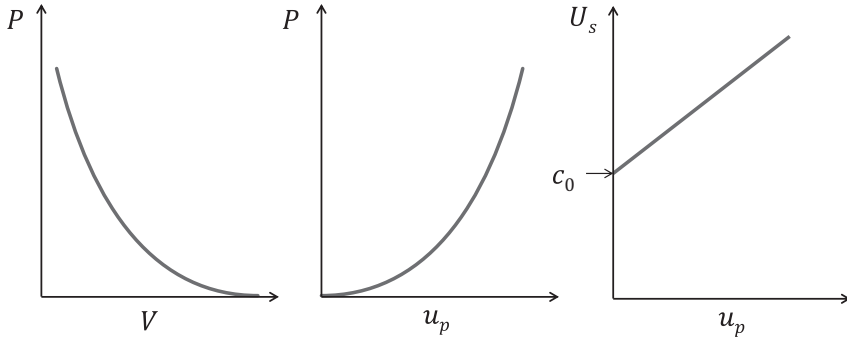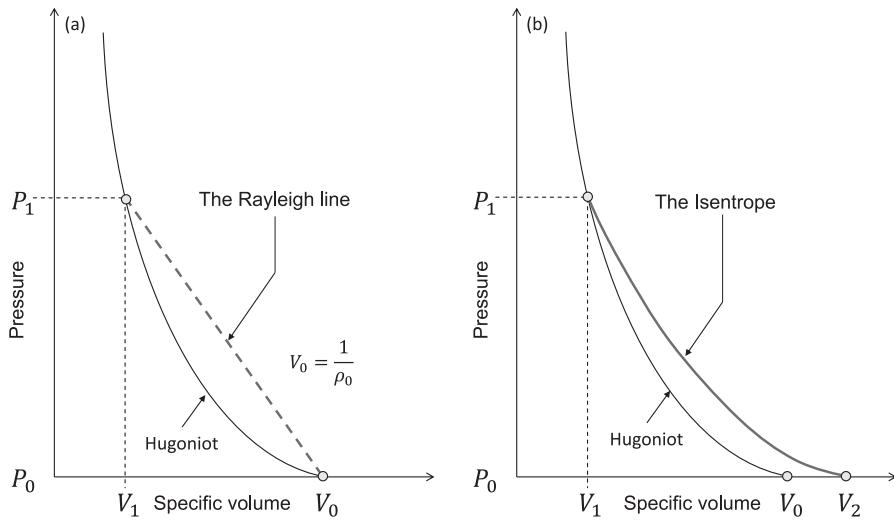
FIGURE 5.14   Hugoniot curves.

FIGURE 5.15   (a) The Hugoniot and Rayleigh line in a strengthless medium and (b) unloading via the isentrope.

The gradient of the Rayleigh line in the P–V plane can be written as

$$R = -\rho_0^2 U_s^2 \qquad (5.68)$$

where ρ_0 and U_s are the bulk (and initial) density and shock velocity, respectively. The shock impedance, Z_s, of the materials is defined as

$$Z_s = \rho_0 U_s \qquad (5.69)$$

and so, the gradient of the Rayleigh line has a direct relationship with the shock impedance.

It is not too difficult to see that this equation is very similar to the equation that was cited for the elastic impedance, where the elastic impedance was written as

$$Z = \sqrt{E\rho_0} = \rho_0 c_0 \tag{5.70}$$

This is a reasonable assumption for where the elastic wave travels at the bulk sound velocity. For cases where the elastic wave is travelling at the longitudinal wave velocity (such as after a plate impact), then c_l is used. Therefore, the equation becomes

$$Z = \rho_0 c_l \tag{5.71}$$

It is also important to point out that despite the classical Hugoniot shapes presented in Figure 5.14, not all materials follow these shapes. Indeed, if the shock incurs a phase change within the material, then this will frequently be represented as a kink or change in gradient.

For most materials (especially metals), it is generally regarded that the Hugoniot, in shock velocity–particle velocity space can be described as being linear of the form

$$U_s = c_0 + S u_p \tag{5.72}$$

where c_0 is the bulk sound speed of the material, and S is a constant.

For metals, c_0 has been correlated with the bulk sound speed of the material, whereas S has been theoretically shown to relate to the first derivative of the bulk modulus with pressure (Ruoff, 1967). This is the standard form of Hugoniot description that fits for many materials and ceramics. In fact, it is highly unusual for the fit to be non-linear for a metal. For polymers, however, some are thought to behave in a non-linear fashion (Porter and Gould, 2006). An example is Dyneema®—a commonly used armour material that crops up in lightweight armour applications—see Figure 5.16. In this case, the Hugoniot for Dyneema is described by

$$U_s = c_0 + a.u_p + b.u_p^2 \tag{5.73}$$

where

c_0 is the bulk sound speed (=1.77 mm/μs).
a is an empirically derived constant (=3.45).
b is an empirically derived constant (=−0.99 μs/mm).

For a straightforward linear Hugoniot (i.e. Equation 5.72), there are various sources for the constants c_0 and S that are reported in the literature. In particular, the compendium published by Marsh gives a good list as do the works of McQueen et al. (1970), Meyers (1994) and Carter and Marsh (1995) for polymers.

A list of parameters (including elastic data) for various materials that may well be used in armour applications is provided in Table 5.3.
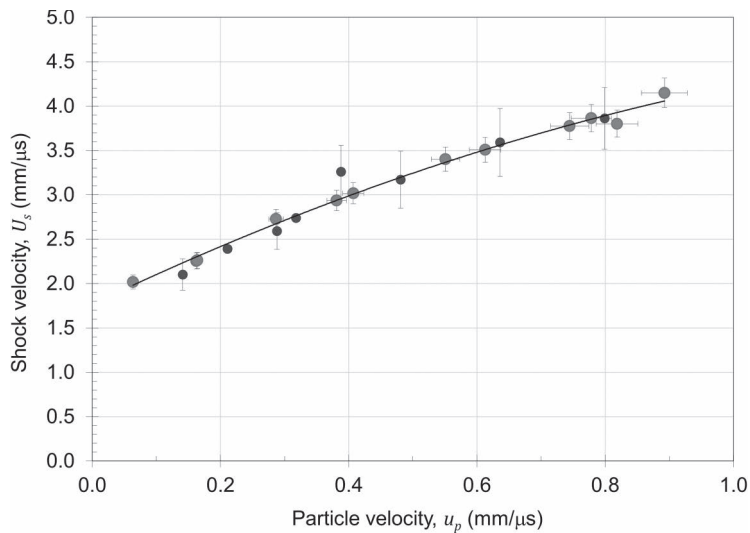
FIGURE 5.16   A measured Hugoniot curve for Dyneema showing a slight non-linear behaviour. (Data from Chapman, D. J. et al. 2009 *AIP Conference Proceedings*, 1195, 1269–1272; Hazell, P. J. et al. 2011 *Journal of Applied Physics*, 110(4), 043504.).

TABLE 5.3

Equation-of-State Parameters for Some Materials That Could Be Used in an Armour Application

Reference	Material	Density (g/cc)	c_0 (mm/µs)	S	c_1[a] (mm/µs)	c_s[a] (mm/µs)
Marsh (1980)	AA 2024	2.784	5.37	1.29	6.36	3.16
Boteler and	AA 5083-H131	2.668	5.29	1.40	6.51	3.20
Dandekar (2006)	AA 5083-H32	2.668	5.14	1.27	6.51	3.20
Marsh (1980)	Comp B (explosive)	1.715	3.06	2.01	3.12	1.71
	Mg (AZ31B)	1.776	4.57	1.21	5.70	3.05
	Steel, 304L	7.903	4.57	1.48	5.79	3.16
Carter and	Epoxy[b]	1.192	2.69	1.51	2.641	1.177
Marsh (1995)	Polycarbonate[c]	1.196	2.33	1.57	2.187	0.886
Dandekar and Benfanti (1993)	Titanium diboride	4.490	8.622	0.795	11.23	7.41

[a] Ultrasonically measured data.

[b] Between $U_s = 0.4–2.8$ mm/µs.

[c] Between $U_s = 0.4–2.6$ mm/µs.
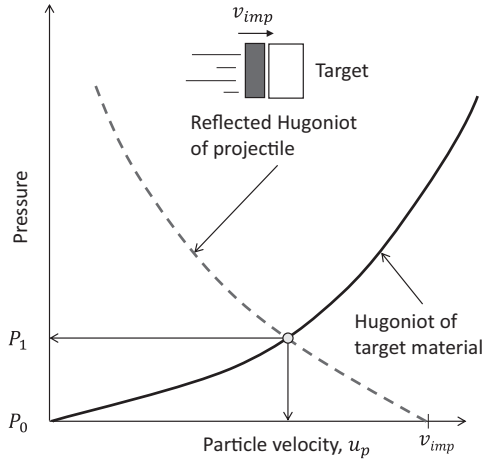
FIGURE 5.17 Calculation of the pressure and particle velocity from two colliding objects. Here the pressure is raised from P_0 to P_1.

5.7.1 CALCULATING THE PRESSURE FROM TWO COLLIDING OBJECTS

For a condition of 1D strain, it is a relatively trivial task to establish the pressure generated in two colliding bodies with knowledge of the Hugoniots of the materials and the impact velocity. Again, it is assumed that the material does not have strength. First, the Hugoniot of the target material is plotted in the $P-u_p$ space. Secondly, the Hugoniot of the projectile, reflected and recentred, is plotted so that the curve intercepts the x-axis at the impact velocity (v_{imp}) (see Figure 5.17). Finally, the pressures and particle velocities in both the target and the projectile are provided by reading from the intercepts between the two curves. This approach is a direct application of what is called 'the impedance matching technique'.

From this approach, it is possible to see that if the impact occurs between two identical materials, then the particle velocity resulting in both materials can be calculated by merely dividing the impact velocity by 2. This is known as a symmetrical impact. Let us have a look at a couple of examples.

Example 5.5

Take a copper projectile striking a copper target at 2 mm/µs. The Hugoniot of copper is well known and can be described by the following polynomial equation:

$$P = \rho_0 \left(c_0 + Su_p\right)u_p \tag{5.74}$$

where $\rho_0 = 8.93$ g/cc, $c_0 = 3.94$ mm/µs and $S = 1.49$.

The equation for the reflected Hugoniot (for the projectile) can be written as

$$P = \rho_0 \left(c_0 + S\left(v_{imp} - u_p\right)\right)\left(v_{imp} - u_p\right) \tag{5.75}$$
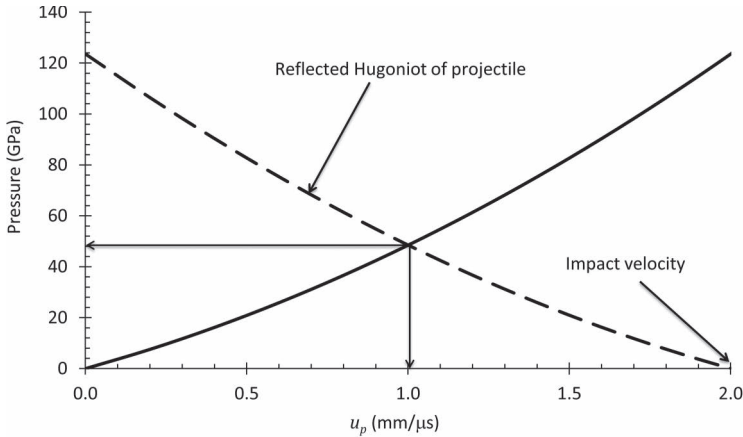
FIGURE 5.18 Calculating the impact pressure and particle velocity from an impact of a Cu projectile striking a Cu target at 2 mm/µs.

Solving these equations simultaneously results in a pressure of 48.5 GPa and u_p value of 1 mm/µs. This is shown graphically in Figure 5.18.

Example 5.6

A 50-mm-long tantalum explosively formed projectile strikes a semi-infinite RHA (steel) target at 2.0 mm/µs such that a shock wave is produced in the steel. Calculate

   a. The pressure in both the tantalum and steel
   b. The particle velocities in the tantalum and the steel
   c. How long it takes the shock wave pulse to travel 50 mm into the steel
   d. How long it takes for the shock pulse to reach the rear free surface of the tantalum projectile

For the sake of this calculation, assume that the impact is 1D (so that it behaves as if it is a plate impact experiment). The Hugoniot properties for the materials are

$$\text{steel}: U_s = 4.16 + 1.73u_p; \rho_0 = 7.84 \text{ g/cc}; c_1 = 5.92 \text{ mm/µs}$$

$$\text{tantalum}: U_s = 3.41 + 1.20u_p; \rho_0 = 16.65 \text{ g/cc}$$

Parts (a) and (b): The first step is to use the impedance matching technique to establish the pressures and particle velocities. From before, it was seen that the Hugoniot for the target can be mathematically described as

$$P = \rho_0 (c_0 + Su_p)u_p = 7.84(4.61 + 1.73u_p)u_p$$

and the reverse Hugoniot for the projectile (with $u_p = v_{imp}$ at $P=0$) will be given by

$$P = \rho_0 \left(c_0 + S(v_{imp} - u_p)\right)(v_{imp} - u_p) = 16.65\left(3.41 + 1.20(2.0 - u_p)\right)(2.0 - u_p)$$
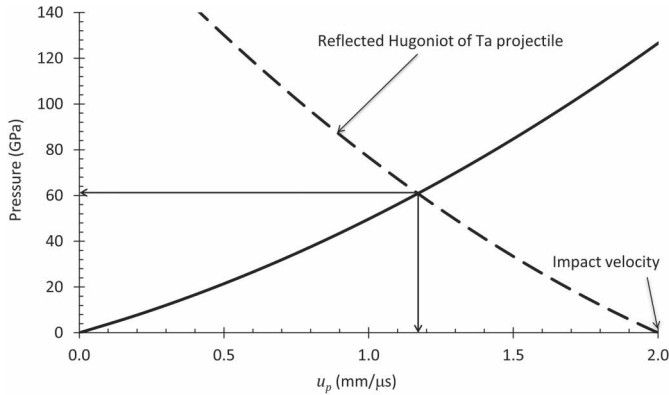
FIGURE 5.19   Calculation of the pressure and particle velocities due to the impact of a tantalum projectile onto steel at 2 km/s.

Solving these two equations simultaneously gives us the pressures and particle velocities in both the projectile and the target; the calculation is shown graphically in Figure 5.19.

So, the results are $P = 60.9\,\mathrm{GPa}$; $u_p = 1.17$ mm/μs for both the tantalum and the steel (a+b)

Part (c): The next step is to calculate the shock pulse width after it has travelled $x = 50\,\mathrm{mm}$ into the steel. The shock propagates into the steel at $U_s = 4.61 + 1.73 \times 1.17 = 6.63$ mm/μs. Therefore, the time taken to travel 50 mm (s) is given to us as

$$t = \frac{x}{U_s} = \frac{50.00}{6.63} = 7.54 \text{ μs}$$

Part (d): The time taken to reach the rear free surface of the tantalum projectile is given in a similar fashion. The shock wave propagates into the Ta projectile at a speed of $U_s = 3.41 + 1.20 \times 1.17 = 4.81$ mm/μs. Therefore, the time taken for the shock wave to reach the rear of the projectile is

$$t = \frac{x}{U_s} = \frac{50.00}{4.81} = 10.40 \text{ μs}$$

5.8   SHOCKS IN ELASTIC–PLASTIC MATERIALS

Up to now, we have been largely concerned with strengthless materials. Of course, real armour materials have strength. Some armour materials such as ceramic are particularly strong in compression, and it is this strength that helps defeat projectiles.

5.8.1   THE HUGONIOT ELASTIC LIMIT

Consider three flyer-plate experiments (uniaxial strain—see Chapter 2) where the shock states are defined by an elastic–plastic Hugoniot (see Figure 5.20a). Instead of the Hugoniot being a straightforward polynomial, there is initially a straight line that
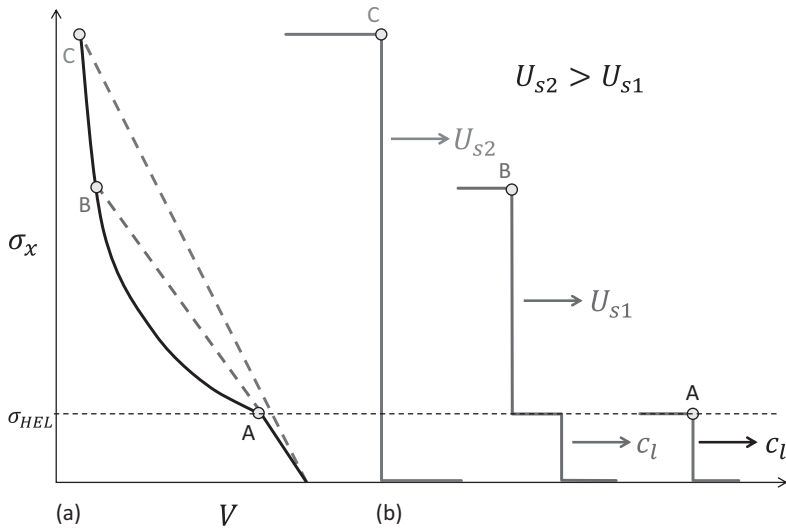
FIGURE 5.20 A Hugoniot and three different shock states resulting in three different wave shapes. The absence of the HEL for the strong shock (C) indicates hydrodynamic behaviour.

breaks into a curve with an upward trajectory. The transition occurs at what is called the Hugoniot Elastic Limit (HEL). This is the point at which the elastic wave velocity transitions to the plastic shock front (see Figure 5.20b). All waves at stresses below the HEL (point 'A') travel at the longitudinal wave velocity, c_l. If the shock stress is increased such that a higher shock state is reached (B), both an elastic wave (again travelling at c_l), and a plastic wave are seen. The plastic wave is travelling at U_{s1}. At very high shock pressures (C), the shock velocity U_{s2} is so high, that the HEL is absent, and the wave propagation can be simulated assuming hydrodynamic behaviour. We will discuss this again later. Note too that $U_{s2} > U_{s1}$.

It turns out, that if a material is shocked, and the shock velocity, U_s, is less than the elastic wave speed in the material, then an elastic wave will always propagate ahead of the main shock front.

From, flyer-plate experiments where the free-surface velocity (u_{fsv}) is being measured with a laser-based system (e.g. VISAR or PDV), the HEL can be calculated from the following:

$$\sigma_{HEL} = \frac{1}{2}\rho_0 c_l u_{fsv} \tag{5.76}$$

where u_{fsv} is the free surface velocity at the HEL. This is the conservation of momentum equation (5.65), but replacing U_s with c_l and also noting that the particle velocity is given by:

$$u_p = \frac{1}{2}u_{fsv} \tag{5.77}$$

The HEL (1D strain) can be related to the yield strength (1D stress) by the following equation:

$$Y = \frac{(1-2v)}{(1-v)}\sigma_{HEL} \qquad (5.78)$$

where v is the Poisson's ratio for the material. Note that here, we describe Y as the yield strength that may or may not be identical to the quasi-static yield strength, Y_0. Thus, it is possible to measure how the shock loading has affected the yield behaviour of the material and whether this has resulted in any strengthening (or indeed, softening) behaviour.

The HELs for various armour-type materials are shown in Table 5.4.

The effect of the HEL on the Hugoniot of a material is shown in Figure 5.21. Adding a HEL to a strengthless Hugoniot shifts the Hugoniot up. For different grades of steel, the Hugoniot will be pretty much identical (the Hugoniot is insensitive to small changes in chemistry). However, as can be seen from Table 5.4, the HEL for armour steel is quite variable.

We can glean more salient information by considering a shock profile. Figure 5.22 shows the results from a hydrocode analysis of a strengthless tungsten flyer plate striking an AA 7075-T6 target at 500 m/s. There are three types of targets considered here: (1) a strengthless target, that is, it is assumed that the material has zero strength and stiffness; (2) an elastic–perfectly plastic target with a dynamic yield strength of 0.5 GPa (this is approximately what you would expect from an AA 7075-T6 target); and (3) an elastic–perfectly plastic target with a dynamic yield strength of 1.0 GPa.

TABLE 5.4

HELs for Various 'Armour-Type' Materials

Reference	Material	ρ_0 (g/cc)	σ_{HEL} (GPa)
Hazell et al. (2012)	Elektron 675 T5 (Mg)	1.903	0.37 ± 0.04
Boteler and Dandekar (2006)	AA 5083-H131	2.668	0.573 ± 0.04
	AA 5083-H32	2.668	0.40 ± 0.03
Wang et al. (2020)	Improved rolled homogeneous armour	7.840	2.5 ± 0.2[a]
	High hardness armour	7.840	3.1 ± 0.1[a]
Nahme and Lach (1997)	Mars 190 (armour steel)	7.840	1.2–2.0
	Mars 240 (armour steel)	7.840	1.2
	Mars 300 (armour steel)	7.840	1.6–2.2
Gust and Royce (1970)	Vascomax 350 (maraging steel)	8.080	4.8 ± 2
	Alumina (AD 85)	3.420	6.1–6.5
	Alumina (AD 995)	3.810	8.3 ± 0.5
Dandekar and Bartkowski (1994)	Alumina (AD 995)	3.880	6.71 ± 0.08
Gust and Royce (1970)	Boron carbide, hot pressed	2.500	13.7–16.2
Yuan et al. (2001)	Silicon carbide (SiC–N)	3.214	11.5 ± 0.4
Gust and Royce (1970)	Titanium diboride	4.520	8.1 ± 0.4

[a] Calculated from the FSV traces from the data presented by (Wang et al., 2020) using $c_l = 5290$ m/s.

This is an exaggerated strength—in reality, the alloy would never be this strong. However, in this case, exaggerating the strength enables us to clearly demonstrate the physics of what is happening. There are several things to note here:

1. Increasing the yield strength increases the magnitude of the HEL.
   So rearranging Equation 5.78, it can be seen that

$$\sigma_{HEL} = \frac{(1-v)}{(1-2v)}Y \qquad (5.79)$$

   Assuming that the Poisson's ratio for the material is 0.34, then for a target with a yield strength of 0.5 GPa, the HEL = 1.03 GPa. For a (dynamic) yield strength of 1.0 GPa, the HEL would be 2.06 GPa. This is what is seen in the shock trace.

2. When the strength of the aluminium target material is increased, the magnitude of the shock 'seen' by the target also increases. This is seen in Figure 5.22 for a $Y = 1.0$ GPa target as $\Delta\sigma_x$. The reason for this is that we need to take into account the strength of the target in our Hugoniot. So, Figure 5.17 now needs to be redrawn (see Figure 5.21). It will be seen that now, the stress has been raised in the target as the Hugoniot is shifted upwards slightly (up and to the left). This is depicted in our shock compression traces shown in Figure 5.22. It is also noted that the compression curve has been shifted up by 2/3 Y. To understand why it has been shifted up by
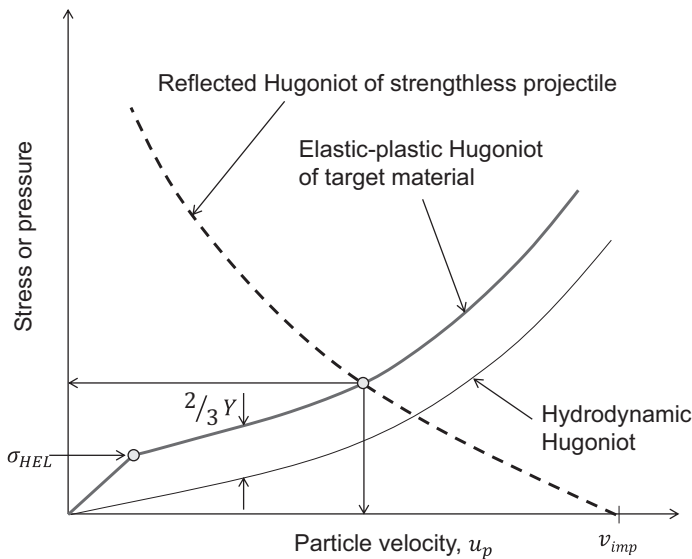
FIGURE 5.21 Calculation of the stress and particle velocity from two colliding objects using an elastic–plastic Hugoniot for the target. The particle velocity at the HEL is usually quite small.
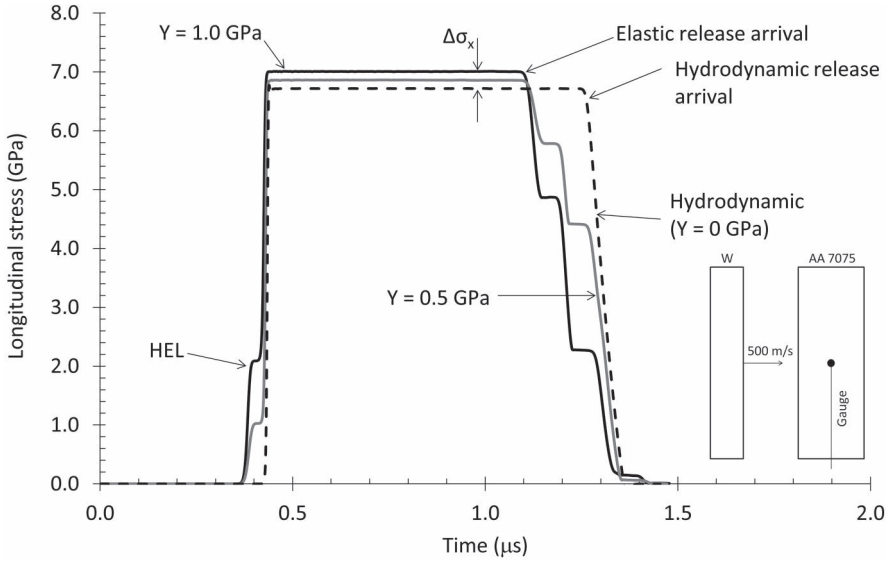
FIGURE 5.22 Shock propagation in (a) a strengthless (hydrodynamic) aluminium (AA 7075) target, (b) an aluminium target with a dynamic yield strength of 0.5 GPa and (c) an aluminium target with a dynamic yield strength of 1.0 GPa.

$2/3\,Y$, the pressure in the sample needs to be considered, which is the average of the three principal stresses, i.e.

$$P = \frac{\left(\sigma_x + \sigma_y + \sigma_z\right)}{3}$$

(5.80)

In the case where the material is loaded in the uniaxial strain, $\sigma_y = \sigma_z$; therefore,

$$P = \frac{\left(\sigma_x + 2\sigma_y\right)}{3}$$

(5.81)

However, from Tresca, it is also noted that the yield strength is given by

$$Y = \sigma_x - \sigma_y$$

(5.82)

Therefore, substituting and rearranging,

$$P = \frac{\left(\sigma_x + 2\sigma_y - 2Y\right)}{3}$$

(5.83)

Simplifying and rearranging in terms of σ_x, we find that

$$\sigma_x = P + \frac{2}{3}Y$$

(5.84)

Therefore, the longitudinal stress in the material when it is shocked is given by the hydrodynamic pressure $+2/3$ yield strength. As $Y = 2\tau$, according to Tresca, Equation 5.84 can also be written as

$$\sigma_x = P + \frac{4}{3}\tau \qquad (5.85)$$

It should be pointed out that this assumes that the material is elastic–perfectly plastic. Some materials pressure-harden, and therefore, the Hugoniot curve will move further away from the hydrodynamic curve as the pressure increases. Some materials pressure-soften. Therefore, the Hugoniot curve moves closer to the hydrodynamic curve as the pressure increases. Equation 5.85 also shows us that the applied load is carried by the hydrostatic pressure and in part by its resistance to shear. Therefore, it is reasonable to assume that if the pressure is very large, one can ignore material strength.

3. Finally, the arrival of the release wave is observed from the rear of the projectile and into the target resulting in the pulse being truncated. The target is initially released elastically followed by a plastic release. The velocity at which the wave structure is eaten away is a function of the particle velocity and the speed of sound in the material at that pressure. The hydrodynamic target appears to maintain its pulse for longer, and this is because the speed of sound is significantly reduced due to the zero stiffness.

5.8.2 EVALUATING THE STRENGTH OF A MATERIAL BEHIND THE SHOCK WAVE

Frequently, it is important to evaluate how the strength of the material varies after a shock wave has passed through the material. This can be done by applying very thin in-material gauges made from such materials as manganin. The beauty of manganin is that it is a piezo-resistive material whose response is essentially insensitive to temperature. Therefore, the rise in temperature associated with a shock wave will have little effect on the response of the gauge.

The experimental technique involves splitting the material into two in a plane perpendicular to the impact direction of a flyer plate (machined flat and parallel) and inserting a suitable gauge. As the target is struck by the flyer plate, the shock that is formed sweeps the target, and although the state of strain is 1D, the state of stress is 2D. In fact, the state of stress can be written as follows:

$$\sigma_x \neq \sigma_y = \sigma_z \qquad (5.86)$$

This is to say that a longitudinal stress (σ_x) state is established that is not (or unlikely to be) equal to the lateral stress, σ_y (except in fluids). With knowledge of σ_x and σ_y, it is possible to establish a value for the shear strength behind the shock front. This is given from the Tresca criteria (which, for a 1D plate-impact experiment is identical to von Mises as $\sigma_y = \sigma_z$) as follows:

$$2\tau = \sigma_x - \sigma_y \qquad (5.87)$$

This relation can then be used to establish the strength of the material behind the shock as the material is squeezed together. The strength behind the shock wave is important—particularly for providing constitutive relationships for the material.

Of course, the gauge technique to establish σ_y is naturally invasive. There have been questions on whether the gauge is measuring a true response of the material that is shocked or whether its response is a feature of the soft gauge encapsulation material (Winter and Harris, 2008; Winter et al., 2008; Appleby-Thomas et al., 2010).

5.8.3 RELEASE (RAREFACTION) WAVES

When a shock wave encounters a free surface, stress will be released at that surface, and a release wave will travel back into the target in the opposite direction of the shock. Release waves will also be travelling from the free surfaces of the projectile that hit the target. When these release waves collide, the target is placed in net tension, and this causes the material to spall.

Looking again at Figure 5.11, the release portion of the wave is curved in nature as the pressure drops from the Hugoniot pressure to zero. This release portion of the wave is sometimes referred to as the rarefaction wave or expansion wave. This is because during the release process, the density of the material that is shocked is reduced, and therefore, in real terms, the material undergoes an expansion.

As mentioned in Section 5.7, shock waves will follow a curve called an isentrope on pressure release. For small compressions, and for what is seen in most ballistic applications, one can assume that the isentrope is very similar to the Hugoniot curve of the material. For elastic–plastic materials (i.e. where hydrodynamic behaviour is no longer assumed), the material will initially be released elastically before following a 'plastic' release path. This can be seen in the simulation results in Figure 5.22.

Release waves travel faster than shock waves and eventually catch up with the wave and 'eat away' at it. The velocity of the rarefaction wave is given by

$$U_R = u_p + c^p \tag{5.88}$$

where u_p is the particle velocity, and c^p is the speed of sound at a given pressure. As the pressure drops in the material, so too does c^p, and this defines the shape of the release portion of the wave.

Figure 5.23 shows how this happens for a simple trapezoidal wave form. The release wave is travelling faster than the shock wave and eventually catches up with it. As it does so, the shock pressure is reduced. This process results in a slower shock wave as the shock-wave velocity is a function of pressure (see Equation 5.43). Furthermore, the trailing edge of the release wave will be moving slower than the shock front at the bulk sound speed of the material (i.e. c^p for $P=0$). Therefore, the shock profile effectively gets shorter and broader until, eventually, it attenuates to nothing.

5.8.4 STRAIN MEASUREMENTS IN SHOCKED MATERIALS

In many engineering applications, it is commonplace to use strain gauges to measure strain in a sample. This is not possible in shocked materials due to the limited
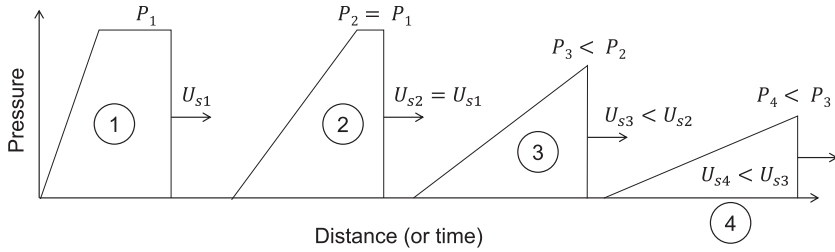
FIGURE 5.23 Change in shape and velocity of a shock wave due to the release wave attenuating the shock.

frequency response of such gauges (i.e. they cannot record the data quick enough) and susceptibility to temperature and pressure. However, we can evaluate strain in shock materials from free-surface velocity measurements.

In a 3D system, there will be orthogonal values of strain (and stress for that matter). These can be defined as ε_x, ε_y and ε_z that correspond to strain along the x, y, z axes. We can reduce ε_x, ε_y and ε_z into a scalar strain, or 'effective' or indeed, 'equivalent' strain according to:

$$\varepsilon_{eq} = \frac{\sqrt{2}}{3} \left[\left(\varepsilon_x - \varepsilon_y \right)^2 + \left(\varepsilon_x - \varepsilon_z \right)^2 + \left(\varepsilon_y - \varepsilon_z \right)^2 \right]^{\frac{1}{2}}$$
(5.89)

We will be introduced to this again when we evaluate constitutive models in Chapter 6 and more information can be provided by texts such as (Dowling, 2013). For the very special case of uniaxial strain (i.e. during a flyer-plate impact, for example where $\varepsilon_x \neq \varepsilon_y = \varepsilon_z = 0$), this reduces to (Meyers, 1994):

$$\varepsilon_{eq} = \frac{\sqrt{2}}{3} \left(2\varepsilon_x^2 \right)^{\frac{1}{2}} = \frac{2}{3} \varepsilon_x$$
(5.90)

Consider an element of material that is compressed in one direction during a uniaxial-strain experiment (e.g. with a flyer plate). An example is shown in Figure 5.24. As the element is squashed along the x-axis, it is strained in one direction only, such that the side l_0 becomes l. However, when the shock has passed, and the element has been subjected to a rarefaction wave, it expands. So, the element is strained in compression and strained during expansion.

In Figure 5.24, the engineering strain (e_x) that the element experiences during shock can be described by:

$$e_x = \frac{l_0 - l}{l_0} = 1 - \frac{l}{l_0} = 1 - \frac{V}{V_0}$$
(5.91)

From the Rankine–Hugoniot relationships we know that,

$$V = V_0 \left(1 - \frac{u_p}{U_s} \right)$$
(5.92)
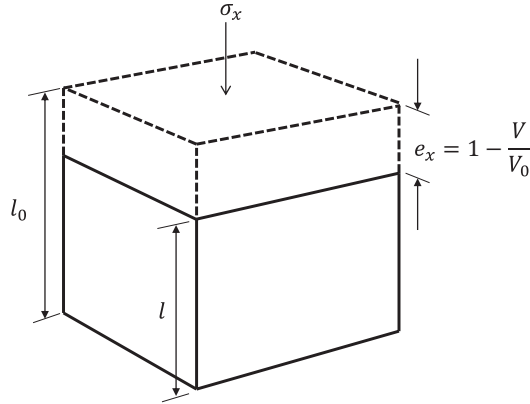
FIGURE 5.24   An element subjected to uniaxial-strain deformation.

Therefore, during shock, the uniaxial engineering strain is given by,

$$e_x = 1 - \frac{V}{V_0} = \frac{u_p}{U_s} \tag{5.93}$$

The true strain along the x direction can be defined by

$$\varepsilon_x = \int_{l_0}^{l} \frac{dl}{l} = \ln\frac{l}{l_0} = \ln\frac{V}{V_0} \tag{5.94}$$

It also should be noted that from a simple analysis of a unit cell being compressed that the shape change causes a shear strain. As solid materials have non-zero shear strengths, the shear strains are resisted and shear stress develops on planes inclined to the shock front (Jones, 1973).

5.8.4.1   Stress–Strain Curves

Most shock data is presented showing a Hugoniot in terms of pressure and volume, or with shock velocity and particle velocity. One can, however, examine shock data in terms of stress and strain. These terms are more familiar to the engineer. Again, going back to a flyer-plate experiment where the target is subjected to uniaxial strain (e_x), the stress–strain response of the target is shown in Figure 5.25.

Initially, the target is stressed to the HEL, beyond which the sample is shocked along the Rayleigh line. The decreasing volume of an element in the target, decreases the interatomic distances, thereby leading to an increase in pressure (not plotted). At point C, the stress is released and the unloading process follows a path of elastic unloading initially (CD), followed by plastic unloading (DE). Thus, after the passage of a single shock wave, a residual strain (AE) is apparent. This strain can also be affected further by the arrival of radial release waves that cause further thinning of the target (to point F in Figure 5.25) (Jones, 1973).
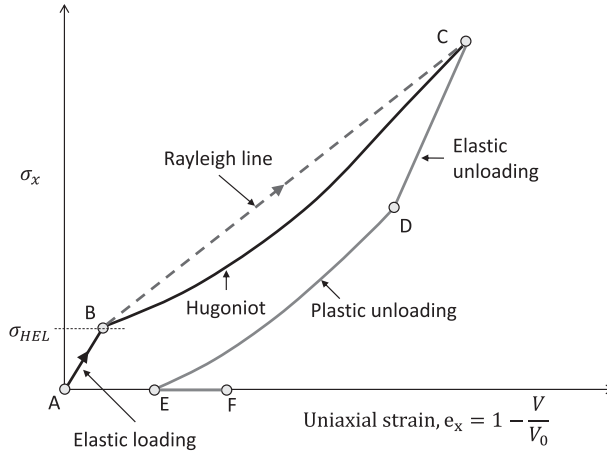
FIGURE 5.25 Stress–strain diagram of a sample under shock. (Adapted from Jones, 1973.)

5.8.4.2 Transitory Strain

As discussed above, during the shock process, the material is compressed, which induces strain and then is released, the subsequent release process also induces strain (unlike in a simple tensile test). Therefore, the total equivalent strain that occurs in the sample during the whole shock process can be described by

$$\varepsilon_{eq} = 2 \times \frac{2}{3} \varepsilon_x = \frac{4}{3} \ln \frac{V}{V_0} \tag{5.95}$$

This is a transitory strain and this definition has been used by a number of researchers, e.g., (Murr et al., 1997, Sencer et al., 2005, Ameri et al., 2021). Now from the conservation equations across a shock front, we know that,

$$\frac{V}{V_0} = \frac{U_s - u_p}{U_s} = 1 - \frac{u_p}{U_s} \tag{5.96}$$

And noting that $U_s = c_0 + S u_p$ we can define the transitory equivalent strain as:

$$\varepsilon_{eq} = \frac{4}{3} \ln \left(1 - \frac{u_p}{c_0 + S u_p} \right) \tag{5.97}$$

where u_p is the maximum particle velocity derived from a free-surface velocity trace.

5.8.5 SPALL IN SHOCKED MATERIALS

The spall behaviour of materials has been studied for decades due to the fact that it is useful to be able to predict when materials fail due to spall. Furthermore, it is found that many weapons systems are designed to create spall failures in materials, and the

HESH round is one such example. Spall is, in essence, a dynamic tensile fracture, and many armour materials are susceptible to spall mainly because of their hard brittle nature.

Grady (1988) has provided a route to predict the spall strength based on readily available material properties and parameters. For brittle spall, Grady deduced that

$$P_s = \left(3\rho_0 c_0 K_c^2 \dot{\varepsilon}\right)^{\frac{1}{3}}$$

(5.98)

whereas for ductile spall,

$$P_s = \left(2\rho_0 c_0^2 Y_0 \varepsilon_f\right)^{\frac{1}{2}}$$

(5.99)

where ρ_0 is the density, c_0 is the bulk sound speed, K_c is the fracture toughness, Y_0 is yield strength, $\dot{\varepsilon}$ is strain rate, and ε_f is failure strain.

For ductile spall, Rosenberg (1987) proposed an alternative predictive approach based on cavity expansion theory. By simply applying Hill's cavity expansion theory to spall from 1D plate-impact experiments, he deduced that

$$P_s = \frac{2}{3} Y_0 \left[2 + \ln\left\{ \frac{E}{2(1-v)Y_0} \right\} \right]$$

(5.100)

The resisting force to cavity expansion is best reproduced by adopting the dynamic yield strength for the material calculated from the HEL. Thus, Y_0 can be replaced by the von Mises equivalent stress, Y in the above equation.

In a plate-impact setup, it is useful to initiate spall in the centre of the target. This is achieved by carrying out a symmetrical impact with identical materials, as shown in Figure 5.26. At time 1, the elastic wave arrives prior to the plastic compression front, which arrives at time 2. The elastic wave is travelling at the longitudinal wave
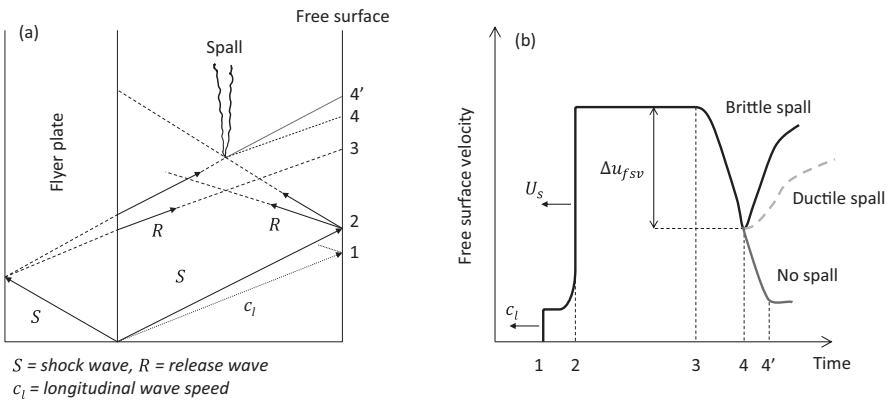
FIGURE 5.26   Schematic of spall initiation showing (a) a simplified wave path in an x-t diagram form, and (b) the free-surface velocity response.

velocity (c_l), whereas the plastic compression front is travelling at the shock velocity, U_s. At the free surface of the target, the shock (S) is reduced by a release wave (R) that propagates back into the target towards the impact surface. Equally, a release wave emanates from the rear free surface of the flyer plate. When release waves emanating from the rear surfaces of the flyer and the target collide, a complex state of tensile stress forms. If the generated stress exceeds the material spall strength, spall (or spallation) occurs. The existence of the spall plane, which is a new free surface within the sample, causes new reflections. The arrival of these reflections at the target free surface occurs at time 4. The rise of the signal after time 4 may elucidate the failure mechanics. Generally speaking, a steep rise from the minimum is indicative of a brittle failure process, whereas a more gradual recovery rate indicates a more ductile failure (Chen et al., 2006). A good review of spall behaviour is given by Antoun et al. (2003).

When the target material is strong enough to withstand the generated tensile stress, no spall will occur. This results in a further release of the shock state within the target and so the free surface velocity value will continue to diminish (see time 4' in Figure 5.26b). Theoretically, this would be expected to reach zero providing a shock trace similar to Figure 5.11. However, this is rarely the case and the arrival of release waves from the periphery of the sample interferes with this process resulting in non-zero values of free surface velocities (see also Figure 5.27). Ringing of the wave backwards and forwards through the thickness of the specimen would also be expected, as shown in Figure 5.27.

It is important to remember that the data for spall strengths are measured using plate-impact experiments either by directly measuring the free-surface velocity of the rear surface or by using manganin gauges trapped between the sample and (typically) some low-density polymer (usually PMMA). The free-surface velocity method is the most common method where free-surface velocity measurements are
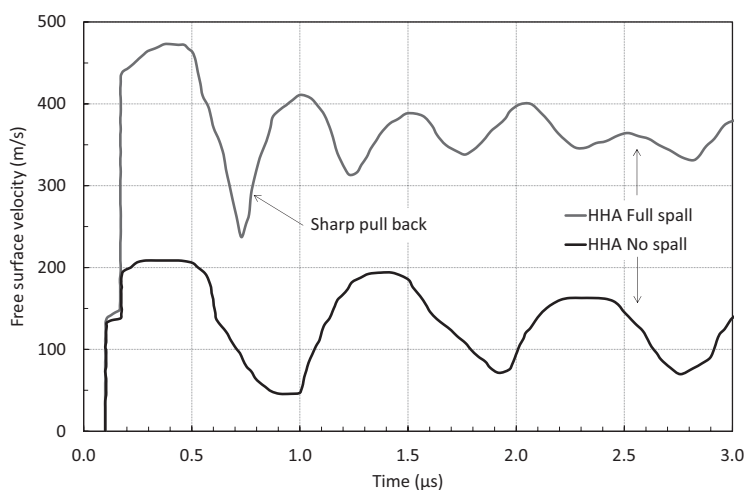
FIGURE 5.27 Spall behaviour of a high hardness armour (HHA) steel for two different shock stress values. (Adapted from the original data presented by Wang et al., 2020.)

made using a laser-based system (usually a velocity interferometer system for any reflector [VISAR]), and the spall strength, σ_{sp}, is calculated as follows:

$$\sigma_{sp} = \frac{1}{2}\rho_0 c_0 \Delta u_{fsv} \tag{5.101}$$

where Δu_{fsv} is the free-surface velocity drop in the sample (see Figure 5.26b), and c_0 is the bulk sound speed in the sample.

Occasionally, spall strength is calculated using the following equation that adds a small correction to the free-surface velocity measurement (Antoun et al., 2003):

$$\sigma_{sp} = \frac{1}{2}\rho_0 c_0 \left(\Delta u_{fsv} + \delta\right) \tag{5.102}$$

where

$$\delta = \left(\frac{x}{c_b} - \frac{x}{c_l}\right)\frac{|\dot{u}_1\dot{u}_2|}{|\dot{u}_1| + \dot{u}_2} \tag{5.103}$$

where x is the spall position, $\dot{u}_1$ is the gradient of the velocity curve into the spall dip and $\dot{u}_2$ is the gradient out of the spall dip. Delta $\left(\delta\right)$ is the correction to the free-surface velocity and added to correct for using a surface measurement to quantify an internal failure process. Strictly, however, the term 'spall strength' is not a failure threshold per se because it is not a constant for a given material and is affected by the loading parameters (peak stress, pulse duration, release strain rate), the material's microstructure and the profile of tensile stresses generated due to the collision of release waves (Kanel, 2019, Ameri et al., 2022). Nevertheless, the term has been widely adopted in the literature.

Another important parameter in the assessment of spall response is the strain rate of decompression. This is given as follows:

$$\dot{\varepsilon} \cong \frac{1}{2c_0}\frac{du}{dt} \tag{5.104}$$

where du/dt is the slope of the release wave immediately following the peak velocity, i.e. the slope of the part between times 3 and 4 in Figure 5.26b. It is important to note that this is an approximation, although widely used.

An example of spall experiments on armour-grade materials has been presented by (Wang et al., 2020). They used a photo doppler velocimeter (PDV) system that shone a 1550 nm laser onto the back surface of the target to track the free surface velocity. Using the flyer-plate technique, impact tests were conducted at three different velocities that resulted in three outcomes: no damage, incipient spall damage, and (nearly)[2] full spall. Two of the results (full spall and no spall) are shown in Figure 5.27. Incipient spall experiments are often carried out as they can help in the understanding of spalling mechanisms during the early stages of damage ('incipient' = beginning to happen). No spall is indicative of the absence of post-mortem damage in the
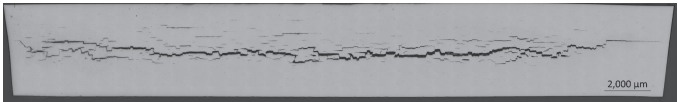
FIGURE 5.28   Sectioned post-shocked sample of an ultra-high hardness steel that has been subjected to a shock using the flyer-plate technique causing a brittle fracture in the steel. This was caused by a steel flyer-plate impacting the target at 320 m/s.

specimen and is generally characterized by a broad trough following the peak stress in the free surface velocity trace (see Figure 5.27). This is caused by the wave reflecting from the front surface of the specimen as opposed to the damage zone. Full spall is indicated by material separation and pull back. 'ringing' behind the peak stress as the shock is trapped in-between the damage zone and the rear surface. As mentioned previously, a sharp pull-back is indicative of brittle spall fracture (which is a quick failure mode) whereas a 'more lazy' rise pull-back signal indicates ductile spall damage (which requires time to take place). An example of a (nearly) fully spalled target recovered after these types of experiments is shown in Figure 5.28.

Some evaluated spall strengths for a selection of armour-grade materials are shown in Table 5.5.

For amour-grade material alloys, the interesting properties are those that lie perpendicular to the rolling direction of the plate. This is known as the short-transverse direction. The reason for this is that a projectile is likely to penetrate in the

TABLE 5.5

Quasi-Static and Tensile Spall Data for Some Armour-Grade Alloys

Reference	Alloy	ρ_0 (g/cc)	c_o (mm/μs)	ε_f	Y_0 (GPa)	Measured Spall Strength (GPa)
Boteler and Dandekar (2006, 2007)	AA 5083-H131	2.668	5.360	0.09	0.240	0.94
Whelchel et al. (2014)	AA 5083-H321 (long)	2.668	5.31	–	–	1.06
	AA 5083-H321 (long transverse)	2.668	5.32	–	–	1.01
	AA 5083-H321 (short transverse)	2.668	5.17	–	–	1.07
Hazell et al. (2014)	AA 7010-T7651 (long)	2.810	5.329	0.16	0.464	1.61
	AA 7010-T7651 (short transverse)	2.810	5.314	0.08	0.426	1.20
Millett et al. (2004)	AA 7017 (peak aged)	2.740	5.211	0.05	0.402	0.63
Wang et al. (2020)	Improved Rolled Homogeneous Armour	7.840	4.57	0.125	1.000	3.6
	High Hardness Armour	7.840	4.57	0.123	1.200	4.3
Nähme and Lach (1997)	Mars 190	7.840	–	–	1.150	3.1–4.5
	Mars 240	7.840	–	–	1.725	3.4–5.9
	Mars 300	7.840	–	–	2.250	5.7–6.2

short-transverse direction due to the way the plate would be offered up as armour. And, usually, it is in the short-transverse direction that the plate is more brittle.

5.9 INTERPRETING FREE-SURFACE VELOCITY SHOCK DATA FROM FLYER-PLATE TESTS

As we have previously seen flyer-plate tests are carried out in conjunction with free-surface velocity measurement techniques to assess the shock conditions in the target. This is often the preferred method used to study shock waves as the technique is non-invasive. Therefore, as we close this chapter, it is perhaps prudent to summarize the important equations that we have seen thus far. These are shown in Table 5.6.

5.10 SUMMARY

We have seen during dynamic loading that it is not just a simple case of examining the plastic deformation of the sample or the penetration of the material by the projectile. Much of these effects are governed by wave dynamics. Stress waves and shock waves are particularly important as ultimately, they can kill you. This is particularly true where spall is seen occurring in materials. This can lead to the separation of the material and fragments carried along by inertia.

This chapter started by reviewing elastic wave transmission and reflection, and there is a lot you can do in the design of an armour structure by knowing the physics of wave transmission and reflection. We have seen that when a wave transmits its way through a high-impedance plate that is joined to a low-impedance plate, tensile waves emanate from the interface. This can be damaging to the armour structure if

---

TABLE 5.6

Important Equations for Interpreting Shock Information from Free-Surface Velocity Measurements (u_{fsv}) Acquired during a Flyer-Plate Test

Purpose	Equation
To calculate the particle velocity, u_{p}	$u_{\mathrm{p}} = \dfrac{1}{2} u_{\mathrm{fsv}}$
To calculate the HEL stress, σ_{HEL}	$\sigma_{\mathrm{HEL}} = \dfrac{1}{2} \rho_0 c_1 u_{\mathrm{fsv}}$
To calculate the peak (Hugoniot) shock stress, σ_{x}	$\sigma_{\mathrm{x}} = \rho_0 U_{\mathrm{s}} u_{\mathrm{p}}$ where $U_{\mathrm{s}} = c_0 + S u_{\mathrm{p}}$
To calculate the spall strength, σ_{sp}	$\sigma_{\mathrm{sp}} = \dfrac{1}{2} \rho_0 c_0 \Delta u_{\mathrm{fsv}}$, or $\sigma_{\mathrm{sp}} = \dfrac{1}{2} \rho_0 c_0 \left(\Delta u_{\mathrm{fsv}} + \delta \right)$
To calculate the *approximate* tensile strain rate (from the slope of the release wave)	$\dot{\varepsilon} \cong \dfrac{1}{2c_0} \dfrac{du}{dt}$
To calculate the uniaxial engineering strain during shock, e_{x}	$e_{\mathrm{x}} = 1 - \dfrac{V}{V_0} = -\dfrac{u_{\mathrm{fsv}}}{2\left(c_0 + 0.5 \times S u_{\mathrm{fsv}}\right)}$
To calculate the transitory equivalent strain in the specimen, $\varepsilon_{\mathrm{eq}}$	$\varepsilon_{\mathrm{eq}} = \dfrac{4}{3} \ln\left(1 - \dfrac{u_{\mathrm{fsv}}}{2\left(c_0 + 0.5 \times S u_{\mathrm{fsv}}\right)}\right)$

the high-impedance plate is brittle. Conversely, if a wave propagates through a low-impedance plate joined to a high-impedance plate, then it is seen that compression waves are reflected back into the front plate. This can be helpful—particularly if we are trying to suppress damage in brittle materials such as ceramics.

We have seen too that enormous stresses in materials can be generated in the laboratory by virtue of loading a material in 1D strain. This allows us to interrogate materials as they are compressed to extremes and thereby provides insight into the properties of the materials deep inside the Earth's crust. These types of tests also reveal the dynamic behaviour of materials that would be shocked because they are overdriven by a penetrating projectile, such as a shaped charge jet.

There is still much to study regarding wave dynamics, and there are numerous papers on the subject. This chapter has only skimmed the surface.

NOTES

1 Inspired by a similar problem in Smith and Hetherington (1994).
2 The term 'nearly' has been used here as strictly the material has not undergone full spall as complete material separation is not evident.

REFERENCES

Ahrens, T. J. 1993. Equation of state. *In:* Asay, J. R. & Shahinpoor, M. (eds.) *High-Pressure Shock Compression of Solids*. New York: Springer.

Ameri, A., Wang, H., Li, Z., Quadir, Z., Gonzalez, M., Hazell, P. J. & Escobedo-Diaz, J. P. 2022. Spall strength dependence on peak stress and deformation history in Lean Duplex Stainless Steel 2101. *Materials Science and Engineering: A*, 831, 142158.

Ameri, A., Wang, H., Li, Z., Quadir, Z., Rickard, W. D. A., Gonzalez, M., Hazell, P. J. & Escobedo-Diaz, J. P. 2021. Ferrite phase transformation in dual-phase steel under shock loading. *Materials Science and Engineering A*, 802, 140690.

Antoun, T., Seaman, L., Curran, D. R., Kanel, G. I., Razorenov, S. V. & Utkin, A. V. 2003. Spall fracture. *In:* Davison, L. & Horie, Y. (eds.) *High-Pressure Shock Compression of Condensed Matter*. New York: Springer.

Appleby-Thomas, G. J., Hazell, P. J., Wilgeroth, J. M. & Wood, D. C. 2010. On the interpretation of lateral manganin gauge stress measurements in polymers. *Journal of Applied Physics*, 108(3), 033524.

Boteler, J. M. & Dandekar, D. P. 2006. Dynamic response of two strain-hardened aluminum alloys. *Journal of Applied Physics*, 100 (5), 054902.

Boteler, J. M. & Dandekar, D. P. 2007. Dynamic response of 5083-H131 aluminum alloy. *In:* Elert, M., Furnish, M. D., Chau, R., Holmes, N. & Nguyen, J. (eds.). *Shock Compression of Condensed Matter – 2007: Proceedings of the Conference of the American Physical Society Topical Group on Shock Compression of Condensed Matter*. Waikoloa; Melville, NY: American Institute of Physics.

Carter, W. J. & Marsh, S. P. 1995. *Hugoniot Equation of State of Polymers*. Los Alamos, NM: Los Alamos National Laboratory.

Chapman, D. J., Braithwaite, C. H. & Proud, W. G. 2009. The response of Dyneema to shock-loading. *AIP Conference Proceedings*, 1195, 1269–1272.

Chen, X., Asay, J. R., Dwivedi, S. K. & Field, D. P. 2006. Spall behavior of aluminum with varying microstructures. *Journal of Applied Physics*, 99(2), 023528.

Dandekar, D. P. & Bartkowski, P. 1994. Shock response of AD995 alumina. *In:* Schmidt, S. C., Shaner, J. W., Samara, G. A. & Ross, M. (eds.). *High Pressure Science and Technology – 1993*. Colorado Springs, CO; Melville, NY: American Institute of Physics.

Dandekar, D. P. & Benfanti, D. C. 1993. Strength of titanium diboride under shock wave loading. *Journal of Applied Physics*, 73(2), 673–679.

Davison, L. 2008. *Fundamentals of Shock Wave Propagation in Solids*, Leipzig: Springer.

Davison, L. & Graham, R. A. 1979. Shock compression of solids. *Physics Reports*, 55(4), 255–379.

Dowling, N. E. 2013 *Mechanical Behavior of Materials: Engineering Methods for Deformation, Fracture, and Fatigue*. Harlow: Pearson.

Grady, D. E. 1988. The spall strength of condensed matter. *Journal of the Mechanics and Physics of Solids*, 36(3), 353–384.

Gust, W. H. & Royce, E. B. 1970. *Dynamic Yield Strengths of Light Armor Materials*. Livermore, CA: Lawrence Radiation Laboratory.

Hazell, P. J., Appleby-Thomas, G. J., Trinquant, X. & Chapman, D. J. 2011. In-fiber shock propagation in Dyneema®. *Journal of Applied Physics*, 110(4), 043504.

Hazell, P. J., Appleby-Thomas, G. J., Wielewski, E., Stennett, C. & Siviour, C. 2012. The influence of microstructure on the shock and spall behaviour of the magnesium alloy, Elektron 675. *Acta Materialia*, 60(17), 6042–6050.

Hazell, P. J., Appleby-Thomas, G. J., Wood, D. C. & Painter, J. D. 2014. The shock and spall response of AA 7010-T7651. *Journal of Physics: Conference Series*, 500(11), 112032.

Jones, O. E. 1973. Shock wave mechanics. *In:* Rohde, R. W., Butcher, B. M., Holland, J. R. & Karnes, C. H. (eds.) *Metallurgical Effects at High Strain Rates*. Boston, MA: Springer US.

Kader, M. A., Islam, M. A., Hazell, P. J., Escobedo, J. P., Saadatfar, M. & Brown, A. D. 2017. Numerical modelling of closed-cell aluminium foams under shock loading. In*: AIP Conference Proceedings* 1793, 120028 Melville, NY: American Institute of Physics.

Kanel, G. I. 2019. *Shock Waves in Solid State Physics*. Boco Raton, FL: CRC Press.

Marsh, S. P. 1980. *LASL Shock Hugoniot Data, Los Alamos Series on Dynamic Material Properties*. Berkeley: University of California Press.

McQueen, R. G., Marsh, S. P., Taylor, J. W., Fritz, J. N. & Carter, W. J. 1970. Chapter VII: The equation of state of solids from shock wave studies. In: Kinslow, R. (ed.) *High-Velocity Impact Phenomena*, pp. 293–417. New York: Academic Press.

Meyers, M. A. 1994. *Dynamic Behaviour of Materials*. New York: John Wiley & Sons, Inc.

Millett, J. C. F., Bourne, N. K. & Edwards, M. R. 2004. The effect of heat treatment on the shock induced mechanical properties of the aluminium alloy, 7017. *Scripta Materialia*, 51(10), 967–971.

Murr, L. E., Meyers, M. A., Niou, C. S., Chen, Y. J., Pappu, S. & Kennedy, C. 1997. Shock-induced deformation twinning in tantalum. Acta Materialia, 45, 157–175.

Nahme, H. & Lach, E. 1997. Dynamic behavior of high strength armor steels. *Le Journal de Physique IV*, 7(3), C3-373–C3-378.

Porter, D. & Gould, P. J. 2006. A general equation of state for polymeric materials. *Journal De Physique IV*, 134, 373–378.

Rosenberg, Z. 1987. Accounting for the spall strength of ductile metals by spherical cavity expansion analysis. *Materials Science and Engineering*, 93, L17–L20.

Ruoff, A. L. 1967. Linear shock-velocity-particle-velocity relationship. *Journal of Applied Physics*, 38(13), 4976–4980.

Sencer, B. H., Maloy, S. A. & Gray III, G. T. 2005. The influence of shock-pulse shape on the structure/property behavior of copper and 316 L austenitic stainless steel. *Acta Materialia*, 53, 3293–3303.

Skidmore, I. C. 1965. An introduction to shock waves in solids. *Applied Materials Research*, 4, 131–147.

Smith, P. D. & Hetherington, J. G. 1994. *Blast and Ballistic Loading of Structures*. Trowbridge, England: Butterworth-Heinemann.

Wang, H., Higgs, S., Ameri, A., Gonzales, M., Mcdonald, B., Hazell, P. J., Li, Z. & Escobedo-Diaz, J. P. 2020. Spall fracture of two high strength armor steels. *In: AIP Conference Proceedings* 2272, 120031. Melville, NY: American Institute of Physics.

Whelchel, R. L., Thadhani, N. N., Sanders, T. H., Kecskes, L. J. & Williams, C. L. 2014. Spall properties of Al 5083 plate fabricated using equi-channel angular pressing (ECAP) and rolling. *Journal of Physics: Conference Series*, 500(11), 112066.

Winter, R. E. & Harris, E. J. 2008. Simulations of embedded lateral stress gauge profiles in shocked targets. *Journal of Physics D: Applied Physics*, 41(3), 035503.

Winter, R. E., Owen, G. D. & Harris, E. J. 2008. Experimental measurement of stress perturbations caused by lateral gauges. *Journal of Physics D: Applied Physics*, 41(20), 202006.

Yuan, G., Feng, R. & Gupta, Y. M. 2001. Compression and shear wave measurements to characterize the shocked state in silicon carbide. *Journal of Applied Physics*, 89(10), 5372–5380.

6 Computational Methods for Armour Design

Computational methods have now become a standard and a well-established methodology for engineering design projects. In ballistics, we use computational modelling for a number of benefits. These are as follows:

1. We can use it as a tool to understand the physics of dynamic events. That is, computational models can inform the physics of the interaction between projectiles and targets, for example.
2. We can also use computational approaches to look at forces, pressures, stresses and strains in objects that have been dynamically loaded. This can help in informing the armour design process.
3. We can use computational models to explore how structures collapse. In particular, we can examine the ways in which porous materials collapse during dynamic loading events.

Furthermore, it goes without saying that many of the academic papers that you read nowadays have a focus on computational techniques. It is now almost unheard of for engineers to avoid computer programs to solve penetration problems and so it is appropriate that we examine computational methods here.

6.1 HYDROCODES

Some of the early computer codes that were used extensively for studying collisions were called 'hydrocodes', and for good reason. We have already seen in Chapter 4 that fluid behaviour is invoked when the impact velocities are high. Further, we have seen in Chapter 5 that for very high-pressure shock waves we can assume hydrodynamic behaviour. This flows from the observation that under uniaxial strain, it has been noted that:

$$\sigma_x = P + \frac{4}{3}\tau \qquad (6.1)$$

That is, the applied load (σ_x) is carried by the hydrostatic pressure (P) and in part by its resistance to shear (τ). Therefore, it is reasonable to assume that if the pressure is very large, one can ignore material strength and $\sigma_x \cong P$. Therefore, 'hydro' behaviour is observed.

Early codes that relied on purely hydrodynamic calculations were called 'hydrocodes'. These were used in early studies of planetary impacts, hypervelocity impact and penetration of satellite shielding, nuclear explosions, and shaped-charge

penetration. However, it was not very long before strength models and failure models were integrated into these codes. Nevertheless, the term 'hydrocode' largely stuck.

The mechanism of how these codes work can be briefly described as follows: Generally speaking, these codes solve the conservation laws of mass and momentum based on initial boundary conditions. The user is prompted for an equation of state that describes the pressure in terms of the internal energy and volume and a constitutive relationship that calculates the flow stress in terms of a number of material-dependent parameters, including strain, strain rate and temperature. Failure models can be introduced to describe the failure.

6.2 THE CONUNDRUM OF MATERIAL FAILURE

One of the largest challenges that still exists with computational techniques is to provide an exact methodology to correctly account for material failure. Why? Well, most computer codes rely on a continuum discretization of the materials where the geometry is replicated by numerous repeated cells or computational zones. An example of this is shown in Figure 6.1. At locations within these zones, there are points or nodes where the mass of that localized zone is recorded in an array. The mass, density, stiffness, yield strength and other material parameters are recorded at these nodes and entered beforehand by the user. However, material failure occurs at the microstructural level where length scales of typically a few microns are relevant. In fact, failure will often *originate* at the sub-micron scale. No computer can adequately account for this level of complexity and the nuances of changes that occur in the properties of the material at the micro-level without enormous amounts of processing power
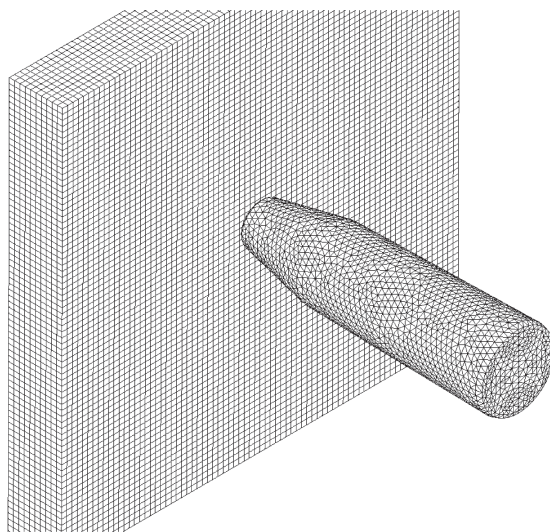
FIGURE 6.1   A finite element mesh showing a projectile about to strike a plate.

and memory. And therefore, most continuum codes are essentially an approximation for the bulk of the material. These can adequately predict the elasticity, strength and pressure–volume characteristics of the material but they often fall short when addressing material failure. This is all the more compounded by the fact that modelling separation in continuum codes is problematic. Nevertheless, advances have been made in recent years and we will discuss these in this chapter.

It is important to note that there is no *specific* requirement to be wed to a particular element shape and in fact triangular, quadrilateral, tetrahedral and cubic elements are commonly used. Without the risk of getting too mathematical, all codes will work on a computational cycle. There are plenty of engineering texts out there that cover the mathematics of finite element/finite difference approaches, and the reader is recommended to consult them for background, e.g. Khennane (2013), Zukas (1990), Zukas (2004) and Hiermaier (2008b).

Most structural problems are carried out using Lagrangian approaches. With a Lagrangian description, the mesh points are fixed to the material and move with the local material velocity. Thus, it is straightforward to track material boundaries as they are defined by the external limits of the mesh. The mass of each cell remains constant however individual cells will compress and expand in volume as the density changes (due to shock compression, for example).

With Eulerian descriptions, on the other hand, velocity, pressure, density etc., are computed at fixed points in a mesh (= nodes). All of the nodes, in this case, remain stationary, however, mass, momentum and energy flow across the cell boundaries. The quantities of flow into and out of the cell are used to calculate the new cell properties. The advantage of this technique is that large deformations can be accommodated and therefore it is commonly used to simulate fluid behaviour and gas dynamics that arise from explosions and the like.

6.3   THE COMPUTATIONAL CYCLE

We can start by looking at what we call the computational cycle. A computational cycle is a common approach for progressing the calculation and is based on an explicit approach. That is, the solution is calculated exactly by the integration of variables by a time-step. Time-steps are generally small packets of time (e.g. 1×10^{-9} s) and generally change for each cycle. Typically, a Lagrangian computation will progress as follows:

1. A cell, which is part of a discretized shape, such as a bullet, is assigned a velocity. The velocities variables are assigned to the nodes. Also recorded are variables associated with the physical and mechanical properties of the material associated with the cell. These variables are stored and updated as the simulation progresses.
2. At the nodes we record global variables. So, we record displacement, compression, the force acting on the cell and so on.
3. At the start of the cycle, the nodal velocities are integrated in time to get the new nodal positions.

4. Once the new nodal positions have been established, we can assess how much the cell has been compressed or stretched (i.e. the cell's strain and strain rate).
5. From this we can deduce the stresses, from the constitutive models (see later) and from the stresses, we can deduce the force on the cell.
6. Once we have the force on the cell (which can be supplemented with boundary forces), we can calculate the acceleration from Newton's second law of motion).
7. The acceleration is integrated to find the new velocities and then the whole process repeats.

6.4   ARTIFICIAL VISCOSITY

One of the many challenges of simulating shock waves in continuum codes is dealing with the fact that, as we have seen in Chapter 5, shock waves are sharp discontinuities. That is, in nature, they are incredibly thin. The solution to this problem is to imply 'smear' the shock wave over several mesh widths so that we are no longer dealing with a steep discontinuity but rather a stress gradient. This is achieved with artificial viscosity and good overviews are provided by Hiermaier (2008b) and Campbell and Vignjevic (2009).

The concept of artificial viscosity was first introduced by Neumann and Richtmyer (1950). The original form of the von Neumann constant, q, for one-dimensional flow (Campbell and Vignjevic, 2009), was:

$$q = -\rho(c_2\Delta x)^2 \frac{\partial v}{\partial x}\left|\frac{\partial v}{\partial x}\right| \tag{6.2}$$

x is the coordinate in the direction of motion of the mesh, Δx is the mesh spacing, ρ is the density of the shocked material, and c_2 is a dimensionless constant ≈ 2. This equation alone was found to be not ideal in that oscillations that arose behind the shock were only slowly damped out. Later, a linear term was added by Landshoff (1955) to compensate for this problem. Therefore, the revised term comprised of a linear term and a quadratic term, viz:

$$q = -\rho c_1 \Delta x c\left|\frac{\partial v}{\partial x}\right| - \rho(c_2\Delta x)^2 \frac{\partial v}{\partial x}\left|\frac{\partial v}{\partial x}\right| \tag{6.3}$$

In this case, c is the local speed of sound (which, for 3D formulations $=c_0$), the constants c_1 and c_2 are defined by the user. The term c_1 is usually set to between 0.05 and 0.5 and the term $c_2 \approx 2$ (Zukas, 2004). However, the default values used in LS-DYNA are $c_1 = 0.06$ and $c_2 = 1.50$ as these have shown to offer a good balance between shock thickness and oscillations behind the shock for a wide range of scenarios (Campbell and Vignjevic, 2009). Users of commercial codes are generally afforded the opportunity to modify the default values however this is rarely done. A schematic showing the effect of artificial viscosity is shown in Figure 6.2 (including the LS-DYNA example).
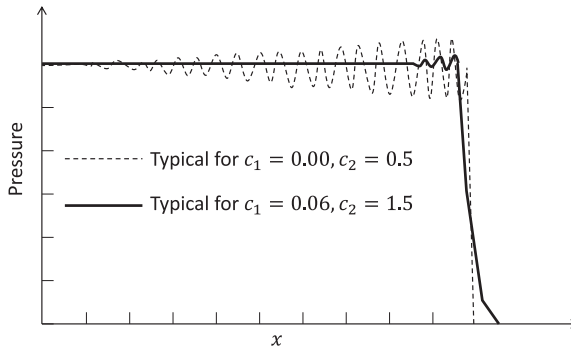
FIGURE 6.2 Shock profile for a 1D calculation showing the effect of varying the coefficients c_1 and c_2 on the shock profile.

6.5 TIME INTEGRATION

Hydrocodes operate by a process of integration with respect to a very short period of time. This time period is referred to as the 'time step', Δt. This is probably the most efficient way of arriving at a solution for a transient problem. As we discussed previously, the problem starts with knowing a set of initial conditions (at $t = t_0$), which includes velocities and positions. Integrating the velocities with respect to Δt provides for cell displacement values. However, the choice of Δt is important as if it is too small the simulation may not be optimized; if the Δt is too large then there is a danger that the mesh becomes unstable as a cell becomes degenerate. This happens when a node is displaced too far (due to a large time-step). Typically, the time-step can be calculated according to

$$\Delta t = \frac{kl}{c} \tag{6.4}$$

where l is a characteristic length of the cell, c is the local sound speed and k is a stability fraction of the order of 0.6–0.9 (Zukas, 2004). It is clear from this equation that as the cells become highly compressed the time step reduces and therefore the run-time increases. The time-step is also determined by the local elastic properties of the materials being simulated (i.e. controlled by the sound speed).

6.6 EROSION

The compression of cells in Lagrange formulations can cause simulations to grind to a halt due to the much-reduced time-step. Furthermore, occasionally it is possible for numerical instabilities to occur that lead to degeneration of cells and unphysical properties (such as negative density, for example). Therefore, it is sometimes advantageous to erode the offending cell(s) to allow the simulation to run to completion. This is usually a simple process of 'deletion' of the cell, with the option of averaging the mass and momentum to the neighbouring nodes. The criterion for deletion is usually determined by an equivalent strain value that is ideally set to a very large value
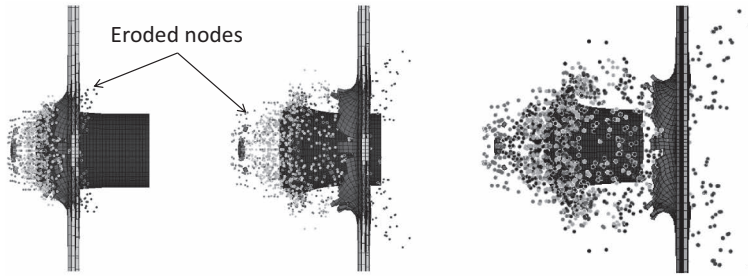
FIGURE 6.3 Penetration of an ultra-high-molecular-weight polyethylene target by a poly-carbonate projectile travelling at 2.1 km/s. Cells are eroded via an equivalent strain criterion whilst retaining inertia. The dots indicate eroded cells. (Adapted from Austin et al., 2017.)

(e.g. 200%). Large values allow for the cell to fail via the failure model prior to erosion, which is desirable. Figure 6.3 shows an example of a Lagrange simulation with very clear evidence of cell erosion (denoted by the dots). Erosion of the cells, in this case, allowed the simulation to run to completion.

Much of the problems associated with erosion can be avoided by using Euler or meshless methods such as smooth particle hydrodynamics (SPH). SPH has the ability to simulate large deformations such as the case when a ductile projectile penetrates an armour target. It is also a technique that has been extensively used to simulate material separation, as would be expected during the impact of brittle targets such as ceramic and during hypervelocity collisions (Hiermaier, 2008b).

6.7 MATERIAL MODELS

Computational models require data on the specific materials that are to be studied. These material models will tell the computer how that material responds to stress and temperature, for example. As we have seen, many materials exhibit a behavioural change when the conditions of pressure, temperature or strain rate are changed; material models (or, constitutive models) are designed to capture those changes.

6.7.1 THE EQUATION OF STATE

Equations of state are an important part of the computational setup and put simply, these define the relationship between pressure, density and internal energy (or temperature), viz:

$$P = fn(\rho, T) \tag{6.5}$$

6.7.1.1 Simple Linear Equation of State

The simplest equation of state is an isothermal Hugoniot, the nature of which we discussed in Chapter 5. Some codes will even allow the user to define a simple linear relationship between pressure and compression, the gradient of which is defined by
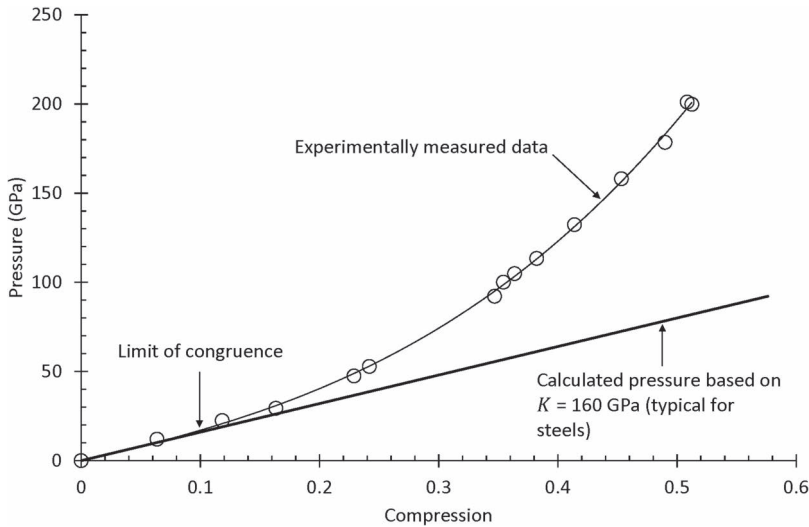
FIGURE 6.4 Experimentally derived Hugoniot for Viscomax 250 maraging steel ($\rho_0 = 8129 \, \text{kg/m}^3$) vs calculated linear Hugoniot assuming $K = 160 \, \text{GPa}$ (typical for steels). (Data from Marsh, 1980.)

the bulk modulus (K), providing an elastic response. This is to approximate the shape of the Hugoniot in the pressure–compression space. And therefore,

$$P = K\mu \tag{6.6}$$

where,

$$\mu = \frac{\rho}{\rho_0} - 1 = \frac{V_0}{V} - 1 \tag{6.7}$$

Where ρ is the density and V is the specific volume, $V = 1/\rho$. The subscript '0' refers to the initial condition.

This equation, however, can only be used for small compressions as the following example shows. Figure 6.4 shows the experimentally derived Hugoniot for Viscomax 250 maraging steel ($\rho_0 = 8129 \, \text{kg/m}^3$). There is a best-fit polynomial relationship that follows according to:

$$P = 153.7\mu + 98.2\mu^2 + 715.8\mu^3. \tag{6.8}$$

Also plotted is the linear calculation $(P = K\mu)$ assuming $K = 160 \, \text{GPa}$. You will see that the limit of congruence occurs at around $\mu = 0.1$ ($P = 16 \, \text{GPa}$) and therefore implies that the simple linear approach is only suitable for relatively small compressions. Around 6% error could be expected in the calculations of pressure for this material up to $\mu = 0.1$. For most ballistic applications, where the velocity of impact is only a few hundred metres-per-second and therefore the anticipated shock pressures

are low, this may be adequate. Where higher shock pressures are expected, then clearly a more complex non-linear Hugoniot is preferred.

This simple approach was used for some early damage models with ceramics as it was relatively straightforward to degrade the bulk modulus (and thus, the pressure) as damage ensued e.g. see Hazell and Iremonger (1997).

6.7.1.2   Polynomial Equation of State

If there is a requirement for a more complex relationship due to higher shock pressures then a polynomial Hugoniot relationship can be used, according to:

$$P = A\mu + B\mu^2 + C\mu^3 \tag{6.9}$$

This is frequently used with a Mie–Grüneisen equation of state.

6.7.1.3   Mie–Grüneisen Equation of State

With this equation of state, we can now integrate the effects of temperature on the pressure–volume response of the material. Each material will have its own unique equation of state in pressure, volume and temperature space thereby resulting in a 3D surface.

Recall that a Hugoniot, in linear shock, particle velocity space is defined as:

$$U_s = c_0 + S u_p \tag{6.10}$$

where U_s is the shock velocity, u_p is the particle velocity and c_0 and S are the bulk sound speed and shock parameter, respectively.

You will recall from Chapter 5 that it is possible to plot a Hugoniot in different ways. Using the Rankine–Hugoniot relationships, we can derive a Hugoniot in pressure–volume ($P_h(V)$) and energy–volume ($e_h(V)$) planes according to the following equations:

$$P_h(V) = \frac{c_0^2(V_0 - V)}{\left(V_0 - S(V_0 - V)\right)^2} \tag{6.11}$$

$$e_h(V) = \frac{1}{2}\frac{c_0^2(V_0 - V)^2}{\left(V_0 - S(V_0 - V)\right)^2} \tag{6.12}$$

Again, where V is the specific volume ($=1/\rho$) and the subscript '0' indicates the initial condition. That is, $V_0 = 1/\rho_0$.

Armed with this knowledge we can now write down the general form of the Mie–Grüneisen equation of state, viz.

$$P - P_h(V) = \frac{\Gamma(V)}{V}\left(e - e_h(V)\right) \tag{6.13}$$

Where v, $P_h(V)$ and $e_h(V)$ are defined above, P is the pressure and e the internal energy. The term $\Gamma(V)$ is the Mie–Grüneisen constant (= Gamma). This equation
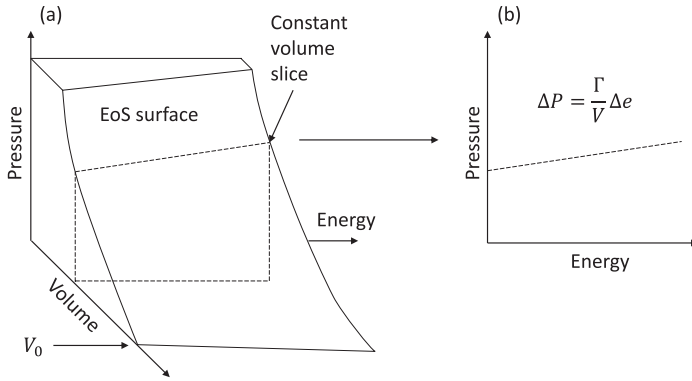
FIGURE 6.5 (a) The Mie–Grüneisen equation of state surface and (b) the view through the pressure-energy plane showing the role of Gamma.

defines the equation of state surface. With knowledge of $\Gamma(V)$, and a well-defined Hugoniot in the shock velocity-particle velocity plane, it is possible to define a surface in terms of P, e, and V.

The best way to understand the Mie–Grüneisen equation of state is to consider Figure 6.5. On the left-hand side, (a), the equation of state surface is plotted in terms of P, e, and V. Note that V_0 is indicated and gets larger as e increases (that is, the material expands as the temperature increases for $P=0$). Also indicated is a slice of constant volume (dashed line). Examining the 'top' of that slice in the $P - e$ plane (Figure 6.5b), you can see that the gradient of that line is defined by Γ/V and therefore what Gamma does is allow us to transform the reference Hugoniot line ($P_h(V)$) into a surface.

From the Mie–Grüneisen equation of state, it is clear that

$$dP = \frac{\Gamma(V)}{V} dE \tag{6.14}$$

and so, using the Chain rule,

$$\Gamma = V\left(\frac{\partial P}{\partial E}\right)_V = V\left(\frac{\partial P}{\partial T}\right)_V\left(\frac{\partial T}{\partial E}\right)_V = \frac{V}{C_v}\left(\frac{\partial P}{\partial T}\right)_V \tag{6.15}$$

$$\left(\frac{\partial P}{\partial T}\right)_V = -\left(\frac{\partial P}{\partial V}\right)_T\left(\frac{\partial V}{\partial T}\right)_P \tag{6.16}$$

$(1/V)(\partial V/\partial T)_P$ is known as the volumetric thermal expansion coefficient (3α) and $-(1/V)(\partial V/\partial P)_T$ is isothermal compressibility (K). Therefore, we can rewrite all of this as follows (Meyers, 1994):

$$\frac{\Gamma}{V} = \frac{3\alpha}{C_v K} \tag{6.17}$$

It is assumed that the ratio (Γ/V) is constant and therefore it follows that:

$$\frac{\Gamma}{V} = \frac{\Gamma_0}{V_0} = \text{const} \tag{6.18}$$

where, Γ_0 and V_0 are the Grüneisen gamma and specific volume at zero (ambient) pressure.

An approximation of Γ_0 is given by Royce (1971):

$$\Gamma_0 = 2S - 1 \tag{6.19}$$

Where S is the slope of the shock velocity-particle velocity Hugoniot, as defined earlier. Therefore knowing Γ_0 and knowing that $V_0 = 1/\rho_0$, where ρ_0 is the material density, we can calculate the ratio of Γ/V. A list of Grüneisen gamma parameters is provided by (Meyers, 1994).

For most materials, Gamma lies in the range of 1.25 ± 0.75. Although we have discussed a couple of ways of calculating it, these should only be seen as a way of establishing an initial value. In reality, the best way of assessing Gamma is by carrying out experiments where the material is shocked more than once. This results in off-Hugoniot states which are very sensitive to the value of Gamma, e.g. see Roberts et al. (2012) and Winter et al. (2004).

It is frequently good practice to check the results from hydrocode calculations with the analytical approaches that we have discussed in Chapter 5. In this following example, we will do this by comparing 'simple' back of the envelope calculations with a hydrocode employing the Mie–Grüneisen equation of state where there is a single shock occurring. Will there be any difference in the results? Let us take a look.

Example 6.1

A steel projectile strikes a high-strength steel target at 1.5 mm/µs. The projectile is 10 mm in diameter and 10 mm in length and is made from 1006 steel. The target is 20-mm thick and is made from AA 7075-T6. The equation of state data for the 1006 steel and the AA 7075-T6 are shown in Table 6.1:

    a. Ignoring the strength of the projectile and target materials, calculate the maximum shock pressure and corresponding particle velocity in the target. Compare these results with a hydrocode simulation using the above parameters.

TABLE 6.1

Equation of State Data for 1006 Steel and AA 7075-T6

Mat'l	ρ_o (kg/m³)	c_o (mm/µs)	S	Γ (Gamma)
1006 steel	7.896	4.57	1.49	2.17
AA 7075-T6	2.804	5.20	1.36	2.20

b. Compare the results seen in (a) with the hydrocode simulations of a 1006 steel flyer plate of 10-mm thickness and 60 mm diameter striking the same target. Explain why there is a difference in the results.

First, lets us calculate the shock pressure and particle velocity using 1D assumptions (i.e. uniaxial strain). It was seen in Chapter 5 that the Hugoniot for the target can be mathematically described as

$$P = \rho_0 (c_0 + Su_p) u_p = 7.896(4.57 + 1.49 u_p) u_p \qquad (6.20)$$

and the reverse Hugoniot for the projectile (with $u_p = v_{imp}$ at $P = 0$) can be given by

$$P = \rho_0 (c_0 + S(v_{imp} - u_p))(v_{imp} - u_p) = 2.804(5.20 + 1.36(1.5 - u_p))(1.5 - u_p) \quad (6.21)$$

Solving these two equations simultaneously we get:

$$P = 19.22 \text{ GPa, and}$$

$$u_p = 1.04 \text{ mm/}\mu$$

Recall that this will be the pressure and particle velocity in both the target and the projectile and in a real situation that would be true initially, at least.

Now let us test this problem with a hydrocode, and for this example, using Ansys Autodyn. We can use an axisymmetrical approach as the problem is symmetrical about a central axis.

Figure 6.6 shows a simulation of a strengthless 1006 steel projectile striking an AA 7075-T6 target (again, strengthless). Initially, a high shock pressure emanates from the interface between the projectile and the target. This high shock pressure is seen to decay as the simulation progresses as radial release waves diminish their magnitude. Using gauge points in Autodyn we can evaluate how the pressure and particle velocity decay as the shock progresses through the target. Lagrangian (moving) gauge points spaced every 4 mm were used (and 1 mm from the central axis), and the results are shown in Figure 6.7. The variable 'x-velocity' is used to track the linear particle velocity.
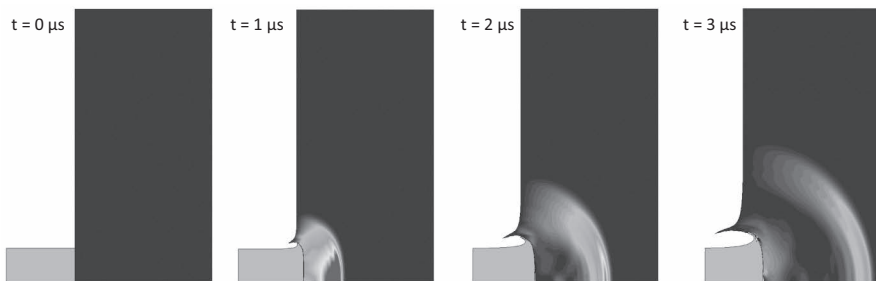
FIGURE 6.6 Autodyn simulation of a strengthless 1006 projectile striking a strengthless AA 7075 target. The red/dark colours within the wave front indicate high shock pressure which decays as the time progresses.
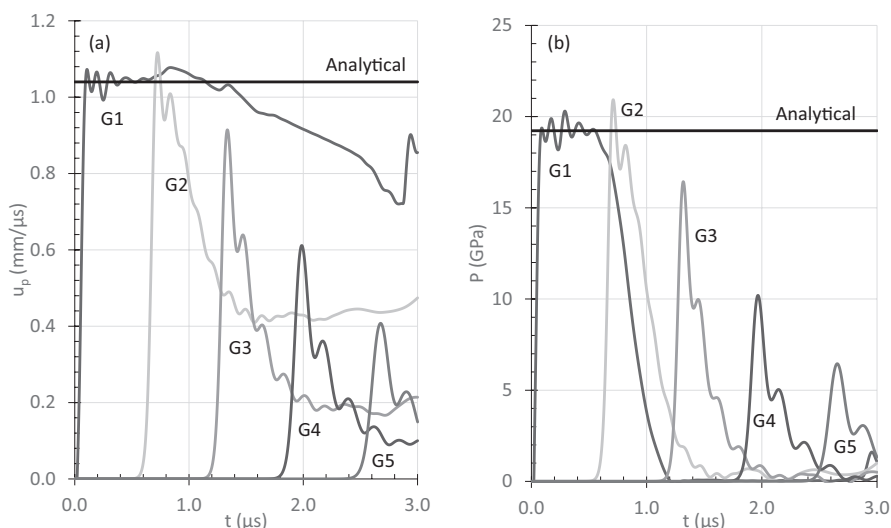
FIGURE 6.7   Simulation results showing the particle velocity (a) and the pressure (b) with time for a steel projectile striking an aluminium target. The 1D analytical solution is also shown.
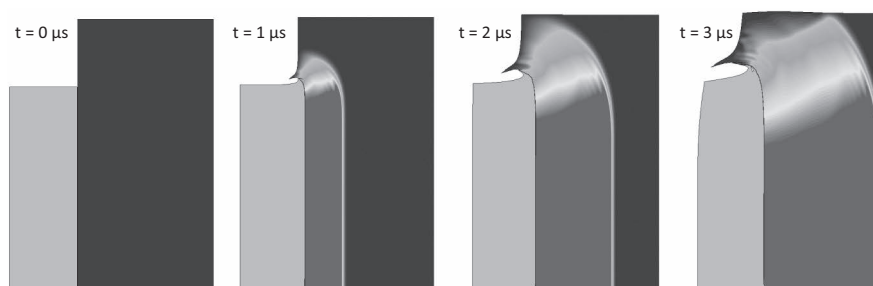
FIGURE 6.8   Autodyn simulation of a strengthless 1006 flyer plate striking a strengthless AA 7075 target. The red/dark colours within the wave front indicate high shock pressure.

Note that the analytical solution matches well with the initial shock pressure and particle velocities however both the pressure and particle velocity quickly decay due to the finite diameter of the projectile and radial release (compare this result to the flyer-plate result—part (b)). Further, the effect of Gamma in the hydrocode calculations is negligible due to a single shock being interrogated here.

Now we can compare these results to a flyer-plate experiment which comprises a plate that is 10-mm thick and has a diameter of 60 mm. This time, the radial release is mitigated by the geometry of the projectile which maintains uniaxial (1D) strain in the target for longer. See Figure 6.8. Therefore, the analytical matches the gauge results well. Much neater! See Figure 6.9.

The results are shown in Figure 6.9. Of course, it should be noted that the computational results matching the analytical approach are to be expected given that the
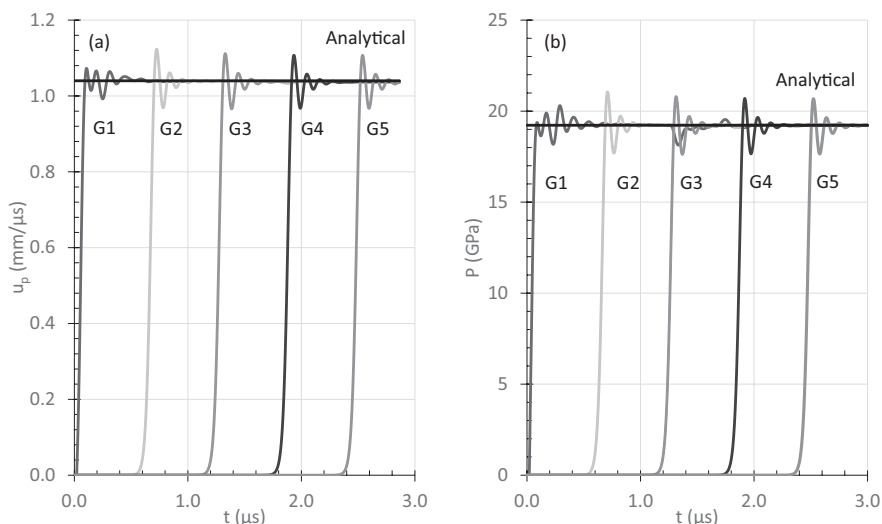
FIGURE 6.9 Simulation results showing the particle velocity (a) and the pressure (b) with time for a steel flyer-plate projectile striking an aluminium target. The 1D analytical solution is also shown and matches very well!

computational model is effectively replicating 1D ideal conditions. Nevertheless, it is a good check that the model works! Note that the shock is relatively lazy as what we would expect to see in real life and 'ringing' occurs in the solution. This is to be expected and is due to the complexities of how computational codes model shock waves, as discussed previously.

6.7.2 Modelling Materials of Strength

Armour is regularly loaded at rates where we would expect to see changes in strength. Furthermore, localized temperature increases can result in thermal softening which will affect an armour's ability to resist the load of the projectile. It is therefore important to understand how materials respond to a variety of loading rates and temperatures and develop appropriate relationships that can be implemented with continuum codes such as Abaqus, LS-DYNA and Ansys Autodyn. We have already been introduced to methods of achieving this with Split Hopkinson Pressure Bars, as discussed in Section 2.7.3.

6.7.2.1 Elastic Behaviour

Before we get to looking at the plastic response of materials, it is important to consider how materials respond elastically. This is defined by the elastic modulus of the material. So far, we have been considering a general stress state in 3D (x, y, z) that can be described by six stress components (normal and shear). However, it is possible to establish coordinate axes such that the shear stresses are zero at a point. Such a set of axes are called the principal axes. There are (at most) three non-zero stress components at that point, called σ_i, where $i = 1, 2, 3$. Computer codes tend to decompose

each stress into a hydrostatic component, P and a deviatoric component, s_i, where $-P$ is the mean of the three stresses, viz:

$$-P = \frac{1}{3}(\sigma_1 + \sigma_2 + \sigma_3) \tag{6.22}$$

And

$$\sigma_i = -P + s_i \tag{6.23}$$

The sign convention for most codes is that pressure is taken as positive in compression whereas stress is taken as negative in tension. Now it is also worth saying a little about the terms 'hydrostatic' and 'deviatoric'. The hydrostatic component accounts for volumetric changes and is derived from the equation of state discussed above. The stress deviators account for a change in shape or the distortion of the object (or cell). We can calculate the elastic stresses according to Hooke's law (which will also give us the elastic stress deviator):

$$\sigma_i = \lambda \frac{\Delta V}{V} + 2G\varepsilon_i \tag{6.24}$$

Where G is the shear modulus and λ is Lame's constant and written in terms of the bulk modulus, K as

$$\lambda = K - \frac{2}{3}G \tag{6.25}$$

Note that we can 'cleverly' expand the equation for the elastic stress (Equation 6.24) as follows (Woodruff, 1976):

$$\sigma_i = \lambda \frac{\Delta V}{V} + 2G\varepsilon_i + \frac{2}{3}G\frac{\Delta V}{V} - \frac{2}{3}G\frac{\Delta V}{V} \tag{6.26}$$

Which simplifies to

$$\sigma_i = \left(\lambda + \frac{2}{3}G\right)\frac{\Delta V}{V} + 2G\left(\varepsilon_i - \frac{1}{3}\frac{\Delta V}{V}\right) \tag{6.27}$$

Thus, comparing Equation 6.23 with 6.27 it can be seen that in the elastic regime:

$$P = -\left(\lambda + \frac{2}{3}G\right)\frac{\Delta V}{V} \tag{6.28}$$

This is because we can also write down a term for elastic hydrostatic compression using the following approach (see Equation 6.6):

$$P = -K\frac{\Delta V}{V} \tag{6.29}$$

Furthermore, we can also see from Equation 6.27 that the following is also true in the elastic regime:

$$s_i = 2G\left(\varepsilon_i - \frac{1}{3}\frac{\Delta V}{V}\right) \tag{6.30}$$

6.7.2.2 Von-Mises

Most computational codes will control plasticity by implementing a von Mises criterion. This is a theory of plasticity that was first suggested in 1913 by Richard Edler von Mises (1883–1953) and serves to describe how a material subjected to a three-dimensional stress state will yield. Mathematically, it is described by a single *equivalent* stress (sometimes, referred to as the *effective stress*). An equivalent stress $\left(\sigma_{eq}\right)$ is a single stress value derived from a multiaxial stress state with multiple stress components acting at the same time and at the same point in the material. So, we can define the von Mises equivalent stress by

$$2\sigma_{eq}^2 = \left(\sigma_1 - \sigma_2\right)^2 + \left(\sigma_2 - \sigma_3\right)^2 + \left(\sigma_3 - \sigma_1\right)^2 \tag{6.31}$$

$\sigma_1, \sigma_2, \sigma_3$ are the three orthogonal principal stresses that are calculated by the computer code.

Importantly, it is possible to define a yielding criterion simply by measuring the yield strength of the material from a test in uniaxial stress, either using a universal testing machine or a SHPB. Yielding of the material occurs when the following is true

$$\sigma_{eq} = Y \tag{6.32}$$

As we have seen in Chapter 2, we can experimentally measure values of the yield strength and conveniently this can be carried out under uniaxial stress. In this case, the material is said to yield when

$$\sigma_1 = Y \tag{6.33}$$

Here we define Y as the equivalent flow stress (that starts at Y_0).

Therefore, the von Mises equation describes a surface of a straight circular cylinder that is inclined in the $\sigma_1, \sigma_2, \sigma_3$ system of coordinates, with a locus of yielding, the radius of which $= \sqrt{2/3}Y$.

For 2D, when $\sigma_3 = 0$, the equation becomes (substituting Y for σ_{eq}):

$$Y^2 = \sigma_1^2 - \sigma_1\sigma_2 + \sigma_2^2 \tag{6.34}$$

Graphically, these equations define surfaces for the stress state on which the material has yielded, and inside which, the material behaves elastically. This provides a nice framework with which to manage elastic–plastic behaviour in a computer code. This surface can stretch or shift depending on the hardening regime as we will see next. See Figure 6.10.
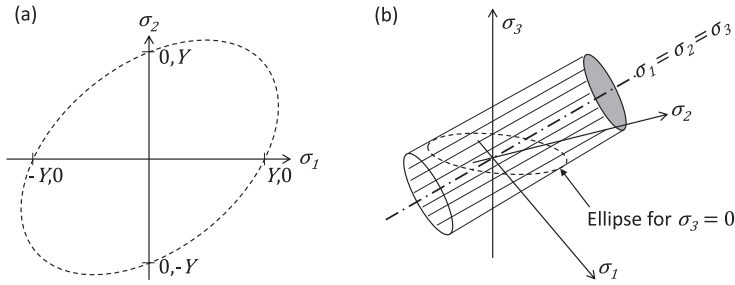
FIGURE 6.10   The von Mises yield locus for a two-dimensional system of stresses (a) and three-dimensional system of stresses (b). Y=equivalent flow strength.

It is important to note that the stress state of any material must lie within or on the yield surface defined by the yield criterion. From here, we can now define the various plasticity models that can be used with explicit codes. As we have discussed in Chapter 2, we know that the plastic response of a material is affected by strain, strain rate, temperature, and even pressure!

It is worth noting too that an equally important yield locus was defined by Henri Tresca (1814–1885) that coincides with von Mises for uniaxial stress states. Tresca is more conservative than von Mises and is defined by a hexagon in the $\sigma_1 - \sigma_2$ plane. The theory derived by von Mises is by far the most popular, however.

6.7.2.3   Elastic–Plastic Behaviour

There are many ballistic problems where a simple elastic–perfectly plastic model is sufficient. An equivalent stress (σ_{eq}) is calculated and compared to Y. If $\sigma_{eq} < Y$, then the material is elastic. However, if $\sigma_{eq} > Y$ the material has flowed plastically and the stresses must be allowed to relax back to the yield surface whilst conserving mass, and momentum.

Importantly, there are often two types of hardening approaches used in hydrocodes and these are *isotropic* and *kinematic*. With isotropic hardening, the centre of the von Mises yield surface is fixed but the radius is a function of the plastic strain. In essence, the yield surface expands proportionally in all directions when the yield stress is exceeded. In kinematic hardening, the radius of the von Mises yield surface is fixed but the centre translates in the direction of the plastic strain. This is best described by the following figure in a 2D stress space (Figure 6.11).

You will note from the isotropic hardening (Figure 6.11a) that effectively once the yield strength has been exceeded and the yield surface has expanded, we get a 'new' yield stress. In other words, the elastic limit will be higher for both compression and tension. With kinematic hardening (Figure 6.11b), the material will strengthen as it did before with isotropic hardening, however as the von Mises yield surface has shifted in the direction of the plastic strain, the elastic zone in compression will now be lower. This can be used to simulate such features as the Bauschinger effect[1] where hardening in tension will lead to a lower yield in subsequent compression. Taking into account the Bauschinger effect is important when simulating the impact
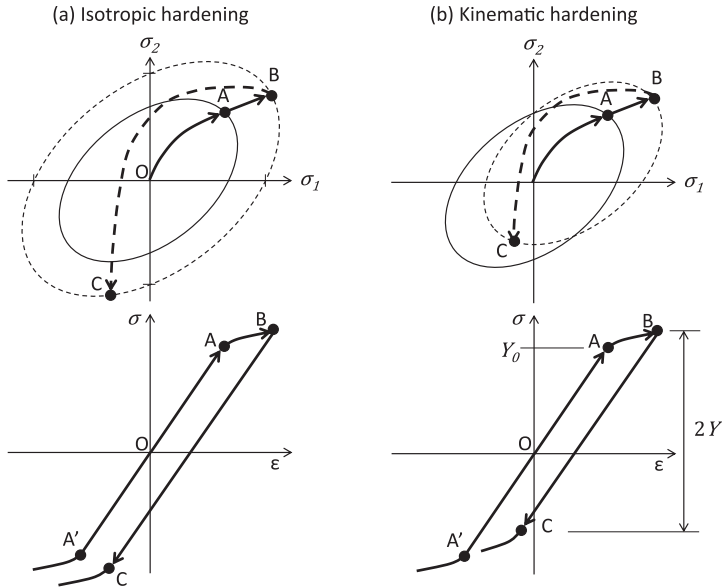
FIGURE 6.11   Isotropic hardening vs kinematic hardening (Y_0=tensile yield strength).

of armour materials that are sensitive to this effect. This is due to the complex compressive and tensile stress states that arise. That is, frequently materials will be loaded in compression and then subsequently released and loaded in tension, where the Bauschinger effect comes into play.

Most hardening in hydrocodes is isotropic but some, such as LS-DYNA, give an option to switch between the two for certain constitutive formulations. Constitutive models (that we will discuss next) define the von Mises yield surface.

6.7.2.4   Strain Hardening Models

As we have seen in Chapter 2, the onset of plasticity will often result in a hardening behaviour. Several empirical equations are often used to describe the experimental stress–strain relationships for materials that are subjected to strain hardening. The four that are the most commonly used describe the von Mises equivalent stress, Y. These are as follows (Kleemola and Nieminen, 1974):

$$\text{Ludwik} : Y = Y_0 + B\varepsilon_p^n \tag{6.35}$$

$$\text{Holloman} : Y = B_1\varepsilon_p^{m_1} \tag{6.36}$$

$$\text{Swift} : Y = B_2\left(\varepsilon_p - \varepsilon_0\right)^{n_2} \tag{6.37}$$

$$\text{Voce} : Y = B_3 - \left(B_3 - A_1\right)exp\left(-n_3\varepsilon_p\right) \tag{6.38}$$

where $B, B_1, B_2, B_3, A_1, n, n_1, n_2, n_3, \varepsilon_0$ are empirically derived (= curve fitting) constants and Y_0 and ε_p are the quasi-static yield strength and plastic strain, respectively. The Ludwick approach is probably the most commonly used model and crops up again in various models, such as Johnson–Cook (see below). However, Kleemola and Nieminen found that for describing the stress–strain curves of annealed and deformed copper, the Voce equation worked best, whereas the Holloman equation appeared to work better in describing the stress–strain curves of steel (Kleemola and Nieminen, 1974).

6.7.2.5   Johnson–Cook Model

We have previously looked at this model in Chapter 2 and it is widely used due to its beautiful simplicity. For completeness we will repeat it again here in that the von Mises equivalent stress in tension is given by (Johnson and Cook, 1985):

$$Y = \left(Y_0 + B\varepsilon_p^n\right)\left(1 + C \ln \dot{\varepsilon}_p^*\right)\left(1 - \left(T^*\right)^m\right) \tag{6.39}$$

where

  Y_0 is the yield strength of the material.
  B and n are the strain (or work) hardening constants.
  ε_p is the amount of equivalent plastic strain.
  $\dot{\varepsilon}_p^*$ is the dimensionless plastic strain rate $\left(\dot{\varepsilon}_p^* = \dot{\varepsilon}_p / \dot{\varepsilon}_0\right)$, for $\dot{\varepsilon}_0 = 1.0 \ s^{-1}$.
  C is a strain-rate constant.
  T^* is the homologous temperature defined by $T^* = (T - T_0)/(T_m - T_0)$.
  T_0 is the ambient or reference temperature (usually 293 K).
  T_m is the melting temperature. The temperatures are measured in degrees
      Kelvin.
  m is the thermal softening exponent.

All of the constants need to be measured experimentally, usually with a SHPB equipped with a furnace.

Some Johnson–Cook parameters for various metals are provided in Table 6.2.

One of the criticisms of the JC model is its oversimplicity and inability to observe the discrete coupling of certain mechanisms (Saleh et al., 2017). A modified version of the Johnson–Cook model was proposed by Børvik et al. (2001). This places greater emphasis on the strain rate sensitivity and is appropriate for high strengths steels (Børvik et al., 2009). The modified version (MJC) is described as:

$$Y = \left(Y_0 + B\varepsilon_p^n\right)\left(1 + \dot{\varepsilon}_p^*\right)^C\left(1 - \left(T^*\right)^m\right) \tag{6.40}$$

Parameters for five high-strength steels were presented by Børvik et al. (2009) and are listed in Table 6.3 along with an AA 7075-T651 from Børvik et al. (2010):

The thermal softening aspect of plasticity models is important, and one can expect that at high strain rates, the bulk of the plastic work is converted to heat.

TABLE 6.2

Properties for the Johnson–Cook Equation for Various Metals

Material	Reference	Y_0 (MPa)	B (MPa)	n	C	m	T_m (K)
AA 2024-T351[a]	Seidt and Gilat (2013)	304	478	0.406	0	2.100	775
AA 5083[b]	Gray III et al. (1994)	270	470	0.600	0.0105	1.200	933
AA 7017	Bobbili et al. (2015)	410	528	0.880	0.01024	0.600	-
AA 7039	Johnson G. R. and Cook, (1983)	337	343	0.410	0.0100	1.000	877
AA 7039[b]	Gray III et al. (1994)	220	500	0.220	0.0160	0.905	933
AA 7075-T651[c]	Senthil et al. (2017)	448	476	0.3948	0.0012	1.290	893
Ti–6Al–4V (low cost)	Meyer Jr and Kleponis (2001)	896	656	0.500	0.0128	0.800	1930
Mild steel (142 HV)[c, d]	Iqbal et al. (2015)	304	422	0.345	0.0156	0.870	1800
1006 steel	Johnson G. R. and Cook (1983)	350	275	0.360	0.0220	1.000	1811
4340 steel	Johnson G. R. and Cook (1983)	792	510	0.260	0.0140	1.030	1793
HSLA-65[e]	Nemat-Nasser and Guo, (2005)	790	1320	0.250	0.0220	0.350	1773
RHA	Gray III et al. (1994)	1225	1575	0.768	0.0049	1.090	1783
HHA	Gray III et al. (1994), Johnson and Holmquist (1989)	1504	569	0.220	0.0030	0.900	1783
ARMOX 500T	Iqbal et al. (2016)	1372	835	0.247	0.0617	0.840	1800
ARMOX 500T	Nilsson (2003)	1470	702	0.199	0.00549	0.811	1800
ARMOX 600T	Nilsson (2003)	1580	958	0.175	0.00877	0.712	1800

[a] In this case, $T_0 = 223$ K.

[b] The plate was obtained directly from the manufacturing line for the Bradley infantry fighting vehicle.

[c] Reference strain rate, $\dot{\varepsilon}_0 = 0.0001$ s^{-1}.

[d] Mild steel with (%) 0.188 C, 0.1855 Si, 0.8375 Mn, 0.0342 S, 0.0213 Cr, 0.0217 Ni and 0.0762 Al.

[e] In this case, $T_0 = 50$ K.

TABLE 6.3

Target Material Constants for the MJC Constitutive Model for High-Strength Armour Steels and an Aluminium Alloy

Material	Y_0 (MPa)	B (MPa)	n	$\dot{\varepsilon}_0$ (s⁻¹)	C	m	T_m (K)
Weldox 500E	605	409	0.50	5×10^{-4}	0.0166	1.0	1800
Weldox 700E	819	308	0.64	5×10^{-4}	0.0098	1.0	1800
Hardox 400	1350	362	1.0	5×10^{-4}	0.0108	1.0	1800
Domex Protect 500	2030	504	1.0	5×10^{-4}	0.0010	1.0	1800
Armox 560T	2030	568	1.0	5×10^{-4}	0.0010	1.0	1800
AA 7075-T651	520	477	0.52	5×10^{-4}	0.0010	1.0	893

Source: After Børvik et al. (2009, 2010).

The temperature increase is assumed adiabatic due to the transitory nature of ballistic events, and each increment can be calculated according to the following relation:

$$\Delta T = \frac{\chi}{\rho_0 C_p} \int_0^\varepsilon \sigma_{eq} d\varepsilon \tag{6.41}$$

Where, C_p is the specific heat of the material, ρ_0 is its density, and χ is a constant. This constant is known as the Taylor–Quinney coefficient, named after G I Taylor and H Quinney, who assessed the fraction of mechanical energy that is transformed to heat in a rapidly deformed solid (Taylor and Quinney, 1934). For material alloys, χ can be set to 0.9 (Meyers, 1994) which leads to the bulk of the plastic work converted into adiabatic heating of the specimen. This appears to give satisfactory results for metal alloys (Børvik et al., 2009).

Other variations of the JC model take into account contributions from the Zerilli–Armstrong model with the intention of a combined model that better represents observed coupled behaviour between temperature and strain rate, e.g. (Lin and Chen, 2010):

$$Y = \left(Y_0 + B\varepsilon_p^n\right) e^{\left(-C_3(T+\Delta T)+C_4(T+\Delta T)\ln\dot{\varepsilon}_p^*\right)} \tag{6.42}$$

Where C_3 and $,C_4$ are material constants.

6.7.2.6 Cowper–Symonds Model

The Cowper–Symonds model (Cowper and Symonds, 1957) is a well-used model and similar to the Johnson–Cook model previously described. It allows the definition of yield strength in terms of isotropic strain hardening and strain-rate dependence. Consequently, the von Mises equivalent stress is defined by:

$$Y = \left(Y_0 + B\varepsilon_{pl}^n\right)\left(1 + \left(\frac{\dot{\varepsilon}_{pl}}{D}\right)^{1/q}\right) \tag{6.43}$$

All the parameters are as defined for the Johnson–Cook model except this time, the strain rate constants are given by D and q. These need to be derived from experimental results with a SHPB.

6.7.2.7 Steinberg–Guinan Model

Steinberg, Cochran and Guinan account for the fact that not only has it been observed that the yield strength increases with strain rate but the shear modulus, G, does as well (Steinberg et al., 1980). Furthermore, even though the yield strength increases with strain rate, one would not expect it to do so without limit. From their observations of flyer-plate tests, they noted that at shock pressures approaching 10 GPa, rate-dependent effects vanished, and the shock profiles could be replicated well with rate-independent models. This was explained by the increase in temperatures with increasing shock stress. In liquids, rate-dependent effects such as viscosity, appear to decrease dramatically with temperature (Andrade, 1934). Steinberg et al. also noted that there were extensive data showing the pressure and temperature variation of G. However, there was no such definitive data for Y. Nevertheless, for materials that do not exhibit strain rate dependency, Y is expected to be proportional to G.

The constitutive relationships for G and Y as functions of ε_p, P and temperature, T, for high strain rates are:

$$G = G_0\left[1 + \left(\frac{G_p'}{G_0}\right)\frac{P}{\eta^{1/3}} + \left(\frac{G_T'}{G_0}\right)(T - 300)\right] \tag{6.44}$$

$$Y = Y_0\left[1 + B\left(\varepsilon_p + \varepsilon_i\right)\right]^n \times \left[1 + \left(\frac{Y_p'}{Y_0}\right)\frac{P}{\eta^{1/3}} + \left(\frac{G_T'}{G_0}\right)(T - 300)\right] \tag{6.45}$$

Subject to a limit of

$$Y_0\left[1 + B\left(\varepsilon_p + \varepsilon_i\right)\right]^n \leq Y_{max} \tag{6.46}$$

Y_0 is the yield strength of the material.

Y_{max} is a limiting maximum yield strength that effectively defines a limit such that materials cannot infinitely strain harden.

B and n are the strain (or work) hardening constants.

η is compression, defined here as $\eta = V_0/V$.

ε_i is initial equivalent plastic strain, normally set to 0.

ε_p is the equivalent plastic strain.

The subscript '0' refers to the reference state ($T = 300$ K, $P = 0$, $\varepsilon_p = 0$) and therefore G_0 is the shear modulus at standard temperature and pressure. Primed parameters with the subscripts 'P' and 'T' imply derivatives of that parameter with respect to pressure or temperature at the reference state.

Table 6.4 lists material values used for this constitutive model (Steinberg et al., 1980). You will see there are several parameters, many of which can be garnered

TABLE 6.4
Numerical Values of Parameters Used in the Steinberg–Guinan Model

Material	G_0 (GPa)	Y_0 (GPa)	Y_{max} (GPa)	B	n	$\dfrac{G_p'}{G_0}$ (TPa⁻¹)	$\dfrac{-G_T'}{G_0}$ (kK⁻¹)	T_{m0} (K)	T_m (K)	γ_0	a
AA 6061-T6	27.6	0.29	0.68	125	0.10	65	0.62	1220	925	1.97	1.5
Au	28.0	0.02	0.225	49	0.39	38	0.31	1970	1336	2.99	2.4
Be (S-200)	151	0.33	1.23	81	0.22	15.5	0.26	1820	1558	1.11	1.0
Cu (OFHC)	47.7	0.12	0.64	36	0.45	28	0.38	1790	1356	2.02	1.5
AZ31B-H24	16.5	0.19	0.48	1100	0.12	103	0.51	1150	903	1.54	1.2
Nb	37.7	0.70	1.4	(5)	(0.2)	12	0	3530	2743	1.66	1.3
Ni (annealed)	85.5	0.14	1.2	46	0.53	16	0.33	2330	1726	1.96	1.5
Pb	8.6	0.008	0.1	110	0.52	116	1.16	760	600	2.74	2.2
Pt (annealed)	63.7	0.03	0.34	1300	0.19	25	0.14	2730	2043	2.74	2.2
SS 304	77.0	0.34	2.5	43	0.35	26	0.45	2380	1783	1.93	1.4
Ta	69.0	0.77	1.10	(10)	(0.1)	14.5	0.13	4340	3253	1.67	1.3
Ti	43.4	0.71	1.45	780	0.065	11.5	0.62	2260	1943	1.23	1.0
U	86.7	0.40	1.68	2000	0.16	35	0.78	1710	1405	2.32	1.8
W	160	2.2	4.0	(7.7)	(0.13)	9.4	0.14	4520	3673	1.67	1.3

Source: After (Steinberg et al., 1980).

from the open literature. The melting temperature is specified as the shear modulus and yield strength are set to zero if the temperature of the material exceeds the specified melting temperature.

It is worth noting that the melting temperature listed by Steinberg et al. (1980) in Table 6.4, lists the melting temperature (T_{m0}) where $V = V_0$. This is different to the normal melting temperature at ambient conditions (T_m) which is also listed for the various materials in Table 6.4. This is based on the assumption that there is an interdependence between shock compression and melting which can be described by a modified Lindemann law (Royce, 1971). Roughly speaking, $T_{m0} \approx 1.3 \; T_m$ and for the values listed in Table 6.4, T_{m0} ranges from 1.16 to 1.47 T_m. Melting is not intimately connected with the Steinberg–Guinan model. In computations, it is only used as a value, which when exceeded, causes a drop in the shear moduli and yield strength of the material to zero. For ballistic applications, where large compressions are not expected, the normal melting temperature (T_m) may produce more realistic results. For a further brief discussion of its applicability, see Steinberg (1987).

The Steinberg–Guinan model was subsequently updated by Steinberg and Lund based on a number of identified deficiencies (Steinberg and Lund, 1989). Consequently, they added an additional strain rate term to extend the Steinberg–Guinan model to strain rates as low as 10^{-4}s^{-1}. This was done by splitting the yield strength calculation into thermal (Y_T) and athermal (Y_A) components. The general form of the equation is presented as follows:

$$Y = \left[Y_T\left(\dot{\varepsilon}_p, T\right) + Y_A f\left(\varepsilon_p\right) \right] \frac{G_{(P,T)}}{G_0} \tag{6.47}$$

where,
$\;\;\;\;\;\;Y_T\left(\dot{\varepsilon}_p, T\right)$ is the thermally activated part of the yield strength and is a function
$\;\;\;\;\;\;\;\;\;\;$of $\dot{\varepsilon}_p$ and T.
$\;\;\;\;\;\;Y_A f\left(\varepsilon_p\right)$ is similar in form to the Steinberg–Guinan model with $f\left(\varepsilon_p\right)$ being
$\;\;\;\;\;\;\;\;\;\;$the work hardening term, a function of equivalent plastic strain, ε_p.
$\;\;\;\;\;\;G_{(P,T)}$ is the pressure and temperature-dependent shear modulus.
$\;\;\;\;\;\;G_0$ is the shear modulus at standard temperature and pressure.

6.7.2.8 Zerilli–Armstrong Model

The Zerilli–Armstrong model was developed on the basis that there was a perceived deficiency in existing constitutive models (Zerilli and Armstrong, 1987). For example, it was noted that generally, there is no account given for grain size even though it is well known that this has a dramatic effect on the strength and ductility of materials. There was also a deficiency in that, until Zerilli and Armstrong, there were no models that took into account the very clear difference in behaviour between FCC materials (e.g. copper) and BCC materials (e.g. iron). For BCC metals, the nature of dislocation interactions dictates there is generally little strain hardening that occurs. Whereas for FCC materials, substantial strain hardening is often observed (Zerilli and Armstrong, 1994).

TABLE 6.5

Zerilli–Armstrong Parameters for OFHC Copper (FCC) and Armco Iron (BCC) from Two Different Sources

Material	Reference	C_0 (MPa)	C_1 (MPa)	C_2 (MPa)	C_3 (K⁻¹)	C_4 (K⁻¹)	C_5 (MPa)	n
OFHC Copper	Zerilli and Armstrong (1987)	65	-	890	0.0028	0.000115	-	0.500
Armco Iron	Zerilli and Armstrong (1987)	65	1033	-	0.00698	0.000415	266	0.289
OFHC Copper	Holmquist and Johnson, (1991)	60	-	656	0.00198	0.000060	-	0.370
Armco Iron	Holmquist and Johnson (1991)	65	3214	-	0.00973	0.000321	332	0.420

For FCC materials, the von Mises equivalent stress is defined as

$$Y = C_0 + C_2 \varepsilon_p^n e^{\left[-C_3 T + C_4 T \ln \dot{\varepsilon}_p \right]}$$

(6.48)

For BCC metals, the equivalent stress is defined as follows:

$$Y = C_0 + C_1 e^{\left[-C_3 T + C_4 T \ln \dot{\varepsilon}_p \right]} + C_5 \varepsilon_p^n$$

(6.49)

where,

$$C_0 = \sigma_G + \frac{k}{\sqrt{d}}$$

(6.50)

where,

This final expression (C_0) is defined by the flow stress contribution due to solutes and initial dislocation density, k is the microstructural stress intensity and d is the average grain diameter. However, usually, C_0 is taken as a *free* constant that is measured independently. Model parameters are provided in Table 6.5.

$C_0, C_1, C_2, C_3, C_4, C_5$ are material constants.

ε_p is the equivalent plastic strain.

$\dot{\varepsilon}_p$ is the dimensionless plastic strain rate.

n is a constant for strain dependence, and in theory, can be set to 0.5. This is commonly done so for FCC materials and some formulations within codes (such as Autodyn) take that to be the case. Therefore, the user is not required to enter a value (i.e. 0.5 is already taken into account in the code's formulae).

T is the temperature.

6.7.2.9   Drucker–Prager

The Drucker–Prager model has been introduced to calculate the yield behaviour of materials where the flow stress varies with pressure. This is important for materials such as concrete (e.g. see Li and Meng (2003)), granular materials and ceramics. This can also be important for understanding the mechanical behaviour of comminuted ceramic material that would be expected to be formed around a penetrating
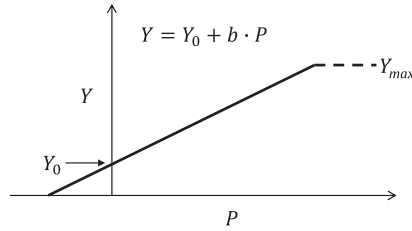
FIGURE 6.12   The Drucker–Prager relationship for brittle materials.

projectile, for example.It was originally proposed by D. C. Drucker and W. Prager for soils (Drucker and Prager, 1952). Put simply, the von Mises flow stress is defined in terms of pressure, usually with a linear relationship (the original Drucker–Prager model) and occasionally, a maximum yield stress. This is done according to the following figure.

Figure 6.12 shows a linear Drucker–Prager relationship. Inset is the simple linear equation where Y_0 and b are material constants, and P is the pressure. Some materials exhibit a cap in their strength as the pressure is increased, and therefore, in this specific case, yielding occurs until the cap (Y_{max}) is reached. Codes frequently offer the user other relationships that describe the von Mises equivalent stress in terms of polynomial or exponential functions.

Commonly, the way that parameters are derived for the Drucker–Prager model is by conducting triaxial compression tests on the sample. Here, a cylindrical sample is loaded into a thick-wall pressure vessel and compressed radially with hydraulic fluid. The specimen is protected from the hydraulic load by virtue of a plastic pliable sleeve. The specimen is then loaded axially.

The von Mises equivalent stress is then defined by:

$$Y = \sigma_z - \sigma_r \tag{6.51}$$

where σ_z is the axial stress on the specimen and σ_r is the radial stress imposed by the hydraulic fluid. The hydrostatic pressure that the specimen is subjected to is calculated from

$$P = \frac{1}{3}(2\sigma_r + \sigma_z) \tag{6.52}$$

Several experiments are required to build up a picture of the yield surface variation with pressure.

Alternatively, another way of deriving a constitutive model for a comminuted material is by performing experiments, modelling those experiments assuming a type of constitutive model, and changing the parameters of the model until the computational results fit with the experiments. Anderson Jr et al. (2008) presented the experimental results of the penetration of an Au rod into both pre-damaged hot-pressed SiC and compacted powder. For the pre-damaged ceramic targets, they compared the experimental

results with computational simulations and varied the constants Y_0 and b to develop a Drucker–Prager relationship for the material. This was done by requiring numerical simulations to match the penetration-velocity versus impact-velocity response.

Examples of data are summarized in Table 6.6 along with the way they were found. These data are all from the same team. Generally, the brittle specimens were damaged by thermally shocking the sample.

However, further work has been presented by Anderson et al., (2009) that suggests that the Drucker–Prager formulation may not be adequate to describe the in situ comminuted (heavily damaged) ceramic material behaviour during penetration. They compared penetration-rate data with that predicted using the Drucker–Prager constants for Au penetrators penetrating pre-damaged SiC confined targets. They noted that no single pair of parameters appeared to be applicable over the entire range of impact velocities when comparing experiments with simulations.

TABLE 6.6
Drucker–Prager Relationships for Intact, Broken and Powdered Brittle Materials

Reference	Material Type	Y_0 (GPa)	b	Y_{max}(GPa)	Derivation
Chocron et al. (2013)	Intact soda-lime glass	1.20	1.26	-	Triaxial tests
Chocron et al. (2013)	Damaged soda-lime glass	0.416	1.25	-	Triaxial tests
Chocron et al. (2013)	Damaged soda-lime glass	0.411	1.19	1.61[a]	Uniaxial compression (sleeve confined)
Chocron et al. (2010)	Intact borosilicate glass	1.59	1.20	-	Triaxial tests
Chocron et al. (2010)	Damaged borosilicate glass[a]	0.423	1.22	-	Triaxial tests
Chocron et al. (2010)	Intact borosilicate glass	1.28	1.10	-	Uniaxial compression (sleeve confined)
Chocron et al. (2010)	Damaged borosilicate glass[a]	0.535	1.23	-	Uniaxial compression (sleeve confined)
Chocron et al. (2012)	Intact B_4C	1.50	1.9	-	Triaxial tests
Chocron et al. (2012)	Damaged B_4C	0.35	1.8	-	Triaxial tests
Anderson Jr et al. (2008)	In situ comminuted SiC	0.0455	2.7	2.56	Ballistic penetration experiments
Anderson Jr et al. (2008)	In situ comminuted SiC	1.0	0.5	-	Ballistic penetration experiments
Chocron et al. (2005)	Fractured SiC	0.028	2.5	-	Mechanical testing
Chocron et al. (2005)	Powdered SiC	-	1.1	-	Mechanical testing

[a] At $P = 1.01$ GPa.

TABLE 6.7
Variations on the Johnson–Holmquist Model

Year	Model	Description	Ref.
1992	JH-1	Instantaneous drop in strength only when the material is deemed to be fully damaged through the accumulation of plastic strain; piecewise description of the strength	Johnson and Holmquist (1992)
1994	JH-2	Gradual softening from intact to damaged strength curves as damage accumulates; analytical description of the strength	Johnson and Holmquist (1994)
2003	JHB	Similar strength behaviour to JH-1; accommodation of a phase change	Johnson et al. (2003)
2011	HJ	Building off the JHB model but with significant differences and applied to glass	Holmquist and Johnson (2011)
2017	HJG	Building off the HJ model that showed sensitivity to the mesh construction. Modification of the strength and damage approach.	Holmquist et al. (2017)

6.7.2.10 Johnson–Holmquist

There are several different types of constitutive models and approaches that are used to simulate the dynamic behaviour and failure of ceramic materials. One of the more widely used models that has been developed and used for understanding the physics of projectile/ceramic interaction was developed by Johnson and Holmquist, and therefore, a brief review is provided here. This model is one of the more elegant of the approaches available and is easily applied in continuum codes such as Ansys Autodyn and LS-DYNA. The model has evolved somewhat since the original 1992 formulation; a summary of the models is found in Table 6.7.

A brief description of the JH-1 model is given in the following description. The schematic illustration of the JH-1 model from Johnson and Holmquist (1992) and (Holmquist and Johnson, 2002) is shown in Figure 6.13. The intact material strength is described as the linear segmented curve where it is assumed that the von Mises equivalent stress is a function of pressure, the dimensionless strain rate, defined by $\dot{\varepsilon}^* = \dot{\varepsilon}/\dot{\varepsilon}_0$ (for $\dot{\varepsilon}_0 = 1.0\,\mathrm{s}^{-1}$) and the damage, D. Any increase in the strain rate under a given pressure increases the equivalent stress and therefore makes the material stronger. This is done according to

$$Y = Y_{\mathrm{p}}\left(1.0 + C \ln \dot{\varepsilon}^*\right) \tag{6.53}$$

where Y is the equivalent stress, Y_{p} is the available strength at $\dot{\varepsilon}^* = 1.0$ and C is the strain-rate constant. When damage to the ceramic occurs, the equivalent stress for a given pressure reduces, and consequently, the material becomes weaker. Damage (D) is defined as the ratio of the total accumulated increment of plastic strain and the equivalent failure strain, viz.,

$$D = \sum \frac{\Delta \varepsilon_{\mathrm{p}}}{\varepsilon_{\mathrm{p}}^f} \tag{6.54}$$
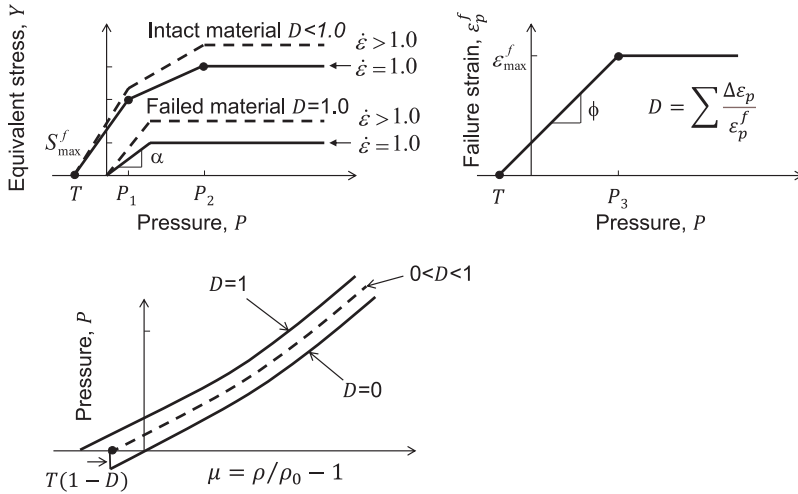
FIGURE 6.13 JH-1 formulation typically used for silicon carbide. (Adapted from Holmquist and Johnson, 2002.)

Where $\Delta\varepsilon_p$ is the increment of equivalent plastic strain during a cycle of integration and ε_p^f is the equivalent plastic strain at failure under a constant pressure, P. The material fails when either pressure reaches the tensile limit T, or damage D is equal to 1.0. After the material has failed, it cannot withstand any tensile loading but can still withstand a limited compressive loading. There can be a limit that can be set to ε_p^f and this is defined as ε_{max}^f, that occurs at a compressive pressure of $P = P_3$ (see Figure 6.13).

Further, an additional pressure contribution can be added to the equation of state to simulate the bulking of the material due to the formation of fracture surfaces.

There have been several papers dealing with the subject of ceramic armour penetration; however, it should be pointed out that of the 14 constants that are required for the Johnson–Holmquist formulation, 2 have to be established through calibration with ballistic trials data. These two constants (for the strength of the failed material and the damage parameter, ϕ) also have a dramatic effect on the ceramic's propensity to cause dwell, and consequently, caution should be exercised in interpreting the data.

6.7.2.11 Orthotropic Strength Models for Composites and Woven Fabrics

Composite materials (that are made up fibres and a matrix) are complex materials mainly due to (1) the multiple materials that are used therein and, (2) the directionality of the elastic, inelastic and failure behaviour. Figure 6.14 pictorially outlines the problem at hand. On the left-hand side, there is a continuum element, whose properties must represent a real composite material (on the right-hand side).

Most[2] composite materials are orthotropic in nature. That is, they have material properties that differ along three mutually orthogonal axes. Necessarily, the key equations governing the material behaviour are complex. There are two fundamental differences between isotropic and orthotropic materials when it comes to pressure (Anderson Jr et al., 1994):
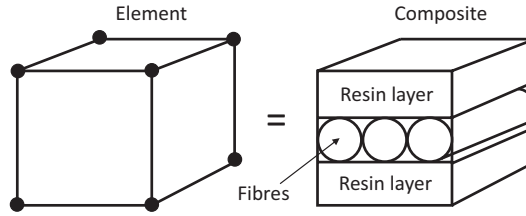
FIGURE 6.14   The challenge of simulating composite materials using continuum codes. On the left is a representation of a continuum element used to build up the geometry of the model. On the right-hand side is a representation of a composite material.

1. Strain is not uniform in all three directions when an orthotropic material is subjected to hydrostatic pressure.
2. Deviatoric strain will cause a change in volume since the coefficients in the stress–strain relationship are not all equal.

These differences dictate changes to the equation of state.

An example of an equation of state that has been implemented into codes (such as Ansys Autodyn) is one proposed by (Anderson Jr et al., 1994). This is shown as follows:

$$P - P_h(V) = \frac{\Gamma(V)}{V}\left(e - e_h(V)\right) - \frac{1}{3}\left[C_{11} + C_{21} + C_{31}\right]\varepsilon_{11}^d$$

$$- \frac{1}{3}\left[C_{12} + C_{22} + C_{32}\right]\varepsilon_{22}^d - \frac{1}{3}\left[C_{13} + C_{23} + C_{33}\right]\varepsilon_{33}^d \qquad (6.55)$$

where C_{ij} are the terms from the orthotropic stiffness matrix for the composite and are functions of the directional elastic properties which can be measured. The term ε_{ii}^d describes the deviatoric strains. The numbers in the subscripts indicate direction.

Hydrocodes compute stresses from the strain fields and consequently the C_{ij} terms are calculated from elastic constants in the orthotropic stiffness matrix according to:

$$\{\sigma\} = [M]\{\varepsilon\} \qquad (6.56)$$

Where $[M]$ is the orthotropic elasticity matrix inverted from the strain–stress formulation. Therefore, as an example,

$$C_{11} = \frac{1 - v_{23}v_{32}}{E_{22}E_{33}\Delta} \qquad (6.57)$$

where

$$\Delta = \frac{1 - v_{12}v_{21} - v_{23}v_{32} - v_{31}v_{13} - 2v_{21}v_{32}v_{13}}{E_{11}E_{22}E_{33}} \qquad (6.58)$$

TABLE 6.8

Linear Us-up Shock Data for Various Polymer Composite Materials

Composite	Type	Density (g/cc)	c_0 (mm/ μs)	S (mm/ μs)	u_p range (mm/μs)	Reference
Aramid epoxy	Aramid/ epoxy	N/K	1.562	2.10	<0.9	Riedel et al. (2004)
Hexcel 5HS/epoxy	CFRP,through- thickness	1.50	3.23	0.92	0.2–0.9	Millett et al. (2007a)
Hexcel 5HS/epoxy	CFRP, in-fibre	1.512	2.27	2.26	0.4–0.9	Hazell et al. (2009)
Toray T700/epoxy	CFRP	1.600	2.161	3.112	0.3–0.7	Xie et al. (2018)
3D carbon–carbon	CFRP	1.97	1.146	4.07	0.2–0.5	Héreil et al. (1997)
Aerospace grade	CFRP	N/K	2.544	1.41	<0.8	Riedel et al. (2004)
Tape-wrapped/phenolic	CFRP	1.46	3.69	0.59	0.1–0.9	Wood et al. (2012)
E Glass/epoxy (5HS)	GFRP	1.885	3.3	0.9	<0.4	Yuan et al. (2007)
S2 Glass fibre/polyester	GFRP	1.942	2.96	1.111	<2.0	Dandekar et al. (2003)
S2 Glass fibre/polyester	GFRP	1.959	3.224	0.960	<0.5	Tsai et al. (2009)
Glass fibre/epoxy	GFRP	2.05	2.89	1.73	0.14–0.66	Millett et al. (2007b)
Glass fibre/epoxy	GFRP	1.79	2.84[a]	1.205[a]	0.16–2.13	Zhuk et al. (1994)

[a]　Derived from presented data.

See Anderson Jr et al. (1994) for a full list of coefficients. The deviatoric strains are calculated during the computational cycle.

$P_h(V)$ can be derived from flyer-plate data as discussed previously (see Section 6.7.1.3) with knowledge of the shock properties for c_0 and S. These are presented in Table 6.8 for various composites (gleaned from the literature).

To simulate the inelastic response in composites there have been a limited number of models that build upon the work of Hill (1948). Hill's extended von Mises' description of an isotropic yield surface to take into account anisotropy in metals. An example of a yield function that is currently implemented in some codes is the extension by Chen et al. (1997). This is described as follows:

$$Y = a_{11}\sigma_{11}^2 + a_{22}\sigma_{22}^2 + a_{33}\sigma_{33}^2 + 2a_{12}\sigma_{11}\sigma_{22} + 2a_{23}\sigma_{22}\sigma_{33}$$

$$+2a_{13}\sigma_{11}\sigma_{33} + 2a_{44}\sigma_{23}^2 + 2a_{55}\sigma_{31}^2 + 2a_{66}\sigma_{12}^2 \tag{6.59}$$

Here the nine plasticity constants a_{ii} shape the yield surface dependent on the degree of anisotropy of the material. The stresses, σ_{ii} refer to the stresses in the principal material directions. This yield criterion reduces to Hill's orthotropic yield function when

$$a_{12} = a_{33} - (a_{11} + a_{22} + a_{33})/2 \tag{6.60}$$

$$a_{13} = a_{22} - (a_{11} + a_{22} + a_{33})/2 \tag{6.61}$$

$$a_{23} = a_{11} - (a_{11} + a_{22} + a_{33})/2 \tag{6.62}$$

Further, the von Mises yield criterion is derived when

$$a_{11} = a_{22} = a_{33} = 2/3 \tag{6.63}$$

$$a_{12} = a_{23} = a_{13} = -1/3 \tag{6.64}$$

$$a_{44} = a_{55} = a_{66} = 1 \tag{6.65}$$

This approach (along with the orthotropic equation of state) has been used successfully by a number of researchers using Autodyn (Ryan et al., 2009, Nguyen et al., 2015, Lässig et al., 2015, Clegg et al., 2006).

6.7.3 MODELLING FAILURE

As mentioned previously, modelling failure in a continuum code is tricky as failure originates at the sub-micron level in materials. Therefore, all failure models in continuum codes, are approximations of reality.

Most models are quite simple where a single parameter is specified that defines failure. In hydrocodes, that ultimately results in prohibiting the cell from carrying any shear stresses or negative pressures (cracks cannot propagate tensile stresses).

6.7.3.1 Simple Bulk (Isotropic) Failure Models

These are used to simulate the failure in cells in an isotropic material. There is no directionality, and the cell is said to have failed when a predetermined parameter is exceeded. This can be due to a negative pressure, for example, according to the P_{min} criteria such that failure in a cell occurs when

$$P \leq P_{min} \tag{6.66}$$

This criterion has been used to simulate the effect of spall under hypervelocity impact conditions, for example, Hiermaier (2008a).

Other models include specifying an equivalent strain, ε_{eq}, of the material, such that the cell fails when it reaches a predetermined value of failure strain, ε_f, viz

$$\varepsilon_{eq} = \varepsilon_f \tag{6.67}$$

6.7.3.2 Cockroft–Latham Failure Model

The Cockroft–Latham failure model (Cockroft and Latham, 1968) is effectively an energy-based failure model where the failure of a cell occurs when a critical value of energy per unit volume is exceeded. This can simply be derived from a simple tensile test (see Section 2.5). This has been used in the simulation of high-strength steels (Børvik et al., 2009) as well as other materials.

In essence, the following applies:

$$W = \int_0^{\varepsilon_{eq}} \sigma_1 d\varepsilon_{eq} \leq W_{cr} \tag{6.68}$$

where σ_1 is the principal stress and ε_{eq} is the equivalent strain. The presence of the brackets implies that $\sigma_1 = \sigma_1$ when tension occurs and $\sigma_1 = 0$ in compression. Thus, failure can only occur during tension. The value of W_{cr} the critical work per unit volume can be derived from a simple true stress–strain curve by measuring the area under the curve. Fracture is reached when $W = W_{cr}$ at $\varepsilon_{eq} = \varepsilon_f$ (i.e. at the failure strain as measured from a simple tensile test). This failure model has been shown to be equally effective as an alternative more complex failure model (Johnson–Cook Damage—see Section 6.7.3.3) when simulating projectile impact on steel plates (Dey et al., 2007).

6.7.3.3   Stress Triaxiality

An important parameter that is used to determine failure in materials is stress triaxiality. This is the ratio of the hydrostatic stress, or mean stress (σ_m) to the von Mises equivalent stress, viz,

$$\sigma^* = \frac{\sigma_m}{\sigma_{eq}} \tag{6.69}$$

Using the previously established notation, we can also write the stress triaxiality as $\sigma^* = -P/\sigma_{eq}$. When yielding has occurred, $\sigma_{eq} \equiv Y$. The measure of triaxiality is important as a greater (negative) triaxiality makes brittle fracture in ceramic increasingly difficult as noted by (Deshpande and Evans, 2008).

   The influence of stress triaxiality is often evaluated using notched tensile test specimens and using universal testing machines or Split Hopkinson Tension Bars to load a coupon to failure. The true strain to failure (ε_f) is calculated after the test by examination of the fracture surfaces and by using the following well-known relationship:

$$\varepsilon_f = \ln\left(\frac{A_0}{A_f}\right) \tag{6.70}$$

where A_0 and A_f are the cross-sectional areas before and after the test, respectively.

   Initial stress triaxiality is calculated according to the analysis carried out by Bridgman (Bridgman, 1952), viz

$$\frac{\sigma_m}{\sigma_{eq}} = \frac{1}{3} + \ln\left(1 + \frac{a_0}{2R_0}\right) \tag{6.71}$$

where a_0 is the original radius in the centre of the notch and R_0 is the initial notch radius. An example of how the fracture strain varies with stress triaxiality in Weldox 460 E steel is presented in Figure 6.15. Both quasi-static and dynamic tests are shown here. The dynamic tests were carried out using a 'pre-loaded' split Hopkinson tension bar setup. A tensile pre-load is applied to the extremity of the input bar, which when released, allows for a tension wave to be transmitted along the input bar and
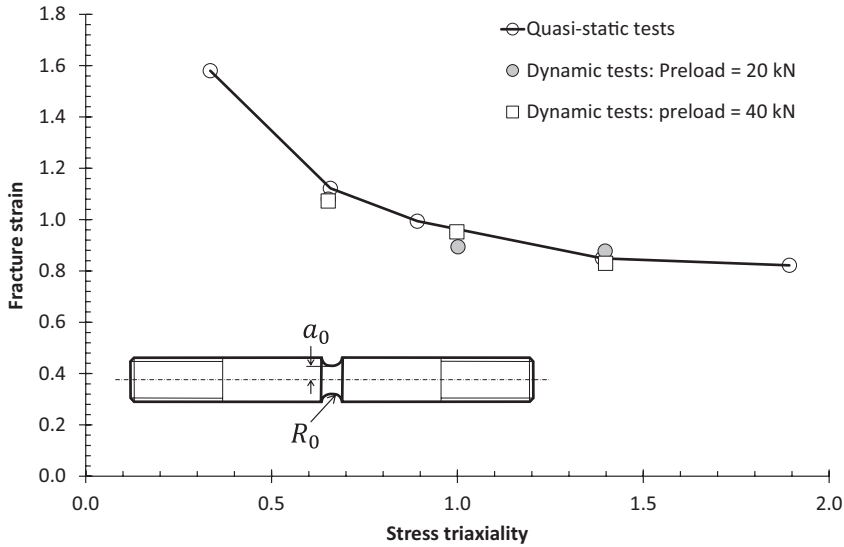
FIGURE 6.15 Quasi-static and dynamic results from tests conducted on notched specimens in tension for Weldox 460 E steel coupons. Inset: a schematic of a typical notched specimen used in the tests. The pre-load is indicative of the loading rate due to the methodology used to induce a tensile wave in the specimen. (Plotted from data provided in Hopperstad et al. (2003) with data also from Børvik et al. (2001).)

into the specimen. The pre-load in this context is indicative of a loading rate with a higher loading rate revealing a higher strain rate (Hopperstad et al., 2003).

It is notable that for both the dynamic and the quasi-static tests the fracture strain decreases with increasing stress triaxiality. Further, it appears from this data that there is little difference in the failure behaviour for quasi-static and dynamic testing conditions (that is, the failure appears independent of strain rate).

Tensile stresses correspond to positive triaxialities, whereas compressive stresses correspond to negative triaxialities.

Johnson and Cook presented a failure model that employs this approach (Johnson and Cook, 1985). This is an often-implemented model in many commercial hydro-codes and postulates that the critical equivalent fracture strain, ε_{eq}^{f} is a function of the stress triaxiality, σ^{*}. In this model, the equivalent strain to failure is modelled as decreasing with increasing hydrostatic tension, σ_{m}.

$$\varepsilon_{eq}^{f} = \left(D_{1} + D_{2}\exp\left(D_{3}\sigma^{*}\right)\right)\left(1 + D_{4}\ln\dot{\varepsilon}_{p}^{*}\right)\left(1 + D_{5}T^{*}\right) \tag{6.72}$$

where

$D_{1} - D_{5}$ are material constants measured from laboratory tests.

$\dot{\varepsilon}_{p}^{*}$ is the dimensionless plastic strain rate $\left(\dot{\varepsilon}_{p}^{*} = \dot{\varepsilon}_{p}/\dot{\varepsilon}_{0}\right)$, for $\dot{\varepsilon}_{0} = 1.0\ \text{s}^{-1}$.

T^{*} is the homologous temperature defined by $T^{*} = \left(T - T_{0}\right)/\left(T_{m} - T_{0}\right)$.

T_{0} is the ambient or reference temperature.

In a similar fashion to the Johnson–Holmquist model, the damage is accumulated according to

$$D = \Sigma \frac{\Delta \varepsilon_{\mathrm{p}}}{\varepsilon_{\mathrm{eq}}^{f}} \tag{6.73}$$

Activation of failure occurs when $D = 1.0$.

6.7.3.4 Orthotropic Failure

Complex failure involves including directionality into the failure processes or taking into account different material phases that possess differing properties. The simplest of all directional failure models involves comparing the three orthogonal principal stresses or strains to criteria set by the user. Generally, measurements are carried out on the structure in the three orthogonal directions (Figure 6.16) to measure the failure stresses/strains and input into the code. Failure is initiated when the predetermined value is reached by one of the three principal stress or strain tensors.

Mathematically, we can write that type of failure model as follows (Hiermaier, 2008a):

$$\max \left\{ \left| \frac{\sigma_{11}}{X_{\mathrm{T,C}}} \right|, \left| \frac{\sigma_{22}}{Y_{\mathrm{T,C}}} \right|, \left| \frac{\sigma_{33}}{Z_{\mathrm{T,C}}} \right|, \left| \frac{\sigma_{12}}{S_{12}} \right|, \left| \frac{\sigma_{13}}{S_{13}} \right|, \left| \frac{\sigma_{23}}{S_{23}} \right| \right\} = 1 \tag{6.74}$$

where the strength parameters, X_{T}, Y_{T}, Z_{T}, X_{C}, Y_{C} and Z_{C} are measured using a universal testing machine in the directions of 1-, 2- and 3- respectively. The subscripts T and C represent either tension or compression. The remaining shear strength parameters (S_{ij}) are measured by shear tests.

Fibre composites often comprise stiff, brittle fibres and a relatively soft polymer matrix. Consequently, it would be expected that the failure would occur in different modes. Hashin developed a model of a unidirectional composite that took into account the different material phases and the potential for different failure modes (Hashin, 1980). This is a well-known failure model and is regularly used in a variety of computational codes. The model is written as follows:
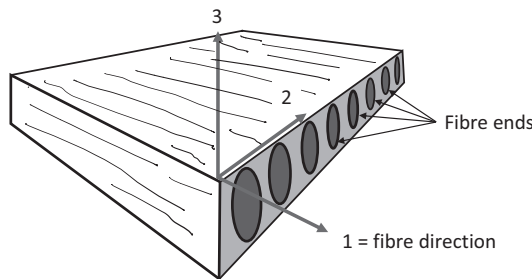
FIGURE 6.16   Elementary coordinates.

For fibre tensile failure, noting this is for a unidirectional composite: $\sigma_{11} > 0$

$$\left(\frac{\sigma_{11}}{X_T}\right)^2 + \frac{\sigma_{12}^2 + \sigma_{31}^2}{S_{12}^2} = 1 \tag{6.75}$$

Or, when ignoring shear components (this is more of a 'drastic' approximation, according to (Hashin, 1980)):

$$\sigma_{11} = X_T \tag{6.76}$$

For fibre compressive failure: $\sigma_{11} < 0$

$$\sigma_{11} = -X_C \tag{6.77}$$

For matrix tensile failure, noting this is for a unidirectional composite: $\sigma_{22} + \sigma_{33} > 0$

$$\frac{1}{Y_T^2}(\sigma_{22} + \sigma_{33})^2 + \frac{1}{S_{23}^2}\left(\sigma_{23}^2 - \sigma_{22}\sigma_{33}\right) + \frac{1}{S_{12}^2}\left(\sigma_{12}^2 + \sigma_{13}^2\right) = 1 \tag{6.78}$$

For matrix compressive mode: $\sigma_{22} + \sigma_{33} < 0$

$$\left[\left(\frac{Y_C}{2S_{12}}\right)^2 - 1\right]\frac{1}{Y_C}(\sigma_{22} + \sigma_{33}) + \frac{1}{4S_{23}^2}(\sigma_{22} + \sigma_{33})^2$$

$$+ \frac{1}{S_{23}^2}\left(\sigma_{23}^2 - \sigma_{22}\sigma_{33}\right) + \frac{1}{S_{12}^2}\left(\sigma_{12}^2 + \sigma_{13}^2\right) = 1 \tag{6.79}$$

Although it appears complicated, the user is only required to measure the following parameters which can be achieved using a universal testing machine:

X_T = tensile failure strength in the fibre direction
X_C = compressive failure strength in the fibre direction (absolute value)
Y_T = tensile failure strength transverse to the fibre direction
Y_C = compressive failure strength transverse to the fibre direction
S_{12} = axial failure stress in shear
S_{23} = transverse failure stress in shear

6.7.3.5   Modelling Delamination

Composite materials are prone to extensive delamination during ballistic penetration. To model this correctly some researchers have adopted a multi-layered mesh approach comprising multiple parts (e.g. see Nguyen et al. (2016)). A benefit of discretizing the model into sub-laminates is that delamination is represented by the through-thickness tensile failure and can be separated from the failure model. An example of a typical model setup is shown in Figure 6.17.
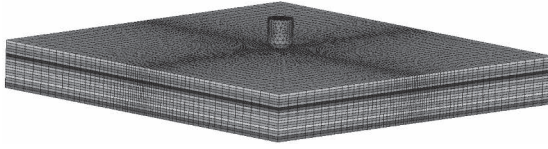
FIGURE 6.17 An example of a multi-layered meshed structure. The target comprises multiple layers of individual parts that are joined by a breakable contact algorithm.

This can be achieved using a breakable contact algorithm combining normal and shear stress to approximate the bond between lamina as represented by

$$\left(\frac{\sigma_n}{S_n}\right)^a + \left(\frac{\sigma_s}{S_s}\right)^b \geq 1 \qquad (6.80)$$

where σ and S are stress and strength values and subscripts n and s are normal and shear components at the interface, respectively. Parameters a and b are material constants and can be set to 1.0 (e.g. see Nguyen et al. (2016)). The strength values S_n and S_s are measured parameters. The parameter S_n can be assessed from spall experiments where the stress required to cause delamination is recorded. Alternatively, the through-thickness tensile strength of the materials can be assessed by pulling apart cubes or cylinders of the composite that have been adhered to the platens of a universal testing machine (see Lässig et al. (2015)). This value can be multiplied to take into account the strain-rate multiplication factor of between 2 and 5, as seen in dynamic spall tests (Riedel et al., 2004). The parameters used to model the behaviour of an ultra-high molecular weight polyethylene under ballistic impact were $S_n = 5.35$ MPa and $S_s = 7.85$ MPa (Nguyen et al., 2016).

An alternative approach is to discretize the problem into multiple small cells and adopt a meso-scale approach as has been done by (Wang et al., 2021) for ultra-high molecular weight polyethylene targets. In these cases, yarns are assumed to be homogeneous continua and modelled explicitly. The properties are assigned to each yarn and avoid complex anisotropic constitutive models but at the expense of more computational cells and therefore longer run-times—see Figure 6.18.

6.8 SUMMARY

Modelling is becoming increasingly important for the prediction of the penetration of armour. It can help us in the understanding of how projectiles interact with target materials and can all-important values of forces and stresses at key locations. However often the limitations of these approaches hinge around how the computational code in question handles failure. Incipient failure in materials occurs at the sub-micron level, and for continuum codes, this presents a problem. Therefore, for the users who do not have access to advanced computing facilities and huge data storage capacities, they must be mindful that for the most part, computational results are an approximation of reality. Therefore, they should be treated as such.
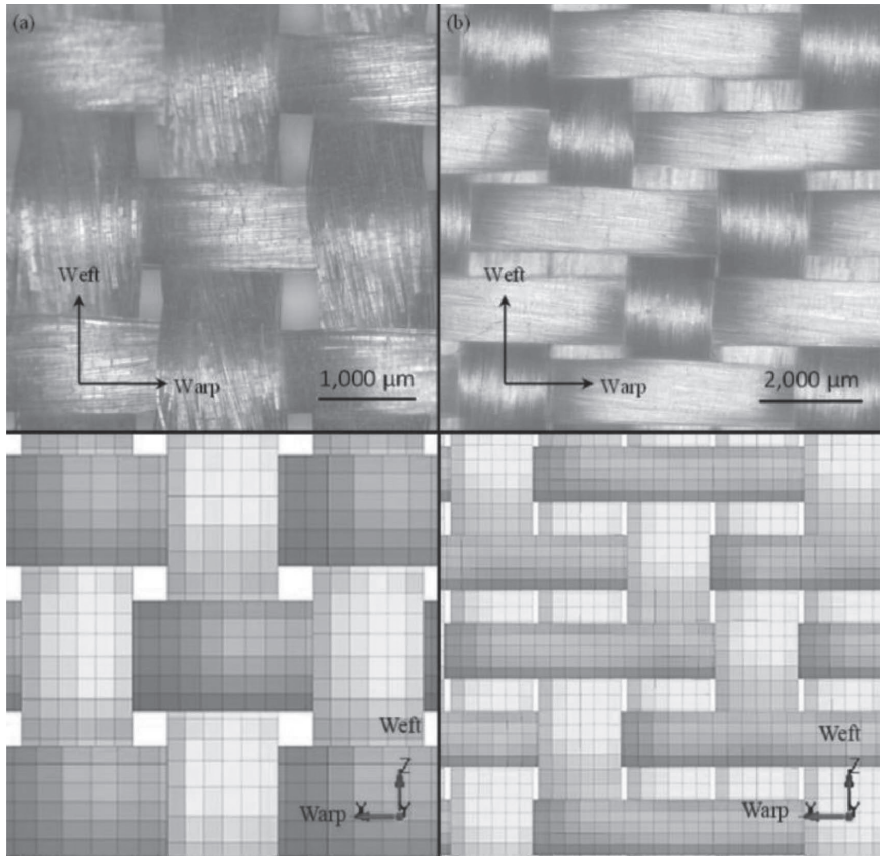
FIGURE 6.18 Actual and computational warp and weft arrangement of an ultra-high molecular polyethylene fabric at two magnifications. (Reproduced from Wang et al. (2021), with permission.)

NOTES

1 The Bauschinger Effect is named after the German engineer Johann Bauschinger (1834–1893).
2 Some composite materials can exhibit a quasi-isotropic behaviour. That is, they can have similar properties in all three orthogonal directions.

REFERENCES

Anderson Jr., C. E., Behner, T., Orphal, D. L., Nicholls, A. E. & Templeton, D. W. 2008. Time-resolved penetration into pre-damaged hot-pressed silicon carbide. *International Journal of Impact Engineering*, 35, 661–673.

Anderson Jr., C. E., Cox, P. A., Johnson, G. R. & Maudlin, P. J. 1994. A constitutive formulation for anisotropic materials suitable for wave propagation computer programs-II. *Computational Mechanics*, 15, 201–223.

Anderson, C. E., Chocron, S. & Behner, T. 2009. A constitutive model for in situ comminuted silicon carbide. *Journal of the American Ceramic Society*, 92, 1280–1286.

Andrade, E. N. D. C. 1934. XLI. A theory of the viscosity of liquids.—Part I. *The London, Edinburgh, and Dublin Philosophical Magazine and Journal of Science*, 17, 497–511.

Austin, S., Brown, A. D., Escobedo, J. P., Wang, H., Kleine, H. & Hazell, P. J. 2017. The high-velocity impact of Dyneema® and Spectra® laminates: Implementation of a simple thermal softening model. Procedia Engineering, 204, 51–58.

Bobbili, R., Ramakrishna, B., Madhu, V. & Gogia, A. K. 2015. Prediction of flow stress of 7017 aluminium alloy under high strain rate compression at elevated temperatures. *Defence Technology*, 11, 93–98.

Børvik, T., Dey, S. & Clausen, A. H. 2009. Perforation resistance of five different high-strength steel plates subjected to small-arms projectiles. *International Journal of Impact Engineering*, 36(7), 948–964.

Børvik, T., Hopperstad, O. S., Berstad, T. & Langseth, M. 2001. A computational model of viscoplasticity and ductile damage for impact and penetration. *European Journal of Mechanics - A/Solids*, 20, 685–712.

Børvik, T., Hopperstad, O. S. & Pedersen, K. O. 2010. Quasi-brittle fracture during structural impact of AA7075-T651 aluminium plates. *International Journal of Impact Engineering*, 37, 537–551.

Bridgman, P. W. 1952. *Studies in Large Plastic Flow and Fracture*. New York: McGraw-Hill.

Campbell, J. & Vignjevic, R. 2009. Artificial viscosity methods for modelling shock wave propagation. *In:* Hiermaier, S. (ed.) *Predictive Modeling of Dynamic Processes: A Tribute to Professor Klaus Thoma*. Boston, MA: Springer US.

Chen, J. K., Allahdadi, F. A. & Sun, C. T. 1997. A quadratic yield function for fiber-reinforced composites. *Journal of Composite Materials*, 31, 788–811.

Chocron, S., Anderson, C. E., Dannemann, K. A. & Nicholls, A. E. 2013. Pressure effects on the compressive response of confined intact and damaged soda-lime glass. *Experimental Mechanics*, 53, 77–89.

Chocron, S., Anderson Jr., C. E., Dannemann, K. A., Nicholls, A. E. & King, N. L. 2012. Intact and predamaged boron carbide strength under moderate confinement pressures. *Journal of the American Ceramic Society*, 95, 350–357.

Chocron, S., Anderson Jr., C. E., Nicholls, A. E. & Dannemann, K. A. 2010. Characterization of confined intact and damaged borosilicate glass. *Journal of the American Ceramic Society*, 93, 3390–3398.

Chocron, S., Dannemann, K. A., Nicholls, A. E., Walker, J. D. & Anderson, C. E. 2005. A constitutive model for damaged and powder silicon carbide. *In:* Swab, J. J., Zhu, D. & Kriven, W. M. (eds.) *29th International Conference on Advanced Ceramics and Composites, Ceramic Engineering and Science Proceedings*. Cocoa Beach, FL: John Wiley and Sons, Inc.

Clegg, R. A., White, D. M., Riedel, W. & Harwick, W. 2006. Hypervelocity impact damage prediction in composites: Part I-material model and characterisation. *International Journal of Impact Engineering*, 33, 190–200.

Cockroft, M. G. & Latham, D. J. 1968. Ductility and the workability of metals. *Journal of the Institute of Metals*, 96, 33–39.

Cowper, G. R. & Symonds, P. S. 1957. *Strain-Hardening and Strain-Rate Effects in the Impact Loading of Cantilever Beams*. Providence, RI: Brown University.

Dandekar, D. P., Hall, C. A., Chhabildas, L. C. & Reinhart, W. D. 2003. Shock response of a glass-fiber-reinforced polymer composite. *Composite Structures*, 61, 51–59.

Deshpande, V. S. & Evans, A. G. 2008. Inelastic deformation and energy dissipation in ceramics: A mechanism-based constitutive model. *Journal of the Mechanics and Physics of Solids*, 56, 3077–3100.

Dey, S., Børvik, T., Hopperstad, O. S. & Langseth, M. 2007. On the influence of constitutive relation in projectile impact of steel plates. *International Journal of Impact Engineering*, 34, 464–486.

Drucker, D. C. & Prager, W. 1952. Soil mechanics and plastic analysis for limit design. *Quarterly of Applied Mathematics*, 10, 157–165.

Gray III, G. T., Chen, S. R., Wright, W. & Lopez, M. F. 1994. *Constitutive Equations for Annealed Metals under Compression at High Strain Rates and High Temperatures*. Los Alamos, NM: Los Alamos National Laboratory.

Hashin, Z. 1980. Failure criteria for unidirectional fiber composites. *Journal of Applied Mechanics*, 47, 329–334.

Hazell, P. J. & Iremonger, M. J. 1997. Crack softening damage model for ceramic impact and its application within a hydrocode. *Journal of Applied Physics*, 82, 1088–1092.

Hazell, P. J., Stennett, C. & Cooper, G. 2009. The effect of specimen thickness on the shock propagation along the in-fibre direction of an aerospace-grade CFRP laminate. *Composites Part A: Applied Science and Manufacturing*, 40, 204–209.

Héreil, P. L., Allix, O. & Gratton, M. 1997. Shock behaviour of 3D carbon-carbon composite. *Le Journal de Physique IV*, 7, C3-529–C3-534.

Hiermaier, S. J. 2008a. Failure models for dynamic loading conditions. *In: Structures under Crash and Impact: Continuum Mechanics, Discretization and Experimental Characterization*. Boston, MA: Springer US.

Hiermaier, S. J. 2008b. Hydrocodes. *In: Structures under Crash and Impact: Continuum Mechanics, Discretization and Experimental Characterization*. Boston, MA: Springer US.

Hill, R. 1948. A theory of the yielding and plastic flow of anisotropic metals. *Proceedings of the Royal Society of London. Series A. Mathematical and Physical Sciences*, 193, 281–297.

Holmquist, T. & Johnson, G. N. 1991. Determination of constants and comparison of results for various constitutive models. *Journal de Physique IV Proceedings*, 01, 853–860.

Holmquist, T. J. & Johnson, G. R. 2002. Response of silicon carbide to high velocity impact. *Journal of Applied Physics*, 91, 5858–5866.

Holmquist, T. J. & Johnson, G. R. 2011. A computational constitutive model for glass subjected to large strains, high strain rates and high pressures. *Journal of Applied Mechanics*, 78, 051003.

Holmquist, T. J., Johnson, G. R. & Gerlach, C. A. 2017. An improved computational constitutive model for glass. *Philosophical Transactions of the Royal Society A: Mathematical, Physical and Engineering Sciences*, 375, 20160182.

Hopperstad, O. S., Børvik, T., Langseth, M., Labibes, K. & Albertini, C. 2003. On the influence of stress triaxiality and strain rate on the behaviour of a structural steel. Part I. Experiments. *European Journal of Mechanics, A/Solids*, 22, 1–13.

Iqbal, M. A., Senthil, K., Bhargava, P. & Gupta, N. K. 2015. The characterization and ballistic evaluation of mild steel. *International Journal of Impact Engineering*, 78, 98–113.

Iqbal, M. A., Senthil, K., Sharma, P. & Gupta, N. K. 2016. An investigation of the constitutive behavior of Armox 500T steel and armor piercing incendiary projectile material. *International Journal of Impact Engineering*, 96, 146–164.

Johnson G. R. & Cook, W. H. 1983. A constitutive model and data for metals subjected to large strains, high strain rates and high temperatures. *In: Proceedings of the 7th International Symposium on Ballistics*. The Hague, The Netherlands: American Defense Preparedness Association.

Johnson, G. R. & Cook, W. H. 1985. Fracture characteristics of three metals subjected to various strains, strain rates, temperatures and pressures. *Engineering Fracture Mechanics*, 21, 31–48.

Johnson, G. R. & Holmquist, T. J. 1989. *Test Data and Computational Strength and Fracture Model Constants for 23 Materials Subject to Large Strains, High Strain Rates, and High Temperatures*. New Mexico: Los Alamos National Laboratory.

Johnson, G. R. & Holmquist, T. J. 1992. A computational constitutive model for brittle materials subjected to large strains, high rates, and high pressure. *In:* Meyers, M. A., Murr, L. E. & Staudhammer, K. P. (eds.) *Shock-Wave and High Strain Rate Phenomena in Materials*. New York: Marcel Dekker Inc.

Johnson, G. R. & Holmquist, T. J. 1994. An improved computational constitutive model for brittle materials. *In:* Schmidt, S. C., Shaner, J. W., Samara, G. A. & Ross, M. (eds.) *High Pressure Science and Technology -1993*. Colorado Springs, CO: AIP.

Johnson, G. R., Holmquist, T. J. & Beissel, S. R. 2003. Response of aluminum nitride (including a phase change) to large strains, high strain rates, and high pressures. *Journal of Applied Physics*, 94, 1639–1646.

Khennane, A. 2013. *Introduction to Finite Element Analysis Using MATLAB® and Abaqus*. Boca Raton, FL: CRC Press.

Kleemola, H. J. & Nieminen, M. A. 1974. On the strain-hardening parameters of metals. *Metallurgical Transactions*, 5, 1863–1866.

Landshoff, R. 1955. *A Numerical Method for Treating Fluid Flow in the Presence of Shocks*. Los Alamos, NM: Los Alamos Scientific Laboratory.

Lässig, T., Nguyen, L., May, M., Riedel, W., Heisserer, U., Van Der Werff, H. & Hiermaier, S. 2015. A non-linear orthotropic hydrocode model for ultra-high molecular weight polyethylene in impact simulations. *International Journal of Impact Engineering*, 75, 110–122.

Li, Q. M. & Meng, H. 2003. About the dynamic strength enhancement of concrete-like materials in a split Hopkinson pressure bar test. *International Journal of Solids and Structures*, 40, 343–360.

Lin, Y. C. & Chen, X.-M. 2010. A combined Johnson–Cook and Zerilli–Armstrong model for hot compressed typical high-strength alloy steel. *Computational Materials Science*, 49, 628–633.

Marsh, S. P. 1980. *LASL Shock Hugoniot Data*. Berkley: University of California Press.

Meyer JR, H. W. & Kleponis, D. S. 2001. Modeling the high strain rate behavior of titanium undergoing ballistic impact and penetration. *International Journal of Impact Engineering*, 26, 509–521.

Meyers, M. A. 1994. *Dynamic Behaviour of Materials*. New York, John Wiley & Sons, Inc.

Millett, J. C. F., Bourne, N. K., Meziere, Y. J. E., Vignjevic, R. & Lukyanov, A. 2007a. The effect of orientation on the shock response of a carbon fibre-epoxy composite. *Composites Science and Technology*, 67, 3253–3260.

Millett, J. C. F., Meziere, Y. J. E. & Bourne, N. K. 2007b. The response to shock loading of a glass-fibre-epoxy composite: Effects of fibre orientation to the loading axis. *Journal of Physics D: Applied Physics*, 40, 5358–5365.

Nemat-Nasser, S. & Guo, W.-G. 2005. Thermomechanical response of HSLA-65 steel plates: experiments and modeling. *Mechanics of Materials*, 37, 379–405.

Neumann, J. V. & Richtmyer, R. D. 1950. A method for the numerical calculation of hydrodynamic shocks. *Journal of Applied Physics*, 21, 232–237.

Nguyen, L. H., Lässig, T. R., Ryan, S., Riedel, W., Mouritz, A. P. & Orifici, A. C. 2015. Numerical modelling of ultra-high molecular weight polyethylene composite under impact loading. *Procedia Engineering*, 103, 436–443.

Nguyen, L. H., Lässig, T. R., Ryan, S., Riedel, W., Mouritz, A. P. & Orifici, A. C. 2016. A methodology for hydrocode analysis of ultra-high molecular weight polyethylene composite under ballistic impact. *Composites Part A: Applied Science and Manufacturing*, 84, 224–235.

Nilsson, M. 2003. *Constitutive Model for Armox 500T and Armox 600T at Low and Medium Strain Rates*. Weapons and Protection, SE-147 25. Tumba: Swedish Defence Research Agency.

Riedel, W., Nahme, H. & Thoma, K. 2004. Equation of state properties of modern composite materials: modelling shock, release and spallation. *AIP Conference Proceedings*, 706, 701–704.

Roberts, A., Appleby-Thomas, G. J. & Hazell, P. J. 2012. Experimental determination of Grüneisen gamma for polyether ether ketone (PEEK) using the shock-reverberation technique. *In:* Elert, M. L., Buttler, W. T., Borg, J. P., Jordan, J. L. & Vogler, T. J. (eds.) *Shock Compression Of Condensed Matter -2011: Proceedings of the Conference of the American Physical Society Topical Group on Shock Compression of Condensed Matter.* Chicago, IL: AIP.

Royce, E. B. 1971. *Gray, A Three-Phase Equation of State for Metals.* Lawrence Livermore Laboratory.

Ryan, S., Wicklein, M. & Mouritz, A. 2009. Theoretical prediction of dynamic composite material properties for hypervelocity simulations. *International Journal of Impact Engineering*, 36, 899–912.

Saleh, M., Edwards, L. & Crouch, I. G. 2017. Numerical modelling and computer simulations. *In:* Crouch, I. G. (ed.) *The Science of Armour Materials.* Duxford: Woodhead Publishing.

Seidt, J. D. & Gilat, A. 2013. Plastic deformation of 2024-T351 aluminum plate over a wide range of loading conditions. *International Journal of Solids and Structures*, 50, 1781–1790.

Senthil, K., Iqbal, M. A., Chandel, P. S. & Gupta, N. K. 2017. Study of the constitutive behavior of 7075-T651 aluminum alloy. *International Journal of Impact Engineering*, 108, 171–190.

Steinberg, D. J. 1987. Constitutive model used in computer simulation of time-resolved, shock-wave data. *International Journal of Impact Engineering*, 5, 603–611.

Steinberg, D. J., Cochran, S. G. & Guinan, M. W. 1980. A constitutive model for metals applicable at high-strain rate. *Journal of Applied Physics*, 51, 1498–1504.

Steinberg, D. J. & Lund, C. M. 1989. A constitutive model for strain rates from 10^{-4} to $10^{6} s^{-1}$. *Journal of Applied Physics*, 65, 1528–1533.

Taylor, G. I. & Quinney, H. 1934. The latent energy remaining in a metal after cold working. *Proceedings of the Royal Society of London. Series A, Containing Papers of a Mathematical and Physical Character*, 143, 307–326.

Tsai, L., Yuan, F., Prakash, V. & Dandekar, D. P. 2009. Shock compression behavior of a S2-glass fiber reinforced polymer composite. *Journal of Applied Physics*, 105, 093526.

Wang, H., Weerasinghe, D., Mohotti, D., Hazell, P. J., Shim, V. P. W., Shankar, K. & Morozov, E. V. 2021. On the impact response of UHMWPE woven fabrics: Experiments and simulations. *International Journal of Mechanical Sciences*, 204, 106574.

Winter, R. E., Whiteman, G., Haining, G. S., Salisbury, D. A. & Tsembelis, K. 2004. Measurement of equation of state of silicone elastomer. *AIP Conference Proceedings*, 706, 679–684.

Wood, D. C., Appleby-Thomas, G. J., Hazell, P. J. & Barnes, N. R. 2012. Shock propagation in a tape wrapped carbon fibre composite. *Composites Part A: Applied Science and Manufacturing*, 43, 1555–1560.

Woodruff, J. P. 1976. *KOVEC User's Manual.* Livermore, CA: Lawrence Livermore Laboratory.

Xie, W., Zhang, W., Guo, L., Gao, Y., Li, D. & Jiang, X. 2018. The shock and spallation behavior of a carbon fiber reinforced polymer composite. *Composites Part B: Engineering*, 153, 176–183.

Yuan, F., Tsai, L., Prakash, V., Rajendran, A. M. & Dandekar, D. P. 2007. Spall strength of glass fiber reinforced polymer composites. *International Journal of Solids and Structures*, 44, 7731–7747.

Zerilli, F. J. & Armstrong, R. W. 1987. Dislocation-mechanics-based constitutive relations for material dynamics calculations. *Journal of Applied Physics*, 61, 1816–1825.

Zerilli, F. J. & Armstrong, R. W. 1994. Constitutive relations for the plastic deformation of metals. *AIP Conference Proceedings*, 309, 989–992.

Zhuk, A. Z., Kanel, G. I. & Lash, A. A. 1994. Glass-epoxy composite behaviour under shock loading. *Le Journal de Physique IV*, 4, C8-403–C8-407.

Zukas, J. A. 1990. *High Velocity Impact Dynamics*. New York: John Wiley & Sons, Inc.

Zukas, J. A. 2004. *Introduction to Hydrocodes*. Amsterdam: Elsevier.

7 Metallic Armour Materials and Structures

7.1 INTRODUCTION

Metals have been used extensively in armour. Generally speaking, there are only four practical metallic contenders for armour applications: aluminium, magnesium, steel and titanium. Steel and aluminium are the most common metals in use today mainly due to the price and their ability to be worked and welded. However, magnesium and titanium, although expensive, have some desirable properties that will be discussed in Sections 7.3.4 and 7.3.5. Figure 7.1 shows a summary of how most armour is made. The vast majority of armour is wrought plate. That is to say that it is processed by rolling or pressing. Some armour is cast, although this has been mostly reserved for the turrets of tanks such as the Chieftain (see Figure 7.2).

To protect against ballistic attack, it is necessary to use a solid homogeneous plate, although there are one or two exceptions, as will be seen later. To protect against blast, this is not necessarily the case. In fact, it has been shown that hollow porous structures can aid in providing protection against blast waves.

7.2 PROPERTIES AND PROCESSING OF METALLIC ARMOUR

7.2.1 WROUGHT PLATE

Wrought plates are mechanically worked either through hot working or cold working the material. The typical ways that this is achieved are as follows:

- *Forging*: where the piece is subjected to successive blows or by continuous squeezing of the metal.
- *Rolling*: where a plate is squeezed in between two rollers. This is by far the most common method of processing wrought armour plate mainly because desirable thicknesses and properties can be achieved through this process.
- *Extrusion*: where the piece is forced through a die to produce the desired shape.
- *Drawing*: where the metal is pulled through a die that has a tapered bore. Rod and wire are commonly fabricated in this way (not used for armour plate).

7.2.2 CAST ARMOUR

Casting metal structures for armour applications, where molten metal is solidified in a mould, has become less attractive in recent years as the strength that can be offered by wrought plates is far superior. However, before and during World War II (WWII),

279
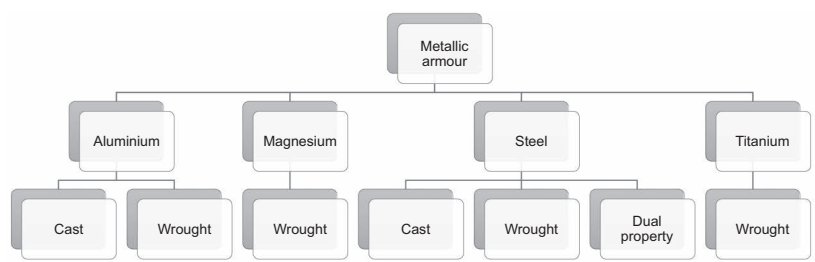
FIGURE 7.1   Classifications of materials that are used in armour applications.

FIGURE 7.2   Chieftain Main Battle Tank (MBT) employing a cast steel turret.

there was a significant amount of cast armour produced. Casting metallic structures (say, for example, for turrets on tanks) can provide some geometric and cost advantages. Accordingly, the Chieftain Main Battle Tank (MBT) employed such a turret. However, castings are notorious for containing porosity and generally possess low toughness values.

Some improvements in the casting of steels occurred in the 1970s when it was shown that cooling the metal in such a way that heat was extracted on one surface led to improvements in properties. This process resulted in columns of grains extended from the chill surface completely through the casting thereby giving the casting microstructural 'texture'. The end result was a casting that had superior ductility and ballistic performance than conventional castings (Papetti, 1980).

7.2.3 Welding and Structural Failure due to Blast and Ballistic Loading

Welding is a very common way of joining metallic plates, and it is particularly important for armoured fighting vehicles (AFVs) that may be exposed to blast loading. Joins are often a source of weakness in structures, and it is these that tend to fail first if the whole structure is subjected to a dynamic stimulus (such as a blast wave). Therefore, it is necessary to get the technique right.

During the welding process, there is a diffusion of the metal so that the join is metallurgical rather than mechanical. Arc and gas welding occurs by a process of melting the work pieces and a filler material (i.e. the welding rod), whilst they are all in contact with one another. When all materials solidify, the filler material provides a join between the work pieces. Unfortunately, there will be a material that is adjacent to the weld that experiences microstructural changes due to being subjected to elevated temperatures. This will lead to change in the localized properties of the material, and this can turn out to be a source of weakness. This area of property alteration is called the 'heat-affected zone' and is sometimes abbreviated as 'HAZ'. There are several reasons why properties are changed in the HAZ, as summarized by Callister (2007):

1. If the material was previously cold worked, the temperature increase due to the welding process may lead to grain growth or recrystallization. This process weakens the material and can lead to a reduction of strength, hardness and toughness in this zone.
2. On cooling, the material experiences residual stresses due to different cooling rates through the thickness of the weld. These residual stresses can lead to a weakness in the joint.
3. For steels, the material may have been heated sufficiently by the welding process to form austenite. On cooling, the phases that are produced are dependent on the cooling rate and the carbon content of the steel. For plain carbon steels, normally, pearlite will form on cooling. However, for alloy steels, martensite can form. This is undesirable as it is brittle. This will be discussed briefly in Section 7.3.2.1.
4. Some stainless steels may become sensitive to inter-granular corrosion in the HAZ. In essence, they begin to corrode due to the formation of a chromium-free zone adjacent to the grain boundaries as chromium carbide precipitates are formed. Therefore, the grain boundaries become susceptible to corrosion.

The HAZ in the weld can be the origin of the failure, as depicted in Figure 7.3, both through structural collapse and through perforation (caused by the local failure of weld material).
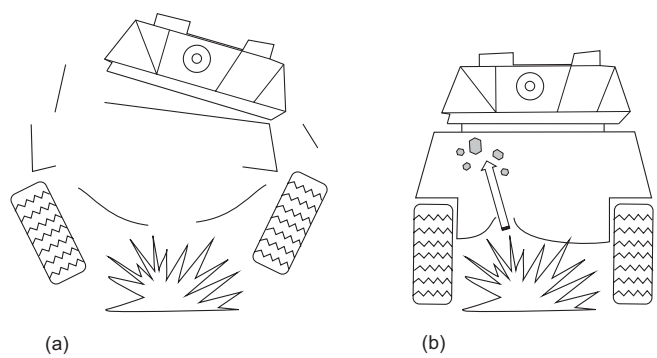
FIGURE 7.3 Failure of an armoured vehicle subjected to blast loading showing (a) structural collapse through the failure of the welds and, (b) perforation of the hull bottom by explosively accelerated debris.
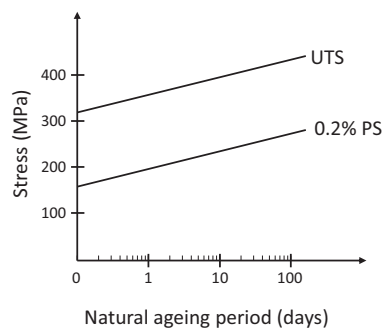
FIGURE 7.4 Natural ageing of 7039 alloy after welding (after (Doig, 2002) showing the increase in the 0.2% proof strength (PS) and the ultimate tensile strength (UTS) with time.

Care should be taken when welding armoured steel—and this is all the more important to consider when carrying out field repairs. Cracking can occur along the weld if inappropriate methods are used. Alkemade (1996) examined the weldability of high-hardness steel armour plate—specifically for the Australian light armoured vehicle (LAV) 25 that is made from welded high-hard steel plate. The purpose of his work was to examine the susceptibility to cracking after fusion welding of Bisalloy® 500 armour plate (0.2% proof strength = 1580 MPa). It was shown that for this armour, hydrogen-induced cracking was seen in the hardened region of the HAZ where the heat input was 0.5 kJ/mm, and the preheat was 75°C or less, whereas no cracking was observed at this heat input when the preheat was raised to 150°C. Additionally, when the heat input was raised to 1.2 kJ/mm, no cracking was observed even when preheat was not used.

Care should also be taken when welding aluminium alloys as a substantial reduction in strength can occur around the HAZ. This has led to the British Army ensuring that the Scorpion armoured fighting vehicle is put on 'light duties' for several months after a repair (Doig, 2002). This allows for the aluminium alloy to 'age harden' (see later). Figure 7.4 shows the effect of natural ageing of the HAZ for a 7039 alloy (after

(Doig, 2002), showing the increase in the 0.2% proof strength (PS) and the ultimate tensile strength (UTS) with time.

A good weld between two armour plates can be achieved by the use of laser beam welding (LBW). LBW uses a highly focused and intense laser beam as a heat source to selectively melt the materials. Often, there is no need to supply a separate filler material, and the process can be employed in a highly automated fashion. The resulting HAZ is usually small due to the fact that the total energy input into the work pieces is small, and the welds are precise. With LBW, it is entirely possible to achieve porosity-free welds with strengths at least equal to the parent metal.

7.3 METALLIC ARMOUR MATERIALS

Four of the more important metal alloys that are used in protection will now be reviewed: steel, aluminium, magnesium and titanium. The United States publish MIL specifications that define the minimum ballistic behaviour of these materials against certain threats, and these are summarized in Table 7.1. A quick Google search will provide the text.

7.3.1 COMPARING THE BALLISTIC PERFORMANCE OF METAL ARMOUR MATERIALS

Apart from a couple of examples, most metal armour materials exhibit relatively similar ballistic properties on a weight-by-weight basis when subjected to impact by armour-piercing projectiles. Figure 7.5 shows the variation of ballistic limit velocities, v_{50}, with the areal densities of various metallic armour plates subjected to impact by a 30-cal AP M2 projectile. Apart from a couple of outliers, the data is bounded by an upper envelope boundary and a lower envelope boundary. The equations for those boundaries are as follows:

$$\text{Upper envelope}: v_{50} = 12.5A_\mathrm{d} - 0.03A_\mathrm{d}^2$$

$$\text{Lower envelope}: v_{50} = 10.0A_\mathrm{d} - 0.03A_\mathrm{d}^2$$

TABLE 7.1
US Military Standards for Steel, Aluminium, Magnesium and Titanium Alloys

Standard	Date	Name
MIL-DTL-12560J	24 July 2009	Homogeneous wrought armour plate
MIL-DTL-46100E	24 October 2008	Armour plate, steel, wrought, high hardness
MIL-DTL-46177C	24 October 1998	Armour, steel plate and sheet, wrought, homogeneous (1/8 to less than 1/4 in. thick)
MIL-DTL-46027K	31 July 2007	Armour plate, aluminium alloy, weldable 5083, 5456 and 5059
MIL-DTL-46063H	14 September 1998	Armour plate, aluminium alloy, 7039
MIL-DTL-32333	29 July 2009	Armour plate, magnesium alloy, AZ31B, applique
MIL-DTL-46077G	28 September 2006	Armour plate, titanium alloy, weldable
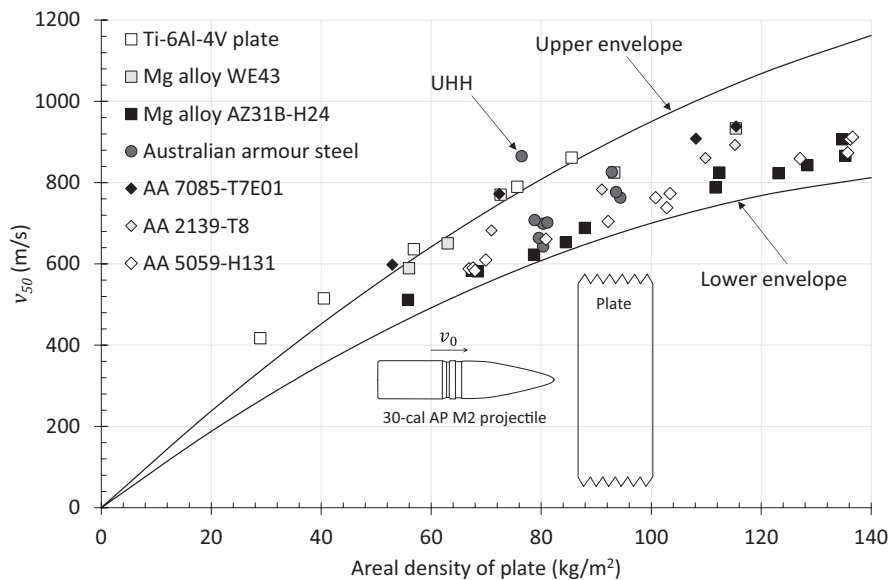
FIGURE 7.5 Comparing the v_{50} ballistic limit velocity for different armour plates showing an upper and lower envelope of commonality; data from (Gallardy, 2012, Jones, 2004, Fanning, 2000, Lloyd et al., 2021, Cheeseman et al., 2008, Showalter et al., 2008, Gooch et al., 2007, Ryan et al., 2016). The higher the value of v_{50}, the better the protection (see Chapter 12).

where the areal density, A_d, is defined as follows in terms of the plate thickness, h, and density, ρ_0 :

$$A_d = \rho_0 h \tag{7.1}$$

These two 'envelope equations' dictate what can be expected from metallic armour materials. If ballistic data for a new alloy sits above the upper envelope, then it can be regarded as a good product. There are a couple of materials that fit that criterion. These are the Ti-6Al-4V plate and AA 7085-T7E01. Titanium alloys are a well-known high-strength solution for many engineering applications, and these will be discussed later. AA 7085 is an aerospace-grade aluminium alloy available in large volume production for the aircraft industry used in bulkheads and wing spars. It has a yield strength of 530 MPa in the T6 temper condition. The temper for this ballistic data (T7E01) was an experimental designation (Gallardy, 2012). One other outlying point is the single point presented by Ryan et al. (2016) for a Bisalloy® UHH plate (hardness = 590 HB). This was due to the high hardness of the plate and the velocity of impact causing the shattering of the projectile's core.

7.3.2 STEEL ARMOUR

Steel is by far the most commonly used material in armoured vehicles to date mainly because steel is a good 'all-rounder'. Toughness, hardness, good fatigue properties,

ease of fabrication and joining and its relatively low cost make steel a popular choice for armoured vehicle hulls. Steel has been used extensively over the centuries and found its first use in armoured vehicles in the tanks of World War I (WWI), and it is still used extensively today.

7.3.2.1   A Quick Word on the Metallurgy of Steel

Steels are Fe–C alloys that possess between 0.008 wt% and 2.14 wt% C. Introductory materials science books discuss in detail the iron–iron carbide phase diagrams (e.g. see Ashby and Jones, 1986). This is a diagram that shows how the microstructure of the steel will develop if allowed sufficient time during cooling such that near-equilibrium conditions are always maintained. One of the remarkable features of Fe is that it undergoes polymorphism. This is the ability of a material to exist in more than one crystal structure and for Fe, this occurs when the temperature is increased. At room temperature, the stable form of iron is called *ferrite*, or α-iron (or α-ferrite) and it has a body-centred cubic (BCC) crystal structure. At 912°C, ferrite undergoes a polymorphic phase transformation to FCC *austenite*, or γ-iron. Increasing the temperature to 1394°C results in the reversion back to a BCC structure with the formation of δ-ferrite. This finally melts at 1538°C. The δ-ferrite is virtually identical to α-ferrite except over which the temperature range it exists.

We class ferrous alloys into three types: iron, steel and cast iron. For C contents of 0.008 wt% and less, α-ferrite is the dominant phase at room temperature (almost exclusively so) and commercially this would be regarded as pure iron. The metal is regarded as being steel for carbon contributions of between 0.008 and 2.14 wt% although in practice carbon concentrations are generally below 1.4 wt%. The 2.14 wt% value is chosen as this corresponds to the maximum solubility of carbon in austenite at 1147°C. Above 2.14 wt% carbon concentrations (and up to 6.70 wt% C) the material is regarded as being cast iron.

Another important component of steel is *cementite*. This is the compound Fe_3C and it is formed when the solubility limit of carbon in Fe is exceeded. It is very hard and brittle, and the strength of steel is enhanced by its presence.

Unlike many non-ferrous alloys, the cooling rate from elevated temperatures plays a large part in how the microstructure (and the resultant mechanical property) is formed. Cooling a steel quickly will have a different effect than cooling it slowly—depending on the quantity of carbon and other alloying elements. For example, slowly cooling a plain carbon steel from around 850°C will result in BCC α grains (ferrite) being formed and nodules[1] of *pearlite*. Pearlite is an alternate plate-like mixture of α-iron and cementite (iron carbide (Fe_3C)). The iron (α) phase is quite soft with a local hardness of about 90 VHN, whereas pearlite is stronger and harder with a typical hardness of 250 VHN. Cooling can be very slow (i.e. in a furnace) or in air, depending on the desired pearlite structure. Slower cooling rates generally result in coarser structures. When cooling is done in the air, the complete process (heating and slow cooling in air) is known as normalizing. Rapid cooling or 'quenching' is done in water or oil. Rapidly cooling the same plain carbon steel in water will result in *martensite* forming. Martensite arises when the quenching rate
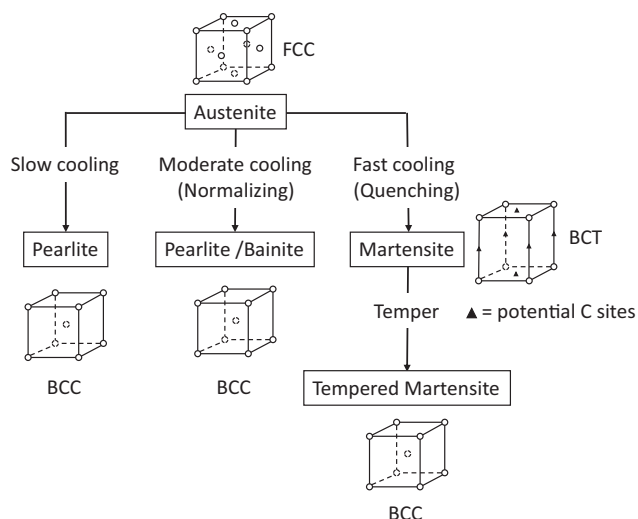
FIGURE 7.6   A summary of the different crystal transformations that can occur during the decomposition of austenite. BCC, body-centred cubic; BCT, body-centred tetraganol; FCC, face-centred cubic.

is so rapid that it prevents the diffusion of the carbon atoms. This means that the FCC austenite undergoes a polymorphic transformation to a body-centred tetragonal (BCT) lattice. This is a body-centred cubic structure that has been elongated along one of its dimensions. The structure is supersaturated with carbon atoms that remain as interstitial impurities but can readily diffuse out when the structure is reheated. Martensite is the hardest constituent obtained in a given steel (800–900 VHN), and the hardness of this phase increases with carbon content. The martensitic microstructure consists of a fine needle-like structure. These steels are hard but brittle, and therefore, they need tempering to allow for an improvement in toughness. The tempering process allows for the diffusion of the martensite into tempered martensite that consists of stable ferrite and cementite phases. Internal stresses are also relieved which results in a strong and tough steel. Several armour plates are manufactured in this fashion. Another constituent that can be formed on cooling in alloy steels is *bainite*. Through careful choice of alloying elements and tempering temperatures, it is possible to produce a super-strong bainite steel with nano-sized grain sizes. This makes the steel very strong with tensile strengths of 2 GPa quite possible. This is obviously very attractive as an armour. A summary of the transformations is shown in Figure 7.6.

There are several labels for steels. These are summarized below:

1. *Low-carbon steels*: These steels generally have a low-carbon content (<0.25 wt%) and are unresponsive to heat treatment. Strengthening the material is generally achieved by cold working. They will have low yield strengths (around 150–250 MPa) and will work-harden easily. Generally,

these steels are not useful for lightweight armour applications as they are too soft, and consequently, large sections are required to stop modern weapon systems. However, they exhibit excellent ductility, are easily machinable and weldable and are generally cheap. Examples of low-carbon steels are AISI 1010 and 1020 grades that have 0.1 and 0.2 wt% carbon content, respectively, and yield strengths of 180 and 205 MPa. High-strength low-alloy steels are also classed as low-carbon steels as they possess low-carbon contents. These steels are stronger with yield strengths approaching 500 MPa. These types of steels are useful for construction and are readily weldable. They have good toughness characteristics and provide a moderate resistance to penetration.

2. *Medium-carbon steels*: These steels have a carbon content of between 0.25 and 0.6 wt%. These steels may be heat treated by austenitizing, quenching and then tempering to improve the mechanical properties. Sometimes referred to as quenched and tempered steels, these steels are used where high strengths are required and can be in an alloyed or unalloyed form. They are readily weldable and when alloyed, provide good options for lightweight armour. An example is Bisalloy® armour HHA500 steel plate, which is an alloy steel with 0.32 wt% C and a tensile strength of 1640 MPa (Anon, 2020a).

3. *High-carbon steels*: These steels have carbon contents in the range between 0.6 and 1.4 wt%. They possess high strength and hardness due to the presence of large amounts of Fe_3C. However, unless they are combined with alloying elements, they can be brittle. They are generally used in hardened and tempered conditions. They are good for wear resistance applications.

4. *High alloy steels*: These generally have more than 12 wt% in alloying elements. For example, stainless steel would fit this class of steel and has a high chromium content (11–25 wt%) for corrosion resistance. Other examples include temperature-resistant steels such as Inconel® which is a nickel–chromium alloy steel. These steels are generally relatively expensive and used in niche applications.

7.3.2.2 Rolled Homogeneous Armour

Rolled homogeneous armour (RHA) has been used extensively as an armour material for nearly a century. It is usually used in depth-of-penetration testing as the benchmark for testing armour materials. It is also used in describing the performance of armour systems or materials in terms of RHA equivalences, that is, the thickness of RHA required to defeat a given projectile when compared to a specific armour system that is able to defeat the same projectile.

RHA is manufactured by hot-rolling ingots of steel that contain a small percentage of alloying elements followed by quench and temper processing to produce a through-hardened tempered martensitic structure. A typical chemical composition of the RHA plate is shown in Table 7.2 with broad limits; the exact composition would depend on the required properties and thickness of the plate to be hardened.

TABLE 7.2

Composition of RHA

C	Mn	Ni	Cr	Mo	S	P
0.18–0.32	0.60–1.50	0.05–0.95	0.00–0.90	0.30–0.60	0.015 (max)	0.015 (max)

Changing the alloying content and treatment of the steel will provide a range of strengths and ductility. For example, the UK Ministry of Defence Standard for Armour Plate (MoD, 2004) specifies five classes of hardened and tempered RHA within the thickness limits of 3–160 mm.

Military specifications normally provide steel suppliers latitude to satisfy the requisite armour mechanical properties and ballistic requirements within a broad range of chemistry and treatment conditions. A typical treatment process for the RHA plate is as follows.

After rolling the steel into shape, the plate would normally be hardened by reheating to between 820°C and 860°C and quenched in oil or water. The resulting product is very strong but brittle due to the formation of the hard and brittle martensite phase. This can be moderated by tempering whereby the steel is reheated in a furnace for a few hours to temperatures in the region of 400°C–650°C. The final product will be relatively ductile and tough and possess a uniform microstructure (hence the reference to homogeneous). The tempering temperature will be selected to give the wanted mechanical and ballistic properties with lower temperatures being used for the thinner harder armours and higher temperatures for the thicker, tougher armour plate.

7.3.2.3 High-Hardness Armour

High-hardness armour (HHA) is the name that is given to a class of homogeneous steel armour with hardness values in excess of 430 BHN.[2] Typically, the method of manufacture is similar to that of RHA involving lower tempering temperatures (~200°C as opposed to 400°C–650°C for RHA). An example of this steel is Bisalloy® armour UHH600 steel, which has a 0.45 wt% C content and a hardness in the range of 570–640 BHN. The tensile strength of this steel is 2050 MPa (Anon, 2020b).

Much of the development of modern high-hard armour steel plate occurred during the Vietnam conflict where there was a requirement for a thin steel plate that could provide protection against 0.30-in. ball ammunition. This was achieved using plates of hardness values of around 500 BHN. Of course, the use of hard armour in fighting vehicles is not new. In fact, the relatively thin plates of steel armour that were used in the tanks of WWI had hardness values within the range of 420–650 BHN (Ogorkiewicz, 1991b). A thin high-hardness plate can be used as quite an effective disruptor for most types of armour-piercing ammunition. However, with increasing hardness, the toughness is compromised, and therefore, these materials can be susceptible to gross cracking.

7.3.2.4 Variable Hardness Steel Armour

There are potential advantages in using a single steel plate with varying through-thickness properties. By surface-hardening one side of a thick low-carbon steel plate, it is possible to incorporate both hard disruptive and tough absorbing properties in a single material. The main advantage offered is that the more ductile backing layer is able to arrest crack propagation in the armour plate, whilst the hard-facing layer is able to deform or fragment the projectile.

A common approach to developing steel armour with varying hardness properties is by a process called face hardening. An early example of this is a process called carburizing, which is described as follows. The surface of the steel is heated to a temperature around 850°C–900°C in intimate contact with a carbon-rich solid (such as wood or bone charcoal), liquid or gas. During this process, carbon atoms, being soluble in the austenite phase that is formed at elevated temperatures, migrate into the steel. Once carbon has entered the steel at the surface, it diffuses inwards at a rate that is dependent upon the composition of the steel. This produces a carbon gradient from the surface of the steel to the inside. Afterwards, the steel is heat-treated to achieve the desired material properties. The result is a plate with a thin hardened face due to the additive carbon, whilst the body of the plate remains relatively tough.

This approach to armouring was first applied to battleships in the 1890s and notably was used by Vickers–Armstrong in the production of tanks during the 1920s and 1930s (Ogorkiewicz, 1991b). The armour plates from these tanks had a facing plate hardness of 600 BHN and a softer rear face of 400 BHN. Although the plate was up to 20 mm thick and was effective at defeating the contemporary armour-piercing projectiles of the time, it was virtually impossible to machine and weld and therefore had to be attached by bolts or rivets.

During WWII, the armour for the German King Tiger tanks (Figure 7.7) was produced by another surface-hardening process known as flame-hardening. This method involves heating the surface of the armour (using a gas flame) up to high temperatures and then rapidly cooling the steel (generally by water quenching) to form a very hard but brittle martensitic layer with decreasing hardness through the thickness of the steel plate (Doig, 2002).

An effective way of producing a plate with dual hardness values is by roll-bonding two different steels together to form a single plate (see Figure 7.8). This provides an armour plate with more discrete hardness values as opposed to a plate with a hardness gradient. This technology, which has been around before WWII in the form of Hadfield duplex armour, has become commonly known as the dual-hardness armour (DHA). This type of plate is manufactured from two separate plates of nickel-alloy steel that are roll-bonded until the two plates form a strong metallurgical bond. The face plate usually contains higher carbon content that leads to higher hardness after heat treatment.

The performance data in Table 7.3 taken from Ogorkiewicz (1991a) demonstrate the effectiveness of DHA. As can be seen from Table 7.3, the ballistic performance of DHA is far superior to that of HHA of comparative hardness when subjected to attack from a steel-cored 7.62-mm AP bullet. However, despite the apparent advantage of using DHA, it is currently out of favour with most mainstream armour manufacturers for military applications—mainly because of the complexity and cost of manufacturing for a relatively limited number of customers.

FIGURE 7.7   King Tiger tank of WWII, which used 'flame-hardened' steel armour.

FIGURE 7.8   (a) Conventional hot rolling and (b) processing of DHA.

7.3.2.5   Perforated Armour

Drilling holes in a high-hardness steel plate has been shown to be an effective means of disrupting the path of an AP projectile leading to its fragmentation or destabilization. The complete armour system consists of a holed or perforated hard but tough

TABLE 7.3

Thickness, Areal Density and Mass Effectiveness Values for the Amount of Steel Required to Protect against 7.62-mm AP Bullets at Point-Blank Range and Normal Incidence

Armour Steel	Density (kg/m³)	Thickness (mm)	Areal Density (kg/m²)	Em
RHA (380 BHN)	7830	14.6	114	1.00
HHA (550 BHN)	7850	12.5	98	1.16
DHA (600–440 BHN)	7850	8.1	64	1.78

Source: Data taken from Ogorkiewicz, R. M. 1991, *International Defence Review*, 4, 349–352.

steel layer spaced at some distance from the base armour of the vehicle (typically 200–300 mm). The spacing provides time for the core of the projectile to tumble or separate into discrete fragments. The base armour must be sufficient to defeat the tumbling projectiles that result after the core has been disrupted by the outer steel-perforated plate. The edges of the holes provide a point for destabilizing the projectile path and, if the conditions are right, can provide a contact point that induces bending loads within the projectile core. Applying 'dynamic' bending loads to a projectile core will induce tensile fracture in the projectile. Optimization of this armour is achieved by choosing the appropriate properties of the plate as well as the hole diameters and spacing.

The primary use of perforated armour systems has been to up-armour armoured personnel carriers (APCs) and infantry-fighting vehicles (IFVs) to protect against armour-piercing small-arms bullets. However, some effort has been made to design a perforated system to protect against APFSDS ammunition, but the results have shown little advantage in doing so (Weber, 2002). Nevertheless, if yaw can be induced into the rod, then the depth of penetration into residual armour can be significantly reduced. Even yaw angles as low as 1.5° can result in the degradation of the rod's performance (Roecker and Grabarek, 1986).

An example of an experimental perforated armour is shown in Figure 7.9.

7.3.2.6 Ballistic Testing of Steel Armour

There are quite a lot of data available on the ballistic penetration capability of steel plates, and various authors have studied the behaviour of various types of projectiles against different target strengths. Probably of most interest is the behaviour of the armour-grade steels, and Børvik et al. (2009a) provide a nice summary of results for 7.62-mm ball and AP projectiles. The Recht–Ipson curve fit was used for this data (see Chapter 4) according to

$$v_r = a\left(v_0^p - v_{bl}^p\right)^{1/p} \tag{7.2}$$

where v_r is the residual velocity of the projectile, v_0 is the impact velocity, and v_{bl} is the ballistic limit velocity. The parameters a and p are the Recht–Ipson parameters (note that for all data presented here, $a = 1.0$).
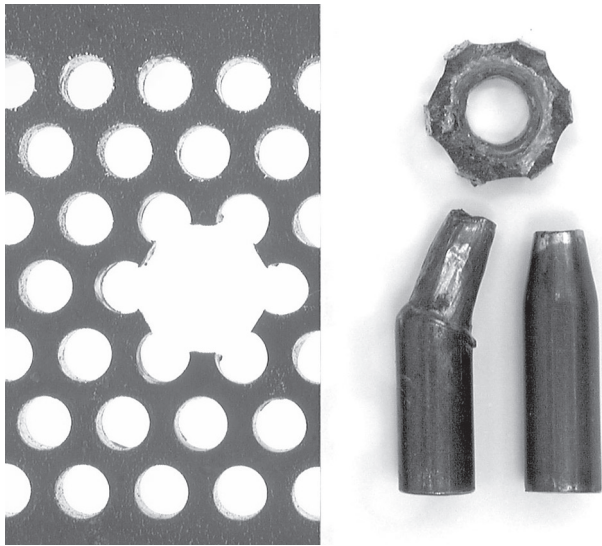
FIGURE 7.9 An example of an experimental perforated plate (left) showing a post-impact and pre-impact projectile core (right). After (Mitchell, 2000).

TABLE 7.4

Ballistic Performance Data (and Recht–Ipson Parameters) for Various Armour-Grade Steel Plates Perforated by a 7.62-mm Ball Projectile (BR6)

Steel Type	Yield Strength (MPa)	Thickness (mm)	Areal Density (kg/m²)	Recht–Ipson Parameter, p	Ballistic Limit Velocity (m/s)
Weldox 500E	605	6.0	47.1	2.3	596
Weldox 700E	819	6.0	47.1	2.6	666
Hardox 400	1148	6.0	47.1	3.0	762
Domex 500	1592	6.0	47.1	3.4	886
Armox 560T	1711	6.0	47.1	3.5	918

Source: Børvik, T. et al. 2009, *International Journal of Impact Engineering*, 36(7), 948–964.
Note: $a = 1.0$.

The ballistic data are summarized in Tables 7.4 and 7.5.

Essentially, as would be expected, as the strength of the plate increases (as we move down Tables 7.4 and 7.5), it is seen that the ballistic limit velocity increases as well.

A selection of additional steel penetration data that has been published in the open literature is presented in Table 7.6.

TABLE 7.5

Ballistic Performance Data (and Recht–Ipson Parameters) for Various Armour-Grade Steel Plates Perforated by a 7.62-mm AP (APM2) Projectile (BR7)

Steel Type	Yield Strength (MPa)	Thickness (mm)	Areal Density (kg/m²)	Recht–Ipson Parameter, p	Ballistic Limit Velocity (m/s)
Weldox 500E	605	2×6.0=12.0	94.2	2.2	624
Weldox 700E	819	2×6.0=12.0	94.2	2.4	675
Hardox 400	1148	2×6.0=12.0	94.2	2.0	741
Domex 500	1592	2×6.0=12.0	94.2	2.1	837
Armox 560T	1711	2×6.0=12.0	94.2	1.5	871

Source: Børvik, T. et al. 2009, *International Journal of Impact Engineering*, 36 (7):948–964.
Note: $a = 1.0$.

TABLE 7.6

Ballistic Penetration of Steel (v50 Tests)

Alloy	Thickness (mm)	Areal Density (kg/m²)	Projectile	Ballistic Limit Velocity (m/s)
Bisplate HHA (530 HB)	11.9	92.8	0.30 APM2	826
Bisplate HHA (477 HB)	19.5	152.1	0.50 APM2	751
Bisplate HHA (530 HB)	11.9	92.8	0.50 FSP	835
Bisplate HHA (477 HB)	19.6	152.9	20-mm FSP	845

Source: Gooch, W. A. et al. 2007a. Ballistic testing of Australian Bisalloy steel for armour applications. *In: Proceedings of the 23rd Symposium on Ballistics, Tarragona, Spain.*

7.3.3 ALUMINIUM ALLOY ARMOUR

The use of aluminium in domestic applications has increased dramatically since 1960 with the transport sector being the largest user. It was around the 1950s and 1960s that aluminium alloys were being used in the design of AFVs including the British combat vehicle reconnaissance (CVR) family of vehicles and the M113 APC. With the M113, the US Army wanted a lightly armoured, air-transportable, air-droppable amphibious vehicle. Aluminium-based armour seemed an appropriate route to take given the relatively low density of aluminium and the discovery that, ballistically, certain wrought alloys performed quite well.

For lightweight and medium-weight vehicle applications, it has been shown to be a good all-rounder, and several AFVs are made from aluminium alloys. These include the Warrior (United Kingdom), CVR family of vehicles (United Kingdom)

and the Bradley AFV and as already mentioned, the M113 (United States). The reason for aluminium's choice for these vehicles is that the areal density of the material required to provide protection against 7.62 and 14.5-mm AP is lower for the wrought aluminium alloys than their steel counterparts.

7.3.3.1 Processing and Properties

The first military use of aluminium was conceived in the mid-nineteenth century in France after an impure form of aluminium was produced by H. Sainte-Claire Deville through the chemical reaction between aluminium chloride and sodium. The new metal soon gathered government support due to Napoleon the Third who thought it could be used in the manufacture of lightweight body armour (Polmear, 1989). Although pure forms of aluminium are too soft to be realistically used in armour applications, certain alloys of aluminium have been used successfully in the production of AFVs, as discussed in Section 7.3.3. And so, Napoleon's ambition has been successfully implemented!

Generally speaking, the aluminium alloys that have been used in AFV armour are wrought alloys. That is to say, they have been mechanically worked during processing. Wrought alloys are described by the International Alloy Designation System (IADS) where the first of a four-digit number designates the major alloying element. Table 7.7 summarizes the designations. Subsequent numbers are added to the H and T conditions to indicate secondary treatments used to influence mechanical properties.

The mechanical properties of aluminium alloys are affected by a range of microstructural features including small grain sizes and control of grain shape and a dislocation substructure produced by cold working and/or a very fine distribution of sub-micron-sized precipitates and coarse intermetallic particles produced by the precipitation-hardening heat treatment process. Many of the armour-grade alloys of aluminium (2xxx, 6xxx and 7xxx) can be hardened in this way. The precipitation-hardening process involves three basic steps: solution treatment, quenching and ageing and is illustrated in Figure 7.10. Consider an alloy with a known composition of an alloying element, B (e.g. Cu). In the first stage, the alloy is heated up to above the solvus line (to T_0), that is, the temperature above which the alloying element is dissolved into solid solution, and soaked until a homogeneous solid solution single (α)

TABLE 7.7

IADS Aluminium Alloy and Temper Designations

Four-Digit Series	Main Alloying Element	Temper Designations (Added as a Suffix Letter)
1xxx	99% Al min.	F – as fabricated
2xxx	Cu	O – annealed wrought
3xxx	Mn	H – strain hardened
4xxx	Si	T – heat treated
5xxx	Mg	
6xxx	Mg + Si	
7xxx	Zn	
8xxx	Others	
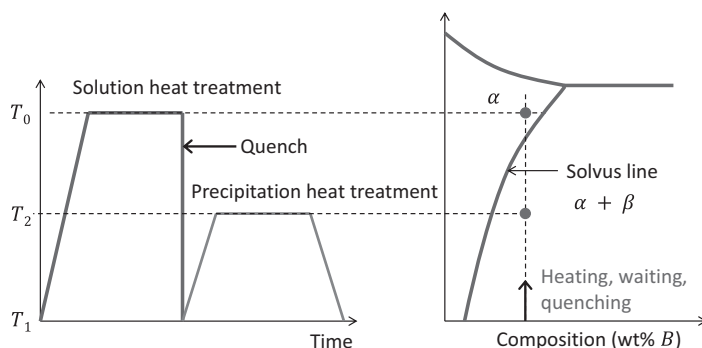
FIGURE 7.10 The precipitation-hardening process for an aluminium alloy. The composition of the final precipitates is dictated by the right-hand side of the phase diagram (not shown).

phase is produced. This is known as *solution heat treatment.* At this point, the Cu atoms would have completely dissolved into the lattice. The second stage involves quenching, usually to room temperature (T_1). During this process, the atoms do not have time to diffuse out and instead are retained in what becomes a highly-stressed non-equilibrium lattice structure. Therefore, a non-equilibrium α-phase exists, saturated with *B* atoms. The third stage involved heating the alloy to a temperature below the solvus line to achieve optimum properties. This is known as *precipitation heat treatment* or *ageing*. In this stage, finely dispersed *β* precipitates come out of the solid solution. The exact nature of these particles is dictated by the heat treatment temperature (T_2) and the ageing time (at this temperature), with their chemistry being prescribed by the phase diagram (not shown). These precipitates act as barriers to dislocation movement as they are now forced to go around the newly formed particles, thus strengthening the alloy. For the alloys that respond well to ageing, it is these finely dispersed precipitates that have a significant effect in raising the yield and tensile strengths of the alloy.

An alternative processing route for an aluminium armour material is through cold rolling and this is often the preferred route for alloys that do not respond well to ageing. This is achieved by forcing the plate in between two rollers and results in a microstructure with elongated grains (see Figure 7.11). The increase in dislocation density through cold rolling increases the strength but does reduce the ductility of the plate. Ultimately, the increased strength of the alloy improves the ballistic performance of the plate.

Most aluminium armour is made from the 5xxx or 7xxx series of aluminium alloys with a relatively small portion manufactured from the 2xxx and even 6xxx plate. For example, the armour on the M113 and the USMC amphibious assault vehicle consists of cold-rolled 5083 aluminium–magnesium–manganese alloy plate. The Type 5083 alloy is formed into a plate by hot rolling, from the ingot, at temperatures in the range of 350°C–400°C. It is then cooled at room temperature and 20% cold-rolled to the desired thickness to provide the required strength. Consequently, the plate has been strain-hardened with 5083—H131 being a typical example. Strain-hardening of the
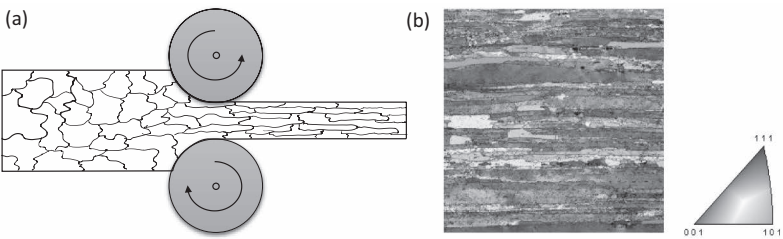
FIGURE 7.11   (a) The rolling process and (b) EBSD of the resulting microstructure after the rolling process for a 7010-T7651 plate (after (Cranston et al., 2016), reproduced with permission).

TABLE 7.8
Material Properties of Some Aluminium Alloys Currently Used in AFVs

Armour-Grade Alloy	Proof Stress (MPa)	UTS (MPa)	Elongation (%)
AA 5083-H131	(0.2%) 285	345	10
AA 5059-H131	(0.2%) 360	405	9
AA 7017-T6	(0.2%) 385	445	11
AA 7039-T6	(0.2%) 375	435	11

Source: Aleris 2010. *Defence Aluminium Product Data Sheet*. Switzerland: Aleris Switzerland GmbH.

alloy will result in a loss of ductility, and therefore, only modest amounts of cold rolling are desirable. Also, it is known that AA 5083 exhibits a modest negative strain-rate sensitivity (Clausen et al., 2004). That is to say that as the loading rate increases, the material effectively gets softer. This is bad news for armour, although the reduction in flow strength is quite small. Typical properties of some armour-grade alloys are summarized in Table 7.8.

An alternative to the 5083 grade is the ballistically superior Type 2024 aluminium–copper age-hardened alloy. However, the 2024 grade is not readily weldable, and that renders it difficult to integrate into structural armour. Certain high strength 7xxx grades of alloy are also difficult to weld without adversely affecting their microstructure and so too their mechanical properties.

7.3.3.2   Ballistic Testing of Aluminium Armour

There have been a large number of studies examining the ballistic penetration of aluminium plates. Some have examined the effect of rigid projectiles as they penetrated the plates, whilst others have examined the effect of deforming projectiles on the ballistic penetration of aluminium. Several studies have centred around the ballistic penetration of armour-grade aluminium alloys and in particular the AA 5083 grade in various treatments by rigid penetrators (Forrestal et al., 1990; Børvik et al., 2004, 2009b). Of particular interest is the close correlation between the cavity expansion-type analytical models and the experimental results. Forrestal and co-authors have

developed closed-form equations that predict the ballistic limit and residual velocities for the perforation of plates by rigid projectiles (Forrestal et al., 1987; Piekutowski et al., 1996). A typical analytical formulation is summarized in the following and applied to AA 5083-H116 plates (Børvik et al., 2009b).

As we have seen previously, for the perforation of an elastic–plastic ductile finite-thickness plate, the conservation of energy equation applies:

$$\frac{m_p}{2}\left(v_0^2 - v_r^2\right) = \pi a^2 h \sigma_r \tag{7.3}$$

where m_p is the mass of the projectile, v_r is the residual velocity, v_0 is the striking velocity, α is the radius offered by the projectile, h is the plate thickness and σ_r is the radial compressive stress acting on the projectile's nose. Note that when the projectile comes to rest in the plate, $v_r = 0$, and therefore, $v_s = v_{bl}$ (the ballistic limit velocity). A further refinement is that the radial stress on the projectile nose is approximated to the quasi-static value of flow stress as the cavity expansion velocity approaches 0. That is to say that $\sigma_r = \sigma_s$ as $v \to 0$. For an elastic–perfectly plastic material, the 1D compressive response is $\sigma = E\varepsilon$ in the elastic reason and $\sigma = Y_0$ in the inelastic reason. Rearranging Equation 7.3 and noting that $\sigma_r = \sigma_s$ gives us

$$v_{bl} = \sqrt{\frac{2\pi a^2 h \sigma_s}{m_p}} \tag{7.4}$$

For the von Mises yield criterion (elastic–perfectly plastic),

$$\sigma_s = \frac{Y_0}{\sqrt{3}}\left(1 + \mathrm{In}\left[\frac{1}{\sqrt{3}}\left(\frac{E}{Y_0}\right)\right]\right) \tag{7.5}$$

where Y_0 is the yield strength and E is Young's modulus. Further modification of this equation is required where hardening occurs (Forrestal et al., 1990; Piekutowski et al., 1996):

$$\sigma_s = \frac{Y_0}{\sqrt{3}}\left(1 + \mathrm{In}\left[\frac{1}{\sqrt{3}}\left(\frac{E}{Y_0}\right)\right]\right)^n \int_0^b \frac{\left[-\mathrm{In}(x)\right]^n}{(1-x)}\,dx\right), \quad b = 1 - \frac{\sqrt{3}Y_0}{E} \tag{7.6}$$

where n is the work hardening exponent. Using this type of approach, Børvik et al. have shown a very good correlation to the prediction of the penetration of aluminium AA 5083-H116 plates amongst other armour plates. Equally, good results for 6061-T651 have been presented by Piekutowski et al. (1996). These results are shown in Figure 7.12.

There have been numerous studies of the penetration of the finite-thickness aluminium alloy plate in the literature, and it is perhaps helpful to provide a snapshot of the results. Most studies have concentrated on establishing a ballistic limit calculation such as a v_{50}. Table 7.9 shows a summary of some results for 0.30 APM2 and 0.50 APM2 bullets.
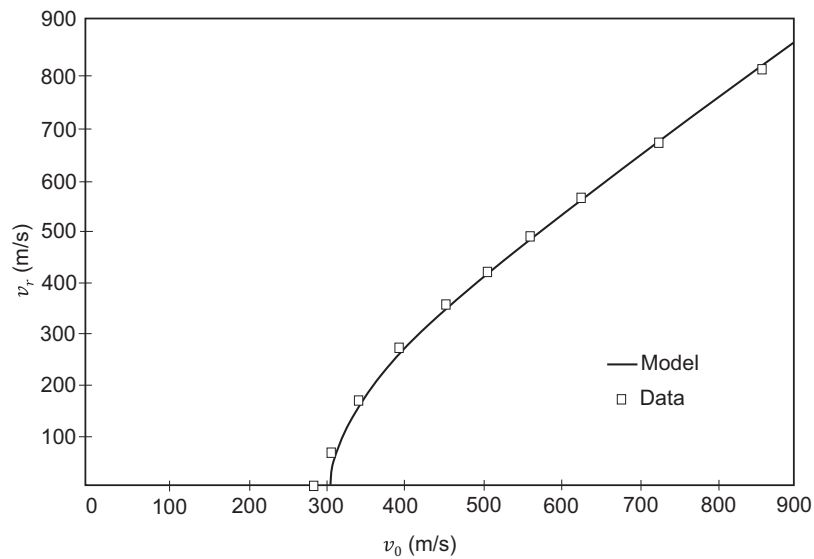
FIGURE 7.12 Relationship between residual and striking velocity showing the comparison between theoretical and experimental results for a non-deforming projectile perforating 26.3 mm of AA 6061-T651; $v_{bl} = 307$ m/s. (Reprinted from Piekutowski, A. J. et al., *International Journal of Impact Engineering*, 18(7–8), 877–887, Copyright 1996, with permission from Elsevier.)

TABLE 7.9
Penetration of Aluminium Alloys by Armour-Piercing Bullets—Ballistic Results

Ref.	Alloy	Thickness (mm)	Areal Density (kg/ m²)	Projectile	Ballistic Limit Velocity (m/s)
Showalter	5059-H131	25.1	66.8	0.30 APM2	588
et al. (2008)	5059-H131	51.2	136.2	0.30 APM2	906
	5059-H131	51.2	136.2	0.50 APM2	680
	5059-H131	77.1	205.1	0.50 APM2	830
Børvik et al.	6082-T6	20.0	54.0	0.30 APM2	414[a]
(2011)	5083-H116	20.0	53.2	0.30 APM2	492[a]
	7075-T651	20.0	56.2	0.30 APM2	628[a]
Gooch et al.	6061-T651	26.0	70.2	0.30 APM2	582
(2007a)	6061-T651	38.8	104.8	0.30 APM2	755
	6061-T651	51.2	138.2	0.30 APM2	882

Note: This table is a snapshot of the data; more details are provided in the references.

[a] Estimated from the Recht–Ipson model (Recht and Ipson, 1963), i.e $v_{bl} = \sqrt{v_0^2 - v_r^2}$

Aluminium alloy armour plates are applied in single thickness sections, and it has been thought that laminating the armour plates would lead to an increase in ballistic performance. This has been shown not to be so. Woodward and Cimpoeru (1998) ballistically tested 2024-T351 plates with various shaped projectiles and compared the results for single thickness (~9.5 mm thick) plates and multiple-thickness plates. They showed that replacing a single thickness of aluminium armour with multiple plates comprising the same thickness had little change on the ballistic limit velocity. Increasing the number of layers (for a given thickness) increases the level of tensile stretching work done during the perforation of the target. However, there is a reduction in other work terms, and therefore, there was little overall change in the energy absorption of the target.

7.3.3.3 Applications of Aluminium Armour

In the late 1960s, the British adopted aluminium for the Alvis Scorpion tracked reconnaissance vehicle (CVR(T)). This was the first vehicle to have a turret as well as a hull welded from the aluminium alloy plate (see Figure 7.13). Due to the strict weight limitations and the level of protection that was required, the 5083-aluminium alloy could not be used. Instead, a new alloy was developed. The result was AA 7039—an aluminium-zinc-magnesium alloy, which derived its strength from a precipitation-hardening heat treatment discussed earlier. This finished aluminium alloy possesses a higher strength and better ballistic properties than AA 5083.

The Type 7039 alloy performed well against AP ammunition when compared to steel armour (RHA). For 14.5-mm ammunition, the advantages of using aluminium alloy over steel are more significant than what would be required to protect against the 7.62-mm ammunition. Yet with both types of ammunition, the disadvantage of using steel narrows as the angle of obliquity increases.

A decade later, a similar aluminium alloy (AA 7017) was adopted for use as the armour plate in the Warrior IFV (Figure 7.14). In this vehicle, the use of the aluminium was limited to the hull, whereas the turret is fabricated from the RHA plate. The
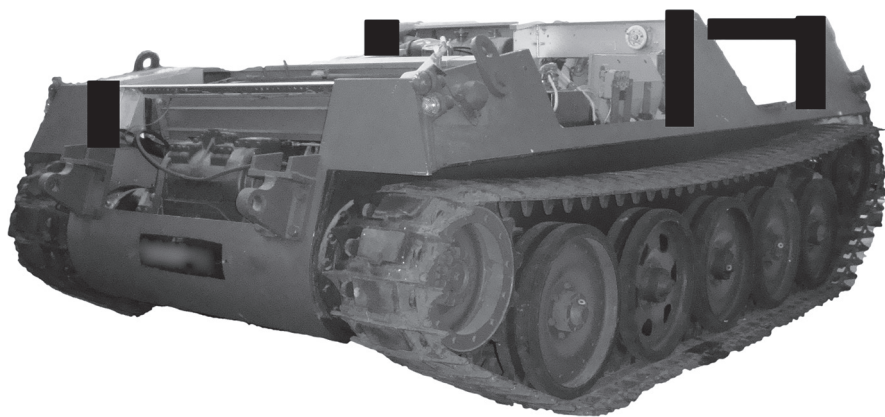
FIGURE 7.13   CVR(T) cutaway chassis with exposed hull profiles blacked out.
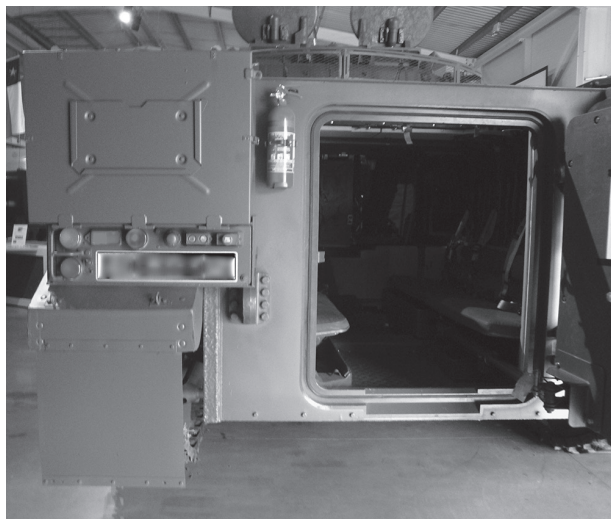
FIGURE 7.14   Rear of a Warrior IFV made from aluminium alloy plate.

reason for the choice of this alloy was to reduce the risk of stress corrosion cracking. This alloy is slightly harder than the AA 7039 alloy but less tough.

Aluminium alloy plate is anisotropic, and therefore, it is convenient to describe a rolled plate's properties in three directions: longitudinal (parallel to the rolling direction), transverse (perpendicular but in plane with the rolling direction) and short transverse (through the thickness). Aluminium alloys tend to be less strong and tough when tested in the short transverse direction, and ballistically, this can lead to a difference in the performance of up to 10% due to cracking; in most applications, this is never a problem as the cross-section to the rolling direction is rarely exposed.

Aluminium alloy armours provide advantages in that, due to their relatively low density, thicker sections can be used to provide optimum protection. This provides the vehicle with additional structural rigidity. For example, the flexural rigidity of a plate is given by the product *EI*, where *E* is Young's modulus, and *I* is the second moment of area of the rectangular cross-section given by the well-known relationship

$$I = \frac{bd^3}{12} \tag{7.7}$$

where *b* is the breadth of the plate, and *d* is the depth.

However, aluminium suffers from a number of disadvantages. The most prominent disadvantage of aluminium alloys in the design of AFVs is that the harder alloys that are suitable for armour applications such as 7039 are susceptible to stress-corrosion cracking. Stress-corrosion cracking occurs when the aluminium alloy is attacked by a corrodant whilst being subjected to tensile stress. It is a particularly insidious failure because the magnitudes of stresses that are required to encourage failure are frequently lower than the yield strengths of the alloy. In fact, residual stresses induced during machining, assembling or welding can lead to failure.

Armour-grade aluminium also possesses a lower spall strength than steel and therefore is more susceptible to 'scabbing'. It is often necessary to employ internal spall shields in vehicles made of aluminium alloys. Furthermore, it possesses a relatively low melting temperature when compared with steel and therefore will soften more when the temperature is elevated (although in practical terms, this is minimal).

7.3.4 MAGNESIUM ALLOY ARMOUR

It may come as some surprise to the reader, but magnesium-based armours are a real possibility. Although they have never been fielded on the battlefield, their high specific strengths lend themselves to armour applications. Magnesium on its own is quite weak and brittle and consequently is never used in engineering applications unalloyed. Adding alloying elements such as aluminium, zinc or some of the rare earth metals provides a route to strengthening through precipitation-hardening heat treatments. Minimum required ballistic limit data for magnesium armour plate are provided by MIL-DTL-32333 (MR).

7.3.4.1 Processing and Properties

The crystal structure of magnesium is hexagonal close-packed (HCP). These types of crystal structures do not lend themselves to good ductility as they have few available slip systems at room temperature. Slip is an important mode of plastic deformation in metals. If a crystal lattice structure has few available slip directions, then it is difficult to plastically deform, and therefore, its ductility is curtailed. At elevated temperatures, thermally activated slip can occur, and this is why magnesium needs processing at elevated temperatures.

At higher strains or higher strain rates (including shock loading), plastic deformation in magnesium is accommodated through a process of twinning. Instead of atoms slipping past one another (as is the case in slip), there is a homogeneous deformation of the crystal structure. This leads to a reorientation across the twin plane. See Figure 7.15.

Generally speaking, magnesium alloys are described by the first two letters that indicate the principal alloying elements. The letter corresponding to the greater alloying element is used first. The two letters are followed by numbers that indicate the wt% composition of each of the respective alloying elements rounded off to the nearest whole number. So for example, AZ61 indicates an alloy Mg–6Al–1Zn comprises 6% Al and 1% Zn (although the exact composition may vary). The heat-treated and work-hardened conditions are specified in the same way as aluminium alloys.

The origin of magnesium-based armour dates back to WWII when work was carried out to examine whether a magnesium alloy would make reasonable aircraft armour (Sullivan, 1943). In this case, the particular grade of magnesium alloy tested (Dowmetal-grade FS) was susceptible to large amounts of spallation and therefore deemed not appropriate for this application. Recently, however, there has been renewed interest in magnesium alloys for armour applications (van de Voorde et al., 2005; Cho et al., 2009) due to improvements in processing technologies.

The attractiveness of magnesium alloys is that they have low densities (typically 1.7–1.9 g/cc), and some of the more modern alloys have strength values that compete
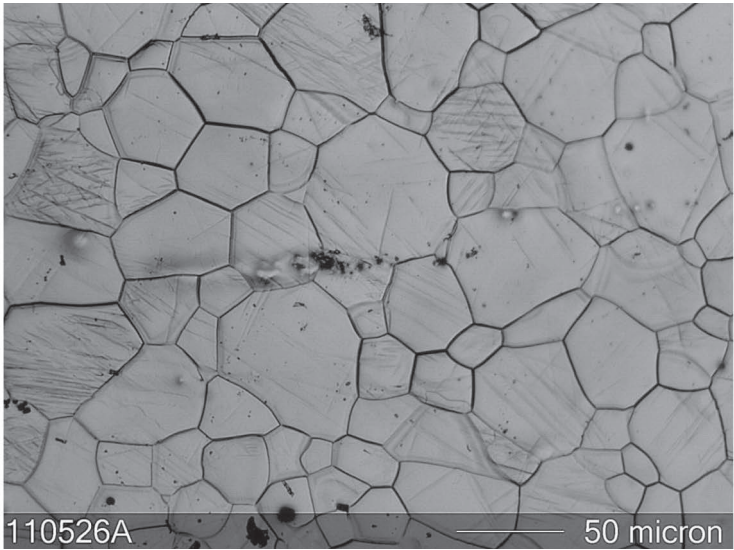
FIGURE 7.15   Optical micrograph showing extensive twinning in grains of a magnesium alloy (Elektron 675) after it has been shocked to 3.4 GPa using the flyer-plate technique (see Chapter 2). After (Hazell et al., 2012).

TABLE 7.10

Properties of Magnesium Alloy Materials (with a Comparison with AA 5083-H116)

Ref.	Alloy	Density (g/cc)	E (GPa)	ν	Y_0 (MPa)
Jones et al. (2007a)	AZ31B-H24	1.77	44.0	0.31	186[a]
Polmear (1989); Millett et al. (2009)	AZ61-F	1.80	43.0	0.31	180[a]
Magnesium Elektron UK (2010); Hazell et al. (2012)	Elektron 675-T5	1.90	45.9	0.31	310[a]
–	5083-H116	2.66	71.0	0.33	228

[a]   0.2% proof stress.

against armour-grade aluminium alloys such as 5083-H32 (Jones et al., 2007a; Magnesium Elektron UK, 2010). Table 7.10 summarizes the elastic and strength properties of some magnesium alloys; an armour-grade aluminium alloy (5083-H32) is provided for comparison.

Although Mg ribbon burns (as the reader may all recall from our high school chemistry classes), larger masses of Mg will not. The reason for this lies in magnesium's high thermal conductivity, which means that any localised heat is very quickly dissipated to the surrounding metal. Its melting point is comparable to aluminium too (650°C), which implies similar thermal softening properties during ballistic

penetration. However, when particulated, it would be expected to burn, therefore posing a pyrophoric risk—particularly when penetrated by a shaped charge jet.

Their low density and relatively low stiffness values mean that these materials tend to have low elastic impedance values. Following on from that, their shock impedances are very low too, and therefore, they will not impart large disruptive stress waves into the projectile. However, for small-arms bullets, where there is a general correlation between strength and ballistic performance, they will perform reasonably well.

7.3.4.2 Ballistic Testing of Magnesium Alloys

There has been relatively little ballistic work that has been done with magnesium alloys.

A selection of ballistic results is shown in Table 7.11.

Careful analysis of Tables 7.9 and 7.11 will show that magnesium alloys have the potential to perform in a comparable manner to armour-grade aluminium alloys on a weight-by-weight basis, although against fragments, the aluminium armour performs better with thicker sections. The likely reason for this is that magnesium alloys have been shown to be susceptible to adiabatic shear band formation during ballistic impact (Zhen et al., 2010; Zou et al., 2011), and therefore, they are susceptible to plugging.

Further data on APM2 projectiles penetrating different grades of magnesium alloys has been presented by (Lloyd et al., 2021). Selected data is summarized for 50 and 30-cal APM2 projectiles—see Figure 7.16. For the AZ31B-H24 the v_{50} follows the following empirical relationship:

$$v_{50} = 62.2\frac{h}{d} + 267.8 \tag{7.8}$$

For the WE43 plate, the following relationship fits the data:

$$v_{50} = 80.1\frac{h}{d} + 281.7 \tag{7.9}$$

where h and d represent the plate thickness and projectile calibre respectively.

TABLE 7.11

Ballistic Results for Magnesium Alloys

Alloy	Thickness (mm)	Areal Density (kg/m²)	Projectile	Ballistic Limit Velocity (m/s)
AZ31B-O	31.5	55.8	0.30 APM2	511
AZ31B-H24	76.5	135.4	0.30 APM2	863
AZ31B-O	7.6	13.5	0.22 FSP	417
AZ31B-H24	7.8	13.8	0.22 FSP	421
AZ31B-O	31.5	55.8	0.50 FSP	639
AZ31B-H24	76.5	135.4	20-mm FSP	897

Source: Jones, T. L. et al. 2007b. *Ballistic Evaluation of Magnesium Alloy AZ31B.* Aberdeen Proving Ground, MD: U.S. Army Research Laboratory.
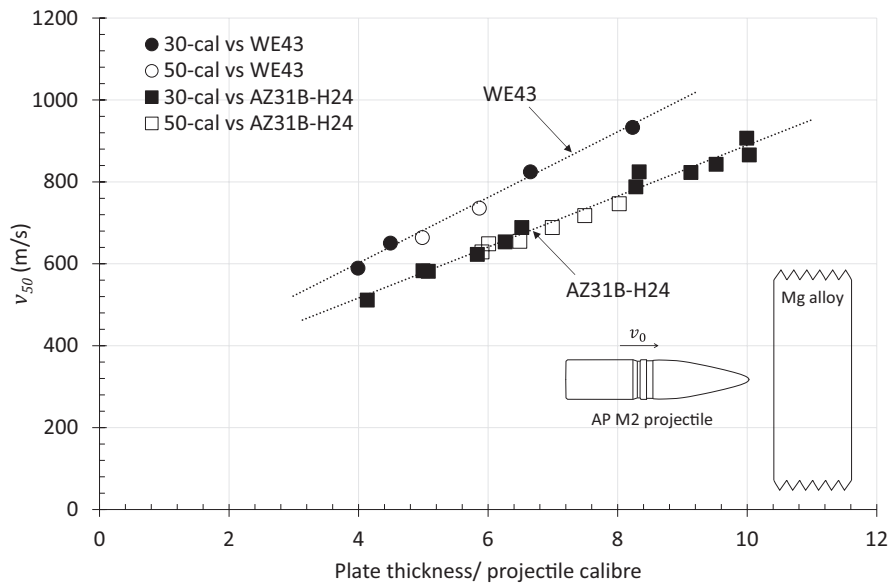
FIGURE 7.16 Perforation of Mg alloy plate by 30-cal and 50-cal AP M2 projectiles. Data extracted from (Lloyd et al., 2021). The higher the value of v_{50}, the better the protection (see Chapter 12).

7.3.5 TITANIUM ALLOY ARMOUR

Titanium is an attractive material for armour designers, and in its ballistic-grade form (Ti–6Al–4V), it possesses a relatively low density (4.45 g/cc) whilst maintaining a relatively high strength and hardness (UTS = 900–1300 MPa, BHN = 300–350). In fact, its properties are not dissimilar to that of RHA of similar hardness. It is also weldable and heat-treatable. However, like magnesium, titanium possesses an HCP structure. In addition, ballistic-grade titanium alloy plate costs around 10–20 times that of steel (depending on the world metal markets).

Titanium alloy armour has been used in several armour applications including the commander's hatch and top armour protection on the M2 Bradley AFV and in some armoured components of the M1A2 Abrams MBT. It has also been used to reduce the weight of the M777 155-mm howitzer by replacing the steel that would be ordinarily used in the trails and recoil cylinders (Montgomery and Wells, 2001). Titanium alloy plate has also been used in applique constructions. The Mobile Tactical Vehicle Light produced for the Canadian Army also used titanium in its protection construction to provide protection against 14.5-mm AP ammunition. Ballistic limit data requirements for testing are provided in MIL-DTL-46077G.

7.3.5.1 Processing and Properties

Pure titanium has a relatively low density (4.5 g/cc) and a high melting temperature (1668°C). Commercially pure titanium possesses the HCP crystal structure, which at room temperature is denoted as α-Ti. Increasing its temperature beyond 882°C

results in the formation of a body-centred cubic (or β) structure. Alloying elements affect this α-β transition (or transus) temperature. The choice of alloying elements will either stabilize the α phase or the β phase and they are therefore known as either 'α stabilizers' or 'β stabilizers'. All titanium falls into one of four categories depending on the phase(s) present after processing. These are as follows:

1. α-titanium alloys are usually alloyed with aluminium or tin. Strengthening is not possible due to the stable α phase (= HCP crystal structure).
2. β-titanium alloys contain sufficient concentrations of β stabilizing elements that enable the β phase to be retained in either a metastable (or non-equilibrium) or stable state. Metastable states are called as such because they will tend to precipitate a second phase (i.e. α) on ageing. These alloys possess a BCC crystal structure.
3. α/β alloys generally contain elements to stabilize both the α phase as well as 4%–6% of stabilizing elements. The most relevant for armour applications is Ti-6Al-4V, which contains 6% of Al (α stabilizer) and 4% of vanadium (β stabilizer). These alloys have the possibility for exceptional strength and toughness and in general, their strength can be improved through heat treatment.
4. Near α alloys are the final type of titanium alloy, containing only a small proportion of β stabilizers compared to α stabilizers. They present higher RT tensile strengths than the fully α-titanium alloys.

The interest in armour applications can be traced back to the 1950s when titanium and its alloys were demonstrated to be a viable option for ballistic protection (Pitler and Hurlich, 1950). A decade later, Ti-6Al-4V, which was developed in the mid-1950s, was shown to offer superior ballistic properties compared to other metals (Sliney, 1964). This alloy has since become one of the more important alloys of titanium and constitutes half of the sales of titanium alloys in both the United States and Europe (Polmear, 1989). This α/β alloy is composed of a dominant HCP α phase and a BCC β phase.

One of the potential drawbacks of using titanium alloy is that it is highly susceptible to adiabatic shear. This occurs when a material is subjected to a large amount of high-rate deformation leading to a temperature increase along localized bands. As the deformation of the material occurs rapidly, there is little or no time for the heat to conduct and diffuse from the plastically deforming zone, and therefore, the process is said to be adiabatic. This localized heating can lead to thermal softening of the material and therefore further plastic flow.

The propensity of a material to fail by adiabatic shear can be assessed by the Culver criterion (Culver, 1973). It can be used to calculate the critical shear strain that is required for material flow to occur and is given by (Walley, 2007)

$$\gamma_i = \frac{\rho_0 C n}{(\partial \tau / \partial T)_{\gamma,\dot{\gamma}}} \tag{7.10}$$

where ρ_0 is the bulk density of the material, C is the specific heat and n is the work-hardening exponent. $\partial \tau / \partial T$ is the rate of change of flow stress with temperature. $\partial \tau / \partial T$ is smaller for pure metals than it is for alloys, and therefore, they are less prone

TABLE 7.12
Properties for the 'Culver Equation'

Material	ρ_0 (kg/m³)	n	γ_i
AA 1100-0	2707	0.32	4.5
AA 6061-T6	2707	0.075	0.43
Cu	8938	0.38	6.4
1020 Steel	7850	0.28	1.9
4130 Steel	7850	0.35	1.2
$\propto$-Ti	4533	0.17	0.32
Ti–6Al–4V	4421	0.08	0.16

Source: With kind permission from Springer Science+Business Media: Thermal instability strain in dynamic plastic deformation, in Metallurgical Effects at High Strain Rates, edited by R. W. Rohde et al., 1973, 519–530, Culver, R. S.

to failure by adiabatic shear. Titanium is a metal that is susceptible to adiabatic shear failure because its properties combine a relatively low n and ρ_0 with a relatively high $\partial\tau/\partial T$. Table 7.12 summarizes the instability strains for several metals.

The Culver criterion cited above is for materials that are assumed to behave with a power law– hardening dependency between strain and stress (i.e. $\tau \propto \gamma^n$). Other criteria exist (for example, with linear work-hardening laws). More details on adiabatic shearing theory are provided in Bai (1990), Bai and Dodd (1992) and Walley (2007).

Due to titanium armour's propensity to fail by adiabatic shear and the fact that it can also suffer from spalling when subjected to ballistic attack, it is normally used in combination with other materials—such as steel. However, experiments in laminating titanium armour with commercially available pure titanium plate to form a dual hardness armour have demonstrated suppressed spall failure and produced increased ballistic efficiency (Bruchey and Burkins, 1998).

7.3.5.2 Ballistic Testing of Titanium Alloy Armour

Gooch et al. (1995) studied the penetration of tungsten alloy and depleted uranium rods with L/d ratios of 10, 13 and 20 into Ti–6Al–4V (BHN = 302–364) and compared the results with RHA (BHN = 241–331). From these data, Gooch et al. deduced that the E_m^3 values of the alloy against such penetrators ranged from 1.5 to 1.8 with approximately 10% more penetration being observed in the titanium alloy than in the RHA semi-infinite targets. Figure 7.17 shows the areal density of target material penetrated by an $L/d = 20$ WHA rod. It is clear that on a weight-by-weight basis that the Ti-6Al-4V target performs much better than the RHA. Further, as the velocity is increased, the difference between the two curves increases. This is due to the density effect where the areal density of the target material penetrated become more influenced by $\sqrt{\rho_t}$, as hydrodynamic effects become more apparent (see Section 4.5.1).

Ballistic data for smaller threats are provided by Montgomery and Wells (2001), Jones (2004) and Burkins (2007). A selection of ballistic limit data is provided in Table 7.13.
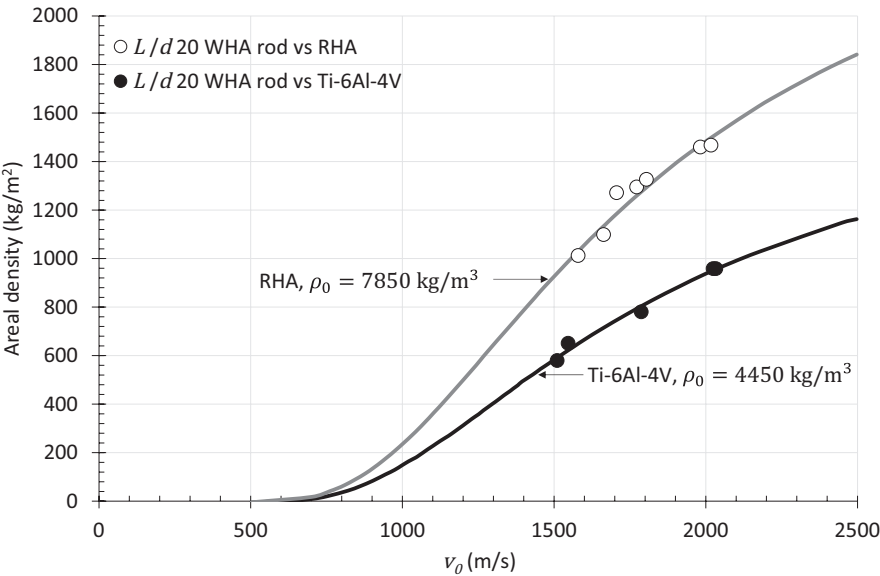
FIGURE 7.17 Areal density of target material penetrated by *L/d* 20 WHA rods comparing the penetration into RHA and Ti-6Al-4V. Data replotted from (Gooch W.A. et al., 1995).

TABLE 7.13
Ballistic Data for Ti–6Al–4V

Alloy	Thickness (mm)	Areal Density (kg/m²)	Projectile	Ballistic Limit Velocity (m/s)
EBCHM Ti–6Al–4V	25.4	111.3	20-mm FSP	1016
EBCHM Ti–6Al–4V	38.8	172.7	20-mm FSP	1493
EBCHM Ti–6Al–4V	64.0	284.8	30-mm APDS	932

Source: Montgomery, J. S., and M. G. H. 2001. Wells, *JOM*, 53(4), 29–32.
Note: EBCHM, Electron-beam cold-hearth melting.

(Fanning, 2000) presented ballistic limit data for different projectiles impacting a range of thickness values of Ti-6Al-4V plate (TIMETAL®6-4). This plate demonstrated exceptional ballistic properties against armour-piercing projectiles—see Figure 7.18. Similar to magnesium alloys, the results showed that a linear fit could be determined for the data when comparing the v_{50} to the ratio of plate thickness (h) to projectile calibre (d), viz:

$$v_{50} = 246.6 \frac{h}{d} + 206.4 \qquad (7.11)$$
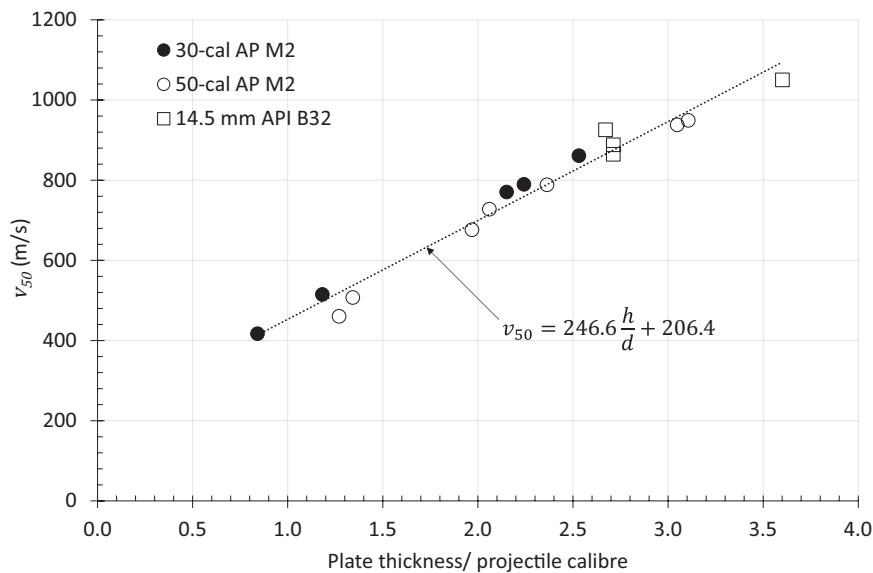
FIGURE 7.18 Measured v_{50} for the penetration of a Ti-6Al-4V plate by various armour-piercing projectiles. Data from (Fanning, 2000). The higher the value of v_{50}, the better the protection (see Chapter 12).

7.4   SANDWICH STRUCTURES

Sandwich systems that comprise either honeycombed, diamond-shaped, corrugated or pyramidal shapes have shown an enhanced ability to absorb the energy from a blast wave—when compared to their monolithic counterparts (Guruprasad and Mukherjee, 2000a, b; Dharmasena et al., 2008). These sandwich panels comprise thin stiff face sheets enveloping a relatively soft or collapsible porous core. The advantage offered by this construction is an increase in the second moment of the area of the structure as well as the ability to absorb energy through plastic compaction. Fleck and Deshpande (2004) presented an analytical assessment of various sandwich core topologies against blast loading. They described a model whereby the structural response of a sandwich beam occurs in three separate stages:

Stage 1: The fluid–structure interaction phase where the blast wave induces a uniform velocity in the outer face sheet.
Stage 2: The core undergoes crushing, and velocities of the core and the outer face sheet equalize as momentum is shared.
Stage 3: The sandwich beam is brought to rest through plastic bending.

Although this work centred on a two-dimensional beam, there is every reason to believe that this will equally apply to a three-dimensional plate problem. Moreover, Fleck and Deshpande noted that in the case of a water blast, an order-of-magnitude

improvement in blast resistance compared to monolithic plates could be achieved. Diamond-celled cores provided the best performance. However, against a sharp air blast shock, their model indicated that sandwich structures would give a moderate gain in blast resistance when compared to a monolithic structure. This was due to the impedance mismatch between the air and the face sheet of a sandwich core being similar to that of a monolithic plate. Therefore, the energy from the blast would be reflected rather than being transferred to a compaction wave in the cellular core. Nevertheless, for deflection-limited designs (where there is a necessity to limit the deformation of a structure due to an air blast), certain sandwich structures appear to be efficient (Dharmasena et al., 2008).

7.4.1 SANDWICH CORE TOPOLOGIES

For a given mass, cellular structures have been shown to exhibit high levels of impact energy absorption. In fact, nature, as ever, has been a long way ahead of us in this. For example, a youthful bone is known to exhibit good impact resistance due to its cellular geometry as are cellular (or porous) materials such as wood and cork (Gameiro et al., 2007; Sousa-Martins et al., 2013). An extensive review of the properties and form of cellular materials is given by Gibson and Ashby (1997). In particular, cellular metallic structures such as metallic foams have shown particular promise in absorbing energy from collisions. Therefore, they offer an attractive option for mitigating blast loading—particularly from underwater blasts.

A cellular material for blast mitigation would almost certainly be incorporated into a sandwich construction comprising two outer layers (either a structural composite such as carbon fibre–reinforced polymer or a monolithic metal plate such as aluminium). A review of these is provided by Yuen et al. (2010).

7.4.1.1 Foams

There are several metals that have been used in the manufacture of metallic foams including aluminium, copper, lead, magnesium, steel, titanium and zinc. These are made through a variety of manufacturing techniques that can be summarized in four families of processes indicated by the starting material (Banhart, 2001). So, to produce a porous metal, one can start from

   i. Liquid metal (e.g. 'foaming' of the material with gas bubbles)
  ii. Solid metal in powdered form (e.g. sintering of hollow spheres to produce a structure of multiple joined spheres)
 iii. Metal vapour or gaseous metallic compounds (e.g. vapour deposition of the material)
  iv. A metal ion solution (e.g. electrochemical decomposition of the material)
        Of the four processes, (i) and (ii) are the most favoured for their ability to produce thick sections. The most common form of metallic foam used is aluminium foam—mainly due to the fact that it offers good specific properties and is relatively cheap.

Loading direction

(a)   (b)
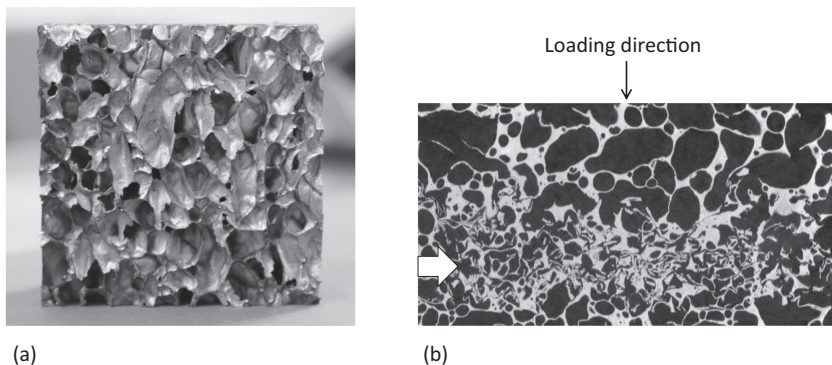
FIGURE 7.19 (a) Closed-cell aluminium foam with the density of this foam is only 300 kg/m³, and (b) 2D μ-CT image of a closed-cell foam tested using a Split-Hopkinson Pressure Bar (SHPB) system with a striker bar velocity of 9.8 m/s and compressed to 54% strain. Damage accumulation occurs where the cell walls are weakest (indicated), after (Islam et al., 2018).

There are two types of foam:

1. Open-cell metallic foams (where the material is composed predominantly of interconnecting cellular voids).
2. Closed-cell metallic foams (where the voids are predominately enclosed by a surrounding material). Two examples of this are shown in Figure 7.19 with Figure 7.19b showing a 2D micro-computed tomography image of a compressed closed-cell foam.

The mechanical behaviour of a porous material is characterized by a relatively constant-plateau stress region over a large range of plastic strains. This is due to the collapse of individual cells during compression. Eventually, the cells become completely compressed, and the measured stress increases as the material approaches full densification (see Figure 7.20). The higher and longer the plateau stress, the larger the amount of energy absorbed.

Aluminium foams show promise as stress wave attenuation layers in composite structural armour panels. Due to the porosity, it has been shown that the presence of an aluminium foam layer in a structural armour can delay and attenuate stress waves propagating to subsequent layers (Gama et al., 2001). That is, of course, before full densification. After the aluminium foam has been completely compressed, no attenuation will occur.

However, the mechanism of accommodating blast loading is complex. It has been known since 1970 that placing a cellular structure in direct contact with the structure that it is trying to protect actually leads to an amplification of the stress imparted (Monti, 1970). So, it is necessary to separate the cellular plate from the protected structure. An extensive review on this phenomenon with open-celled metallic foams is provided by Seitz and Skews (2006). It has also been observed that stress waves are able to propagate through the cellular structure prior to the material achieving full densification. The nature of these waves and how they affect the cell walls are not clear.
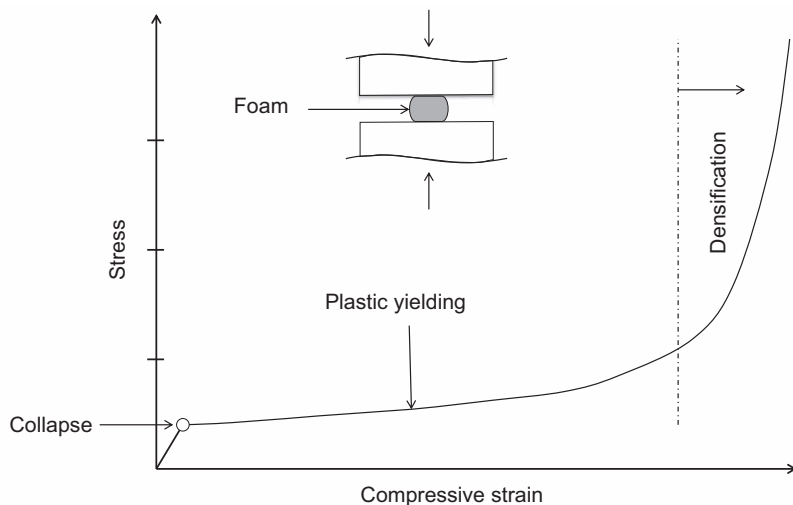
FIGURE 7.20   Typical stress–strain response for a metallic foam in compression.

7.4.1.2   Architectured Core Topologies

As mentioned in Section 7.4, honeycombed materials have also been investigated as potential structures for blast mitigation (Dharmasena et al., 2008). The impulsive blast wave energy causes the honeycomb structure to collapse. The more inelastic strain energy that is expended by the collapse, the better.

An emerging possibility for blast mitigation may lie in the use of micro-lattice or micro-architectured materials. These are most frequently made through a process of systematically selective laser melting of metallic powders (usually SS 316L or Ti–6Al–4V) using a high-energy density laser (e.g. see (Rashed et al., 2016)). It is an additive manufacturing process so that the excess powders that remain after the process can be gathered up and reused (Tsopanos et al., 2010). So far, studies on the blast response of steel lattice structures have been carried out by relatively few researchers (McKown et al., 2008; Smith et al., 2011), and it is generally recognized that there is still room to optimize the performance of these materials. The structures that have been studied to date are of the BCC form (see Figures 7.21 and 7.22). Recovered specimens after both types of experiments (quasi-static and blast loading) demonstrated that similar collapse mechanisms and energy absorption mechanisms had occurred. However, to manufacture even small samples of these structures takes a long time; therefore, they are relatively expensive compared to other cellular structures such as metallic foams, and realistically, it is unlikely that useable technologies would be made available in the next decade until the demand for these uniquely engineered structures takes off.

In addition to lattice structures, additive manufactured ordered cellular structures have shown promise in absorbing energy (Bonatti and Mohr, 2019). The advantage that these structures have over strut-based structures, is that the geometric smoothness of shell-lattices and the absence of joints prevent stress concentrations. These
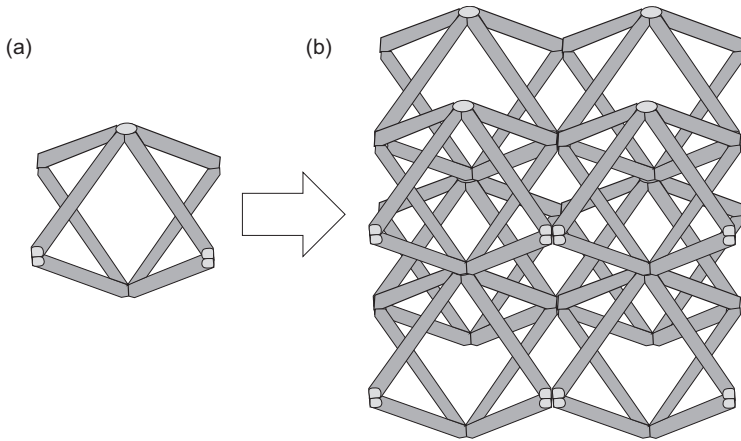
FIGURE 7.21   (a) Micro-lattice unit cell and (b) cells in a 2×2 matrix.
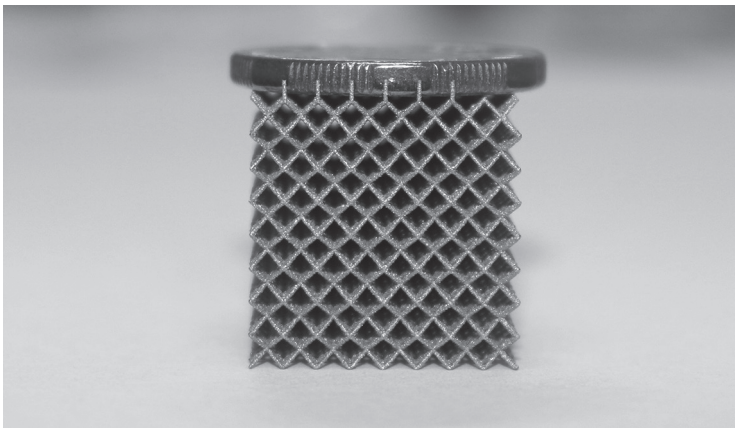
FIGURE 7.22   BCC Ti–6Al–4V micro-lattice structure supporting an Australian dollar coin (for scale).

are currently being investigated for low-velocity collision applications but may show promise in sandwich panels subjected to blast. Examples of this type of structure are shown in Figure 7.23.

7.4.1.3 Auxetic Structures

Auxetic structures are structures that exhibit a negative Poisson's ratio when applied with a load. That is, when under compression a structure would contract inwards, or when under tension the structure would expand outward (see Figure 7.24). This is counterintuitive as usually one would expect the opposite to occur. However, this behaviour is realized simply through the clever design of an architectured system. Nevertheless, there are several natural auxetic materials that have been discovered in
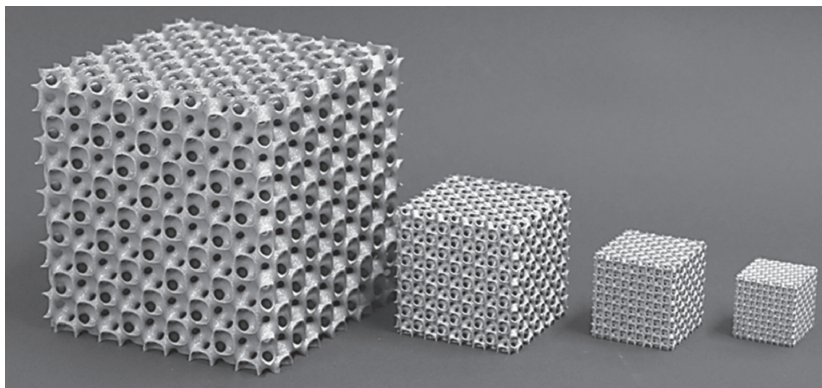
FIGURE 7.23 View of four smooth-shell lattice specimens manufactured by selective laser melting with a 316 L stainless steel powder. Relative densities from left to right: 0.1, 0.2, 0.3 and 0.4. (Reproduced with permission from Bonatti and Mohr (2019).)
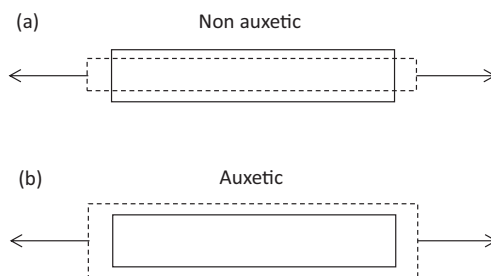
FIGURE 7.24 (a) Non-auxetic material behaviour and (b) auxetic material behaviour under tension.

single crystals of arsenic and cadmium as well as other materials. Biological auxetic examples also exist in cow teat skin and cat skin, see (Evans and Alderson, 2000).

Auxetic structures appear to have some benefits in protecting against blast loading. Through numerical modelling studies, auxetic composite panels have been shown to absorb more impulsive energy when compared with monolithic panels. Further, they have been shown to be able to reduce the back face's maximum velocity considerably compared to monolithic examples (Imbalzano et al., 2016). They also appear to behave better than other equivalent porous structures when subjected to blast loading. For example, they have been shown to provide reduced back-face deformation when compared with equivalent honeycombed structures, when both are subjected to equivalent loads (Imbalzano et al., 2018).

Auxetic structures have also shown some promise when it comes to resistance to ballistic penetration too and this is thought to be due to the accumulation of the auxetic wall materials ahead of the projectile during ballistic penetration (Yang et al., 2013). Similar results have been seen by (Qi et al., 2017) with heavy drop-weight tests and close-in blast loads of auxetic panels mounted on concrete slabs.

7.5 SUMMARY

Metallic materials have been used for millennia in armour. Steel has historically been used as it is a good all-rounder—combining reasonable hardness with good ductility and toughness. Moreover, it is relatively cheap and is a well-understood material to work with. It was not until the 1950s that aluminium alloys were used in AFV design and are more attractive than steel for protecting against large bullets such as the 14.5-mm B32—especially at low angles of obliquity. Titanium and magnesium alloys are relatively high-performing materials, but their cost is currently prohibitive for large production volumes.

As will be seen in Chapters 8 and 9, there are several lighter-weight non-metallic options such as high-strength fibres that have been used in personal protection, and these types of materials are largely yet to be adopted by vehicle manufacturers for structural applications. Consequently, the use of metal in armour is likely to be carried on for some time. This is all the more probable given the developments in porous or micro-architectured structures that show promise in attenuating blast loads.

NOTES

1. Note that pearlite is a mixture of two separate phases, and therefore, it is not referred to as a 'grain' but rather a 'nodule'.
2. In this book, I have used the scales of hardness, VHN and BHN, referring to Vickers hardness number and Brinell hardness number, respectively.
3. Here, the definition of E_m is slightly different from the one defined in this book. It is simply the ratio of the areal densities of the material penetrated of RHA to titanium alloy for the same impact velocity and in a semi-infinite target configuration.

REFERENCES

Aleris. 2010. *Defence Aluminium Product Data Sheet*. Switzerland: Aleris Switzerland GmbH.

Alkemade, S. J. 1996. *The Weld Cracking Susceptibility of High Hardness Armour Steel*. Melbourne, Vic: DSTO.

Anon 2020a. *Bisalloy Armour UHH500 Steel Product Datasheet*. Unanderra, Australia: Bisalloy Steels Group Limited.

Anon 2020b. *Bisalloy Armour UHH600 Steel Product Datasheet*. Unanderra, Australia: Bisalloy Steels Group Limited.

Ashby, M. F. & Jones, D. R. H. 1986. *Engineering Materials 2: An Introduction to Microstructures, Processing and Design*, vol. 39, International Series on Materials Science and Technology. Exeter, UK: Pergamon Press.

Bai, Y. 1990. Adiabatic shear banding. *Res Mechanica*, 31(2), 133–203.

Bai, Y. & Dodd, B. 1992. *Adiabatic Shear Localization: Occurence, Theories and Applications*. Oxford, UK: Pergamom Press.

Banhart, J. 2001. Manufacture, characterisation and application of cellular metals and metal foams. *Progress in Materials Science*, 46(6), 559–632.

Bonatti, C. & Mohr, D. 2019. Mechanical performance of additively-manufactured anisotropic and isotropic smooth shell-lattice materials: Simulations & experiments. *Journal of the Mechanics and Physics of Solids,* 122, 1–26.

Børvik, T., Clausen, A. H., Hopperstad, O. S. & Langseth, M. 2004. Perforation of AA5083-H116 aluminium plates with conical-nose steel projectiles – Experimental study. *International Journal of Impact Engineering*, 30(4), 367–384.

Børvik, T., Forrestal, M. J., Hopperstad, O. S., Warren, T. L. & Langseth, M. 2009a. Perforation resistance of five different high-strength steel plates subjected to small-arms projectiles. *International Journal of Impact Engineering*, 36(7), 948–964.

Børvik, T., Forrestal, M. J., Hopperstad, O. S., Warren, T. L. & Langseth, M. 2009b. Perforation of AA5083-H116 aluminium plates with conical-nose steel projectiles – Calculations. *International Journal of Impact Engineering*, 36(3), 426–437.

Børvik, T., Olovsson, L., Dey, S. & Langseth, M. 2011. Normal and oblique impact of small arms bullets on AA6082-T4 aluminium protective plates. *International Journal of Impact Engineering*, 38(7), 577–589.

Bruchey, W. J. & Burkins, M. S. 1998. Suppression of material failure modes in titanium armors. *In: Proceedings of the 17th International Symposium on Ballistics, Midrand, South Africa, 23–27 March*. Van Niekerk, C., (ed)., Publisher: South Africa Ballistics Organisation, Moreleta Park, South Africa.

Burkins, M. 2007. Ballistic performance of thin titanium plates. *In: Proceedings of the 23rd International Symposium on Ballistics, Tarragona, Spain, 16–20 April 2007*. Galvez,F., Sanchez-Galvez, V. (eds) Lancaster, PA: Destech Publications.

Callister, W. D. 2007. *Materials Science and Engineering: An Introduction*, 7th ed. New York: John Wiley & Sons, Inc.

Cheeseman, B. A., Gooch, W. A. & Burkins, M. S. 2008. Ballistic evaluation of aluminum 2139-T8. *In:* Bless, S. & Walker, J. (eds.). *Proceedings -24th International Symposium on Ballistics, Ballistics 2008*, pp. 651–659. Lancaster, PA: Destech Publications.

Cho, K., Sano, T., Doherty, K., Yen, C., Gazonas, G., Montgomery, J., Moy, P., Davis, B. & DeLorme, R. 2009. *Magnesium Technology and Manufacturing for Ultra Lightweight Armored Ground Vehicles*. Aberdeen Proving Ground, MD: Army Research Laboratory.

Clausen, A. H., Børvik, T., Hopperstad, O. S. & Benallal, A. 2004. Flow and fracture characteristics of aluminium alloy AA5083-H116 as function of strain rate, temperature and triaxiality. *Materials Science and Engineering A*, 364(1–2), 260–272.

Cranston, A. L., Hazell, P. J., Appleby-Thomas, G. J., Zakaria, Q. M. & Escobedo, J. P. 2016. *Effects of Microstructural Anisotropy on the Mechanical Properties of Aluminum Alloy AA 7010 — T7651*. Cham: Springer International Publishing, pp. 929–936.

Culver, R. S. 1973. Thermal instability strain in dynamic plastic deformation. *In:* Rohde, R. W., Butcher, B. M., Holland, J. R. & Karnes, C. H. (eds.) *Metallurgical Effects at High Strain Rates*, pp. 519–530. New York: Plenum Press.

Dharmasena, K. P., Wadley, H. N. G., Xue, Z. & Hutchinson, J. W. 2008. Mechanical response of metallic honeycomb sandwich panel structures to high-intensity dynamic loading. *International Journal of Impact Engineering*, 35(9), 1063–1074.

Doig, A. 2002. *Military Metallurgy*. London, UK: Maney Publishing.

Evans, K. E. & Alderson, A. 2000. Auxetic materials: Functional materials and structures from lateral thinking! *Advanced Materials*, 12, 617–628.

Fanning, J. C. 2000. Ballistic evaluation of TIMETAL 6-4 plate for protection against armor piercing projectiles. *In:* Gorynin, I. V. & Ushkov, S. S. (eds.) *Titanium '99 Science and Technology*. St. Petersburg, Russia: Central Research Institute of Structural Materials (CRISM) Prometey.

Fleck, N. A. & Deshpande, V. S. 2004. The resistance of clamped sandwich beams to shock loading. *Journal of Applied Mechanics, Transactions ASME*, 71(3), 386–401.

Forrestal, M. J., Luk, V. K. & Brar, N. S. 1990. Perforation of aluminum armor plates with conical-nose projectiles. *Mechanics of Materials*, 10(1–2), 97–105.

Forrestal, M. J., Rosenberg, Z., Luk, V. K. & Bless, S. J. 1987. Perforation of aluminum plates with conical-nosed rods. *Journal of Applied Mechanics, Transactions ASME*, 54(1), 230–232.

Gallardy, D. 2012. *Ballistic Evaluation of 7085 Aluminum*. Aberdeen Proving Ground: ARL.

Gama, B. A., Bogetti, T. A., Fink, B. K., Yu, C. J., Dennis Claar, T., Eifert, H. H. & Gillespie Jr., J. W. 2001. Aluminum foam integral armor: A new dimension in armor design. *Composite Structures*, 52(3–4), 381–395.

Gameiro, C. P., Cirne, J. & Gary, G. 2007. Experimental study of the quasi-static and dynamic behaviour of cork under compressive loading. *Journal of Materials Science*, 42(12), 4316–4324.

Gibson, L. J. & Ashby, M. F. 1997. *Cellular Solids: Structure and Properties*, 2nd ed., Cambridge Solid State Science Series. Cambridge, UK: Cambridge University Press.

Gooch, W. A., Bukins, M. S. & Squillacioti, R. J. 2007a. Ballistic testing of commercial aluminum alloys and alternate processing techniques to increase the availability of aluminum armor. *In: Proceedings of the 23rd International Symposium on Ballistics, Tarragona, Spain, 16–20 April.*

Gooch W.A., Burkins, M. S., Ernst, H. F. & Wolf, T. 1995. Ballistic penetration of titanium alloy Ti-6Al-4V. *In: Proceedings of the Lightweight Armour Systems Symposium.* Shrivenham, Oxfordshire: The Royal Military College of Science.

Gooch, W. A., Showalter, D. D., Burkins, M. S., Thorn, V., Cimpoeru, S. J. & Barnett, R. 2007. Ballistic testing of Australian Bisalloy steel for armor applications. *In:* Galvez, F. & Sanchez-Galvez, V. (eds.) *Proceedings of the 23rd Symposium on Ballistics*. Tarragona, Spain; Lancaster, PA: Destech Publications.

Guruprasad, S. & Mukherjee, A. 2000a. Layered sacrificial claddings under blast loading. Part I – Analytical studies. *International Journal of Impact Engineering*, 24(9), 957–973.

Guruprasad, S. & Mukherjee, A. 2000b. Layered sacrificial claddings under blast loading. Part II – Experimental studies. *International Journal of Impact Engineering*, 24(9), 975–984.

Hazell, P. J., Appleby-Thomas, G. J., Wielewski, E., Stennett, C. & Siviour, C. 2012. The influence of microstructure on the shock and spall behaviour of the magnesium alloy, Elektron 675. *Acta Materialia*, 60, 6042–6050.

Imbalzano, G., Linforth, S., Ngo, T. D., Lee, P. V. S. & Tran, P. 2018. Blast resistance of auxetic and honeycomb sandwich panels: Comparisons and parametric designs. *Composite Structures*, 183, 242–261.

Imbalzano, G., Tran, P., Ngo, T. D. & Lee, P. V. S. 2016. A numerical study of auxetic composite panels under blast loadings. *Composite Structures*, 135, 339–352.

Islam, M. A., Brown, A. D., Hazell, P. J., Kader, M. A., Escobedo, J. P., Saadatfar, M., Xu, S., Ruan, D. & Turner, M. 2018. Mechanical response and dynamic deformation mechanisms of closed-cell aluminium alloy foams under dynamic loading. *International Journal of Impact Engineering*, 114, 111–122.

Jones, T. L. 2004. *Ballistic Performance of Titanium Alloys: Ti-6Al-4V versus Russian Titianium*. Aberdeen Proving Ground, MD: Army Research Laboratory.

Jones, T. L., Burkins, M. S. & Gooch, W. A. 2007a. *An Analysis of Magnesium Alloy AZ31B-H24 for Ballistic Applications*. Aberdeen Proving Ground, MD: U.S. Army Research Laboratory.

Jones, T. L., DeLorme, R. D., Burkins, M. S. & Gooch, W. A. 2007b. *Ballistic Evaluation of Magnesium Alloy AZ31B*. Aberdeen Proving Ground, MD: U.S. Army Research Laboratory.

Lloyd, J. T., Jannotti, P. A. & Jones, T. L. 2021. An overview of penetration behavior in magnesium alloys. *Mechanics of Materials*, 162, 104038.

Magnesium Elektron UK. 2010. *Elektron 675 Preliminary Data Sheet, Data Sheet 102*. Swinton, Manchester, UK: Magnesium Elektron UK.

McKown, S., Shen, Y., Brookes, W. K., Sutcliffe, C. J., Cantwell, W. J., Langdon, G. S., Nurick, G. N. & Theobald, M. D. 2008. The quasi-static and blast loading response of lattice structures. *International Journal of Impact Engineering*, 35(8), 795–810.

Millett, J. C. F., Bourne, N. K., Stirk, S. M. & Gray III, G. T. 2009. The shock response of the magnesium-aluminium alloy, AZ61. *AIP Conference Proceedings*, 1195, 957–960.

Mitchell, A. P. 2000. An Investigation into Perforated Armour Systems. *DTC MSc reports*. Shrivenham: RMCS, Cranfield University.

MoD, UK. 2004. *Ministry of Defence Defence Standard 95–24: Armour Plate, Steel (3–160 mm)*. Glasgow, UK: UK Ministry of Defence Standards.

Montgomery, J. S. & Wells, M. G. H. 2001. Titanium armor applications in combat vehicles. *Journal of the Minerals, Metals & Materials Society*, 53(4), 29–32.

Monti, R. 1970. Normal shock wave reflection on deformable solid walls. *Meccanica*, 5(4), 285–296.

Ogorkiewicz, R. M. 1991a. Advances in armour materials. *International Defence Review*, 4, 349–352.

Ogorkiewicz, R. M. 1991b. *Technology of Tanks II*, vol. 2. Coulsdon, Surrey, UK: Jane's Information Group.

Papetti, D. J. 1980. Metallic armor materials. *In:* Laible, R. C. (ed.) *Ballistic Materials and Penetration Mechanics*, pp. 145–167. New York: Elsevier.

Piekutowski, A. J., Forrestal, M. J., Poormon, K. L. & Warren, T. L. 1996. Perforation of aluminum plates with ogive-nose steel rods at normal and oblique impacts. *International Journal of Impact Engineering*, 18(7–8), 877–887.

Pitler, R. & Hurlich, A. 1950. *Some Mechanical and Ballistic Properties of Titanium and Titanium Alloys*. Watertown: Watertown Arsenal Laboratory.

Polmear, I. J. 1989. Light alloys: Metallurgy of the light metals. *In:* Honeycombe, R. W. K. & Hancock, P. (eds.) *Metallurgy and Materials Science*, 2nd ed.. London: Edward Arnold.

Qi, C., Remennikov, A., Pei, L. Z., Yang, S., Yu, Z. H. & Ngo, T. D. 2017. Impact and close-in blast response of auxetic honeycomb-cored sandwich panels: Experimental tests and numerical simulations. *Composite Structures,* 180, 161–178.

Rashed, M. G., Ashraf, M., Mines, R. A. W. & Hazell, P. J. 2016. Metallic microlattice materials: A current state of the art on manufacturing, mechanical properties and applications. *Materials & Design*, 95, 518–533.

Recht, R. F. & Ipson, T. W. 1963. Ballistic perforation dynamics. *Journal of Applied Mechanics*, 30(3), 384–390.

Roecker, E. & C. Grabarek. 1986. The effect of yaw and pitch on long rod penetration into RHA at various obliquities. *In: Proceedings of the 9th International Symposium on Ballistics, 29 April–1 May*. Shrivenham, Swindon, UK: The Royal Military College of Science.

Ryan, S., Li, H., Edgerton, M., Gallardy, D. & Cimpoeru, S. J. 2016. The ballistic performance of an ultra-high hardness armour steel: An experimental investigation. *International Journal of Impact Engineering*, 94, 60–73.

Seitz, M. W. & Skews, B. W. 2006. Effect of compressible foam properties on pressure amplification during shock wave impact. *Shock Waves*, 15(3–4), 177–197.

Showalter, D. D., Placzankis, B. E. & Burkins, M. S. 2008. *Ballistic Performance Testing of Aluminum Alloy 5059-H131 and 5059-H136 for Armor Applications*. Aberdeen Proving Ground, MD: Army Research Laboratory.

Sliney, J. L. 1964. Status and potential of titanium armor. *In: Proceedings of the Metallurgical Advisory Committee on Rolled Armor*. Watertown: U.S. Army Materials Research Agency.

Smith, M., Cantwell, W. J., Guan, Z., Tsopanos, S., Theobald, M. D., Nurick, G. N. & Langdon, G. S. 2011. The quasi-static and blast response of steel lattice structures. *Journal of Sandwich Structures and Materials*, 13(4), 479–501.

Sousa-Martins, J., Kakogiannis, D., Coghe, F., Reymen, B. & Teixeira-Dias, F. 2013. Behaviour of sandwich structures with cork compound cores subjected to blast waves. *Engineering Structures*, 46, 140–146.

Sullivan, J. F. 1943. *Aircraft Armor – Ballistic Characteristics of a Magnesium Alloy, Dowmetal (Type FS)*. Watertown, MA: Watertown Arsenal Laboratory.

Tsopanos, S., Mines, R. A. W., McKown, S., Shen, Y., Cantwell, W. J., Brooks, W. & Sutcliffe, C. J. 2010. The influence of processing parameters on the mechanical properties of selectively laser melted stainless steel microlattice structures. *Journal of Manufacturing Science and Engineering, Transactions of the ASME*, 132(4), 0410111–04101112.

van de Voorde, M. J., Diederen, A. M. & Herlaar, K. 2005. Preliminary investigations of potential lightweight metallic armour applications. *In: Proceedings of the 22nd International Symposium on Ballistics*. Vancouver, BC. Flis, W. & Scott B. (eds) Lancaster, PA: DEStech Publications, Inc.

Walley, S. M. 2007. Shear localization: A historical overview. *Metallurgical and Materials Transactions A: Physical Metallurgy and Materials Science A*, 38(11), 2629–2654.

Weber, K. 2002. Protection efficiency of structured targets against KE projectiles. *In: Proceedings of the 20th International Symposium on Ballistics*. Orlando, FL. Carleone J., & Orphal D. (eds) Lancaster, PA: DEStech Publications, Inc.

Woodward, R. L. & Cimpoeru, S. J. 1998. A study of the perforation of aluminium laminate targets. *International Journal of Impact Engineering*, 21(3), 117–131.

Yang, S., Qi, C., Wang, D., Gao, R., Hu, H. & Shu, J. 2013. A comparative study of ballistic resistance of sandwich panels with aluminum foam and auxetic honeycomb cores. *Advances in Mechanical Engineering*, 5, 589216.

Yuen, S. C. K., Nurick, G. N., Theobald, M. D. & Langdon, G. S. 2010. Sandwich panels subjected to blast loading. *In:* Shukla, A., Ravichandran, G. & Rajapakse, Y. D. S. (eds.) *Dynamic Failure of Materials and Structures*, pp. 297–325. New York: Springer.

Zhen, L., Zou, D. L., Xu, C. Y. & Shao, W. Z. 2010. Microstructure evolution of adiabatic shear bands in AM60B magnesium alloy under ballistic impact. *Materials Science and Engineering: A*, 527(21–22), 5728–5733.

Zou, D. L., Zhen, L., Xu, C. Y. & Shao, W. Z. 2011. Characterization of adiabatic shear bands in AM60B magnesium alloy under ballistic impact. *Materials Characterization*, 62(5), 496–502.

8 Ceramic Armour

8.1 INTRODUCTION

The term 'ceramic' comes from the Greek word *Keramikos*, which literally means 'burnt things'. This tells us something about the way that the early Greeks manufactured ceramic pots, cisterns and the like. Consequently, a ceramic can be defined as an inorganic solid compound that is formed by the application of heat and sometimes heat and pressure. Ceramic armour materials are composed of at least one metal and non-metallic elemental solid with the raw material for ceramic production extracted from the earth and processed.

Readers will be familiar with the ceramic materials that are used in the kitchen or bathroom, and these have been termed 'traditional ceramics' and are largely based on clay. These tend to be quite porous and open structures with limited strength. However, around 70 years ago, progress was made in the development of what is now understood as 'advanced ceramics'. These are materials that have unique properties and are the type of ceramic that is used in armour. Armour ceramics, in particular, are strong in compression—their microstructures are carefully controlled during manufacture, and they possess limited porosity.

An early hint of the potential for using a hard brittle material in armour occurred when Major Neville Monroe-Hopkins found that a thin layer of enamel improved the ballistic performance of a steel plate (Dunstan and Volstad, 1984). This work was carried out in 1918. Enamel is made by fusing powdered glass to a substrate at temperatures between 750°C and 850°C and given that glass is a type of ceramic, this was the first ceramic-faced armour. Indeed, many early designs from the 1960s onwards have employed a hard ceramic face backed by a relatively ductile material, thereby employing the disruptor (or 'disturber')/absorber recipe that is used widely in armour systems today.

8.2 STRUCTURE OF ARMOUR CERAMICS

The atomic bonding of ceramic materials ranges from being purely ionic to completely covalent, and many ceramics exhibit a combination of these two bonding types.

The ceramics that are used in armour applications are polycrystalline materials that comprise numerous grains (or crystallites). These grains are defined by the extent of repeatability of the ordered arrangement of atoms and are separated by a grain boundary that may include single or multiple phases of sintering-aid materials (see Figure 8.1).

In addition, the microstructure is likely to contain a certain amount of porosity left behind during manufacture. Sometimes, separate phases of a material exist within the microstructure as particles as is commonly found in reaction-bonded ceramics.

319
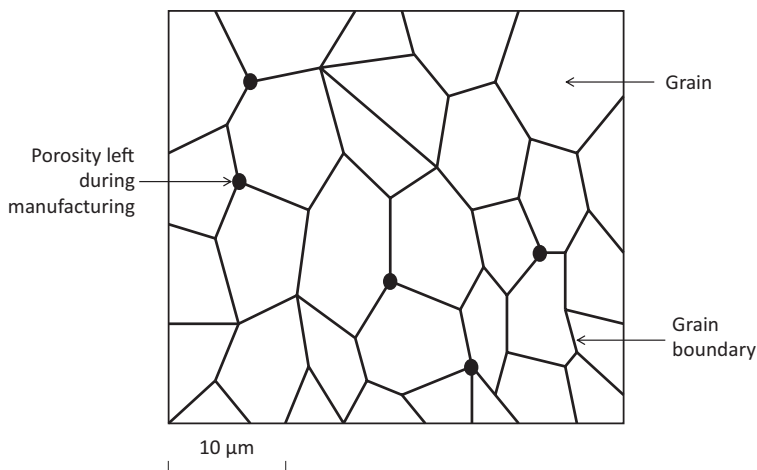
FIGURE 8.1 Schematic of a typical polycrystalline ceramic's microstructure.

Viewed as a polished section, we cannot see the full three-dimensional nature of the grain. It is found that grains of many different polycrystalline materials have a limited range of faces—usually between 9 and 18, and each face will have around four to six edges. The tightness and packing of the structure, along with the sizes and weights of the elements in the ceramic, will determine its density. The bulk density of the ceramic will take into account the porosity, all lattice defects and the phases that are present within the material. This is the measured density, which is referred to in this book. The theoretical density of the material is the ideal density that can be calculated from the continuous defect-free lattice—taking into account the multiple phases that may exist. Elements of low atomic number and atomic weight (H, C, Si, Al, B and so on) will result in materials with a low theoretical density. Elements of high atomic number and atomic weight (W, U, Zr, Th and so on) will result in materials with a relatively high theoretical density. Therefore, tungsten carbide (WC) has a theoretical density of over six times that of boron carbide (B_4C). Armour ceramics consist of a relatively small number of self-selecting elements. These are Al, B, C, N, O, Si and Ti. These elements combine together with a good number of strong bonds that provide the desired strength and stiffness characteristics of ceramic armour materials.

8.3 PROCESSING OF CERAMICS

A base ceramic powder is fabricated into a required shape and then densified by a process called sintering. The base powder is usually very fine (<5 μm), and when it is packed together and heated to a specific temperature (hence, the term 'burnt things' was used to describe the early ceramics), the particles sinter, that is, they form very small 'joins' to one another. When the joins grow, the surface area of the particles is reduced, and the material densifies. The theoretical density is not achieved with this method due to the presence of small pores, which have a small effect on the final mechanical strength. A schematic of the sintering process is shown in Figure 8.2.
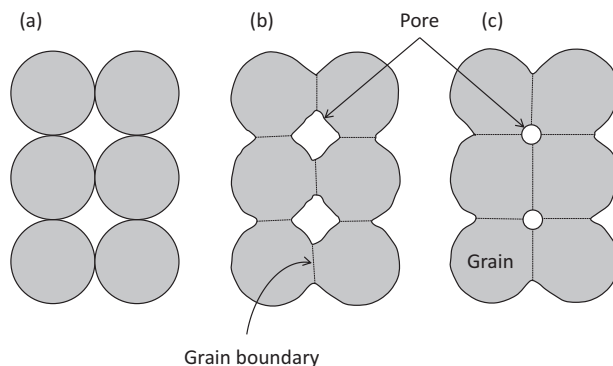
FIGURE 8.2 Sintering process showing (a) pressed powder (six particles), (b) the start of sintering and the emergence of grain boundaries and (c) the changes to pores as sintering proceeds.

For example, aluminium oxide (Al_2O_3) occurs naturally as the mineral corundum and can be produced in large quantities from the mineral bauxite (aluminium hydroxide) by the Bayer process. This involves the selective leaching of the useful mineral by caustic soda (sodium hydroxide) and precipitation of the purified aluminium hydroxide ($Al(OH)_3$). This is then thermally converted to alumina:

$$2Al(OH)_3 = Al_2O_3 + 3H_2O \tag{8.1}$$

The resulting material is then milled and sieved to provide a very fine powder that can be then used to manufacture a sintered or hot-pressed product. Prior to sintering, the powder can be pressed into the desired shape by cold pressing in a uniaxial or isostatic press. Alternatively, for complex shapes, a process of slip casting can be used where ceramic particles are suspended in water and cast into porous plaster moulds. The water is sucked out through the pores in the porous mould over time, leaving a closely packed deposition of particles that are ready for densification.

During the sintering process, an agent is added to help in the bonding process and reduce the temperatures that are required during the sintering step. These sintering agents lead to a reduction in the mechanical properties of the ceramic because they form relatively soft grain boundaries with low melting temperatures. Smaller particles sinter much faster than coarse particles because the surface area is larger, and the diffusion distances are smaller. Furthermore, the rate of sintering varies with temperature.

Liquid-phase sintering (LPS) is commonly used to densify engineering ceramics. This process makes use of low-melting-point sintering aids that form a viscous liquid at the firing temperature. The liquid thoroughly wets the solid particles and increases the rate at which sintering occurs. When cooled, it forms a glassy phase in between the grain boundaries. Typical sintering-aid materials are compounds of silicon dioxide (SiO_2), magnesium oxide (MgO) and calcium oxide (CaO). Because the glassy phase will melt again at a relatively low temperature compared to the crystalline lattice, liquid-phase sintered materials have a compromised high-temperature strength.

Higher densities and small grain sizes can be achieved by hot pressing. This is achieved when, simultaneously, pressure and temperature are applied to the powder. The application of pressure increases the contact stresses between particles and rearranges them to optimize their packing arrangement. This leads to a reduced densification time and can lead to a reduction in the temperature required to sinter—thereby reducing the amount by which the grains grow. This will lead to a final product with an increased final strength compared to a ceramic that was densified using pressureless sintering. Hot pressing can provide a near-theoretical density material with a very fine grain structure and therefore optimized strength, and therefore most suitable for armour applications. The same types of fine-grained powders suitable for pressureless sintering are usually suitable for hot-pressing applications. In most cases, a grain growth inhibitor will be added to inhibit grain growth to achieve a maximum density with minimum grain size.

Hot pressing is usually conducted at temperatures of approximately half the melting temperature of the material, which is usually a lower temperature than is used with pressureless sintering, which will be approximately two-thirds of the melting temperature. Nevertheless, this means that careful choice of the pressing die material is made such that it can withstand high thermal loads and thermal stresses. It also needs to be inert so that it will not react with the ceramic powder. Graphite is a popular material for hot-pressing machinery mainly because of its high-temperature capability and that it does not react with most materials. It is also suitable for heat by electrical induction. However, graphite will oxidize and therefore must be used in a vacuum or with an inert atmosphere of nitrogen, helium or argon. These issues make hot-pressing machinery very expensive. A schematic of a typical hot die press is shown in Figure 8.3.

An alternative method of processing a ceramic material is reaction bonding. Although the process has been around since the 1950s, it has only recently been used to produce armour ceramics. Two ceramics that are commonly manufactured by this method are silicon carbide and silicon nitride. With this process, densification occurs via a chemical reaction.

If pure silicon powder is heated in nitrogen gas, the following reaction occurs:

$$3Si + 2N_2 = Si_3N_4 \tag{8.2}$$

Alternatively, for reaction-bonded silicon carbide, a reaction between pure silicon and pure carbon powders can be created; thus,

$$Si + C = SiC \tag{8.3}$$

Usually, reaction-bonded silicon carbide is manufactured by infiltrating a preform of silicon carbide and carbon particles with molten or vapourized silicon (Si). The silicon and the carbon react to form silicon carbide (as above), which bonds the original silicon carbide particles together. The resulting structure will be a composite of silicon and silicon carbide. The carbon is usually completely consumed.

Boron carbide can also be made from reaction bonding and has been suggested as a lightweight material for armour applications mainly because the boron carbide particles have superior properties when compared to similar sized silicon carbide particles.
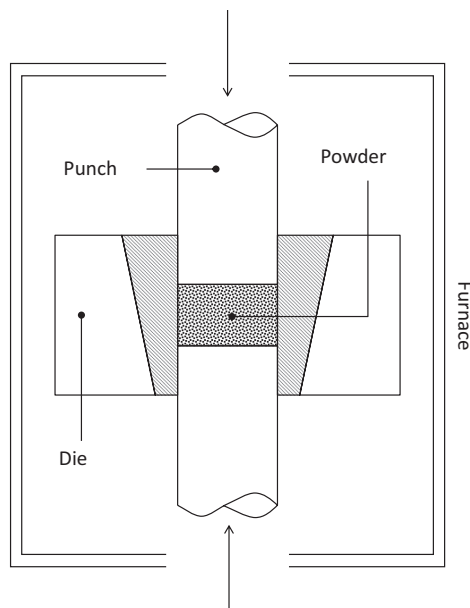
FIGURE 8.3   Schematic of hot-press system for ceramic powder densification.

Reaction bonding has several advantages relative to other processing routes. The main advantage is that during the process, the volume change is relatively small (less than 1%), and this provides good dimensional control. Additionally, the process requires relatively low operating temperatures and no applied pressure, which reduces the operating and capital costs. The disadvantage of this approach is that, inevitably, some unreacted silicon is left behind, and therefore, the resulting ceramic is a composite of silicon and silicon carbide. Consequently, the relatively soft silicon compromises the ballistic performance. Nevertheless, there have been a number of reaction-bonded silicon carbides produced for armour applications, and ballistic penetration studies have shown that approximately 8 mm of suitably constrained reaction-bonded SiC with ~10% Si content is sufficient to defeat steel-cored armour-piercing ammunition (Hazell et al., 2005).

8.4   PROPERTIES OF CERAMIC

Advanced ceramics display limited plasticity at room temperature and in fact often fracture in the elastic region. Fracture toughness values for ceramics are low and much lower than predicted by theory. The reason for this is the presence of flaws within the structure that act as stress raisers, which can cause a crack to form once the stress is applied. These flaws may be interior micro-cracks, internal pores or impurities. Stress raisers can even occur at the junction between neighbouring grains—which is unavoidable. In addition, boundary materials (such as the presence of a sintering aid) tend to be weaker than the grains, and therefore, they are more

susceptible to failure. However, in compression, the flaws do not act as stress raisers, and therefore, much higher strengths are achievable. On average, it is found that the ceramic's strength in compression is approximately tenfold that of what it is in tension. This is good news for armour applications – as the material will be loaded in compression for at least the early stages of projectile penetration.

Compared to ductile materials, brittle materials such as ceramics exhibit a relatively broad range of stresses that cause failure in the material. This has led to a probabilistic approach in defining failure of ceramics. The Swedish engineer Weibull (1951) proposed the following way of handling statistical variations of failure strengths. He defined the survival probability $P_s(V_0)$ in terms of two material constants, m and σ_0. If we have a large number of identical samples of volume V_0, then the survival probability $P_s(V_0)$ would be given by the fraction of samples that survived testing to a stress σ. This can be written as

$$P_s(V_0) = \exp\left\{-\left(\frac{\sigma}{\sigma_0}\right)^m\right\}$$

(8.4)

When the applied stress $\sigma=0$, then as expected, all samples survive, and $P_s(V_0)=1$. As the applied stress is increased, more and more samples fail; as $\sigma \rightarrow \infty$, so $P_s(V_0) \rightarrow 0$. Further, if we set $\sigma=\sigma_0$, then $P_s(V_0)=1/e=0.37$. Therefore, σ_0 can be described as the stress at which we will expect to see 37% of our samples survive. The constant m is described as the Weibull modulus, and this is a constant that defines how quickly the strength falls as we move from $P_s(V_0)=0$ to 1. Figure 8.4 shows a Weibull distribution function for a selection of materials where $\sigma_0=250$ MPa, and m varies from 3 to 100. Firstly, it is possible to see that when the applied stress$=250$ MPa, then the
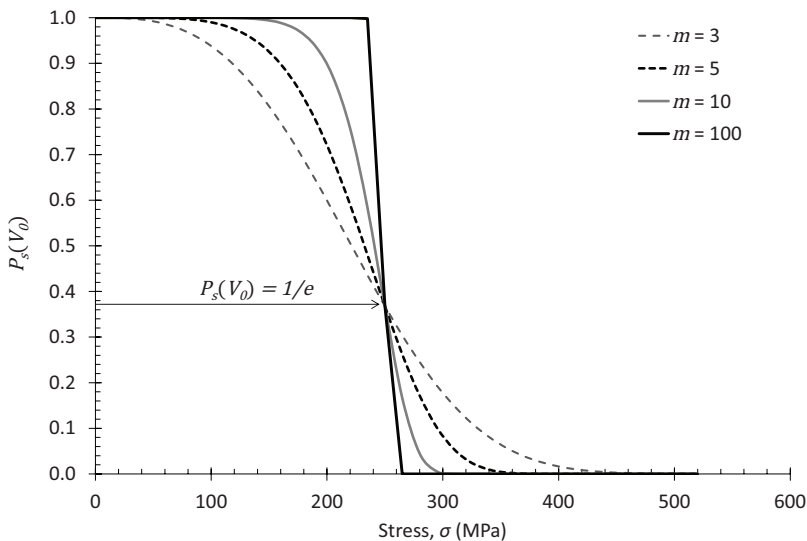
FIGURE 8.4 Weibull distribution function showing the survival probability changes due to changes in the Weibull modulus, m; $\sigma_0=250$ MPa.

survival probability $P_s(V_0) = 1/e = 0.37$. Secondly, it is also possible to see that for the sample where $m = 3$, there is a much larger range of stresses that result in failure of samples, whereas when $m = 100$, failure of the samples occurs over a relatively narrow range of stresses. Advanced ceramics will have an m value in the range of 5–10, whereas metals will have an m value in the range of 90–100. Traditional ceramics such as pottery and brick will have an m value that is less than 3 (Meyers and Chawla, 1999).

8.4.1 FLEXURAL STRENGTH OF CERAMICS

Ceramics are unable to be tested in a simple uniaxial tensile test like metals principally due to their incredibly low strain to failure at room temperature and their high-hardness values. Their high hardness also makes it very difficult to produce the characteristic dog bone-shaped specimen that can be produced for testing metals. A ceramic specimen is also difficult to grip without using inducing failure in the specimen. Therefore, ceramic samples are usually tested using either a three-point or four-point bend test with either cylindrical or rectangular cross-sections. This method is discussed in Chapter 2. It should be noted that the three-point test configuration subjects a relatively small portion of the specimen to the maximum stress in bending. Therefore, three-point flexural strengths are likely to be much higher than four-point flexural strengths. Therefore, the four-point bending test is preferred and recommended for most characterization purposes. A relevant standard for testing is published by the American Society for Testing and Materials International (ASTM, 2013).

8.4.2 FRACTURE TOUGHNESS OF CERAMICS

The fracture toughness value for a ceramic can be calculated by the following equation:

$$K_{\text{Ic}} = Y\sigma\sqrt{\pi a} \tag{8.5}$$

This is the plane strain fracture toughness. This is for the case where the crack dimension is much smaller than the thickness of the plate. Y is a dimensionless shape factor, σ is the stress applied and a is the half-length of an internal crack. It can be seen from Equation 8.5 that for a given fracture toughness value, the larger the value of the inherent flaw, the lower the applied stress required to cause fracture.

Examples of fracture toughness values for selected ceramic and glass materials are presented in Table 8.1 (after Callister (2007)).

8.4.3 FRACTOGRAPHY

There are two principal modes of cracking with polycrystalline ceramics: (1) inter-granular cracking, where the crack propagates around the grain boundaries in the weaker inter-granular material, and (2) trans-granular cracking, where the cracks propagate through the grains. Usually, when a ceramic fails, there will be a

TABLE 8.1

Plain Strain Fracture Toughness and Strength Values for a Selection of Glass and Ceramic Materials

Ceramic	Type	Fracture Toughness (MPa m$^{1/2}$)	Flexural Strength (MPa)
Aluminium	99.9% pure	4.2–5.9	282–551
oxide	96% pure	3.85–3.95	358
Glass	Borosilicate	0.77	69
	Soda–lime	0.75	69
Glass ceramic	Pyroceram	1.6–2.1	123–370
Silicon nitride	Hot pressed	4.1–6.0	700–1000
	Reaction-bonded	3.6	250–350
	Sintered	5.3	414–650
Silicon carbide	Hot pressed	4.8–6.1	230–825
	Sintered	4.8	96–520

Source: Callister, W. D. 2007 *Materials Science and Engineering: An Introduction*, 7th ed. Copyright
            Wiley-VCH Verlag GmbH & Co. KGaA. Reproduced with permission.

combination of the two failure modes, but this will depend on the packing structure and the strength of the grain boundary material.

During the initial stages of projectile penetration into a ceramic armour material, both inter-granular and trans-granular cracking are likely to occur. For resisting penetration, inter-granular cracking in the ceramic is frequently more attractive than trans-granular cracking. This is because, with inter-granular cracking, the cracks have to travel along more convoluted pathways around the grains, thereby increasing the time for comminution to occur (that is, the reduction of intact ceramic to very small fragments). Furthermore, when the material is subjected to large confining pressures due to the projectile penetration, if the grains cleave in two, it is likely that the two fragments will be able to move cooperatively more readily than closely inter-locked grains that have been separated by inter-granular cracking.

The maximum velocity at which cracks grow in ceramics is determined by the speed of sound of the material. After the crack tip has reached some critical terminal velocity, it will tend to divide (or bifurcate). This process will be repeated until a network of cracks has been formed in the material and the material begins to separate.

This multi-crack propagation process that results from the penetration of a projectile means that ceramics have limited multi-hit capability. However, pre-existing single cracks do not compromise the ballistic performance per se. Horsfall and Buckley (1996) showed that the ballistic limit velocity for a through-thickness pre-cracked (full width) 6-mm-thick alumina tile backed by a 9-mm-thick glass fibre-reinforced polymer panel (17 ply, plain weave) only dropped by ~3% when penetrated by a 7.62-mm AP projectile when compared to non-cracked targets. Their ceramic tiles had a limited impact-face constraint in the form of a single layer of woven fibreglass bonded to the front surface using polyester resin. However, they noted that the effect

TABLE 8.2

Ballistic Limit Data (v_{50}) for a 7.62-mm Armour-Piercing (Fabrique Nationale P80) Projectile Penetrating a Ceramic-Faced Armour (6-mm Alumina/9 mm GFRP) Showing the Results of Penetrating a Non-Cracked and Cracked Target

	No Pre-Existing Crack in Ceramic		Pre-Existing Crack in Ceramic, Projectile Impact within 5 mm of the Crack	
v_{50} Calculation	Range of Results (m/s)	v_{50} (m/s)	Range of Results (m/s)	v_{50} (m/s)
Over 6 shots	27	765	33	741
Over 8 shots	33	763	51	742

Source: Horsfall, I. & Buckley, D. 1996, *International Journal of Impact Engineering*, 18(3), 309–318.

TABLE 8.3

Approximate Knoop Hardness (100-g Load) for Several Ceramic Materials

Material	Approximate Knoop Hardness
Diamond	7000
Boron carbide (B_4C)	2800
Silicon carbide (SiC)	2500
Tungsten carbide (WC)	2100
Aluminium oxide (Al_2O_3)	2100
Quartz	800
Glass	550

Source: Callister, W. D. 2007 *Materials Science and Engineering: An Introduction*, 7th ed. Copyright Wiley-VCH Verlag GmbH & Co. KGaA. Reproduced with permission.

of pre-crack was simply to increase the variability in ballistic limit data, which in turn produced a small reduction in the measured ballistic limit velocity. Their ballistic limit data (v_{50}—see Section 12.2.3) results are summarized in Table 8.2.

8.4.4 HARDNESS

For polycrystalline ceramics, as with metals, plastic deformation occurs by the motion of dislocations. One of the reasons why ceramic materials tend to be hard and brittle is the difficulty of these materials to accommodate slip (or dislocation motion). This is true for both ionic and highly covalently bonded ceramics. Consequently, it is often difficult to measure plastic deformation in ceramics at room temperature before fracture. However, it is possible to use a Vickers or a Knoop indenter (Chapter 2) to incur local plastic deformation in the sample. These methods can be used to establish the hardness of ceramic materials. Typical Knoop hardness values of ceramics are provided in Table 8.3.

8.4.5 EFFECT OF POROSITY ON THE PROPERTIES OF CERAMICS

Due to the fact that during fabrication, the precursor material is in the form of a powder, this inevitably results in porosity in the sample. The effect of porosity on the flexural strength and stiffness of a ceramic sample has been well known since the 1950s (Coble and Kingery, 1956). For example, it has been shown that the porosity of certain ceramics follows the following relationship (Callister, 2007):

$$E = E_0 \left(1 - 1.9p + 0.9p^2\right) \tag{8.6}$$

where E is Young's modulus, E_0 is Young's modulus for the non-porous material and p is the volume fraction of porosity. When measuring the flexural strength of the sample, porosity also affects the strength of the ceramic. This is for two principal reasons:

1. The pores themselves reduce the cross-sectional area of the material carrying the load.
2. They act as a stress raiser to the extent that for an isolated spherical pore, the applied tensile stress is effectively doubled.

Experimentally, it has been shown that the flexural strength decreases exponentially with porosity (p) according to Callister (2007)

$$\sigma_{fs} = \sigma_0 \exp\left(-np\right) \tag{8.7}$$

where σ_0 is the non-porous strength, and n is an experimental constant. In Figure 8.5, the effect of porosity on the transverse strength of an alumina sample is clearly seen from the data presented by Coble and Kingery. Here, the best fit to the experimental data in SI units is given by $\sigma_0 = 195.6\,\text{MPa}$ and $n = 3.6$. They tested alumina samples of 5%–50% porosity with comparable grain sizes and showed that the strength and stiffness reduced markedly as the volume fraction of porosity was increased.

Ultimately, this has implications for ceramic armour in that increased porosity will lead to an increased probability of fracture in compression (as the bullet penetrates into the samples and collapses the pores) and failure in tension as stress waves are reflected off the free surface of the ceramic to produce tensile waves. Therefore, ceramic armour materials tend to be processed so as to minimize the extent of porosity.

8.5 EARLY STUDIES ON CERAMIC ARMOUR

Patents for a ceramic-based armour were filed by the Goodyear Aerospace Company, with the first filed in 1963 and granted in 1970 (Cook, 1970; Cook et al., 1979). The initial patent application detailed a ceramic-faced armour composed of an alumina facing attached to a woven substrate (see Figure 8.6). Subsequent research into the mechanics of ceramic-armour penetration was carried out by Wilkins (1967, 1968), Wilkins et al. (1967), Florence and Ahrens (1967) and Florence (1969).
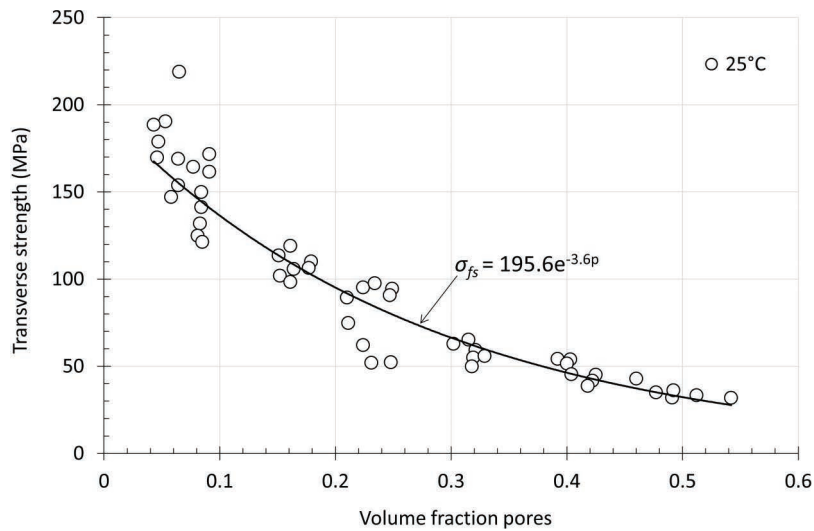
FIGURE 8.5 Effect of porosity on transverse strength on alumina samples at 25°C. (Adapted from Coble, R. L. & Kingery, W. D. 1956, *Journal of the American Ceramic Society*, 39(11), 377–385.)
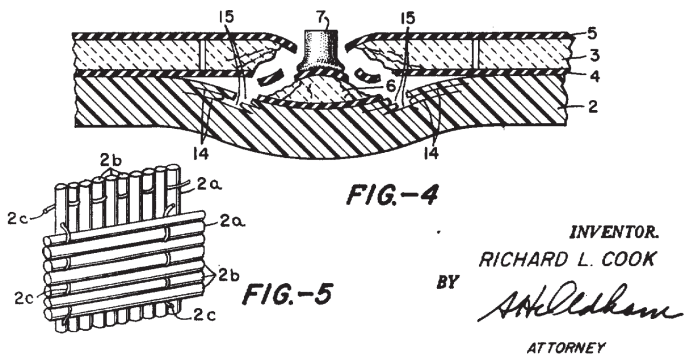
FIGURE 8.6 R. L. Cook's ceramic-faced armour from 1963. (From Cook, R. L. 1970 *Hard-Faced Ceramic and Plastic Armor*. Delaware: Goodyear Aerospace Corporation.)

Wilkins recognized that in order to optimize a two-component ceramic armour system, it is necessary to understand the interaction between the target and the projectile. Using high-speed photography, flash X-ray and numerical modelling techniques, they were able to evaluate the ballistic failure processes.

From their numerical simulations of a sharp steel projectile impacting an 8.64-mm alumina tile backed by 6.35 mm of aluminium at 853 m/s, they deduced the following:

- During the initial stages of penetration (0–9 µs), the projectile tip is destroyed, and the back plate yields at the ceramic interface. A crack is initiated at the rear surface of the ceramic as it tends to follow the motion
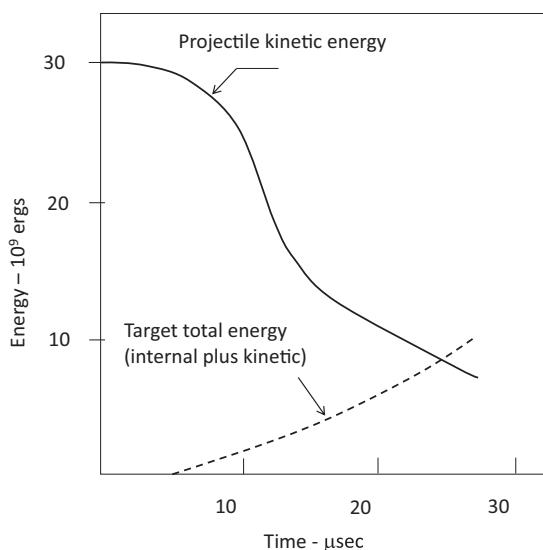
FIGURE 8.7   Energy versus time for an impact at 2800 ft./s (853 m/s) of a sharp steel pro-jectile with an AD85–faced aluminium target; 1 erg $= 10^{-7}$ J. (Adapted from Cline, C. F. & Wilkins, M. L. 1969 The importance of material properties in ceramic armor. *In: Proceedings of the Ceramic Armour Technology Symposium, Columbus, OH, 29–30 January.*)

of the backplate. This grows in magnitude in the direction of the impact face. Furthermore, a fracture conoid grows from the interface between the projectile and the target and grows in the direction of the projectile travel.

- Between 9 and 15 μs, the projectile is eroded, and the ceramic has become rubble by multiple cracks intersecting and coalescing. The projectile erodes by a process of yielding and plastic flow in a direction perpendicular to the projectile travel. Erosion takes place because the stress level in the projectile is greater than its strength. Approximately 40% of the projectile mass and initial energy are carried off by eroded projectile material.
- After 15 μs, the erosion of the projectile ceases, and the remainder of the energy in the target–projectile system is absorbed by the backplate.

An energy balance analysis of ballistic penetration, referring to the above events, is shown in Figure 8.7.

8.6   CONE FORMATION

One of the notable and helpful factors in offering resistance during ceramic armour penetration is the cone of damage that is produced ahead of the penetrator. An exam-ple is captured by Cook's early patent and shown in Figure 8.6. Sometimes, a cone is formed that remains intact, and these have been seen to evolve in real time in glass (Chaudhri and Walley, 1978). Cone formation is also a characteristic of quasi-static indentation. They follow paths of maximum tensile stress in the material. These paths
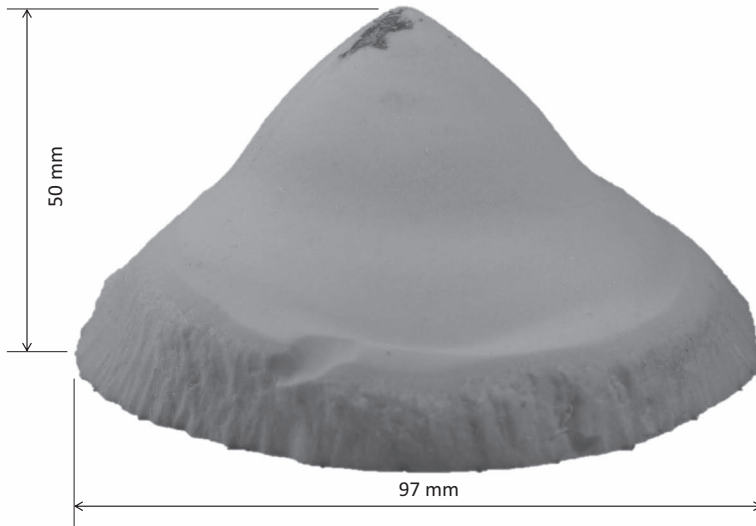
FIGURE 8.8 Ceramic cone produced from an impact from a bullet into a thick block (50 mm) of alumina.

were first plotted by Hertz (1882, 1896a, b). An example of such a cone is provided in Figure 8.8. Here, a steel bullet was fired at a thick tile of alumina (50 mm thick). The cone is seen to broaden at its base, and this is due to the stress wave interactions from the free-surface reflections. Note too that, in this case, the diameter of the base of the cone is approximately twice the thickness of the tile.

The advantage of the ceramic armour is that the formation of the cone spreads the load of the projectile over a wider surface area. Therefore, essentially, the kinetic energy density of the projectile is reduced. A much tougher and ductile layer is then placed at the rear of the ceramic to 'catch' the cone and the projectile fragments.

It has been shown that the degree of pre-stress confinement will affect the morphology of the cone formation. Pre-stress of a ceramic can be achieved either through the mechanical application of a 'wedged' confinement jig (see Sherman and Ben-Shushan (1998)) or through shrink fitting a high-strength metallic collar onto a cylindrical tile. Both techniques have been shown to improve the ballistic behaviour of the ceramics, see Zhang et al. (2020) and Hazell et al. (2021). In fact, it has been well-known since the 1950s that pre-stressing ceramics improve their impact resistance (Johnston et al., 1953).

The shrink fitting process involves heating up high-strength steel collars to ~550°C and slipping over the room-temperature ceramic tiles. The subsequent cooling of the steel collars results in a lateral confinement of the ceramic tile. The required radial mismatch at room temperature (δ) to give the desired pre-stress can be estimated from the 'press-fit' theory (Lundberg et al., 2016).

$$\sigma_{cf} = \frac{\delta}{R} \left[\frac{1-v}{E} + \frac{(1-v_s)R^2 + (R+t)^2(1+v_s)}{tE_s(2R+t)} \right]^{-1} \qquad (8.8)$$
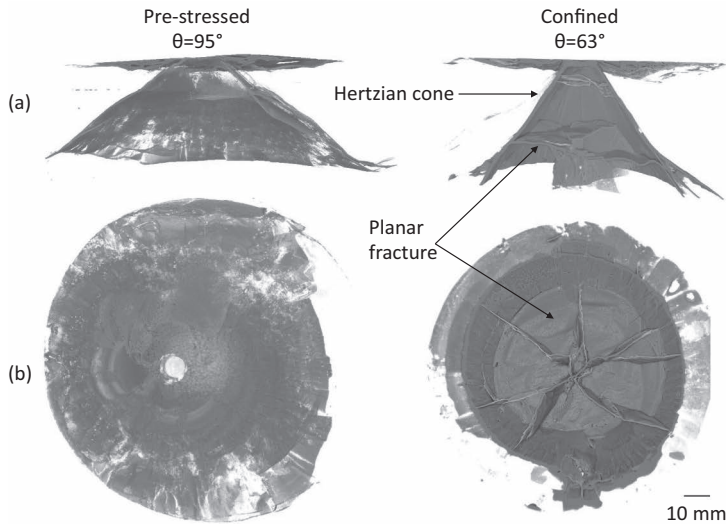
FIGURE 8.9 Micro-computed tomography scan images of post-impacted ceramic samples showing the internal damage caused from a pre-stressed sample (left) and a non-stressed confined sample (right). (a) Looking through the cone crack and (b) looking from the bottom up. Also included is the included angle of the initial trajectory of each cone, θ. (After Hazell et al., 2021.)

where σ_{cf} is the shrink-fit confining pre-stress, E is Young's modulus, ν is Poisson's ratio, R is the radius of the ceramic, t is the wall thickness of the steel surround. Subscript 's' represents the steel and no subscript indicates the property of the ceramic.

The improvement of ballistic performance due to pre-stress is thought to be largely due to the suppression of crack growth within the ceramic (Sherman and Ben-Shushan, 1998). Pre-stressing the ceramic has been shown through modelling to lead to greater negative stress triaxiality (a ratio of the pressure to the equivalent stress) and this has been linked to damage suppression in ballistically loaded ceramic targets (Deshpande and Evans, 2008). Further, it has been hypothesized that pre-stress will suppress the formation and growth of the cone cracks by lowering the stress that would otherwise drive cone crack growth (Lundberg et al., 2016). Indeed, it has been shown that when ceramic tiles are pre-stressed, the cone crack morphology appears shallower compared to unstressed ceramic targets (Sherman and Ben-Shushan, 1998, Hazell et al., 2021)—see Figure 8.9. In the context of a two-component ceramic armour system, it would be expected that the force of the penetrating projectile would be spread over a larger surface area implying a better resistance to penetration.

8.7 HIGH-VELOCITY IMPACT STUDIES

The high-velocity impact of ceramic materials has gained considerable interest in recent years in the drive to provide better protection against tank rounds and shaped
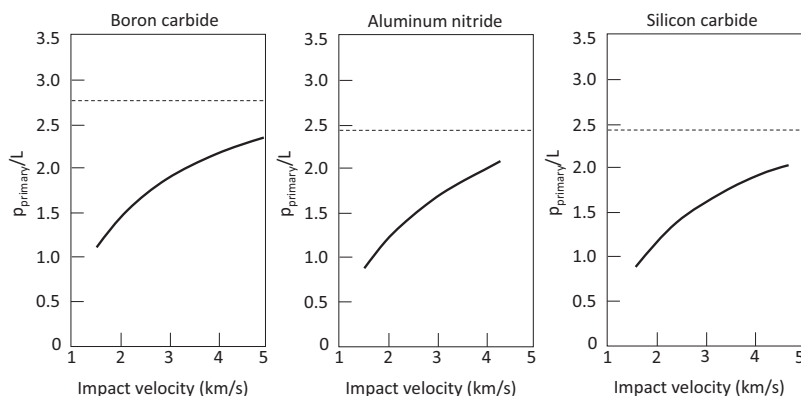
FIGURE 8.10   Primary penetration depth normalized by penetrator length for three differ-ent ceramics (dashed lines from hydrodynamic theory). (Adapted from Franzen, R.R. et al., *International Journal of Impact Engineering*, 19(8), 727–737.)

charge jets. The experiments designed for rods have usually involved the use of the reverse-ballistic technique (essentially, where the 'target' is launched towards the 'projectile'—see Section 12.2.7). For tungsten-alloy penetrators impacting steel, fully hydrodynamic penetration will not occur until an impact velocity of ~3 km/s. This velocity is known as the 'hydrodynamic limit'—see Section 4.5. Up to this veloc-ity, the strength of the target is important and therefore acts to decelerate the rod. However, the required velocity for full hydrodynamic interaction (where the target and the projectile interaction are assumed to behave in a fluid-like fashion) depends on the materials and for ceramic can be many kilometres per second (Kozhushko et al. 1991), and therefore, this type of penetration regime will only be approached by very high-velocity rod projectiles and shaped charge jets. At 5 km/s, the penetration is still substantially less than that which is predicted by hydrodynamic theory as the results, as presented by Franzen et al. (1997) (see Figure 8.10).

Shockey et al. (1990) investigated the long-rod penetration of a variety of ceramic materials by firing tungsten–nickel–iron penetrators at confined ceramic targets. The velocities of the projectiles ranged from 0.8 to 1.4 km/s and therefore far below the hydrodynamic threshold discussed previously in this section. Nevertheless, Shockey's results inform how ceramic armour would respond when subjected to impact from a tank-fired armour-piercing rod. Post-mortem analysis of the ceramics revealed that tensile fracture occurs soon after impact, close to the rod periphery. They built up a picture of the penetration process, which is summarized as follows.

1. The stress fields are initially elastic, and the largest tensile stresses are in the radial direction. Therefore, the cracks that form are ring cracks con-centric about the impact site. These cracks initially grow to approximately 1 mm below the surface. From these ring cracks, several large Hertzian cone cracks extend throughout the tile, assuming trajectories 25°–75° from the initial normal-to-the-surface direction.

2. As the rod continues to advance, the compressive strength is exceeded in the material directly below the penetrator. Microcracking occurs in a shallow zone near the penetrator tip, and the stress field changes in character.
3. The principal tensile stresses are now hoop stresses that invoke 6–12 large radial cracks propagating outward from the impact centre like spokes in a bicycle wheel.
4. A fourth type of crack finally develops beneath the impact surface and runs parallel to it. These intersect cone and radial cracks to form the residual crater and to produce fragmentation with a large proportion of the projectile's kinetic energy being converted to the kinetic energy of the fragments.

8.7.1 SHAPED-CHARGE PENETRATION OF CERAMIC MATERIALS

Ceramic materials provide good passive armour solutions to protect against shaped-charge penetration—especially when confined (Held, 2002; Hornemann and Holzwarth, 1997). Figure 8.11 shows a schematic of a shaped charge penetrating a confined ceramic target. The confinement has a higher shock impedance than the ceramic (e.g., steel) and that allows for the reflection of a compression wave from the periphery of the ceramic. As the jet penetrates the front cover plate and the ceramic, a high-intensity shock wave propagates into the ceramic (see Figure 8.11a). Behind, the shock, large shear stresses cause damage to the ceramic. When the wave encounters the surrounding confinement, it is reflected as a compression wave (c). These reflected waves cause the damaged material surrounding the crater wall to move into the penetration channel (d) and thus interact with the shaped-charge jet (e).
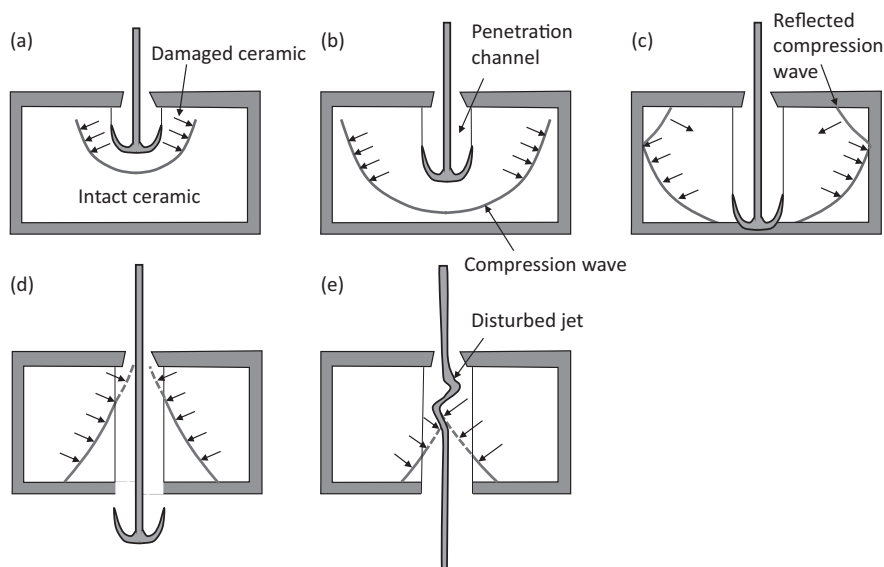
FIGURE 8.11 Penetration of a confined ceramic target.

The high strength of ceramics helps with the defeat of shaped-charge jets as strong materials will not produce large cavities. That is, penetration of ceramics by a shaped-charge jet results in relatively narrow cavities when compared to metals. Shock waves travel quickly in ceramics too and therefore the reflection off the confinement can cause the crater to collapse in a short time period, as discussed above.

Glass also has an unusual ability to resist penetration by shaped-charge jets and this has been known since World War II. When a jet penetrates a glass target, the penetration path opens up to its maximum diameter within a few microseconds and then closes rapidly after the penetration front passes. It is thought that the closure of the penetration cavity is caused by rapid elastic recovery from high pressure near the penetration front (Hauver et al., 1991). This behaviour has been turned 'spring back' and is similar in behaviour to highly shock-compressed material rapidly releasing and expanding around the crater wall (Held, 1998). It has also been observed that permanent densification of the glass occurs when it is subjected to high pressure (Bridgman and Šimon, 1953) and this may also contribute to the resistance to penetration. Dilatancy, associated with a brittle fracture is thought to make a secondary contribution. This is unlike ceramics, where this plays a major role in jet interference.

Figure 8.12 shows a sequence of images from an experiment where a shaped-charge jet is visualized penetrating a target comprising of a stack of 25-mm thick glass targets. The penetration path, the permanently densified volume surrounding the penetration path, the trailing fracture and the fracture initiated at the interface between the glass plates are visible. Also visible is the partial necking of the penetration path due to the 'spring back' of the permanently densified region.
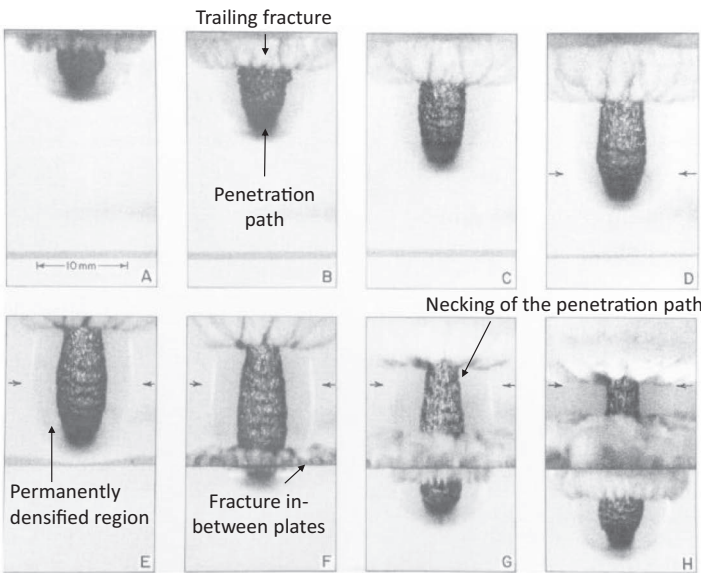
FIGURE 8.12 Penetration of a target comprising of stacked 25-mmm soda–lime glass plates by a shaped charge jet with images taken at every 1 μs (after (Hauver et al., 1991)).

8.8   STUDIES ON THE SUBJECT OF DWELL

There appeared to be little interest in ceramic armour during the 1970s after the work of Wilkins; however, Cold War pressures meant that there was to be a resurgence in interest in ceramic armour during the early 1980s. One of the more notable discoveries during that period was that under certain ballistic loading conditions, the projectiles could be seen to 'dwell' on the surface of the ceramic (Hauver et al., 1992). These targets were mostly highly confined, thick targets to reduce the propensity of tensile (release) waves propagating into the penetration zone, thereby exacerbating failure. Studies in dwell are of great interest as they may provide a route to enhancing the performance of ceramic armours. Ceramic 'dwell' occurs when a high-velocity projectile impacts a ceramic target and flows out radially with little significant penetration. When the projectile is completely eroded at the ceramic's surface, this is called 'interface defeat'. Notably, Wilkins had previously observed similar behaviour with small-arms bullets with very thick (75 mm) alumina targets (Holmquist et al., 2010).

An example of dwell in small-arms bullets has been demonstrated by Wilkins using flash X-ray. A sequence of flash X-ray radiographs of the penetration sequence for a surrogate 7.62-mm APM2 bullet is shown in Figure 8.13. It can be seen from the sequence that penetration does not occur for the first 20 µs. Instead, the tip of the projectile is progressively blunted. After 15.8 µs, a certain degree of penetration occurs; however, the radial flow of the penetrator is extensive. Eventually, it is possible to see some evidence of conoid formation (at 25.2 µs), which appears to have a relatively large included angle. This is most likely due to the large contact area between the projectile and the ceramic due to the presence of the radially extended projectile material. Ultimately, the extended elements break off, and the projectile continues to penetrate (35.5 µs).

Dwell has also been observed with transparent armour systems. Straßburger (2009) showed that using a thin (4 mm) layer of sub-micrometre grain-sized alumina added to a transparent armour (3×9 mm of borosilicate glass with a 3-mm polycarbonate backing) resulted in a dwell phase that lasted approximately 10 µs. In this case, the projectile was a 7.62×51 mm armour-piercing (steel-cored) projectile; the impact velocity was 850 m/s. It has also been seen in strong bullet cores made from tungsten carbide. In this case, the projectiles were penetrating silicon carbide (Hazell et al., 2013). Figure 8.14 shows the stages of penetration. By 19.2 µs after impact (Figure 8.14b), the strong tungsten carbide core is seen to flow out radially from the central penetration axis in a fashion previously seen by Wilkins with a steel-cored projectile. There is also evidence of conical fracture due to the way in which the projectile is flowing into the target. Ultimately, by 28.2 µs (Figure 8.14c), the core has been completely destroyed.

With high-velocity rods, the majority of the work has been carried out with small-scale projectiles using the reverse-ballistic techniques mentioned in Section 8.7 (with the exception of G. E. Hauver's initial findings, e.g. Hauver et al. (1992)). These studies have mostly focused on borosilicate glass (Anderson, Jr. et al. 2010), boron carbide (Lundberg et al., 1998), silicon carbide (Lundberg et al., 2000, 2001; Lundberg and Lundberg 2005), alumina (Espinosa et al., 2000) and titanium diboride (Espinosa et al., 2000; Lundberg et al., 2000).
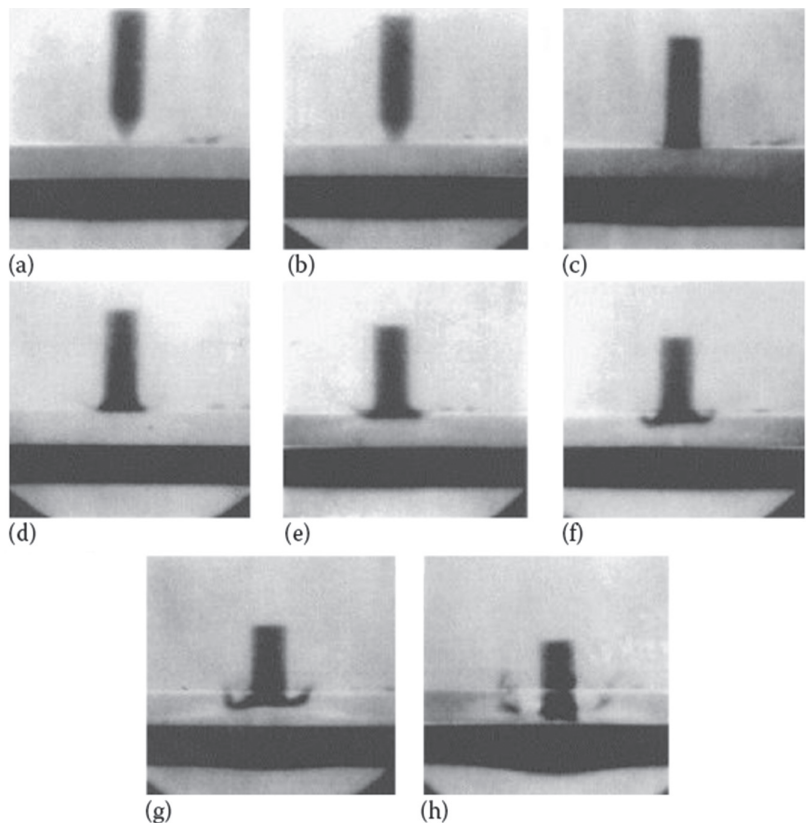
FIGURE 8.13 Flash X-ray shadowgraphs of AP surrogate projectile impacting 7.24-mm B4C/6.35-mm 6061-T6 at 701 m/s. Penetration after (a) 1.8, (b) 3.8, (c) 8.9, (d) 11.8, (e) 15.8, (f) 19.8, (g) 25.2 and (h) 35.5 μs. (Reprinted from Anderson, Jr., C. E. & Walker, J. D., *International Journal of Impact Engineering*, 31(9), 1119–1132, Copyright 2005, with permission from Elsevier.)
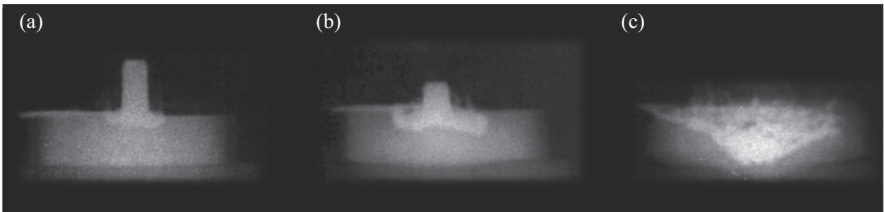
FIGURE 8.14 Series of radiographs of an FFV (tungsten carbide) core completely penetrating a ceramic-faced projectile. Timings (from core contact) were as follows: (a) 10.2, (b) 19.2 and (c) 28.2 μs. (Reprinted from Hazell, P. J. et al., *International Journal of Impact Engineering*, 54, 11–18, Copyright 2013, with permission from Elsevier.)

It has been shown that below a certain threshold velocity, the strength of the ceramic during the ballistic event appears relatively high. As a result, the material of the penetrator flows outwards in a radial fashion without significant penetration of the ceramic material. Also, above a threshold velocity, the ceramic behaves as if its strength is reduced, and normal penetration ensues. That is to say that sufficient damage is accumulated at the tip of the penetrator allowing for penetration. This interface-defeat-to-penetration transition behaviour is observed over a fairly narrow range of ordnance velocities (Lundberg et al., 2000). Interface defeat is also more likely when the ceramic is confined with the confinement being of a good acoustic impedance match to the ceramic (Hauver et al., 1992) and offering sufficient rear-face support to prevent the flexure of the ceramic during ballistic loading. The extent of penetrator dwell is also determined by the geometry of the target—with semi-infinite targets exhibiting more dwell than thin targets. This is due to the return of tensile release waves from the rear surfaces occurring over a shorter time period in the thin targets than with relatively thick semi-infinite targets. The extent of penetrator dwell has also been shown to be affected by the degree of pre-stress that the ceramic target is subjected to, as discussed earlier.[1] To test this, Lundberg et al. carried out high-velocity reverse-ballistic experiments with scaled-rod projectiles impacting pre-stressed ceramic targets (Lundberg et al., 2016). Impact experiments with different levels of target pre-stress showed that pre-stress increased the velocity at which the transition from interface-defeat-to-penetration occurred. For example, they showed, in one experiment, that the velocity of transition of one unconfined sample was increased from 982 to 1367 m/s by adding a confining pre-stress of 56 MPa.

Work has also focused on the use of buffer plates to elucidate the mechanisms of dwell (Holmquist et al., 2010). Although it is known that specially designed cover plates extend the dwell time for SiC targets (Lundberg et al., 2001), it has been shown that using Cu buffer plates can lead to an increase in the impact velocity that requires the dwell-to-penetration transition to occur. The reason for this is that the buffer plate attenuates the shock from the projectile thereby leading to a (relatively) gradual loading profile on the surface of the ceramic (Holmquist et al., 2005). Similar results have also been seen by encapsulating the projectile in polycarbonate (Malaise et al., 2000).

The exact microstructural mechanisms of penetrator dwell are not well understood, although the effect has been successfully modelled using macroscopic pressure hardening and strain-dependent damage laws (Holmquist and Johnson, 2002) suggesting that some kind of pressure hardening of the intact (or indeed, failed) material is occurring. It is also thought that when confined pressures are applied, certain ceramics exhibit ductility. Therefore, if sufficient confining pressure is realized during the penetration event, the ceramic can accommodate relatively high strains.

8.9   SHOCK STUDIES IN CERAMIC MATERIALS

The shock response of ceramic materials has also been of interest in recent years, although it is debatable whether the target is shocked during a ballistic impact. There is, however, a small 1D zone that exists at the penetrator/target interface that can

lead to the formation of shocks. Nevertheless, these would be quite short-lived. Despite all of this, carrying out plate-impact experiments can inform the researcher on the mechanics of ceramic yield and failure at high rates of strain. In particular, the transition from elastic behaviour to plastic flow has captured some interest in recent years.

Probably the three most important properties that can be gleaned from the plate-impact test are the following: the dynamic shear strength, the Hugoniot elastic limit (HEL) and the spall strength. These are discussed in some detail in Chapter 5. The HEL (which represents the yield strength under 1D strain conditions, in metals at least) is the transition from elastic to inelastic behaviour as a compression wave propagates through the material. However, in ceramics, it was widely accepted that this is the point that microcracking began. This viewpoint has been challenged by some researchers who have found evidence of damage within the elastic region (Rosenberg and Yeshurun, 1985; Louro and Meyers, 1989).

The HEL, which is a measure of strength in 1D strain conditions, is important for ballistic applications in that it can be used to calculate the dynamic yield strength (Y) in 1D stress conditions and compared to yield strengths from universal testing machine results. This is achieved knowing the Poisson's ratio, v; thus,

$$Y = \frac{(1 - 2v)}{(1 - v)} \sigma_{\text{HEL}}$$

(8.9)

where σ_{HEL} is the HEL of the material that would have been measured under uniaxial strain conditions.

This in turn has been historically linked to the performance of a selection of ceramic tiles by Rozenberg and Yeshurun (1988) by correlating ballistic performance with average yield strength, which is an average of the quasi-static (Y_0) and dynamic values, viz.,

$$\bar{Y} = \frac{Y_0 + Y}{2}$$

(8.10)

8.10   UNDERSTANDING THE ROLE OF COMMINUTION

Comminution is the break-up of the ceramic into very small fragments, and these fragments can interact with one another during the ballistic penetration process. The importance of this process in understanding the ballistic penetration processes of ceramic materials was underlined by Curran et al. (1993) who developed a micro-mechanical model for comminution and granular flow of brittle materials. From their model, they inferred that the most important ceramic properties that govern the depth of penetration into thick ceramic targets were the friction between comminuted granules, the unconfined compressive strength of the intact material and the compaction strength of the comminuted material. In addition, it has been noted from the experiments of Shockey et al. (1990) that properties such as the dynamic compressive failure energy and the friction, flow and abrasive properties of the comminuted material govern the penetration resistance of thick confined ceramics.
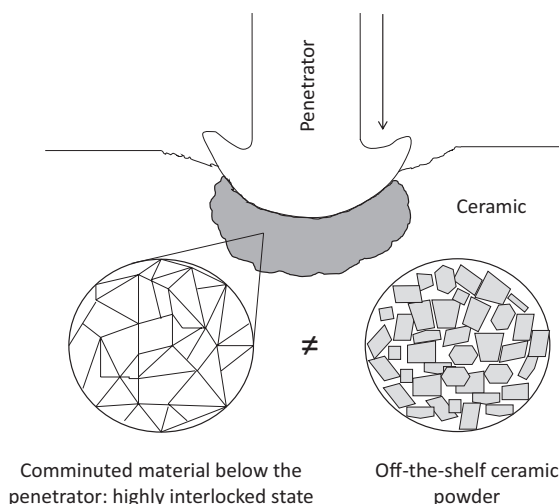
FIGURE 8.15   Penetration of a ceramic: comparison between the highly interlocked state and example of a material that one can buy off the shelf. They are not equivalent.

Indeed, it was observed during high-velocity rod penetration experiments into thick ceramic sections that the comminuted material produced at the leading edge of the rod flowed around and behind the rod, closing the hole made by the rod. Hardness and scratch tests indicated strengths of the compacted powder comparable to that of the unimpacted material.

So how can such behaviour be simulated? Well, a good start is to try and assess the shear strength of powder compacts at various pressures and use these as an analogue for the comminuted material. However, one must be cautious here as comminuted ceramic starts off as highly interlocked fragments, whereas purchasing ceramic powder off the shelf and compacting it will result in a material with lots of voids and broken edges (see Figure 8.15). This material is more representative of the material that flows away from the rod during penetration. Nevertheless, it is a good start.

There have been several studies examining the properties of damaged ceramic material under both dynamic and quasi-static loading conditions in an attempt to understand the behaviour of the comminuted material. Horsfall et al. (2010) have examined the impact behaviour of explosively shattered alumina and compressed ceramic powder using an instrumented drop-weight tower and ballistic experiments. They showed that the elastic stiffness of the highly fractured alumina tile was reduced to ~130 GPa by the explosive loading process as compared to the intact tile's modulus of 330 GPa. Further, they noted that the ballistic efficiency of the fractured material was approximately 70% of the monolithic tile.

Other works that have sought to elucidate a constitutive relationship for comminuted ceramic material have involved the use of triaxial tests on damaged materials and powder compacts. Good examples are presented by Wilkins et al. (1969), Meyer and Faber (1997), Zeuch et al. (2001) and Anderson, Jr. et al. (2012). Data for these types of studied are covered in Section 6.7.2.
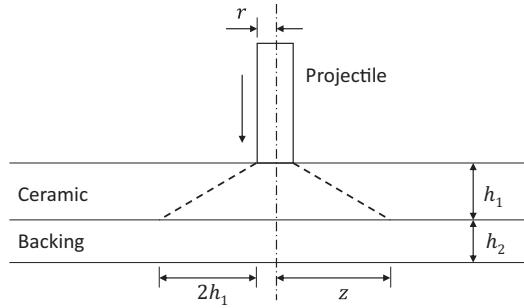
FIGURE 8.16 The 'Florence model' concept.

8.11 OPTIMIZING TWO-COMPONENT SYSTEMS

Florence (1969) derived an analytical model that provided a reasonable estimate for the ballistic limit velocity that could be achieved by using a two-component ceramic-faced armour. His approach was as follows (see Figure 8.16):

- The projectile is assumed to be a non-deforming rigid body and therefore does not lose mass during penetration.
- The backing layer is assumed to behave as an elastic membrane of uniform mass that is fixed at the periphery of the base of the cone that is formed in the ceramic.
- The base of the (Hertzian) cone that is formed on impact is roughly equal to half the calibre of the projectile plus two times the thickness of the ceramic tile. (This was based on experimental observations—although it should be pointed out that conoid dimensions are largely dependent on the relative properties of the impactor and the target. Nevertheless, Figure 8.8 suggests that this is not far off the mark.)
- The kinetic energy of the projectile is equated to the work done in stretching a membrane until it reaches the breaking point.

Using this approach, the following expression is derived that describes the ballistic limit velocity (v_{bl}) for the system:

$$v_{bl} = \left(\frac{S \cdot \varepsilon}{0.91 \cdot m_p \cdot f(z)} \right)^{\frac{1}{2}} \tag{8.11}$$

where $S = \sigma \times h_2$, σ is the breaking stress of the back plate, h_1 and h_2 are the thickness of the front and back plates, respectively, m_p is the projectile mass and ε is the breaking strain of the back plate. Furthermore,

$$f(z) = \frac{m_p}{\left(m_p + \left(h_1 \cdot \rho_1 + h_2 \cdot \rho_2 \right) \pi \cdot z^2 \right) \pi \cdot z^2} \tag{8.12}$$

where $z = r + 2h_1$ (and is the anticipated radius of the base of the Hertzian cone – see Figure 8.16), r is the radius of the projectile, which is cylindrical in shape, and ρ_1 and ρ_2 are the densities of the front plate and backplate, respectively.

This model has been used by Hetherington (1992a) to predict the optimum ratio of front tile to backing plate tile thickness for an alumina-faced aluminium-alloy composite-armour system. It was around 2.5. Further, validation was carried out using a non-deforming armour-piercing projectile (7.62×51-mm FFV) that was fired at a target comprising various thicknesses of Sintox™ FA (alumina) ceramic backed by a 5083 aluminium plate. For each validation shot, the areal density was kept the same (approximately 50 kg/m²). Good correlation was noted between the experimental and analytical results (see Figure 8.17).

Of course, it should be noted that the above model does not take into account the relative hardness values of the projectile and the target, and therefore, it cannot discriminate between ceramics and projectiles of different mechanical strengths. However, it can provide a very helpful approximation of the velocity required to perforate a two-component ceramic-faced armour.

Hetherington also considered the energy absorbed by the composite ceramic. For this calculation, it would be commonplace to calculate the residual velocity from an overmatched target using energy considerations. As we have seen previously in Chapter 4, the residual velocity from thin plates can be calculated according to the Recht–Ipson method (Recht and Ipson, 1963), viz

$$\frac{1}{2} m_p v_0^2 = \frac{1}{2} m_p v_r^2 + \frac{1}{2} m_p v_{bl}^2 \tag{8.13}$$
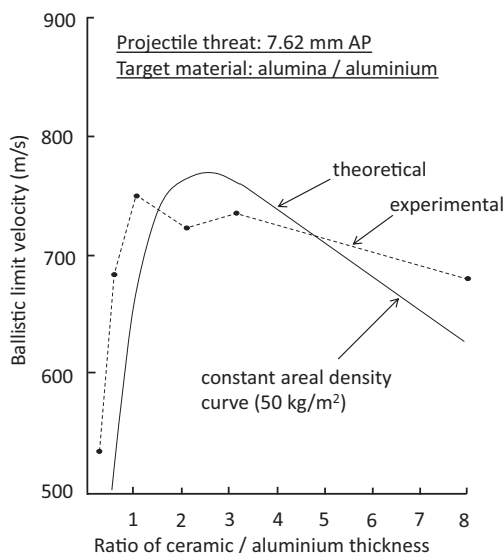
FIGURE 8.17 Dependence of v_{50} on ceramic/aluminium thickness for constant areal density—comparison of theoretical and experimental results. (Adapted from Hetherington, J. G., *International Journal of Impact Engineering*, 12(3), 409–414.)

and therefore,

$$v_r = \sqrt{v_0^2 - v_{bl}^2}$$ (8.14)

However, Hetherington argued that for a flexible system in which failure is determined by the tensile strain in the backing plate, it is the impulse delivered by the round, rather than its kinetic energy which is critical (Hetherington, 1992b). Therefore, the residual velocity should be calculated from a momentum balance:

$$m_p (v_o - v_r) = m_p v_{bl}$$ (8.15)

Thus,

$$v_r = v_0 - v_{bl}$$ (8.16)

So, which is the correct way for calculating the residual velocity of the projectile? Hetherington argued that for flexible targets the latter was more accurate. That is, the impulse to a flexible target during which it was perforated can be approximated to the impulse delivered to the target that just stops the projectile. Whereas for 'stiff' targets (such as RHA) the former should be true.

And the analysis appears to back that conclusion. Figure 8.18 shows the experimental energy absorbed by a two-layered composite armour (from (Hetherington and
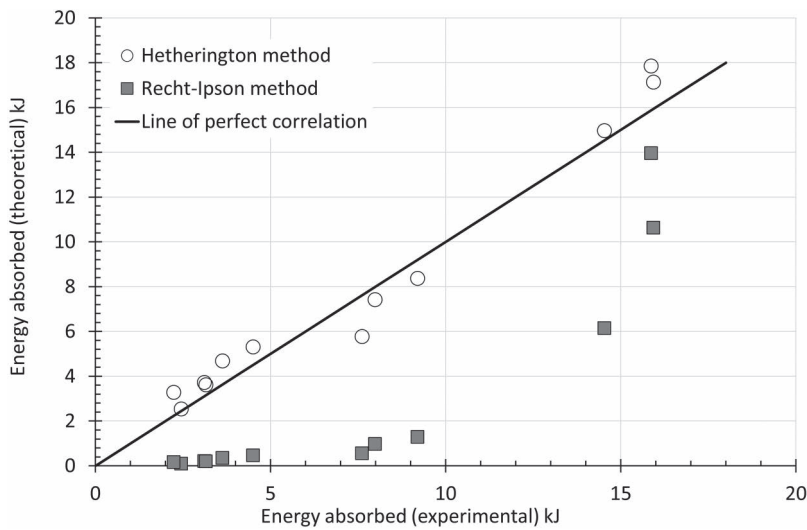
FIGURE 8.18 Comparison of two methods for establishing the theoretical energy absorbed by the target when perforated by a 12.7 mm Ball projectile. (This data has been plotted from data provided in Hetherington and Rajagopalan (1991) and based on the analyses in Hetherington (1996b) and Hetherington (1992b). This Figure is based on Figure 2 in Hetherington (1996).)

Rajagopalan, 1991)) with the theoretical prediction either using the residual velocity calculated from the Recht–Ipson method (Equation 8.14), or the 'Hetherington method' (Equation 8.16). The 'Hetherington method' appears to provide a superior correlation.

Example 8.1

You are required to develop a ceramic-faced armour with an areal density of 45 kg/m² to provide some help in stopping a 12.7-mm Ball projectile ($m_p = 46.8$ g). This is to be part of a much larger armour system. Using the Florence model, calculate the optimum ratio of ceramic to backing thicknesses for a ceramic-faced armour that has a density of 3200 kg/m³ and a composite backing layer that has a density of 2230 kg/m³. Assume the backing plate has a breaking strain of 4% and a breaking stress of 1 GPa.

First, we must establish the ratios of the material thickness, which are bounded by the areal density (A_d). Recalling that:

$$A_d = \rho h \qquad (8.17)$$

And therefore, for our problem,

$$A_d = \rho_1 h_1 + \rho_2 h_2 \qquad (8.18)$$

Rearranging

$$h_1 = \frac{A_d - \rho_2 h_2}{\rho_1} \qquad (8.19)$$

TABLE 8.4
Calculated Thickness Values for Optimized Ceramic-Faced Armour Using the Florence Model

h_1 (mm)	h_2 (mm)	h_1/h_2
13.4	1.0	13.4
12.7	2.0	6.3
12.0	3.0	4.0
11.3	4.0	2.8
10.6	5.0	2.1
9.9	6.0	1.6
9.2	7.0	1.3
8.5	8.0	1.1
7.8	9.0	0.9
7.1	10.0	0.7
6.4	11.0	0.6
5.7	12.0	0.5

We can tabulate h_1 in terms of h_2 by incrementally increasing h_2 and maintaining the areal density of 45 kg/m². These data are shown in Table 8.4.

The simplest way to complete this problem is by using a spreadsheet analysis as an individual calculation for each h_1/h_2 ratio would be time-consuming. Nevertheless, a manual calculation for $h_1 = 9.9$ mm ($h_2 = 6.0$ mm) is provided below.

The first step is to calculate the various functions:

$$S = \sigma \times h_2 = 1.0 \times 10^9 \times 6.0 \times 10^{-3} = 6.0 \times 10^6 \ \text{N}/\text{m}$$

$$z = r + 2h_1 = 6.35 \times 10^{-3} + 2 \times 9.9 \times 10^{-3} = 26.15 \times 10^{-3} \text{m}$$

$$f(z) = \frac{46.8 \times 10^{-3}}{\left(46.8 \times 10^{-3} + \left(9.9 \times 10^{-3} \times 3200 + 6.0 \times 10^{-3} \times 2230\right) \times \pi \left(26.15 \times 10^{-3}\right)^2\right) \times \pi \left(26.15 \times 10^{-3}\right)^2}$$

$$= 152.6$$

$$v_{bl} = \left(\frac{S \cdot \varepsilon}{0.91 \cdot m \cdot f(z)}\right)^{\frac{1}{2}} = \left(\frac{6.0 \times 10^6 \times 0.04}{0.91 \times 46.8 \times 10^{-3} \times 152.6}\right) = 192.2 \ \text{m/s}$$

This step can be repeated to develop a range of values for varying h_1/h_2 ratios. Ultimately, this will result in Figure 8.19.

From Figure 8.19 it is therefore a trivial task to read off the maximum ballistic limit velocity and for this example. This happens to be at the point of the worked calculation (i.e. 192.2 m/s) and therefore the model predicts that the optimum ratio of ceramic to composite backplate thickness = 1.6 for a 12.7 mm projectile impact.
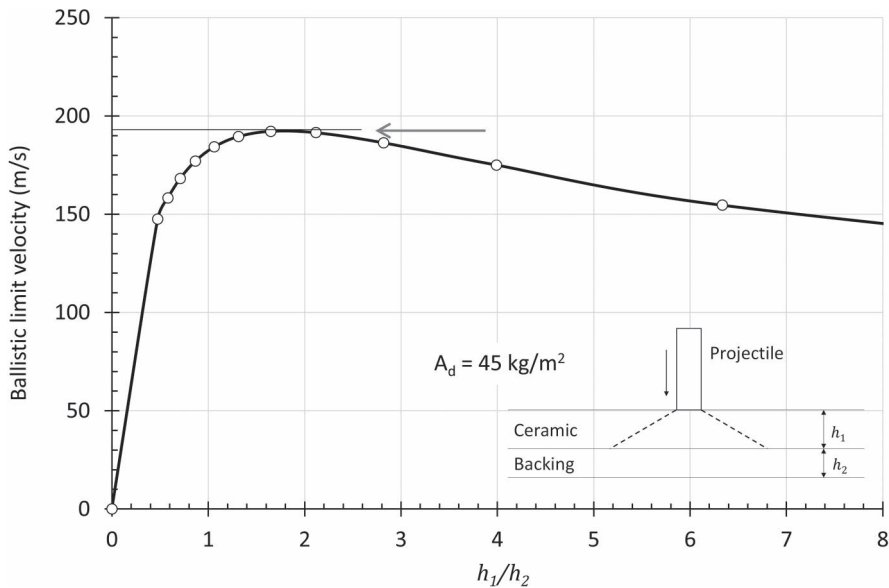
FIGURE 8.19 Dependence of v_{bl} on ceramic/composite thickness for constant areal density.

8.12   MULTILAYERED CERAMIC/STEEL SYSTEMS

Multilayered systems are extensively used in armoured fighting vehicles and the employment of glass (or, in some cases, ceramic) interlayers, sandwiched inbetween steel plates have been shown to be beneficial at disturbing shaped-charge jets. An example of how these can be used is shown in Figure 8.20. The composite armour comprises three metallic (usually steel) layers that sandwich two glass layers. As the jet penetrates from the first steel and into the glass layer, a shock emerges at the interface between the two materials. This is principally, due to the high velocity of the jet, the density of the penetrating material (= copper, $\rho_0 = 8930\,kg/m^3$) and the relatively low density of the glass layer ($\rho_0 = 2500\,kg/m^3$) resulting in a supersonic penetration regime (see Chapter 4). The jet continues to penetrate the composite target, however below the axis of penetration, the shock reflects off the subsequent steel layer, due to the steel's relatively high impedance when compared with glass. The reflected compression wave causes a rearward movement of the first steel layer, thereby driving some parts of the metal into the path of the jet. Simultaneously, already fractured glass material is also pushed towards the jet resulting in the narrowing of the crater. Above the axis of penetration, a shock wave also propagates,
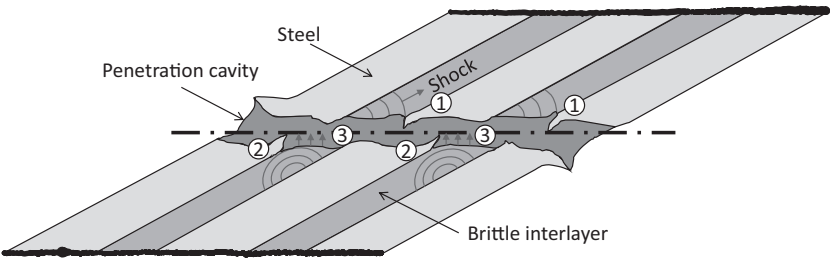
FIGURE 8.20   Penetration of a multilayered system by a high-velocity penetrator showing: 1. Forward moving elements of the target, 2. Rearward moving elements of the target and, 3. Fractured interlayered material being pushed into the penetration cavity. (Adapted from Held, 2002.)

TABLE 8.5
Relative Cost of Ceramic Materials for Armour Applications

Ceramic	Bulk Density (kg/m³)	Hardness (HV)	K_{IC} (MPa m$^{1/2}$)	Relative Cost
98% Al_2O_3	3800	1600	4.5	1.0
RB SiC	3100	1200/2200	~4.5	2.5
Sintered SiC	3150	2700	3.2	4.5
HP SiC	3220	2200	5.0	9.0
HP B_4C	2520	3200	2.8	16.0

Source: Roberson, C. 2004 Ceramic materials for lightweight armour applications. *In: Proceedings of the Combat Vehicle Survivability Symposium, RMCS, Shrivenham, UK, 8–10 December.*

pushing elements of the already-perforated second steel layer into the path of the jet. The process is repeated for subsequent layers. The resistance to penetration is also aided by the spring-back nature of the glass interlayer as previously discussed in Section 8.7.1.

8.13 CURRENT APPLICATION AND CHALLENGES

8.13.1 CERAMIC MATERIAL CHOICES

In many cases, the choice of the ceramic material that is purchased is determined by cost as well as performance. It is very difficult to put an absolute price on ceramic materials because it will vary depending on the quantity and the size and shape of the tiles that are required. However, if a 98% liquid phase-sintered alumina is taken as a baseline material, then Table 8.5 gives some indication of the relative costs of these materials for armour applications.

Alumina (Al_2O_3) has been the benchmark ceramic for a number of years and in its sintered state is a relatively cheap ceramic to manufacture compared to its non-oxide hot-pressed rivals. However, it possesses a relatively low hardness and high density compared with silicon carbides and boron carbides. High-purity alumina (~99.5%) is the hardest and provides the most weight-efficient protection against hard-cored AP rounds.

Silicon carbide (SiC) is becoming more common in the design of armour systems because of its superior mechanical properties to those of alumina. Silicon carbide powders are commercially produced by the reaction of a mixture of SiO_2 (sand) and coke. The resulting compound possesses a very strong covalent bond that makes sintering difficult, and therefore, special processes have to be applied to manufacture

TABLE 8.6
Advantages and Disadvantages of Ceramic-Based Systems Compared to Metallic Systems when Applied to an Armoured Vehicle

No.	Advantage over a Metal Armour	Disadvantage over a Metal Armour
1	Good level of ballistic resistance for a given thickness	Not good at multi-hit impacts.
2	Lightweight solution for a given threat	Parasitic and therefore cannot be used as part of the vehicle's integral load-bearing structures.
3	Hard material	Low fracture toughness and therefore susceptible to damage in transit or use.
4	Relatively cheap logistic load to transport in large quantities (for a given volume)	Relatively expensive to manufacture high-performing materials.
5	–	Compared with armour-grade metals, high-performing armour ceramics are not readily available due to complex manufacturing processes.

high-density silicon carbide. Silicon carbide for armour applications can be made via three routes: pressureless sintering, hot pressing and reaction bonding. Pressureless sintering is a common yet relatively difficult process to undertake as it requires firing temperatures in excess of 2000°C. Hot pressing provides a very high-performing ceramic for armour applications, but the cost is high (as discussed previously). Conversely, reaction bonding is a relatively cheap method of manufacture, but the ballistics performance of these ceramics is relatively poor.

Boron carbide (B_4C) was one of the original ceramic materials that were used in armour applications. It is similar to silicon carbide in that the most useful form of this material is produced via the hot-pressing route, although some boron carbide samples have been made for armour applications by reaction bonding. It has been shown that despite its promise of very high hardness and relatively low density compared to other ceramics ($2500\,kg/m^3$), boron carbide does not perform well when subjected to very high shock stresses due to rapid brittle failure and hence strength degradation. In fact, at sufficient shock stress levels, its performance is not much better than a sintered alumina.

Titanium diboride (TiB_2) is a relatively dense ceramic ($4500\,kg/m^3$) that is normally hot-pressed mainly because it is difficult to sinter. TiB_2 is a very high-performing ceramic but is relatively expensive—some three to four times that of hot-pressed silicon carbide. This material is electrically conductive, which has the benefit of being able to be machined using electro-discharge methods, which is very handy because it is notoriously difficult to grind in its hot-pressed form.

Tungsten carbide (WC) has also shown some promise as an armour material because of its relatively high hardness (Gooch et al., 2000). However, in many cases, it is an unusual choice of ceramic for armour applications mainly because of its relatively high density. Nevertheless, against tungsten-alloy rods in a semi-infinite DOP-type target arrangement, it has demonstrated a performance that is better than RHA on a weight-by-weight basis and thickness. Most tungsten carbides that are produced today are in fact cermets—that is, an alloy of a ceramic and metal binder such as cobalt or nickel. These cermets are frequently used in ammunition design and are frequently manufactured by LPS. However, for the fully dense WC ceramic ($15,700\,kg/m^3$), Cercom Inc. has developed a hot-pressing route that produces a 99.6% pure ceramic. This material is electrically conductive (like TiB_2) and can therefore be machined using electro-discharge methods.

Aluminium nitride (AlN) is an interesting material that is becoming widely used in the electronics and semiconductor processing industries. This material can be made using the pressureless sintering route; however, the best quality materials are hot pressed. It is believed that this material undergoes a brittle-to-ductile transition at elevated strain rates.

Silicon nitride (Si_3N_4), like silicon carbide, can be formed through the reaction bonding process where shaped silicon powder is fired in a nitrogen-rich environment. However, the porosity of the product manufactured in this way is relatively high and therefore renders the material inappropriate for ballistic applications. Nevertheless, silicon nitride can be sintered or hot pressed and has found some niche applications in defeating small arms. However, against hard-cored AP projectiles, its performance is similar to a high-quality alumina.

8.13.2 CERAMIC ARMOUR APPLICATIONS

It should be no surprise to the reader that ceramic-based armours have been extensively used in protective structures such as helicopter seats, helicopter floor plates, engineering vehicles, armoured fighting vehicles, body armour and so on.

The first battle use of ceramic armour technology was in US helicopters during the Vietnam conflict where low-level sorties made the helicopter and crew vulnerable to small-arms fire. Therefore, in 1965, the first ceramic-based aircrew body armour vest was manufactured as this was the most weight-efficient means of providing protection (Rolston et al., 1968). Also, in 1965, the UH-I 'Huey' was fitted with a 'hard-faced composite' armour kit used in the armoured seats for the pilot and co-pilot. The seats provided protection against 7.62-mm AP ammunition on the seat bottom, sides and back using a boron–carbide-faced fibreglass. Similar systems were installed on AH-1 Cobra helicopter gunships. In 1966, the first monolithic ceramic body armour vest was issued to the helicopter crews along with other protection improvements including the use of airframe-mounted armour panels. It has been estimated that, between 1968 and 1970, these improvements in aircrew armour reduced the number of non-fatal wounds by 27% and fatalities by 53% (Dunstan and Volstad, 1984).

In the 1980s, the majority of the ceramic-based armour systems that were used in battlefield applications used alumina. Alumina is relatively inexpensive to manufacture, and even quite thin sections can stop high-velocity small-arms bullets. Whereas, when silicon carbide and boron carbide systems were used, the added ballistic performance (against small-arms projectiles) was small for a considerable additional cost. Although the curve has changed somewhat since the 1980s, the lesson is still the same. There is a high-cost trade-off for a relatively small improvement in ballistic performance. Nevertheless, the advantage of added ballistic protection (albeit small) can be attractive if minimal weight is required—such as in aircraft or body armour systems.

Boron carbide is a high-performing material. Nevertheless, apart from the incredible hardness that this material possesses and its low density, it does have one potential drawback. In recent years, there has been some evidence to suggest that this hard and strong material has been shown to not perform as well as expected when penetrated by high-velocity dense-cored bullets. This is thought to be due to physical changes that occur to the material when subjected to a high shock stress that is induced by these rounds (Chen et al., 2003). In fact, when tested with a semi-infinite aluminium backing material, there is some evidence to suggest that against specific tungsten–carbide-based projectiles, certain grades of boron carbide perform just as well as alumina targets (Roberson et al., 2005). This is despite boron carbide's superior hardness. It has also been found that when boron carbide is bonded to a high-performance fibre-reinforced laminate, a 'shatter gap' phenomenon occurs (Moynihan et al., 2002), that is, where two v_{50} velocities are found (see Chapter 12). The discovery of two v_{50} velocities has traditionally been attributed to a transition from intact projectile perforation of the target to the shattered projectile defeat of the target at higher velocities. However, Moynihan et al. have shown that the upper v_{50} velocity of a boron carbide–faced composite occurs with a change in fragmentation behaviour of the ceramic. Nevertheless, the upshot from these results means
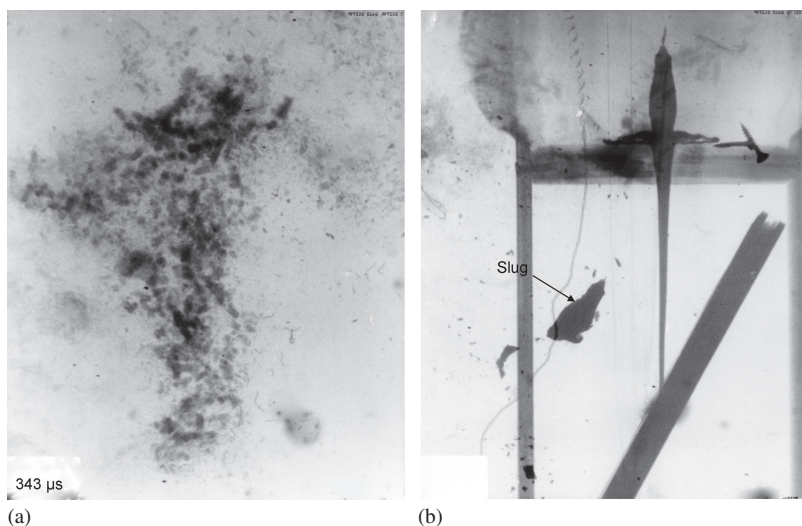
FIGURE 8.21 Flash X-ray of a ceramic plate showing two exposures: (a) the cloud of ceramic debris 343 μs later (with the slug from the disturbed jet) and (b) contact between the shaped-charge jet and the ERA at $t = 0$ μs. (After Hazell, P. J. et al. 2012, *International Journal of Applied Ceramic Technology*, 9(2), 382–392.)

that the thickness of the boron carbide plate is required to be higher than originally anticipated to defend against these dense high-velocity projectile cores. Against steel armour-piercing projectiles, there is plenty of evidence to show that boron carbide is a very good ceramic to use.

Among the new possibilities for ceramic materials is their application in the use of explosive-reactive armour packages. Against shaped charge jets, ceramic materials perform well, and recent results suggest that they could also be used as part of an explosive reactive armour configuration (Koch and Bianchi, 2010; Hazell et al., 2012). The advantage of using ceramic materials as opposed to steel as the flyer plates is that the ceramic very rapidly breaks down into small fragments, thereby minimizing any collateral damage (see Figure 8.21). This is particularly useful for lightweight armoured vehicles that may be operating in urban areas. And ceramics perform just as well as steels (and potentially better) (Hazell et al., 2012). Notably, glass also performs well. In fact, glass (such as traditional float glass or borosilicate glass) will have a tendency to become powdery very quickly thereby rendering the risk to personnel, other vehicles and military platforms somewhat obsolete (see Figure 8.22).

8.13.3 COMPARING WITH OTHER MATERIALS

Ceramic armour systems clearly have some advantages over other materials or structures that would be used for protection; however, there are some disadvantages too. Table 8.6 provides a comparison with metal systems when applied to an armoured fighting vehicle.
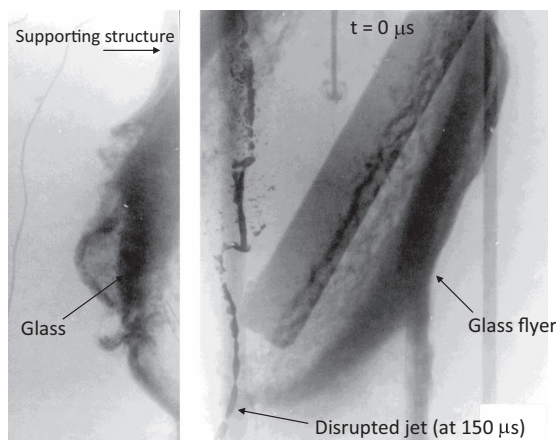
FIGURE 8.22 Flash X-ray of a glass ERA system showing the shaped-charge jet prior to contact ($t = 0$ μs) and the glass flyer plates and disrupted jet 150 μs later: (After Hazell, P. J. et al. 2012, *International Journal of Applied Ceramic Technology*, 9(2), 382–392.)

8.13.4 IMPROVING PERFORMANCE

Improving performance can be done through two routes: either through engineering solutions, where the structure of the ceramic is designed as part of a wider system, or through material science, where understanding how the projectile interacts with the ceramic material informs the design of novel ceramic microstructures. In recent years, a large amount of effort has been put into engineering solutions for the battlefield, including adding confinement with or without pre-stress, carefully controlling the geometry of the tile or by segmenting the ceramic inserts with polymer interlayers. Even small modifications (such as using hexagonal tiles to maximize the distance from interfaces for a given area) can often help.

Notably, confinement plays a large role in restricting the movement of the comminuted materials and enhancing the erosion of the penetrator. This was achieved in the 1970s by Aeronautical Research Associates of Princeton and ABEX/Norton Ceramics (Gooch, Jr. 2011) by using precision metal castings to house ceramic tiles. A further enhancement of this approach is to hot isostatically press (HIP) metal structures onto ceramic tiles; this has shown an improvement in enhancing dwell characteristics and a doubling of ceramic tile ballistic efficiencies. Further enhancements are thought possible if the ceramic is subjected to a compressive pre-stress (Hazell et al., 2021) and minimizing the effect of the lateral interfaces as was discussed in Section 8.6. This can be achieved by heat shrinking collars onto ceramic tiles that are usually hexagonal or circular in nature. Equally, it has been shown that fielding a 'pelletized' ceramic armour increases the multi-hit capability of the system. Such armours include Light Improved Ballistic Armour (LIBA™) manufactured by Mofet Etzion Ltd., Israel, and Super Multi-Hit Armor Technology (SMART™) manufactured by Plasan Sasa, Israel. These offer advantages in that the damage is limited to one 'cell' of the armour, and thereby, the scale of the damage is limited.

All of these modifications, however, are achieved through engineering the structure. An early example of this was presented by R. L. Cook in the 1970s (Cook et al., 1979).

The challenge is to seek paths through which the improvement of the performance of the ceramic armour can be achieved through material science. Some notable examples of this have been (or could be) the following: (1) engineering a ceramic's structure to fail preferentially during ballistic impact and penetration so that the comminuted material's resistance is enhanced (Nanda et al., 2011); (2) increasing the strength of the ceramic by reducing the grain size of the ceramic to sub-micron values, e.g. Strassburger et al. (1999); and (3) reinforcing ceramic structures with carbon nanotubes or through the design of functionally graded armour materials. This later example was originally suggested in the late 1960s by Wilkins et al. (1969). This can be achieved by using functionally graded materials (FGMs) that attempt to provide a single material construction that maximizes the benefits of ceramic (hardness and compressive strength) and metals (ductility and toughness). Such materials would normally consist of a ceramic or cermet front face with subsequent sintered layers with greater metallic content. One published example of this technique was presented by Gooch et al. (1998). Here, the titanium monoboride is densified as a cermet and consisted of seven layers each with higher contents of titanium as the sample is examined from the front (impact surface) to the rear. The rear surface consisted of pure titanium. Against the 14.5-mm B32 projectile, an FGM-faced aluminium-alloyed armour provided an $E_m{}^2$ value of 2.02 when compared to RHA. However, in this case, the authors report that this target system was not optimized for ballistic protection, and further improvements are thought possible. In this case, the multi-hit capability was not tested.

There has also been some recent interest in high-density ceramics such as tungsten carbide (Gooch et al., 2000). The advantage of these materials is that their high density and stiffness ($\rho_0 = 15,700\,\text{kg/m}^3$; $E = 696\,\text{GPa}$) impart a large stress into the shank of the projectile on impact. Further, the high density and high hardness lead to good space effectiveness factors, meaning that the armour can be relatively thin compared to other means of protection. This is important where space, rather than weight, can be a driving factor such as on heavily armoured fighting vehicles.

8.14   TRANSPARENT ARMOUR MATERIALS

Providing protection whilst maintaining transparency is a particular challenge as often the materials that are naturally transparent (i.e. glass) are particularly brittle. This means that projectile impacts or blast waves will form very small shards of glass materials, which in themselves can become lethal projectiles, that is, if the glass material is not contained.

8.14.1   BULLET-RESISTANT GLASS

To date, almost all bullet-resistant glass comprises float or tempered glass with rubbery interlayers (such as polyurethane or polyvinyl butyral) and a backing layer of polymer, usually polycarbonate. The backing layer is optimized to contain all

of the comminuted glass particles during penetration and prevent scabbing of the rear surface layer. A glass face is used as the disruptor, the hardness of which will be in the region of 400–500 HV. This will fragment or deform the penetrator and therefore redirect its kinetic energy. As with ceramic armour, only a very small amount of the kinetic energy of the penetrator is absorbed as the glass cracks and comminutes.

Commonly, soda–lime glass or slightly stronger and tougher borosilicate glass is used. Soda–lime glass contains a high percentage of soda ash to help with the manufacturing process; borosilicate glass contains a certain percentage of boron oxide, which provides better strength and thermal characteristics. The interlayers provide a flexible separation between layers of glass to account for thermal expansion and serve to contain any fractured glass. Depending on the threat level, different combinations of these layers form an array to prevent perforation by the projectile and provide a multi-hit capability.

However, silica-based glass plates tend to have relatively low hardness values when compared to the cores of armour-piercing ammunition. They also possess low toughness values ($K_{Ic} = 0.6–0.8$ MPa m$^{1/2}$). Therefore, to provide satisfactory multi-hit protection against heavy or hard threats usually requires quite thick and hence heavy constructions. For example, to stop a 7.62-mm AP bullet, the thickness of glass armour required would be in the region of 60–100 mm depending on the nature of the round and the construction of the laminate. As the thickness increases, transparency reduces, and eventually, the weight can become prohibitive for lighter-weight vehicles. Historically, to get around this problem, smaller vision blocks have been used in vehicles, but these can compromise the situational awareness of the occupants let alone the ability to drive the vehicle. If a system can be manufactured that uses a relatively hard disrupting face, then the thicknesses (and hence the areal densities) of these armours will reduce. This will allow vehicle designers to use larger areas of transparent armour.

8.14.2 CERAMIC OPTIONS

One possibility for enhancing glass-based transparent armour is by using transparent crystalline ceramic. There are currently three transparent crystalline ceramics of interest to the armour community: aluminium oxynitride or 'AlON', magnesium aluminate spinel or 'spinel' and a single crystal aluminium oxide (sapphire). The key to producing a transparent crystalline ceramic is first to use a material that is intrinsically transparent, that is, the electrons present within the atoms do not absorb the photon energy. Cubic crystal structures, unlike others, are advantageous as they have refractive index values that are independent of direction. Secondly, we can either do away with grain boundaries altogether (as we do with sapphire) or, with polycrystalline materials, minimize porosity and impurities that will refract, reflect, diffract or perturb the photons of light. It is also possible to make transparent ceramics if the grains are reduced to a size below the wavelength of visible light (0.40–0.72 μm) whilst eradicating porosity and impurities. However, this is currently very difficult to do without resorting to very expensive processing techniques.

Sapphire (Al_2O_3) is a single crystal and therefore has no grain boundaries to diffract light and, when grown and polished, can provide a very hard replacement for bullet-resistant glass systems. Sapphire possesses a hardness value within the range of 2500–3000 HV. The main problem with sapphire is that to achieve a sample of suitable size for armoured window applications that is sufficiently free from flaws is quite time-intensive and therefore expensive. Usually, achieving any significant size of window requires joining two or more tiles together with an appropriate bonding agent.

Aluminium oxynitride ($Al_{23}O_{27}N_5$) can be produced as a transparent polycrystalline ceramic via processing routes that are used for conventional opaque engineering ceramics. Usually, AlON will be manufactured from a pre-synthesized powder that can then be shaped (via pressing or slip casting) and then sintered in a nitrogen atmosphere.

Spinel ($MgAl_2O_4$) can be densified from commercially available powder either by hot pressing or by pressureless sintering. Usually, there is a requirement to HIP the samples to increase further the mechanical properties and improve transparency. Hot isostatically pressing is a process of simultaneously applying a uniform gas pressure with heat to the sample. Its main advantage over uniaxial hot pressing is that the pressure is applied equally in all directions rather than just in one direction. This results in greater material uniformity and microstructures without preferred orientations, resulting in higher strengths, Weibull modulus and transparency—the latter being very important for this type of ceramic. Both Spinel and AlON have cubic crystal structures and consequently benefit from isotropic optical properties.

All of these ceramics are still relatively immature technologies compared to opaque ceramic materials and currently are used in niche applications such as radomes. They are therefore currently very expensive materials—despite being very attractive materials to use as optical lenses. However, if the properties that they have to offer are considered, it can be seen why they may prove to be exciting alternatives to silica–glass materials in the future. Both spinel and AlON have hardness values in the range of 1200–1400 HV depending on the processing method used and have approximately 2.5 times the fracture toughness of float glass.

8.15 SUMMARY

Since the work of Cook, Wilkins and Florence, our understanding of the behaviour of ceramic materials under impact loading conditions has been enhanced by models coupled with laboratory testing techniques that probe the high strain-rate response. However, despite the numerous studies on the impact response of these materials, we still have a lot to learn, and there are still rich avenues of study to pursue, ranging from their quasi-static behaviour to the shock response of these materials where strain rates of $10^5-10^6 s^{-1}$ are common. Current themes of research include the following: attempts to understand the flow characteristics of the comminuted material, methods for enhancing interface defeat, strength behaviour under shock loading and particularly the processing techniques to enhance their performance. The key to all of this is to understand the mechanisms by which a projectile penetrates (or 'interacts') with the ceramic and thereby deduce the important properties that maximize performance.

This may appear a trivial task, but the time durations during which a penetrator is in contact with a ceramic are typically short, and this often makes analysis difficult. Furthermore, ceramic materials are required to cope with diverse threats from bullets to shaped charge jets where the mechanism of interaction is quite different. Consequently, the properties that are useful in defeating shaped charge jets (such as the fragmentation and subsequent flow characteristics of the material) differ from those that are best for defeating high-velocity bullets such as hardness and acoustic impedance, and particularly how the armour system is engineered. Even if one particular threat is considered, it has been known for some time that it is not one isolated material property that defines the behaviour of a ceramic during penetration, which is why it is important to study these materials using a range of different techniques.

NOTES

1 See Section 8.6.
2 This metric is based on a depth-of-penetration test that will be discussed in Chapter 12.

REFERENCES

Anderson Jr., C. E., Chocron, S., Dannemann, K. A. & Nicholls, A. E. 2012. Testing boron carbide under triaxial compression. *In: Shock Compression of Condensed Matter – 2011: Proceedings of the Conference of the American Physical Society Topical Group on Shock Compression of Condensed Matter*. Chicago. Mark L. Elert, William T. Buttler, John P. Borg, Jennifer L. Jordan and Tracy J. Vogler (eds). Publisher: Melville, NY: AIP

Anderson Jr., C. E., Holmquist, T. J., Orphal, D. L. & Behner, T. 2010. Dwell and interface defeat on borosilicate glass. *International Journal of Applied Ceramic Technology*, 7(6), 776–786.

Anderson Jr., C. E. & Walker, J. D. 2005. An analytical model for dwell and interface defeat. *International Journal of Impact Engineering*, 31(9), 1119–1132.

ASTM. 2013. *ASTM C1161 – Standard Test Method for Flexural Strength of Advanced Ceramics at Ambient Temperature*. West Conshohocken, PA: ASTM.

Bridgman, P. W. & Šimon, I. 1953. Effects of very high pressures on glass. *Journal of Applied Physics*, 24, 405–413.

Callister, W. D. 2007. *Materials Science and Engineering: An Introduction*, 7th ed. New York: John Wiley & Sons, Inc.

Chaudhri, M. M. & Walley, S. M. 1978. Damage to glass surfaces by the impact of small glass and steel spheres. *Philosophical Magazine A: Physics of Condensed Matter, Structure, Defects and Mechanical Properties*, 37(2), 153–165.

Chen, M., McCauley, J. W. & Hemker, K. J. 2003. Shock-induced localized amorphization in boron carbide. *Science*, 299(5612), 1563–1566.

Cline, C. F. & Wilkins, M. L. 1969. The importance of material properties in ceramic armor. *In: Proceedings of the Ceramic Armour Technology Symposium*. Columbus, OH.

Coble, R. L. & Kingery, W. D. 1956. Effect of porosity on physical properties of sintered alumina. *Journal of the American Ceramic Society*, 39(11), 377–385.

Cook, R. L. 1970. *Hard Faced Ceramic and Plastic Armor*. Delaware: Goodyear Aerospace Corporation.

Cook, R. L., Hampshire, W. J. & Kolarik, R. V. 1979. *Ballistic Armor System*. Delaware: Goodyear Aerospace Corporation.

Curran, D. R., Seaman, L., Cooper, T. & Shockey, D. A. 1993. Micromechanical model for comminution and granular flow of brittle material under high strain rate application to penetration of ceramic targets. *International Journal of Impact Engineering*, 13(1), 53–83.

Deshpande, V. S. & Evans, A. G. 2008. Inelastic deformation and energy dissipation in ceramics: A mechanism-based constitutive model. *Journal of the Mechanics and Physics of Solids*, 56, 3077–3100.

Dunstan, S. & Volstad, R. 1984. *Flak Jackets: 20th Century Military Body Armour*. London: Osprey Publishing Ltd.

Espinosa, H. D., Brar, N. S., Yuan, G., Xu, Y. & Arrieta, V. 2000. Enhanced ballistic performance of confined multi-layered ceramic targets against long rod penetrators through interface defeat. *International Journal of Solids and Structures*, 37(36), 4893–4913.

Florence, A. L. 1969. *Interaction of Projectiles and Composite Armor*. Menlo Park, CA: Stanford Research Institute.

Florence, A. L. & Ahrens, T. J. 1967. *Interaction of Projectiles and Composite Armor: Final Report*. Menlo Park, CA: Stanford Research Institute.

Franzen, R. R., Orphal, D. L. & Anderson Jr., C. E. 1997. The influence of experimental design on depth-of-penetration (DOP) test results and derived ballistic efficiencies. *International Journal of Impact Engineering*, 19(8), 727–737.

Gooch Jr., W. A. 2011. Overview of the development of ceramic armor technology: Past, present and the future. *Ceramic Engineering and Science Proceedings*, 32(5), 195–213.

Gooch, W. A., Burkins, M. S. & Palicka, R. 2000. Ballistic development of U.S. high density tungsten carbide ceramics. *Journal de Physique IV France*, 10, 741–746.

Gooch, W. A., Burkins, M. S., Palicka, R., Rubin, J. & Ravichandran, R. 1998. Development and ballistic testing of a functionally gradient ceramic/metal applique. *In: Proceedings of 17th International Symposium on Ballistics*. Midrand, South Africa. Van Niekerk, C. (ed) Moreleta Park, South Africa: South Africa Ballistics Organisation.

Hauver, G. E., Netherwood, P. H., Benck, R. F., Gooch, W. A., Perciballi, W. J. & Burkins, M. S. 1992. Variation of target resistance during long rod penetration into ceramics. *In: Proceedings of the 13th International Symposium on Ballistics*. Stockholm, Sweden. Persson, A., Andersson K., Bjorck E. B. (eds) Sundbyberg, Sweden: National Defence Research Establishment.

Hauver, G. E., Netherwood, P. H., Benck, R. F. & Melani, A. 1991. *Penetration of Shaped-Charge Jets into Glass and Crystalline Quartz*. Maryland: US Army Laboratory Command.

Hazell, P. J., Appleby-Thomas, G. J., Philbey, D. & Tolman, W. 2013. The effect of gilding jacket material on the penetration mechanics of a 7.62 mm armourpiercing projectile. *International Journal of Impact Engineering*, 54, 11–18.

Hazell, P. J., Donoghue, S. E., Roberson, C. J. & Gotts, P. L. 2005. The penetration of armour piercing projectiles through reaction bonded ceramics. *Ceramic Engineering and Science Proceedings, 26(7), 143–150.*

Hazell, P. J., Lawrence, T. & Stennett, C. 2012. The defeat of shaped charge jets by explosively driven ceramic and glass plates. *International Journal of Applied Ceramic Technology*, 9(2), 382–392.

Hazell, P. J., Wang, H., Lin, T., Saleh, M., Luzin, V., Kader, M. A., Saadatfar, M., Ameri, A. & Ellis, C. 2021. On the improvement of the ballistic performance of a silicon carbide tile through pre-stress: Experiments and simulations. *International Journal of Impact Engineering*, 151, 103836.

Held, M. 1998. Glass armour and shaped charge jets. *Propellants, Explosives, Pyrotechnics*, 23, 105–110.

Held, M. 2002. Lecture notes from the survivability of armoured vehicles course (18–20 March). *In:* Coombs, M. E. C. (ed.). *The Royal Military College of Science*. Shrivenham: Cranfield University.

Hertz, H. 1882. On the contact of elastic solids. *Journal für die Reine und Angewandte Mathematik*, 92, 156–171.

Hertz, H. 1896a. On the contact of elastic solids. *In:* Jones, D. E. & Schott, G. A. (eds.) *Miscellaneous Papers by Heinrich Hertz*, pp. 146–162. London: Macmillan.

Hertz, H. 1896b. On the contact of rigid elastic solids and on hardness. *In:* Jones, D. E. & Schott, G. A. (eds.) *Miscellaneous Papers by Heinrich Hertz*, pp. 163–183. London: Macmillan.

Hetherington, J. G. & Rajagopalan, B. P. 1991. An investigation into the energy absorbed during ballistic perforation of composite armours. *International Journal of Impact Engineering*, 11, 33–40.

Hetherington, J. G. 1992a. The optimization of two component composite armours. *International Journal of Impact Engineering*, 12(3), 409–414.

Hetherington, J. G. 1992b. Reply. *International Journal of Impact Engineering*, 12, 325–327.

Hetherington, J. G. 1996. Energy and momentum changes during ballistic perforation. *International Journal of Impact Engineering*, 18, 319–337.

Holmquist, T. J., Anderson Jr., C. E. & Behner, T. 2005. Design, analysis, and testing of an unconfined ceramic target to induce dwell. *In: Proceedings of the 22nd International Symposium on Ballistics*, vol. 2, pp. 860–868 Flis, W. & Scott, B. (eds) Lancaster, PA: DEStech Publications, Inc.

Holmquist, T. J., Anderson Jr., C. E., Behner, T. & Orphal, D. L. 2010. Mechanics of dwell and post-dwell penetration. *Advances in Applied Ceramics*, 109(8), 467–479.

Holmquist, T. J. & Johnson, G. R. 2002. A detailed computational analysis of interface defeat, dwell and penetration for a variety of ceramic targets. *In: Proceedings of the 20th International Symposium on Ballistics*. Orlando, FL Carleone, J. & Orphal, D. (eds) Lancaster, PA: DEStech Publications.

Hornemann, U. & Holzwarth, A. 1997. Shaped charge penetration in alumina targets. *International Journal of Impact Engineering*, 20, 375–386.

Horsfall, I. & Buckley, D. 1996. The effect of through-thickness cracks on the ballistic performance of ceramic armour systems. *International Journal of Impact Engineering*, 18(3), 309–318.

Horsfall, I., Edwards, M. R. & Hallas, M. J. 2010. Ballistic and physical properties of highly fractured alumina. *Advances in Applied Ceramics*, 109(8), 498–503.

Johnston, R. D., Chipman, R. D. & Knapp, W. J. 1953. Prestressed ceramics as a structural material. *Journal of the American Ceramic Society*, 36, 121–126.

Koch, A. & Bianchi, S. 2010. Protection efficiencies of steel and ceramic confinement plates for explosive reactive armours against shaped charges. *In: Proceedings of the 25th International Symposium on Ballistics*. Beijing, China. Zhong-yuan, W., Xiaobing, Z., Yude, A., (eds) Beijing, China: China Science and Technology Press

Kozhushko, A. A., Rykova, I. I. & Sinani, A. B. 1991. Resistance of ceramics to penetration at impact velocities above 5 km/s. *Journal de Physique IV France*, 1(C3), C3-117–C3-122.

Louro, L. H. L. & Meyers, M. A. 1989. Effect of stress state and microstructural parameters on impact damage of alumina-based ceramics. *Journal of Materials Science*, 24(7):2516–2532.

Lundberg, P., Holmberg, L. & Janzon, B. 1998. An experimental study of long rod penetration into boron carbide. *In: Proceedings of the 17th International Symposium on Ballistics*. Midrand, South Africa Van Niekerk, C., (ed) Moreleta Park, South Africa: South Africa Ballistics Organisation.

Lundberg, P. & Lundberg, B. 2005. Transition between interface defeat and penetration for tungsten projectiles and four silicon carbide materials. *International Journal of Impact Engineering*, 31(7), 781–792.

Lundberg, P., Renström, R. & Andersson, O. 2016. Influence of confining prestress on the transition from interface defeat to penetration in ceramic targets. *Defence Technology*, 12, 263–271.

Lundberg, P., Renström, R. & Holmberg, L. 2001. An experimental investigation of interface defeat at extended interaction times. *In: Proceedings of the 19th International Symposium on Ballistics*. Interlaken, Switzerland Crewther, I. R. & Marti, F. (eds) Thun, Switzerland: Vetter Druck AG.

Lundberg, P., Renström, R. & Lundberg, B. 2000. Impact of metallic projectiles on ceramic targets: Transition between interface defeat and penetration. *International Journal of Impact Engineering*, 24(3), 259–275.

Malaise, F., Tranchet, J. & Collombet, F. 2000. Effects of a dynamic confinement on the penetration resistance of ceramics against long rods. *AIP Conference Proceedings 505,* 1121–1124.

Meyer, L. W. & Faber, I. 1997. Investigations on granular ceramics and ceramic powder. *Le Journal de Physique IV*, 7(3):C3-565–C3-570.

Meyers, M. A. & Chawla, K. K. 1999. *Mechanical Behavior of Materials*. Upper Saddle River, NJ: Prentice Hall.

Moynihan, T. J., LaSalvia, J. C. & Burkins, M. S. 2002. Analysis of shatter gap phenomenon in a boron carbide/composite laminate armor system. *In: Proceeding of the 20th International Symposium on Ballistics*. Orlando, FL. Carleone J. & Orphal D. (eds) Lancaster, PA: DEStech Publications.

Nanda, H., Appleby-Thomas, G. J., Wood, D. C. & Hazell, P. J. 2011. Ballistic behaviour of explosively shattered alumina and silicon carbide targets. *Advances in Applied Ceramics*, 110(5), 287–292.

Recht, R. F. & Ipson, T. W. 1963. Ballistic perforation dynamics. *Journal of Applied Mechanics*, 30, 384–390.

Roberson, C. 2004. Ceramic materials for lightweight armour applications. *In: Proceedings of the Combat Vehicle Survivability Symposium*. Shrivenham, UK: RMCS.

Roberson, C. J., Hazell, P. J., Gotts, P. L., Pickup, I. M. & Morrell, R. 2005. The effective hardness of hot pressed boron carbide with increasing shock stress. *Ceramic Engineering and Science Proceedings* 26(7), 151–159.

Rolston, R. F., Bodine, E. & Dunleavy, J. 1968. Breakthrough in armor. Space/Aeronautics, July, 55–63.

Rosenberg, Z. & Yeshurun, Y. 1985. Determination of the dynamic response of AD-85 alumina with in-material Manganin gauges. *Journal of Applied Physics*, 58(8), 3077–3080.

Rozenberg, Z. & Yeshurun, Y. 1988. The relation between ballistic efficiency and compressive strength of ceramic tiles. *International Journal of Impact Engineering*, 7(3), 357–362.

Sherman, D. & Ben-Shushan, T. 1998. Quasi-static impact damage in confined ceramic tiles. *International Journal of Impact Engineering*, 21, 245–265.

Shockey, D. A., Marchand, A. H., Skaggs, S. R., Cort, G. E., Burkett, M. W. & Parker, R. 1990. Failure phenomenology of confined ceramic targets and impacting rods. *International Journal of Impact Engineering*, 9(3), 263–275.

Straßburger, E. 2009. Ballistic testing of transparent armour ceramics. *Journal of the European Ceramic Society*, 29(2), 267–273.

Strassburger, E., Senf, H., Rothenhausler, H., Lexow, B. & Krell, A. 1999. Influence of grain size and microstructure on the ballistic resistance of alumina. *In: Proceedings of the 18th International Symposium on Ballistics*. San Antonio, TX Reinecke, W. G. (ed) Lancaster, PA: Technomic Publishing Co.

Weibull, W. 1951. A statistical distribution function of wide applicability. *Journal of Applied Mechanics* 18:293–297.

Wilkins, M. L. 1967. *Second Progress Report of Light Armor Program*. Livermore, CA: Lawrence Radiation Laboratory.

Wilkins, M. L. 1968. *Third Progress Report of Light Armor Program*. Livermore, CA: Lawrence Radiation Laboratory.

Wilkins, M. L., Cline, C. F. & Honodel, C. A. 1969. *Fourth Progress Report on Light Armor Program*. Livermore: Lawrence Radiation Laboratory, University of California.

Wilkins, M. L., Honodel, C. A. & Swale, D. 1967. *An Approach to the Study of Light Armor*. Livermore: Lawrence Radiation Laboratory.

Zeuch, D. H., Grazier, J. M., Argüello, J. G. & Ewsuk, K. G. 2001. Mechanical properties and shear failure surfaces for two alumina powders in triaxial compression. *Journal of Materials Science*, 36(12), 2911–2924.

Zhang, R., Han, B. & Lu, T. J. 2020. Confinement effects on compressive and ballistic performance of ceramics: A review. *International Materials Reviews*, 66(5), 287–312.

9 Woven Fabrics and Composite Laminates for Armour Applications

9.1 INTRODUCTION

In this chapter, we review the composite materials and woven fabrics that are commonly used in the manufacture of armour systems and examine why they are used. In particular, we will focus on the structure of composite materials and why the structure and fibre choice leads to a good level of protection.

9.2 BASICS

A composite is a material that is made up of two or more discrete materials that are combined together in such a way to achieve desirable properties. There are several types of composite materials including natural and engineered composites. Commonly, the composite will consist of a matrix material and some kind of reinforcement. Composite materials are now used in an increasing number of applications ranging from sporting gear to telegraph poles. Rigid composite materials have also found their way into protective structures such as in armoured vehicles.

Woven fabrics, on the other hand, do not necessarily employ matrix materials but rather make use of the high tensile strength of the fibres (~2–3 GPa) and their low densities (~1000–1500 kg/m³). Fibres that are used in ballistic applications generally have reasonable strains to failure (~3%–6%), and that means that they have excellent energy-absorbing abilities (denoted by the area under the stress–strain curve). Of course, composite laminates can also be woven with high-strength fibres before being embedded in the matrix. A summary of some of the mechanical properties of fibres that are used in military applications is presented by Edwards (2002) and is summarized in Table 9.1.

It can be seen from Table 9.1 that the specific strength and stiffness of these fibres are high (specific strength and stiffness are calculated by dividing the relevant term by the density). All of these fibres (apart from carbon) can be used in blast or ballistic protection applications. Carbon fibres are too brittle for these types of applications, and as a result, they have poor translaminar strengths. However, if there is a requirement to inhibit bending in a structural component that is subjected to blast (for example), then carbon-based composites can be an excellent solution for this by positioning the CFRP behind the face plate. Graphene may be a useful protection material too, and although there have been examples of woven structures of graphene, these are still at a very small scale, and it is unclear as to whether it will perform with

TABLE 9.1

Mechanical Properties of Some Fibres That Are Found in the Military Environment

Fibre	Density (kg/m³)	Tensile Strength (MPa)	Specific Strength (m²/s²)	Elastic Modulus (GPa)	Specific Stiffness (m²/s²)	Failure Strain (%)
Aramid (low modulus)	1440	2900	2.01×10^6	60	4.17×10^7	3.6
Aramid (high modulus)	1450	2900	2.00×10^6	120	8.28×10^7	1.9
Polyethylene (low modulus)	970	2700	2.78×10^6	89	9.18×10^7	3.5
Polyethylene (high modulus)	970	3200	3.30×10^6	99	1.02×10^8	3.7
E-glass	2600	3500	1.35×10^6	72	2.77×10^7	4.8
S-glass	2500	4600	1.84×10^6	86	3.44×10^7	5.2
Carbon (high strength)	1780	3400	1.91×10^6	240	1.35×10^8	1.4
Carbon (high modulus)	1850	2300	1.24×10^6	390	2.11×10^8	0.5

Source: Edwards, M. R. 2002. *Proceedings of the Institution of Mechanical Engineers, Part G: Journal of Aerospace Engineering*, 216 (2), 77–88.

exceptional ballistic performance when technology allows for macro-sized experiments. Certainly, against miniaturized bullets at the nanoscale, this material appears to offer good ballistic performance compared to steel (on a weight basis; see Lee et al., 2014).

9.2.1 Terminology and Notation

Before we proceed, here are several definitions that you might find useful along the way:

Lamina (or ply)—a layer of unidirectional (UD) fibres or woven fabric in a matrix

Laminate—two or more laminae stacked together at various orientations with a material present that acts as a bonding agent (the matrix material)

Matrix material—usually consists of a polymer-based 'in-fill' for the fibres

Reinforcement—usually referring to the fibres

Laminates are manufactured by stacking individual layers of plies with the fibres positioned along varying directions. Consequently, a code has been developed that describes these directions. Essentially, each lamina is defined by the angle between the fibre direction and an axis (in this case, across the paper). Furthermore, individual adjacent laminae are separated by a slash if their angles are different. Where laminates are symmetrical about a mid-plane, only half the stacking sequence is recorded with the symmetry denoted by the subscript 's'. Where there are an odd number of laminae, the overscore
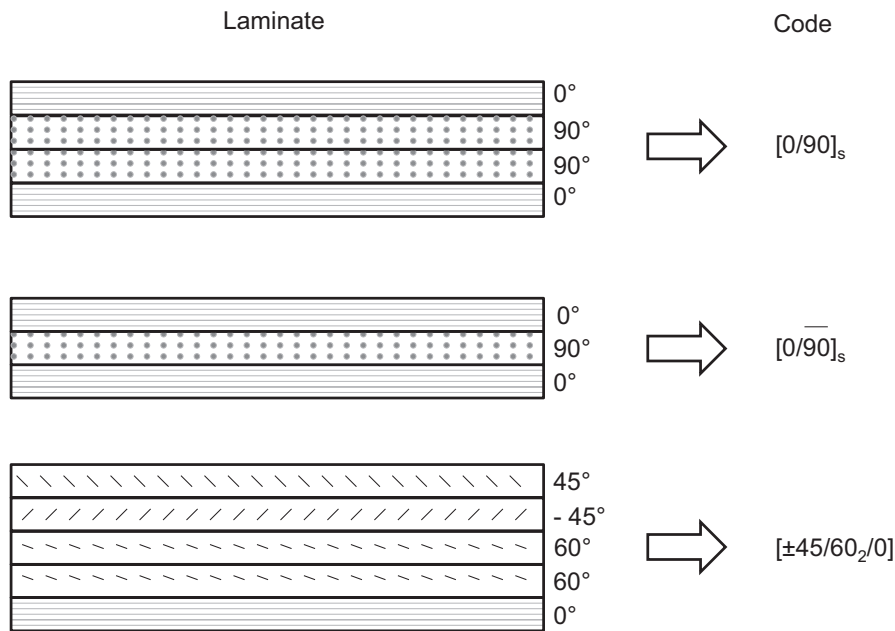
Laminate   Code

FIGURE 9.1   Examples of laminate orientation codes.

indicates that half of that laminate lies on either side of the plane of symme-
try. A repeat of a particular lamina can be summarized by a subscript of the
number of laminae in sequence, e.g. '2' for two laminates in sequence. See
Figure 9.1 for a few examples of these.

9.3   MANUFACTURING PROCESSES OF COMPOSITE LAMINATES

There is a wide variety of ways of manufacturing composite materials, and a book
of this type cannot do this subject justice. Therefore, we will restrict our attention
to methods that are used to manufacture plate-like composite panels as these are the
ones that are most typically used in rigid amour applications.

9.3.1   COMPRESSION MOULDING

Compression moulding is a process whereby pre-impregnated composite plies are
compressed together in a mould that is heated. The pre-impregnated composite plies
(or pre-pregs) can be bought off the shelf and provide a very simple way of construct-
ing a plate. The principal advantage of pre-pregs is that the resin that coats the rein-
forcement is mixed by the suppliers and is generally of high quality; the disadvantage
is that they are expensive compared to dry reinforcement and have a finite life.

Pre-pregs can be shaped within one side of the mould to form a more complex
shape. As the pressure is applied, the plies are heated, and this allows the resin to
flow around the reinforcement to produce the final part.

Compression moulding is best suited to high-volume manufacturing.

9.3.2 Autoclave Moulding

Autoclave moulding is very similar to compression moulding, except that this time, a vacuum is applied to a bagged workpiece. Essentially, an autoclave is a pressure vessel with pipework to allow for a vacuum to be established in the sample. This allows for greater levels of consolidation of the resin and reinforcement. Using an autoclave is generally a slow process, and the capital cost of the equipment is high; however, the quality of the finished product—particularly where the change of sections occurs and where there are tight radii—is high.

9.3.3 Resin Transfer Moulding

The resin transfer moulding (RTM) process is suitable for high-volume manufacturing. This method starts with the skeleton of the fibres or a woven fibre mat, or multiple mats, that is placed into a mould of the final desired shape. The mould is then clamped together, and resin is pumped into the mould expelling the air from the edges until the mould has been filled. The heating of the mould cures the resin, and usually, relatively low temperatures (~40°C) are required. Once cured, the mould parts are separated to reveal the finished product. The advantages of this process are that good dimensional tolerances are achieved, and it is possible to produce complex shapes such as corner sections. A wide variety of reinforcements can be used too. The key is in the choice of the resin. This needs to sufficiently permeate the reinforcement and wet the fibre bundles and then undergo the curing process to produce a rigid matrix. This manufacturing process has been widely adopted by the automotive and aerospace sectors.

9.4 FIBROUS MATERIALS FOR ARMOUR APPLICATIONS

The majority of composite materials that are used for ballistic protection today are fibrous in nature. That is to say that they consist of multiple plies (or layers) of fibres. These tend to be used in body armour systems with the most famous of the fibres being Kevlar®, which is mostly used in a woven fabric construction.

Of course, it should be of little surprise that fibrous composites are used in protection systems given the very early use of leather as armour. Leather is fibrous in nature with the outer layer (the grain) consisting of the epidermis of the animal, whereas the corium underneath provides a loose fibrous structure. The structure is tough, and consequently, it has been used for hundreds of years dating back to before the Qin dynasty of ancient China (ca. 221 BC). Arguably, wood (another fibrous composite) has been known for millennia for its protective properties and, in particular, its ability to absorb the energy of a low-velocity impact.

9.4.1 General Factors That Affect Performance

There have been several reviews on what factors affect the ballistic performance of composite materials. These have been nicely summarized by Cheeseman and Bogetti (2003), Tabiei and Nilakantan (2008) and various publications by Abrate (1991, 1994).

The ballistic penetration resistance offered by fabric and rigid composites involves a number of different parameters, and therefore, it is not possible to single out a variable that will provide enhanced protection. For example, one might think that increasing fibre toughness is an important factor in providing enhanced ballistic protection. However, if toughness was a single parameter that improved ballistic performance, then nylon fibres would be expected to perform better than Kevlar fibres—which we know is not the case (Prosser et al., 2000).

However, a metric that is often used to compare fibres for blast and ballistic protection application involves both the specific energy absorption capability of the fibre and the sonic or elastic wave speed in the fibre.

You will recall from Chapter 2 that the energy absorbed per unit volume can be calculated from the area under a tensile test, and for a high-performance fibre, this can be approximated by

$$U_r = \frac{1}{2}\sigma_t\varepsilon_t \tag{9.1}$$

where
σ_t is the tensile stress at rupture.
ε_t is the tensile strain at rupture.

This assumes a linear stress–strain response until rupture under tension and therefore for some fibres is a crude approximation; ultra-high-molecular-weight polyethylene (UHMWPE) fibres in particular show a distinct inelastic curve as the strain approaches rupture.

The specific energy absorption (per unit volume) can be calculated by

$$U_{sp} = \frac{1}{2}\frac{\sigma_t\varepsilon_t}{\rho_0}. \tag{9.2}$$

The elastic velocity follows the well-known relationship

$$c_0 = \sqrt{\frac{E}{\rho_0}} \tag{9.3}$$

The multiplication of c_0 and U_{sp} provides an indication of the ballistic effectiveness of an individual fibre in a composite and can be used as a metric to compare fibres. It is therefore given as (Cunniff, 1999)

$$U^* = \frac{1}{2}\frac{\sigma_t\varepsilon_t}{\rho_0}\sqrt{\frac{E}{\rho_0}} \tag{9.4}$$

A high elastic wave velocity is important as this allows for the rapid delocalization of the stresses from the point of impact. The specific energy absorption (or specific toughness) of the fibre is a measure of how much of a projectile's kinetic energy (KE) can be absorbed on impact.

TABLE 9.2

Specific Energy Absorption Ability and Speed of Sound Comparisons between Fibres

Fibre	ρ_0 (kg/m³)	E (GPa)	σ_t (GPa)	ε_t (%)	c_0 (m/s)	$U^{*1/3}$(m/s)
PBO	1560	169	5.20	3.10	10,408	813
Spectra® 1000	970	120	2.57	3.50	11,123	802
SK60 (Dyneema®)	970	87	2.70	3.50	9471	773
600-denier Kevlar® KM2	1440	83	3.40	3.55	7592	682
850-denier Kevlar® KM2	1440	74	3.34	3.25	7154	681
1500-denier Kevlar® 29	1440	74	2.90	3.38	7188	625
1140-denier Kevlar® 49	1440	120	3.04	1.20	9129	612
Carbon fibre	1800	227	3.80	1.76	12555	593

Further evolution of this equation has been undertaken by Cunniff to compare a dimensionless v_{50} velocity by dividing the v_{50} velocity of a fabric by the cube root of Equation 9.4. This was then compared to a dimensionless system parameter comprising the projectile's presented area, the system's areal density and the projectile's mass (Cunniff, 1999). Some fibre parameters are shown in Table 9.2 with some of the parameters from Cunniff (1999).

There is also evidence that coating fibres in a substance leads to an improvement in ballistic performance. Indeed, it has been known for two decades that shear thickening fluid (STF) impregnation is a technique that can improve the impact resistance of high-performance fabrics (more on this in Section 9.4.2.1). Researchers have reported that coating fibres in a thin polymeric coating can also show benefit—particularly for soft fabric armour (e.g., see Kim et al, 2020). This simply increases the inter-fibre friction thereby leading to an increase in energy absorption. For example, Ignatova et al. (2020) used polyvinyl acetate (PVA) to coat a multilayer fabric armour based on Twaron® 709 and observed a substantial increase in ballistic performance of their armour over and above the non-coated system. Other researchers have seen similar improvements with zinc oxide nanowire coatings of UHMWPE fabrics (Steinke and Sodano, 2021).

9.4.2 ARAMID-BASED FIBRES FOR ARMOUR APPLICATIONS

Kevlar was first developed by DuPont in the 1960s from aromatic polyamides. This and similar fibres such as Twaron, manufactured by Teijin Aramid, are known as aramids and are derived from polymer molecules containing benzene rings. These molecules readily align parallel to each other to form highly ordered structures and consequently demonstrate excellent properties along the direction of the fibres. The fibres, however, are highly anisotropic due to the weak inter-chain bonding between each of the molecules and therefore are susceptible to splitting. This is illustrated by the experiments of Cheng et al. (2004, 2005) who measured the longitudinal and transverse properties of a single Kevlar KM2 fibre. The longitudinal modulus is significantly higher. See Table 9.3.

TABLE 9.3

Transverse and Longitudinal Measurements of a Kevlar KM2 Fibre

Fibre	E_1 (Transverse Modulus)	E_3 (Longitudinal Modulus)
Kevlar KM2	1.34 ± 0.35 GPa	84.62 ± 4.18 GPa

Source: Cheng, M. et al. 2005. *Journal of Engineering Materials and Technology, Transactions of the ASME*, 127 (2), 197–203.

TABLE 9.4

Properties of Kevlar Fibres

Fibre	Density (kg/m³)	Tenacity (GPa)	Young's Modulus (GPa)	Elongation to Break (%)	Decomposition Temp (°C)
Kevlar 29	1440	2.92	70.50	3.6	427–482
Kevlar 49	1440	3.00	112.40	2.4	427–482
Kevlar KM2	1440	3.88 ± 0.40	84.62 ± 4.18	4.52 ± 0.37	–

Source: DuPont. 2001. *KEVLAR Aramid Fibre – Technical Guide*. Richmond, VA: DuPont; Cheng, M. et al. 2005. *Journal of Engineering Materials and Technology, Transactions of the ASME*, 127 (2), 197–203.

Aramid fibres tend to fail in a ductile manner, and although the strain to failure of the fibres is small, necking occurs in the fibres followed by a localized drawing of the material forming fibrils (microfibres). This is an energy-expensive process and is an attractive mode of failure—particularly for when we need the material to stop a bullet.

Kevlar has been used extensively in the design of body armour, and many police officers and soldiers owe their life to this material (and its inventor—Stephanie Kwolek). The best types of woven systems will consist of multiple fabric layers of tightly woven material. These will be arranged in either a plain or basket weave. Loosely woven materials lead to an inferior ballistic performance (Cheeseman and Bogetti, 2003). The properties of three common brands of Kevlar fibres are presented in Table 9.4.

9.4.2.1 Kevlar Fibres and Shear-Thickening Fluids

Improvements to the performance of fibres can be achieved via a couple of routes. In particular, it has been shown that the addition of shear-thickening fluids (STFs) to Kevlar fibres results in an enhancement of ballistic protection (Lee et al., 2003). Shear thickening is a non-Newtonian process characterized by a significant increase in viscosity with shear stress. Non-Newtonian 'thickening' behaviour tends to occur in colloidal suspensions where small (nanometre-sized) particles are deposited in a matrix fluid. As the rate of shear is increased, the suspended
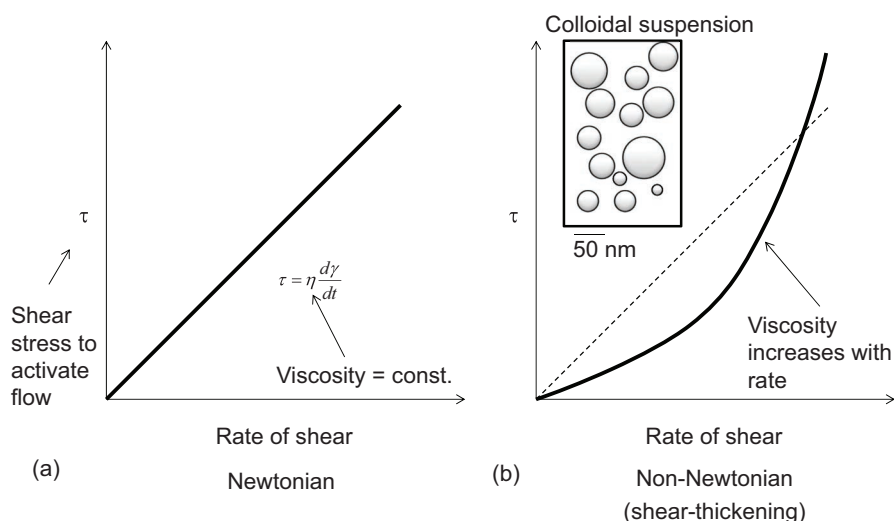
FIGURE 9.2 (a) Newtonian response and (b) a non-Newtonian response where the viscosity increases with the rate of shear; inset—an example of a colloidal suspension.

particles cluster together to provide a resistance to flow in a process called 'hydro-clustering'. Figure 9.2a and b shows how a Newtonian fluid responds to applied shear and a non-Newtonian fluid (shear thickening) responds to shear, respectively. It can be seen that for the STF, the viscosity of the fluid increases as the rate of shear is increased. This means that the fluid gets thicker (the term 'thickness' here is not referring to a geometrical thickness but rather a viscosity effect). The opposite of this is a shear-thinning fluid where the viscosity decreases with the increase in the rate of shear. This is particularly useful in the application of paint where applying a paint-loaded brush to a wall will result in the paint flowing smoothly (due to a reduced viscosity). However, remove the brush and the viscosity of the paint increases, thereby limiting the number of drips that are formed. Colloidal suspensions can undergo shear thinning at low shear rates and shear thickening at high shear rates.

So, why does adding an STF to Kevlar fibres increases their ballistic performance? Lee et al. (2003) fired fragment-simulating projectiles (FSPs) into composite materials woven with Kevlar fibres impregnated with colloidal STF (silica particles dispersed in ethylene glycol). The Kevlar targets were backed with clay, and the depth of penetration into the clay was recorded. They showed an enhancement in the energy absorption of the Kevlar fabric where the STF materials were applied. In addition, they found that the shear-thickening effects were proportional to the volume of the STF applied to the fabric. It was thought that the performance enhancement was due to an increase in yarn pullout force on the transition of the STF to a rigid state (Lee et al., 2003). Similar improvements in performance have been found in stab-resistant STF-treated Kevlar and nylon fabrics (Decker et al., 2007).

9.4.3 GLASS FIBRES FOR ARMOUR APPLICATIONS

Glass fibre-based materials have been used in all types of military environments ranging from mine countermeasure vessels such as HMS Wilton (Mouritz et al., 2001) to armoured fighting vehicles (Fecko, 2006). To date, several technology demonstrators of armoured fighting vehicles have been used in an attempt to develop what became known in the popular media as the 'plastic tank'. In fact, for the most part, that is exactly the aim, i.e. to produce an armoured vehicle where 30%–40% of the vehicle's structure is an epoxy resin (plastic).

Glass fibre–reinforced plastics (GFRPs) have been used in developmental trial vehicles such as the Advanced Composite Armoured Vehicle Programme in the United Kingdom (see Figure 9.7) and the various Composite Armoured Vehicle programmes running in the United States. However, to date, only weight savings of approximately 10%–15% have been achieved when compared to metallic systems with similar protection levels. It is thought that further weight savings can be achieved by moving from an E-glass fibre to an S-glass fibre system if cost allows.

It is important to note that composite materials on their own will not provide sufficient protection against large ballistic threats or hard-cored AP rounds, and therefore, a ceramic or high-hardness armour plate would be attached to provide a disruptor face (Ogorkiewicz, 1976; Hetherington and Rajagopalan, 1991). However, glass fibre–reinforced polymers do provide useful protection against spall fragments, and therefore, spall shields are often constructed from these types of materials.

Repairing composite material plates that have delaminated due to penetration or have been perforated by a projectile is a relatively straightforward process—if the damage is cosmetic rather than structural. It is possible to remove the damaged zone by drilling out a core of a material and replacing it with a cylinder of a new composite material by using an adhesive to glue the contacting surfaces together. Such repairs have been ballistically tested and have been shown to have the same performance as the original composite material—even with bullets fired at the joints (Edwards, 2000).

GFRP materials generally demonstrate a good resistance to shock loading, and unlike carbon-based composites, they demonstrate reasonable energy absorption when subjected to ballistic attack. Consequently, for armour applications, glass-based composite materials are considered more important.

9.4.3.1 The Effect of Stitching

There have been several studies that have focused on the penetration and failure mechanisms of stitched composite materials. Mines et al. (1999) studied the penetration behaviour of woven, z-stitched (± 45° z-stitch E-glass fabrics supplied by Tech Textiles) and through-thickness z-stitched glass polyester laminates for a number of laminate thicknesses, a number of geometries and masses of projectiles. They identified three modes of energy absorption: local perforation, delamination and friction between the projectile and the panel. They also reported that the woven and the z-stitched samples behaved in a similar manner. Their evidence suggested that the local energy absorption was dominated by shear effects during penetration. Similar evidence has also been seen by Naik and Shrirao (2004), Gama et al. (2005), Naik et al.

Direction of stitching (transverse)

(a)

Direction of stitching (parallel)

Coupons for testing

(b)

Direction of stitching

Through thickness

Modified lock stitch

(c)

Water

Explosive

Coupon (clamped and with an air backing)
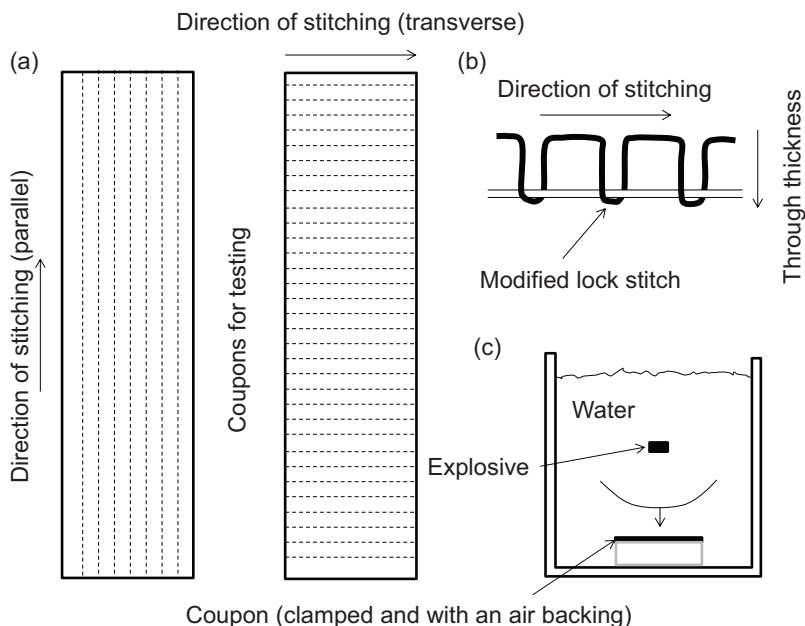
FIGURE 9.3 Experimental details showing (a) the coupons used in the testing, (b) the type of stitching employed and (c) the explosive test set-up. (From Mouritz, A. P. 1995. *Composites Science and Technology*, 55, 365–374.)

(2006) and Naik and Doshi (2008). In particular, Gama et al. partitioned the penetration mechanisms into five stages, namely: impact contact, hydrostatic compression of the composite, compression–shear, tension–shear and structural vibration. Stitching composites does have some benefit where the composite is subjected to blast loading and it provides this by limiting delamination. This was shown by Mouritz who tested GFRP coupons (270×70 mm) that had been stitched in the through-thickness with a Kevlar thread stitched in either the parallel or transverse direction of the coupon (see Figure 9.3a; Mouritz, 1995). The stitch was a modified lock stitch as shown in Figure 9.3b. Mourtiz showed that when subjected to underwater blast loading (see Figure 9.3c), the area of delamination damage was reduced by the stitching, with the greatest reductions occurring at a higher stitched density and when the stitches were parallel to the coupon's longest dimension. However, as the coupons bent due to the pressure exerted by the shock wave, the stitches act to produce a stress concentration, which resulted in a high amount of damage around the stitching. Significantly, bending failure is a prominent failure mechanism when coupons are subjected to bending by explosive loading (Mouritz et al., 1994; Mouritz, 1996).

Stitching should also have an effect on the ballistic behaviour of the composite principally because of the improved impact damage tolerance offered by the presence of the stitching. However, Mouritz (2001) has shown that against ballistic impact, the effect of stitching is minimal on the damage reduction, whereas against blast loading, it is much more significant.

9.4.3.2 3D Woven Structures

3D woven composites offer the possibility of providing enhanced ballistic protection by virtue of the architecture providing strength and stiffness in the z-plane and enhanced damage tolerance (Mouritz et al., 1999). There have been relatively few studies that have explored the advantages of these types of materials under ballistic loading, although they have been shown to offer improvements over 2D composites in the design of ceramic-faced armour systems (Grogan et al., 2007). Under dynamic impact tests, there have been several studies that show that 3D woven composites exhibit higher energy-absorbing abilities under repeated impact when compared to 2D composites. Importantly, it has been shown that under low-velocity impact, 3D composites spread the damage from the impact over a wider area than 2D composites (Baucom et al., 2006). However, the question still remains as to whether this behaviour is translated for higher-rate ballistic impacts. Jia et al. (2011) studied the ballistic behaviour of these materials computationally and experimentally and noted that during ballistic penetration, delamination was inhibited due to the presence of the z-plane reinforcement. They concluded that the energy absorption was predominately due to shear failure on the impact surface and tensile and shear failure on the rear surface of the target ultimately leading to target failure. On the other hand, Walter et al. (2009) experimentally investigated the ballistic performance of a thick 3D-woven glass-based composite made of 27 layers of tows stacked in a cross-ply arrangement and showed that under high-velocity impact, the z-plane reinforcement did not stop delamination. They also noted very different failure mechanisms due to different bullet morphologies underlining the complex failure mechanisms of these materials (Walter et al., 2009).

9.4.3.3 Thickness Effects

It has also been shown that changes in thickness have an important role in the penetration mechanisms. Gellert et al. (2000) noticed that the penetration of varying thicknesses of GFRP materials resulted in a bilinear relationship when the KE of the projectile at the ballistic limit was plotted against target thickness. This was also found to be the case for a broad range of reported ballistic impact data. Increasing the thickness of the GFRP target resulted in two characteristic patterns of delamination (illustrated schematically in Figure 9.4). For thin targets, the damage was in the form of a cone of delamination opening towards the target's rear surface. This cone increased in diameter and height with increasing target thickness until, with sufficiently thick targets, a cone of delamination opening towards the impact side was also added.

The reason for this was due to the way in which the target failed during ballistic penetration. A change in perforation mechanism was observed from largely dishing in thin targets to a combination of indentation and dishing for thick targets and was largely affected by projectile shape and diameter (see Figure 9.5). For thin targets, the projectile nose shape (flat-nosed or conical) did not affect the energy absorption characteristics of the target; however, for the thick targets, the conical projectiles were more effective. This is contrary to the observations in carbon/epoxy targets where conical projectiles appeared to perform less well compared to flat-ended projectiles
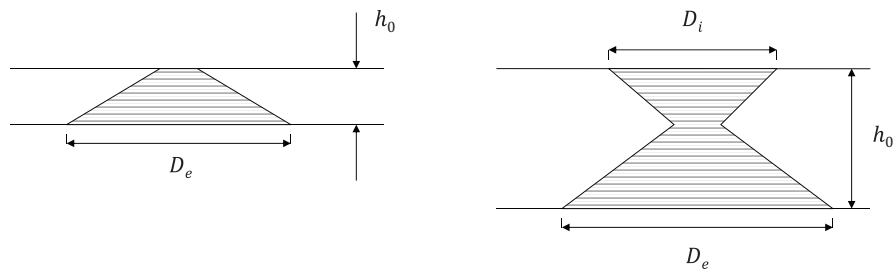
FIGURE 9.4 Differences in the type of damage for thin and thick GFRP targets. h_0 is the laminate thickness, whereas D_i and D_e represent the delamination extent on the target's incidence and exit sides, respectively. (Adapted from Gellert, E. P. et al. 2000. *International Journal of Impact Engineering*, 24(5), 445–456.)
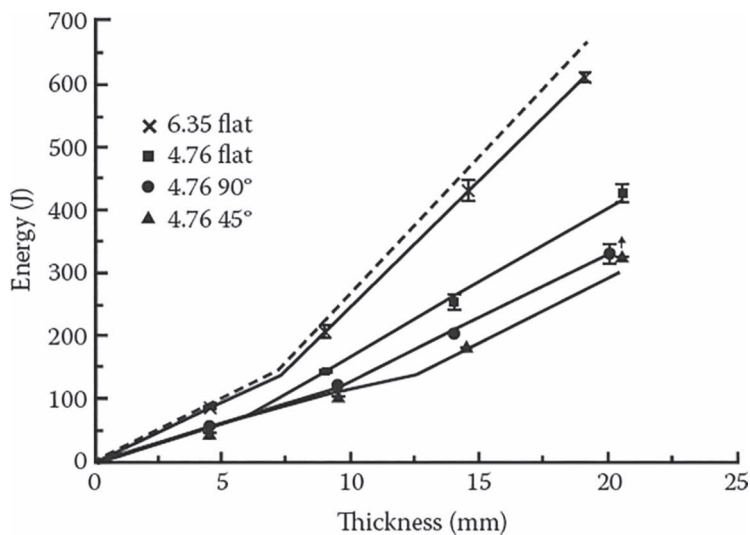
FIGURE 9.5 KE at ballistic limit versus target thickness for projectiles impacting GFRP targets. (Reprinted from Gellert, E. P. et al. 2000. *International Journal of Impact Engineering*, 24 (5), 445–456, Copyright 2000, with permission from Elsevier.)

(Ulven et al., 2003). Notably, this is due to the carbon/epoxy target failing by shear plugging at elevated velocities. Importantly, Gellert et al. (2000) concluded that the indentation phase is a significant absorber of energy in GFRP targets and indicated that it should be maximized in any bonded composite armour design.

For thin composite materials, it is anticipated that the strength and the strain to failure of the fibres are particularly important to accommodate the tensile strains that occur due to the dishing. Consequently, for these structures, using the higher-strength S-glass fibres as opposed to the E-glass fibres is desirable.

Naik et al. (2005) have also shown how impact energy is partitioned during ballistic impact loading. Using an analytical formulation, they showed how the energy absorption can be partitioned during the ballistic penetration of 2D-woven E-glass epoxy composite ($t = 2\,mm$; $\rho_0 = 1750\,kg/m^3$). The result shown in Figure 9.6 is for a calculation where the composite is impacted at just below the ballistic limit (i.e. where the projectile has not completely penetrated the composite). The main energy-absorbing mechanisms were fracture of primary yarns and deformation of secondary yarns. In particular, a significant amount of the KE of the projectile was transferred to the KE of a cone of the material that was ejected from the rear surface as well as deforming the secondary yarns.

Damage from ballistic impact conditions can also be affected by the number of simultaneous impacts that the laminate experiences such as the situation where an exploding artillery munition propels multiple projectiles to the target. Using a unique gas–gun arrangement, with three barrels with an angular separation of 120°, Deka et al. (2009) showed that the progressive time-dependent damage due to sequential impacts resulted in an increased performance of an S2 glass/epoxy laminate when compared to simultaneous impacts. Specimens subjected to sequential impact
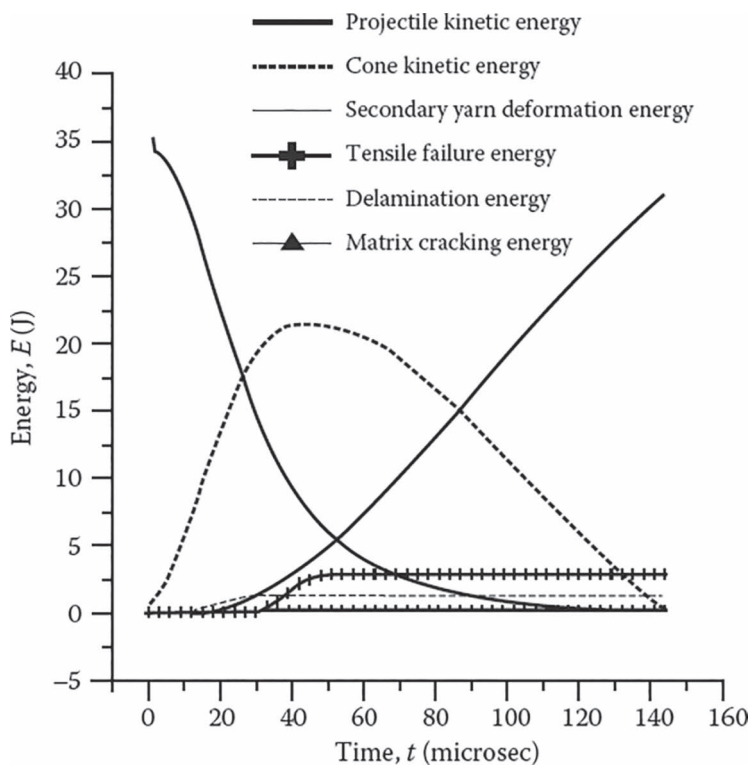
FIGURE 9.6 Energy absorbed by different mechanisms during ballistic impact events, $v_0 = 158\,m/s$, projectile mass $= 2.8\,g$, $h = 2\,mm$, d $= 5\,mm$. (Reprinted from Naik, N. K. et al. 2005. *Materials Science and Engineering A*, 412 (1–2), 104–116, Copyright 2005, with permission from Elsevier.)

exhibited an average of 10% greater energy absorption with a corresponding 18% increase in delamination damage than specimens impacted simultaneously. The energy absorption of the laminate was influenced by the stress wave interactions, particularly along the primary yarns and the amount of delamination that developed.

9.4.3.4 The Effect of Laminate Make-Up on Ballistic Performance

Various attempts have been made to analyze the penetration of composite materials, and these are generally based on energy-balance equations where the KE of the projectile is balanced with the energy required to cause the shear failure of the composite, delamination, tensile failure of the yarns, KE of the resulting fragments and so on, e.g. Sun and Potti (1996) and Morye et al. (2000). Some choose to decompose the resistance offered by the composite into two stress terms—namely the static and dynamic resistive component—and derive terms for each based on the shape of the projectile penetrating the composite and the energy required to penetrate the depth, e.g. Wen (2001). Nevertheless, in the formulation of analytical models (and of course, validation of computational models), the geometry of failure is also important. Also important is the strain wave propagation along the length of the fibres/yarns, which, for soft fabric constructions at least, is one of the several mechanisms of absorbing energy (Cheeseman and Bogetti, 2003). The addition of the matrices of either the thermoset or thermoplastic type clearly has an effect on the penetration mechanisms. This has been shown by Lee et al. (2001) who compared dry fabrics (i.e. without a resin in place) to a composite structure (where either a vinyl ester resin or aliphatic ester-type polyurethane was used) on the ballistic performance of Spectra 900–reinforced composites. The effect of adding the resin reduced yarn mobility and ultimately resulted in higher energy absorption through yarn fracture. However, they noted that the resin matrix itself does not absorb much energy in itself. Nevertheless, small improvements in the ballistic performance of GFRP composites have been seen with the addition of carbon nanotubes to the resin (Trovillion et al., 2010).

It is perhaps no surprise that the type of reinforcement used in rigid composite construction is also critical. Wrzesien (1972) has shown that complementing the glass–fibre reinforcement with a steel wire added the resistance to ballistic penetration. Although there is an obvious weight penalty due to the addition of the relatively dense steel (and in this case, brass coated), on a weight-by-weight basis, it has shown to be efficient at resisting penetration. Consequently, increasing the strength of the fibres should improve the ballistic performance of the composite.

On the other hand, Woodward et al. (1994) examined the ballistic performance of semi-infinite (very thick) composite materials with various reinforcements including (S2) glass, nylon and Kevlar materials (all with different tensile strength values). Unusually, they tested target structures that were at least 150 mm square and 150 mm thick, and therefore, the projectile was subjected to inertial confinement throughout the penetration phase. Using a simple energy balance, a value for the mean stress was established and found to be highest when the glass-reinforced material was tested. The mean resisting stress was calculated according to

$$\sigma_r A d = \frac{1}{2} m_p v_0^2 \qquad (9.5)$$

where

σ_r is the mean resisting stress.

A is the cross-sectional area of the cavity that is formed by the projectile.

d is the diameter of the projectile.

m_p is its mass.

v_0 is the velocity.

For GFRP, they measured a value of 1190 MPa, which was twice that measured for the Kevlar-based composite (615 MPa). It was demonstrated that for GFRP, crushing fracture of the composite occurred immediately ahead of the penetrator, and they pointed out that this was seen to be responsible for a large amount of energy absorption during the early stages of penetration in finite-thickness targets. High tensile modulus and good bonding between the fibre and the matrix were identified as important parameters for ballistic resistance. However, it should be pointed out that as this was effectively a semi-infinite target (i.e. where the thickness exceeded the penetration depth), some of the 'break-out' mechanisms seen by others were not evident.

The post-impact structural behaviour of composites is of particular interest when consideration is given to where they would be applied. In loadbearing structures such as ships and composite armoured vehicles (such as the Advanced Composite Armoured Vehicle Platform; see Figure 9.7), it is critical to understand the degradation of strength and stiffness when the material has been subjected to blast and impact loading. And, certainly, for blast-loaded structures, this has been a critical path of study.

FIGURE 9.7 Qinetiq advanced composite armoured vehicle programme technology demonstrator.

9.4.4 Basalt Fibres for Armour Applications

Basalt fibres are derived from igneous rock that is readily available in the Earth's crust. The advantage of basalt is that, due to its abundance and the ease at which it can be mined, it is relatively cheap. It also can be readily extruded into fibres, and therefore, it is possible to manufacture ballistic protection systems that can compete against E-glass and S2-glass systems. It is also pretty good at accommodating high temperatures and therefore would not be susceptible to thermal softening at extreme temperatures (unlike UHMWPE). Basalt fibres also retain their properties at low temperatures, do not degrade in ultraviolet radiation and are inert. Given that these fibres are derived from igneous rock, they are wonderfully environmentally friendly too. To date, there is relatively little research on the viability of basalt fibres for ballistic protection. Nevertheless, some work on this product at the Army Research Laboratory at Aberdeen Proving Ground (United States) has shown that this material shows some promise. They showed that against FSP projectiles, basalt-based composites perform in a comparable fashion to S2 glass epoxy laminates (Spagnuolo et al., 2011).

9.4.5 UHMWPE Fibres for Armour Applications

UHMWPE-based composites are fairly unique in that the fibre material is accommodated in a matrix made from the same type of polymer used to manufacture the fibre. The fibres consist of a specially manufactured UHMWPE such that the carbon chain of the PE molecule is aligned along the fibre. This makes the fibres very strong. The fibre is made through a process of 'gel spinning' where the long-chain molecules of UHMWPE are dissolved in a solvent (to form a gel) and then extruded through a spinneret and cooled to form the fibre with a high degree of molecular orientation. Two principal brands exist: Dyneema (DSM) and Spectra (Honeywell). The properties of a Dyneema fibre (SK60) are provided in Table 9.5 (van Dingenen, 1989).

UHMWPE fibres have two advantageous properties for goods ballistic protection for lightweight armour solutions (Jacobs and Van Dingenen, 2001):

1. A high specific energy absorption capability
2. A high elastic wave velocity

This can be seen in Table 9.2.

A typical structure of the composite is shown in Figure 9.8. In this case, the composite is a ballistic-grade material (HB50) and is laid up according to a 0°/90° fashion.

TABLE 9.5

Properties of Dyneema SK60

Fibre	Density (kg/m³)	Young's Modulus (GPa)	Tenacity (GPa)	Elongation to Break (%)
SK60	970	87	2.7	3.5

Source: van Dingenen, J. L. J. 1989. *Materials & Design*, 10 (2), 101–104.
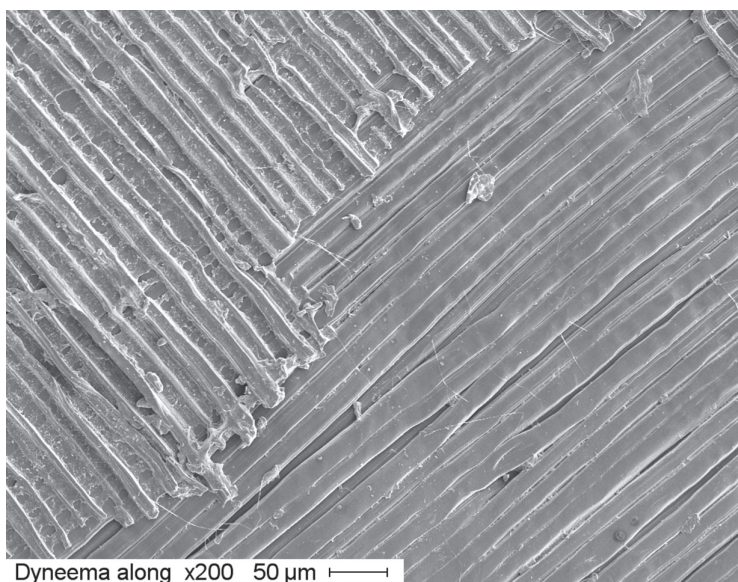
FIGURE 9.8 A micrograph of a Dyneema composite (HB50).

The PE fibres run in a UD ply and are stacked on top of one another with each fibre direction at an orthogonal angle to the previous.

Dyneema is one of the most weight-efficient composites to use for the lower threat spectrum, and for Standardization Agreement (STANAG) Level 1, which encompasses soft-cored high-velocity rifle bullets such as the 7.62 × 51-mm NATO ball round, around 30 mm for this ballistic-grade composite is sufficient. Coupled with its low density (~970 kg/m³), this translates to an areal density of 28.5 kg/m². Of course, weight-efficient ballistic protection comes at a price, and consequently, this composite material is not cheap.

This type of composite is also used as a spall shield for armoured fighting vehicles such as the Patria XA188 in service with the Netherlands Army. However, being a PE-based composite, its decomposition temperature is relatively low compared with other composite options. The fibres melt at around 144°C–152°C, and therefore, their performance will be considerably reduced as the temperatures approach these values.

9.4.5.1 Ballistic Penetration of Dyneema

Dyneema can be used as part of a ceramic-faced system, or it can be used as a stand-alone armour material. Figure 9.9 shows a 22-mm-thick Dyneema plate penetrated by a 5.56 × 45 mm SS109 (L2A2) bullet. It can be seen that the plate has stopped the bullet, but there are several important effects that have occurred during the penetration process. Firstly, it appears that on contact with the panel, the bullet has begun to compress the plies and individual fibres subjected to shear failure. Approximately a quarter of the way through the sample, the resistance offered by the panel has led to the deformation/disruption of the projectile. Delamination of the plies has
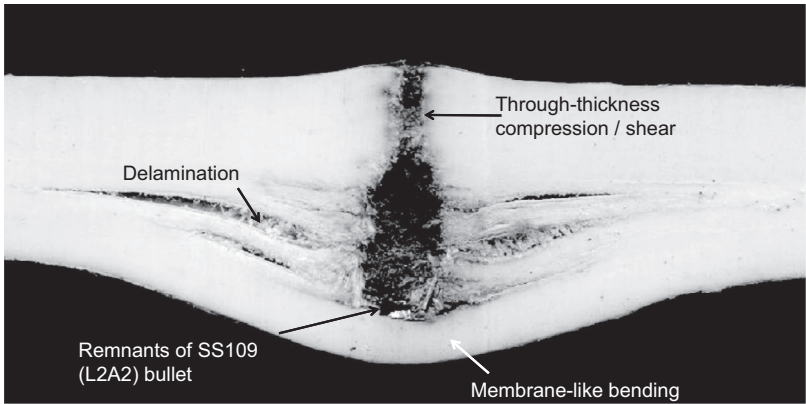
FIGURE 9.9 22-mm-thick Dyneema plate penetrated by a 5.56×45 mm SS109 (L2A2) bullet; impact velocity = 838 m/s. (From Iremonger, M. J. 1999. Polyethylene composites for protection against high-velocity small arms bullets. *In: Proceedings of the 18th International Symposium on Ballistics, San Antonio, Texas*; Image of Dyneema courtesy of Dr. M. J. Iremonger.)

TABLE 9.6

Ballistics Performance of HB1 Dyneema Panels against L2A2 Bullets

Target		Response of Target to Impact by an L2A2 Bullet at a Range of Impact Velocities			
Thickness (mm)	A_d (kg/m²)	600 m/s	700 m/s	800 m/s	900 m/s
4.2	4.0	–	–	–	G
11.0	10.5	G	G	G	G
15.0	13.7	–	O	O	G
22.0	21.0	U	U	U	U
32.0	31.0	U	U	U	U

Source: Iremonger, M. J. 1999. Polyethylene composites for protection against high-velocity small arms bullets. *In: Proceedings of the 18th International Symposium on Ballistics*. San Antonio, TX.

G, grossly overmatched by bullet; O, overmatched; U, undermatched (stopped).

also occurred. However, probably the most important resistance is offered during the membrane-bending action of the rear portion of the panel. Here, the high-tenacity fibres are being placed in tension, and the energy absorbed through the stretching of these fibres leads to the arrest of the projectile mass. The ballistic penetration data of Dyneema are provided by Iremonger (1999)—see Table 9.6; the fractographic analysis of a projectile penetrating this material is provided by Greenhalgh et al. (2013)

Additional ballistic results are presented in Table 9.7 (Nguyen et al, 2015).

TABLE 9.7

Ballistic Performance of HB26 Dyneema Panels against FSPs

Target				
Thickness (mm)	A_d (kg/m²)	Projectile	v_{50} (m/s)	Standard Deviation (m/s)
9.1	8.9	12.7-mm FSP	506.0	26.4
20.0	19.6	12.7-mm FSP	825.8	17.2
25.2	24.7	12.7-mm FSP	1021.4	8.5
35.1	34.4	12.7-mm FSP	1250.3	36.1
50.4	49.4	12.7-mm FSP	1656.5	16.3
10.0	9.8	20-mm FSP	393.9	43.0
20.0	19.6	20-mm FSP	620.1	19.6
36.2	35.5	20-mm FSP	901.4	9.8
75.6	74.1	20-mm FSP	1527.6	104.6
101.7	99.7	20-mm FSP	2001.8	91.8

Source: Nguyen, L. et al. 2015. *International Journal of Impact Engineering*, 75 (0), 174–183.
Note: Areal densities calculated assuming $\rho_0 = 980$ kg/m³.

9.4.5.2 Shock Loading of Dyneema

The shock properties have been studied by Chapman et al. (2009) and Hazell et al. (2011). It was shown over a limited pressure range (up to 4 GPa) that the Hugoniot followed the well-known relationship (see Chapter 5)

$$U_s = c_0 + a \cdot u_p + b \cdot u_p^2 \tag{9.6}$$

where U_s is the shock velocity, c_0 is the intercept (that we have assumed to be the bulk sound speed), a and b are the polynomial coefficients and u_p is the particle velocity. The measured values for *a*, *b* and c_0 were 3.45, −0.99 and 1.77 mm/µs, respectively (Hazell et al., 2011).

At elevated shock stresses, it was found that the Dyneema appeared to have melted. Figure 9.10 shows the micrographs of post-shocked target material recovered from the target chamber. In these cases, the shock-induced particle velocities increase from left to right according to (a) 0.16, (b) 0.55 and (c) 0.86 mm/µs. At lower particle velocities, the recovered material showed evidence of fibre definition indicating that the fibres remained intact during shock loading, whereas at the elevated values, melting of the fibres and matrix had occurred.

An assessment of the temperature rise during shock loading can be approximated by examining the temperature along the adiabat (T_a) according to the following equation:

$$T_a = T_0 \exp\left[\Gamma - \Gamma\left(\frac{V}{V_0}\right) \right] \tag{9.7}$$

Increasing shock stress

(a)   (b)   (c)
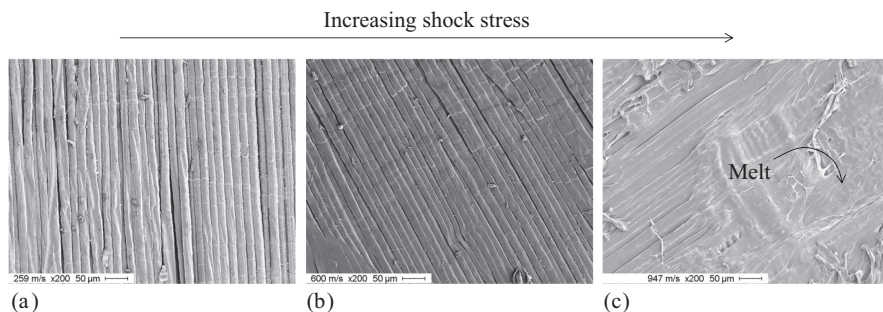
FIGURE 9.10 Recovered Dyneema target after being struck by a flyer plate; showing the fibres recovered from a shocked target up to (a) 0.16 mm/µs, (b) 0.55 mm/µs and (c) 0.86 mm/µs.

where

Γ is Grüneisen gamma (see Section 6.7.1.3).

T_0 is the initial temperature of the sample (300 K).

V is the specific volume due to shock ($1/\rho$).

V_0 is the initial specific volume prior to shock ($1/\rho_0$).

Assuming a value of $\Gamma = 1.6$ as taken for PE, the temperature along the adiabat for a compressed Dyneema sample can be calculated, and it was shown that the melting of the samples corresponding to the calculated temperature increase due to the passage of the shock wave (Hazell et al., 2011). Localized melting has also been observed in Dyneema panels that have been subjected to air-blast loading (Fallah et al., 2014).

9.4.6 PBO Fibres

There are several other fibres that have shown promise in recent years and are currently not extensively used for blast and ballistic protection. This is due to one of two possibilities. Either it is because it is widely believed that improvement in mechanical properties is achievable but not yet sufficient to warrant extensive use, or alternatively, their mechanical properties are excellent, although their physical properties are not desirable for military applications.

One such fibre that has the strength potential and has already been used in body armour applications with controversial outcomes is poly p-phenylene-2, 6-benzobisoxazole (PBO) currently manufactured under the trade name Zylon®. This fibre has a tensile strength of 5.2 GPa and, according to Table 9.2, will perform as an excellent ballistic-grade material. However, a report from the National Institute of Justice (United States) suggested that it degrades due to environmental conditions (moisture and heat; see Walsh et al., 2006a) and this, it is thought, was a contributing factor to the failure of a vest worn by a police officer who was mortally wounded. Furthermore, the report implied that a visual inspection of a Zylon-based body armour would not indicate whether the intended ballistic performance was maintained (Hart, 2005). There have been subsequent attempts to stabilize PBO fibres, but to date, these have been deemed as not being successful (Walsh et al., 2006b).

9.4.7 CARBON FIBRE COMPOSITES

Carbon-based composites have enjoyed wide usage over the past several decades ranging from bicycle frames to aircraft fuselages. However, generally speaking, carbon fibre-based composites are not suitable for providing ballistic protection. In fact, the response of carbon fibre composite materials to impulsive loads is poor, and this is due to the brittleness of the epoxy resin and the low strain to failure of the carbon fibres (<1%) leading to a poor translaminar strength. However, they are very stiff and very strong when tested in plane (along the direction of the fibres). Consequently, they are used on military platforms where lightweight structural rigidity is required. They have also been shown to provide some benefit in contributing to the strength of structural armour in aerospace applications where the presence of the CFRP layer preserves the structural integrity of the panels after ballistic impact (Horsfall et al., 2000).

They have excellent stiffness properties as well as good tensile properties, whereas their bulk densities are relatively low, typically around 1500 kg/m^3. Carbon fibres in particular have very good stiffness and strength values with the tensile modulus reaching as high as 1000 GPa and tensile strengths reaching values of 3.8 GPa. They also possess a very low (in fact, slightly negative) coefficient of thermal expansion as well as good thermal and electrical conductivity.

There exists a large body of work examining the low-velocity impact regime of carbon composite targets. These are thoroughly summarized in review publications by Abrate (1991, 1994, 1998) and Cantwell and Morton (1991).

9.4.7.1 Failure during Ballistic Loading

Despite carbon fibre laminates finding their way into military aircraft structures as early on as the 1960s, it took an additional 15 or so years for extensive studies on these materials' high-velocity impact response to be published. Early published works of Cantwell et al. (1986), Cantwell (1988) and Cantwell and Morton (1989a, b, 1990) showed a number of facets to the high-velocity impact response of these materials. Through a series of impact experiments, they have shown that high-velocity impacts generate large areas of matrix cracking, fibre fracture and delamination within the target. With relatively low-impact energies, where the projectile was a 6-mm-diameter steel sphere, they showed that damage initiated at ply on the rear side of the target due to flexural bending. In thicker, stiffer targets, damage occurs in the uppermost plies caused by the large contact stresses around the projectile. In further studies, they showed that increasing the velocity of the projectile resulted in a localized response to the target, which is somewhat different from low-velocity impacts where the areal geometry of the target is important.

The analysis of the failure modes carried out by Cantwell and Morton on the perforated samples revealed the formation of a conical-shaped shear plug. This resulted in a shear surface extending away from the point of contact at approximately 45°. For low-velocity impacts, they suggested that three energy-absorbing mechanisms were active, namely, elastic deformation, delamination and shear out.

At higher velocities, it appears that these materials become extensively particulated, and the effect of the delamination on the projectile's KE absorption becomes negligible. The sequence of events for a high-velocity projectile striking a target at 1199 m/s is shown in Figure 9.11 and highlights how brittle these
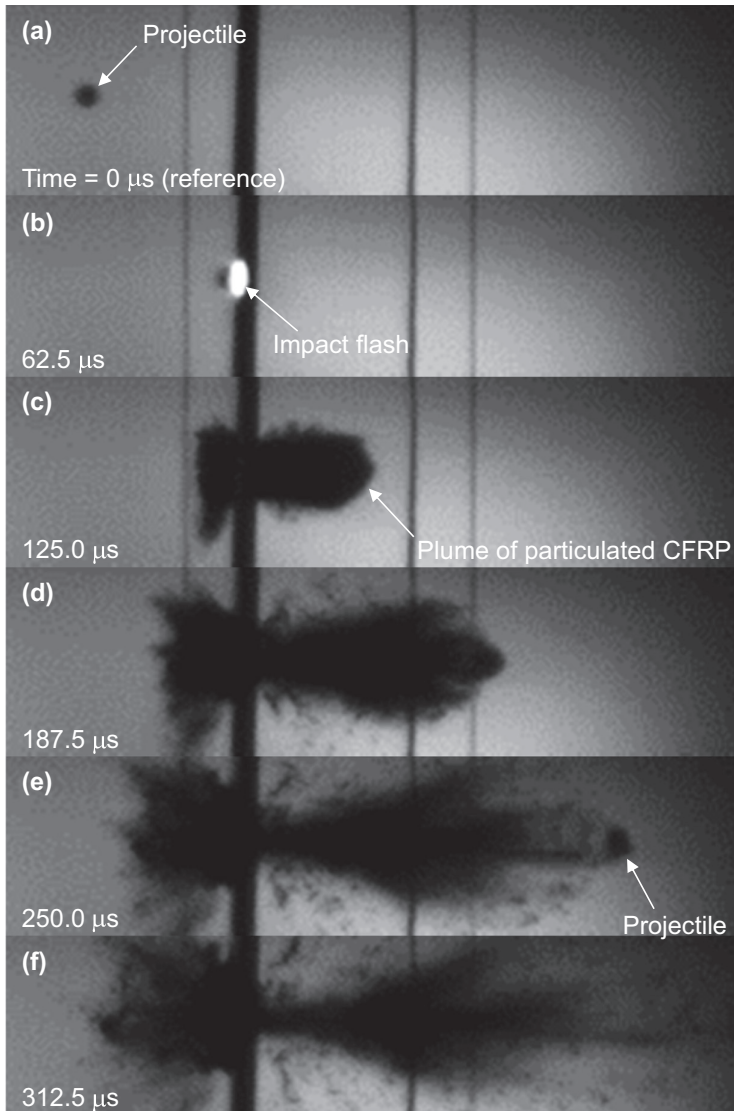
FIGURE 9.11 High-speed video images taken at 16,000 frames per second showing the perforation of a 6-mm CFRP laminate; impact energy = 5150 J (1199 m/s). (a) Time = 0 μs (reference), (b) 62.5 μs, (c) 125.0 ps, (d) 187.5 μs, (e) 250.0 μs and (f) 312.5 μs. (Reprinted from Hazell, P. J. et al. 2009. *International Journal of Impact Engineering*, 36 (9), 1136–1142, Copyright 2009, with permission from Elsevier.)
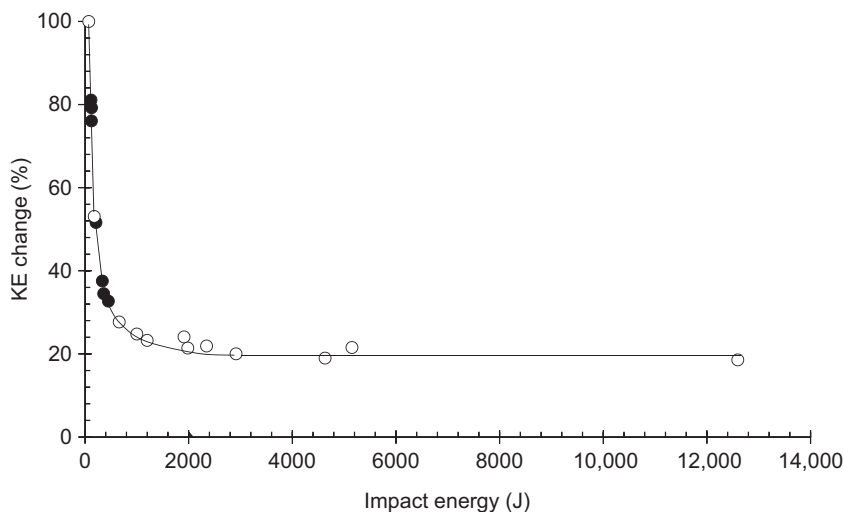
FIGURE 9.12   Percentage change in KE due to the perforation of a 5HS 6-mm-thick CFRP laminate; the different shading in data points indicates two separate experimental trials. (Reprinted from Hazell, P. J. et al. 2009. *International Journal of Impact Engineering*, 36 (9), 1136–1142, Copyright 2009, with permission from Elsevier.)

materials are. As the projectile contacts the CFRP material, light is emitted (frame B). At 125 µs, a plume of particulated CFRP material has been formed, the forward front of which precedes the projectile. Material is ejected backwards from the impact surface. At 187.5 µs, the projectile starts to emerge from the cloud of dust. The material ejected from the impact surface of the panel appears to be moving at a lower velocity than the material ejected from the rear surface. At 250 µs (frame E), the projectile is clearly defined. The large fragments formed maintain a velocity similar to the projectile (1062 m/s), whereas the large volume of lighter-weight particles is slowed. By 312.5 µs (frame F), the lighter-weight particles are moving with an average linear velocity of 200 m/s (Hazell et al., 2009).

The percentage of KE absorbed by the laminate appears to reach a plateau at elevated velocities, that is, for 5HS woven laminates at least. Figure 9.12 shows the percentage change of KE due to the perforation of a 6-mm-thick CFRP laminate. Here, the maximum impact velocity was 1875 m/s. It can be seen that above an impact energy of ~2000 J, the percentage KE of the projectile that is absorbed is constant. This work also showed that the level of delamination in the sample was roughly constant, implying that at increased impact velocities, the majority of the energy that is dissipated in the CFRP laminate is from the comminution of the CFRP material and in the KE transferred to the particulated material. Given the low translaminar strength of these CFRP laminates and the weakness of the exposed fibres caused by the matrix particulation, the majority of the projectile energy would be given up to the KE of the particulates. In any case, it is clear that these materials do not respond well to ballistic impact.

9.5   SPALL SHIELDS

Most spall shields that are used in AFV design use the composite material construction that has been discussed in this chapter. The reason for this is that composite panels are

- Lightweight
- Mouldable to the internal structure of the vehicle
- Adept at 'catching' blunt fragments

The purpose of a spall shield is to catch any fragment that is produced when a metallic hull is perforated and limit the damage and injury that may happen inside the vehicle. This is all the more important when an attack by shaped charge devices is considered. These shaped charge jets frequently overmatch the armour and can result in the formation of high-velocity fragments. Early ballistic tests by FMC showed that placing one-half inch of Kevlar in contact with the aluminium armour of the M113A1 APC captured more than 90% of the spray from a 66-mm M72 LAW shaped-charge warhead (Kennedy, 1983).

Spaced metallic plates have been shown to effectively reduce the number of fragments produced during shaped charge attack (Horsfall, 2005), and adding a 22-mm-thick plain weave E-glass polyester composite considerably improves performance by reducing the angle of debris that is ejected (Horsfall et al., 2007). Horsfall et al. showed that more than 600 fragments were created by the penetration of a single 10-mm mild steel plate by a shaped-charge warhead. This produced a spall cone (a cone containing 95% of all fragments) with an included angle of ~80°. Introducing the E-glass polyester composite panel behind this steel plate reduced the included angle of the spall cone to <40°. This can significantly enhance survivability prospects for the crew of AFVs (see Figure 9.13).

9.6   A WORD ABOUT SANDWICH CONSTRUCTIONS

We have already touched on the use of metallic sandwich constructions in Chapter 7 and seen that those with porous fillings can be useful in mitigating blast. Sandwich composite constructions are largely attractive for maintaining a high stiffness whilst ensuring good energy-absorbing abilities without excessive weight. Therefore, they are able to offer good specific strength and stiffness properties and have been attractive materials for aerospace structures.

One example of a sandwich construction that has been used in the aerospace sector is glass laminate aluminium–reinforced epoxy (GLARE). This is a fibre–metal laminate that has been used in the manufacture of the Airbus A380. It is composed of layers of aluminium alloy (usually AA 2024 T0) interspersed with layers of a glass fibre composite. The layers are bonded to each other with an epoxy resin. Several variants have been developed; a schematic of GLARE 3 is shown in Figure 9.14.

GLARE has shown improved prospects for blast mitigation when compared to a monolithic aluminium plate (Langdon et al., 2009); it has also been shown to have improved ballistic performance too when compared to plates of aluminium alloy of similar areal densities (Hoo Fatt et al., 2003).
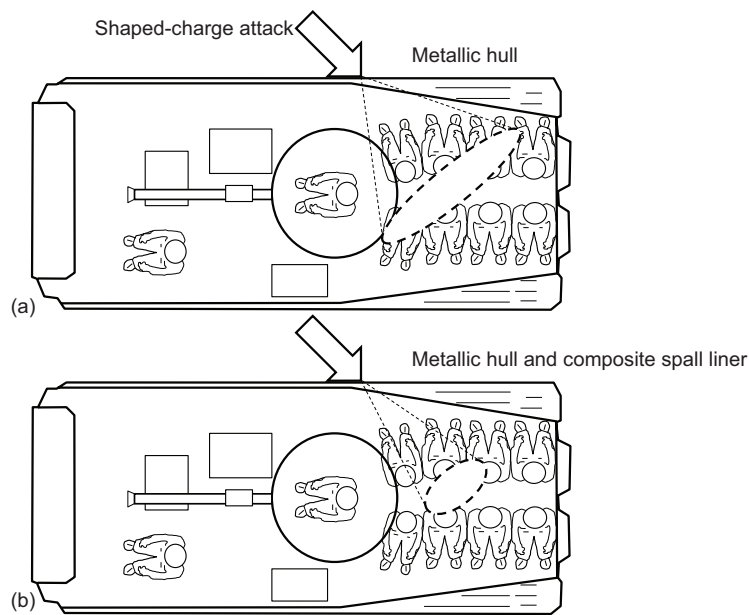
FIGURE 9.13   Spall debris formed when a shaped-charge perforates the hull of an AFV with (a) no spall liner fitted and (b) with a spall liner fitted.
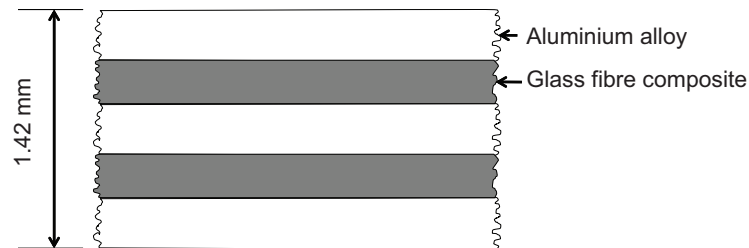
FIGURE 9.14   A schematic of GLARE.

There are multiple options for developing sandwich constructions for blast and ballistic loading, and more information on some of these structures that have been subjected to blast is given by Langdon et al. (2014).

9.7   SUMMARY

In this chapter, some of the fibres that can be used in the construction of rigid composite panels and flexible woven materials have been reviewed. The former are commonly found in military vehicles, whereas the latter are more commonplace in personal protection applications.

The use of high-performing fibres and composite materials in the aerospace sector is well established (Soutis, 2005). The reason for their use in aerospace structures is clear: they have excellent stiffness properties as well as good tensile properties, whereas their bulk densities are relatively low. They also lend themselves to vehicle design too and have good properties for blast mitigation as well as stealthy properties for reduced acoustic and thermal emissions. However, apart from a handful of demonstrators, at the time of writing, there is still a reluctance to push forward with the development of composite materials for armoured vehicle hull applications. The reason for this is probably that metallic hulls are well understood—particularly by the traditional suppliers of armoured vehicles.

The important part of the armour construction is the fibre. And it has mainly been due to the extensive research efforts dating back to the 1960s that have given us these high-strength fibres that are stronger than even the hardest steels. This, I suppose, underlines the importance of material science in the development of armour materials. If it was not for the conscientious scientists that were working away at these materials, then our ability to offer protection would have been inhibited. We can look forward to what science can produce in the coming years.

REFERENCES

Abrate, S. 1991. Impact on laminated composite materials. *Applied Mechanics Reviews*, 44(4), 155–190.

Abrate, S. 1994. Impact on laminated composites: Recent advances. *Applied Mechanics Reviews*, 47(11), 517–544.

Abrate, S. 1998. *Impact on Composite Structures*. Cambridge: Cambridge University Press.

Baucom, J. N., Zikry, M. A. & Rajendran, A. M. 2006. Low-velocity impact damage accumulation in woven S2-glass composite systems. *Composites Science and Technology*, 66(10), 1229–1238.

Cantwell, W. J. 1988. The influence of target geometry on the high velocity impact response of CFRP. *Composite Structures*, 10(3), 247–265.

Cantwell, W. J., Curtis, P. T. & Morton, J. 1986. An assessment of the impact performance of CFRP reinforced with high-strain carbon fibres. *Composites Science and Technology*, 25(2), 133–148.

Cantwell, W. J. & Morton, J. 1989a. Comparison of the low and high velocity impact response of CFRP. *Composites*, 20(6), 545–551.

Cantwell, W. J. & Morton, J. 1989b. The influence of varying projectile mass on the impact response of CFRP. *Composite Structures*, 13(2), 101–114.

Cantwell, W. J. & Morton, J. 1990. Impact perforation of carbon fibre reinforced plastic. *Composites Science and Technology*, 38(2), 119–141.

Cantwell, W. J. & Morton, J. 1991. The impact resistance of composite materials – A review. *Composites*, 22(5), 347–362.

Chapman, D. J., Braithwaite, C. H. & Proud, W. G. 2009. The response of Dyneema to shock-loading. *AIP Conference Proceedings*, 1195, 1269–1272.

Cheeseman, B. A. & Bogetti, T. A. 2003. Ballistic impact into fabric and compliant composite laminates. *Composite Structures*, 61(1–2), 161–173.

Cheng, M., Chen, W. & Weerasooriya, T. 2004. Experimental investigation of the transverse mechanical properties of a single Kevlar® KM2 fiber. *International Journal of Solids and Structures*, 41(22–23), 6215–6232.

Cheng, M., Chen, W. & Weerasooriya, T. 2005. Mechanical properties of Kevlar® KM2 single fiber. *Journal of Engineering Materials and Technology, Transactions of the ASME*, 127(2), 197–203.

Cunniff, P. M. 1999. Dimensionless parameters for optimization of textile-based body armor systems. *In: Proceedings of the 18th International Symposium on Ballistics*. San Antonio, TX. Reinecke, W. G. (ed) Lancaster, PA: Technomic Publishing Co.

Decker, M. J., Halbach, C. J., Nam, C. H., Wagner, N. J. & Wetzel, E. D. 2007. Stab resistance of shear thickening fluid (STF)-treated fabrics. *Composites Science and Technology*, 67(3–4), 565–578.

Deka, L. J., Bartus, S. D. & Vaidya, U. K. 2009. Multi-site impact response of S2-glass/epoxy composite laminates. *Composites Science and Technology*, 69(6), 725–735.

DuPont. 2001. *KEVLAR Aramid Fibre – Technical Guide*. Richmond, VA: DuPont.

Edwards, M. 2000. Land-based military applications. *In:* Bader, M. G., Kedward, K. T., Sawada, Y. (eds.) *Comprehensive Composite Materials*, vol. 6, Design and Applications, pp. 681–699. Oxford: Elsevier.

Edwards, M. R. 2002. Materials for military helicopters. *Proceedings of the Institution of Mechanical Engineers, Part G: Journal of Aerospace Engineering*, 216(2), 77–88.

Fallah, A. S., Micallef, K., Langdon, G. S., Lee, W. C., Curtis, P. T. & Louca, L. A. 2014. Dynamic response of Dyneema® HB26 plates to localised blast loading. *International Journal of Impact Engineering*, 73, 91–100.

Fecko, D. 2006. High strength glass reinforcements still being discovered. *Reinforced Plastics*, 50(4), 40–44.

Gama, B. A., Waliul Islam, S. M., Rahman, M., Gillespie Jr., J. W., Bogetti, T. A., Cheeseman, B. A., Yen, C. F. & Hoppel, C. P. R. 2005. Punch shear behavior of thick- section composites under quasi-static, low velocity, and ballistic impact loading. *SAMPE Journal*, 41(4), 6–13.

Gellert, E. P., Cimpoeru, S. J. & Woodward, R. L. 2000. Study of the effect of target thickness on the ballistic perforation of glass-fibre-reinforced plastic composites. *International Journal of Impact Engineering*, 24(5), 445–456.

Greenhalgh, E. S., Bloodworth, V. M., Iannucci, L. & Pope, D. 2013. Fractographic observations on Dyneema® composites under ballistic impact. *Composites Part A: Applied Science and Manufacturing*, 44, 51–62.

Grogan, J., Tekalur, S. A., Shukla, A., Bogdanovich, A. & Coffelt, R. A. 2007. Ballistic resistance of 2D and 3D woven sandwich composites. *Journal of Sandwich Structures and Materials*, 9(3), 283–302.

Hart, S. V. 2005. *NIJ Special Report: Third Status Report to the Attorney General on Body Armor Safety Initiative Testing and Activities*. Washington, DC: U. S. Department of Justice, Office of Justice Programs, National Institute of Justice.

Hazell, P. J., Appleby-Thomas, G. J., Trinquant, X. & Chapman, D. J. 2011. In-fiber shock propagation in Dyneema®. *Journal of Applied Physics*, 110(4), 043504.

Hazell, P. J., Cowie, A., Kister, G., Stennett, C. & Cooper, G. A. 2009. Penetration of a woven CFRP laminate by a high velocity steel sphere impacting at velocities of up to 1875 m/s. *International Journal of Impact Engineering*, 36(9), 1136–1142.

Hetherington, J. G., and B. P. Rajagopalan. 1991. An investigation into the energy absorbed during ballistic perforation of composite armours. *International Journal of Impact Engineering*, 11(1), 33–40.

Hoo Fatt, M. S., Lin, C., Revilock Jr., D. M. & Hopkins, D. A. 2003. Ballistic impact of GLARE™ fiber–metal laminates. *Composite Structures*, 61(1–2), 73–88.

Horsfall, I. 2005. The effect of spaced armour on the penetration of shaped charge warheads. *In: Proceedings of the 22nd International Symposium on Ballistics*. Vancouver, Canada. Flis, W. & Scott, B. (eds) Lancaster, PA: DEStech Publications, Inc.

Horsfall, I., Austin, S. J. & Bishop, W. 2000. Structural ballistic armour for transport aircraft. *Materials and Design*, 21(1), 19–25.

Horsfall, I., Petrou, E. & Champion, S. M. 2007. Shaped charge attack of spaced and composite armour. *In: Proceedings of the 23rd International Symposium on Ballistics*, Tarragona, Spain. Galvez, F. & Sanchez-Galvez, V. (eds) Lancaster, PA: DEStech Publications, Inc.

Ignatova, A. V., O. A. Kudryavtsev, and M. V. Zhikharev. 2020. Influence of surface polymer coating on ballistic impact response of multi-layered fabric composites: Experimental and numerical study. *International Journal of Impact Engineering*, 144, 103654–103654.

Iremonger, M. J. 1999. Polyethylene composites for protection against high velocity small arms bullets. *In: Proceedings of the 18th International Symposium on Ballistics*. San Antonio, TX. Reinecke, W. G. (ed) Lancaster, PA: Technomic Publishing Co.

Jacobs, M. J. N. & Van Dingenen, J. L. J. 2001. Ballistic protection mechanisms in personal armour. *Journal of Materials Science* 36 (13):3137–3142.

Jia, X., Sun, B. & Gu, B. 2011. Ballistic penetration of conically cylindrical steel projectile into 3D orthogonal woven composite: A finite element study at microstructure level. *Journal of Composite Materials*, 45(9), 965–987.

Kennedy, D. R. 1983. Improving combat crew survivability. *Armor*, 9, 16–22.

Kim, Y. H., S. K. Sathish Kumar, Y. Park, H. Kwon, and C. G. Kim. 2020. High-velocity impact onto a high-frictional fabric treated with adhesive spray coating and shear thickening fluid impregnation. *Composites Part B: Engineering*, 185, 107742–107742.

Langdon, G. S., Cantwel, W. J., Guan, Z. W. & Nurick, G. N. 2014. The response of polymeric composite structures to air-blast loading: A state-of-the-art. *International Materials Reviews*, 59(3), 159–177.

Langdon, G. S., Chi, Y., Nurick, G. N. & Haupt, P. 2009. Response of GLARE© panels to blast loading. *Engineering Structures*, 31(12), 3116–3120.

Lee, B. L., Walsh, T. F., Won, S. T., Patts, H. M., Song, J. W. & Mayer, A. H. 2001. Penetration failure mechanisms of armor-grade fiber composites under impact. *Journal of Composite Materials*, 35(18), 1605–1633.

Lee, J.-H., Loya, P. E., Lou, J. & Thomas, E. L. 2014. Dynamic mechanical behavior of multilayer graphene via supersonic projectile penetration. *Science*, 346(6213), 1092–1096.

Lee, Y. S., Wetzel, E. D. & Wagner, N. J. 2003. The ballistic impact characteristics of Kevlar® woven fabrics impregnated with a colloidal shear thickening fluid. *Journal of Materials Science*, 38(13), 2825–2833.

Mines, R. A. W., Roach, A. M. & Jones, N. 1999. High velocity perforation behaviour of polymer composite laminates. *International Journal of Impact Engineering*, 22(6), 561–588.

Morye, S. S., Hine, P. J., Duckett, R. A., Carr, D. J. & Ward, I. M. 2000. Modelling of the energy absorption by polymer composites upon ballistic impact. *Composites Science and Technology*, 60(14), 2631–2642.

Mouritz, A. P. 1995. The damage to stitched GRP laminates by underwater explosion shock loading. *Composites Science and Technology*, 55, 365–374.

Mouritz, A. P. 1996. The effect of underwater explosion shock loading on the flexural properties of GRP laminates. *International Journal of Impact Engineering*, 18(2), 129–139.

Mouritz, A. P. 2001. Ballistic impact and explosive blast resistance of stitched composites. *Composites Part B: Engineering*, 32(5), 431–439.

Mouritz, A. P., Bannister, M. K., Falzon, P. J. & Leong, K. H. 1999. Review of applications for advanced three-dimensional fibre textile composites. *Composites Part A: Applied Science and Manufacturing*, 30(12), 1445–1461.

Mouritz, A. P., Gellert, E., Burchill, P. & Challis, K. 2001. Review of advanced composite structures for naval ships and submarines. *Composite Structures*, 53(1), 21–24.

Mouritz, A. P., Saunders, D. S. & Buckley, S. 1994. The damage and failure of GRP laminates by underwater explosion shock loading. *Composites*, 25(6), 431–437.

Naik, N. K. & Doshi, A. V. 2008. Ballistic impact behaviour of thick composites: Parametric studies. *Composite Structures*, 82(3), 447–464.

Naik, N. K. & Shrirao, P. 2004. Composite structures under ballistic impact. *Composite Structures*, 66(1–4), 579–590.

Naik, N. K., Shrirao, P. & Reddy, B. C. K. 2005. Ballistic impact behaviour of woven fabric composites: Parametric studies. *Materials Science and Engineering A*, 412(1–2), 104–116.

Naik, N. K., Shrirao, P. & Reddy, B. C. K. 2006. Ballistic impact behaviour of woven fabric composites: Formulation. *International Journal of Impact Engineering*, 32(9), 1521–1552.

Nguyen, L. H., Ryan, S., Cimpoeru, S. J., Mouritz, A. P. & Orifici, A. C. 2015. The effect of target thickness on the ballistic performance of ultra high molecular weight polyethylene composite. *International Journal of Impact Engineering*, 75, 174–183.

Ogorkiewicz, R. M. 1976. Composite armour. *Composites*, 7(2), 71–72.

Prosser, R. A., Cohen, S. H. & Segars, R. A. 2000. Heat as a factor in the penetration of cloth ballistic panels by 0.22 caliber projectiles. *Textile Research Journal*, 70(8), 709–722.

Soutis, C. 2005. Fibre reinforced composites in aircraft construction. *Progress in Aerospace Sciences*, 41(2), 143–151.

Spagnuolo, D. M., Napadensky, E., Sano, T. & Wolbert, J. P. 2011. *Investigation of Basalt Woven Fabrics for Military Applications*. Aberdeen Proving Ground, MD: Army Research Laboratory.

Steinke, K., and H. A. Sodano. 2021. Improved inter-yarn friction and ballistic impact performance of zinc oxide nanowire coated ultra-high molecular weight polyethylene (UHMWPE). *Polymer*, 231, 124125.

Sun, C. T. & Potti, S. V. 1996. A simple model to predict residual velocities of thick composite laminates subjected to high velocity impact. *International Journal of Impact Engineering*, 18(3), 339–353.

Tabiei, A. & Nilakantan, G. 2008. Ballistic impact of dry woven fabric composites: A review. *Applied Mechanics Reviews*, 61(1), 010801.

Trovillion, J. C., Boone, R. N. & Fink, R. L. 2010. Improving the ballistic performance of E-glass composite panels using carbon nanotubes. *In: The 27th Army Science Conference*. Orlando, FL.

Ulven, C., Vaidya, U. K. & Hosur, M. V. 2003. Effect of projectile shape during ballistic perforation of VARTM carbon/epoxy composite panels. *Composite Structures*, 61(1–2), 143–150.

van Dingenen, J. L. J. 1989. High performance Dyneema fibres in composites. *Materials & Design*, 10(2), 101–104.

Walsh, P. J., Hu, X., Cunniff, P. & Lesser, A. J. 2006a. Environmental effects on poly-p-phenylenebenzobisoxazole fibers. I. Mechanisms of degradation. *Journal of Applied Polymer Science*, 102(4), 3517–3525.

Walsh, P. J., Hu, X., Cunniff, P. & Lesser, A. J. 2006b. Environmental effects on poly-p-phenylenebenzobisoxazole fibers. II. Attempts at stabilization. *Journal of Applied Polymer Science*, 102(4), 3819–3829.

Walter, T. R., Subhash, G., Sankar, B. V. & Yen, C. F. 2009. Damage modes in 3D glass fiber epoxy woven composites under high rate of impact loading. *Composites Part B: Engineering*, 40(6), 584–589.

Wen, H. M. 2001. Penetration and perforation of thick FRP laminates. *Composites Science and Technology*, 61(8), 1163–1172.

Woodward, R. L., Egglestone, G. T., Baxter, B. J. & Challis, K. 1994. Resistance to penetration and compression of fibre-reinforced composite materials. *Composites Engineering*, 4(3):329–341.

Wrzesien, A. 1972. Improving the impact resistance of glass-fibre composites. *Composites*, 3(4), 172–174.

10 Reactive Armour Systems

10.1 INTRODUCTION

The shaped-charge or high-explosive anti-tank warhead has been around since before World War II. As seen in Chapter 3, the way it works is simple and elegant. A high explosive, contained within a metal casing, is detonated resulting in a fast-moving shock front. This fast-moving front eventually encounters a copper liner that is essentially collapsed and turned inside out forming a stretching, fast-moving jet of material, sometimes referred to as a 'Munroe jet'. Remarkably, contrary to popular myth, the material that forms the jet is not molten but rather a stretching plastically deforming rod. It is usually referred to as a 'jet' mainly because it is assumed that it behaves like a fluid during penetration. However, due to the very high velocity of the tip (even velocities of over 12 km/s are possible), the jet possesses very high energy concentrated over a very small area. This means that it is able to penetrate a large amount of steel armour such as rolled homogeneous armour (RHA). It is this fact that potentially makes armoured fighting vehicles (AFVs) vulnerable to attack from warheads such as the RPG 7[1] (see Figure 10.1), and consequently, it is a dangerous as well as a prolific threat. There are several approaches that are used to defeat these types of threats; these are reviewed in this chapter.

10.2 EXPLOSIVE-REACTIVE ARMOUR

It may seem non-sensical to use explosives in an armour. However, the role of explosives in intercepting high-velocity Munroe jets was established towards the end of World War II. This approach was later discounted as it was largely thought that surrounding a tank with explosives was not practical or desirable. Other possibilities included the use of oxidizing agents such as nitrates and chlorates, dry sand and water. Based on a limited number of experiments, it was deduced that sodium carbonate decahydrate (washing soda) was the most effective oxidizing agent (Roberts and Ubbelohde, 1944). Even 'luting' (liquid clay/cement) was considered and measured to be as high as five times as effective as steel on a weight-by-weight basis at providing protection against shaped-charge warheads (Anon, 1944).

   Explosive-reactive armour, or 'ERA' is probably one of the more widely recognized 'bolt-on' armour technologies mainly due to the fact that it stands out quite obviously on a vehicle (usually a tank). It is famous for its success in several conflicts too—especially when protecting against some of the older, simpler shaped-charge warheads. Much in the same way that the formation of a shaped-charge jet is simple and elegant, its defeat by ERA is also simple and elegant. Discovered by Manfred Held back in the early 1970s (Held, 1970), the simplest construction of ERA consists of two steel plates sandwiching a layer of high explosive (see Figure 10.2). These

FIGURE 10.1   A (PG 7) munition for an RPG-7 anti-tank grenade launcher.
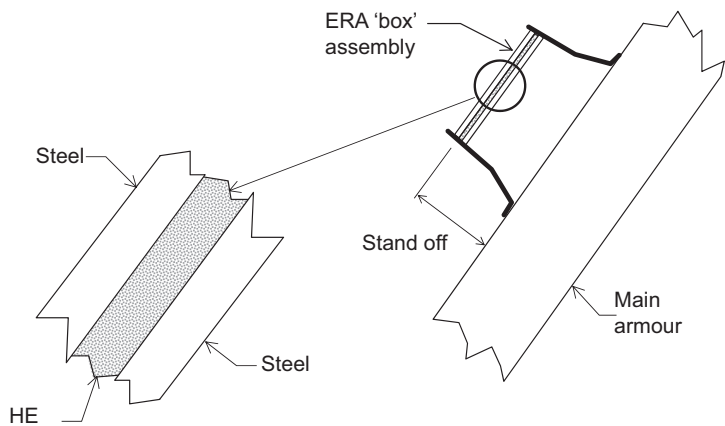
FIGURE 10.2   A conventional 'tri-plate' arrangement of ERA.

layers are usually contained in a robust mild steel housing to prevent operational and environmental damage. When the jet penetrates the outer housing and the first steel plate, it rapidly compresses the high explosive. The rapid compression of the explosive leads to detonation, propelling the steel sandwich plates apart. Frequently, the leading edge of the jet perforates through both plates before the flyer plate starts to move and therefore escapes any interaction. This portion of the jet is called the precursor, and its length is somewhat determined by the obliquity of the cassette and the velocity of the jet. It is this part, as will be seen later, that proves to be a challenge for lightweight AFVs. To maximize protection, it is necessary to accelerate the plates to a very high velocity to maximize the amount of material offered to the jet. The plate velocity depends on the mass of the plate and the type and mass of explosive— the first parameters to be varied in the pursuit of an efficient system. Finally, for optimum disruption, the ERA cassette is angled to the incoming threat. Therefore, the outer steel plate moves across the path of the jet thereby continually offering fresh steel to perforate—cutting a slot in the moving plate or plates. Disruption to the jet can also be caused at normal incidence (Brown and Finch, 1989), and this is due to the impact of inverted jet material on the tail of the jet as the jet perforates the armour (Rosenberg and Dekel, 1999). To have a substantial effect and be able to disrupt the jet at normal incidence, the explosive thickness should be at least twice the diameter of the jet (Brown and Finch, 1989).

A typical specification of an ERA system is outlined in Table 10.1.

TABLE 10.1

Typical Specification of an ERA System Required to Protect an Armoured Vehicle

No.	Specification	Reason	How Will This Be Achieved?
1	At least two flyer plates should be used.	So that interaction with the jet will occur when impacted at the bottom of the tri-plate or the top.	By using at least one sandwich structure.
2	The flyer plate should be moving as quickly as possible.	So that the mass of material interacts with the jet as much as possible.	By using a relatively large mass of high-performing explosive as the interlayer.
3	The ERA should be able to accommodate attack from a range of incidence angles including a normal-incidence strike.	So that the performance of the armour is not compromised.	By using at least two tri-plate assemblies of different angles stacked on top of one another.
4	The ERA should be set at a distance from the main armour.	So that the rear flyer plate can travel and interact with the jet.	By using suitable fixtures.
5	The ERA should not be detonated by small-arms fire or other easily deployable weapon systems.	So that it is not easily cleared.	By using explosive materials that are not sensitive to impact.
6	Collateral damage should be minimized.	So that the risk of injury to surrounding personnel is low.	By using soft or frangible plates.
7	The ERA should be water-tight and survive extreme environmental conditions.	So that its performance is not compromised by temperature changes, wind and rain.	Coatings and coverings.
8	The ERA should be easily removable for maintenance.	So that it is easily maintained.	By using suitable fixtures.
9	The ERA should be replaceable if it is activated.	So that the vehicle can maintain good levels of protection.	By using suitable fixtures.

ERA works best when there is an oblique angle between the incoming jet and the cassette. The tri-plate configuration also provides good protection. Other configurations are possible, but the outcome is often less than satisfactory. Figure 10.3 shows the advantage of an oblique tri-plate arrangement when compared to other configurations (Held, 2002). Even a single plate at an oblique angle can be reasonably effective at disturbing the jet when centrally impacted (Figure 10.3d). Equally, other researchers have shown that the disruptive effect of an ERA cassette is maximized when a heavier plate is positioned at the rear of the target (in an asymmetric configuration) (Brown and Finch, 1989).
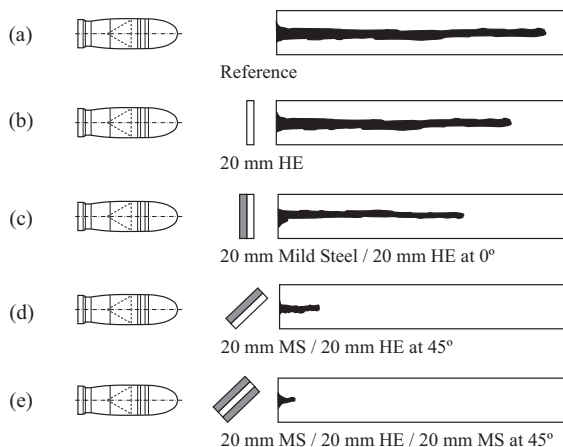
FIGURE 10.3 The effect of changing the configuration of the ERA on the residual depth of penetration into a steel reference target (Held, 2002).

10.2.1 HISTORICAL DEVELOPMENT

During 'Operation Peace for Galilee' in Lebanon in 1982, the IDF fielded its M60 main battle tanks (MBTs) with Blazer. This was the first bolt-on operational ERA package available for the market. Blazer was designed and developed by the RAFAEL Armament Development Authority. Blazer can be fitted to any tank and is simply fitted by welding threaded studs to the MBT's hull. The armour is then simply bolted onto the vehicle using the threaded studs. It is claimed that, when fitted to an MBT in appropriate locations, it can completely defeat the 125-mm diameter Russian Kolomna KBM 9K11 ATGW at 60° incidence as well as the RPG 7. The armour is, however, defeated if the missile contains more than a single warhead.

At that time, there was still considerable mystery surrounding ERA, and the raised studs observed on Centurion and M60 MBTs resulted in a number of speculative questions amongst military planners. Of course, the Soviets were not far behind in their use of ERA. The former Soviet Union has always been rather fond of applying ERA to their MBTs, and although much of the development of the armour occurred in the 1970s (soon after Held's discovery), it was not until the 1980s that they started using them on their tanks with the introduction of the 'Kontakt' series. A common form of the armour believed to have been fielded on the T 80 consisted of two explosive tri-plates within a single mild steel housing (see Figure 10.4). Two tri-plates are, of course, better than one. The additional tri-plate provides enhanced contact with the shaped-charge jet. It also provides some defence to tandem warheads. If the first ERA sandwich is able to defeat the first shaped-charge jet, the second ERA sandwich can be retained to defeat the main shaped-charge warhead. Further, with the two tri-plates orientated at different angles, it is possible to minimize the reduced performance that would have otherwise been caused by two parallel plates colliding. It was believed that this type of ERA was capable of reducing the effectiveness of a 93-mm diameter shaped-charge warhead by up to 98% when orientated at 70° obliquity.
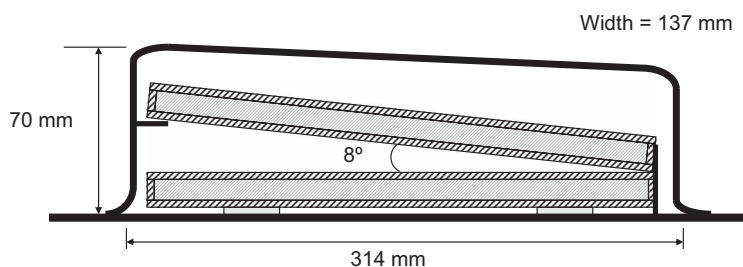
FIGURE 10.4   Early Soviet ERA twin-tri-plate assembly.
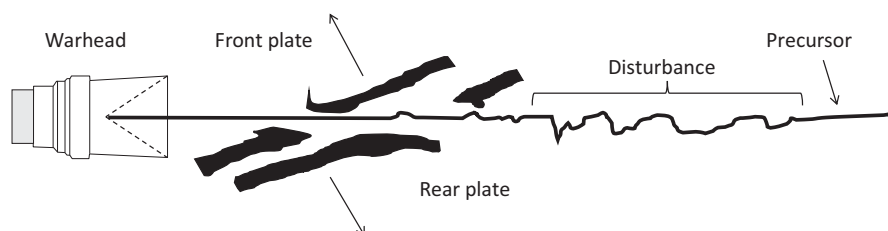
FIGURE 10.5   Perforation of ERA by a shaped-charge jet.

Typically, the explosive used was an RDX-based composition. An MBT would typically be fitted with between 200 and 300 boxes per vehicle.

10.2.2   THEORETICAL CONSIDERATIONS

In 1984, Mayseless et al. presented a theoretical model that showed how the flyer plates interacted with a fast-moving jet (Mayseless et al., 1984). They explained some of the characteristic patterns observed in flash X-rays of the ERA inducing a disturbance in the jet. Figure 10.5 shows a schematic of a shaped-charge jet perforating ERA. At the tip of the jet, there is an undisturbed region called the precursor. Moving back towards the warhead, there exists a region of disturbed jet material that appears to have an inherent waviness. Mayseless et al. observed that this disturbance was principally caused by the rear plate (they referred to this plate as the forward-moving plate or 'F-plate' — as it was moving in the same direction as the jet). That is, the F-plate was more effective at interacting with the jet and inducing a disturbance (i.e. see Mayseless, 2011). They also proposed a model that they termed the 'pebblestone model' as the jet's interaction with the plates was analogous to a pebblestone skipping on a pond.

On contact with the steel, the jet would cause the crater in the steel to grow at a velocity, v_e (Figure 10.6); this was estimated to be about half the jet velocity based on hydrodynamic penetration theory. The crater would grow until it was no longer stimulated by the jet material. Concurrently, the plate continues to move, being accelerated to the Gurney velocity (see Section 3.8.1) by the impulse delivered to it by the explosive. Eventually, the crater wall of the flyer plate will come back into contact
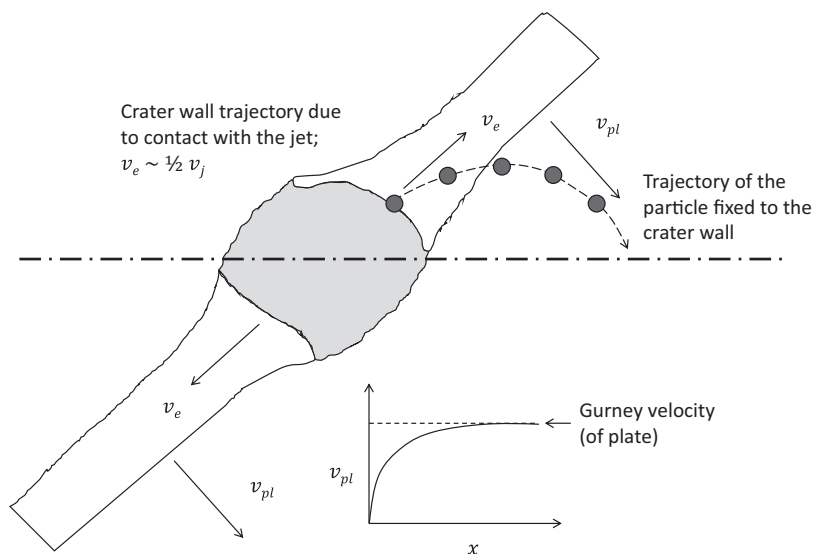
FIGURE 10.6 The 'Pebblestone model' to explain the jet 'skipping'. (Adapted from Mayseless, M. et al., 1984. Interaction of shaped-charge jets with reactive armor. *In: Proceedings of the Eighth International Symposium on Ballistics, Orlando, FL, 23–25 October.*)

with the jet, and the process repeats. So, again, the crater wall is accelerated out radially in a direction parallel to the plate until it escapes the influence of the jet. The plate continues to move and so on.

If the motion of a particle (or Lagrangian gauge point) that was attached to the crater sidewall was examined such that it was not eroded by the contact with the jet, then that particle would follow a parabolic motion due to the combination of crater growth and forward plate motion (see Figure 10.6). This process leads to the skipping motion that is seen in the disturbance of the jet.

Mayseless et al. deduced that the most important property in an ERA system was the mass flux (or mass flow) of material that was passed into the jet.

Held (2004) reported on a similar property to the mass flux, namely, the 'the dynamic plate thickness'. The dynamic plate thickness (Δs) is a rather arbitrary term that is a function of the plate velocity (v_{pl}), the interaction of time with the jet (Δt) and the angle between the jet and the normal to the plate. It is defined by Held (2004)

$$\Delta s = \frac{v_{pl}\Delta t}{\cos \theta} \tag{10.1}$$

The increase in plate velocity can be achieved by increasing the mass of the explosive in between the flyer plates. Held (2006) observed that increasing the mass of explosive increased the performance of 1-mm-thick flyer plates when penetrated by a shaped-charge jet. Although Held did see a reduction in penetration into a mild steel witness plate (see Section 10.2.6), it was noted that increasing the thickness

of the explosive beyond 3 mm resulted in a diminishing return in performance. Nevertheless, the overall improvement in performance was thought to be linked to the increase in plate velocities as the explosive mass was increased.

In summary, it is probable that there are several factors that come into play during the penetration of a shaped-charge jet into an ERA, and therefore, there are several parameters that can lead to the improvement in the performance of ERA systems. These can be summarized as

- The interaction between the jet and the cavity of the flyer plate (Mayseless et al., 1984)
- The interaction between the intensely turbulent explosive products and the jet (i.e. see Mayseless et al., 1984; Brown and Finch, 1989)
- The dynamic plate thickness, which takes into account the velocity of the flyer plate (Held, 2004).

In particular, Brown and Finch showed that the disruptive effect of the armour can be improved, even at zero-degree obliquity, as long as the explosive thickness is not too thin (at least 2 or more jet diameters thick), as mentioned earlier.

10.2.3   DEFEATING LONG-ROD PENETRATORS

The former Soviet Union was always interested in the defeat of armour-piercing fin-stabilized discarding sabot (APFSDS) rounds too. This interest was largely driven by the fierce tank battles that occupied the minds of military planners during the Cold War. Such a projectile travels much slower than the tip of the shaped-charge; however, they are made from heavy metallic tungsten–nickel alloys or depleted uranium alloys. The diameters of these rods are much larger too with diameters of 20–30 mm as opposed to 2–3 mm commonly seen in shaped-charge jets (see Section 3.3). Consequently, they are much more difficult to disrupt than the relatively thin jet of copper from a shaped-charge warhead. Nevertheless, some early Soviet-era armours claimed to be able to do this. Mostly, APFSDS-defeating ERA consists of heavier and harder plates and larger volumes of high explosives. Probably the most famous example is Kontakt 5, which has been deployed on T80Us and T90s. Some reports suggest that it adds 300 mm of equivalent RHA protection against APFSDS rounds by the propulsion of a 15-mm-thick front flyer plate. However, thicker plates mean that you have to use thicker explosive layers.

Held (1999) presented results that showed the effectiveness of a 40/10/25 system (corresponding to 40 mm of steel, 10 mm of high explosive backed by 25 mm of steel) against long-rod penetrators. His results showed that such armour reduced the residual penetration of a modern APFSDS projectile into a backing plate of RHA from 800 to 190 mm by the addition of the ERA.

Offering the flyer plates to the incoming projectile at an oblique angle is essential. This is because the main mechanism of defeating the long-rod projectile is the process of momentum transfer. That is, the flyer plate hits the projectile sufficiently hard so that it knocks it off course. More importantly, the rod is fragmented during the interaction, and therefore, more accurately, it is the fragments from the rod that

are knocked off course. The explosive itself has relatively little effect on the rod compared to the flying metal, and therefore, nearly all of the disrupting work needs to be done by the plates themselves. There is also the considerable risk behind armour debris too as such armour only breaks the rod into fairly large fragments. Despite the fact that these fragments of the projectile are deviated from their path with some degree of yaw, it is highly likely that a considerable mass of armour is required to 'mop up' these fragments. Consequently, this type of armour is only applicable to MBTs.

Very few manufacturers want to talk about how their armour responds to explosively formed projectiles (EFPs) that would be launched from top-attack or off-route mine weapons systems. Although many manufacturers claim very impressive non-initiation criteria, the EFP provides a particularly difficult problem for ERA. This is for two reasons. First, well-formed EFPs tend to have relatively flat noses when compared to the sharp ogival form of small-arms projectiles. This can create a situation analogous to a plate impact experiment where a high-intensity shock wave is formed in contact with the steel. They travel at relatively high velocities too and can reach impact velocities as high as 2000–3000 m/s. Both of these factors increase the propensity to cause shock initiation of the explosive in between the steel sandwich layers of the ERA. Secondly, EFPs tend to be short and fat projectiles as opposed to long and thin jets or rods. This makes it particularly difficult to disrupt the projectile by the moving steel plates unless the plates are sufficiently thick. Certainly, ERA that has been designed to defeat shaped-charge jets will have very little effect on this type of projectile, whereas those that have been designed to cope with large-calibre long-rod penetrators will fare better.

10.2.4 LOW COLLATERAL DAMAGE

So, if ERA is a very weight-efficient system, why has it taken Western countries so long to adopt the technology? In recent years, there has been a drive towards providing so-called low collateral damage reactive armour systems. This has mainly come about due to political and operational pressures. Reactive armour systems, by their very nature, can prove to be a risk to anybody that is happened to be standing around the AFV when it has been hit by an RPG (although arguably, the explosive and the fragments from the warhead alone would pose considerable danger to nearby individuals). It can also prove to be a problem for any low-flying aircraft too—mainly because of the high velocity that is reached when the plates are accelerated. A calculation using the Gurney equation reveals the velocities achieved possible from a simple tri-plate assembly.

Example 10.1

An ERA tri-plate assembly includes a $3 \times 150 \times 100$ mm plate of steel ($\rho_0 = 7800$ kg/m³) that is propelled vertically into the air by 3 mm of high explosive ($\rho_0 = 1770$ kg/m³). Calculate the velocity that it reaches. The plate velocity can be evaluated by using the well-known Gurney analysis (Gurney, 1943), and for a symmetrical sandwich, this can be calculated by

$$v_{pl} = \sqrt{2E}\left(\frac{M}{C}+\frac{1}{3}\right)^{-\frac{1}{2}} \tag{10.2}$$

where v_{pl} is the velocity of the flyer plate, M is the total mass of the flyer plates, C is the charge mass and $\sqrt{2E}$ is Gurney constant that is specific to the explosive composition used. Assume a $\sqrt{2E}$ of 2.93 mm/μs (a value that is used for RDX (Meyers, 1994)).

- The mass of a single steel plate and explosive can be calculated to be 0.351 kg and 0.0797 kg, respectively. Note that in this case, M is the *total* mass of the metal flyer plates, viz:

$$M = 2\times0.351 = 0.702 \text{ kg.}$$

- From Equation 10.2, the velocity of the flyer plates can be calculated to be 969 m/s. That is,

$$v_{pl} = 2.93\left(\frac{0.7020}{0.0797}+\frac{1}{3}\right)^{-\frac{1}{2}} = 0.969 \text{ mm/μs} = 969 \text{ m/s}$$

From this example, it can be seen that plates can fly at very high velocities and travel very large distances; ranges of up to 80–100 m are not uncommon. A possible sensitivity to this issue by Western armed forces is exemplified by the Challenger I and Challenger II. Originally, the Challenger I was fitted with ERA modules during Operation Desert Storm and subsequently to the Challenger II for operations in the Balkans. These were fitted to the lower glacis plate only. Consequently, any activity from the plates would merely lead to flyer plates being driven into the ground thereby reducing the risk to others. However, some argue that the risk to any surrounding personnel is largely unfounded because any shaped-charge warhead contains enough high explosive and hard casing material to kill all individuals in close proximity to the vehicle.

Modern ERA packages also must provide sufficient protection against small-arms ammunition, and the explosive employed must be sufficiently insensitive so that it is not detonated by fragments. Protection against heat sources such as that provided by exposure to napalm is also desirable.

Protection behind the main ERA cassette is also very important for lightweight vehicles that employ ERAs. ERAs do not stop the precursor portion of the jet. An MBT has relatively thick armour behind the explosive-reactive appliqué and therefore is capable of stopping all of the jet. Lightweight vehicles, on the other hand, generally have relatively thin hull armour; therefore, the jet is more likely to perforate. This is highlighted by the common threat to lightweight armoured vehicles—the RPG-7 grenade, which is capable of penetrating 300 mm of armour steel. Whilst ERA can reduce this penetration by 90%, this still leaves the jet penetrating 30 mm of steel—a thickness greater than that offered by the hulls of lightweight vehicles.

A workaround is simply adding more steel behind the ERA cassettes. This was done when ROMOR-A, a Royal Ordnance development, was fitted to Italian Centauro

vehicles for operation in Somalia in the early 1990s. However, adding sufficient steel to mop up the precursor of the jet increased the weight of the vehicles significantly. Reinforcing the vehicle's hull is also sometimes necessary when the ERA is fitted to thin-skilled vehicles such as the M113 or the FV432 (these are two similar AFVs). The rear plate will also have quite considerable kinetic energy and can cause a considerable shock effect to the vehicle's structure. Aluminium-hulled vehicles such as the M113 are particularly vulnerable as armour-grade alloys such as the 5083 type have a tensile strength that is somewhat lower than that of armoured steel. If the rear flyer plate hits the vehicle's aluminium hull with sufficient velocity, there is a risk that serious damage could occur to the armour.

Other advances in the use of ERAs include using polyethylene flyer plates as opposed to steel plates. This approach is behind Verseidag Ballistic Protection and Dynamit Nobel Defence's Composite Lightweight Adaptable Reactive Armour (CLARA). When each module explodes, the flyer plates shatter into relatively harmless fibre shards (Ogorkiewicz, 2007). Consequently, the risk to dismounted troops and civilians in the local area of the vehicle is considerably reduced. Each CLARA bolt-on module weighs 18.5 kg and is only 100 mm thick excluding the stand-off required. CLARA has also been tested on a Rheinmetall Marder 1A5 Infantry Fighting Vehicle using a surrogate RPG warhead. Although the surrogate warhead was capable of penetrating 320 mm of RHA without any reactive armour protection in place, the jet was almost completely destroyed by the action of CLARA with only 6 mm of penetration into the steel armour.

Kaufman and Koch (2005) used a 50-mm diameter shaped-charge warhead to test a variety of candidate flyer materials. They examined a variety of materials including steel, aluminium, polycarbonate, polyethylene and a GFRP as candidate ERA flyer plates. Their work showed two important results. Firstly, the protection efficiency of the low-density materials is good compared to steel, and secondly, to reduce the collateral damage, it is advantageous to use brittle materials, producing small and lightweight fragments. These results are consistent with a sound theoretical and long-understood principle. The fact that low-density materials are in fact useful at stopping shaped-charge jets is not new. Using plates that are broken into small and lightweight fragments is also attractive, and that is why others have chosen to use flyer plates constructed from brittle materials such as ceramic and glass (Koch and Bianchi, 2010; Hazell et al., 2012). Smaller fragments will decelerate faster in the air than heavier fragments and consequently will pose less of a risk to personnel.

10.2.5 Explosive Compositions

The use of low-sensitivity explosives in ERA is important in maximizing commercial gains that can be made in the armour business. Many countries, such as the United Kingdom, are only prepared to adopt insensitive munition-compliant products in service. Explosives that are very difficult to accidentally initiate are almost universally cast polymer bonded explosive (PBX)-based materials. These materials are very difficult, if not impossible, to initiate unless a very violent stimulant such as a shaped-charge jet penetrates them. Due to the very high-pressure region incurred in the explosive composition by the jet, it is relatively simple to guarantee initiation when desired whilst at the same time remaining safe at all other times. There are a number of tests that are done to check this. The most stringent of tests are done
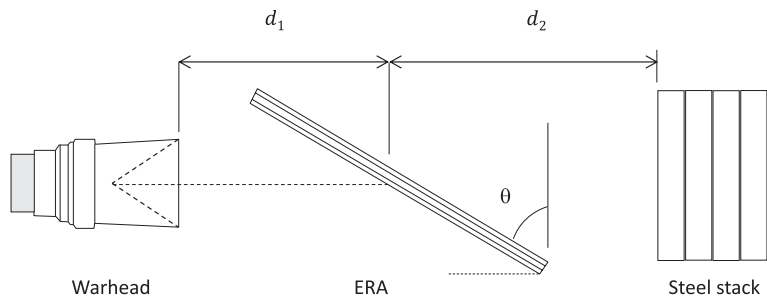
FIGURE 10.7 Standard ERA test.
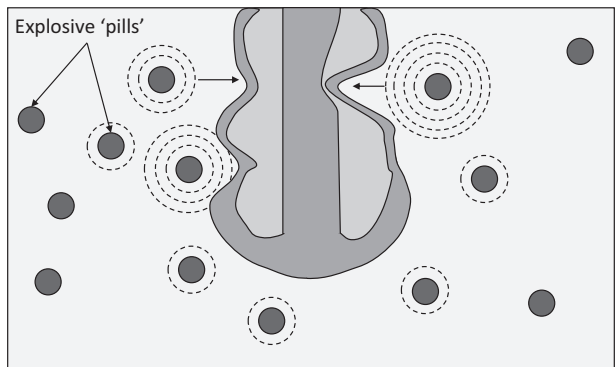
FIGURE 10.8 Explosive 'pill armour'. (Adapted from Held, 2002.)

according to STANAG 4496 where a steel fragment-simulating projectile is fired at the armour at around 2500 m/s to test whether the explosive is shock initiated. This is the worst-case scenario for an impact from high-velocity fragment that has been propelled from a 155-mm HE shell.

10.2.6 TESTING AND PERFORMANCE IMPROVEMENT

Testing of the ERA assemblies is not always that straightforward as warhead quality can be quite variable. The commonly used approach used to evaluate the ERA's performance is by using the standard depth-of-penetration approach (see Chapter 12). A common set-up is shown in Figure 10.7 where the performance of the armour is evaluated by measuring the depth of penetration in the steel stack. Sometimes, it is advantageous to insert a thin (~5-mm) steel plate set at some distance from the ERA cassette to 'clean' the front of the jet and to improve consistency.

10.2.7 EXPLOSIVE 'PILL' ARMOUR

A modification of the tri-plate arrangement discussed above is the explosive pill armour concept whereby explosive pills (or pellets) are integrated into a plate (Held, 1993). This can be achieved by building up multiple layers of material in between

which explosive pills are located in pre-machined recesses. As the shaped-charge jet penetrates, the shock imparted to the target during penetration initiates the detonation of the pills, which go on to disturb the jet as the material is driven into the jet axis. See Figure 10.8.

Although the explosive pill armour is not as high performing as ERA, it has the advantage that little debris is projected from the armour during penetration and therefore the collateral damage is minimized.

10.3   BULGING ARMOUR

The safety and lethality implications of ERA have led to the development of a reactive armour system that employs an inert rather than an explosive interlayer material. Non-ERA consists of an inert low-density interlayer material sandwiched between two parallel steel plates. This concept was first patented by Held in 1973. The plates do not separate from the armour cassette at high velocity and therefore do not pose a threat to dismounted troops and civilians. However, because the velocity of the plate separation is relatively small when compared to conventional ERA, it does not perform as well.

A generalized view of how this system works was postulated by Gov et al. (1992). A shaped-charge jet that perforates the outer layer of steel deposits considerable energy into the interlayer. The interlayer is compressed by a hemispherical 'piston' that consists of the bulging front-plate material backed by the eroding jet. The filler acquires both internal energy as it compresses and kinetic energy as it moves axially and radially away from the penetrating 'piston'. The compressed interlayer presses against the rear plate of the cassette along the axis of jet penetration and accelerates it. This portion of the rear plate is also accelerated further when the jet comes into contact with it. Furthermore, a shock wave emanates from the region of local compression and propagates in a radial fashion away from the central axis accelerating the plates apart. For a cassette placed at a relatively high angle of obliquity, the plates that are accelerated apart come into contact with the shaped-charge jet and disturb it thereby reducing its lethality.

The main defeat mechanism is due to the interaction between the steel plates and the shaped-charge jet—it is, therefore, advantageous for the holes that are formed by the jet to be as small as possible. This can be achieved by using high-hardness steels to ensure that the hole growth is limited as the jet perforates the front plate. Other factors include the thickness and choice of the interlayer materials (Thoma et al., 1993), which can greatly affect the bulging velocity of the plates and hence the interaction with the jet (Rosenberg and Dekel, 1998). For example, low-density polymers such as Dyneema® have been previously used as effective interlayer materials (Held, 2001).

Because of their relatively simple construction, these passive sandwich assemblies are relatively cheap and easy to apply. However, because these systems only work by minimizing the residual penetration achieved by a jet after perforating the armour, they are often applied in multiple assemblies or in tandem with other effective armour systems.

However, they have also been shown to provide notable disruption to scaled long-rod penetrators. For these threats, as the bulging ensues, the expansion of the interlayer causes movement of the steel plates thereby disrupting the rod (Fras, 2021).
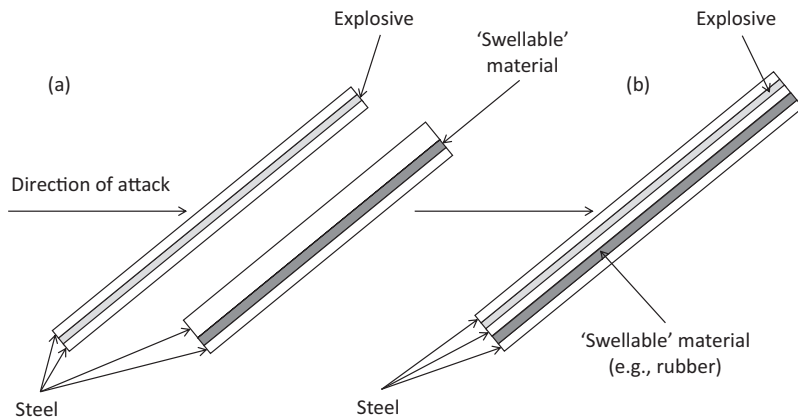
FIGURE 10.9 Two passive-reactive cassette options as suggested by Benyami et al. (1991). (From Benyami, M. et al., 1991. Combined reactive and passive armor. *In: Google Patents*. Israel: The State of Israel, Ministry of Defense, Rafael Armament.)

10.3.1 The Passive-Reactive Cassette Concept

A notable improvement to ERA cassette design involved incorporating a bulging armour assembly with the conventional tri-plate ERA assembly (Benyami et al., 1991). This has been shown to lead to a reduction in the length of the precursor element of the jet (Brand et al., 2001). The diagrams of two possible configuration options are shown in Figure 10.9.

10.4 LIQUID-FILLED COLUMNS AND COMPRESSIBLE TARGETS

Held (1993) proposed a form of protection against shaped-charge jet using liquid-filled columns (or containers). Liquids have the advantage in that they are mechanically simple in structure and generally low cost. In some ways, these work in a similar way to bulging armour in that it is possible to use the shock wave formed during the penetration process to our advantage by causing the material to interfere with the jet. The mechanisms of shaped-charge defeat are shown below in Figure 10.10. Initially, the shaped-charge jet penetrates the liquid-filled column. The 'supersonic' penetration (noting the density mismatch between the penetrating jet and the target liquid) results in a shock wave emanating from the jet/crater interface. This shock wave reflects off the rigid containment and proceeds to accelerate the liquid material into the jet. This mechanism is similar to the heavily confined glass and layered ceramic armour targets discussed in Section 8.12.

It is worth noting that certain low-density materials can exhibit excellent resistance to penetration by virtue of their compressibility. That is, the capacity of the material to be squashed by a given pressure, usually due to a shock. This is even without the benefit of shock reflections from strong containment as discussed above. For highly compressible targets, work is expended by the penetrator to compress the sample (so-called pressure–volume, or PV work) as well as for the formation of the shock wave. White III et al. (1982) demonstrated this effect by comparing the
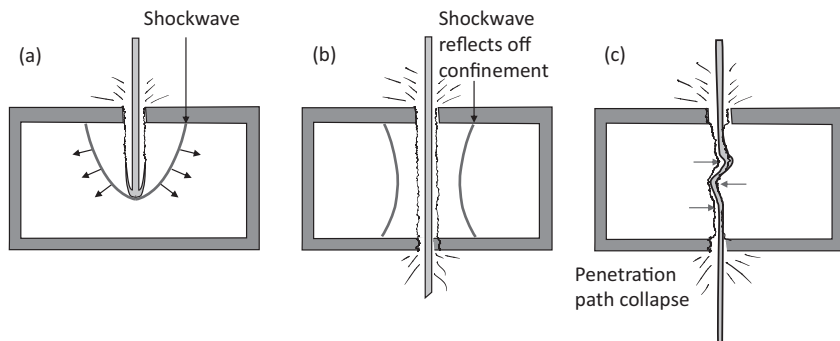
FIGURE 10.10 The 'liquid-filled' columns concept showing: (a) initial penetration of the jet into the fluid region, (b) the reflection of the shock wave from the containment and, (c) the liquid contents being 'driven' into the shaped-charge jet by the shock wave and causing interference.
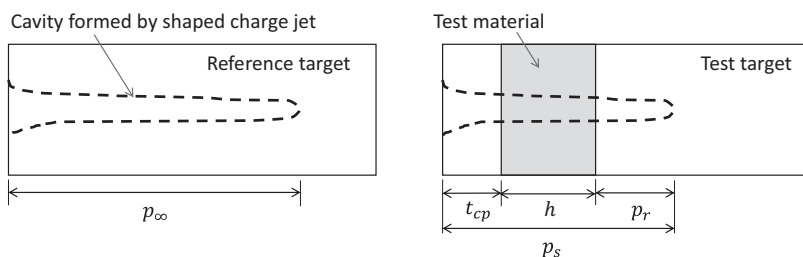
FIGURE 10.11 Definition of parameters to establish T_e for shaped-charge jet penetration studies.

residual penetration of a shaped-charge jet into mild steel (type 1020) after penetrating a 76.2-mm target containing three materials: glycerol, methanol and Plexiglass. Mild steel was also compared, and a 25-mm thick cover plate (4340 steel) was used in each case.

There are several ways to evaluate the ballistic resistance of materials (see Chapter 12), and White III et al., used an 'effective thickness' measure. This is the sample's equivalent effective thickness of the reference target material and is evaluated as follows.

Consider Figure 10.11. The definition of effective thickness is given by

$$T_e = \frac{p_\infty - p_{st}}{h} \tag{10.3}$$

where

p_∞ is the penetration into a semi-infinite reference target (steel)

p_{st} is the total penetration of the steel (including the cover plate and the residual penetration) in the test target.

h is the sample thickness in the test target.

$$p_{st} = t_{cp} + p_r = p_s - h \tag{10.4}$$

Therefore, substituting,

$$T_e = \frac{p_\infty - p_s + h}{h} \tag{10.5}$$

and

$$T_e = 1 + \frac{p_\infty - p_s}{h} \tag{10.6}$$

Another way to evaluate such penetration effectiveness is to consider the areal density of the reference material and compare it with the area density of the material penetrated in the test target (see Chapter 12). This is given by:

$$E_m = \frac{\rho_{st} p_\infty}{\rho_{st}\left(t_{cp} + p_r\right) + \rho_h h} \tag{10.7}$$

where ρ_{st} and ρ_h are the material densities of the steel reference material (and cover plate) and sample, respectively. In some ways, this is a simpler and more straightforward metric. Both metrics are shown with relevant data in Table 10.2.

Probably the most important metric in Table 10.2 is the ratio of T_e/T_{hd} where T_{hd} is the sample equivalent effective thickness assuming pure hydrodynamic penetration. This is given by,

TABLE 10.2
Shaped-Charge Jet Penetration Data into Four Low Strength Materials

Material	Density, ρ_h (g/cc)	Isothermal compressibility $(10^{-12}\ Pa^{-1})$	p_r (mm)	$T_e{}^a$	T_{hd}	T_e/T_{hd}	E_m
Methanol	0.792	1210	92.7±6.1	0.82	0.32	2.58	1.53
Plexiglass	1.18	150	74.7±4.3	1.06	0.39	2.72	1.77
Glycerol	1.26	220	130.8±0.2	0.32	0.40	0.80	1.08
1020 steel	7.83	9.2	79.0±2.3	1.00	1.00	1.00	1.00

Source: Adapted from (White III et al., 1982). The value of p_r was measured for the 50% most penetrating jets to avoid bias for poor performing jets.

[a] To calculate T_e, White III et al., corrected the thickness of the sample from 76.2 to 64.5 mm in order to partially account for penetration reduction occurring if the sample was a vacuum. The data presented here is based on the original value of 76.2 mm. The conclusions remain the same, however.

$$T_{hd} = \sqrt{\frac{\rho_h}{\rho_{st}}} \qquad (10.8)$$

where ρ_{st} and ρ_h are the material densities of the steel reference material (and cover plate) and sample, respectively. The high values of methanol and Plexiglass imply that the penetration resistance values of these materials are at least twice the expected values based on simple hydrodynamic theory. This is also revealed in the single metric, E_m, which shows that on a weight-by-weight analysis, both methanol and Plexiglass perform very well. The fact that Plexiglass performed well relative to steel was unexpected and White III et al. (1982) suggested that other factors are coming into play for this material. These may include cavity rebound and/or brittle fracture, or scission of chemical bonds at high pressure, for example. Irrespective, this work showed that methanol, a simple liquid, can have high penetration resistance.

Remarkably, diesel has also been shown to be an excellent resisting penetration by shaped-charge jet penetration (White III and Wahll, 1981). The implications of this mean that over the years, armoured fighting vehicle manufacturers have generally moved the fuel from crew spaces and placed it within thick cells between a thin outer armour shell and a thick inner armour hull. This provides much-needed added protection (Kennedy, 1983). On the other hand, lithium-ion batteries are more susceptible to combustion and not so protective and therefore it will be a long time before we see the advent of the all-electric AFV!

10.5 ELECTRIC AND ELECTROMAGNETIC DEVELOPMENTS

In recent years, it has been realized that it is possible to disrupt a shaped-charge jet by virtue of applying a short burst of electrical energy through it. This was first proposed by Walker (1973). The concept is shown in Figure 10.12. The system works by delivering a large electrical current ($\sim 10^2$ kA) through the jet when it makes contact
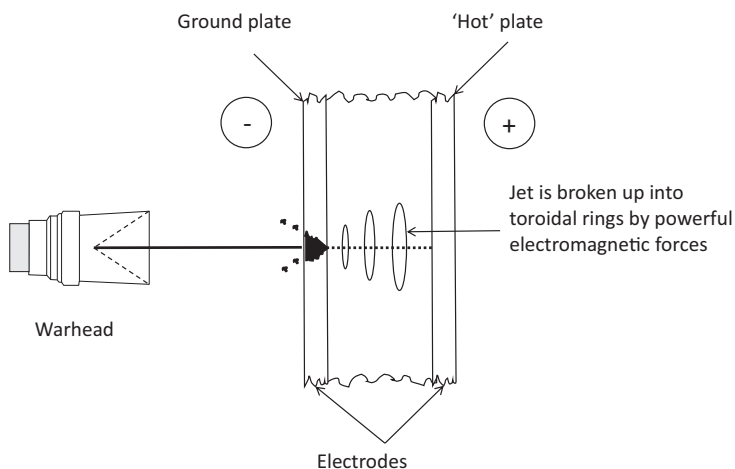
FIGURE 10.12 The electric armour concept.

with the 'hot' plate, as seen in Figure 10.12. Essentially, the jet acts like a switch—making contact with the outer ground plate and the inner 'hot' plate simultaneously. This results in powerful electromagnetic forces disrupting the jet causing it to split up into discrete toroidal rings through a process called magnetohydrodynamic pinch (Littlefield, 1991; Shvetsov et al., 1999; Swatton et al., 2001). Experimental evidence has shown that these rings expand with a radial velocity of up to 200 m/s when a 200–250-kA current is applied to the jet (Appelgren et al., 2010). A lesser disruptive effect through lateral dispersion also occurs arising from the forces that occur due to the interaction between the current in the jet and the magnetic field generated by the plates. The dispersed/toroidal parts of the jet are then stopped by the vehicle's base armour.

Other concepts include using electromagnetic energy to propel steerable electromagnetically driven flyer plates into the direction of an incoming threat (Sterzelmeier et al., 2001). The concept is similar to ERA, except that in this case, the plates are electromagnetically driven. These are more akin to hard-kill defensive aid suites (DASs) that will be discussed next.

10.6 HARD-KILL DAS

A relatively modern phenomenon in the protection industry is the development of intelligent protection systems that are able to detect, track and engage an incoming projectile threat. This is not a trivial task as many of the weapon systems are travelling towards their target (i.e. you) at very high velocity. To illustrate how difficult this is to engineer, Table 10.3 lists several anti-tank weapon systems and their velocities and the time they take to travel 500 m (assuming that this is a mean engagement distance). Now, clearly, there is going to be a velocity drop-off due to air drag; however, these data give a good rough order of magnitude in terms of the required response time that one has to defeat the incoming threat.

Notably, for APFSDS projectiles travelling at 1500 m/s (a typical muzzle velocity for these types of projectiles), a system will need to respond, identify the threat and track the incoming projectile and deploy a countermeasure (or 'effector') within a very quick timeframe.

TABLE 10.3
Typical Anti-Tank Weapon Systems, Their Velocities and the Time Taken to Travel 500 m

Threat	Typical Mean Velocity (m/s)	Time Taken to Travel 500 m (s)
M72 LAW	145	3.45
Swingfire	185	2.70
RPG-7	295	1.69
BGM-71 TOW	300	1.67
AGM-114 Hellfire	425	1.18
APFSDS	1500	0.34

An integral part of the active protection system is the sensor technology employed to detect and track the threat. The sensors are required to be sensitive enough to detect the threat at a suitable distance so that the active protection system has time to respond. Detection distances of up to 30–50 m are often claimed. A common way of detecting the threat is by using millimetric-wave radar. The low wavelength of this type of radar enables good resolution to the extent that even the distinguishing features of a threat are observable. However, using such active radar continuously can have the adverse effect of advertising your position to the enemy. Consequently, radar is often cued into action by passive infrared sensors that look for a flash associated with a missile or gun-launched penetrator.

Ultimately, all this information needs to be processed somehow, and consequently, all systems are fitted with an onboard computer. If established technology is used, the electronic components in themselves can be relatively cheap. However, all systems need to be suitably rugged for the military environment, and it is this requirement that often pushes the price up. In particular, today's modern army places high demands on its equipment due to the variety of extreme locations and circumstances in which battles are fought.

There are two principal ways of attacking an incoming fast-moving threat. This is achieved using an 'effector' and can be done in two ways:

a. Delivering a directed explosive blast towards the object (Lidén et al., 2013), or by
b. Delivering a fast-moving projectile/fragment to intercept the incoming object

Delivering a directed explosive blast is more attractive for active protection applications for two reasons (Heine et al., 2013):

1. The very fast reaction times can be achieved from the detonation of the explosive to the propagation of the blast wave over several metres. This means that an impulse can be offered to the flying object in a very short period of time.
2. As the blast wave decays rapidly, there is less likely to be any collateral damage problem that would otherwise occur if the effector was a projectile.

10.6.1 PROJECT DASH-DOT

Project Dash-Dot was a 1950s endeavour to develop a suitable tank defence against high-velocity projectiles. The concept originated at Picatinny Arsenal although later development occurred by the US Ordnance Corps at the Diamond Ordnance Fuze Laboratories. Figure 10.13 summarizes the early concept. The system, which was revolutionary for the time, comprised of (Straub et al., 1960):

1. An array of defending shaped charges located on the tank periphery orientated to intercept and defeat an approaching warhead.
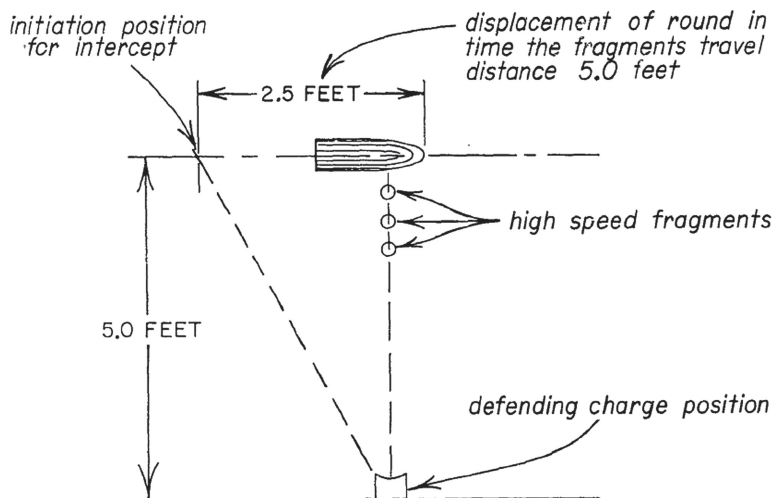
FIGURE 10.13 Project Dash-Dot. (Reproduced from Straub et al., 1960.)

2. A sensing computing system that would detect the incoming warhead at around 1 m from the tank, compute its trajectory, decide on whether or not it was dangerous, select a defending charge in the most appropriate location and transmit a firing pulse to that charge at the correct time to defeat the attacking warhead.

Previous success in using shaped charges had been demonstrated in 1956. These comprised of 'linear cutting charges' (otherwise known as Picatinny Arsenal Devices, or 'PADs') that were 2 in. wide (50.8 mm) and 10 in. (254 mm) long with either a Fe or Cu liner. The test explosive was Comp B, with a mass of 0.73 kg. These charges offered considerable promise for protection against chemical energy ammunition of the HEP and HEAT types of 90 and 106 mm calibre, respectively. Whereas against 90 mm armour-piercing ammunition, the defence was less satisfactory (Pillersdorf, 1956).

The project was terminated due to problems with the detection system. Nevertheless, although at the time the detection and tracking system did not lend itself to tank defence, the report noted that the approach used was well suited to solve other defence problems.

There have been a few notable active protection systems deployed on armoured vehicles. Some are now briefly discussed.

10.6.2 Drozd

One of the earliest active protection systems fielded and probably the best known is the Drozd or 'Thrush'. This system was first fielded in the early 1980s by Soviet forces. The system was developed by the Konstruktorskoe Buro Priborostroeniya (KBP) Instrument Design Bureau to defeat North Atlantic Treaty Organization

(NATO) missiles such as the Tow and Milan. Both missiles deploy precursor shaped charges, thereby potentially rendering ERA less effective. Therefore, having the ability to kill the missile before contact with the armour is an attractive ability. The Drozd system uses two millimetric-wave radar antennae mounted on each side of the turret to detect an incoming missile. When the radar system detects an incoming missile, an unguided 107-mm diameter rocket is launched, and at a calculated time, the rocket detonates propelling a cone of fragments towards the flight path of the incoming missile. In the vertical plane, the protection zone given by the system is +20° through to −6° and in the horizontal plane, ±40°. The system consists of a full complement of eight missiles permitting eight separate defences; crew replenishment time is 10 minutes. The original Drozd system was only fitted facing forwards of the turret leaving the flanks and rear of the vehicle vulnerable to attack. A subsequent system, Drozd 2, comprises a total of 18 individual launch tubes arranged around the turret. Each of these launch tubes covers an arc of 20° and from −6° to +20° in the azimuth. The updated system apparently weighs no more than 800 kg making it a possible system for lightweight armoured vehicles. The system is not activated by small-arms fire and can happily deal with incoming missiles travelling at between 50 and 700 m/s.

The Drozd system does highlight one of the more unfortunate aspects of active protection systems—the risk of collateral damage. Consequently, the Drozd system is fitted with an interlock system so that the unguided countermeasures cannot fire when the hatches of the tank are open. The ejection of a cone of small fragments from a detonating munition poses a very dangerous risk to dismounted troops or civilians. Some would argue that this is largely a moot point because any personnel within the vicinity of the vehicle would be killed by the blast and fragments from the incoming warhead anyway. However, it is unclear as to the extent of the danger radius for the Drozd system.

The sort of fragmenting munitions that are fired from the active protection systems can propel small fragments up to velocities of 1500 m/s, and consequently, they can be lethal to quite large distances. If explosively driven steel plates are used instead of fragments, then distances of up to 100 m can be achieved from relatively thin layers of explosive.

10.6.3 ARENA

The Arena system was developed in the 1990s partly as an evolution of the Drozd system. This system can weigh up to 1300 kg depending on the vehicle that it has been applied to, and it has been exhibited on the T 80 Main Battle Tank and the BMP 3 infantry fighting vehicle. A radar mounted towards the rear of the turret detects the incoming missile at around 50 m from the vehicle. An onboard computer then decides which of 22 projectiles to launch towards the incoming threat. Like the Drozd 2 system, there is potentially 360° coverage around the vehicle; however, there is a small dead zone behind the radar making attack from behind a dangerous possibility. Moreover, the radar system is, due to its size and prominence, a vulnerable asset to the vehicle. It is supported by three legs that are most probably susceptible to damage by sustained heavy machine gun fire. Whether or not the main unit is
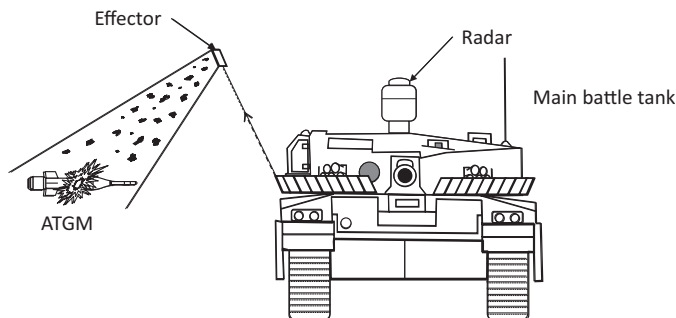
FIGURE 10.14   The ARENA system in operation. Fragments are projected to defeat the incoming anti-tank guided missile (ATGM).

susceptible to heavy machine gun fire is unknown. A schematic of its operation is shown in Figure 10.14.

10.6.4   TROPHY

It is not just the former Soviet states that have been heavily involved in the development of active protection systems. In 2004, Israel revealed the Trophy active protection system that had been in development for approximately 10 years.

The Trophy active protection systems have been touted as defeating all types of anti-tank guided missile systems as well as rockets at a significant distance from the platform. There are two key parts to this active protection. The radar system is coupled to four-panel antennae that are located at the front and rear sides of the vehicle that is being protected. This configuration can supposedly detect top-attack munitions. The other system of importance is the hard-kill system. Relatively few details are known of how the active protection system works; however, it is rumoured that the hard-kill part of the system works on firing a focused 'beam' of explosive energy (Ogorkiewicz, 2007). That is, an explosive charge is detonated that is focused towards the incoming threat. This seems plausible as the developers have claimed that the missile can be defeated at significant distances from the vehicle with minimal collateral damage. If a fragmenting munition is used, then collateral damage becomes a problem, as discussed in Section 10.2.4. It is also known that the system will only be activated when a direct threat to the vehicle is detected. Missiles that are predicted to miss the vehicle are deliberately ignored. The further attractive feature of Trophy is that it weighs less than 500 kg—considerably lighter than Drozd or Arena. And, it can be fitted to lightweight vehicles too—such as a high mobility multipurpose wheeled vehicle (HMMWV) (Foss, 2011).

10.6.5   IRON FIST

Iron Fist is a hard-kill active protection system developed by Elbit Systems Ltd. The system has been designed by keeping lightweight-to-medium vehicles in mind. The effector comprises of a small canister-looking object that is propelled from tubes

located on the vehicle. Fins are deployed on exit from the tube to stabilize the trajectory of the effector as it heads towards the incoming threat. The casing is made from a lightweight material to minimize the collateral damage risk, and the system solely relies on the shock wave from a powerful explosive to neutralize the incoming threat. Heavier systems are reported to be efficient at destroying tank rounds such as HEAT and APFSDS (Anon, 2019). The lethality of the latter is reduced by inducing significant yaw into the projectile (see Section 10.6.6).

10.6.6 DEFEATING LONG-ROD PENETRATORS

The ability of an active protection system to defeat long-rod penetrators is a particular engineering achievement. Unlike missiles and rockets, the projectile consists of a single lump of dense metal, usually depleted uranium or a tungsten alloy, the performance of which cannot usually be compromised by small fragments. One possible way of defeating a long-rod penetrator is by using the force of a shock wave to deflect the incoming projectile some distance out from its target. There are a number of technical challenges that need to be overcome to achieve this; here are a few:

1. High-fidelity detection and tracking systems are required to detect and track the incoming projectile that potentially will be travelling at between four and five times the speed of sound.
2. The countermeasure needs to be positioned very close to the penetrator at detonation as the amount of energy delivered to the projectile by the shock will rapidly diminish with distance.
3. The composition of the explosive must be such that it can withstand setback forces resulting from the acceleration to the required relatively high intercept velocities.

The main purpose is often to induce yaw into the incoming rod where the yaw is defined as the angle between the trajectory of the projectile and its axis (see Figure 10.15). Even small angles of yaw can lead to dramatic penetration ability (Hohler and Behner, 1999; Anderson, Jr. et al., 2013). Hohler and Behner showed that for a rod with a length/diameter ratio of ~20, and a yaw angle (α) of 20°, the penetration into a steel target was reduced by 60% compared to a non-yawed rod—see Figure 10.15.

Other methods that have been discussed in open forums include the use of explosively driven projectiles of relatively high mass. These are again designed to induce a small degree of yaw or alternatively cause the rod to fracture—thereby reducing its effective length offered to the target (see Figure 10.16). A sufficient impulse delivered to the side of a flying rod can potentially cause this effect. This method is particularly attractive if the rod is made from depleted uranium. This is because depleted uranium is less stiff than the commonly used tungsten alloy materials and consequently will mean that it should be easier to induce failure by bending.

Once the rod has been fragmented, the effectiveness of the rod is reduced considerably. This is due to two principal reasons. Firstly, the penetration depth is very much dependent on the length of the penetrator, and consequently breaking the rod up will reduce the amount of penetration in the target. Secondly and perhaps more
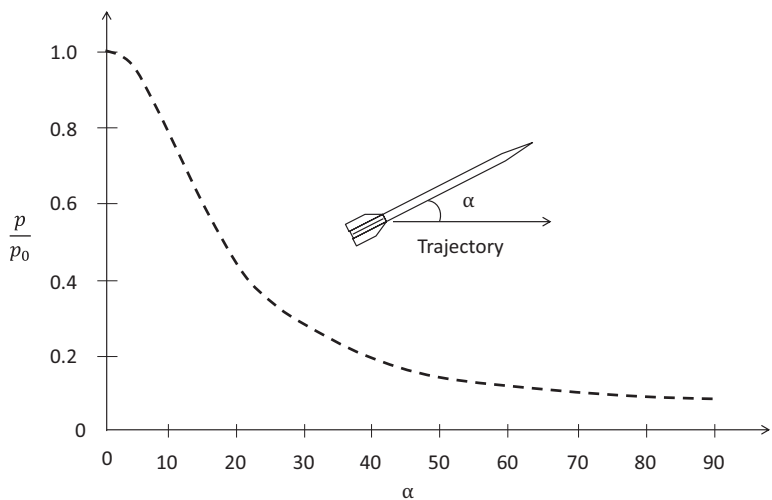
FIGURE 10.15 The drop-off in normalized penetration into steel (p/p_0) as the yaw angle of penetrator (α) is increased, where p is the penetration measured into a semi-infinite steel plate where yaw is preferentially induced before impact and p_0 is the penetration into the steel with no yaw ($\alpha=0$). Inset: a diagram of a yawed projectile. (Adapted from Hohler, V., and Th. Behner. 1999. Influence of the yaw angle on the performance reduction of long-rod projectiles. *In: Proceedings of the 18th International Symposium on Ballistics, San Antonio, TX, 15–19 November.*)
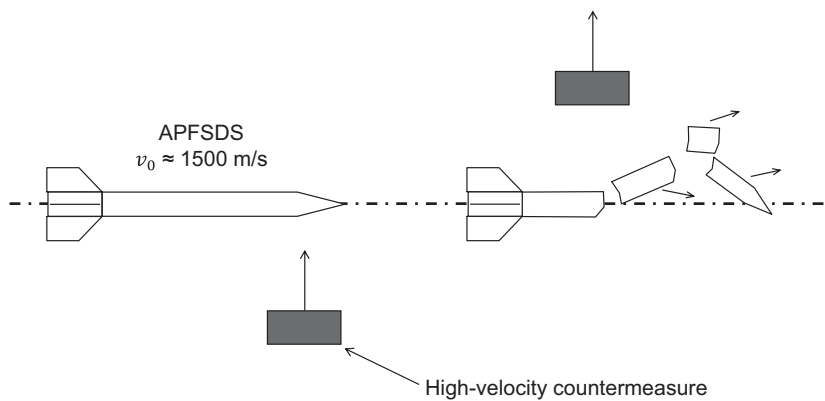
FIGURE 10.16 Inducing fragmentation in an APFSDS round by delivering an impulse.

importantly, the other advantage of fragmenting the rod is that the impulse delivered to the rod will induce yaw in the fragments. This leads to a significant reduction in penetration depth. Of course, this also highlights the importance of armour to 'mop up' the fragments that still could be lethal despite their effectiveness being dramatically diminished.
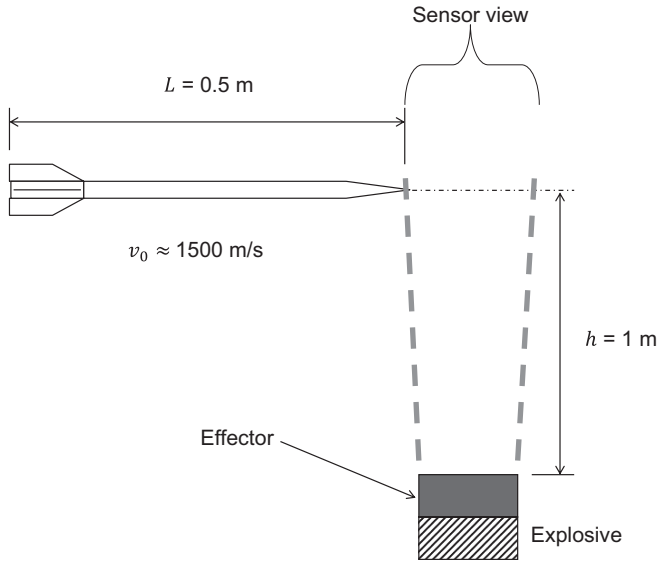
FIGURE 10.17 A hypothetical design of a hard-kill countermeasure system designed to engage an APFSDS projectile.

So, how far away do I need to be to adequately engage an APFSDS projectile? Let us consider this problem:

Consider a hypothetical case where the sensor view is restrained to just overhead of the countermeasure. The problem is described in Figure 10.17. The system is required to engage with a 0.5-m long APFSDS projectile and needs a tungsten countermeasure to contact with the projectile halfway along its length. What is the average velocity required by the countermeasure to make contact with the rod, assuming that the rod passes over at a height of 1 m at a velocity of 1500 m/s?

Firstly, the time taken for the rod to traverse 0.25 m (half its length) is given by $t = s/v_0$ (where s and v_0 are displacement and projectile velocity, respectively). Therefore, $t = 167 \times 10^{-6}$ s. So, the tungsten countermeasure needs to travel 1 m in 167×10^{-6} s (167 µs). Basically, it needs to be accelerated to a truly enormous velocity.

10.6.7 A DEVELOPING TREND

It is possible to use a deployed airbag to detonate an incoming RPG (Fong et al., 2007). Although using an airbag to defeat threats is not a new idea, it is an interesting development as such a system considerably reduces the collateral damage risk. Similar systems have been suggested for providing hidden yet rapidly deployable protection against small-arms bullets. These systems principally use the relative speed of the threat and the airbag to cause a disruptive effect. In the case of the RPG, this will involve detonation of the high explosive at a decent stand-off so that the shaped-charge jet does not perforate the armour. The concept

that was presented by Fong et al., involved a 4-in. tactical airbag munition that was deployed to intercept the incoming RPG. The airbag tested was from a Ford Taurus. Due to the spherical nature of the deployed airbag, the system is aerodynamically stable, which is useful when you are trying to hit a projectile travelling at high velocity.

The airbag approach is very attractive due to the reduction of the risk of collateral damage. This is particularly true if the airbag can disable the fuze system.

10.7 SUMMARY: WHAT ABOUT THE FUTURE?

So, what of the future? Sadly, we are still a long way from the magical invisible shields of *Star Trek* fame, but there are still some exciting possibilities that are available to us from known science.

We have seen with electric armour that it is possible to use electricity to defeat shaped-charge jets, but what about using electrical energy to defeat an incoming missile before it strikes the vehicle? Projectiles can, for example, be electromagnetically driven towards the incoming threat. This can be achieved by adopting a design similar to a linear motor. Linear motors are commonly used to propel trains to high speed, although the acceleration required in these applications is far less than would be desired from an active protection system. Similar systems have been proposed for weapon systems such as coil guns. With this system, electromagnetically generated forces are able to accelerate the projectile to a high velocity. The advantage of this type of system for active protection systems is that it affords the possibility of accelerating projectiles of various geometries including meshes or grids. This is unlike explosively driven projectiles that require a large surface on which the explosive products can act. Therefore, it is possible to use a lower mass projectile that reduces the risk of collateral damage whilst maximizing the possibility of contact with the threat. With grids or meshes, a larger surface area is afforded for the same mass as a relatively small solid plate, and therefore, it is possible to maximize the probability of contact with the threat.

There are a number of challenging problems to overcome before we will see such a system fielded—most notably a suitably small capacitor bank that is able to deposit the large amount of electrical energy that is required to drive a projectile large enough to have a disruptive effect.

Other possibilities of using electricity to defeat incoming threats include the use of lasers. There are two notable programmes that have been developed with US funding: Tactical High-Energy Laser and the US Air Force's Airborne Laser. Both are designed to destroy missiles with the latter being mounted in the nose-cone of a Boeing 747. However, both systems are very large and in no way could be integrated into an armoured fighting vehicle—mainly due to the high power demands of such systems.

Whatever the future holds, the author sincerely hopes that however advanced active protection systems become, the importance of passive armour is never diminished. After all, a suitably thick plate of RHA or equivalent provides occupants the guaranteed security that at least there are certain threats that will not make it through to the crew compartment.

NOTE

1 RPG, Rocket-Propelled Grenade.

REFERENCES

Anderson Jr., C. E., Behner, T. & Hohler, V. 2013. Penetration efficiency as a function of target obliquity and projectile pitch. *Journal of Applied Mechanics*, 80(3), 031801.

Anon 1944. *The Protection of Steel Targets from Attack by Shaped Charges*. London, UK: Ministry of Supply.

Anon 2019. *Iron Fist Series of Active Protection Systems - Product Data Sheet*. Israel: Elbit Systems Ltd.

Appelgren, P., Skoglund, M., Lundberg, P., Westerling, L., Larsson, A. & Hurtig, T. 2010. Experimental study of electromagnetic effects on solid copper jets. *Journal of Applied Mechanics, Transactions ASME*, 77(1), 1–7.

Benyami, M., Erlich, Y., Friling, S., Partom, Y., Rosenberg, G. & Shevach, H. 1991. Combined reactive and passive armor. U.S. Patent 5,070,764. Israel: The State of Israel, Ministry of Defense, Rafael Armament.

Brand, M., Mayseless, M. & Genussov, R. 2001. Analytical model to analyze the passive reactive cassettes. In: *Proceedings of the 19th International Symposium on Ballistics*. Interlaken, Switzerland Crewther, I. R. (ed).

Brown, J. & Finch, D. 1989. The shaped charge jet attack of confined and unconfined sheet explosive at normal incidence. In: *11th International Symposium on Ballistics*. Brussels, Belgium.

Fong, R., Ng, W., Rottinger, P. & Tang, S. 2007. Application of airbag technology for vehicle protection and non-lethal applications. In: *Proceedings of the 23rd International Symposium on Ballistics*. Tarragona, Spain. Galvez, F. & Sanchez-Galvez, V. (eds) Lancaster, PA: DEStech Publications, Inc.

Foss, C. F. 2011. Rafael expands Trophy family. *Jane's International Defence Review*, 29 September.

Fras, T. 2021. Experimental and numerical study on a non-explosive reactive armour with the rubber interlayer applied against kinetic-energy penetrators—the 'bulging effect' analysis. *Materials,* 14, 3334.

Gov, N., Kivity, Y. & Yaziv, D. 1992. On the interaction of a shaped charge jet with a rubber filled metallics case. In: *13th International Symposium on Ballistics*. Stockholm, Sweden. Persson, A., Andersson, K. & Bjorck E. B. (eds) Sundbyberg, Sweden: National Defence Research Establishment

Gurney, R. W. 1943. *The Initial Velocities of Fragments from Bombs, Shell and Grenades*. Aberdeen Proving Ground, MD: Ballistic Research Laboratories.

Hazell, P. J., Lawrence, T. & Stennett, C. 2012. The defeat of shaped charge jets by explosively driven ceramic and glass plates. *International Journal of Applied Ceramic Technology*, 9(2), 382–392.

Heine, A., Wickert, M. & Thoma, K. 2013. Future vehicle protection-technologies for ultra-fast close-distance active protection systems. In: *Proceedings of the 27th International Symposium on Ballistics*. Freiburg, Germany.

Held, M. 1970. Explosive Reactive Armour Patent. No. 2008156, filed on 2, February 1970, Germany.

Held, M. 1973. *Schutzeinrichtung gegen Geschosse, insbesondere Hohlladungsgeschosse (Protection Device against Projectiles, Especially Shaped Charges)*. Germany.

Held, M. 1993. Armour. *In:* Murphy, M. J. & Clark, M. N. (eds.) *Proceedings of the 14th International Symposium on Ballistics*. Quebec: National Defence Research Establishment.

Held, M. 1999. Comparison of explosive reactive armour against different threat levels. *Propellants, Explosives, Pyrotechnics*, 24(2), 76–77.

Held, M. 2001. Disturbance of shaped charge jets by bulging armour. *Propellants, Explosives, Pyrotechnics*, 26(4), 191–195.

Held, M. 2002. Lecture notes from the survivability of armoured vehicles course (18–20 March). *In:* Coombs, M. E. C. (ed.). *The Royal Military College of Science*. Shrivenham: Cranfield University.

Held, M. 2004. Dynamic plate thickness of ERA sandwiches against shaped charge jets. *Propellants, Explosives, Pyrotechnics*, 29(4), 244–246.

Held, M. 2006. Stopping power of ERA sandwiches as a function of explosive layer thickness or plate velocities. *Propellants, Explosives, Pyrotechnics*, 31(3), 234–238.

Hohler, V. & Behner, T. 1999. Influence of the yaw angle on the performance reduction of long rod projectiles. In: *Proceedings of the 18th International Symposium on Ballistics*. San Antonio, TX.

Kaufmann, H. & Koch, A. 2005. Terminal ballistic effects of low density materials used as confinement plates for explosive reactive armour. In: *Proceedings of the 22nd International Symposium on Ballistics*. Vancouver, BC.

Kennedy, D. R. 1983. Improving combat crew survivability. *Armor*, 9, 16–22.

Koch, A. & Bianchi, S. 2010. Protection efficiency of steel and ceramic confinement plates for explosive reactive armours against shaped charges. In: *25th International Symposium on Ballistics*. Beijing, China.

Lidén, E., Odell, A. & Lundgren, J. 2013. Focused blast against small cylindrical targets. In: *Proceedings of the 27th International Symposium on Ballistics*. Freiburg, Germany.

Littlefield, D. L. 1991. Finite conductivity effects on the MHD instabilities in uniformly elongating plastic jets. *Physics of Fluids A: Fluid Dynamics (1989–1993)*, 3(6), 1666–1673.

Mayseless, M. 2011. Effectiveness of explosive reactive armor. *Journal of Applied Mechanics, Transactions ASME*, 78(5), 051006.

Mayseless, M., Erlich, Y., Falcovitz, Y., Rosenberg, G. & Wheis, D. 1984. Interaction of shaped-charge jets with reactive armor. In: *Proceedings of the Eighth International Symposium on Ballistics*. Orlando, FL.

Meyers, M. A. 1994. *Dynamic Behaviour of Materials*. New York: John Wiley & Sons, Inc.

Ogorkiewicz, R. M. 2007. Shifting focus: Armoured vehicle protection adapts to new threats. *Jane's International Defence Review*, 12 January.

Pillersdorf, A. 1956. *Preliminary Tests of Picatinny Arsenal Device (Linear Cutting Charge) against Dynamically Fired Ammunition*. Aberdeen Proving Ground, MD: Development and Proof Services.

Roberts, C. E. & Ubbelohde, A. R. 1944. *Target Damage by Munroe Jets. Protection of Steel Targets by Non-Metallic Substances with Special References to Oxidising Agents.*. Fort Halstead: Armament Research Department.

Rosenberg, Z. & Dekel, E. 1998. A parametric study of the bulging process in passive cassettes with 2-D numerical simulations. *International Journal of Impact Engineering*, 21(4), 297–305.

Rosenberg, Z. & Dekel, E. 1999. On the interaction between shaped charge jets and confined explosives at normal incidence. *International Journal of Impact Engineering*, 23(1 Part II), 795–802.

Shvetsov, G. A., Matrosov, A. D., Babkin, A. V., Ladov, S. V. & Fedoov, S. V. 1999. Disruption of shaped-charge jets due to axial current. In: *Proceedings of the 18th International Symposium on Ballistics*. San Antonio, TX.

Sterzelmeier, K., Brommer, V. & Sinniger, L. 2001. Active armor protection- conception and design of steerable launcher systems fed by modular pulsed- power supply units. *IEEE Transactions on Magnetics*, 37(1), 238–241.

Straub, H. W., Arthaber, J. M., Copeland, A. L., Melamed, L., Miller, J. E., Moore, W. J., Paradis, R. J., Ulrich, R. R. & Vrataric Jr., F. 1960. *Terminal Report: Developmental Sensing Computing System for Project Dash-Dot (U)*. Washington, DC: Diamond Ordnance Fuze Laboratories.

Swatton, D. J. R., Pack, D. C., Brown, J., Endersby, P. C. & Ratcliff, P. R. 2001. The effect of obliquity and conductivity on the current distributions within electric armour. In: *Proceedings of the 19th International Symposium on Ballistics*. Interlaken, Switzerland.

Thoma, K., Vinkier, D., Kiemier, J., Deisenroth, U. & Fucke, W. 1993. Shaped charge jet interaction with highly effective passive systems. *Propellants, Explosives, Pyrotechnics*, 18, 275–281.

Walker, E. H. 1973. *Defeat of Shaped Charge Devices by Active Armor*. Aberdeen Proving Ground, MD: US Army Ballistic Research Laboratory.

White III, J. J. & Wahll, M. J. 1981. Shaped charge jet interactions with liquids. *In:* Backofen Jr., J. E. (ed.) *Proceedings on the 6th International Symposium on Ballistics*. Orlando, FL: American Defense Preparedness Association.

White III, J. J., Wahll, M. J. & Backofen Jr., J. E. 1982. Observation of compressibility-related effects in shaped charge jet penetration. *Journal of Applied Physics,* 53, 4515–4517.

11 Human Vulnerability

11.1 INTRODUCTION

When providing protection, it is sensible that we develop an understanding of how the human body responds to impact and penetration by projectiles and to blast. In this chapter, some of the more pertinent discoveries will be reviewed with regard to the mechanics of wounding. We will also look at some of the techniques used in armoured vehicles to minimize injury and therefore maximize survivability.

In most conventional wars to date, fragment wounds have outnumbered bullet wounds quite considerably. With jungle warfare and the conditions associated with urban terrorism, bullets are the most common threat (Table 11.1). This is likely to be due to greater sniping activities in these environments as well as less intense artillery use. Possibly, the less apparent use of artillery and more urban-based conflict are also the reasons why there were fewer fragmentation injuries in the 2003 Gulf War compared to the 1991 conflict (Hinsley et al., 2005).

In more recent years, understanding the mechanisms of blast-related injury has become all the more important—particularly with regard to injuries sustained to vehicle occupants during an improvised explosive device (IED) attack. This will be explored in more detail in this chapter.

TABLE 11.1

Cause of Wounds to Casualties (%) from Various Conflicts; Data Taken from Different Sample Sizes and over Different Time Durations during the Conflicts

Conflict	Bullets	Fragments	Other (e.g. Traumatic Amputation due to Blast)
World War I	39	61	–
World War II	10	85	5
Korea	7	92	1
Vietnam	52	44	4
Borneo	90	9	1
Northern Ireland	55	22	20
Israel 1982	11.6	53	35.5
Falkland Islands	31.8	55.8	12.4
Gulf War 1991	20	80	–
Gulf War 2003	37	62	1

Source: Ryan, J. M. et al., 1991. *Annals of the Royal College of Surgeons of England*, 73(1), 13–20; Spalding, T. J. W. et al., 1991. *British Journal of Surgery*, 78(9), 1102–1104; Hinsley, D. E. et al., 2005. *British Journal of Surgery*, 92(5), 637–642.

Note: The Israeli data are complicated by the inclusion of psychiatric casualties in the group 'Other'.

11.2 HUMAN RESPONSE TO BALLISTIC LOADING

11.2.1 HISTORY

Much of the early work on wound ballistics was carried out by Emil Theodor Kocher (Fackler and Dougherty, 1991). Kocher was born in Bern, Switzerland in 1841 and became a professor of surgery at the University of Berne in 1872. Around that time, it was widely thought that the wounding mechanism of tissue by a bullet was caused by three factors:

1. A partial melting of the bullet on impact,
2. The centrifugal force of the spinning bullet fired from a rifled barrel and
3. Hydraulic pressure (that is to say, a high-pressure region emanating from the bullet and expanding out radially behind it).

Kocher fired at several targets including metals, glass bottles, pig bladders and pig intestines and human cadavers. Most pertinently, he fired a lead alloy bullet from a Vetterli rifle into a water-filled box faced with a pig bladder. The box was 1.5 m long faced with a pig's bladder (which covered a hole in the box). Kocher observed that the bullet pierced the pig's bladder and struck the rear wall of the box. Also, the box burst catastrophically at the seams due to the passage of the bullet through the water. Kocher concluded that hydraulic pressure (i.e. a high-pressure region radiating out from the bullet to form a temporary cavity) caused the box to burst and therefore was primarily responsible for tissue disruption. Consequently, Kocher concluded that partial bullet melting and centrifugal forces were of little importance to wounding.

At the time of Kocher, 'fishing' with dynamite was a commonplace pastime, and in 1898, it was shown that firing a bullet close to a fish resulted in its death without any obvious injury (*The New York Times*, 1898). It was reported that an Italian officer, Major Michelini, fired an Italian (0.256-in. calibre) rifle[1] at the water at an angle of 45° resulting in a dead fish floating to the surface. It was deduced that the death of the fish was due to the hydraulic shock caused by the bullet penetrating the water. Although this phenomenon was referred to as 'hydraulic shock', the death of the fish would have almost certainly been down to the temporary displacement of the water behind the penetrating bullet. This was the same phenomenon that caused Kocher's box to burst.

Since the work of Kocher, it is generally recognized that there are two principal modes of wounding due to projectile penetration. These are shown in Figure 11.1. A bullet will compress and shear tissue during penetration to form a permanent cavity. At the same time, tissue is propelled outward from the bullet's path and forms a temporary cavity.

A third phenomenon is also shown in Figure 11.1 — this is the sonic pressure wave. This has sometimes (quite incorrectly) been referred to as the shock wave and is different from the hydraulic pressure observed by Kocher that forms a temporary cavity behind the bullet. The sonic pressure wave travels at the speed of sound in tissue (~1450 m/s), and this is much faster than the impact velocity of all high-velocity rifle bullets. There is still some debate as to whether this sonic pressure wave can cause remote injuries, and it has been suggested that damage to the brain can be
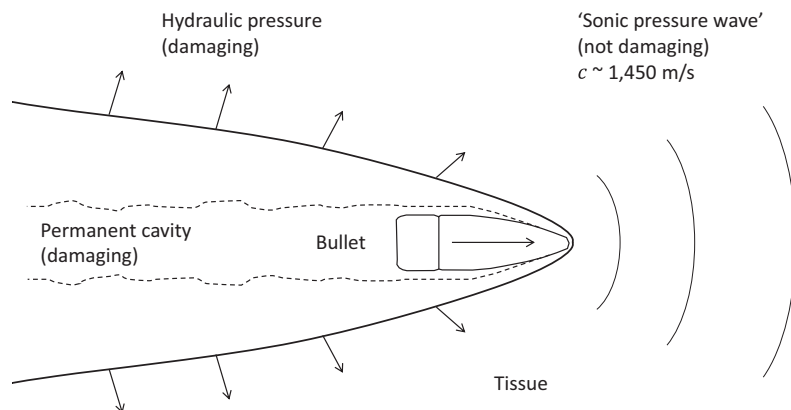
FIGURE 11.1   The effects of a projectile penetrating through tissue.

caused by these waves (Courtney and Courtney, 2007). It has also been argued that flat-nosed projectiles could form a disruptive shock wave due to the way the tissue would be placed in uniaxial strain (much in the same way that a plate-impact experiment works). However, this effect would be severely limited in size due to the fast release of the shock front, as discussed in Chapter 5, and probably lost by the damage caused by the penetrating projectile.

In 1947, Harvey et al. examined the effect of the sonic pressure wave on tissue by suspending frogs' hearts in a water vat and shooting a projectile near them (Harvey et al., 1947). They recorded the experiment using high-speed photography. Due to the fact that the sonic pressure wave travels ahead of the projectile, they were able to observe with the camera what exactly damaged the heart and decouple the effect of the hydraulic pressure and the sonic pressure wave. They noted that the disruption of the tissue accompanied changes in pressure due to the formation of the temporary cavity and not the sonic pressure wave. This classic work has often been used to conclude that sonic pressure waves have no wounding effect.

11.2.2   PENETRATION MECHANISMS

How a bullet penetrates flesh depends on a number of factors. The principal factors of importance are:

- The bullet's velocity,
- The bullet's geometry and
- The bullet's material properties.

The bullet's velocity (along with its mass) determines how much kinetic energy the bullet has. However, the kinetic energy of the bullet alone does not determine the injury mechanism per se but rather the energy delivered to the tissue (Santucci and Chang, 2004). So, it is possible to design a bullet that is very fast (i.e. it possesses

high kinetic energy) that simply passes through the target resulting in little-to-no energy transfer. In fact, in one notorious case, the British military introduced a new high-velocity rifle in 1890 whilst fighting in India. It was assumed that the increased muzzle energy provided by the new full-metal-jacket 0.30-in. calibre ammunition would provide an enhanced stopping power. To the dismay of the military planners, the opposite occurred as the new projectiles did not deform on impact as much as the previously used larger-calibre lead projectiles. This meant that less energy was being delivered to the target's body—particularly when the projectile passed straight through the assailant. This led to the British filing down the tips of the bullets in the Dum-Dum arsenal to increase their damage mechanism. This approach was later outlawed in the Hague Peace Conference in 1899.

The bullet's geometry is a factor that will determine how much the bullet will deform, slow down or tumble and thus determine the extent of tissue damage. The AK-47/Chinese Samozaryadnyj Karabin sistemy Simonova (SKS) military bullet (7.62×39 mm) is one of the most widely used bullets (see Figure 3.3). It generally does not deform in tissue and will travel 260 mm before yawing (Fackler, 1996). The reason for this is due to its short stubby geometry.

The material properties of the bullet too affect the behaviour during penetration. Softer-cored projectiles will have a tendency to deform during penetration, whereas harder-cored bullets will not. Some projectiles will fragment during penetration—particularly if they come into contact with harder tissue. Even similar types of bullets can demonstrate differences in behaviour. For example, it has been shown that with the 7.62×51-mm NATO bullet, US-manufactured bullets have a tendency to stay intact during penetration due to the strength and thickness of the jacket, whereas non-US-manufactured bullets will fragment on impact (Santucci and Chang, 2004).

11.2.3 Penetration of Human Skin

Understanding the penetration of human skin is problematic due to the complex nature of the organ and the variety of 'backing materials' that it covers in the human body. Skin varies in thickness too, depending on the location on the body, and it is well known that the mechanical response varies with age and gender. The mechanical behaviour is also affected by the local environmental conditions. Furthermore, skin is anisotropic in nature.

To get an idea of the ballistic resistance offered by human skin, it is necessary to carry out ballistic penetration experiments on a skin sample or a reliable simulant. Colonel Journée, a French infantry officer, was the first person to investigate skin penetration (Journée, 1907). It has been reported that Journée started his investigations with horse skin and noted that skin appeared to be more resistant to ballistic penetration than muscle tissue (DiMaio, 1981). Projectiles of relatively low velocity (80–200 m/s) would rebound from the skin whereas when the skin of the horse was removed, the projectile was able to penetrate through 20 cm of muscle. Further experiments were conducted where 11.25-mm diameter lead spheres, weighing 8.25 g, were fired at human cadavers. These results revealed that an impact of 46 m/s produced only a contusion to the skin. Increasing the velocity to 60 m/s resulted in

superficial skin damage whereas an impact at 70 m/s perforated the skin and penetrated into the underlying muscle for several centimetres (DiMaio, 1981).

Further work on the penetration of skin was carried out by Sperrazza and Kokinakis (1968). They fired steel cubes, cylinders and spheres with masses up to 15 g and velocities of up to 2000 m/s into human skin and goat skin as well as into soldiers' winter combat clothing of the time. The skin was removed from a cadaver's thigh and was 3 mm thick (average thickness); goat skin was removed from the goat's thigh with the hair removed and was also 3 mm thick on average.

They showed that the v_{50} could be related to the ratio of the area of the fragment to its mass (Sperrazza and Kokinakis, 1968), viz:

$$v_{50} = K\frac{A}{m} + b \tag{11.1}$$

where
    A = the area of the fragment (cm^2)
    m = the mass of the fragment (g)
    K, b = empirically derived constants (m/s)

With reference to Equation 11.1, they showed that for the clothing (which is composed of six layers: sateen, oxford, frieze, ripstop, shirting and underwear), K and b were 261.07 and 73.51 m/s, respectively, whereas for skin, K and b were 124.71
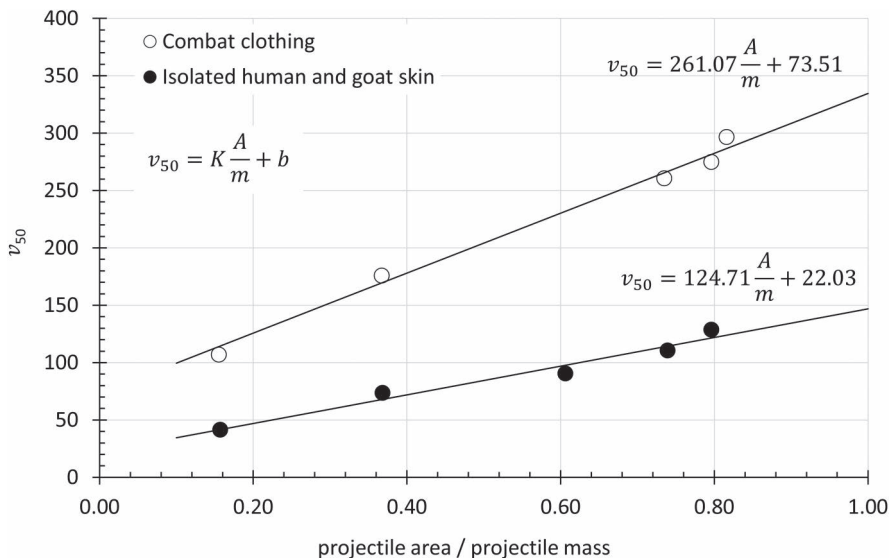
FIGURE 11.2 Ballistic limit data for combat winter clothing an isolated human and goat skin (3 mm thick) penetrated by 15 g steel cubes, spheres and cylinders. The data points represent average values with as many as 30 measurements carried out for each data point. Data from Sperrazza and Kokinakis (1968).

TABLE 11.2
Ballistic Limits for Steel Sphere against Winter Uniform Clothing and Skin

	Ballistic Limit, v_{50} (m/s)	
Projectile Mass (g)	**Uniform**	**Skin**
1	154	60
2	137	52
10	111	40

Source: Sperrazza, J. & Kokinakis, W. 1968, *Annals of the New York Academy of Sciences*, 152(1), 163–167. With permission from John Wiley & Sons, Inc.

and 22.03 m/s, respectively, see Figure 11.2. No significant differences were noted between the behaviour of goat skin and human skin with their ballistic resistance being similar. Table 11.2 provides some representative ballistic limit data for steel spheres against winter uniform clothing and skin. Further data are summarized by Breeze and Clasper (2013).

Further data has also been presented by Bir et al. (2005) that reports the estimated energy density for skin penetration at various locations around the human body with a 12-gauge fin-stabilized rubber rocket (non-lethal round). They conducted 166 impacts on several cadavers of varying age and gender. They showed that the area on the body where the lowest energy density required for penetrating injuries was between two ribs with an energy density of 33.14 J/cm². Whereas the location on the body where the highest energy density was required for penetration was on a posterior rib which required an energy density of 55.90 J/cm² for penetration.

11.2.4 THE WOUND CHANNEL

The response of tissue to penetration by non-deforming but yawing projectile is nicely shown in the diagram presented by Fackler (1996) and reproduced here in Figure 11.3. These experiments are usually carried out in ballistic gelatin or similar tissue simulants.

The AK-47 bullet enters the tissue and travels approximately 260 mm before beginning to yaw. The penetration results in two cavities being formed: temporary and permanent. The temporary cavity is due to momentum being imparted to the tissue by the penetrating projectile. The tissue behaves in an elastic fashion and therefore mostly returns to a rested state after the passage of the projectile. The permanent cavity is caused by the inelastic compression of tissue resulting in damage. It can be seen from Figure 11.3 that the AK-47 bullet does not deform, but rather, the geometry of the permanent cavity is caused by the tumbling of the projectile.

Considerably more trauma is afforded to the patient when fragmentation of the bullet occurs such as when a hollow-point projectile penetrates flesh. Again, we resort to Fackler (1996). Figure 11.4 shows the wound track that would typically
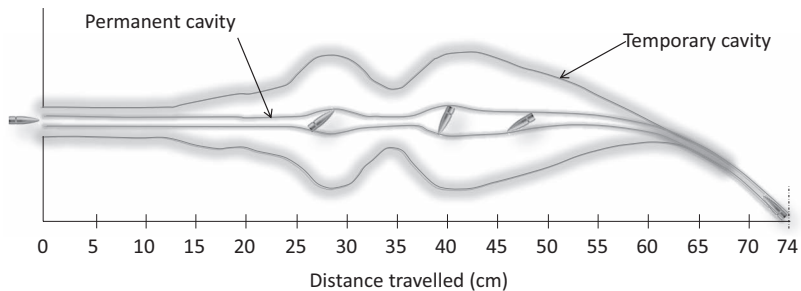
FIGURE 11.3   Wound profile produced by the Russian AK-47 (7.62×39 mm). (Adapted from Fackler, M. L. 1996. *Annals of Emergency Medicine*, 28 (2), 194–203.)
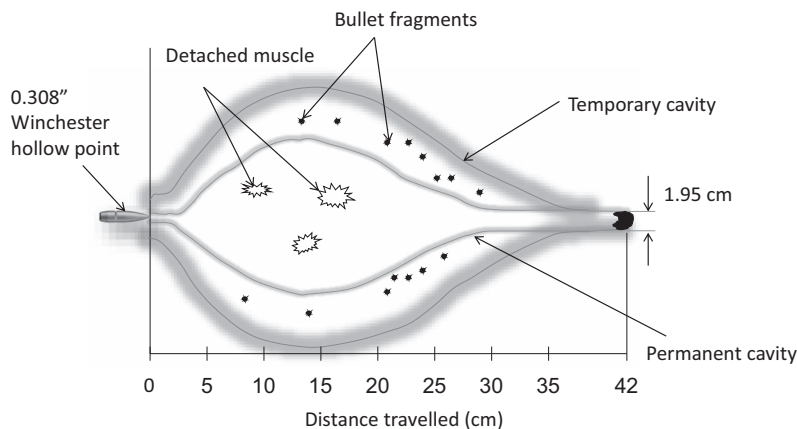
FIGURE 11.4   Wound profile produced by a hollow-point projectile. (Adapted from Fackler, M. L. 1996. *Annals of Emergency Medicine*, 28 (2), 194–203.)

result from the impact of a hollow-point projectile on a human body. The fragmentation of the bullet results in an extra dimension to patient treatment. This bullet expands to more than double its original diameter and loses about one-third of its weight in fragments, within 25 mm or so of striking tissue. These fragments cause multiple perforations of the tissue surrounding the bullet path. The large temporary cavity then displaces this tissue, which has been weakened by multiple perforations by fragments.

11.2.5   BLUNT TRAUMA

It is quite common for wearers of soft body armour to experience injury due to the behind armour blunt trauma (BABT) after a bullet has been stopped. This is where excessive bruising of the flesh occurs due to a blunt impact. Unfortunately, this is the

consequence of stopping a lethal bullet in a very short distance by using compliant materials that stretch and deform.

The effect of BABT is tested regularly with backing layers of Plastilina®, ballistic soap and clays that record the temporary movement of the body armour materials into the body.

11.3 HUMAN RESPONSE TO BLAST LOADING

Many of the vehicles deployed in recent conflicts have faced enormous blast loads on their structures and occupants, and so there has been a considerable effort in recent years to understand the way that out-of-vehicle blast loading can be managed to mitigate the injury to the occupants.

There are four classical types of injury that can occur to an individual that is subjected to a blast loading event (Zuckerman, 1952). These are primary, secondary, tertiary and quarternary. The clinical effects and some of the mitigation requirements

TABLE 11.3

Summary of Human Effects from a Blast Mine on Human Occupants

Blast Injury	Mechanism	Clinical Effects	Mitigation Requirements	Vehicle Mitigation
Primary	Blast/shock wave	Blast lung; traumatic amputation; soft tissue deformation and injury	Reduce blast transfer into the vehicle cabin	Increased stand-off; inclusion of blast-mitigation materials; V-shaping of hull
Secondary	Fragments from mine products, soil ejecta or vehicle structure	Penetrating wounds	Provide protection against fragments	Improved armour protection of the vehicle floor; improved personal protection
Tertiary	Global—vehicle acceleration; local—floor pan deformation	Significant axial loading leading to lower-limb injuries, pelvic and spinal injuries; head injuries from collision with the roof	Reduce vehicle acceleration; reduction in the trapping of the blast wave by the vehicle's structure; resistance of floor plate deformation	Increased stand-off; V-shaping of the hull; occupants use restraints; feet lifted off the floor pan
Quaternary	Thermal effects	Burns	Protect against burns	Fire-resistant materials in vehicles; fire-retardant clothing

Source: Ramasamy A. et al. 2009. *Journal of the Royal Army Medical Corps*, 155(4), 258–264. With permission from BMJ Publishing Group Ltd.

that can be taken into account when developing an armoured fighting vehicle (AFV) are shown in Table 11.3 (Ramasamy et al., 2009).

These four types of injury will now be discussed.

11.3.1 PRIMARY INJURY

Primary injury occurs simply because of the interaction between the blast wave and the human body. This is sometimes referred to as direct blast effects and is associated with the change in environmental pressure due to the passage of the blast wave. Much of our understanding of the expected human response to blast has come from experiments with animals. For example, experiments involving 2097 animals subjected to blast were compiled by Bowen et al. (1968). They observed that species with larger lung volumes for a given mass had a higher probability of survivability.

Further, the factors that affect the level of injury in animals due to a blast wave are summarized by Baker et al. (1983). These are:

- The magnitude of the incident, reflected and dynamic overpressure,
- The rate of rise to peak overpressure after the arrival of the blast wave,
- The duration of the blast wave and its specific impulse,
- Ambient atmospheric pressure,
- The size and type of the subject animal and
- The age of the animal (possibly).

Of all the organs that are most vulnerable to injury, the ones containing air are the most significant. The ear is the most sensitive and can respond to pressures as little as 2×10^{-5} Pa, and therefore, the large overpressures are generated from an explosion risk 'overloading' the ear drum.

Many of the studies that have been carried out to understand the behaviour of the ear drum to blast loading have used animals (pigs, dogs, monkeys, etc.) or human cadavers, and there is a wide variability in response. From a review of overpressure studies in a wide variety of experimental set-ups, circumstances and species, Hirsch (1968) concluded that the threshold pressure for damage to the middle ear structures is about 5 psi (34.5 kPa) and that at overpressures of near 15 psi (103.4 kPa), eardrum rupture will occur in about 50% of the cases.

The lungs are also prone to extensive damage due to fast compression of the chest wall. The tissue cannot respond as quickly, and the end result is shearing failure of the tissue.

The location of the individual is also important to assess survivability. The least survivable position is where the person is close to a reflective surface so that a reflected wave will lead to pressure enhancement. This is demonstrated in Figure 11.5 where the passage of a blast wave has been computed. The pressure reflection at the rigid surface leads to an amplification of pressure in the locality of the wall—higher than the pressure that would have been encountered if the wall was absent. This is the most damaging of scenarios. Better survivability occurs where the individual is standing in free space with better-still survivability derived from lying down in free
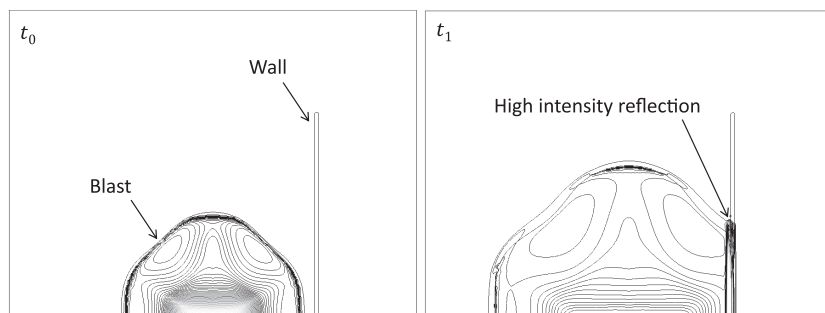
FIGURE 11.5 Computed reflection of a blast wave at a wall. The reflection results in an amplification of the pressure close to the wall.
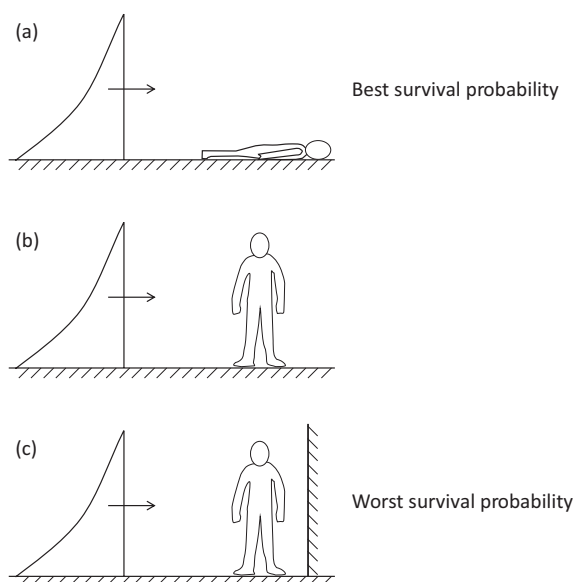
FIGURE 11.6 Human vulnerability to a blast wave: (a) lying down in a free space with the body oriented in the direction of travel of the blast (best survival probability), (b) standing up in free space and (c) standing in close proximity to a vertical wall (worst survival probability).

space where the long axis of the body is orientated in the direction of travel of the blast (see Figure 11.6).

A useful summary of the expected effects on an unprotected person from a primary blast overpressure of short duration is provided by and summarized in Champion et al. (2009). These are injuries that are likely to be sustained when an unprotected person is subjected to a short-duration primary blast overpressure:

- At between 30 and 40 psi (207–276 kPa), there is a slight probability of lung injury.

- At around 80 psi (552 kPa), there is a 50% probability of lung injury.
- At 100–120 psi (690–827 kPa), there is a slight probability of death.
- At 130–180 psi (896–1241 kPa), there is a 50% probability of death.
- At 200–250 psi (1379–1724 kPa), death is the most probable outcome.

11.3.2 SECONDARY INJURY

The secondary injury occurs when there is injury from fragments from an explosion. These fragments can be from a shell casing or simply from stones and soil accelerated from a buried mine. Injury due to fragment impact can be divided into two categories:

1. *Penetrating injuries*: These can cause severe lacerations resulting in loss of blood and ultimately death.
2. *Non-penetrating injuries*: These result in blunt trauma (heavy bruising) and are caused by large, non-penetrating fragments.

In recent conflicts in Iraq and Afghanistan, IEDs that propel explosively formed projectiles at high velocity (see Chapter 3) have been used and proven to be deadly. In Iraq, particularly, they have been a leading cause of death of coalition troops, and despite the close proximity of a casualty to the explosive, primary blast injury is the least common form of wounding (although the mass of explosive used in EFP-based devices tends to be relatively small compared to blast-based IEDs). Between January and October 2006, Ramasamy et al. (2008) recorded 100 consecutive casualties at the British Military Field Hospital Shaibah[2] that were killed or injured in hostile action. Their study centred on roadside devices directed against coalition force vehicles. Fifty-three individuals were subjected to an IED attack during this period, and the injury profile of these casualties is summarized in Table 11.4. Of all the 53 casualties that were subjected to IEDs, all of them displayed open wounds, whereas only two casualties displayed any evidence of being subjected to significant primary blast injury to the lungs.

TABLE 11.4

Casualties Recorded from January 2006 in Iraq from the British Military Field Hospital Shaibah (Iraq)

No. of casualties injured from IEDs	53
No. of casualties displaying primary blast injuries (to lungs)	2 (3.8%)
No. of casualties with open wounds	53 (100%)
No. of casualties displaying fractures	28 (52.8%)
No. of casualties displaying quaternary (thermal) injuries	8 (15.1%)

Source: Ramasamy, A. et al. 2008. *Journal of Trauma and Acute Care Surgery*, 65 (4), 910–914.

TABLE 11.5

Injury Criteria for Tertiary Effects Involving (Decelerative) Impact

Tolerance	Impact Velocity (m/s)[a]
Skull Fracture	
Mostly 'safe'	3.05
Threshold	3.96
50% fracture	5.49
Near 100% fracture	7.01
Total Body Impact Tolerance	
Mostly 'safe'	3.05
Lethality threshold	6.40
50% lethality	16.46
Near 100% lethality	42.06

Source: White, C. S. 1971. Nature of problems involved in estimating immediate casualties from nuclear explosions. *In: Civil Effects Study*. Springfield, VA: Lovelace Foundation for Medical Education and Research.

[a] Converted from ft./s in the original document.

11.3.3 TERTIARY INJURY

The tertiary injury occurs due to the acceleration (or deceleration) of the whole body due to an explosive impulse. Such examples are where a mine blast accelerates a vehicle upward or where local deformation of the floor plate is pushed up into the crew compartment. Other injury scenarios would be where the blast wave picks up an individual and throws them into a wall. Injury can occur during an accelerative phase or during decelerative impact. However, the latter tends to be more serious.

White (1968, 1971) has summarized velocity thresholds for the human body. White's most recent (and updated) summary from 1971 is presented in Table 11.5. It should be noted that these values are crude estimates as ascertaining certainty from prior observations and statistical history can be difficult.

For personnel travelling in an armoured vehicle where they would be either seated or stood, a blast wave could lead to a vertical translation of the vehicle. Equally, there could arise a situation where the floor plate is driven upward, thereby effectively impacting the heels, feet and legs of the occupants. White derived that if the heels, feet and legs were impacted at a velocity of between 4.0 and 4.9 m/s, then fracture of the bones would occur (White, 1971).

11.3.4 QUATERNARY INJURY

This is mostly to do with burns as a result of a fireball from an explosion or the resulting fire that would ensue. It also encompasses toxic gas inhalation (explosives can generate a reasonable amount of carbon monoxide) and injury from environmental contamination.

FIGURE 11.7   Shaped-charge jet penetration of armour (courtesy of J Backofen Jr).

11.4   IMPROVING SURVIVABILITY TO VEHICLE OCCUPANTS

A large number of blast mines and IEDs are used to attack vehicles. The reason for this is that vehicles can carry lots of people and follow reasonably predictable routes (roads). As a consequence of that, there has been a concerted effort in recent years to improve the survivability of vehicle occupants.

11.4.1   BEHIND ARMOUR DEBRIS AND THE 'VAPOURIFIC EFFECT'

As we have seen, shaped-charge jets pose a substantial risk to armour. Figure 11.7 shows the effect as a shaped-charge jet perforates armour. It is clear that there is a large debris cloud that emerges from the plate.

However, what is not clear from this radiograph are the other effects that accompany perforation. There will be:

- Heat
- Light
- Noxious fumes
- Smoke
- Blast.

Both steel and aluminium armour can be susceptible to what is known as the vapourific effect. This is when the small particulates of the armour metal are oxidized under extreme heat and pressure. Aluminium when it is oxidized under these conditions releases nearly 20,000 calories (84 kJ) per cubic centimetre. This is roughly ten times the energy density that can be expected during the detonation of a military-grade explosive (Kennedy, 1983). Various anti-tank warheads have been designed over the years to exploit this vapourific effect. These include the AGM-65 Maverick missile and the FFV AT-4. Both of these employ aluminium alloy liners to enhance the vapour explosion behind the armour. The AT-4 has been known to produce 1 bar overpressure and light intensities of the order of 100 times brighter than sunlight (Kennedy, 1983).

11.4.2 Occupant Survivability

Modern test procedures now require the use of an anthropomorphic test device (ATD) or crash test dummy to evaluate the loads on the human body (NATO, 2011). This is not an exact science per se as certain individuals will have a higher threshold for survivability than others. However, for the purpose of establishing a baseline survivability threshold, it is a sensible guide. Current testing guidelines (NATO, 2011) specify a 50th percentile male Hybrid III ATD, which is fitted with accelerometers (to measure the accelerations) and force–moment transducers (to measure bending loads). Blast overpressure injury to the lungs is also monitored using a pressure transducer fitted to that location. Accelerations and forces are measured in the head, neck, thorax, pelvis femur and tibia. Forces and accelerations are then compared to threshold injury criteria derived from automotive car crash data to establish a pass or fail (NATO, 2011). In general, the longer the duration of the acceleration phase, the less tolerance there is for the human body. Very intense head accelerations are tolerable if they are very brief. However, the head becomes much less tolerable as the pulse duration exceeds 10 or 15 ms (Versace, 1971).

11.4.3 V-Shaping

For improving occupant survivability by way of reducing acceleration to the occupants, much of the effort has centred on the deflection of the blast wave away from the vehicle. And so, most modern armoured vehicles have V-shaped hulls to achieve this. Two examples are shown in Figure 11.8.

Blast defection through V-shaping was developed in the early 1970s by the South Africans. During this time, they modified a WWII-vintage Swedish SKPF M/42 APC by integrating a special-shaped steel capsule with a 43° V-shaped bottom (Hoffman et al., 1991). Generally speaking, geometry dictates that the smaller the included angle of the V-shaping, the more the blast energy will be deflected, and therefore, a lower vertical impulse will be delivered to the vehicle. However, the height of the vehicle will also increase with the potential to make handling and stability more
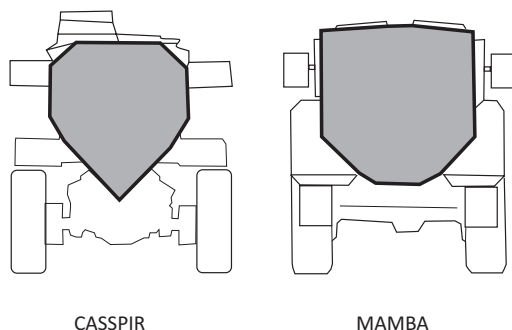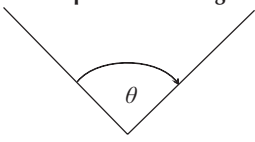
CASSPIR   MAMBA

FIGURE 11.8 Two approaches to V-shaping—the Casspir and the Mamba armoured personnel carriers.

TABLE 11.6

Included Angle of the V-Shaping on Certain Rhodesian Armoured Vehicles

		V-Shape Included Angle
		(diagram of V-shape with angle θ)
No.	**Vehicle**	
1	Camel	46°
2	Hyena	90°
3	Rhino	90°

Source: Hoffman, B. et al. 1991. *Lessons for Contemporary Counterinsurgencies: The Rhodesian Experience*. Santa Monica, CA: RAND.
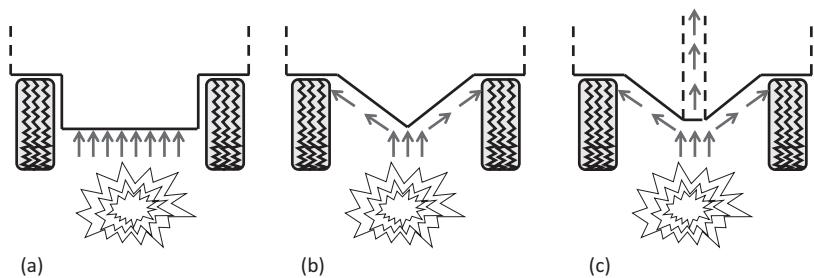
FIGURE 11.9   Different concepts for AFV hull design showing the pathways taken by a blast wave. (a) Flat bottom, (b) 'V' shaped and (c) blast chimney concept.

problematic. Table 11.6 lists some of the included angles of vehicles used by the Rhodesians. Notably, the Camel was named so due to its 'ungainly' appearance.

For vehicles where it is simply not possible to introduce a V-shape to the hull due to height and handling problems that may arise, it is possible to introduce a 'double V'-shape (or essentially a 'W'-shape). With this concept, instead of the blast being solely directed to the outside of the vehicle, a double V-shaped arrangement means that some of the blast is directed into the centre of the vehicle (Lee, 2013). The blast is then spread fore and aft along the vehicle's central axis using a suitably reinforced 'duct' that is concave downward. The deformation of the internal angled parts leads to a downward 'pull' on the central concave part thereby countering some of the upward impulse from the blast. Therefore, this provides a route to provide some meaningful blast protection in vehicles that would otherwise not be able to accommodate a full 'V'-shape.

A slight modification to this concept is the structural blast chimney method where a small (approximately laptop-sized) chimney is integrated into the centre of the vehicle (Tunis and Kendall, 2013). This chimney provides a vent for the blast and therefore minimizes the upward acceleration of the vehicle (see Figure 11.9).

FIGURE 11.10   A South African Buffel showing the V-shaped hull design. The Christmas decorations are not usually part of the camouflage.

11.4.4   GENERAL TECHNIQUES FOR MINE PROTECTION

Other techniques for increasing the survivability in armoured vehicles can include using 'breakable' wheel axles so that the blast is not trapped by the wheel structure, energy-absorbing materials to accommodate the blast-wave energy and sufficient spacing from the blast to reduce the energy density of the waves in contact with the structure. The Buffel (a South African troop carrier) used some of these techniques (see Figure 11.10).

As long as the occupants are sufficiently strapped down, and there are no loose projectiles to fly around the cabin, a principal factor to consider is the acceleration to the occupant. This is why it is often expedient to 'insulate' the individual from fast-deforming structures such as floor plates. However, where the occupant is subject to acceleration (due to the upward movement of the vehicle), or where the occupant is in direct contact with an accelerating structure such as a floor plate, then serious injury can occur.

A typical schematic of protection measures that are usually employed by an AFV is shown in Figure 11.11 in conjunction with Table 11.7.

In the same fashion that the V-shaping leads to an increased deflection prospect for blast-wave energy, having angled hull leads provide that advantage from a side-on blast. This can reduce the propensity of the vehicle to roll over (or be shunted sideways) when being subjected to a blast wave. Angled hulls are also advantageous from a ballistic point of view, as seen in Chapter 4. Having a decent amount of armour is obviously going to help survivability. The sides of hulls are particularly vulnerable to attack from IED fragments, explosively formed projectiles, shaped-charge jets and high explosive shell fragments and, of course, bullets. It is also necessary to add
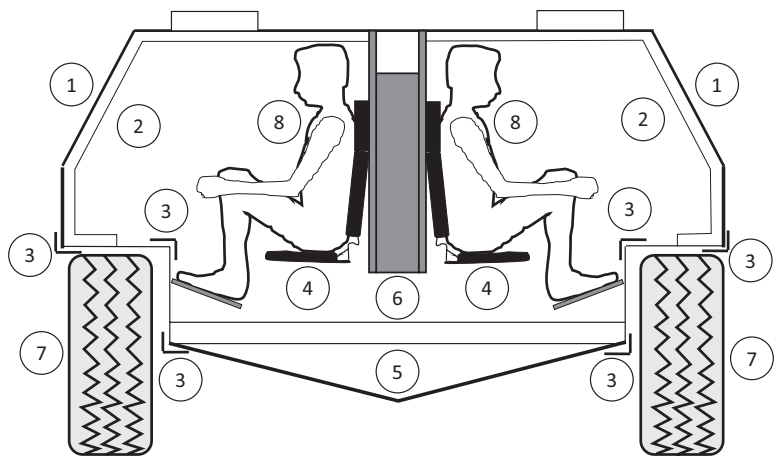
FIGURE 11.11   Protection measures employed in an AFV.

TABLE 11.7
Protection of AFVs from Mine and IED Blast

No.	Description
1	Sufficient armour to protect against fragment attack; angled for greater ballistic resistance and to deflect blast-wave energy from a side attack
2	Spall shields to protect against spalled armour and/or to limit fragment dispersion after the hull has been perforated
3	Reinforced welds
4	Suspended seats and foot rests to lift feet off the floor
5	Hull V-shaping to deflect blast-wave energy
6	Armoured floor
7	Quick-release axles to provide a release of blast-wave energy
8	Harnesses to restrain occupants

a spall shield. These are generally constructed from glass fibre–reinforced plastic or ultra-high-molecular-weight polyethylene composite materials. Their advantage is that during a high-velocity attack, the diameter of the cone of fragments that is produced will be reduced. This leads to less lethality and greater survivability of the crew (see Section 9.5).

The reinforcement of the welds is also crucial to ensure that the vehicle does not suffer structural failure during blast loading. Welds are often the weak point in a structure, and therefore, good quality control needs to be maintained.

Additionally, it is beneficial to keep the occupant away from any dynamically deforming part—such as a floor plate. During a blast, the floor plate can be subjected to high accelerations that can lead to serious injury—particularly in the lower leg. Therefore, suspended seats and footrests are used for this purpose.
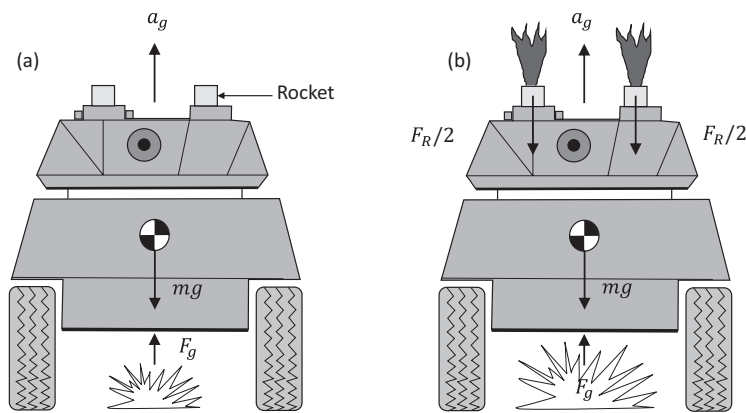
FIGURE 11.12 The principle of the ABBS system to improve occupant survivability in the event of a mine blast (a) before rocket initiation and (b) after initiation.

A novel and recent development has also included the use of installing rockets on the rooves of Armoured Fighting Vehicles. A system, developed by Advanced Blast & Ballistic Systems Ltd. (ABBS) in the UK, is claimed to reduce the acceleration of occupants substantially when their vehicle is the victim of an under-floor mine blast. The technology is based on the well-known Newtonian laws that dictate that it is possible to reduce the acceleration of an object by applying a force acting in the opposite direction to its motion. An example of how it would work in principle is shown in Figure 11.12.

In Figure 11.12a, an AFV of mass m is subjected to an underbelly mine blast that exerts a global force on the vehicle of magnitude F_g. A sensor detects the shock wave from the explosion and initiates two rocket systems (in this example) located on the roof. Each of them exerts a downward force on the vehicle such that the total value of the downward thrust due to the rockets $= F_R$. This occurs in Figure 11.12b. Therefore, the net global acceleration of the vehicle (including the downward force due to the vehicle's weight, mg) is therefore given by:

$$a_g = \frac{F_g - mg - F_R}{m} \tag{11.2}$$

Clearly, the closer the sum of $mg + F_R$ is to F_g, the lower the global acceleration and the less the expected injury to the vehicle occupants. Drag forces due to air resistance would be negligible.

To maximize effectiveness, the impulse delivered by the rockets' thrust would match the impulse conveyed by the explosive blast (see Section 3.4.2). However, this would be challenging given the potential variety of explosive threats. In any case, any substantial downward thrust is likely to improve the survivability prospects of the vehicle's occupants.

11.5 BALLISTIC SIMULANTS

There are several tissue simulants that are available in the market and these range from ballistic gelatin (basically very similar in touch and feel to the jelly that you buy from a supermarket), ballistic soap and even a dielectric gel (Sylgard) that reportedly behaves in a similar fashion to the human brain. And then you have the bone simulants such as BoneSim™ and Synbone® and although there have been several attempts to compare these simulants to living tissue e.g., there has been a limited success (Brown et al., 2019). The truth is that living tissue is necessarily complex in structure. Furthermore, dead tissue is no substitute either due to dehydration.

Nevertheless, let's look at some examples of the materials that have been used in ballistics research in an attempt to gain insight into injury mechanics.

11.5.1 Ballistic Gelatin

Ballistic gelatin is a soft, pliable visco-elastic gelatin very similar to the jelly that you would eat! It is also transparent, which makes it an excellent medium with which one can visualize a temporary cavity. It is usually mixed in a concentration of either 1000 g of gelatin per 9000 mL water to give a 10% solution, or 2000 g of gelatin per 8000 mL of water to provide a 20% solution. The results seen in a 10% ballistic gelatin have correlated well with the penetration and fragmentation seen in living swine leg tissue (Fackler and Malinowski, 1985).

It is usually made by adding powdered gelatin to water (which should be cold, 7°C–10°C) followed by agitation to wet all of the gelatin particles. The product is then placed in a refrigerator at 4°C for a couple of hours followed by heating. It is
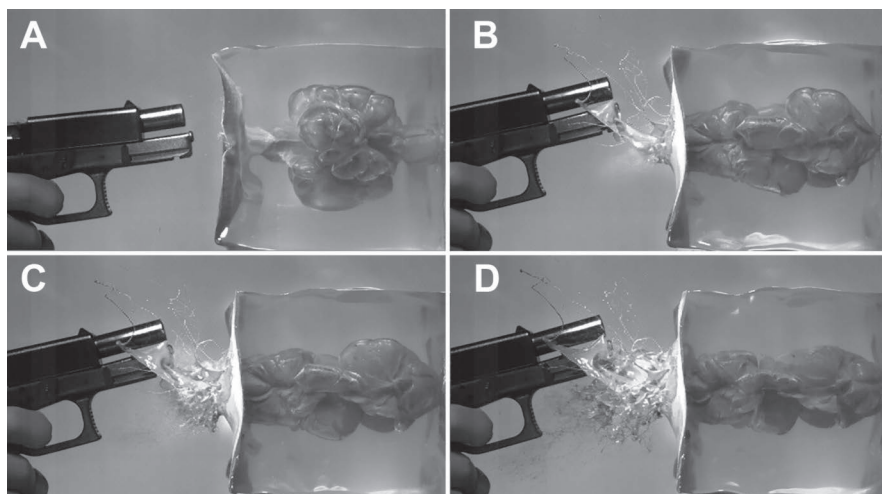
FIGURE 11.13 Nine millimetre Luger shot at 10 mm distance. After the collapse of the temporary cavity (6 ms) the cavity expands again (A = 7.2 ms), a jet is squeezed out and is transformed into spray by escaping gases (B = 12.5 ms, C = 13.3 ms, D = 14.2 ms). Reproduced from Schyma et al. (2021), with permission.

important that the mixture is not heated above 40°C, otherwise erroneous results are possible (e.g., see Fackler and Malinowski (1988)). The gelatin is then poured into molds and placed in cold storage overnight to set. For best consistency, it is recommended that after removal from the molds, the product is stored in a refrigerator in airtight plastic bags for at least 36 hours before use (Fackler and Malinowski, 1988).

An example of ballistic gelatine in use is shown in Figure 11.13, reproduced from Schyma et al. (2021). Here it has been used to study backspatter due to the firing a 9-mm Luger shot at 10 mm distance from the gelatine. The gelatine targets have been doped with a liquid mixture of acrylic paint to reveal the backspatter. The formation and collapse of the temporary cavity are shown.

11.5.2 BALLISTIC SOAP

Ballistic soap is very similar to common bathroom soap in terms of rigidity. The advantage of using a soap to investigate wound tracks is that you would not need high-speed cameras to visualize the temporary cavity. In fact, the temporary cavity otherwise seen in gelatin would be captured by the permanent deformation of the soap. Therefore, with relative ease, the geometry of the cavity produced can elucidate the comparative effectiveness of projectiles (Dyckmans et al., 2003).

11.5.3 BONE SIMULANTS

Bone is a complex hierarchal structured material with varying porosity and mechanical properties. As with all ballistic simulant materials, correlation with real tissue can only be achieved where the simulant's properties match that of the human tissue
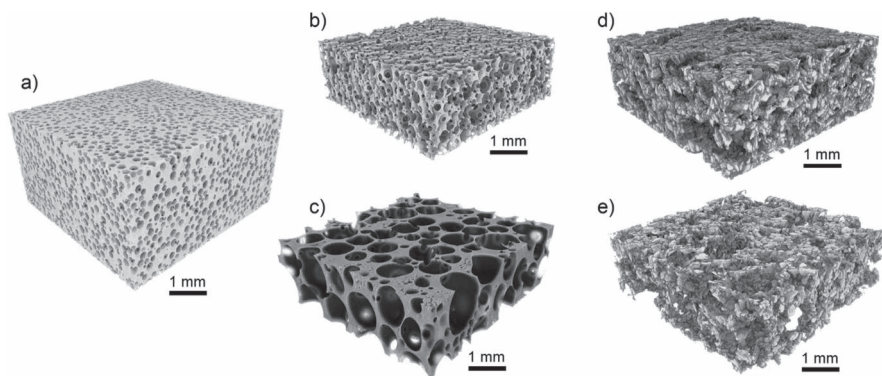
FIGURE 11.14 Computed tomography renderings of commercially available bone surrogates (a) Synbone®, (b) Sawbone A- rigid solid polyurethane foam centre, (c) Sawbone B-closed-cell polyurethane foam centre, (d) Bonesim X- 600 kg/m³ centre and (e) Bonesim Y- 800 kg/m³ centre. Reproduced from Brown et al. (2019), with permission.

in question. Most mechanical property studies on bone have been done at relatively low rates. This may not be a problem per se; however, ballistic processes are clearly fast.

Figure 11.14 shows examples of computed tomography of five commercial bone simulants. These tend to be made from porous polyurethane. Their main purpose is to provide a structure with which orthopaedic surgeons can train skills such as manipulation and sawing and so on. Therefore, it would make sense that their properties match that of human bone tissue reasonably closely.

There is tentative evidence that ballistically, bone simulants can show some similarities to bone tissue. For example, it has been shown that 5-mm flat plates of Synbone® appear to behave similar to porcine bone tissue in gelatine blocks when subjected to ballistic impact. However, 6- and 12-mm plates appeared to behave in a less than satisfactory fashion in terms of the number of fragments produced, energy deposition and projectile tract diameter (Pullen et al., 2021). Similarities between Synbone® and porcine tissue samples when subjected to ballistic impact have also been studied by Henwood and Appleby-Thomas (2020). They noted broad similarities in fracture behaviour. They concluded that Synbone®'s model may be a suitable analogue for bone tissues. However, they added a caveat in that the damage at the impact site in many of their models was not identical to that of bone tissue. Broad similarities from a macroscopic point of view have also been noted when comparing impacts to Synbone® spheres with that of human skulls. However, when examined in closer detail the damage indicated a range of dissimilarities that called for caution in extrapolating such results to real bone (Smith et al., 2015). Other studies have been more damming when assessing similarities. When focusing on fracture morphology of femur samples during ballistic impact it has been reported that two surrogates, Sawbone® and Synbone®, appeared to be found wanting when compared to cadaver samples (Bir et al., 2016). In any case, it seems that one thing is apparent from these studies in that there is a requirement to develop a suitable ballistic simulant that can offer identical ballistic properties to that of bone tissue. Given the variation in properties of human bone tissue depending on the type, age, gender and location in the body, this will be challenging.

11.6   SUMMARY

In this chapter, some of the injury processes due to projectile and blast attacks have been reviewed. Early work in the late nineteenth century showed that there were two principal wounding mechanisms due to projectile or fragment penetration. These are crushing or shearing of the tissue due to the physical penetration and the local propulsion of tissue to form a temporary cavity. The latter causes the tissue to stretch, and if that tissue is resistant to such forces, then relatively little wounding from this process can be expected. Examples of such 'elastic' tissue reside in the lung, the bowel wall and muscles (Fackler, 1988). However, solid organs such as the liver are not accommodating to these temporary strains.

Recent conflicts have shown that the IED is a prolific threat to coalition troops. We have also seen that there are approaches by which armoured vehicles can be

designed to maximize protection from blast and IED attacks. The human body is surprisingly resilient to very-short-duration accelerations; however, our tolerance diminishes very quickly as the duration increases. This is particularly problematic from the point of view of mine and IED blast protection, and there are a number of techniques that have been discussed here that can be employed for maximizing protection. Many of these techniques employ ways of deflecting the blast energy, maximizing the distance between the blast and the occupant and the use of energy-absorbing materials.

NOTES

1 Probably a 6.5×52-mm Mannlicher–Carcano rifle. This is the same type of rifle used in the assassination of President John F. Kennedy.
2 The British Military Field Hospital Shaibah was the military hospital supporting coalition forces in *Southeastern* Iraq. It was the location for treating both coalition troops and Iraqi civilian casualties.

REFERENCES

Baker, W. E., Cox, P. A., Westine, P. S., Kulesz, J. J. & Strehlow, R. A. 1983. *Explosion Hazards and Evaluation*, vol. 5, Fundamental Studies in Engineering. Amsterdam: Elsevier Science.

Bir, C., Andrecovich, C., Demaio, M. & Dougherty, P. J. 2016. Evaluation of bone surrogates for indirect and direct ballistic fractures. *Forensic Science International*, 261, 1–7.

Bir, C. A., Stewart, S. J. & Wilhelm, M. 2005. Skin penetration assessment of less lethal kinetic energy munitions. *Journal of Forensic Sciences*, 50, 1426–1429.

Bowen, I. G., Fletcher, E. R. & Richmond, D. R. 1968. *Estimate of Man's Tolerance to the Direct Effects of Air Blast*. Albuquerque, NM: Lovelace Foundation for Medical Education and Research.

Breeze, J. & Clasper, J. C. 2013. Determining the velocity required for skin perforation by fragment simulating projectiles: A systematic review. *Journal of the Royal Army Medical Corps*, 159(4), 265–270.

Brown, A. D., Walters, J. B., Zhang, Y. X., Saadatfar, M., Escobedo-Diaz, J. P. & Hazell, P. J. 2019. The mechanical response of commercially available bone simulants for quasi-static and dynamic loading. *Journal of the Mechanical Behavior of Biomedical Materials*, 90, 404–416.

Champion, H. R., Holcomb, J. B. & Young, L. A. 2009. Injuries from explosions: Physics, biophysics, pathology, and required research focus. *Journal of Trauma and Acute Care Surgery*, 66(5), 1468–1477.

Courtney, A. & Courtney, M. 2007. Links between traumatic brain injury and ballistic pressure waves originating in the thoracic cavity and extremities. *Brain Injury*, 21(7), 657–662.

Dimaio, V. J. M. 1981. Penetration and perforation of skin by bullets and missiles. A review of the literature. *American Journal of Forensic Medicine and Pathology*, 2, 107–110.

Dyckmans, G., Ndompetelo, N. & Chabotier, A. 2003. Numerical and experimental study of the impact of small caliber projectiles on ballistic soap. *J. Phys. IV France*, 110, 627–632.

Fackler, M. L. 1988. Wound ballistics. A review of common misconceptions. *Journal of the American Medical Association*, 259(18), 2730–2736.

Fackler, M. L. 1996. Gunshot wound review. *Annals of Emergency Medicine*, 28(2), 194–203.

Fackler, M. L. & Dougherty, P. J. 1991. Theodor Kocher and the scientific foundation of wound ballistics. *Surgery Gynecology and Obstetrics*, 172(2), 153–160.

Fackler, M. L. & Malinowski, J. A. 1985. The wound profile: A visual method for quantifying gunshot wound components. *J Trauma*, 25, 522–529.

Fackler, M. L. & Malinowski, J. A. 1988. Ordnance gelatin for ballistic studies. Detrimental effect of excess heat used in gelatin preparation. *American Journal of Forensic Medicine and Pathology*, 9, 218–219.

Harvey, E. N., Korr, I. M., Oster, G. & McMillen, J. H. 1947. Secondary damage in wounding due to pressure changes accompanying the passage of high velocity missiles. *Surgery*, 21(2), 218–239.

Henwood, B. J. & Appleby-Thomas, G. 2020. The suitability of Synbone® as a tissue analogue in ballistic impacts. *Journal of Materials Science*, 55, 3022–3033.

Hinsley, D. E., Rosell, P. A. E., Rowlands, T. K. & Clasper, J. C. 2005. Penetrating missile injuries during asymmetric warfare in the 2003 Gulf conflict. *British Journal of Surgery*, 92(5), 637–642.

Hirsch, F. G. 1968. Effects of overpressure on the ear – A review. *Annals of the New York Academy of Sciences*, 152(1), 147–162.

Hoffman, B., Taw, J. M. & Arnold, D. 1991. *Lessons for Contemporary Counterinsurgencies: The Rhodesian Experience*. Santa Monica, CA: RAND.

Journée, C. 1907. Rapport entre force vive des balles et la gravite des blessures qu'elles peuvent causer. *Rev. d'Artillerie*, 70, 81–120.

Kennedy, D. R. 1983. Improving combat crew survivability. *Armor*, 9, 16–22.

Lee, R. K. H. 2013. W-shaped hull. In *Google Patents*. London, ON, Canada: General Dynamics Land Systems—Canada Corporation.

NATO. 2011. *AEP-55. Procedures for Evaluating the Protection Level of Armoured Vehicles – Volume 2: Mine Threat*. Brussels, Belgium: NATO.

Pullen, A. E., Kieser, D. C., Hooper, G. & Plummer, T. C. H. 2021. A study into the viability of Synbone® as a proxy for Sus scrofa (domesticus) ribs for use with 7.62×51 mm full metal jacket ammunition in ballistic testing. *Forensic Science*, *Medicine, and Pathology*, 17, 665–669.

Ramasamy, A., Harrisson, S. E., Clasper, J. C. & Stewart, M. P. M. 2008. Injuries from roadside improvised explosive devices. *Journal of Trauma and Acute Care Surgery*, 65(4), 910–914.

Ramasamy, A., Hill, A. M., Hepper, A. E., Bull, A. M. & Clasper, J. C. 2009. Blast mines: Physics, injury mechanisms and vehicle protection. *Journal of the Royal Army Medical Corps*, 155(4), 258–264.

Ryan, J. M., Cooper, G. J., Haywood, I. R. & Milner, S. M. 1991. Field surgery on a future conventional battlefield: Strategy and wound management. *Annals of the Royal College of Surgeons of England*, 73(1), 13–20.

Santucci, R. A. & Chang, Y. J. 2004. Ballistics for physicians: Myths about wound ballistics and gunshot injuries. *Journal of Urology*, 171(4), 1408–1414.

Schyma, C., Baumann, F., Madea, B. & Gotsmy, W. 2021. Study of backspatter using high-speed video of experimental gunshots. *Forensic Science, Medicine and Pathology*, 17, 36–46.

Smith, M. J., James, S., Pover, T., Ball, N., Barnetson, V., Foster, B., Guy, C., Rickman, J. & Walton, V. 2015. Fantastic plastic? Experimental evaluation of polyurethane bone substitutes as proxies for human bone in trauma simulations. *Legal Medicine*, 17, 427–435.

Spalding, T. J. W., Stewart, M. P. M., Tulloch, D. N. & Stephens, K. M. 1991. Penetrating missile injuries in the Gulf war 1991. *British Journal of Surgery*, 78(9), 1102–1104.

Sperrazza, J. & Kokinakis, W. 1968. Ballistic limits of tissue and clothing. *Annals of the New York Academy of Sciences*, 152(1), 163–167.

The New York Times. 1898. Science and industry. The New York Times, 27 November 1898. Available at http://query.nytimes.com/mem/archive-free/pdf?_r=1&res=9F01EED6113 9E433A25754C2A9679D94699ED7CF, accessed 5 January 2015.

Tunis, G. C. & Kendall, S. 2013. Vehicle with structural vent channels for blast energy and debris dissipation. U.S. Patent 8,578,834. Pocomoke City, MD: Hardwire, LLC.

Versace, J. 1971. A review of the severity index. *In: Proceedings of the 15th Stapp Car Crash Conference*. Coronado, CA. Warrendale, Pennsylvania: Society of Automotive Engineers.

White, C. S. 1968. The scope of blast and shock biology and problem areas in relating physical and biological parameters. *Annals of the New York Academy of Sciences*, 152(1), 89–102.

White, C. S. 1971. Nature of problems involved in estimating immediate casualties from nuclear explosions. *In: Civil Effects Study*. Springfield, VA: Lovelace Foundation for Medical Education and Research.

Zuckerman, S. 1952. Vulnerability of human targets to fragmenting and blast weapons. *In: Textbook of Air Armament*, pp. 1–243. London: HMSO.

12 Blast and Ballistic Testing Techniques

12.1 INTRODUCTION

There are a variety of techniques that can be used to test the performance of an armour system. Some testing techniques have been developed for the sole purpose of carrying our research into the performance of individual elements of armour, whereas others are well suited to understanding how well a platform responds to a given threat. Some of these will be reviewed here.

First off, it would be worth mentioning that strictly, there is no foolproof testing regime that is ever going to give you 100% confidence that the people who are protected by the armour are going to escape injury—or even death. If there was, then we would never lose soldiers on the battlefield. There are many unknowns in conflict. In fact, to quote United States Secretary of Defense Donald Rumsfeld in his speech to the United Nations in the run-up to the 2003 Gulf War—there are many *known unknowns* and many *unknown unknowns*. Frequently, it is not absolutely clear how large a threat is going to be faced by the soldier, although military intelligence is of course important.

12.2 BALLISTIC TESTING TECHNIQUES

In the drive to understand penetration mechanisms, and to achieve a route to optimize the thickness or properties of individual elements in an armour system, several ballistic tests have been developed.

12.2.1 DEPTH-OF-PENETRATION TESTING

A commonly used test is carried out by attaching an armour tile to a semi-infinite ductile backing material and firing at the target, recording the resulting depth of penetration (DoP) in the backplate and comparing that value to a value of penetration depth achieved without the armour tile in place. This DoP technique was originally developed by Rosenberg et al. (1988, 1990) as a method to suppress the tensile stresses in a ceramic tile that would otherwise be present when a thin backing was used. Over the past 20 years, there have been numerous studies that have used this technique to study the response of target materials impacted by small-arms bullets and rods. The advantage of this method is that it is relatively cheap to establish performance criteria for the armour tile in question; however, its disadvantage is that the semi-infinite backing is not representative of an armour system, and therefore, its value is in assessing comparative tile performance. These performance criteria are derived from the measured reduction in penetration and the mass of material required to reduce the penetration depth (see Figure 12.1). However, where the core
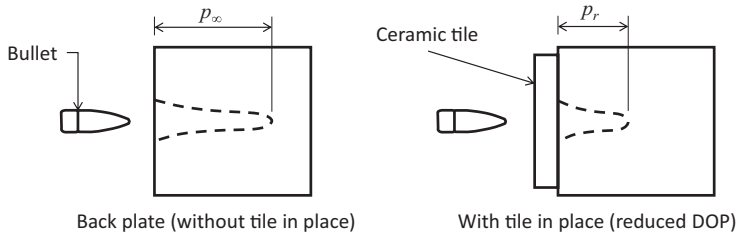
FIGURE 12.1 The DoP technique.

of the bullet remains intact, it has been shown that the DoP test essentially measures the hardness of the ceramic tile (which is an expensive way of carrying out a hardness test; see Hazell (2010)).

A number of performance factors can be calculated from the data generated by the DoP test. Three of the most common factors reported in the open literature are: (1) The mass efficiency factor; (2) The differential tile efficiency factor and (3) The critical thickness. These are now discussed below.

The mass efficiency (E_m) factor (or mass effectiveness) compares the ballistic performance of the target (e.g. a ceramic) with that of a baseline target. Rolled homogeneous armour (RHA) is frequently used for high-velocity rod-based projectiles, whereas softer and lower-density materials such as polycarbonate and aluminium are used for bullet-impact studies. E_m is defined as follows:

$$E_m = \frac{p_\infty \rho_{st}}{h_c \rho_c + p_r \rho_{st}}$$
(12.1)

where the subscripts 'st' and 'c' refer to steel and ceramic, respectively, h is the thickness and ρ is the density. p_∞ is the penetration into the semi-infinite RHA (steel) baseline target without a ceramic tile. E_m represents the factor by which the areal density must be multiplied if an entire armour combination, consisting of a ceramic of thickness h_c and an RHA plate of thickness p_r, was to be replaced by RHA or equivalent to provide the same protection. But actually, when calculated from DoP measurements, the presence of the semi-infinite backing will enhance the protection offered by the backing plate, and therefore, p_∞ and p_r will be less than the thickness of plates that would be required; one rarely has the luxury of using semi-infinite backing materials in armour systems.

The differential tile efficiency (Δe_c) is the factor by which the areal density of backing plate material penetrated is reduced by the addition of a ceramic tile, normalized by the target material's areal density. It is given as

$$\Delta e_c = \frac{(p_\infty - p_r) \rho_{st}}{h_c \rho_c}$$
(12.2)

One further calculation can be undertaken to estimate the performance of an armour system from a single experiment and establish a critical thickness of material required to stop the round. This critical thickness (T_{cr}) is given by

$$T_{cr} = \frac{p_\infty h_c}{(p_\infty - p_r)} \tag{12.3}$$

However, where there is more than a single point of data representing a single thickness of ceramic (as is normally the case), or if you have data for multiple thicknesses, it is normally better to plot the penetration into the witness plate against the corresponding thickness of the ceramic. It is then a simple task to fit a line of regression to estimate the critical thickness that will be required to result in no penetration in the witness plate.

The choice of the back plate is important for ceramic-faced targets as it will affect the final result of the test. Rosenberg et al. (1990) have shown that increasing the strength of the back-plate results in an increase in the mass efficiency (according to Equation 12.1). They showed that comparing results between three different back-plate materials (AISI 1020 steel, RHA and HHA) led to an increase in resistance. The reasoning for this behaviour is that a ceramic tile behaves better when it faces a stronger (or denser) material as it is less likely to fail by bending.

12.2.2 Non-Linear Behaviour

DoP testing is best designed to provide a snapshot of a given tile performance at a particular velocity. And, for ceramic tiles, DoP testing will tend to improve as the thickness of the tile is increased as the impact face is moved further away from the interface between the backing plate and the ceramic tile. At very high velocities (>2000 m/s), it is possible that impacting the metal backing plate alone will lead to projectile disruption and a drop in DoP at some critical impact velocity. Figure 12.2 shows the result of a 6.35-mm steel sphere impacting an aluminium alloy target
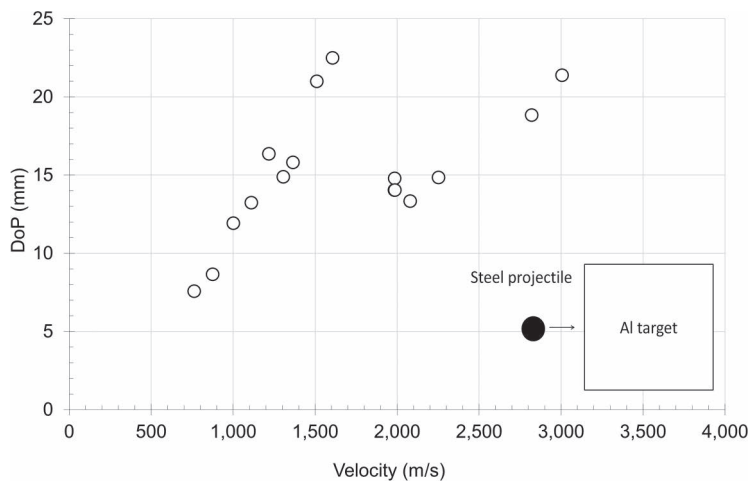
FIGURE 12.2 DoP measurements from a 6.35-mm diameter steel projectile striking an aluminium plate at high velocities. (After Hazell, P. J. et al. 1998. *International Journal of Impact Engineering,* 21 (7), 589–595.)

(AA 6082-T6) at a range of velocities. At approximately 1600 m/s, it can be seen that there is a drop in DoP. This data was discussed in some detail in Chapter 4. There has also been a similar velocity drop off noted in rod-like projectiles—see Section 4.4. So, measuring the ballistic efficiency over the broad range of velocities will result in a highly non-linear relationship with velocity.

12.2.3   BALLISTIC-LIMIT TESTING

Another method for testing performance is by using the v_{50} approach, and this is usually reserved for actual armour systems where bending stresses would be seen on the rear surface of the ceramic. This is an important test for evaluating the ballistic performance of actual armour systems. The advantage of this technique over the DoP-test technique is that the complete system is tested rather than the component of the system (i.e. the ceramic), and it will provide an indication of the performance of the armour. To carry out a ballistic-limit test, you need

- A ballistics range (obviously)
- A means of measuring the projectile velocity
- A means by which the projectile velocity can be 'tweaked' either by changing the mass of the propellant or by warming the propellant in the cartridge a little

The rationale behind ballistic-limit testing is that for a given armour plate, there is going to be a range of mixed results across a fairly narrow velocity band. So, below the velocity that we shall call v_0, all projectiles will be stopped by our armour (see Figure 12.3). If 10 firing shots were carried out at $v = v_0$, then all projectiles would
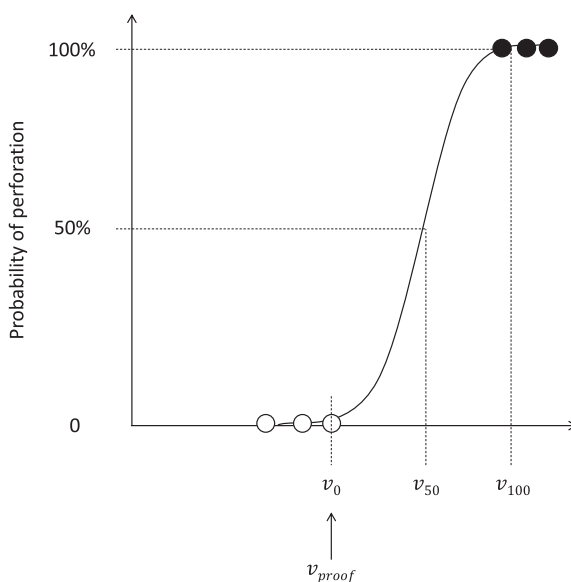
FIGURE 12.3   Ballistic-limit testing.

be expected to be stopped. Equally, above a slightly higher velocity, which we shall call v_{100}, then we would expect all the projectiles to perforate the target. Out of 10 firings, we would expect 10 perforations when $v = v_{100}$. In between v_0 and v_{100}, we would expect to see a range of mixed results where some of the projectiles are stopped, and some are not. In fact, in this zone, it is quite possible that one projectile that is stopped by the armour has an impact velocity that is higher than a similar projectile that perforates the armour. The principal reason for this is that it is pretty much impossible to tie down every variable in a ballistic test. Even for seemingly identical ammunition and targets, there can be small differences in

- The geometry of the bullet
- The mass of the core of the bullet
- The pitch or yaw of the bullet at the point of impact
- The strength or hardness of the armour plate at the point of impact
- The microstructure of the armour plate at the point of impact
- The thickness of the armour plate at the point of impact

Thus, it is sometimes convenient to establish a v_{50} velocity where it would be expected that 50% of our projectiles would be stopped by the plate, and 50% of the projectiles would perforate.

Of course, how is perforation or failure of the armour target defined? Early tests of gun shields followed a prescribed format as outlined by O. M. Lissak (1907, pp. 475–476) such that

> The shield, firmly supported by a backing of oak timbers, is subjected to three shots from a 5-inch gun. The striking velocity of the shot is 1500 feet [per second] and the normal impact. On the first impact, near the center of the shield, no portion of the projectile shall get through the shield, nor shall any through crack develop to an edge of the shield. The other two impacts are so located that no point of impact shall be less than three calibers of the projectile from another point of impact or from an edge of the shield. At the second or and third impacts no projectile or fragment of projectile shall go entirely through the shield.

So for Lissak's gun shields, the first projectile is not allowed to break the rear surface, whereas the other two projectiles are allowed to break the rear surface of the target but not carry on through in their entirety.

Others would be less prescriptive and dictate that perforation only occurs when an impacting projectile results in itself, a piece of the projectile or target debris passing through a witness plate located behind the target such that there is a clearly visible hole in the witness plate. This is the requirement for AEP-55 Vol. 1 (NATO, 2011a). Further details can also be found in military standards (e.g. MIL-STD-662F [US Army Research Laboratory, 1997]).

The following example outlines how to determine the v_{50}:

Example 12.1: How to Calculate the v_{50}

A series of ballistic tests have been carried out on an 8-mm steel plate with a 7.62-mm NATO ball projectile. The impact velocity and the result are recorded as well

TABLE 12.1
Ballistic Test Results

Test No.	Velocity of Impact (m/s)	Result
1	750	CP
2	720	PP
3	735	PP
4	749	CP
5	734	PP
6	748	PP

CP, complete penetration; PP, partial penetration.

TABLE 12.2
Further Ballistic Test Result to Satisfy MIL-STD-662F

Test No.	Velocity of Impact (m/s)	Result
7	763	CP

CP, complete penetration; PP, partial penetration.

as the result. CP=complete penetration (i.e. perforation), and PP=partial penetration (i.e. no perforation). The results are provided in Table 12.1. Determine the v_{50} according to MIL-STD-662F with a velocity span of 40 m/s.

Note that MIL-STD-662F allows for the v_{50} to be calculated by taking the arithmetic mean of an equal number of the highest partial and the lowest complete penetration impact velocities within an allowable velocity span as defined by the contracting officer, in this case, 40 m/s (this is the span as dictated by STANAG 2920—a different military standard). Unfortunately, the results do not satisfy the requirements for the test as Test 6 was a PP despite it being very close to Test 4 at 749 m/s, which was a CP.

Therefore, a further test (or further tests) is required; this is given in Table 12.2.

Test 7 now satisfies our requirement as we have the three highest velocities where there was a PP (735, 734, 748 m/s) and the three lowest velocities that resulted in a CP (750, 749, 763 m/s) within 40 m/s, and so, the arithmetic mean of all six firings can be taken. This is 746.5 m/s, and therefore,

$$v_{50} = 746.5 \text{m/s}$$

It should be noted that MIL-STD-662F has strict advice on velocity increments and decrements for each subsequent firing, and these have been approximated here.

12.2.4   SHATTER GAP

An interesting nuance of a ballistic-limit testing is that occasionally, it is evident that two ballistic-limit curves occur. This can occur for a couple of reasons, and it is
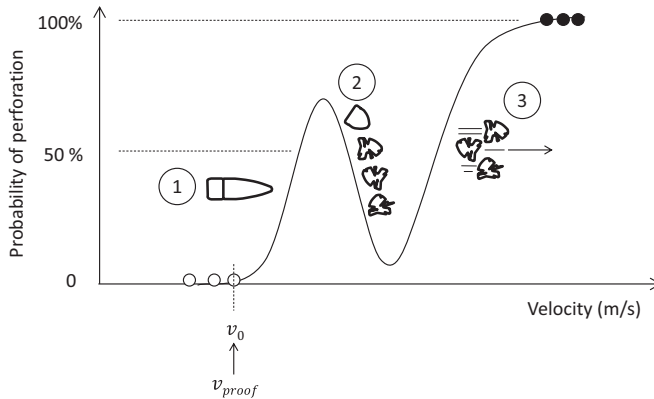
FIGURE 12.4 What happens during a series of tests that exhibit shatter gap.

mostly associated with ceramic-faced armour tiles. An example of the appearance of shatter gap is shown in Figure 12.4. Initially, at $v = v_0$, as before, no projectile perforates the target. Increasing the velocity of the projectile results in perforation (1) until the velocity is increased, and the projectile begins to fragment or shatter (2). At this point, the projectile has been broken up by the target, and therefore, it is more difficult for it to perforate the target. Therefore, the probability of perforation reduces. That is until at (3), the velocity of the projectile is travelling fast enough to perforate the target irrespective of shattering during penetration. The end result is that it is possible to establish two v_{50} velocities, and this can (understandably) create a bit of confusion for the tester. See Appendix D in AEP-55 Vol. 1 (NATO, 2011a).

12.2.5 PERFORATION TESTS

If the projectile is non-deforming, and the target does not fragment, it is possible to consider a crude energy balance for the perforation process. This was a popular lab demonstration at Cranfield University (Shrivenham campus).

Consider a projectile striking a plate at velocity v_0 with a mass of m_i that leaves the rear of the plate with a velocity v_r and with a mass of m_r. The velocities can be measured by a suitable system located before and after the target. The percentage of kinetic energy (%KE) transferred in the penetration process is given by the following:

$$\%\text{KE} = \left(\frac{\frac{1}{2} m_i v_0^2 - \frac{1}{2} m_r v_r^2}{\frac{1}{2} m_i v_0^2} \right) \times 100 \tag{12.4}$$

If the mass of the projectile remains constant throughout (i.e. $m_i = m_r$), this can be simplified to

$$\%\text{KE} = \left(\frac{v_0^2 - v_r^2}{v_0^2} \right) \times 100 = \left[1 - \left(\frac{v_r}{v_0} \right)^2 \right] \times 100 \tag{12.5}$$
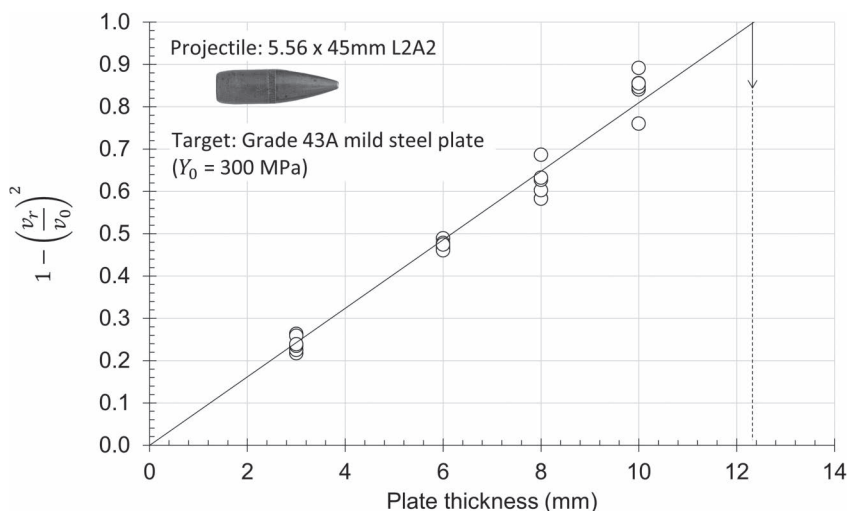
FIGURE 12.5 Fraction of KE transferred from the bullet during the perforation of a mild steel plate by a 5.56×45-mm L2A2 bullet. The trend line indicates the thickness at which this bullet would be stopped (at muzzle velocity ~920 m/s), which indicates a value of just over 12 mm.

In reality, there will always be mass lost by the projectile due to the jacket being stripped away or soft parts of the core (where Pb is used) being dispersed during the penetration process.

Plotting %KE against the plate thickness of several thicknesses of the plate will provide the ballistic limit for the plate. This provides a fairly good approximation even for cases where the projectile is expected to deform and lose mass. Figure 12.5 shows an example of some recorded data of a bullet perforating a plate. At small plate thicknesses, the fraction of KE transferred holds to small groupings, whereas at larger plate thicknesses the dispersion of the data is as one would expect. Nevertheless, plotting an averaged trend line through the data (and through the origin) gives a reasonable prediction of what thickness of the plate would result in the projectile being stopped. In this case, it is just over 12 mm, which is about right for this target plate.

12.2.6   USING A BALLISTIC PENDULUM

A ballistic pendulum is a device that sits behind a target and measures the momentum of a projectile that has passed through a target. In its simplest form, it comprises a steel 'catching tube' that is suspended from the roof of the ballistics range. Before the main experiments are carried out, the pendulum is calibrated by firing various projectiles, of known mass, at varying (measured) velocities. As a bullet enters the pendulum's catching tube, the pendulum will swing. The height of the swing is thus calibrated with the momentum of the bullet. Therefore, knowing the momentum of a bullet before impact and the momentum of the projectile after perforation, it is possible to calculate the impulse delivered to the target plate. A similar device can also be used to measure the impulse due to an explosive charge.
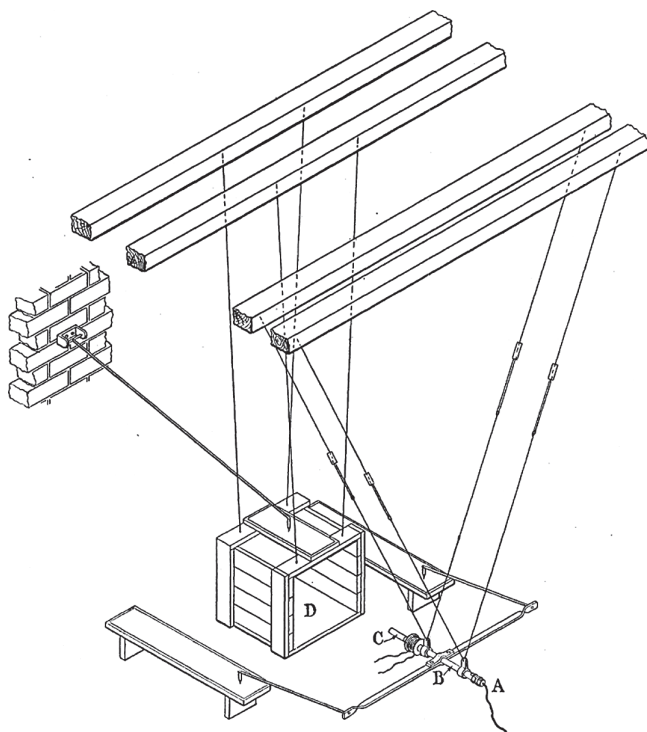
FIGURE 12.6 The ballistic pendulum setup as used by B. Hopkinson. (From Hopkinson, B. 1914. *Philosophical Transactions of the Royal Society,* 213 (10), 437–452.)

A problem with this approach arises when there are multiple high-velocity ejecta from the rear surface of the target. If this occurs, it is challenging to decouple the momentum of the bullet from that of the ejecta.

B. Hopkinson (1914) used a ballistic pendulum to assess the approximate shape and magnitude of a stress wave in a steel bar. Hopkinson's experiments consisted of firing a lead-cored projectile at a steel bar. At the rear end of the bar, a rod of identical diameter was magnetically attached, which flew off into a ballistic pendulum. Thus, by measuring the momentum trapped in the flying rod (by the momentum given to the ballistic pendulum), a portion of the stress–time integral in the bar due to the impact could be established. By varying the length of the 'flyer' rod, a picture of the shape and magnitude of the stress pulse was derived. These experiments were also repeated by detonating gun cotton at the end of the bar. A setup of Hopkinson's famous experiment is shown in Figure 12.6.

12.2.7 THE REVERSE BALLISTIC TEST

A lot of recent work has focused on using a reverse ballistic approach to investigate mechanisms—particularly of interface defeat and dwell and to examine the effect of bullet jackets on ballistic performance. With this technique, the 'target'

is accelerated towards a stationary 'projectile'. Of course, the definition of target is switched around, and now, the projectile that would be fired in forward ballistic experiments becomes the target. There are several advantages. These are as follows:

1. It is easier to set up, position and align the target at a pre-defined orientation.
2. It allows for experiments to be done in a laboratory setting using existing large-calibre gas guns.
3. It avoids any unwanted yaw or spin that may otherwise arise due to the use of a conventional forward ballistic approach.
4. The projectile package is simple to manufacture in that it comprises the sabot made from either acetal or polycarbonate with the armour material to be tested attached to the front (similar to a plate-impact experiment projectile).

However, there are substantial disadvantages in that the lateral extent of the target is limited by the calibre of the gun. Consequently, for brittle targets, confined specimens are usually required to limit the effect of the release waves emanating from free surfaces—particularly for thick samples.

A typical reverse ballistic setup is shown in Figure 12.7 where the target is suspended on a support at the end of the muzzle of the gun. This technique has been used successfully by a variety of researchers to study the penetration of ceramic and metals. In each case, the diameter of the ceramic is very small and is surrounded by either a titanium or aluminium sleeve. Furthermore, very low diameter rods are used with rods with diameters as low as 0.762 mm being reported (Orphal et al., 1996).
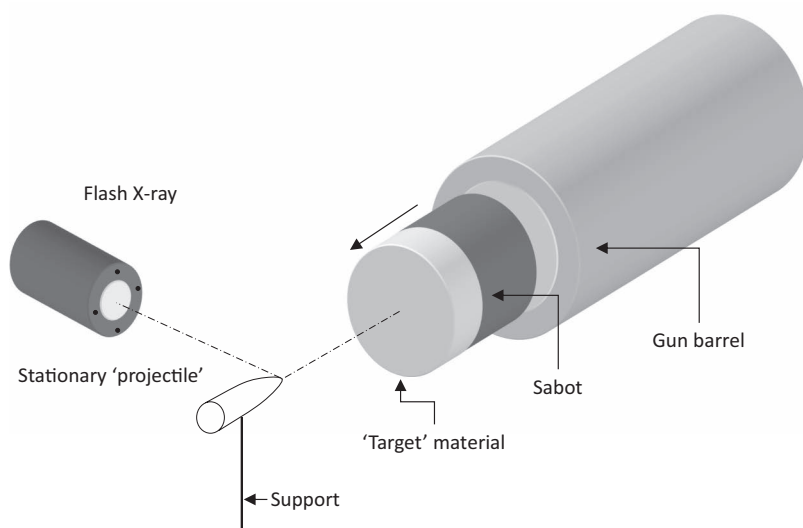
FIGURE 12.7   Schematic of the reverse ballistic experimental approach showing the stationary 'projectile' and the incoming 'target'.

12.3 BLAST AND FRAGMENTATION TESTING TECHNIQUES

Blast wave testing of a material, system or structure has historically been carried out on large open plan ranges that have a pre-defined limit on the mass of explosive and the degree of fragmentation hazard that can be accommodated. Once upon a time, blast testing was a fairly crude affair where an explosive was detonated, and the only metric that was applied was to establish how 'bent the metal was'. Nowadays, range testing with explosives adopts a much more scientific approach, and this has largely been driven by the price of high-speed diagnostics and cameras becoming more affordable and the fact that there has been a significant drive to understand the effect of blast waves on vehicles and personnel since the 2003 Gulf War.

12.3.1 Fragment Simulators

One of the challenges of assessing the response of a material or structure to a fast-moving fragment propelled by an exploding shell or improvised explosive device is the problem that very often, the shape, size, velocity, angle of attack and drag characteristics of the fragment are not known. The detonation of a high-explosive shell would produce a distribution of fragments of varying mass and velocity.

Figure 12.8 shows the velocity distribution of fragments from 155- to 105-mm artillery shells (US Army Test and Evaluation Command, 1983). There is a central 'main spray' region of 25° where high-velocity fragments are propelled. The
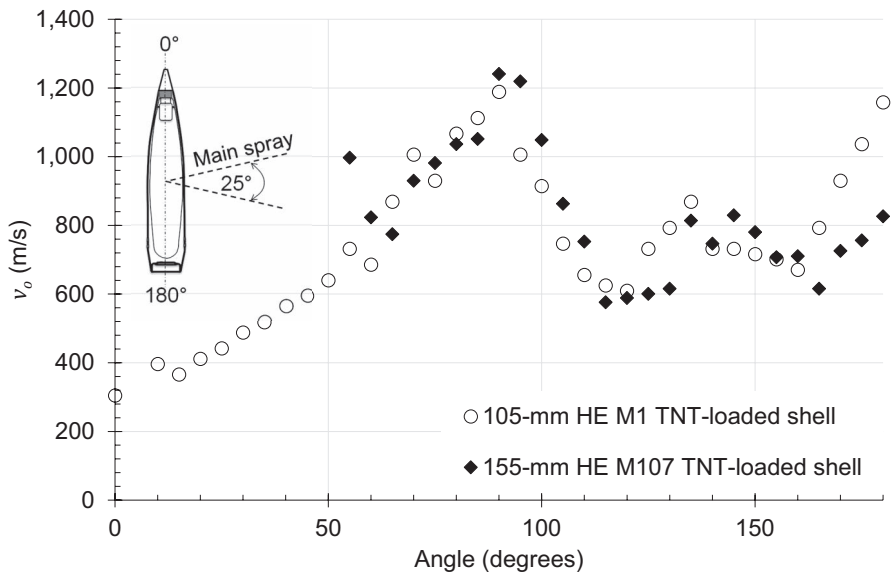
FIGURE 12.8 Initial velocity of fragments (v_o) and distribution due to the detonation of a 105-mm M1 shell and a 155-mm M107 artillery shell. (Data from US Army Test and Evaluation Command, 1983. *Fragment Penetration Tests of Armor*. Aberdeen Proving Ground, MD: US Army Aberdeen Proving Ground [STEAP-MT-M].)

TABLE 12.3
FSP Velocities for Testing against Different STANAG 4569 Protection Levels

Protection Level[a]	Range of Burst (m)	20-mm FSP Velocity (m/s)
6	10	1250
5	25	960
4	25	960
3	60	770
2	80	630
1	100	520

Source: NATO, AEP-55 2011a. *Procedures for Evaluating the Protection Level of Armoured Vehicles-Volume 1: Kinetic Energy and Artillery Threat*. Brussels, Belgium: NATO.

[a] For STANAG 4569, levels 1–3 are not required.

maximum velocity of the fragments is around 1250 m/s. This means that it is just about achievable to replicate this velocity using a conventional barrel in a Small Arms Range.

Accordingly, STANAG 4569 levels of protection for vehicles are defined by six levels of protection where the highest level of protection must protect against a fragment simulator impacting at 1250 m/s (see Table 12.3). This velocity diminishes for extended ranges (and hence protection levels). For extended ranges (levels 1–3), where air bursts would be expected to be at about 60–100 m range, fragment simulating projectile (FSP) testing is not commonplace. This is due to:

1. Anticipated high drag forces acting on the fragment leading to relatively low impact velocities.
2. The probability of impact being low at ranges of 60–100 m.
3. A highly probable low angle of attack on the vehicle's roof (which would result in ricochet).

Therefore, the defined KE threats at these levels are regarded as being sufficiently potent to assess protection.

A typical schematic of a 20-mm FSP and a photo of a slightly smaller (14.5-mm) FSP are shown in Figure 12.9. These will be made from cold-rolled, annealed steel (i.e. AISI 4340H) with a yield strength of ~475 MPa. The protruding flare at the tail of the FSP is larger than the 20-mm calibre. The reason for this is so that it engages in the rifling of the barrel when fired. These FSPs are pushed into conventional gun cartridges (i.e. 20 or 14.5 mm in this case), and the ammunition is then loaded in a conventional fashion. The lengths of the FSPs shown below are 24 and 20 mm for the 20- and 14.5-mm FSPs, respectively. Further details on FSP designs can also be found in NATO (2003) with some earlier designs provided by MIL-P-46593A(ORD) (US Army, 1962).

19.89 ± 0.05

20.83 +0.08

(a)   (b)
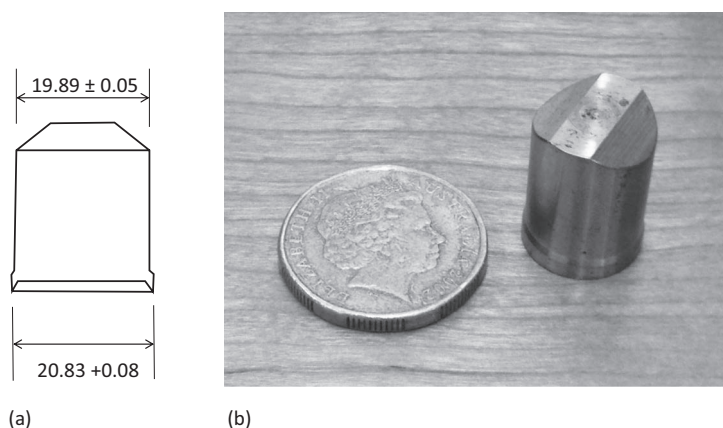
FIGURE 12.9 (a) A 20-mm FSP (From NATO, AEP-55, 2011a. *Procedures for Evaluating the Protection Level of Armoured Vehicles – Volume 1: Kinetic Energy and Artillery Threat.* Brussels, Belgium: NATO) and (b) a photograph of a slightly smaller 14.5-mm FSP next to an Australian dollar coin; dimensions in mm.

12.3.2 BLAST AND SHOCK SIMULATORS

It is often desirable to produce the type of impulse and reflected pressure that would be expected from an explosive blast—but without the use of an explosive. There are several reasons why this is attractive to research groups. Firstly (and probably most importantly), there is no requirement to store explosive materials. The storage of explosive materials usually requires a licence and has to be done safely and securely by appropriately trained staff. Therefore, explosive storage will carry a cost overhead. Secondly, the experiments can be done in a 'cleaner' laboratory environment that is usually well aligned with other activities. Thirdly, there is more control of the direction of the blast. That is to say that the 'blast' wave can be directed at the structure in one direction.

A very simple form of blast simulator involves the use of a shock tube. In simple terms, a shock tube consists of a cylindrical section of the tube part which contains a high-pressure region separated from an ambient-pressure region with a diaphragm. Once the diaphragm is burst by the operator, the high-pressure gas expands rapidly thereby compressing the air in the ambient-pressure region. Thus, a blast wave is simulated. However, it is somewhat more complex than is outlined here, and careful attention needs to be applied to the ambient-pressure tube so that reflections of surfaces do not provide a false pressure–time profile.

Similar to the shock-tube concept outlined above, it is possible to simulate an underwater shock on a material or structure by launching a projectile at a column of water to produce a wave that can be used to test shocks from underwater explosions. An example is outlined by Deshpande et al. (2006). Here, they used a tube arrangement that was 1.4 m in length with an internal diameter of 45 mm and a wall thickness of 7 mm. At one end, the test piece is placed, whilst at the other end, an aluminium piston is configured to receive a blow from a projectile (diameter = 28.5 mm).

It is important that air is not trapped in the water column as this can attenuate the shock generated within the water. Consequently, a bleed valve was integrated into the aluminium piston to account for this. The pressure–time profile of the shock is measured using a piezoelectric transducer and confirmed with measurements of the hoop strain. The hoop strain, ε_h, is related to the thin-walled cylindrical pressure by

$$P(t) = \frac{2Ew\varepsilon_h(t)}{d+w} \tag{12.6}$$

where
   E is the Young's modulus of the tube material,
   w is the wall thickness of the tube and
   d is the internal diameter of the tube.

The specifications of the piezoelectric transducer that Deshpande et al. used are summarized in Table 12.4. The gauge length of the strain gauge to measure the hoop strain was 1 mm to maintain a suitable frequency response.

12.3.3 BLAST MINE SURROGATES

Approximately 80% of the mines that are encountered by armoured vehicles are blast mines. It, therefore, is necessary to provide a suitable replicable method of testing how a mass of explosive interacts with a vehicle structure. Consequently, there have been several mine surrogates specified that fulfil this requirement (NATO, 2011b). There are four protection levels for occupants of armoured vehicles for grenade and blast mine threats. Protection level is decided based on

- Explosive mass (10 kg for protection level 4);
- Surrogate mine location (i.e. under the wheel/track or under the vehicle's belly).

In addition, the type of soil that the mine is buried in is particularly important as the moisture content of the soil will ultimately affect the load transmitted to the vehicle.

TABLE 12.4
Piezoelectric Pressure Transducer Specifications for an Underwater Shock Simulator

Type	Model 102A03 of PCB Piezotronics Inc.
Dynamic pressure range	0–69 MPa
Rise time	<1 μs
Resonant frequency	>500 kHz

Source: Deshpande, V. S. et al. 2006. *Proceedings of the Royal Society A: Mathematical, Physical and Engineering Sciences*, 462(2067), 1021–1041.

TABLE 12.5
Two Level 1 Surrogate Mines; the Second Is the More Severe

Level	Explosive Mass (g)	Explosive Type	Fragments	Expected Fragment Velocity (m/s)
1	>300	C4, Comp B (high explosive)	Pre-fragmented 0.4-g hard steel spheres (750 minutes)	1150–1200
1	550 + 20-g booster	Cast TNT	Pre-fragmented 3.9-g hard steel cylinders (350 minutes)	950

For example, in sand, it has been shown that the presence of moisture leading to a 22% increase in density resulted in a 27% increase in momentum being transferred to a flat plate located above the explosion (Anderson, Jr et al., 2011).

The main point about a surrogate is that it provides consistency in the loading to the structure, and therefore, the results are repeatable. Placing the explosive in a steel pot also increases the reproducibility of tests. Two Level 1 surrogates, as stated in NATO (2011b), are presented in Table 12.5.

12.3.4 EXPLOSIVE BULGE TEST

The explosive bulge test is designed to test how a material deforms due to an incoming shock wave that has been generated by an underwater shock or air blast. It was originally developed by Pellini in 1952 to test welds and understand the crack propagation characteristics of a plate that had a 'synthetic' notch machined into it by means of a grinding wheel (Pellini, 1952). However, it is also useful to assess how the plate bulges and whether or not the bulging will lead to failure.

Plates are positioned in either circular dies (for balanced biaxial loading) or elliptical dies (for unbalanced biaxial loading). Pellini used 381-mm (15-in.) diameter circular dies and 317.5×457.2-mm (12.5×18-in.) elliptical dies for the weld tests. The explosive is then set at a distance from the plate such that

    a. Uniform loading of the plate is achieved by the gas pressure of the explosive.
    b. An area of uniform strain that encompasses the area of interest (i.e. the weld) is achieved.
    c. Brisance (explosive shattering) is minimized.

The explosive blast pushes the plate into the die resulting in a bulged plate. This is then analyzed for failure.

12.4 SUMMARY

In this chapter, some of the blast and ballistic testing techniques that are commonly used on ranges to assess the performance of materials and structures have been summarized. It is important to point out that when carrying out such experiments,

the acquisition of as much data as possible is desirable. This is mainly due to the destructive nature of the tests and the short time duration over which they occur. High-speed framing cameras or flash X-ray equipment are useful for capturing the response of the material and can serve as a good diagnostic where there is an unexpected result. Of course, we all like to think that there will never be such a thing as an unexpected result.

REFERENCES

Anderson Jr., C. E., Behner, T., & Weiss, C. E. 2011. Mine blast loading experiments. *International Journal of Impact Engineering*, 38(8–9), 697–706.

Deshpande, V. S., Heaver, A. & Fleck, N. A. 2006. An underwater shock simulator. *Proceedings of the Royal Society A: Mathematical, Physical and Engineering Sciences*, 462(2067), 1021–1041.

Hazell, P. J. 2010. Measuring the strength of brittle materials by depth-of-penetration testing. *Advances in Applied Ceramics*, 109(8), 504–510.

Hazell, P. J., Fellows, N. A. & Hetherington, J. G. 1998. A note on the behind armour effects from perforated alumina/aluminium targets. *International Journal of Impact Engineering*, 21(7), 589–595.

Hopkinson, B. 1914. A method of measuring the pressure produced in the detonation of high explosives or by the impact of bullets. *Philosophical Transactions of the Royal Society*, 213(10), 437–452.

Lissak, O. M. 1907. *Ordnance and Gunnery: A Text Book*, 1st ed. New York: John Wiley & Sons, Inc.

NATO. 2003. *STANAG 2920 Edition 2: Ballistic Test Method for Personal Armour Materials and Combat Clothing*. Brussels, Belgium: NATO Standardisation Agency (NSA).

NATO. 2011a. *AEP-55. Procedures for Evaluating the Protection Level of Armoured Vehicles – Volume 1: Kinetic Energy and Artillery Threat*. Brussels, Belgium: NATO.

NATO. 2011b. *AEP-55. Procedures for Evaluating the Protection Level of Armoured Vehicles – Volume 2: Mine Threat*. Brussels, Belgium: NATO.

Orphal, D. L., Franzen, R. R., Piekutowski, A. J. & Forrestal, M. J. 1996. Penetration of confined aluminum nitride targets by tungsten long rods at 1.5–4.5 km/s. *International Journal of Impact Engineering*, 18(4), 355–368.

Pellini, W. S. 1952. *Use and Interpretation of the NRL Explosion Bulge Test*. Washington, DC: Naval Research Laboratory.

Rosenberg, Z., Bless, S. J., Yeshurun, Y. & Okajima, K. 1988. A new definition of ballistic efficiency of brittle materials based on the use of thick backing plates. In: *Impact Loading and Dynamic Behaviour of Materials*. Oberursel, Germany: DGM Informationsgesellschaft mbH.

Rosenberg, Z., Yeshurun, Y. & Tsaliah, J. 1990. More on the thick-backing screening technique for ceramic tiles against AP projectiles. *In: Proceedings of the 12th International Symposium on Ballistics*, . San Antonio, TX, 30 October–1 November.

US Army Research Laboratory. 1997. *MIL-STD-662F. Department of Defense Test Method Standard: V50 Ballistic Test for Armor*. Aberdeen Proving Ground, MD: US Army Research Laboratory, Department of Defense.

US Army Test and Evaluation Command. 1983. *Fragment Penetration Tests of Armor*. Aberdeen Proving Ground, MD: US Army Aberdeen Proving Ground (STEAP-MT-M).

US Army. 1962. MIL-P-46593A (ORD). Projectile calibers .22, .30, .50 and 20 mm fragment-simulating. US Army (Ord).

Glossary

Absorber   The part of an armour system that can transfer the kinetic energy of the projectile or fragments to a lower form of energy, usually by a process of plastic deformation or delamination.

Adiabatic shear   A process where, during the penetration of a projectile in a target, the rate of thermal softening exceeds the rate of work hardening leading to the formation of shear failure bands. There is no heat transfer from (or to) the heat-affected area.

Alloy   A mixture of two or more elements where at least one of them is a metal.

Ammunition   Any munition of war whether filled with solid shot or explosive.

Amorphous   A noncrystalline state where the arrangement of atoms has no periodicity.

Angle of obliquity   The angle between the projectile trajectory and the normal to the surface of impact.

Anisotropic   Possessing different material properties along different axes in three-dimensional space; not isotropic.

Anti-tank guided weapon (ATGW)   A vehicle- or infantry-launched warhead that is capable of being guided or guiding itself to attack a target – usually with a shaped-charge warhead. Sometimes referred to as an anti-tank guided missile (ATGM).

Areal density   The mass of a plate divided by its cross-sectional area. It can also be calculated by multiplying the bulk density of the plate material by its thickness.

Armoured fighting vehicle (AFV)   The generic name for a military vehicle, tracked or wheeled, that is designed to engage in warfighting.

Armoured personnel carrier   An armoured vehicle (tracked or wheeled) designed to carry troops into a conflict zone.

Armour piercing   Projectile with a hard core designed to penetrate and perforate hard targets.

Armour-piercing discarding sabot   A sub-calibre solid shot of relatively low length/diameter ratio (~5) that is carried along a gun barrel by a sabot that is discarded when exiting the muzzle. It is usually spin-stabilized.

Armour-piercing fin-stabilized discarding sabot   A sub-calibre solid shot of relatively high length/diameter ratio (~15) that is carried along a gun barrel by a sabot that is discarded when exiting the muzzle. It is usually drag stabilized.

Armour-piercing incendiary   Projectile with an armour-piercing core and a low-explosive material encased in the tip that deflagrates when the bullet impacts armour.

Attenuate   To reduce in force or value. The term is frequently used to describe the weakening of a stress or shock wave.

Austenite   A relatively soft crystalline structure that is formed in steels at elevated temperatures. It is occasionally present with martensite in drastically quenched steels.

Azimuth   A directional bearing but usually used in reference to protection in terms of a 90° arc – that is, from the zenith to the horizon.

Bainite   A constituent of steel that can form when a steel is cooled from the austenitic region. Under a microscope it can be seen as a fine plate-like structure of cementite and ferrite that is very strong. It is named after Edgar Collins Bain (1891–1971).

Ballistic limit velocity   The velocity at which there is a specific probability that a known projectile will just perforate the target. Therefore, a v_{50} is the velocity at which 50% of the projectiles will just perforate the target.

Ballistic pendulum   A device for measuring the momentum of a projectile or fragment(s).

Bauxite   A mineral that is extracted from the earth's crust containing oxides of aluminium, silicon and iron and from which alumina powder is extracted.

Behind armour effects   The fragmentation, or blast and overpressure, that occurs after a projectile or shaped charge jet perforates armour.

Blast wave   A destructive wave produced by the detonation of an explosive.

Blunt trauma   Injury that occurs when a body armour vest is not perforated, but the momentum transfer of the impact causes large deformation in the backing layer. It can lead to bruising, serious injury to major organs, or even death.

Brinell indenter   A spherical hard steel indenter that is used to measure the hardness of a material – usually metal.

Brittle fracture   This occurs when a projectile strikes a target with a low *fracture toughness*. Typically, the target will shatter into a large number of fragments. Examples of materials that suffer from brittle fracture are brick, ceramic and glass. Very little energy is required to form new fracture surfaces.

Bullet   A projectile that is fired from a gun and is usually encased in a metallic jacket that engages with the gun's rifling to enable spin stabilization.

Calibre   The nominal diameter of the bore of a gun. For a rifled barrel, it is measured across the lands of the rifling.

Carburizing   The diffusion of carbon into a material from a carbon-rich environment with the application of heat.

Cementite   A compound (Fe_3C) that is formed when the solubility limit of carbon into Fe is exceeded. It is very hard and brittle and the strength of steel is enhanced by its presence.

Ceramic   A solid compound that is formed by the application of heat, and sometimes heat and pressure, comprising at least one metal and one nonmetallic elemental solid.

Cermet   A composite material composed of ceramic and metallic materials. A metal is used as a binder for an oxide, boride or carbide (for example, tungsten carbide). The metallic elements normally used are nickel, molybdenum and cobalt.

Charge   Enclosed quantity of high explosive or propellant with its own integral means of ignition.

CJ point   With reference to a detonating high explosive material, this is the pressure of the detonation products at the cusp of the detonation wave. Named in honour of David Chapman (1869–1958) and Jacques Charles Émile Jouguet (1871–1943).

Combat body armour   A UK body armour that consists of an aramid and nylon construction to which ceramic-faced armour can be applied as an insert to protect the major organs.

Comminution   A collection of small fragments or rubble. A comminuted zone of material is formed when a projectile penetrates a ceramic.

Complete penetration   See *perforation*.

Composite   A structure comprising two or more materials often engineered so that the properties of the materials are complementary, and therefore, the structure is more than the sum of its parts.

Critical thickness   With reference to semi-infinite depth-of-penetration (DoP) experiments with a ceramic-faced witness material: the thickness of ceramic required so that there is no penetration in the witness material.

Crystalline   A material that possesses a structure that consists of an ordered array of atoms.

Delamination   With reference to a composite armour system, it is the process by which the individual layers (or laminae) become separated from one another – usually due to the penetration or perforation of a projectile.

Detonation wave   A chemically-supported shock wave that propagates in an explosive during detonation.

Differential tile efficiency   With reference to semi-infinite DoP experiments with a ceramic-faced witness material: the factor by which the areal density of the witness material penetrated is reduced by the addition of a target tile normalized by the areal density of the applied target material. It has the symbol Δe_c.

Disruptor   The part of the armour system that causes the projectile to fracture and fragment. Usually, these are made from materials of high hardness and/or impedance.

Drawing   Where a metal is pulled through a die that has a tapered bore. Rod and wire are commonly fabricated in this way.

Driving band   A malleable or pre-engraved band that is pressed around the rim of the projectile, which, when engaged with the rifling of the barrel, imparts spin to the projectile.

Ductile fracture   The growth and coalescence of voids within a ductile medium under stress such that separation of the material is inevitable.

Ductile hole growth   With reference to a projectile penetrating a ductile target: this occurs when the material plastically deforms such that the material is pushed out of the way of the penetrator. It is important to realize that no localized increase in density occurs around the hole formed from the penetrator; rather, the whole plate deforms to take into account the hole that is formed – that is, the volume remains constant.

Dwell   Lateral flow of a penetrator's tip across the surface of a hard target due to the apparent strength of that target overmatching the strength of the penetrator.

Elastic   A material is said to be elastic if it returns back to its original shape after being stretched or squeezed.

Elastic impedance   An elastic property of a material calculated by $\sqrt{(E \cdot \rho)}$. It can also be calculated by multiplying the bulk density of the material by its elastic wave speed.

Engineer   a person of a noble profession that gets excited about things that nobody else really cares about.

Enhanced body armour   A UK body armour that is designed to protect the wearer from 12.7-mm calibre bullets. It incorporates a boron-carbide insert as the disruptor.

Equation of state   A fundamental constitutive equation that relates a material's response to pressure in terms of density and internal energy.

Explosively formed projectile   A projectile that is formed from a thin geometric shape (usually a 'dish') by the action of a detonating high explosive. Also sometimes referred to as a 'self-forging fragment'.

Explosive-reactive armour   An armour system that works by intercepting a penetrator or shaped charge jet with explosively driven plates in order to cause disruption.

Extrusion   Where a metal piece is forced through a die to produce the desired shape.

Face hardening   The process of hardening the surface of a material – usually by work hardening, flame hardening or carburizing.

Flame hardening   A process of heating the surface of steel (by using a gas flame) up to very high temperatures and then rapidly cooling (quenching) to form a very hard but brittle layer with decreasing hardness through the thickness of the steel plate.

Flexural rigidity   The multiplication of the Young's modulus and second moment of area.

Forging   Where a metal is subjected to successive blows or by continuous squeezing.

Fracture The separation of material.

Fracture toughness   A term that defines a material's ability to resist the extension of a crack when the material is placed under load.

Glacis plate   The sloping plate of armour located at the front and top of an armoured fighting vehicle (AFV).

Grain   A single crystal of material. Polycrystalline materials exhibit multiple grains.

Gross cracking   A process that results in large crack formation.

Hardness   A measure of resistance to indentation, abrasion and wear.

HAZ   Heat affected zone (formed around the weld during welding).

High-carbon steel   A steel that has a high carbon content, usually in the range of between 0.6 and 1.4 wt%.

Hot isostatic press   A system for simultaneously applying heat and uniform (gas) pressure to a sample.

Hot pressing   A process used to densify ceramic by simultaneously applying heat and (usually) uniaxial pressure.

Hugoniot The Hugoniot is a material property that describes the locus of states that are achievable due to the passage of a shock wave and is commonly used to derive an equation of state. A Hugoniot curve can be plotted, for example, as a relationship between pressure and density or as a relationship between shock and particle velocity.

Hugoniot elastic limit Under uniaxial strain loading conditions, the point at which the material ceases to behave elastically and starts to behave inelastically.

Hydrocode An explicit transient dynamic computational code where the conservation and the constitutive equations for the materials are solved simultaneously and iteratively using either finite difference or finite element techniques.

Hydrodynamic limit The maximum penetration achievable according to hydrodynamic theory.

Hydrodynamic penetration Penetration of a projectile or shaped charge jet into a target material where the penetrator and target behave as if they possess no strength. This tends to occur at elevated velocities of impact where the shock pressures generated are orders of magnitude higher than the strengths of materials.

Incipient spall The beginnings of spall.

Inelastic Not elastic – that is, plastic.

Interface defeat Resistance to penetration of a hard target due to the penetrator being completely eroded at the target's surface via dwell.

Internal energy Energy that a material possesses because of the motion of its atoms and molecules.

Isentrope A curve, usually plotted in terms of pressure and volume, along which there is a release of pressure (or stress) after the passage of a shock wave. It is similar to a Hugoniot curve, and for small compressions can be assumed identical to it.

Isotropic Possessing identical material properties in all directions in three-dimensional space.

Kinetic energy Energy due to mass and velocity. It can be calculated by taking half the mass and multiplying it by the velocity squared ($1/2\ mv^2$).

Knoop indenter An elongated pyramidal indenter that is used to measure the hardness of a material.

Kolsky bar See *Split-Hopkinson Pressure Bar.*

Liquid-phase sintering Used in the manufacture of ceramics, this process makes use of low-melting-point sintering aids that form a viscous liquid at the firing temperature. The liquid thoroughly wets the solid particles and, when cooled, forms a glassy phase in-between grain boundaries. Typical sintering-aid materials are compounds of silicon dioxide (SiO_2), magnesium oxide (MgO) and calcium oxide (CaO). Because the glassy phase will melt again at a relatively low temperature compared to the crystalline lattice, liquid phase–sintered materials have a compromised high-temperature strength.

Long-rod penetrator A solid rod-like shot, usually sub-calibre and drag stabilized, which is used in attacking armour (see *armour-piercing fin-stabilized discarding sabot*).

Low-carbon steel   A steel that has a low carbon content (<0.25 wt%).

Martensite   A fine needle-like structure that is the hardest constituent obtained in steel. It is an iron phase that has been supersaturated with carbon and formed during the rapid quenching of steel at the austenitic temperature.

Mass effectiveness   The factor by which the areal density of armour will be multiplied if a specific armour system is replaced with a single witness material – usually RHA. It has the symbol E_m.

Mass efficiency factor   See *mass effectiveness*.

MBT   Main battle tank

Medium-carbon steel   A steel that has a carbon content of between 0.25 and 0.6 wt%.

Metal matrix composite   Similar to a cermet. A metal matrix composite is a composite of two or more materials with one material forming the matrix and another forming the reinforcement that is embedded within the matrix. At least one of the materials must be a metal (hence metal matrix composite); the other material(s) can be metallic, ceramic or organic.

Meyer hardness   The hardness measured by dividing the applied load on the indenter by its projected area instead of the surface area of the indentation. Commonly calculated for the Brinell indenter but can be used with other indenters too.

Microcrack   A very small crack.

Mine   An explosive munition that is primarily designed to remain passive until initiated by contact with the target or after a specified amount of lapsed time.

Neutral axis   The longitudinal axis that suffers zero direct stress when a beam is subjected to bending. For a symmetrical section of a uniform beam that is being subjected to pure bending, the neutral axis will be the same as the central axis.

Normalizing   The process of heating a ferrous alloy above the austenitizing temperature and allowing the metal to cool by exposing it to room temperature air.

Passive armour   Armour that works to defeat an incoming projectile or shaped charge jet by mechanical properties.

Partial penetration   Not *perforation*.

Penetration   The process of a projectile moving through a material.

Penetrator   A projectile that penetrates.

Penetrator dwell   The process of a projectile being unable to penetrate a ceramic until its strength has been diminished. The penetrator therefore appears to dwell on the surface of the target. If the strength of the ceramic does not diminish in the timescale of penetrator erosion, then interface defeat occurs.

Perforation   The process of the projectile moving through the material and exiting from the rear surface. Perforation is synonymous with complete penetration.

Phase   A distinct state of matter in a system.

Plane strain   A state of strain where an element or material is being subjected to a two-dimensional in-plane strain such that the strain normal to the two-dimensional plane is zero.

Plane stress   Similar to plane strain. A state of stress where an element or material is being subjected to a two-dimensional in-plane stress such that the stress normal to the two-dimensional plane is zero.

Plate-impact experiment   An experimental method used to create shock waves of a controlled magnitude and duration in solids. The experimental set-up consists of a flyer plate that is accelerated toward the target and impacts it at a predetermined velocity. The geometry of the plates is such that a one-dimensional state of strain exists within the flyer plate and target.

Plugging   With reference to a projectile impacting and penetrating a target: if the material is susceptible to shear failure, a plug can be detached from the armour. This forms a secondary projectile that can result in catastrophic behind-armour effects. If plugging failure does occur, the total energy that the armour absorbs will be less. This is because the failure is localized and does not allow for gross plate plastic deformation. In armour materials, plugging is usually a result of adiabatic shear.

Polycrystalline   With reference to a material: a structure that consists of multiple crystals (or 'grains') that are joined together.

Polymorphism   A condition whereby two or more crystal states can exist for the same material.

Primary explosive   A sensitive explosive that is generally used in initiating devices.

Proof stress   An arbitrary yield stress calculated for materials that do not have an obvious yield point – such as aluminium. A line is drawn parallel to the linear elastic part of the stress–strain curve but is offset by some standard amount of strain (for example, 0.1%). The intersection of the offset line and the stress–strain curve is the proof stress. Sometimes referred to as the *offset yield stress.*

Propellant   An explosive that burns to propel a projectile or missile through the expansion of high-pressure gases.

Quenching   The process of hardening steel by rapidly cooling it from some elevated temperature. Water is the most commonly used medium for quenching, although oils are sometimes used.

Radial fracture   Cracking that resembles the pattern of spokes in a bicycle wheel.

Rayleigh line   The path by which a shock jumps from one state on a Hugoniot to another.

Reaction bonding   An exothermic chemical reaction that produces a ceramic as the end product.

Reactive armour   Armour that works to defeat an incoming projectile or jet by detecting the presence of the threat during penetration and responding kinetically.

RHA   See *Rolled homogeneous armour.*

Roll bonding   A process of rolling two metal plates (of differing mechanical properties) together at elevated temperature to form a strong metallurgical bond between the two plates.

Rolled homogeneous armour (RHA)   Rolled steel plate for armour applications that possesses relatively high hardness and good through-thickness properties. It usually contains carbon, manganese, nickel and molybdenum.

Rolling   Where a plate is squeezed in between two rollers. This is by far the most common method of processing wrought armour plate mainly because the desirable thicknesses and properties can be achieved through this process.

RHA equivalences   The thickness of RHA required to defeat a given projectile when compared to a specific armour system that is able to defeat the same projectile. Therefore, if a ceramic-faced armour system has an RHA-e of 100 mm, then the protection offered by this armour is equivalent to 100 mm of RHA.

Sabot   A lightweight full-calibre casing designed to carry a sub-calibre projectile along the gun tube. It is usually discarded after the projectile leaves the muzzle.

Secondary penetration   Penetration that occurs in a target after a long-rod penetrator has been completely eroded by it.

Self-forging fragment   See *explosively formed projectile*.

Self-propagating high-temperature synthesis   A process whereby raw powdered starting materials are heated to a specific temperature that enables a highly exothermic chemical reaction to propagate and produce a final product.

Shatter gap   Occasionally, it is possible to measure two distinct v_{50} velocities when increasing the velocity over a wide range. That is, it is possible to perforate the target at relatively low velocities followed by partial penetrations at higher velocities. Perforation of the target again occurs when the velocity of the projectile is increased further. This occurs because the penetration mechanism of the projectile changes as the velocity is increased.

Shock wave   A propagating discontinuity of pressure, temperature (or internal energy) and density that is spread over a very thin front.

Sintering   Densification by the welding together of ceramic powders by the application of heat; sometimes, pressure is also used.

Sintering aid   A chemical used to reduce the temperature required for sintering.

Slip casting   A process for shaping ceramic powders into complex geometries before densification. Typically, ceramic particles are suspended in water and cast into porous plaster moulds. The water is sucked out through the pores in the porous mould over time leaving a close-packed deposition of particles that are ready for densification.

Slipping driving band   A malleable band that is able to spin around the rim of a projectile or sabot to minimize the spin imparted by the rifling of a gun barrel. It is used for launching drag-stabilized projectiles in rifled gun barrels.

Solvus temperature   In metal processing, this is the temperature (read from a phase diagram) that indicates a limit of solid solubility. The material on either side of the solvus line on the phase diagram will still be solid but have a different microstructure.

Spall   Dynamic tensile failure caused by stress wave interactions.

Spall liner   A sheet of material that is applied on the inside of a vehicle hull to minimize the lethal effects of a perforating projectile or jet.

Split-Hopkinson Pressure Bar (SHPB)   A device for measuring the dynamic response of materials in terms of stress, strain and strain-rate. Named after Bertram Hopkinson (1874–1918) and sometimes called a *Kolsky bar*.

Strain   The deformation of a material measured, in uniaxial tests, by the extension or contraction of a material divided by its original length.

Strain hardening   See *work hardening*.

Strain rate   The rate at which deformation occurs.

Stress   Force divided by the cross-sectional area over which the force is applied.

Stress corrosion cracking   This occurs when a metal is attacked by a corrodant whilst being subjected to tensile stress. It is a particularly insidious failure because the magnitudes of stresses that are required to encourage failure are frequently lower than the yield strengths of the metal. In fact, residual stresses induced during machining, assembling or welding can exacerbate this type of failure. Aluminium alloys used in some AFVs were susceptible to this type of failure.

Sub calibre   Where the diameter of the projectile that strikes the target is smaller than the calibre of the gun that fired it. The projectile would have to be carried by some form of sabot.

Tempering   A process of heating a metal to relieve internal stresses and to produce the desired quantities of hardness and toughness.

Ultimate tensile strength   The maximum stress as measured from an engineering stress–strain curve.

Uniaxial strain   A state of strain that is acting in a material in one direction only.

Uniaxial stress   A state of stress that is acting in a material in one direction only.

Vickers indenter   A pyramidal indenter with an apex angle of 68° that is used to measure the hardness of a material.

Wave shaper   A material whose geometry and impedance are designed to redirect the detonation wave in a high explosive. These are usually used in shaped charge–type warheads to maximize the collapse of the liner into a slug or jet. It is sometimes referred to as an explosive lens.

Work hardening   Hardening of a material due to the application of work. This process is due to the presence of lattice dislocation pile-up and is sometimes referred to as *strain hardening*.

Yield strength   See *yield stress*.

Yield stress   The stress at which the material ceases to behave elastically. Also referred to as the *yield strength*.

Index

Note: **Bold** page numbers refer to tables and *italic* page numbers refer to figures.